THE UNIVERSITY of ADELAIDE

Advanced Engineering of Nanoporous Anodic Alumina Photonic Crystals for Optical Sensing Applications

Cheryl Suwen Law

A thesis submitted for the degree of Doctor of Philosophy

The University of Adelaide

School of Chemical Engineering

March 2019

Table of Contents

Abstract

Conventional analytical systems have intrinsic limitations that restrict their applicability, including high costs, bulkiness, time-consuming processing, and require highly trained personnel. This triggers an increasing demand of optical sensing technologies that can address these limitations, while offering enhanced sensing capabilities over benchmark analytical techniques. Current progress in nanotechnology is enabling development of rapid, sensitive, user-friendly, and cost-competitive optical sensors integrated into lab-on-a-chip platforms with broad applicability across different disciplines, including medicinal, industrial and environmental applications.

This thesis presents the development of cutting-edge optical sensing systems based on the combination of nanoporous anodic alumina photonic crystals (NAA-PCs) and reflectometric interference spectroscopy (RIfS). Fundamental and applied advances of the proposed sensing systems towards ultrasensitive and selective detection of target analytes are achieved through rational structural engineering of NAA-PCs and surface chemistry architectures. A collection of NAA-PCs was generated by innovative pulse-like anodisation methods aimed at engineering the optical properties of these photonic crystals to harness light–matter interactions at the nanoscale. The sensing characteristics of these optical sensing systems in terms of selectivity and sensitivity were further optimised by engineering the surface chemistry architecture of NAA-PC platforms with multiple functional molecules. The sensitivity and reliability of the proposed sensing systems were demonstrated through real-time detection of heavy metal ions (i.e. gold (III) and mercury (II) ions) and other analytes. The work completed in this thesis advances both fundamental understanding and applied knowledge on the sensing performance of NAA-PCs with optimised geometrical, chemical and optical properties integrated with RIfS, pushing the boundaries of science a step closer to fully functional and marketable analytical tools for real-life medical, environmental, industrial and defence applications.

Preface

This thesis is submitted as a “thesis by publications” in accordance with “Specifications for Thesis 2019” of The University of Adelaide. The journal articles and conference proceedings generated are listed as follow.

List of Publications

1. **Law, C.S.**, S.Y. Lim, A.D. Abell, N.H. Voelcker, and A. Santos, *Nanoporous anodic alumina photonic crystals for optical chemo- and biosensing: fundamentals, advances, and perspectives*. Nanomaterials, 2018. **8**(10): p. 788. **(IF 3.504)**
2. **Law, C.S.**, S.Y. Lim, R.M. Macalincag, A.D. Abell, and A. Santos, *Light-confining nanoporous anodic alumina microcavities by apodized stepwise pulse anodization*. ACS Applied Nano Materials, 2018. **1**(9): p. 4418-4434. **(IF NA) New Journal**
3. **Law, C.S.**, S.Y. Lim, A.D. Abell, and A. Santos, *Real-time binding monitoring between human blood proteins and heavy metal ions in nanoporous anodic alumina photonic crystals*. Analytical Chemistry, 2018. **90**(16): p. 10039-10048. **(IF 6.042)**
4. **Law, C.S.**, S.Y. Lim, A.D. Abell, L.F. Marsal, and A. Santos, *Structural tailoring of nanoporous anodic alumina optical microcavities for enhanced resonant recirculation of light*. Nanoscale, 2018. **10**(29): p. 14139-14152. **(IF 7.233)**
5. **Law, C.S.**, S.Y. Lim, and A. Santos, *On the precise tuning of optical filtering features in nanoporous anodic alumina distributed Bragg reflectors*. Scientific Reports, 2018. **8**(1): p. 4642. **(IF 4.122)**
6. **Law, C.S.**, G.M. Sylvia, M. Nemati, J. Yu, D. Losic, A.D. Abell, and A. Santos, *Engineering of surface chemistry for enhanced sensitivity in nanoporous interferometric sensing platforms*. ACS Applied Materials & Interfaces, 2017. **9**(10): p. 8929-8940. **(IF 8.097)**
7. **Law, C.S.**, A. Santos, M. Nemati, and D. Losic, *Structural engineering of nanoporous anodic alumina photonic crystals by sawtooth-like pulse*

anodization. ACS Applied Materials & Interfaces, 2016. **8**(21): p. 13542-13554. **(IF 8.097)**

8. Lim, S.Y., **C.S. Law**, M. Markoviç, J.K. Kirby, A.D. Abell, and A. Santos, *Engineering the slow photon effect in photoactive nanoporous anodic alumina gradient-index filters for photocatalysis*. ACS Applied Materials & Interfaces, 2018. **10**(28): p. 24124-24136. **(IF 8.097)**
9. Lim, S.Y., **C.S. Law**, L.F. Marsal, and A. Santos, *Engineering of hybrid nanoporous anodic alumina photonic crystals by heterogenous pulse anodization*. Scientific Reports, 2018. **8**(1): p. 9455. **(IF 4.122)**
10. Sukarno, **C.S. Law**, and A. Santos, *Realisation and optical engineering of linear variable bandpass filters in nanoporous anodic alumina photonic crystals*. Nanoscale, 2017. **9**(22): p. 7541-7550. **(IF 7.233)**
11. Nemati, M., A. Santos, **C.S. Law**, and D. Losic, *Assessment of binding affinity between drugs and human serum albumin using nanoporous anodic alumina photonic crystals.* Analytical Chemistry, 2016. **88**(11): p. 5971-5980. (**IF 6.042**)
12. Santos, A., **C.S. Law**, D.W.C. Lei, T. Pereira, and D. Losic, *Fine tuning of optical signals in nanoporous anodic alumina photonic crystals by apodized sinusoidal pulse anodisation*. Nanoscale, 2016. **8**(43): p. 18360-18375. **(IF 7.233)**
13. Santos, A., T. Pereira, **C.S. Law**, and D. Losic, *Rational engineering of nanoporous anodic alumina optical bandpass filters*. Nanoscale, 2016. **8**(31): p. 14846-14857. **(IF 7.233)**
14. Santos, A., **C.S. Law**, T. Pereira, and D. Losic, *Nanoporous hard data: optical encoding of information within nanoporous anodic alumina photonic crystals*. Nanoscale, 2016. **8**(15): p. 8091-8100. **(IF 7.233)**
15. Lim, S.Y., **C.S. Law**, M. Markoviç, L.F. Marsal, N. Voelcker, A.D. Abell, and A. Santos, *Rational management of photons for enhanced photocatalysis in structurally-colored nanoporous anodic alumina photonic crystals*. ACS Applied Energy Materials, 2019. 2(2): p. 1169-1184. **(IF NA) New Journal**
16. Kaur, S., **C.S. Law**, N.H. Williamson, I. Kempson, A. Popat, T. Kumeria, and A. Santos, *Environmental copper sensor based on polyethyleneimine-functionalized nanoporous anodic alumina interferometers*. Analytical Chemistry, 2019. **(IF 6.042)**

Book Chapters

1. **Law, C.S.**, S.Y. Lim, L.F. Marsal, and A. Santos, *Electrochemically engineered nanoporous photonic crystal structures for optical sensing and biosensing*, in *Handbook of Nanomaterials for Analytical Chemistry*. 2019, Elsevier. (Accepted)

Conference Proceedings

1. **Law, C. S.**, Lim, S.Y., and Santos, A. *Fine tuning of transmission features in nanoporous anodic alumina distributed Bragg reflectors*. in *Nanophotonics Australasia 2017*. 2018. International Society for Optics and Photonics.
2. Lim, S.Y., **Law, C.S.**, and Santos, A. *Surface modification of nanoporous anodic alumina photonic crystals for photocatalytic applications*. in *Nanophotonics Australasia 2017*. 2018. International Society for Optics and Photonics.

Conference Presentations

1. **C.S. Law**, S.Y. Lim, A.D. Abell, A. Santos, Real-time binding monitoring between human blood proteins and heavy metal ions in nanoporous anodic alumina photonic crystals, CNBP 2018 Conference, Lorne, December 2018 (Poster and Oral Presentation).
2. **C.S. Law**, S.Y. Lim, A.D. Abell, A. Santos, Real-time binding monitoring between human blood proteins and heavy metal ions in nanoporous anodic alumina photonic crystals, South Australia Physical Chemistry Symposium, Adelaide, November 2018 (Poster Presentation).
3. **C.S. Law**, S.Y. Lim, A. Santos, Fine tuning of transmission features in nanoporous anodic alumina distributed Bragg reflectors, SPIE Nanophotonics Australasia 2017, Melbourne, December 2017 (Poster Presentation).
4. **C.S. Law**, A. Santos, M. Nemati, D. Losic, Photonic coatings based on nanoporous anodic alumina photonic crystals produced by sawtooth-like pulse anodisation, 8th International Conference on Technological Advances of Thin Films and Surface Coatings, Singapore, July 2016 (Poster Presentation).

Invited Seminar Presentations

1. **C.S. Law**, Advanced Engineering of nanoporous anodic alumina photonic crystals: towards precise control of light, IPAS Seminar, University of Adelaide, Adelaide, August 2017 (Oral Presentation).

HDR Thesis Declaration

I certify that this work contains no material which has been accepted for the award of any other degree or diploma in my name, in any university or other tertiary institution and, to the best of my knowledge and belief, contains no material previously published or written by another person, except where due reference has been made in the text. In addition, I certify that no part of this work will, in the future, be used in a submission in my name, for any other degree or diploma in any university or other tertiary institution without the prior approval of the University of Adelaide and where applicable, any partner institution responsible for the joint-award of this degree.

I acknowledge that copyright of published works contained within this thesis resides with the copyright holder(s) of those works.

I also give permission for the digital version of my thesis to be made available on the web, via the University's digital research repository, the Library Search and also through web search engines, unless permission has been granted by the University to restrict access for a period of time.

I acknowledge the support I have received for my research through the provision of an Australian Government Research Training Program Scholarship.

Signature : _____ Date: 3rd March 2019

Name : Cheryl Law Suwen

Acknowledgements

I would like to express my gratitude to my supervisors, Dr. Abel Santos and Prof. Andrew D. Abell for overseeing my PhD study from start to finish and ensuring a smooth-sailing journey of PhD. To Abel, for all the support and guidance in my professional development and personal growth. No words can express how grateful I am to him, it is his tremendous support, contributions and sacrifices that drive and push my PhD study to the finish line. He is not only a supervisor and mentor, but also a friend and someone I will always look up to. To Andrew, for his valuable advice, insight and feedback on the manuscripts. I am appreciative of having both accomplishing researchers like Abel and Andrew as my supervisors for their invaluable supervision, guidance and knowledge.

I would like to acknowledge the University of Adelaide for providing me an opportunity and scholarship to pursue PhD, as well as School of Chemical Engineering for the facilities.

Lastly, I would like to thank my parents for their love and support. It is always encouraging knowing they are always there for me. I also thank my friends for their company and help.

Chapter 1

Introduction

1. Introduction

1.1 Introductory Background

Conventional systems such as gas chromatography, mass spectrometry and atomic absorption play critical roles across different disciplines, including environmental, industrial, and clinical applications (e.g. water quality monitoring, disease diagnosis and prognostics) [1,2]. Though these analytical systems provide reliable results, they are time- and power-consuming, expensive, and bulky. Further to that, traditional analytical methods require considerable instrumentation and highly trained personnel for operation and maintenance. These factors constrain the use of conventional systems in resource-limited and remote areas. Thus, there is a growing demand for affordable, sensitive, rapid, and user-friendly sensing technologies that can overcome logistical, social and technical barriers associated with benchmark analytical techniques.

Amongst the available sensing technologies, optical sensors have attracted significant interest for integrated diagnostic devices due to their relative ease of use, high sensitivity, highly informative content (spectroscopic signatures), and operational flexibility. As a result, optical sensors have found widespread application in healthcare, environmental monitoring, chemo- and bio-sensing, and defence and homeland security [3]. Optical sensors rely on light-matter interactions, which are translated into quantifiable optical signal shifts when analyte molecules immobilised onto a sensing platform alter electromagnetic waves. Advances in nanotechnology have created new opportunities to engineer optical sensing systems by integrating nanomaterials, prepared by self-ordering synthesis, as optical transducers. In particular, nanoporous anodic alumina (NAA) has a unique set of chemical and physical properties, including chemical resistance, thermal stability, biocompatibility, and large surface area [4]. The versatile fabrication process of NAA allows the production of a variety of photonic crystal (PC) structures such as Fabry-Pérot interferometers, gradient index filters, distributed Bragg reflectors, and microcavities. The nanoporous matrix of NAA is an effective medium platform that can be engineered in a multidimensional fashion and with precision by means of different anodisation parameters and approaches.

The major factor that governs light-matter interactions in NAA-based photonic crystals (NAA-PCs) is their nanoporous structure and optical activity, where its photoluminescence, transmittance, reflectivity and absorbance. The structure and composition of NAA-PCs can be tailored to modulate, guide, emit, reflect, transmit, and enhance incident electromagnetic waves across the broad spectral regions, from UV to IR [5]. NAA-PCs feature well-resolved and narrow photonic stop bands (PSBs), the spectral shifts of which upon selective immobilisation of target analytes can be readily used as sensing principle [6,7]. The large surface-to-volume-ratio of NAA-PCs amplifies optical signals to further enhance sensitivity [4]. The surface chemistry of NAA-PCs can be tailored to attain chemical selectivity and specificity toward target analytes. Surface functionalisation of NAA-PCs can be performed by multiple methods, the objective of which is to immobilise functional molecules to tune the chemical properties of NAA-PCs for specific sensing applications in environmental and clinical analysis, industrial and food quality control [4]. This versatility makes NAA-PCs unique platform materials to engineer optical sensing systems that provide enhanced sensitivities by optimisation of nanoporous structure and surface chemistry.

NAA-PCs can be combined with optical techniques such as surface plasmon resonance (SPR), photoluminescence (PL) spectroscopy, surface-enhanced Raman scattering spectroscopy (SERS), and reflectometric interference spectroscopy (RIfS) [4]. Among these, RIfS offers a relatively straightforward and direct approach based on the interference of white light at the interface of NAA-PCs (sensing platforms) [4]. Compared to other methods, RIfS provides real-time, in-situ, and precise acquisition of optical signals (i.e. change in optical thickness) [8]. The set-up of RIfS is cost-effective, robust, and miniaturised [9]. Thus, RIfS has been widely used as detection technique for NAA-based optical sensors, as demonstrated by various sensing applications such as label-free detection of DNA molecules [10], antigens and antibodies [11], small molecules and ions [12], and gas sensing [13]. These properties make RIfS-NAA-based sensors a promising alternative to conventional analytical tools.

The main motivation of this PhD thesis lies on the urgent demand of optical sensing systems that provide prompt response, simplicity, reliability, and automatisation capabilities for field applications. Despite significant advances in this field, more extensive fundamental research must be carried out to optimise individual

components for a feasible optical sensor combining NAA-PCs and RIfS. This thesis will focus on the structural optimisation of NAA-PCs and their integration with RIfS to develop ultrasensitive optical sensing systems that can detect trace levels of analytes. These sensors will establish the basis for a new generation of analytical tools with broad applicability in medical and environmental fields.

1.2 Objectives of thesis

The aim of this thesis is to develop optical sensing platforms based on nanoporous anodic alumina (NAA) with optimised structural and sensing properties to be combined with reflectometric interference spectroscopy (RIfS).

The detailed objectives of the thesis are:

1. To design and engineer nanoporous anodic alumina photonic crystals (NAA-PCs) with different nanoarchitectures (e.g. distributed Bragg reflectors – DBRs, gradient index filters – GIFs, optical microcavities – μCVs).
2. To optimise the optical properties of NAA-PCs (position, width, and quality of photonic stop bands) by means of effective medium engineering approaches.
3. To endow NAA-PCs with chemical selectivity toward heavy metal ions through surface chemistry modifications using different functionalisation strategies.
4. To assess detection performance, reliability and sensitivity of chemically modified NAA-PCs as sensing platforms toward heavy metal ions by RIfS.

1.3 Scope and structure of thesis

Chapter 2 provides a critical review on the use of NAA-PCs in optical sensing and biosensing applications. This chapter encompasses the fabrication and properties of NAA as well as surface chemistry modifications to create chemically selective platforms. This chapter also reviews relevant literature about the application of NAA-PCs as optical sensing platforms, where the performances of NAA-PCs with various nanostructures combined with different sensing techniques are compared and evaluated.

Chapter 3 reports the fabrication of a new type of NAA-PC produced by sawtooth-like pulse anodisation, demonstrating the tunablility of the optical properties of these PCs

by means of several anodisation parameters. The applicability of these NAA-PCs as optical sensing platforms in combination with RIfS is also assessed.

Chapter 4 presents an apodisation strategy to fabricate NAA distributed Bragg reflectors (NAA-DBRs) with finely engineered light-filtering features across the spectral regions. The sensitivity of these PCs as sensing platforms is evaluated as a function of refractive index changes using RIfS.

Chapter 5 is a comprehensive study on the development and comparison of two types of NAA optical microcavities (NAA-μCVs). Optical properties such as quality factor, position and width of resonance bands are demonstrated to be tuneable and optimisable by manipulation of several anodisation parameters.

Chapter 6 further explores the structural optimisation of NAA-μCVs using an anodisation strategy combining apodisation and stepwise pulse anodisation. Through a systemic modification of anodisation parameters, their resulting optical properties in terms of quality factor and position of resonance band are examined.

Chapter 7 investigates different surface engineering strategies to enhance the sensitivity of NAA-PCs as sensing platforms. A range of thiol molecules with different functional groups and length are used to selectively functionalise the surface of NAA-PCs. The sensitivity of these chemically modified NAA-PCs to gold ions is monitored in real-time by RIfS.

Chapter 8 reports the binding assessment between heavy metal ions and human blood proteins immobilised onto NAA-PCs by RIfS, where the binding kinetics, affinity and mechanisms are evaluated.

Chapter 9 summarises the recent advances in structural engineering of NAA-PCs and their application as optical sensing platforms in combination with RIfS, providing an outlook about future work in this research area.

Appendix is a peer-reviewed conference proceeding relevant to this study, in which modulation of the effective medium of NAA-DBRs by stepwise pulse-like anodisation is accomplished for the first time by an apodisation strategy.

1.4 References

1. Yetisen, A.K., et al., *Photonic nanosensor for colorimetric detection of metal ions.* Analytical chemistry, 2015. **87**(10): p. 5101-5108.
2. Potyrailo, R.A., et al., *Towards outperforming conventional sensor arrays with fabricated individual photonic vapour sensors inspired by Morpho butterflies.* Nature communications, 2015. **6**: p. 7959.
3. Chamberlain, J.W. and D.M. Ratner, *Label-free biosensors for biomedical applications: The potential of integrated optical biosensors and silicon photonics*, in *Biological and Medical Sensor Technologies*. 2012, CRC Press. p. 71-104.
4. Santos, A., T. Kumeria, and D. Losic, *Nanoporous anodic aluminum oxide for chemical sensing and biosensors.* TrAC Trends in Analytical Chemistry, 2013. **44**: p. 25-38.
5. Santos, A., *Nanoporous anodic alumina photonic crystals: fundamentals, developments and perspectives.* Journal of Materials Chemistry C, 2017. **5**(23): p. 5581-5599.
6. Ilyas, S., et al., *Porous silicon based narrow line-width rugate filters.* Optical Materials, 2007. **29**(6): p. 619-622.
7. Lorenzo, E., et al., *Porous silicon-based rugate filters.* Applied optics, 2005. **44**(26): p. 5415-5421.
8. Huang, Y., et al., *Competitive protein adsorption on biomaterial surface studied with reflectometric interference spectroscopy.* Acta Biomaterialia, 2010. **6**(6): p. 2083-2090.
9. Hänel, C. and G. Gauglitz, *Comparison of reflectometric interference spectroscopy with other instruments for label-free optical detection.* Analytical and bioanalytical chemistry, 2002. **372**(1): p. 91-100.
10. Pan, S. and L.J. Rothberg, *Interferometric sensing of biomolecular binding using nanoporous aluminum oxide templates.* Nano Letters, 2003. **3**(6): p. 811-814.
11. Alvarez, S.D., et al., *A label-free porous alumina interferometric immunosensor.* Acs Nano, 2009. **3**(10): p. 3301-3307.

12. Kumeria, T., A. Santos, and D. Losic, *Ultrasensitive nanoporous interferometric sensor for label-free detection of gold (III) ions.* ACS applied materials & interfaces, 2013. **5**(22): p. 11783-11790.
13. Kumeria, T. and D. Losic, *Reflective interferometric gas sensing using nanoporous anodic aluminium oxide (AAO).* physica status solidi (RRL)–Rapid Research Letters, 2011. **5**(10-11): p. 406-408.

Chapter 2

Literature Review

2. Literature Review

This section is presented as published review article by **Law, C.S.**, S.Y. Lim, A.D. Abell, N.H. Voelcker, and A. Santos, *Nanoporous anodic alumina photonic crystals for optical chemo- and biosensing: fundamentals, advances, and perspectives*. Nanomaterials, 2018. **8**(10): p. 788.

Statement of Authorship

Title of Paper	Nanoporous Anodic Alumina Photonic Crystals for Optical Chemo- and Biosensing: Fundamentals, Advances, and Perspectives
Publication Status	☑ Published ☐ Accepted for Publication ☐ Submitted for Publication ☐ Unpublished and Unsubmitted w ork w ritten in manuscript style
Publication Details	Law, C.S., S.Y. Lim, A.D. Abell, N.H. Voelcker, and A. Santos, *Nanoporous anodic alumina photonic crystals for optical chemo- and biosensing: fundamentals, advances, and perspectives*. Nanomaterials, 2018. **8**(10): p. 788.

Principal Author

Name of Principal Author (Candidate)	Cheryl Suwen Law		
Contribution to the Paper	Under the supervision of A. Santos and A. D. Abell, I wrote the manuscript for submission.		
Overall percentage (%)	50		
Certification:	This paper reports on original research I conducted during the period of my Higher Degree by Research candidature and is not subject to any obligations or contractual agreements with a third party that would constrain its inclusion in this thesis. I am the primary author of this paper.		
Signature		Date	23/11/2018

Co-Author Contributions

By signing the Statement of Authorship, each author certifies that:

i. the candidate's stated contribution to the publication is accurate (as detailed above);
ii. permission is granted for the candidate in include the publication in the thesis; and
iii. the sum of all co-author contributions is equal to 100% less the candidate's stated contribution.

Name of Co-Author	Siew Yee Lim		
Contribution to the Paper	I aided in the constructing the manuscript. I give consent for Cheryl Suwen Law to present this paper for examination towards the Doctorate of Philosophy.		
Signature		Date	14/11/2018

Name of Co-Author	Andrew D. Abell		
Contribution to the Paper	I aided in the evaluation of final version of manuscript. I give consent for Cheryl Suwen Law to present this paper for examination towards the Doctorate of Philosophy.		
Signature		Date	23/11/2018

Name of Co-Author	Nicolas Voelcker		
Contribution to the Paper	I aided in the evaluation of final version of manuscript. I give consent for Cheryl Suwen Law to present this paper for examination towards the Doctorate of Philosophy.		
Signature		Date	17/11/2018

Name of Co-Author	Abel Santos		
Contribution to the Paper	I acted as primary supervisor for the candidate, aided in developing and revising the manuscript and evaluating the final version of the manuscript. I give consent for Cheryl Suwen Law to present this paper for examination towards the Doctorate of Philosophy.		
Signature		Date	23/11/2018

nanomaterials

MDPI

Review

Nanoporous Anodic Alumina Photonic Crystals for Optical Chemo- and Biosensing: Fundamentals, Advances, and Perspectives

Cheryl Suwen Law [1,2,3], Siew Yee Lim [1,2,3], Andrew D. Abell [2,3,4,*], Nicolas H. Voelcker [5,6,7,8,*] and Abel Santos [1,2,3,*]

1 School of Chemical Engineering, The University of Adelaide, Adelaide SA 5005, Australia; suwen.law@adelaide.edu.au (C.S.L.); siew.lim@adelaide.edu.au (S.Y.L.)
2 Institute for Photonics and Advanced Sensing (IPAS), The University of Adelaide, Adelaide SA 5005, Australia
3 ARC Centre of Excellence for Nanoscale BioPhotonics (CNBP), The University of Adelaide, Adelaide SA 5005, Australia
4 Department of Chemistry, The University of Adelaide, Adelaide SA 5005, Australia
5 Melbourne Centre for Nanofabrication, Victorian Node of the Australian National Fabrication Facility, Melbourne 3168, Australia
6 Drug Delivery, Disposition and Dynamics, Monash Institute of Pharmaceutical Sciences, Monash University, Melbourne 3052, Australia
7 Commonwealth Scientific and Industrial Research Organisation (CSIRO), Melbourne 3168, Australia
8 INM-Leibniz Institute for New Materials, Campus D2 2, 66123 Saarbrücken, Germany
* Correspondence: andrew.abell@adelaide.edu.au (A.D.A.); nicolas.voelcker@monash.edu (N.H.V.); abel.santos@adelaide.edu.au (A.S.); Tel.: +61-8-8313-5652 (A.D.A.); +61-03-9902-9097 (N.H.V.); +61-8-8313-1535 (N.H.V.)

Received: 15 September 2018; Accepted: 1 October 2018; Published: 4 October 2018

Abstract: Optical sensors are a class of devices that enable the identification and/or quantification of analyte molecules across multiple fields and disciplines such as environmental protection, medical diagnosis, security, food technology, biotechnology, and animal welfare. Nanoporous photonic crystal (PC) structures provide excellent platforms to develop such systems for a plethora of applications since these engineered materials enable precise and versatile control of light–matter interactions at the nanoscale. Nanoporous PCs provide both high sensitivity to monitor in real-time molecular binding events and a nanoporous matrix for selective immobilization of molecules of interest over increased surface areas. Nanoporous anodic alumina (NAA), a nanomaterial long envisaged as a PC, is an outstanding platform material to develop optical sensing systems in combination with multiple photonic technologies. Nanoporous anodic alumina photonic crystals (NAA-PCs) provide a versatile nanoporous structure that can be engineered in a multidimensional fashion to create unique PC sensing platforms such as Fabry–Pérot interferometers, distributed Bragg reflectors, gradient-index filters, optical microcavities, and others. The effective medium of NAA-PCs undergoes changes upon interactions with analyte molecules. These changes modify the NAA-PCs' spectral fingerprints, which can be readily quantified to develop different sensing systems. This review introduces the fundamental development of NAA-PCs, compiling the most significant advances in the use of these optical materials for chemo- and biosensing applications, with a final prospective outlook about this exciting and dynamic field.

Keywords: optical sensing; photonic crystals; anodization; nanoporous anodic alumina; surface chemistry

1. Introduction

Optical sensors are a class of devices that utilize different forms of light–matter (i.e., photon–atom) interactions to detect, interrogate, and quantify molecules for multiple applications. They contain a light source to generate electromagnetic waves, a sensing platform in which light–matter interactions occur, and a detector to identify and quantify spectral shifts in electromagnetic waves upon interaction and exposure to analytes [1–3]. Typically, the sensing principle in optical sensors relies on shifts in the characteristic spectral fingerprint of the optical platform upon interaction with analyte molecules. These spectral changes are subsequently translated into quantitative and/or qualitative measurements of molecules of interest. The design and engineering of the sensing platform is of paramount importance since this is where interactions between electromagnetic waves and analyte molecules occur [4,5]. Solid state optical sensing platforms can be produced in the form of thin films, fibers, and nanoparticles, which can guide, enhance, reflect, transmit, modulate, or absorb electromagnetic waves in different ways. The rapid development of nanotechnology has opened new opportunities and paths to develop optical sensing platforms with finely tuned optical properties. These platforms can be combined with spectroscopic techniques to produce outstanding sensing systems such as surface plasmon resonance spectroscopy (SPR) [4,5], localized surface plasmon resonance spectroscopy (LSPR) [6–9], surface enhanced Raman spectroscopy (SERS) [10,11], photoluminescence spectroscopy (PL) [12,13], and reflectometric interference spectroscopy (RIfS) [14,15].

Photonic crystals (PCs) are a type of optical materials that mold the flow of electromagnetic waves by multiple Bragg scattered interferences defined by Bloch modes [16–18]. Light propagation in PCs can be controlled with precision by engineering the structural features of the PCs in a multidimensional fashion (i.e., 1D, 2D, or 3D). Nanoporous PCs are particularly good candidates to develop ultra-sensitive optical sensing platforms since they provide (i) light-modifying capabilities to alter and engineer the flow of photons at specific broadband spectral regions (i.e., from UV to IR), (ii) a nanoporous structure that facilitates mass transport of molecular species involved in binding events, and (iii) high specific surface area that increases the number of functional binding sites within the optical platform [19]. Furthermore, nanoporous PCs can be produced by a range of cost-competitive, fully scalable self-organization approaches that provide excellent control over the PC's features at the nanoscale. For example, inverted opal structures produced by a combination of self-organization of silica nanospheres and deposition of oxides or metals are one of the most representative types of nanoporous PCs [20,21]. However, these nanostructures have limited versatility to tune the photonic stopband (PSB) of PCs, are restricted to 3D nanostructures, feature defects that act as light scattering centers, require long synthesis processes (>24 h), and are constrained to small areas (mm^2–cm^2) [22]. Another prime example of nanoporous PC platform material is porous silicon (pSi), which is typically produced by electrochemical etching of silicon in hydrofluoric acid (HF)-based electrolytes [23–25]. Although, pSi presents excellent optoelectronic properties to develop optical sensing systems, its practical application is limited by its poor chemical stability without additional passivation steps, its fragile mechanical strength, and its fabrication process, which requires the use of extremely hazardous HF-based electrolytes [26,27]. Among other alternatives, nanoporous anodic alumina photonic crystals (NAA-PCs) produced by electrochemical oxidation (i.e., anodization) of aluminum—an industrially scalable and low-cost nanofabrication approach used in industry for decades—has been devised as an excellent alternative/complementary platform material to develop optical sensing systems in combination with a broad range of photonic technologies [28]. The nanoporous structure of NAA can be engineered by means of different anodization approaches to produce PC structures with finely tuned optical properties across the spectral regions. NAA provides controllable and versatile nanopore geometry, chemical and physical stability, stable and tunable optical signals, and mechanical strength. Furthermore, NAA's surface chemistry can be modified with a broad range of functional molecules to achieve chemical selectivity toward analytes of interest [29].

Recent advances in anodization technology have focused on engineering the nanoporous structure of NAA to control optical properties and have paved the way for advanced NAA-PC-based sensing

systems with promising performances and broad applicability (Figure 1). This review provides a comprehensive perspective about the fundamentals of NAA-PC technology, introducing the different fabrication processes and aspects of this singular PC platform material (i.e., chemical and physical properties, nanoporous structure and optical features, surface chemistry modification protocols, etc.) that make it an excellent candidate for optical chemo- and biosensing systems. The most significant advances in the development of NAA-PC-based optical sensing systems are commented upon in detail, with outstanding representative examples of applicability. Finally, this review concludes with a general overview and a prospective outlook on the future trends in this exciting and dynamic field.

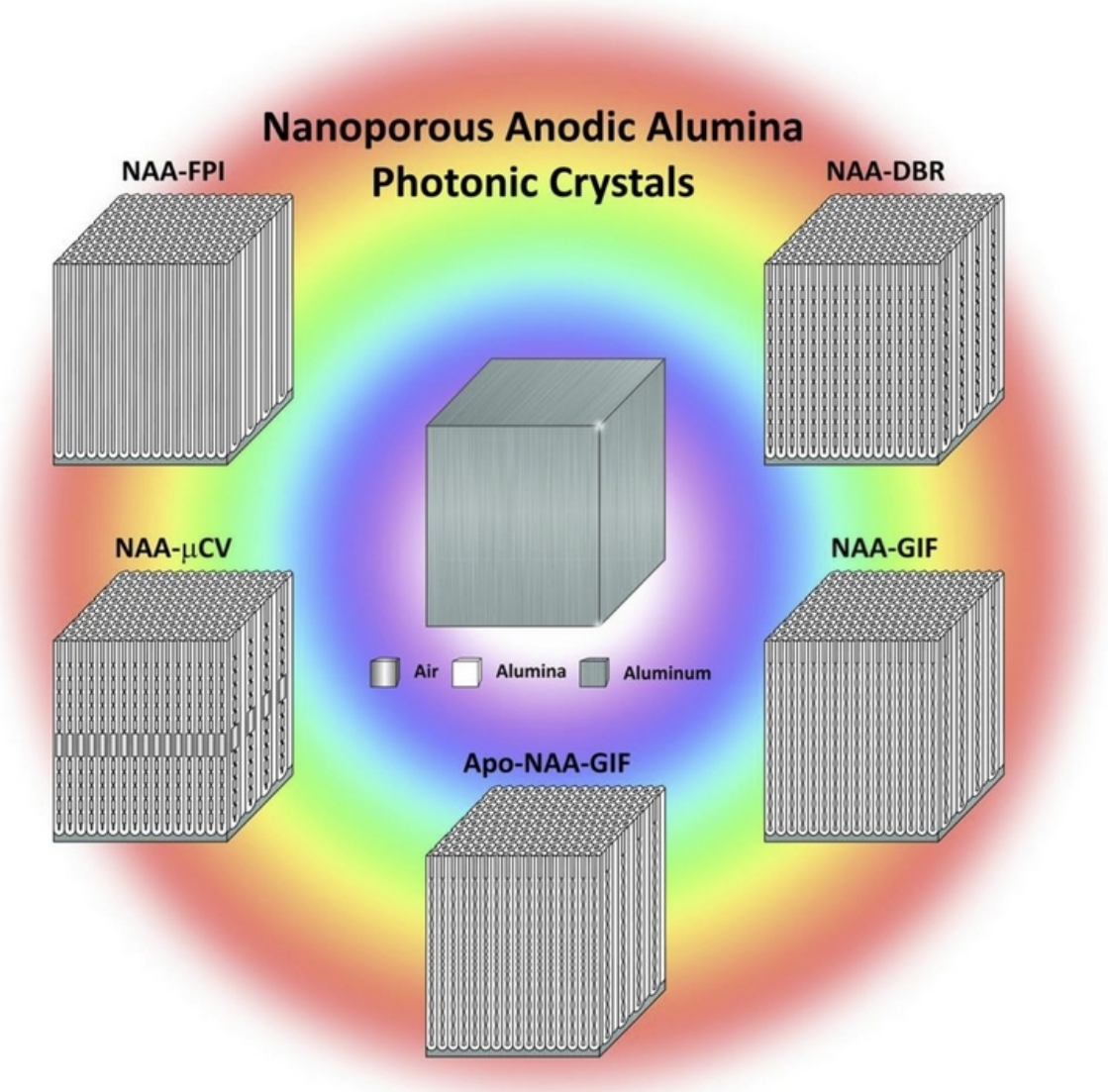

Figure 1. Nanoporous anodic alumina photonic crystals as effective medium platforms to control light–matter interactions for chemo- and biosensing applications. Schemes of representative NAA-PC structures: NAA-FPI—Fabry–Pérot interferometer; NAA-μCV—optical microcavity; NAA-APO-GIF—apodized gradient index filter; NAA-GIF—gradient index filter; NAA-DBR—distributed Bragg reflector.

2. Fabrication and Properties: Nanoporous Anodic Alumina as Effective Medium

2.1. Fabrication of Self-Organized Nanoporous Anodic Alumina

Nanoporous anodic alumina (NAA) is a thin film composed of a matrix of alumina (aluminum oxide—Al_2O_3) featuring arrays of straight cylindrical nanopores with closed hemispherical bottom tips that grow at the center of hexagonal cells normally aligned to the underlying aluminum substrate (Figure 2a) [28]. Under specific fabrication conditions, the nanopores of NAA self-organize in a hexagonal fashion, leading to a characteristic honeycomb-like nanoporous structure with tuneable geometric features. NAA is produced by electrochemical oxidation of aluminum substrates in different mild acid electrolytes, the most representative of which are oxalic, sulfuric, and phosphoric acids [30–32]. This electrochemical process, so-called 'anodization', has been extensively and intensively used in metal finishing industry for more than a century. For example, anodization is used to modify the properties of valve metal parts and structures such as corrosion protection, adhesion, color and appearance, hardness, and impact and erosion resistance. However, despite its intensive use in industry, anodization of aluminum only gained significant attention in nanotechnology after the milestone works of Masuda and coworkers in the mid-1990s, with the introduction of the self-ordered NAA and the two-step anodization process [30–32]. These seminal works boosted an increasing and dynamic research activity in this field, spreading the applicability of these nanomaterials across disciplines and fields.

The two-step anodization process is a top-down nanofabrication approach that consists of three stages: (i) formation of a sacrificial layer of NAA with randomly distributed nanopores at its top (i.e., first step); (ii) selective removal of the resulting NAA film by wet chemical etching; and (iii) re-anodization of the aluminum substrate (i.e., second step) (Figure 2b). During the first anodization step, nanopores grow randomly across the surface of the NAA film and self-organize as they grow due to a combination of mechanical stress between adjacent nanopores and electric field-assisted dissolution and growth of the oxide barrier layer at the electrolyte-oxide and oxide-metal interfaces, respectively (Figure 2c). This mechano-electrochemical self-ordering process patterns the surface of the underlying aluminum substrate, which is a negative replica of the bottom part of the sacrificial NAA layer featuring self-organized hemispherical caps (Figure 3a). During the second anodization step, nanopores grow at the center of each hemispherical void patterned on the aluminum substrate surface and propagate from top to bottom maintaining the self-ordered distribution. This simple approach enables the generation of highly ordered nanoporous structures (Figure 3b) without the need of sophisticated lithographic methods, opening new opportunities to generate a broad range of nanostructures in a fast, simple, and cost-competitive manner.

Anodization of aluminum is an electrochemical process in which two electrodes (i.e., anode = aluminum and cathode = platinum) are partially immersed in a mild acid electrolyte (Figure 2c). The growth of NAA is driven by the application of a voltage or current density between the two electrodes that leads to competing oxidation (i.e., formation of oxide at the metal–oxide interface) and dissolution (i.e., dissolution of oxide at the oxide–electrolyte interface) processes occurring simultaneously at the interfaces of the oxide barrier layer located at the nanopore bottom tips (Figure 2c). Anodization is an electric field-assisted electrochemical process in which the application of an external electric field drives the flow of ionic species (i.e., Al^{3+}, O^{2-}, OH^-, and H^+) involved in the formation and dissolution of oxide at the interfaces of the oxide barrier layer (i.e., metal/oxide and oxide/electrolyte interfaces) [28]. NAA structures can be produced by two anodization regimes: (i) mild anodization (MA), which is performed at low anodization voltage/current density and moderate acid electrolyte temperatures, and (ii) hard anodization (HA), which is characteristically carried out at high anodization voltage/current density and low acid electrolyte temperatures [33]. Whereas the characteristic growth rate of NAA under MA conditions is slow (i.e., 3–8 μm h^{-1}), the growth of NAA films produced under HA regime is fast (i.e., 50–70 μm h^{-1}) (Figure 3c). Furthermore, NAA produced under MA and HA conditions also differ in their geometric features

and chemical composition (i.e., level of impurities). For example, whereas NAA-MA films produced in oxalic acid have a characteristic porosity of ~10%, the porosity of NAA-HA films is typically ~3%. Some excellent review articles covering different fabrication methods and characteristics of NAA are given in the literature [28,34,35].

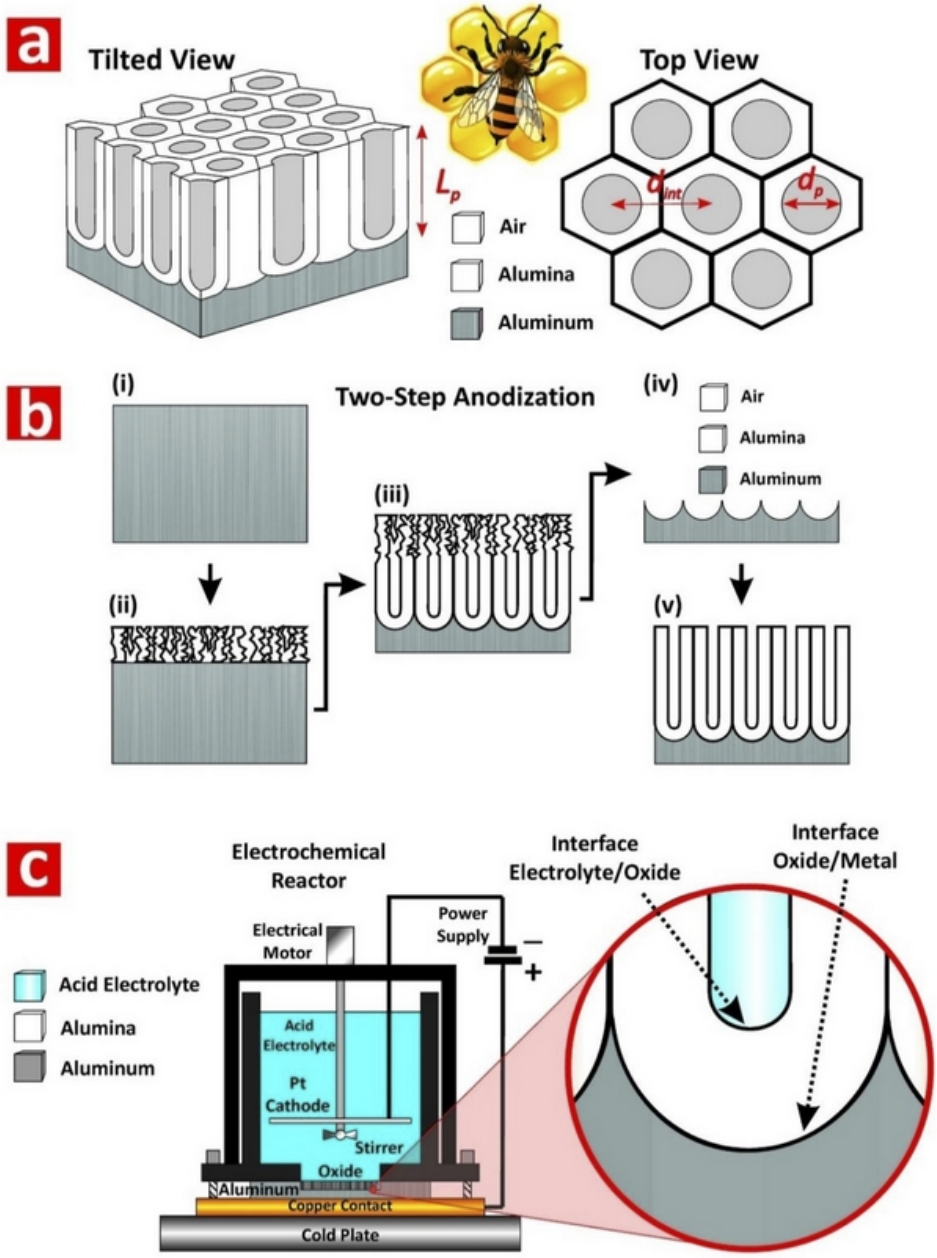

Figure 2. Self-organized nanoporous anodic alumina (NAA). (**a**) Structure and geometric features of NAA produced by two-step anodization with tilted 3D view of NAA structure (**left**) (L_p—nanopores length) and top view of NAA structure (**right**) (d_{int}—interpore distance and d_p—nanopores diameter). (**b**) Schematic diagram illustrating the two-step anodization process: (**i**) aluminum substrate, (**ii**) nanopores nucleation—first step, (**iii**) nanopores development—first step, (**iv**) sacrificial oxide layer removal, and (**v**) cross-sectional view of self-organized NAA structure—second step. (**c**) Schematic illustration of an electrochemical reactor used to NAA by anodization (**left**) and details of the oxide barrier layer located at the bottom tip of the nanopores where the electrochemical reactions (i.e., oxidation and dissolution) occur at the interfaces metal/oxide and oxide/electrolyte.

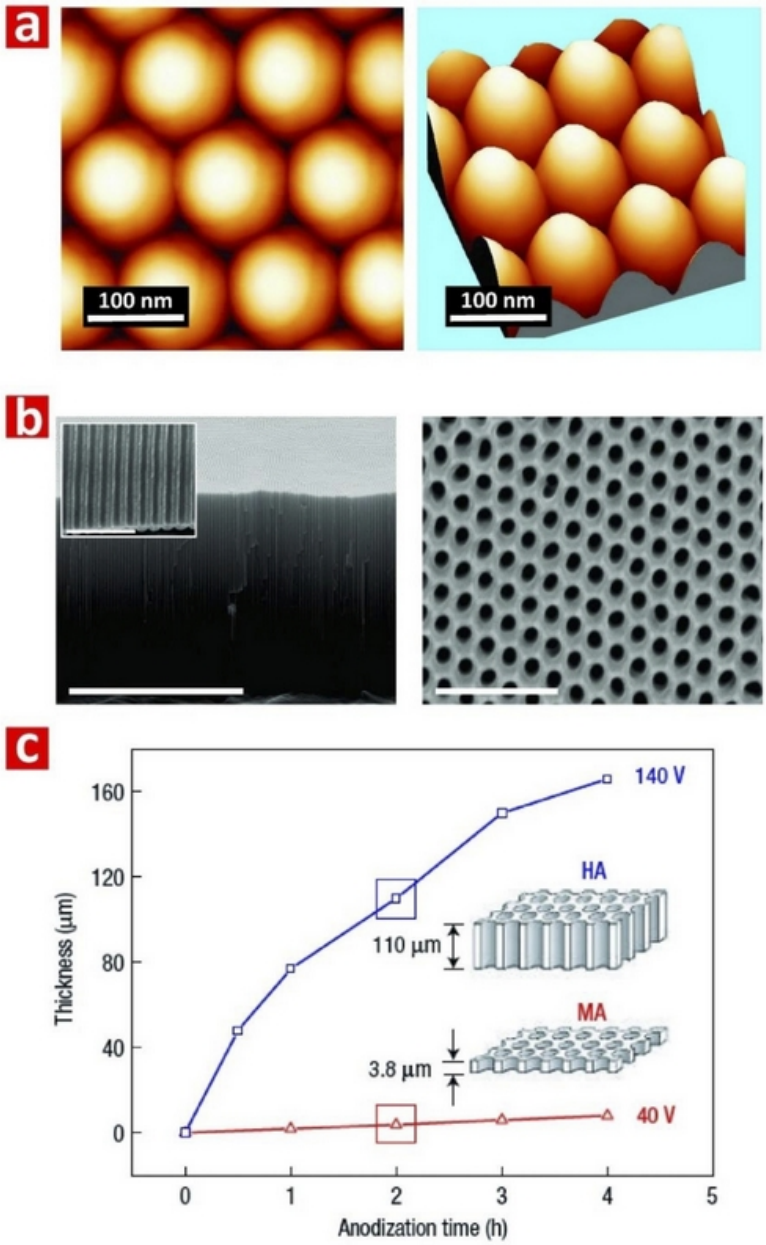

Figure 3. Self-organized nanoporous anodic alumina (NAA). (**a**) Atomic force microscopy images showing details of the hemispherical caps located at the bottom side of NAA produced by two-step anodization. (**b**) General cross-sectional FEG-SEM view of NAA featuring straight cylindrical nanopores from top to bottom (scale bar = 5 μm) with inset showing a magnified view of the oxide barrier layer (scale bar = 500 nm) and top FEG-SEM view of hexagonally arranged cylindrical nanopores in NAA (scale bar = 500 nm). (**c**) Film thickness as a function of anodization time at mild (MA at 40 V—red line) and hard anodization (HA at 140 V—blue line) with schematics showing the different thicknesses of anodic oxides after 2 h of anodization. Reproduced from [33], with copyright permission from Springer Nature, 2006.

2.2. *Physical Properties of Nanoporous Anodic Alumina*

NAA is a mechanically hard and brittle oxide that can withstand high pressures and temperatures. As-produced NAA has an onion-like chemical structure basically composed of Al_2O_3 with some water and impurities incorporated from the acid electrolyte during anodization (Figure 4a). NAA undergoes changes in its crystallographic phase when its structure is annealed (i.e., amorphous Al_2O_3

~T_{room}–1000 °C; gamma Al_2O_3 ~700–1200 °C; alpha Al_2O_3 ~1100–1500 °C), making it extremely resistant to acid or basic chemical etching (Figure 4b) [36]. With a refractive index of ~1.70 RIU, NAA has good transmittance (i.e., ~80–90%) in the UV-visible-NIR spectral region, although it significantly absorbs light in the UVC region (i.e., <280 nm) due to its intrinsic photoluminescence (PL) properties (Figure 4c). The origin of NAA's PL relies on two types of PL centers: (i) F^+ centers associated with ionized oxygen vacancies present in the structure of alumina and (ii) F centers attributable to impurities incorporated into the alumina structure from the acid electrolyte during anodization [37,38]. The PL of NAA is intrinsically dependent upon different fabrication parameters such as anodizing current density/voltage, type and concentration of acid electrolyte, crystallographic phase, and pore-widening treatment [39]. Typically, NAA features PL when it is excited at wavelengths <350 nm and its characteristic PL spectrum can be approximated to a Gaussian bell, the central wavelength and intensity of which can be tuned by the fabrication conditions (Figure 4d). Several studies have demonstrated that the characteristic PL spectrum of NAA films fabricated with certain geometric features (i.e., porosity and thickness) shows optical interference fringes generated by constructive reflection of internal light emission by Fabry–Pérot effect (Figure 4d) [39–43]. This intrinsic property of NAA can be readily used to develop optical sensing systems.

From an optical standpoint, the most attractive property of NAA is its versatile and highly controllable nanoporous structure, which can be readily utilized as an effective medium platform to develop unique PC structures to modulate and control the flow of electromagnetic waves with precision [29]. NAA is a binary composite matrix formed by air (i.e., 1 RIU) and alumina (i.e., ~1.70 RIU), in which the spatial distribution of these two components at the micro/nanoscale establishes the macroscopic optical properties of this nanomaterial (Figure 5a). The optical properties of NAA-PCs (i.e., effective refractive index and effective dielectric constant) can be estimated by averaging the properties of the individual constituents (i.e., air and alumina) as described by different effective medium approximation models, including Maxwell–Garnett, Bruggeman, Lorentz–Lorenz, Monecke, Drude, and Looyenga–Landau–Lifshitz. Selection of the most optimal effective medium model to correlate and describe the optical properties of the composite PC material is strongly dependent on the spatial distribution (i.e., PC structure—e.g., distributed Bragg reflector, gradient-index filter, etc.) and the intrinsic properties of the different components (i.e., refractive indices/dielectric constants) [44]. It is worth noting that the nanoporous structure of NAA also enables the generation of composite PCs by filling or coating its nanopores with other materials by means of different deposition techniques (e.g., electrodeposition, atomic layer deposition, infiltration, etc.). This approach provides multiple opportunities to create PC structures with extraordinary optical properties to attain a versatile control of light across the spectral regions (Figure 5b) [45].

Pioneering studies on NAA-PCs focused on analysis of light–matter interactions in NAA-PC platforms featuring hexagonally arranged straight cylindrical nanopores from top to bottom produced by a combination of nanoimprint lithography and one-step anodization or self-organized NAA-PCs produced by two-step anodization [46–49]. Light in these NAA-PCs is modulated when photons flow transversally across the composite matrix of alumina featuring cylindrical nanopores filled with air (Figure 5c). The seminal studies by Masuda and coworkers and Gösele and coworkers revealed that organized NAA-PCs feature a characteristic photonic stopband (PSB) in their optical spectrum, the position of which can be finely tuned by the interpore distance (i.e., lattice constant—distance between the center of adjacent nanopores) and porosity (i.e., pore diameter) of the NAA-PC platform. During the last decade, intensive research activity has aimed at extending the self-organization regime of NAA toward longer interpore distances (i.e., from 60 to 700 nm) by using different acid electrolytes (e.g., sulfuric, oxalic, selenic, malonic, phosphoric, phosphonic, tartaric, citric, phosphonoacetic, etidronic, etc.) [50–64] (Figure 5d). However, the versatility of these PCs to control light across the spectral regions is constrained by the range of available interpore distances. It is worth noting that the photonic band structure of NAA raising from its nanopore periodicity has yet to be utilized in optical sensing applications. Pulse-like anodization approaches have overcome this limitation by enabling

the in-depth and multidimensional engineering of the NAA's effective medium through structural engineering, paving the way for NAA-PC structures with controllable photonic features across the spectral regions.

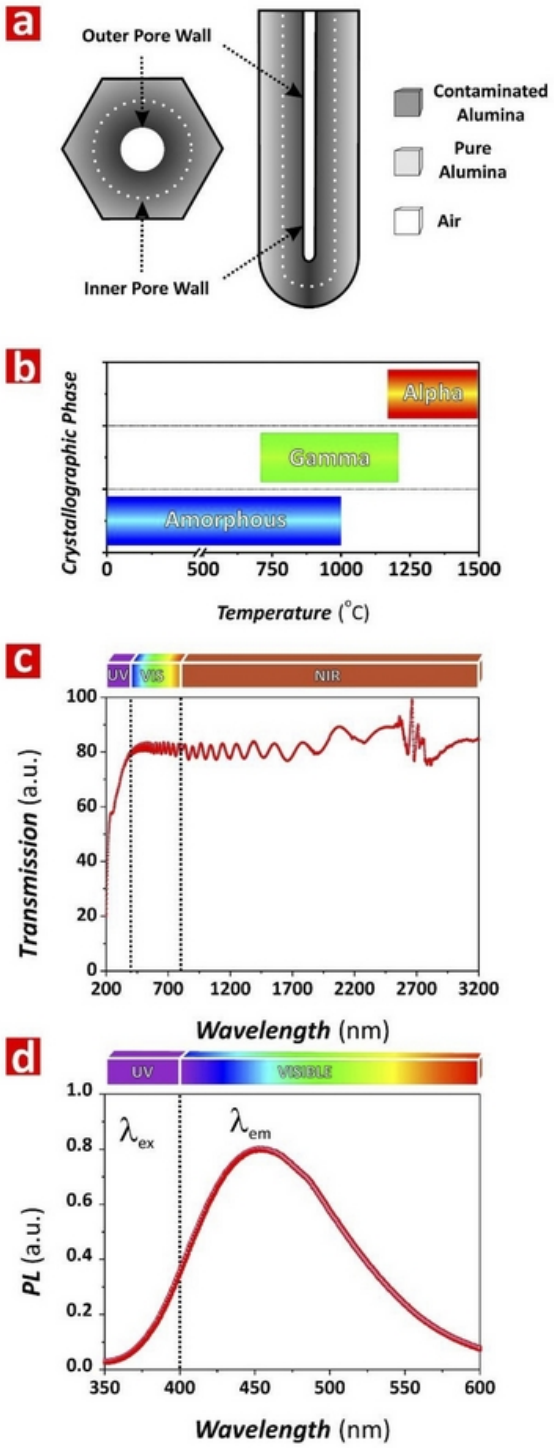

Figure 4. Physical properties of nanoporous anodic alumina (NAA). (**a**) Onion-like chemical structure of NAA with impurities distribution around the central nanopore. (**b**) Crystallographic phases of NAA as a function of temperature. (**c**) Representative UV-visible-near-infrared (NIR) transmission spectrum of NAA (note: NAA produced by two-step anodization under MA regime in oxalic acid electrolyte). (**d**) Representative photoluminescence spectrum of NAA (note: NAA produced by two-step anodization under MA regime in oxalic acid electrolyte).

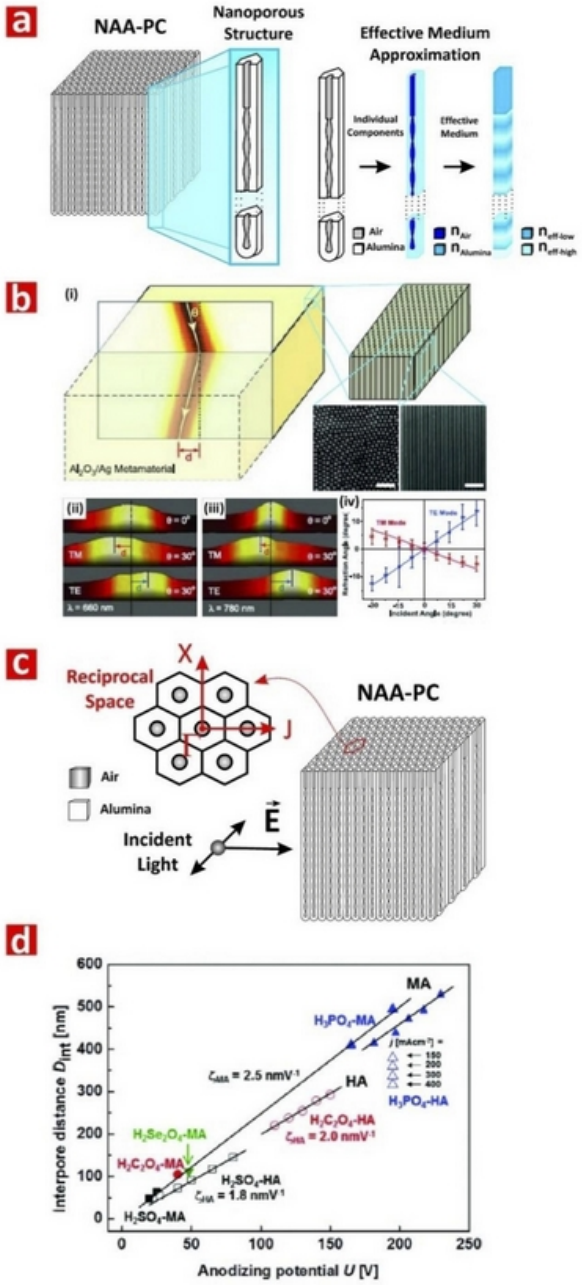

Figure 5. Intrinsic relationship between nanoporous geometry and optical properties in nanoporous anodic alumina photonic crystals (NAA-PCs). (**a**) Structural engineering of effective medium of NAA-PCs with details of the intrinsic relationship between nanoporous geometry and effective medium approximation. (**b**) NAA-PC as a metamaterial platform with negative refraction of light (reproduced from [45], with copyright permission from The American Association for the Advancement of Science, 2008). (**i**) Illustration showing negative refraction from air into composite NAA-PC filled with silver nanowires (**left**) and schemed showing the structure of the composite NAA-PC-Ag nanowires and SEM images of these photonic structures (scale bars = 500 nm); (**ii**) and (**iii**) beam intensities at the surface of the composite NAA-PC-Ag nanowires at 660 and 780 nm, respectively; (**iv**) dependence of refraction angles on incident angles and polarizations at 780 nm wavelength. (**c**) Schematic showing the structure of a 2D NAA-PC with incident light flowing perpendicularly to its nanopores. (**d**) Self-ordering regimes in MA (filled symbols) and HA (open symbols) in the most representative acid electrolytes used to produce NAA. Reproduced from [28], with copyright permission from American Chemical Society, 2014.

2.3. Structural Engineering of Nanoporous Anodic Alumina

Pioneering studies by O'Sullivan and Wood established a direct relationship between the anodization voltage and the nanopore diameter in NAA, where the latter varies at a rate of ~1.29 nm V^{-1} with the former [65,66]. Therefore, pulse-like dynamic modifications of the anodization voltage during the growth of NAA could be used to induce nanopore modulations and engineer the structure of NAA. However, the oxide barrier layer located at the nanopore bottom tips of NAA is an electrical and ionic insulator that limits the direct translation of anodization voltage/current density modifications into nanopore diameter modulations. The thickness of the oxide barrier layer is directly proportional to the applied anodization voltage at an average rate of ~1 nm V^{-1} [67]. When the external electric field is suddenly modified during anodization, the flow of ionic species across the oxide barrier layer is altered, undergoing a recovery process that is strongly dependent upon the electric field change and the thickness of the oxide barrier layer [68–70].

In a series of pioneering works, Lee and coworkers developed pulse-like anodization approaches to engineer and modulate the porosity of NAA in a multidimensional fashion. The combination of anodizing voltage or current density pulses switched between MA and HA regimes was demonstrated as an effective approach to engineer the inner porosity of NAA with precision [71–74]. These strategies, based on the finding of different porosity levels between HA and MA (e.g., ~3 and ~10% in oxalic acid for HA and MA regimes, respectively), were devised by Lee and coworkers to controllably engineer the inner nanoporous structure of NAA with precision and versatility [33]. An optimal design of the anodization conditions such as the pulse anodization profile, acid electrolyte, and temperature enable the effective translation of electric field variations into nanopore diameter modulations, overcoming the limitations imposed by the oxide barrier layer while preventing nanopore branching [68–70]. These approaches inspired and boosted further fundamental and applied research to develop new anodization methods to engineering the nanoporous structure of NAA to generate PC structures.

While MA-HA pulse-like anodization approaches enable the precise modulation of the nanopore geometry in NAA, they do face some challenges due to the limited controllability of anodization under HA conditions. For instance, the growth rate of NAA under HA is extremely fast (i.e., 50–70 μm h^{-1}) and it relies upon the nanopore length. Furthermore, the generation of Joule's heat during HA requires the process to be performed at low acid electrolyte temperatures (i.e., ~0 °C). Alternative pulse-like anodization strategies performed under MA conditions provide a controllable means of tuning the optical properties of NAA-PCs. Although the slow oxide growth rate under MA conditions (i.e., 3–8 μm h^{-1}) is a limiting factor, it enables the precise engineering of the NAA's effective medium to attain a better control over the features of the photonic stopband (PSB) of NAA-PCs across the spectral regions.

In recent years, numerous studies have realized and developed different NAA-PC architectures, the most representative examples of which are Fabry–Perót interferometers (NAA-FPIs), optical microcavities (NAA-μCVs), and 3D NAA-PCs. In addition to these, different architectures of NAA-based distributed Bragg reflectors (DBRs) have been realized, including NAA-DBRs—this term will henceforth refer to NAA-DBRs produced by stepwise pulse anodization, gradient-index filters (NAA-GIFs), apodized DBRs and GIFs (Apo-NAA-DBRs and Apo-NAA-GIFs), bandpass filters (NAA-BPFs), and linear variable bandpass filters (NAA-LVBPFs). Figure 6 shows schematic illustrations of the structure of these NAA-based PC structures along with examples of anodization profiles used to produce these NAA-PCs and their representative optical spectra depicting the characteristic features of the PSB as a function of the NAA-PC architecture. Some excellent review articles have recently described the fundamental concepts and realization of NAA-PCs [29,34]. This review article provides a fresh and comprehensive collation of the most recent developments and applications of NAA-PCs in chemo- and biosensing applications, including surface chemistry modifications.

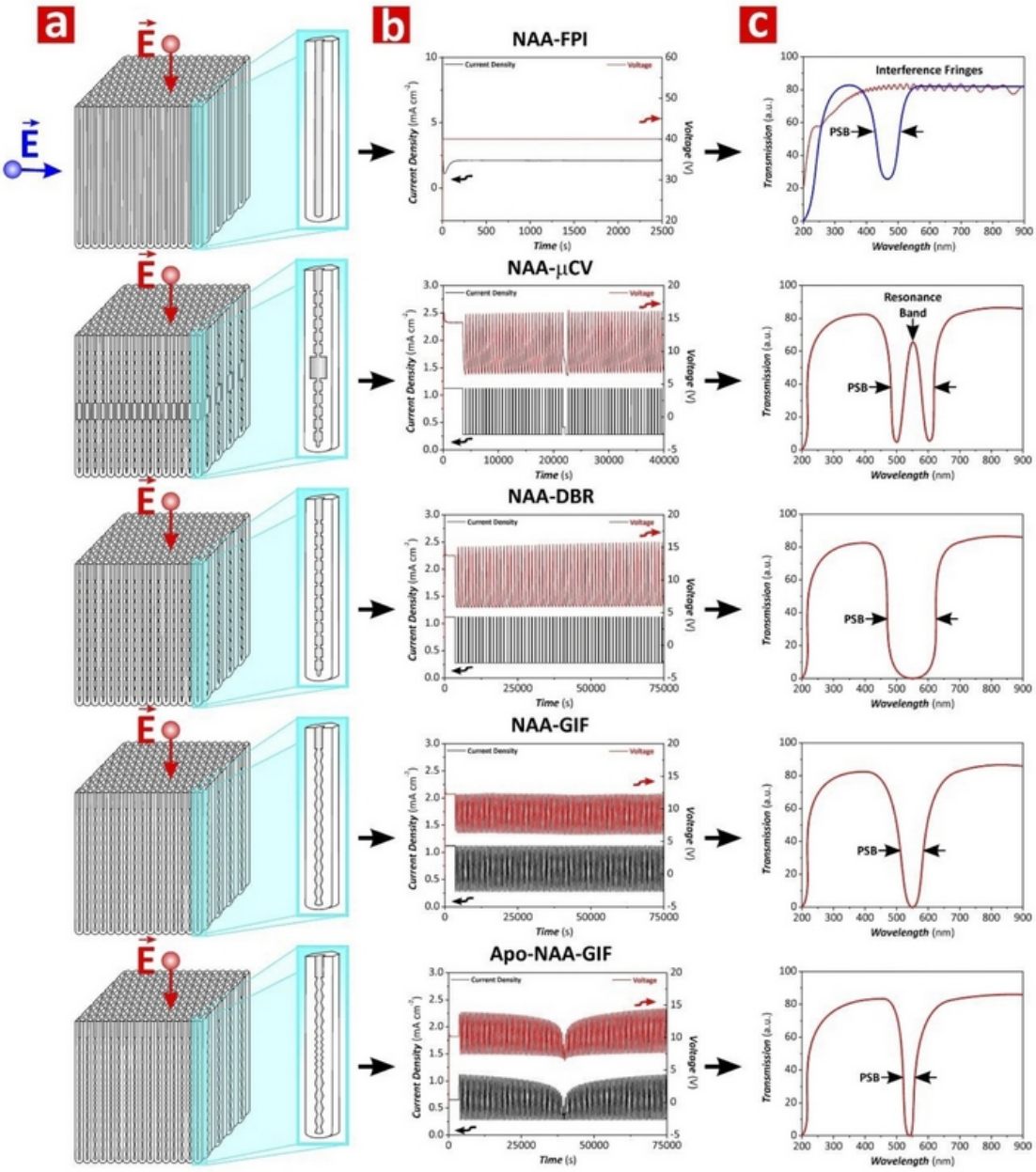

Figure 6. Characteristic nanoporous geometry, anodization profile, and optical properties of representative nanoporous anodic alumina photonic crystals (NAA-PCs) (from top to bottom: NAA-FPI—NAA Fabry–Pérot interferometer; NAA-μCV—NAA optical microcavity; NAA-DBR—NAA distributed Bragg reflector; NAA-GIF—NAA gradient-index filter; Apo-NAA-GIF—apodized NAA gradient-index filter). (**a**) Schematic showing details of the nanoporous structure of NAA-PCs where $\vec{E}$ indicates the direction of the electromagnetic field. (**b**) Representative experimental anodization profiles used to produce NAA-PCs. (**c**) Illustration of optical transmission spectra showing the characteristic photonic features of NAA-PCs.

NAA-DBRs can be produced by stepwise pulse anodization (STPA) approach performed under different conditions (i.e., MA or MA-HA pulses) [75,76]. The structure of these NAA-PCs is characterized by a stepwise modulation of porosity, where the STPA profile is translated into nanopore diameter modulations that correspond to high and low levels of anodizing voltage or current density. The transmission spectra of these NAA-PCs show a characteristically broad PSB, the position and features of which can be readily tuned by different anodization parameters. NAA-GIFs feature a

sinusoidal modulation of porosity and are fabricated by sinusoidal pulse anodization (SPA), a process in which the anodization voltage or current density is pulsed between high and low values in a sinusoidal fashion [77].

Transmission spectra of NAA-GIFs are characterized by a narrow, well-defined, and spectrally tunable PSB, which is a result of a smooth modulation of effective refractive index driven by the SPA profile. Apo-NAA-DBRs and Apo-NAA-GIFs are produced by apodizing STPA and SPA anodization profiles, respectively [78–81]. The characteristic PSB of these NAA-PCs is similar to that of their nonapodized counterparts but with much narrower width due to the apodization of their effective medium. Several studies have demonstrated the successful application of different apodization functions to STPA and SPA profiles to engineer the photonic features of NAA-DBRs and NAA-GIFs [78–81]. NAA-μCVs are a class of NAA-PCs that confine light to small volumes by resonant recirculation of electromagnetic waves [82–84]. Typically, the structure of NAA-μCVs is composed of a physical cavity layer featuring straight cylindrical nanopores, which is sandwiched between two highly reflective mirrors (e.g., NAA-DBRs, NAA-GIFs, etc.). However, other NAA-μCV architectures have been identified [85]. Light reflection by the mirrors forming the structure of NAA-μCVs is maximum at those wavelengths where light interferes in these PCs in a constructive fashion, which is denoted by the characteristic PSB. The introduction of a cavity layer between the mirrors forming the structure of NAA-μCVs creates destructive interferences that lead to the generation of a resonance band within the characteristic PSB. The characteristics of the cavity layer and the mirrors establish the conditions where light confinement is at a maximum. NAA-FPIs are composed of straight cylindrical nanopores that feature a homogeneous distribution of effective refractive index in depth. The optical spectrum of these NAA-PCs has a characteristic PSB when light flows transversally through the NAA-FPIs' structure, which is established by the interpore distance (i.e., lattice constant) and porosity (i.e., nanopore diameter) [46–49]. NAA-BPFs are PC structures that allow the transmission of a specific portion of the light spectrum in a selective manner while impeding the pass of light of all other wavelengths [79,86]. NAA-BPFs can be classified into three categories according to the range of allowed wavelengths: (i) longpass filters, which allow the transmission of light of long wavelengths, (ii) shortpass filters, which allow the pass of light of short wavelengths, and (iii) bandpass filters, which allow the transmission of a band of wavelengths while blocking the pass of light of shorter and longer wavelengths. However, other types of NAA-BPFs with complex transmission bands (i.e., several transmission bands located at different sections of the UV-visible-NIR spectrum) can be fabricated. NAA-LVBPFs have a PSB with variable central wavelength, the position of which is shifted across the surface of the filter in a linear fashion. This effect is achieved by a selective etching of the nanoporous structure of NAA-LVBPFs to engineer their effective medium in the perpendicular direction to the nanopores' growth [87].

3. Surface Modification of Nanoporous Anodic Alumina Photonic Crystals

NAA-PCs have an onion-like layered structure consisting of two main layers: an inner layer away from the central nanopore at the aluminum-alumina interface and an outer layer close to the central nanopores located between the inner layer and the alumina-electrolyte interface (Figure 3a) [88]. The major constituent of the inner layer is pure alumina (Al_2O_3), whereas the outer layer contains anionic contaminants incorporated from the acid electrolyte during anodization such as sulfate, oxalate, and phosphate [29]. Some studies reveal the presence of more than two chemical layers in NAA-PCs. Yamamoto et al. identified three layers in NAA, as suggested by the PL spectrum of NAA after discontinuous pore-widening steps [89]. Santos et al. identified four layers in the chemical structure of NAA with an increasing concentration of impurities toward the layer near the central nanopore by real-time monitoring of pore-widening of NAA using reflectometric interference spectroscopy [90]. During anodization, heterolytic dissociation of water molecules occurs at the oxide-electrolyte interface, leading to the generation of hydroxyl groups on inner surface of NAA-PCs [91]. The presence of hydroxyl groups on the inner surface of NAA-PCs allows surface modifications by binding different

functional molecules with desirable functionalities for specific sensing applications [92]. A number of different surface modification methodologies is still available and these can be categorized into soft and hard techniques (Figure 7) [93].

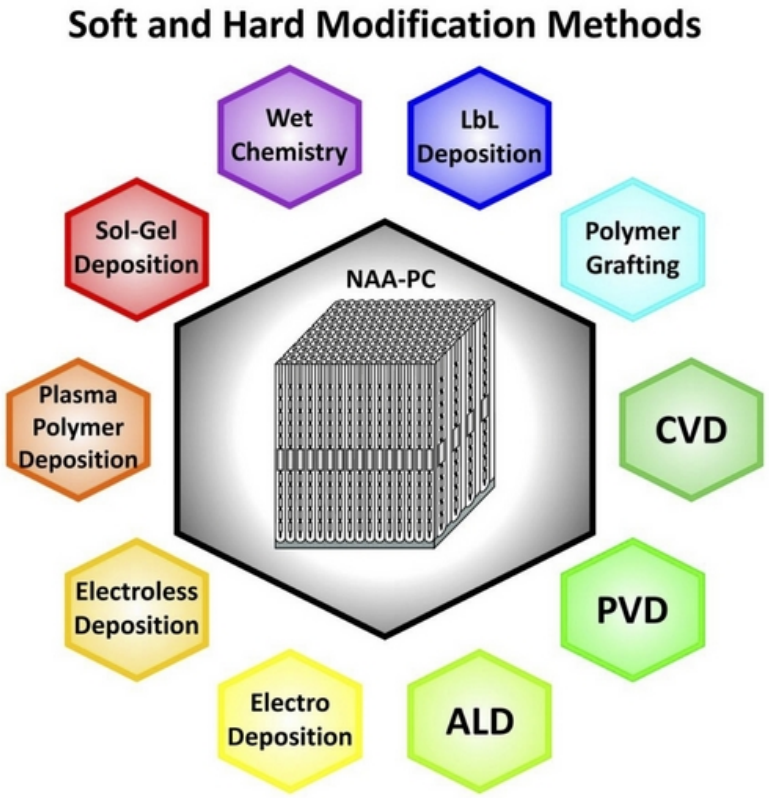

Figure 7. Soft and hard deposition methods used to modify the physical and chemical properties of NAA-PCs.

3.1. Soft Chemical Modification Techniques

3.1.1. Wet Chemistry

The formation of self-assembled monolayers (SAMs) provides a method to functionalize NAA-PCs with organic functional molecules (i.e., aliphatic and aromatic) via anchoring groups such as thiols, disulfides, amines, silanes, and acids. The formation of SAMs is induced by spontaneous strong chemisorption or physisorption of the functional moiety of organic molecules to a solid substrate, which leads to the orderly arrangement of organic films with controlled thickness. When a substrate is immersed in a diluted solution of absorbate for a given time, the organic molecules attach and arrange themselves in an energetically stable form at the solid–liquid interface, imparting the substrate functional entities for different applications [93]. Despite some limitations such as potential oxidation, electric field-induced, and thermal desorption, SAMs generated by wet chemical technique provide many advantageous properties. These include a tight and dense packing configuration of functional groups to attain chemical selectively toward target analytes, chemical stability after immobilization of target molecules, anti-biofouling properties, and flexibility of functional moiety and molecular size. For instance, SAMs of alkanoic acid can be generated in NAA-PCs to alter their surface chemistry [93]. Tao et al. and others studied and analyzed the formation of SAMs based on n-alkanoic acids with chain lengths from C4 to C20 and C24 in NAA [94–96]. SAMs of alkanoic acids with different side functional groups and fluorinated alkanoic acid can also be generated onto the surface of NAA by anchoring carboxylate groups to its surface while providing other functionalities on the outer edge of the monolayer [97,98]. SAMs of alkanoic acids with dual functional groups allow the secondary functional

group to be available for further functionalization with other molecules (i.e., immunoglobulin G and octylamine) [96,98]. Organophosphates form highly stable and densely-packed SAMs due to their phosphonic acid head group (i.e., phosphorus tetrahedrally bonded to carbon, oxygen atoms, and two hydroxyl groups), which forms a covalent bond with hydroxyl groups present on the inner surface of NAA [99]. Organophosphate-modified NAA can be used to detect transition metals for ion exchange, selective sorption, and catalysis [100]. Organophosphate SAMs can also be used as linkers to organic matrices such as pyrrole-containing molecules and graphene oxide in multicomponent systems [91]. Various phosphonic acids such as alkylphosphonic acid [101], fluorinated phosphonic acid [102], and ester-containing phosphonic acid [103] have been used to modify NAA platforms by forming organophosphorus SAMs. SAMs based on bifunctional phosphonic acids and allow further surface reactions of the terminal group with other functional molecules such as polymers, biomolecules, and small molecules [97,104,105].

Other popular organic molecules used to form SAMs on NAA platforms are organosilanes, which are a group of chemical compounds derived from silanes containing one or more organic groups. The silanol group of organosilanes attaches covalently to the hydroxyl groups present on the surface of NAA [88]. These functional molecules can be immobilized onto NAA platforms by wet chemical technique and chemical vapor deposition (CVD), by which evaporated organosilane molecules deposit and self-organize on NAA [106]. A variety of silanes has been explored to modify the properties of as-produced NAA for different purposes, including tuning its surface wettability, improving its biocompatibility, or altering the effective pore geometry for chemical selectivity in various applications such as molecular transport and separation, immunoisolation, hydrophylization, and sensing. SAMs of silanes with hydrophobic terminal groups increase the hydrophobicity of NAA [107], SAMs of perfluoroalkylchorosilanes reduce the effective pore diameter of NAA for molecular transport [108], poly(ethylene glycol)silane SAMs improve the biocompatibility of NAA for immunoisolation [109], and SAMs of mercaptosilanes have been used for sensing applications [110–113]. Similar to SAMs of alkanoic and phosphonic acids, SAMs of organosilanes can act as chemical linkers for further immobilization of biomolecules [114–116], polymers [116], and nanoparticles [117]. Furthermore, organosilanes containing different terminal functionalities (e.g., amine, thiol, carboxyl, etc.) can be deposited onto the inner surface of a single NAA platform in a differential fashion to provide desirable gradient functionalities for specific applications such as and multiplexed sensing [118,119]. Organosulfur is also used to create SAMs on NAA by wet chemical route. The formation of organosulfur-based SAMs requires the pretreatment of NAA platform, which involves the deposition of a thin layer of gold by electroless, electrodeposition, or sputtering technique [91]. The sulfhydryl or disulfide moiety of organosulfur molecules has strong affinity toward gold, leading to relatively strong bonds that form stable SAMs [120,121]. The resulting organosulfur-based SAMs can be used for various applications such as support layer for lipid bilayer formation [122] as well as further functionalization for chemo- and biosensing [123]. Alkene and alkynes are able to form SAMs on NAA by thermally-induced wet chemical technique [97,124]. Alkene- and alkyne-based SAMs modify the hydrophobicity of NAA platforms and enable further chemical functionalization for sensing applications [97,125]. SAMs of alkynes are more stable than their alkene-based equivalents. The instability of alkene-based SAMs is attributed to the different molecular species formed after binding to hydroxyl groups present on the surface of NAA [97]. Alkene SAMs undergo a rapid decrement of carbon content and contact angle upon exposure to phosphate buffer saline solution, which denotes their faster degradation rate as compared to their alkene counterparts. Comparative studies have evaluated the stability and quality of SAMs formed on the surface of NAA platforms using different functional molecules. Bhairamadgi et al. tailored the surface of NAA with SAMs of phosphonic acid and alkyne molecules and assessed their hydrolytic and thermal stability. Phosphonate monolayers on NAA were relatively stable when immersed in acidic and neutral solutions but showed poorer stability under alkaline conditions. The thermal stability of phosphonate-based SAMs on NAA was found to be exceptional, with only a 10% loss of monolayer due to thermally induced desorption at

temperatures as high as 562 °C [124]. This was associated with the strong binding of phosphonic acids to hydroxyl groups on NAA via monodentated, bidentated, or tridentated structures [126]. On the other hand, alkyne monolayers on NAA showed weaker hydrolytic and thermal stabilities as compared to phosphonate-based SAMs. These SAMs showed a decreasing contact angle and carbon-to-aluminum ratio with temperature as well as a lower temperature at 10% monolayer desorption (284 °C) [124]. Similar to phosphonates, alkynes are capable of forming bidentate structures with surface hydroxyl groups present on the surface of NAA [125]. However, the nature of the chemical bond (Al–O–C) is more prone to dissociation as compared to that of phosphonates (Al–O–P) [97]. Debrassi et al. evaluated the stability of chemically modified NAA platforms with SAMs of phosphonate, carboxylate, alkene, alkyne, and silane molecules. The order of stability based on the amount of carbon on SAMs-modified NAA immersed in phosphate buffer saline solution was found to be phosphonate > silane > alkyne > alkene > alkanoic acid [97]. The stronger stability of phosphonate-based SAMs on NAA was further proven over a range of pHs (pH 4–8) and temperatures (25–80 °C) [127]. The strengths and weaknesses of different types of SAMs are summarized in Table 1.

Table 1. Comparison of properties of self-assembled monolayers (SAMs) of different molecules.

SAM	Advantages	Limitations	Quality
Alkanoic acid	- Wide range of carboxylates with different functionalities available - Environmentally friendly - Densely packed SAMs	- Hydrolytically unstable in aqueous media - Relatively easy desorption and exchange	Good
Organophosphonates	- Stable and highly resistant to hydrolysis - Densely packed SAMs	- Potential precipitation of phosphonates	Excellent
Organosilanes	- Rapid covalent binding with substrates - Further chemical modification without compromising the integrity of SAMs	- Difficult to obtain uniform SAMs with limited packing density - High reactivity - Hydrolytically unstable under aqueous and humid conditions - Limited reproducibility	Excellent
Organosulfurs	- Simple and well-established self-assembly process	- Prone to oxidation upon air exposure - Rapid decomposition at high temperature - Undergo displacement when exposed to adsorbates - Conformational defects and cross-contamination	Good
Alkenes and alkynes	- Good stability in water and high temperature - Ease of further (bio)functionalization	- Disordered SAMs - Low surface coverage due to poor reaction kinetics	Excellent

Wet chemical techniques can also be used to build substrate-supported biomimetic lipid membranes. The adsorption of lipid vesicle dispersions to NAA platforms yields lipid bilayers that mimic cell membranes, which can be used as a model to investigate molecular processes occurring at membrane level, concomitant membrane structural and fluidity changes, as well as a support for biological sensing events between membrane and proteins [128]. The formation of lipid bilayers usually involves fusion of lipid vesicles on either bare or functionalized NAA platforms [122]. Typically, bare NAA platforms are directly exposed to lipid vesicle dispersions by either immersion or wetting by droplets, leading to the formation of lipid nanotube arrays [129,130]. On the other hand, NAA platforms can be pretreated as a preparation for subsequent lipid functionalization. In this process, NAA is coated with a gold layer that is used to capture thiol-containing lipids and to link molecules

with sulfhydryl moiety for subsequent lipid binding [122,131]. Another approach to deposit lipid molecules on NAA is by utilizing a support layer of silane, sometimes coupled with cross-linkers (e.g., polymers and streptavidin-biotin), where lipid molecules bind to the reactive surface functional groups electrostatically or covalently [128,132,133]. Wet chemical technique also offers a simple route for the immobilization of charged molecules onto the inner surface of NAA via electrostatic interactions [134]. Protonated hydroxyl groups and exposed cationic aluminum ions present on the surface of NAA can interact with anions when NAA is incubated in a solution of functionalizing molecules. It is important to ensure that the incubation time is long enough for effective electrostatic immobilization. An additional hydroxylation step can be performed in order to create more hydroxyl groups on the surface of NAA. In these electrostatic interactions, proteins that are negatively charged at pH higher than their isoelectric point (e.g., protein A, urea, and bovine serum albumin) can be immobilized onto positively-charged NAA. These functional layers can be used to develop a broad range of optical biosensor [135–137].

3.1.2. Layer by Layer Deposition

Layer by layer deposition (LbL) is a versatile and simple surface modification technique to create functional and multilayered thin films on solid or nanoporous platforms. The thin film is created by alternating dipping stages of a substrate into solutions containing functional molecular species with an intermediate rinsing step in between for removal of weakly-adsorbed molecules and minimization of cross-contamination. Although dip coating is an efficient and automatable approach, this technique is time consuming due to the multiple steps at low speed required to achieve homogeneous coatings. Alternative methods such as alternated spray deposition and spin coating can address this limitation, although these techniques have other intrinsic drawbacks such as waste of depositing solutions and limited area of deposition. LbL of a wide variety of functional molecules can be applied to various surfaces such as planar substrates, colloids, nanoparticles, and porous materials [138]. The underlying principle of LbL assembly is based on electrostatic interactions between positively and negatively charged molecules. However, other approaches such as LbL of layers by chemical interactions such as hydrogen bonding, metal-ligand coordination chemistry, hydrophobic interactions, and biological recognition are possible [139]. These approaches allow the deposition of LbL films beyond conventional and functional polyelectrolytes, including biomolecules (i.e., DNA, nucleic acids, proteins, and viruses), nanoparticles, organic dyes, dendrimers, and inorganic molecules [140,141]. The thickness of thin films created by LbL can be controlled with nanometric precision, with multiple interactions between the layers of the resulting film providing enhanced stability [141]. The LbL method has been used to tailor the surface chemistry of NAA in terms of transport properties and permeability as well as further functionalization [108]. Polyelectrolytes such as poly(stryrene sulfonate) and poly(ally amine hydrochloride) are commonly used for deposition of LbL films on NAA [142–144]. Multilayered polyelectrolyte films can also be generated on NAA using templated polyelectrolytes and functional polyelectrolytes such as dendrimers [145,146]. This approach enables further functionalization with nanoparticles [147,148], drug molecules [149], antibodies [149], DNA [150], and ions [151]. DNA strands and proteins (i.e., glucose oxidase, hemoglobin, and cytochrome C) can be assembled layer by layer inside the nanopores of NAA by hybridization and by protein immobilization agents based on covalent bonding and electrostatic adsorption [152,153]. Typically LbL assembly on NAA platforms may require pretreatment with silanes to generate a positively-charged surface [142,146].

3.1.3. Polymer Grafting

The inner surface of NAA can be modified by polymers using two approaches: (i) the "grafting-to" method involving the anchoring of polymer brushes to a solid interface and (ii) the "grafting-from" method in which the initiator molecules lead to the grow polymer chains on the inner surface of NAA [154]. Although the former method is relatively simple, it only provides limited grafting

densities of polymer brushes and film thickness [155]. On the other hand, the "grafting-from" approach offers a better control over the polymeric film in terms of structure, thickness and density. Among different surface-initiated polymerization techniques (i.e., reversible addition-fragmentation chain-transfer polymerization, ring opening metathesis polymerization, and iniferter polymerization), atom-transfer radical polymerization (ATRP) have been extensively explored for the generation of polymer brushes. Unlike LbL films, polymers grown from surfaces display a more extended and less cross-linked configuration, which is more suitable to develop swollen films that are able to bind a higher number of biomacromolecules [156]. Polymerization of NAA often requires a prefunctionalization step such as silanization, gold coating for adsorption of thiol-containing initiators, generation of hydroxyl groups for subsequent attachment of initiators or grafting of polymers such as poly(N-isopropylacrylaminde, poly(methacrylic acid), and poly(oligo (ethylene glycol) methyl ether methacrylate) [157,158]. Modification of NAA by polymer grafting enables the tuning of the surface properties of NAA such as permeability, wettability, and chemical selectivity [159,160] as well as other features, including immobilization of molecules such as proteins, nanoparticles, and steroids [161–163]. Surface-initiated polymerization techniques can be combined to create films based on different polymers within NAA [164]. This technique is also compatible with the LbL method to construct composite polymer films inside the nanopores of NAA [165].

3.2. Hard Chemical Modification Techniques

3.2.1. Chemical Vapor Deposition

The surface properties of NAA can be modified by chemical vapor deposition (CVD), technique by which the inner surface of NAA is coated by a thin film of the deposited material through dissociation and chemical reaction between a gaseous reactant and the surface of NAA with the aid of heat, light, or plasma. CVD enables the generation of uniform coatings with controllable structure and good conformal coverage. This functionalization method is versatile and allows the deposition of many different chemical precursors such as metals, carbides, oxides, sulfides, silanes, and semiconductors. However, the deposition of multicomponent films by CVD is limited by due to different vaporization rates of precursors [166]. CVD is commonly used to grow nanotubes and nanowires based on semiconductor materials, carbons, and polymers [167–170]. CVD is also employed for the formation of silane monolayers onto NAA as an alternative modification to conventional wet chemistry approaches due to its high reproducibility, reduced chance of particle contamination, and silanol oligomerization [171]. Organosilane modification of NAA by CVD allows further functionalization such as molecule immobilization and polymerization [116,170,172]. These CVD modification methods have been used to develop drug delivery systems, sensors, and electronic devices [173,174].

3.2.2. Physical Vapor Deposition

Physical vapor deposition (PVD) is a hard modification technique used to deposit thin films of elements, alloys, and compounds on NAA platforms [175]. PVD involves the physical transformation of analytes to gaseous state by thermal evaporation or impact process followed by their deposition onto the surface of NAA [176]. PVD can be classified into different categories such as electron beam evaporation, thermal evaporation, sputter deposition, pulsed laser deposition, and molecular beam epitaxy [28]. Properties such as conductivity, reflectivity, and chemical stability and, also, for further chemical modifications, enhancing interactions with various chemical and biological species for optical sensing and molecular separation applications can be improved by modification of the structure of NAA platforms with different coatings produced by PVD [92]. Gold, platinum, nickel, indium-tin oxide, manganese, silver, semiconductor oxides, and mixtures of these are often deposited onto NAA platforms by electron beam evaporation, sputtering or shadow evaporation to produce nanostructured material platforms for sensing, imaging, photocatalysis, and photovoltaics due to

their desirable plasmonic and optoelectronic properties [121,177,178]. These functional coatings enable further chemical modifications of NAA with a wide range of molecules such as thiolates, lipids, and polyelectrolytes [120,179,180].

3.2.3. Atomic Layer Deposition

Atomic layer deposition (ALD) is another hard modification method used to deposit thin and conformal films that provides precise control over the thickness and composition of the film at atomic scale. ALD is based on a self-limiting and layer-by-layer approach that enables the deposition of a broad range materials including oxides, nitrides, phosphates, sulfides, and metals. ALD involves alternating saturate surface reactions of pulsing and purging precursors [181]. The main advantage of ALD is its ability to form homogenous monolayers over large areas and high aspect ratio nanoporous substrates due to its three-dimensional nature [182]. Furthermore, monolayers formed by ALD are versatile in their composition and thickness. However, ALD has some intrinsic drawbacks such as its slow deposition rates, potential cross-contamination of thin films by residual precursors, and high costs for certain materials [183,184]. Despite these limitations, ALD provides high reproducibility and flexibility and it has been extensively used to modify NAA platforms for various applications [129,185]. Conformal single and doubled layered structures based on a broad range of materials such as silicon dioxide, titanium oxide, sulfides, palladium, and platinum deposited onto NAA platforms by ALD have been explored not only for surface modifications, but also to fabricate nanostructures by template synthesis such as nanotubes and nanowires [186,187]. ALD-modified NAA has been used to develop sensors, energy materials, and membranes [188–190]. Polymers such as polyimide can also be deposited onto NAA membranes via ALD for separation applications [191]. Furthermore, ALD coatings deposited onto NAA platforms provide a means for further functionalization, opening up new opportunities for advanced sensing applications [192].

3.2.4. Electrochemical Deposition

Electrochemical deposition has also been used to modify NAA with metal and alloys, where the coating is produced by current or voltage driven electrochemical reduction reactions within NAA platforms [193]. Metals are typically deposited inside the nanoporous network of NAA from electrolytes, which serves as cathode during this process. Despite its limitations, such as low deposition rate and single use of host template, electrodeposition is an attractive approach to surface-modify NAA platforms and prepare nanostructures such as nanotubes or nanowires since it is cost-effective, simple, and it can be performed with simple laboratory equipment at room temperature [194,195]. Nanostructures based on different metals (i.e., copper [196], nickel [197], and antimony [198]) have been successfully synthesized in NAA platforms by electrodeposition, enabling the precise tailoring of the properties of these materials for specific applications such as sensing and catalysis [28,199]. Metal oxides and alloys can also be electrodeposited in NAA platforms to produce nanowires and nanotubes [200,201]. The versatility of this technique is further demonstrated by its ability to synthesize nanoparticles, nanocomposites, and multilayered nanostructures in NAA platforms [198,202,203]. These structures can be further functionalized with thiols, alkanoic acids, and proteins for various purposes such as drug delivery and sensing [204,205]. However, the composition of multilayered nanostructures is not limited to metals since other composite structures such as conducting polymers (e.g., polypyrrol) can be successfully integrated with gold to produce multisegmented nanowires [206].

3.2.5. Electroless Deposition

Electroless deposition can be used to deposit metals and alloys onto NAA platforms without the need of external current as it is based on a purely chemical process (i.e., displacement and autocatalytic deposition) based on oxidation-reduction reactions in aqueous or nonaqueous solutions [207]. Electroless deposition requires reducing agents such as formaldehyde and polydroxyl alcohols or surface activation agents. The advantage of electroless deposition is that this method can be applied to

coat the surface of nonelectronically conductive platforms such as NAA [91]. The coatings formed by electroless deposition are uniform, continuous, and replicate the geometrical characteristics of nanoporous templates. NAA has been long devised as a template for electroless deposition of metals in the form of nanotubes and nanoparticles including cobalt, nickel and zinc [208–210]. The formation of gold coatings in NAA platforms by electroless deposition provides plasmonic and catalytic properties and these initial gold layers can be used as a precursor for further functionalization [210–213].

3.2.6. Plasma Polymer Deposition

Plasma polymerization is also used to functionalize the surface of NAA platforms with polymer films. This process utilizes organic and inorganic precursors to grow polymeric thin films with the aid of plasma discharge to catalyze these chemical reactions [214]. Polymeric films formed by plasma polymerization are highly cross-linked, randomly branched, and lack regular repeating units, making them mechanically, chemically, and thermally strong. Compared to other polymer deposition methods, plasma polymer deposition offers a high degree of versatility and control as the chemical composition and thickness of the resulting films can be manipulated easily by means of the deposition parameters and the nature of the precursors. Furthermore, this technique uses a small amount of reactants for polymeric film deposition at low temperature, making it cost-effective [214]. Nonetheless, polymer plasma deposition cannot achieve sufficient penetration depth to coat the inner surface of nanoporous materials such as NAA, being limited to surface-based applications [106]. Modification of NAA platforms with plasma polymer deposition enables the tuning of the hydrophobicity of the surface by polymerizing fluorocarbon monomers using argon or oxygen plasma [215]. Plasma polymer deposition also changes the chemical and geometrical properties of NAA as platform material in drug delivery systems, where drug release from NAA can be controlled and extended over longer periods of time [216,217]. This technique also allows the deposition of functional monomers to create chemically reactive polymeric surfaces that can be further functionalized for various applications including molecular separation, optical sensing, and drug delivery [218].

3.2.7. Sol-Gel Chemistry Deposition

The sol-gel method can be used to alter the surface chemistry and geometrical characteristics of NAA platforms and to fabricate various nanostructures by template synthesis. This process is divided into three steps: (i) hydrolysis and partial condensation of a precursor solution by immersion, dipping, or spin coating, (ii) gel formation by polycondensation, and (iii) solvent evaporation and gel drying [219,220]. A variety of materials can be obtained via the sol-gel method as it allows direct preparation of sol-gel composite films with controllable stoichiometry and homogeneity at low processing temperature. Sol-gel derived films possess high specific surface area and a surface with rich chemistry that allows ease of functionalization [221]. On the other hand, the sol-gel process has some disadvantages such as limited thickness and mechanical weakness of the resulting film [222]. Careful consideration and handling of precursors must be done since some precursors are too unstable to form sol-gel films [219]. However, sol-gel chemistry modification is an extensively used method to tune the surface characteristics of NAA platforms and to synthesize nanocomposite materials. The flexibility of sol-gel chemistry to modify NAA platforms is demonstrated by the wide range of materials that can be deposited by this technique such as metal oxides (i.e., titanium dioxides [223], silica [224], and zinc oxide [224]) as well as mixtures of inorganics [225,226]. The surface modification of NAA by sol-gel can be further expanded via the immobilization of molecules onto the sol-gel derived films. Sol-gel modified NAA platforms can be endowed with biofunctionalities by immobilization of biomolecules, gold nanoparticles, and drug-bearing polymers. These platforms can be applied in immunoassays, biosensing, and drug delivery applications [227,228]. Furthermore, sol-gel derived functional coatings synthesized within NAA platforms (i.e., titanium and tin oxides) provide composite photocatalyst materials for environmental remediation and green energy generation applications [223,229].

4. Nanoporous Anodic Alumina Photonic Crystals as Optical Sensing Platforms

NAA-PCs show much potential as advanced and versatile optical sensing platforms due to their unique physical, chemical, and optical properties. To engineer the effective medium and surface chemistry of NAA-PCs enhances the sensing performance and capabilities of NAA-based optical sensing system in terms of selectivity, sensitivity, and specificity. The geometric features of nanopores in NAA-PCs can be precisely engineered by different anodization approaches to selectively filter molecules by size-exclusion and increase the available binding functional sites due to the high specific surface area to volume ratio of these nanoporous PCs. Furthermore, the surface chemistry of NAA-PCs can be modified with different functional molecules through well-established protocols to achieve chemical selectivity toward target molecules and analytes [34]. NAA-PCs are active optical platforms that confine, guide, reflect, emit, and transmit incident light, generating stable optical signals for chemo- and biosensing applications based on different spectral shifts upon exposure to analyte molecules such as reflectivity, photoluminescence, transmittance, waveguiding, absorbance, or color changes. Different forms of NAA-PCs (e.g., distributed Bragg reflectors, grading-index filters, optical microcavities, Fabry–Pérot interferometers, etc.) can be integrated with various optical techniques such as reflectometric interference spectroscopy (RIfS), reflection and transmission spectroscopy, and photoluminescence spectroscopy (PL) (Table 2) [29,87,230]. This section summarizes the most representative examples of chemo- and biosensing systems combining NAA-PC structures with optical techniques.

4.1. Nanoporous Anodic Alumina Distributed Bragg Reflectors (NAA-DBRs)

NAA-DBRs are typically fabricated by stepwise pulse anodization (STPA) process, in which the anodizing current density or voltage is pulsed in a stepwise fashion by means of MA or MA-HA pulses. The nanoporous structure of NAA-DBRs features a stepwise modulation of porosity, with stacks of NAA layers of alternating porosity that follow the high and low levels of anodization voltage or current density applied during the STPA. NAA-DBRs have a broad PSB, which shifts its position when the effective medium of these PCs is modified upon exposure to analytes of interest. This property can be used to develop a series of optical chemo- and biosensing systems.

Chen et al. fabricated NAA-based DBRs by galvanostatic pulse anodization under mild conditions in sulfuric acid electrolyte. The structure and optical properties of these NAA-DBRs where tuned across the spectral regions by a systematic modification of anodization period (T_p) and the number of pulses (N_p) (Figure 8a) [231]. The optical properties of these NAA-DBRs were assessed by reflectometric interference spectroscopy (RIfS) and compared in terms of sensitivity (*S*), low limit of detection (*LLoD*), and linearity (R^2). The effective medium of these NAA-DBRs was infiltrated with solutions of different reactive index (i.e., D-glucose, ethanol, and isopropanol), leading to quantifiable changes in the effective optical thickness (ΔOT_{eff}) of these NAA-PCs by RIfS. NAA-DBRs produced with T_p = 1035 s and N_p = 150 pulses showed the highest sensitivity toward changes in the effective medium, with *S* = 37,931 nm RIU^{-1}, *LLoD* = 0.352 RIU, and R^2 = 0.9876. These NAA-PCs were then utilized as sensing platforms for selectively detection of gold (III) ions (Au^{3+}) in combination with RIfS. The surface chemistry of NAA-DBRs was modified with 3-(mercaptopropyl)-trimethoxysilane (MPTMS) by CVD to generate thiol functionalities onto the inner surface of these PCs. A linear correlation between ΔOT_{eff} and the concentration of Au^{3+} ($[Au^{3+}]$) was used to establish the characteristic sensing parameters of these platforms, which were *S* = 22.2 nm μM^{-1}, *LLoD* = 0.16 μM, and R^2 = 0.9983. In another study by Chen et al., the authors developed an optical sensing system combining NAA-DBRs with RIfS for the detection of vitamin C (Figure 8b) [232]. A set of NAA-DBRs with different optical and geometric properties was fabricated by a systematic manipulation of T_p, anodization temperature (T_{an}), and time ratio of high and low current density values (R_t) in the STPA profile. The nanopores of these NAA-DBRs were infiltrated with a mixture of ethanol and isopropanol in different ratios to assess the effective medium sensitivity in terms of *S*, *LLoD*, and R^2 by RIfS. The highest sensitivity (*S* = 27,553 nm RIU^{-1}) was achieved by NAA-DBRs fabricated with T_p = 675 s, T_{an} = 3 °C, and R_t = 6:1. A set of these NAA-DBRs was then

functionalized with (3-aminopropyl)-trimethoxysilane (APTES) to achieve chemical specificity toward vitamin C molecules.

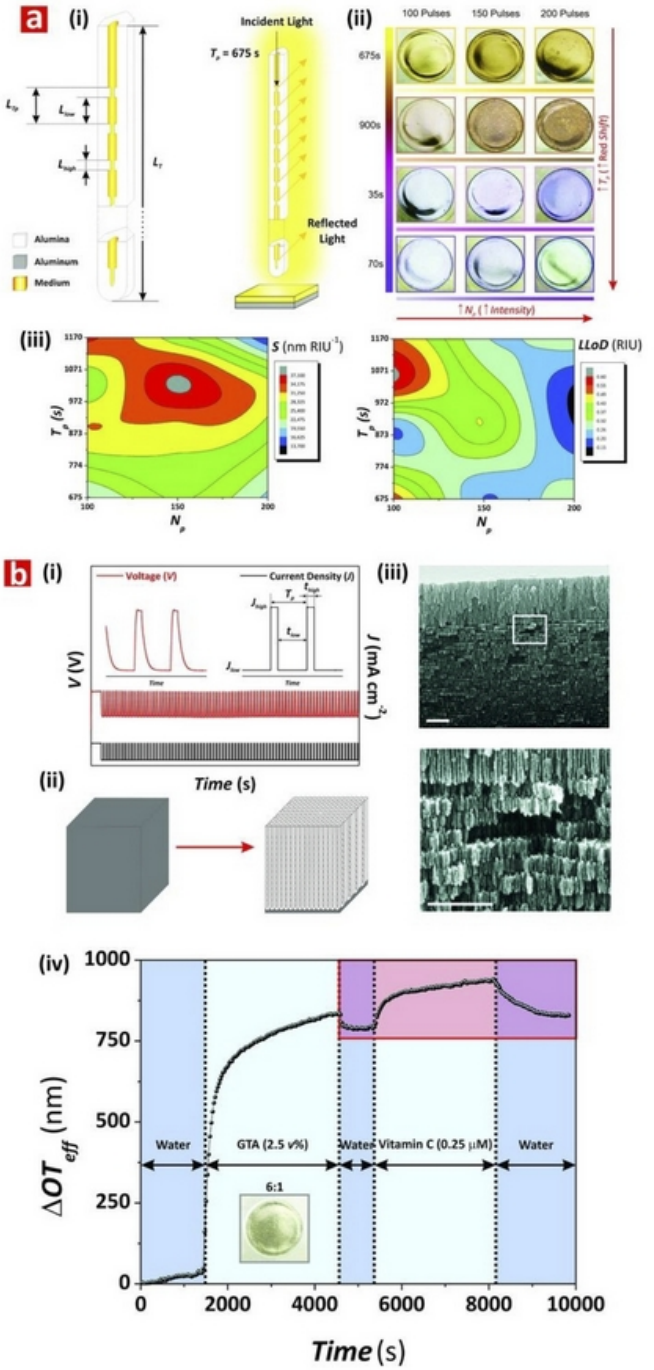

Figure 8. Examples of applicability of NAA-PCs in chemo- and biosensing applications. (**a**) (**i**) Schematic showing details of the structure of Nanoporous anodic alumina-distributed Bragg reflectors (NAA-DBRs) produced by STPA, (**ii**) digital pictures showing the interferometric colors displayed by these NAA-PCs, and (**iii**) sensitivity and low limit of detection as a function of the fabrication parameters. Reproduced from [231], with copyright permission from American Chemical Society, 2015. (**b**) (**i**) STPA profile used to produce NAA-DBRs, (**ii**) schematic showing the fabrication of NAA-DBRs by STPA, (**iii**) SEM images of NAA-DBRs, and (**iv**) real-time effective optical thickness change for each sensing stage of vitamin C. Reproduced from [232], with copyright permission from American Chemical Society, 2015.

Different concentrations of vitamin C solutions were used to characterize the sensing performance of APTES-functionalized NAA-DBRs through real-time measurements of ΔOT_{eff} using RIfS. The performance of this sensing system for vitamin C was S = 227 nm μM^{-1}, $LLoD$ = 20 nM, and R^2 = 0.9985. These NAA-DBRs displayed vivid interferometric colors, which were demonstrated to be precisely tunable (i.e., brown, gold, pink, purple, and green) by modifying different fabrication parameters (i.e., anodization temperature, anodization period, ratio between time at high, and low current density) [232]. Color changes in these NAA-PCs were used as a sensing principle to develop platforms for colorimetric sensing. NAA-DBR films were broken down into nanoporous microparticles by sonification and infiltrated with media of different refractive index such as air and isopropanol. Color changes associated with effective medium changes were then quantified in terms of RGB values. These NAA-DBR nanoporous microparticles are suitable to develop microsensors and self-reporting nanocarriers.

Law et al. applied apodization to the STPA profile used to produce Apo-NAA-DBRs under current density control conditions [233]. The effective medium of these NAA-DBRs was systematically engineered by modifying T_p, from 1100 to 1700 s, and the pore-widening time (t_{pw}), from 0 to 6 min. The sensitivity of apodized and nonapodized NAA-DBRs was assessed by infiltrating their nanopores with mediums of different refractive index (i.e., air, ethanol, and water). Spectral shifts in the position of the characteristic PSB of these NAA-DBRs upon infiltration with different mediums were monitored in real-time by RIfS and used to assess the optical properties of these NAA-PCs. The linear correlation between shifts in the position of PSB and the refractive index of the medium filling the nanopores demonstrated that apodized NAA-DBRs were ~16% more sensitive (S = 392 nm RIU^{-1}) than their nonapodized counterparts (S = 339 nm RIU^{-1}). The obtained results also revealed that a longer T_p (1700 s) and a moderate t_{pw} (4 min) enhance the sensitivity of NAA-DBRs for optical sensing applications. Kumeria et al. fabricated NAA-DBRs produced with porosity modulated in a pseudosinusoidal fashion. These NAA-PCs were used as sensing platforms in combination with RIfS to develop an optical system for the detection of mercury ions (Hg^{2+}) under specific adsorption conditions [111]. Functionalization of the inner surface of these NAA-DBRs with thiol-silane molecules provided NAA-DBRs with chemical selectivity toward Hg^{2+}. Changes in the position of the characteristic reflection band of NAA-DBRs upon exposure to different concentrations of Hg^{2+} were monitored in real-time by RIfS. This sensing system achieved a sensitivity of 0.0115% μM^{-1}, a low limit of detection of 4.20 µM, and R^2 = 0.994. Guo et al. demonstrated the use of NAA-based Bragg stacks as chemical sensors for in situ monitoring of organics with varied refractive index [230]. NAA-DBRs were used as colorimetric sensing platforms, where color in NAA-DBRs changed from blue to green upon exposure to ethanol. To further characterize the sensitivity of these NAA-PCs, the transmission spectra of NAA-DBRs exposed to a series of alkanes (i.e., n-hexane, n-octane, and n-decane) and alcohols (i.e., anhydrous ethanol, 2-propanol, 1-butanol, and 1-hexanol) were analyzed.

Spectral shifts in the characteristic photonic stopband in the transmission spectrum of NAA-DBRs were used to establish a relationship with the refractive index of media filling the nanopores. The sensitivity of these NAA-PCs was 71.4 and 61.9 nm RIU^{-1} for alcohols and alkanes, respectively. The use of NAA-DBRs as visual sensing tool was further explored by Chen et al. for chemically selective detection of mercury ions (Hg^{2+}) [110]. A palette of structurally colored NAA-DBRs was produced as a function of T_p (from 675 to 1170 s) and T_{an} (from −1 to 3 °C). These NAA-DBRs red-shifted their characteristic interferometric color upon infiltration of their nanoporous matrix with ethanol. An analysis of color changes and ΔOT_{eff} measured before and after infiltration by RIfS established that NAA-DBRs produced at T_p = 1035 s and T_{an} = −1 °C displayed the sharpest change in color and the highest effective optical thickness change. A set of these NAA-DBRs was then further developed as a chemically selective visual sensing platform to detect mercury ions. These NAA-DBRs underwent quantifiable color changes during the different sensing stages, including functionalization with thiol-terminated functional groups and exposure to Hg^{2+}. RGB values of NAA-DBRs as a function of the concentration of Hg^{2+} ($[Hg^{2+}]$) revealed a linear correlation between the intensity of the blue and

green channels in the RGB color and [Hg^{2+}] from 10 to 100 mM. An analysis of the sensing performance established a sensitivity and a low limit of detection of 0.81 a.u. μM^{-1} and 1.25 μM for the blue channel and of 29.4 a.u. μM^{-1} and 37.3 μM for the green channel, respectively. Guo et al. developed NAA-DBR platforms to detect organic molecules through shifts in the characteristic photonic stopband in the transmission spectrum of these NAA-PCs (Figure 9a) [234]. NAA-DBRs were produced by a modified two-step anodization process and exposed to a series of alcohols (i.e., anhydrous ethanol, 2-propanol, 1-butanol, and 1-hexanol) and alkanes (i.e., *n*-hexane, *n*-octane, and *n*-decane). Spectral shifts in the PSB of these NAA-PCs upon exposure to analytical solutions demonstrated that NAA-DBRs have higher sensitivity toward alcohols and alkanes of longer chains due to the higher refractive index of these analyte molecules. Ruiz-Clavijo et al. developed a colorimetric sensor based on NAA-DBRs with periodic composition of high-porosity and low-porosity layers (Figure 9b) [235]. The colorimetric sensing properties of these NAA-DBRs were assessed in terms of interferometric color shift upon infiltration of nanopores with water and background substrate. The color variations in NAA-DBRs were quantified by the CIE color space chromaticity diagram.

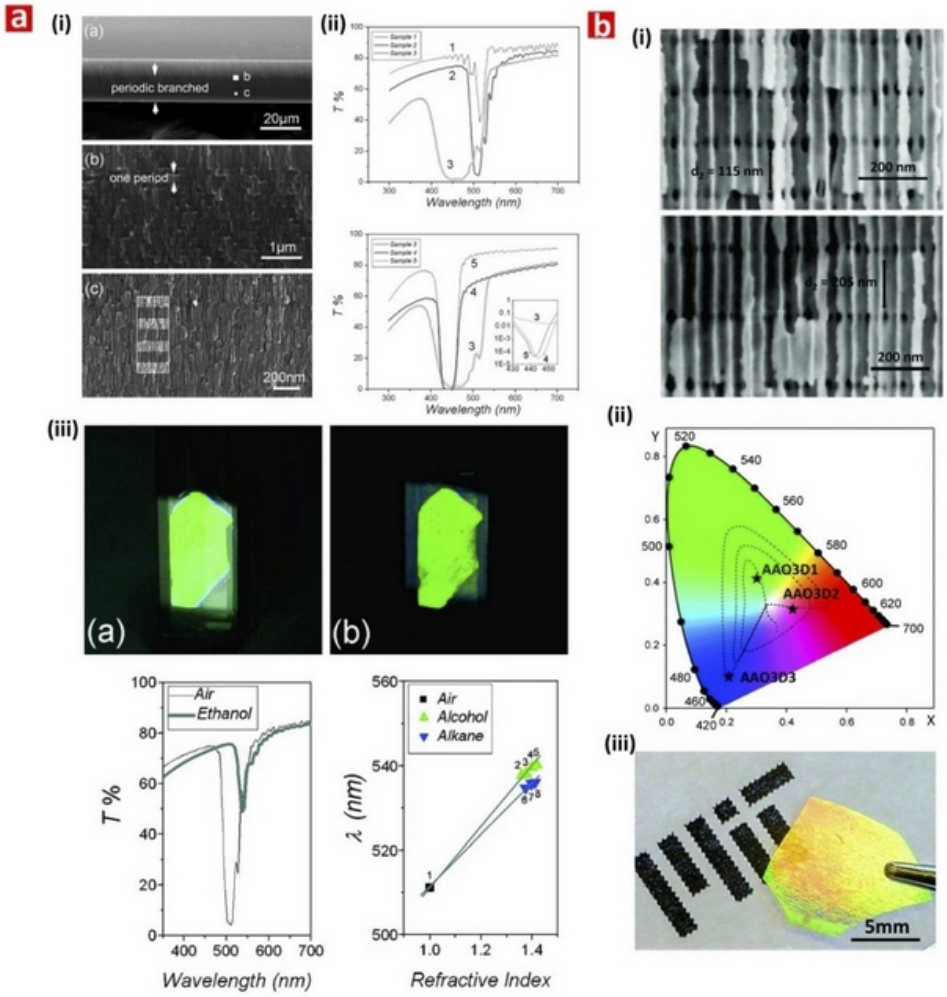

Figure 9. Examples of applicability of NAA-PCs in chemo- and biosensing applications. (**a**) (**i**) SEM images of NAA-DBRs, (**ii**) transmission spectra of NAA-DBRs as a function of the fabrication conditions, and (**iii**) interferometric colors, transmission spectra, and position of the PSB for different media filling, Reproduced from [234], with copyright permission from American Chemical Society, 2008. (**b**) (**i**) SEM images of NAA-DBRs, (**ii**) position within the CIE color space, and (**iii**) digital images showing the interferometric color of NAA-DBRs at different fabrication conditions. Reproduced from [235], with copyright permission from American Chemical Society, 2018.

4.2. Nanoporous Anodic Alumina Gradient-Index Filters (NAA-GIFs)

NAA-GIFs show a sinusoidally periodic variation of effective refractive index that is typically produced by the sinusoidal pulse anodization process (SPA). This smooth variation of effective refractive index gives rise to a much narrower and well-defined PSB, which is more sensitive toward changes in the effective refractive index of the NAA-PC platform [236,237].

Kumeria et al. fabricated NAA-GIFs by a modified two-step anodization process, in which the second step consisted of a pseudosinusoidal voltage profile controlled by total charge under potentiostatic conditions [238]. The sensitivity of NAA-GIFs toward changes in their effective refractive index were assessed by RIfS. NAA-GIFs were exposed to aqueous analytical solutions of D-glucose with concentration ranging from 0.01 to 1.00 M, equivalent to a modification of refractive index from 1.333 to 1.363 RIU. Shifts in the position of the characteristic PSB produced by changes in effective refractive index upon infiltration were used to establish a linear correlation between spectral shift and refractive index of media filling the nanopores. These NAA-based PCs achieved a sensitivity for glucose of 4.93 nm M^{-1} (i.e., 164 nm RIU^{-1}), with a *LLoD* of 0.01 M, and a R^2 of 0.998. These NAA-GIFs also displayed vivid interferometric colors that could be precisely tuned across the visible spectral region by the anodization parameters and pore-widening time. The infiltration of the nanoporous network of NAA-GIFs with acetone led to dynamic color changes from intense green to intense red due to alteration of the effective medium of these NAA-PCs. This demonstrated the capability of NAA-GIFs as colorimetric platforms to develop visual sensing tools.

Santos et al. developed an optical sensing system combining protein-modified NAA-GIFs and RIfS to assess the pharmacokinetic profile of drugs (Figure 10a,b) [77]. NAA-GIFs were fabricated by sinusoidal pulse anodization under galvanostatic conditions using sulfuric acid as an electrolyte. These NAA-PCs were chemically functionalized with silane molecules and human serum albumin (HSA) molecules were immobilized onto the surface of APTES-modified NAA-GIFs via glutaraldehyde activation. HSA-modified NAA-GIFs were exposed to indomethacin, a model drug, and the binding events occurring between immobilized HSA molecules and free indomethacin molecules were monitored in real-time by RIfS. The position of characteristic PSB of HSA-modified NAA-GIFs was found to red-shift when these PC platforms were exposed to different concentrations of indomethacin. A linear correlation between spectral shift and concentration of drug was used to establish the sensing performance of this system, with results: S = 0.63 nm mM^{-1}, *LLoD* = 0.065 mM, and R^2 = 0.9935. This study demonstrated the applicability of the proposed system for pharmacokinetic assessment of drug–protein interactions. In an extension of this study, Nemati et al. assessed systematically the binding affinity between a set of drug molecules and HSA using optimized NAA-GIFs as sensing platforms and RIfS [171]. Spectral shifts in the characteristic PSB and changes in the effective optical thickness of HSA-functionalized NAA-GIFs upon exposure to various drug molecules (i.e., sulfadymethoxine, coumarin, warfarin, indomethacin, and salicylic acid) were assessed as a function of the concentration of model drug. The affinity between HSA-modified NAA-GIFs and drug molecules, defined by the slope of the linear fitting between the sensing parameter and the concentration of drug, was found to be dependent on the sensing parameter used (i.e., PSB shift or effective optical thickness change).

Kumeria et al. combined NAA-GIFs with RIfS to develop an optical sensing system to detect Hg^{2+} in aqueous solutions [112]. The sensing principle of this system relies on red shifts in the position of characteristic PSB of NAA-GIFs produced by the selective binding of Hg^{2+} to the thiol-functionalized surface of NAA-GIFs. The system's performance was assessed for a range of concentrations from 1 to 750 μM. A linear fitting between the spectral shift and [Hg^{2+}] established an S of 0.072 nm μM^{-1}, a *LLoD* of 1 μM, a linearity of 0.992, and a linear working range from 1 to 100 μM. The chemical selectivity of this system was demonstrated through exposure of thiol-modified NAA-GIFs to analytical solutions containing interfering metal ions (e.g., Cu^{2+}, Pb^{2+}, and Fe^{3+}) and aqueous matrices of different complexity such as ultrapure, tap, and river water. The obtained results verified the high selectivity of the sensing system toward Hg^{2+} without further chemical treatments, despite the presence of

interfering elements. Marcias et al. fabricated NAA-GIFs using an apodized sinusoidal current density profile and assessed the sensing capabilities of these NAA-PCs upon infiltration of their nanoporous structure with media of different refractive index (Figure 11a) [81]. Spectral shifts in the characteristic PSB of NAA-GIFs after infiltration with air, ethanol and deionized water were determined by reflection spectroscopy. The sensing system was able to detect small changes in refractive index, with a sensitivity of 48.8 nm RIU^{-1}.

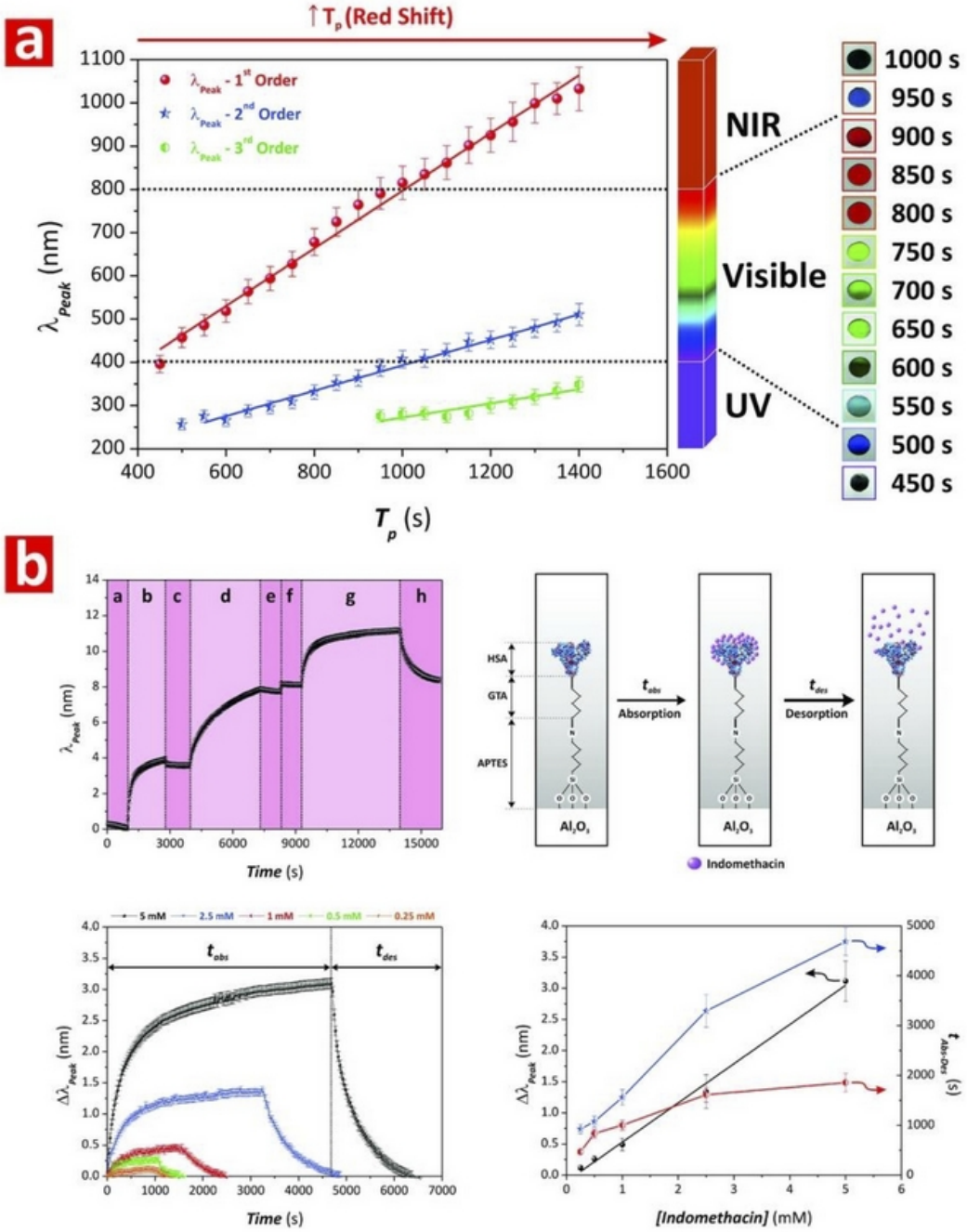

Figure 10. Examples of the applicability of NAA-PCs in chemo- and biosensing applications. (**a**) Dependence of position of PSB and anodization period of NAA-GIFs produced by SPA with digital pictures showing the interferometric colors displayed by these NAA-PCs. (**b**) Sensing process and description of sensing stages used to assess the affinity between drugs and human serum albumin using NAA-GIFs as sensing platforms. Reproduced from [77], with copyright permission from Royal Society of Chemistry, 2016.

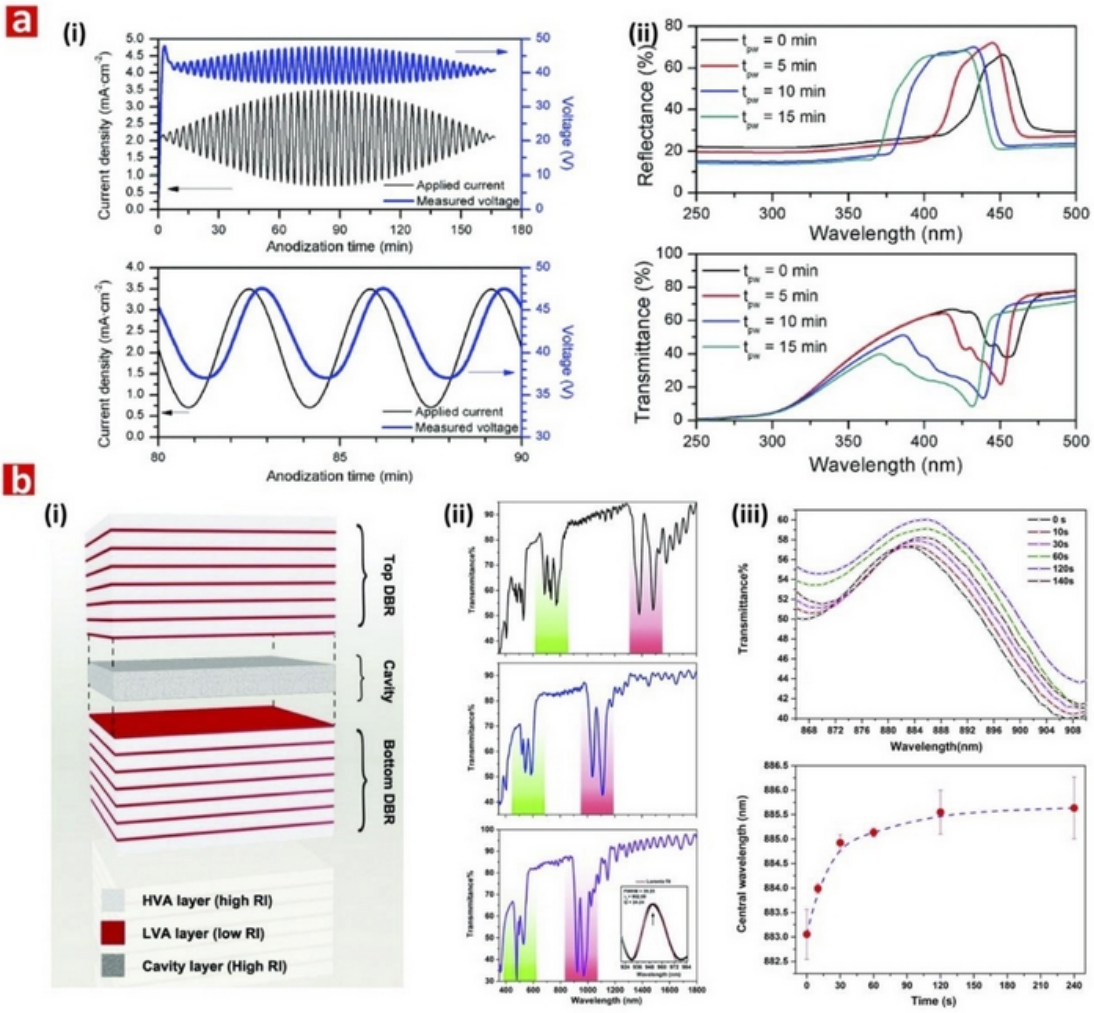

Figure 11. Examples of applicability of NAA-PCs in chemo- and biosensing applications. (**a**) (**i**) SPA profile used to produce NAA-GIFs and (**ii**) reflection and transmission spectra of NAA-GIFs as a function of the pore-widening time. Reproduced with permission from authors of a previous paper [81]. Copyright Springer, 2014. (**b**) (**i**) Schematic showing the structure of NAA-μCVs with two NAA-DBR mirrors and a layer of constant porosity in between, (**ii**) transmission spectrum of NAA-μCVs showing how the resonance band blue-shifts with the pore-widening time, and (**iii**) detection of humidity level based on red shifts in the resonance band of NAA-μCVs. Reproduced from [83], with copyright permission from American Chemical Society, 2015.

4.3. Nanoporous Anodic Alumina Optical Microcavities (NAA-μCVs)

NAA-μCVs are a class of NAA-PCs that confine electromagnetic waves to microvolumes by resonant recirculation of light. The nanoporous structure of NAA-μCVs is typically composed of two highly reflective mirrors (e.g., NAA-DBRs, NAA-GIFs, etc.) between which a physical cavity layer featuring straight cylindrical nanopores is sandwiched. However, other forms of NAA-μCV architecture have been demonstrated.

Wang et al. engineered two types of NAA-μCV architectures by stepwise pulse anodization in oxalic acid electrolyte (Figure 11b) [83]. These PCs were used as platforms to develop a humidity sensor. The resonance band within the characteristic PSB in the transmission spectra of NAA-μCVs underwent red shifts when the sensing platforms were exposed to water vapor at different time intervals. The condensation of water molecules within the nanoporous structure of NAA-μCVs modified the effective medium of these NAA-PCs, leading to a red shift of the resonance band position of 2.58 nm. This study established the foundation for the use of NAA-μCVs in gas sensing applications.

Yan et al. fabricated NAA-μCVs with a defect layer created by a constant voltage step in between a periodic sawtooth-like pulse voltage profile [84]. These NAA-PCs featured narrow resonance bands that were used as sensing parameter when the nanoporous network of NAA-μCVs was filled with liquids of different refractive index such as water, ethyl alcohol, and ethylene glycol. Shifts in the resonance band position upon infiltration were evaluated as a function of the refractive index of infiltrating medium. This sensing system was demonstrated to be capable of identifying analytes based on shifts in the resonance band position, with a sensitivity of 424.4 nm RIU^{-1}. Lee et al. engineered NAA-μCVs by tuning the electrolyte temperature during a stepwise pulse anodization process [82]. NAA-μCVs were immersed in a series of polar (i.e., water, anhydrous ethanol, and isopropyl alcohol) and nonpolar (i.e., *n*-hexane, cyclohexane, and trichloroethylene) analytical solutions and red shifts in the position of the characteristic resonance band were used to establish the sensing performance of the system. This refractometric sensor was found to have a sensitivity of 441 nm RIU^{-1}. The use of this sensing system as a colorimetric tool, based on structural color changes upon infiltration, was also demonstrated. NAA-μCVs were infiltrated with analytes of different refractive index such as air, water, isopropyl alcohol, cyclohexane, and trichloroethylene, which triggered dynamic colorimetric responses. Color changes were analyzed in terms of lightness and chromaticity in the CIELab 19,130 tristimulus color space. NAA-μCVs colorimetric sensors were able to detect refractive index differences of ~0.01 RIU, with a perceptual color change over the whole visible range. An et al. produced NAA-μCVs by a periodic pulse anodization approach with an effective voltage compensating strategy [239]. NAA-μCVs were chemically modified with rhodamine B by adsorption to form rhodamine B-NAA-μCVs composite sensing platforms. NAA-μCVs enhanced the photoluminescence intensity of the functional molecules absorbed onto the inner surface of NAA-μCVs. Although no sensing application was demonstrated, this system could potentially be used to develop PL-based sensors.

4.4. Nanoporous Anodic Alumina Fabry–Pérot Interferometers (NAA-FPIs)

NAA-FPIs feature straight cylindrical nanopores from top to bottom with a homogeneous distribution of effective refractive index. NAA-FPIs interfere constructively with electromagnetic waves, generating a characteristic interference pattern with distinctive fringes, which are a result of the Fabry–Pérot effect. Alterations of the effective medium of NAA-FPIs leads to shifts in their characteristic interference pattern, which can be used as sensing principle to create optical systems with broad applicability.

Kumeria et al. demonstrated the use of NAA-FPIs for optical sensing under both nonspecific and specific adsorption conditions [111]. NAA-FPIs were fabricated via two-step anodization in oxalic acid electrolyte. These NAA-PCs were exposed to different analytical solutions of glucose and their RIfS spectrum was analyzed to establish the effective optical thickness changes (ΔOT_{eff}) as a function of the refractive index of the glucose solution. The nonspecific infiltration of the effective medium of NAA-FPIs achieved an S = 18.42% RIU^{-1}, a *LLoD* of 0.084 RIU, and a R^2 of 0.998. NAA-FPIs were further assessed as chemically selective platforms for the detection of Hg^{2+}. The performance of this sensing system for selective Hg^{2+} detection was S = 0.0009% μM^{-1}, *LLoD* = 22.82 RIU, and R^2 = 0.854.

Law et al. developed a sensing system combining NAA-FPIs and RIfS to monitor gold–thiol interaction [123]. NAA-FPIs were functionalized with a range of thiol-containing with different molecular features and backbone sizes. The sensing performance of the system was evaluated using analyte solutions of gold ions, which have high affinity toward thiol functional groups. Shifts in the effective optical thickness of NAA-FPIs upon exposure to gold ions were used as sensing principle to establish the sensing characteristics of the system. The highest sensitivity value, 5.6 nm μM^{-1}, was achieved by NAA-FPIs featuring a dual functionalization of the inner and top surface with 6-amino-1-hexanethiol and 1,6-hexanedithiol, respectively. Rajeev et al. combined NAA-FPIs with RIfS to develop a biosensor for chronic wound care, using tumor necrosis factor-alpha (TNF-α) in buffer and simulated wound fluid as a biomarker [240]. The inner surface of NAA-FPIs was chemically modified

with anti-TNF-α antibodies via silanization to achieve selectivity toward TNF-α. The sensitivity of this sensing system for TNF-α in buffer, assessed through ΔOT_{eff} from varying TNF-α concentration, was determined to be 22.384 nm (ng $mL^{-1})^{-1}$, with a *LLoD* of 0.13 μg mL^{-1}. The selectivity and specificity of this biosensor to TNF-α was also verified in simulated wound fluid containing other interfering molecules.

The combination of NAA-FPIs with RIfS as a biosensing system to detect circulating tumor cells (CTC) was demonstrated by Kumeria et al. [241]. NAA-FPIs functionalized with biotinylated anti-EpCAM antibody through several surface modification steps have been used to detect Human pancreatic cancer cells (PANC-1) in whole blood and buffer. The different sensing stages were characterized in terms of ΔOT_{eff} and CTC concentration by RIfS. The developed sensor was capable of selective detection of cancer cells with a concentration range from 1000 to 100,000 cells mL^{-1}, with a *LLoD* < 1000 cells mL^{-1}. The sensing capabilities of NAA-FPIs combined with RIfS for gas sensing were assessed by Kumeria et al. [242]. The adsorption of hydrogen sulfide gas (H_2S) on gold-coated NAA-FPIs induced a concentration-dependence shift in the effective optical thickness of these films due to modification of the effective medium of these PC platforms. Real-time oral malodor monitoring was performed using the proposed device for a concentration range from 0.2 to 0.4 μg L^{-1}. Casanova et al. monitored gas adsorption and liquid desorption of organic vapors in NAA-FPIs using optical interferometry to demonstrate the potential of NAA-FPIs combined with RIfS as gas sensor [243]. The interaction of toluene and isopropanol with the nanopores were translated into ΔOT_{eff}. The sensing performance was found to be dependent on the partial pressure of the gas. This system was able to discern between different phase transitions such as monolayer–multilayer adsorption and capillary condensation. Santos et al. used a combination of NAA-FPIs and RIfS to monitor nonspecific and specific adsorption of glucose and L-cysteine, respectively [43]. A linear correlation between ΔOT_{eff} and the concentration of analytes adsorbed in NAA-FPIs established a sensitivity of 0.007% mM^{-1} with a *LLoD* of 100 mM under nonspecific adsorption conditions and a sensitivity of 0.026% mM^{-1} and *LLoD* of 5 mM under specific adsorption conditions.

Kumeria et al. presented an ultrasensitive NAA-FPI sensor to detect Au^{3+} ions in aqueous matrices using RIfS [119]. Chemical selectivity was attained by functionalizing the inner surface of NAA-FPIs with 3-mercaptopropyl-triethoxysilane (MPTES), which contain a thiol functional group with high affinity toward gold (III) ions. Interactions between gold ions and thiol functional groups induced ΔOT_{eff}, the magnitude of which was found to be dependent on the concentration of Au^{3+}. The proposed sensor had a working range from 0.1 to 80 μM with a sensitivity of 1.09 nm μM^{-1} and a *LLoD* of 0.1 μM. The chemical selectivity of the system toward Au^{3+} was verified through a series of selectivity tests with solutions containing potential interfering ions. Furthermore, the system's performance for real-life applications was demonstrated by detecting Au^{3+} in tap water and phosphate buffer solution. An interferometric sensor based on the combination of gelatin-functionalized NAA-FPIs and RIfS was developed by Nemati et al. for the selective detection of trypsin enzyme (Figure 12a,b) [244].

The selectivity, affinity, and specificity of gelatin-modified NAA-FPIs toward trypsin were verified by exposing a set of these PC platforms to nonspecific enzymes (i.e., chymotrypsin and horseradish peroxidase) as well as hemoglobin-modified NAA-PFIs to trypsin. The digestion of gelatin immobilized on the inner surface of NAA by trypsin enzyme was quantified by ΔOT_{eff} as a function of the concentration of trypsin. This enzymatic sensor achieved a sensitivity of −106.9 nm (mg $mL^{-1})^{-1}$, a *LLoD* of 0.025 mg mL^{-1}, and a R^2 of 0.9140. This system enabled the quantification of the kinetics of gelatin digestion (i.e., Michaelis–Menten parameters) by the reaction velocity, defined by ΔOT_{eff} and reaction time and the concentration of gelatin. Krismastuti et al. developed an enzymatic sensor combining NAA-FPIs and RIfS to detect levels of proteinase K (Figure 13a,b) [142]. The surface chemistry of NAA-FPIs was modified with polyelectrolytes by the LbL deposition technique. The enzymatic degradation of the LbL layers by proteinase K was characterized by ΔOT_{eff} as a function of exposure time and concentration of proteinase K. The sensitivity of the enzymatic sensor was 12.311 nm (mg $mL^{-1})^{-1}$ with a *LLoD* of 0.06 mg mL^{-1}. This sensor was also able to detect

the presence of proteinase K in human wound fluid, demonstrating the potential of this system for detection of bacterial infections in chronic wounds.

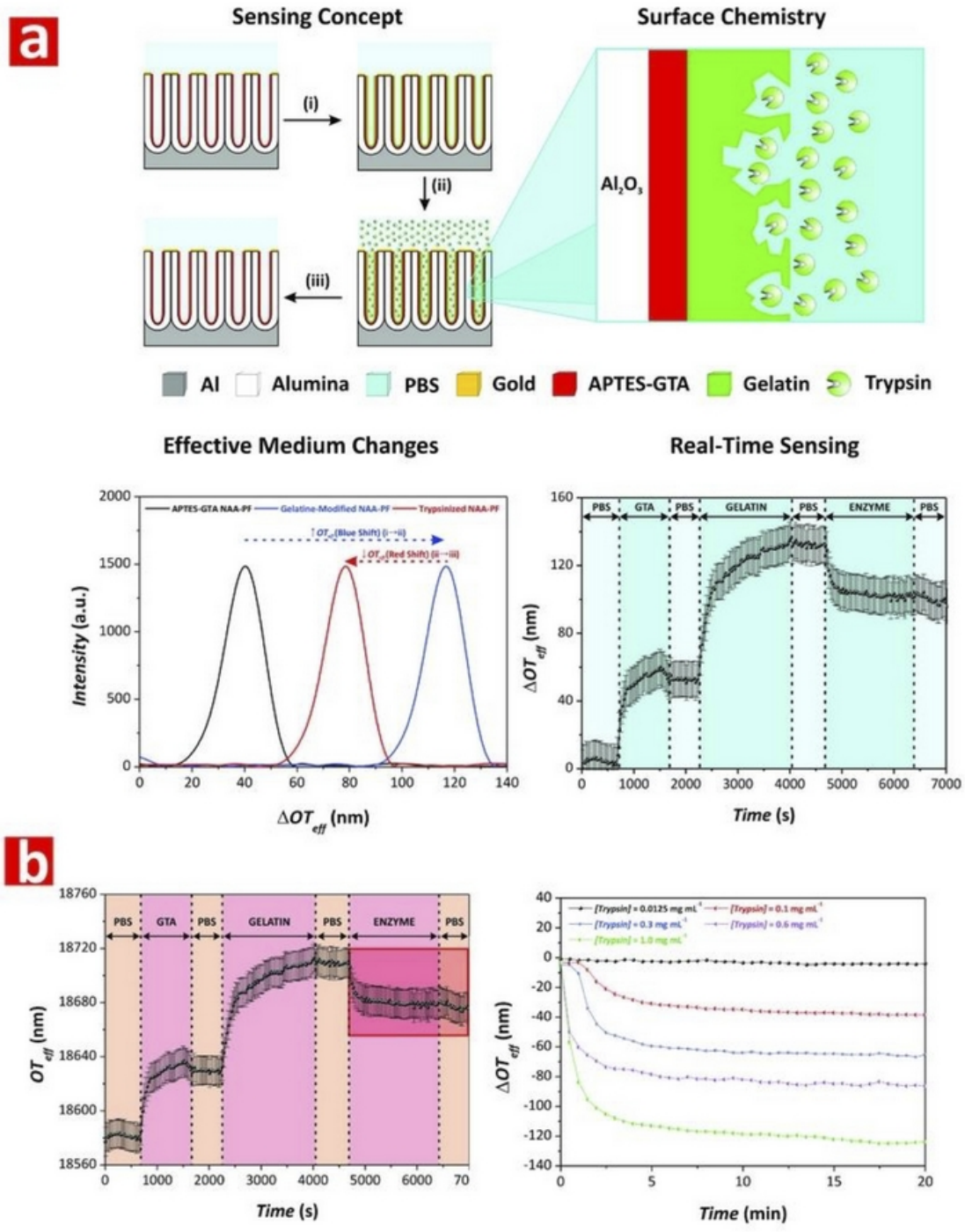

Figure 12. Examples of applicability of NAA-PCs in chemo- and biosensing applications. (**a**) Sensing concept, surface chemistry, and sensing principle for enzymatic sensor combining gelatin-functionalized NAA- Fabry–Perót interferometers (FPIs) and reflectometric interference spectroscopy (RIfS). (**b**) Real-time monitoring of effective optical thickness changes as a function of enzyme concentration. Reproduced from [244], with copyright permission from American Chemical Society, 2015.

Table 2. Characteristics and optical properties of representative NAA-PCs.

NAA-PC	Anodization *	Photonic Features	Refs. **
NAA-FPI	- One-step anodization - Two-step anodization	- Interference fringes (out-of-plane) - PSB (in-plane)	[43] [46–49] [111] [119] [125] [142] [240–244] [244]
NAA-μCV	- STPA with constant step between mirrors - SPA with constant step between mirrors - SATPA with constant step between mirrors - PSTPA with constant step, progressive variation of electrolyte temperature, or phase shift between mirrors	- Resonance band within PSB	[82–85] [239]
NAA-DBR	- STPA - PSTPA	- Broad PSB	[75] [81] [110,111] [231,232] [234,235]
NAA-GIF	- SPA - PSTPA	- Narrow PSB	[77] [80] [112] [171] [238]
Apo-NAA-DBR	- ASTPA	- Narrow PSB	[80] [85] [233]
Apo-NAA-GIF	- ASPA	- Ultra-narrow PSB	[78–81]
3D NAA-PC (DBR)	- SPA with final etching	- Broad PSB (in-plane and out-of-plane)	[75,76]
NAA-BPFs	- STPA - PSTPA - STPA + SPA	- Versatile PSB or PSB across the spectral regions	[79] [86]
NAA-LBPFs	- SPA with asymmetric etching	- Narrow PSB with position variable across the surface	[87]

* STPA = stepwise pulse anodization; SPA = sinusoidal pulse anodization; SATPA = sawtooth pulse anodization; PSTPA = pseudo-stepwise pulse anodization; ASTPA = apodized stepwise pulse anodization; ASPA = apodized sinusoidal pulse anodization. ** Representative references.

Lee et al. combined NAA-FPIs as biochip substrate with RIfS to design an optical sensor for quantification of β-galactosidase [245]. NAA-PFIs were functionalized with prolinker A via silane-linking chemistry. Blue shifts in the Fabry–Perót fringe pattern, due to molecular interactions, were translated into ΔOT_{eff} as a function of β-galactosidase concentration. This protein sensing system had a linear working range from 0.05 to 5 units enzyme mL^{-1} and a sensitivity of 39.04 nm (unit $mL^{-1})^{-1}$. Bae et al. fabricated a hybrid plasmon-coupled NAA-FPIs sensing system, where the sensing platforms were produced by conventional two-step anodization and coated with a layer of gold [246]. This sensing system was able to detect changes in the effective refractive index of NAA-FPIs upon infiltration of Cargille refractive index fluids, achieving a maximum sensitivity of 324 nm RIU^{-1}.

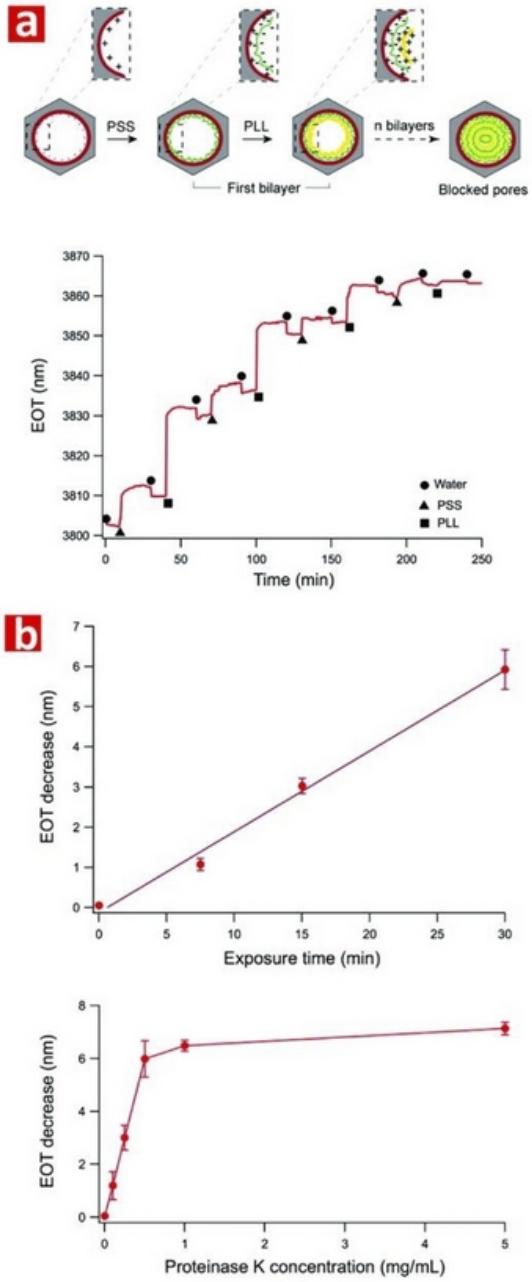

Figure 13. Examples of applicability of NAA-PCs in chemo- and biosensing applications. (**a**) Real-time monitoring of chemical functionalization of NAA-FPIs by polyelectrolyte layers using RIfS. (**b**) Sensing performance of enzymatic sensor as a function of exposure time and concentration upon digestion of polyelectrolyte layers. Reproduced from [142], with copyright permission from American Chemical Society, 2015.

Changes in the refractive index of the medium filling the nanopores produced visible shifts in the characteristic interferometric color of NAA-FPIs. Image analysis of these liquid-infiltrated NAA-FPIs was performed in the CIELab 1931 space as a function of Euclidean distance between two color points, which yielded a perceptual refractive index change (i.e., lower limit of colorimetric sensing performance) of 0.006. Santos et al. developed a photoluminescent enzymatic sensor using NAA-FPIs produced by two-step anodization in oxalic acid electrolyte as sensing platforms [247]. Functionalization of the inner surface of nanopores with trypsin was carried out through several stages,

which were monitored by the characteristic interferometric PL spectra in terms of number, intensity, and position of PL oscillations.

Each functionalization step yielded a shift in effective optical thickness of these NAA-FPIs obtained from the PL spectra. This methodology allowed accurate detection and quantification of immobilized enzyme within NAA-FPIs. Santos et al. developed a barcode system based on the characteristic PL spectrum of NAA-FPIs, in which shifts in the characteristic interferometric pattern of NAA-FPIs were used as a principle to develop a sensing system [13]. NAA-FPIs were infiltrated with glucose and oxazine dye, which caused red shifts in the position of the characteristic PL oscillations. Shifts in oscillations in the characteristic PL spectrum upon infiltration were translated into exclusive barcodes that characterize these processes. Santos et al. developed a PL-based sensor using NAA-FPI platforms for nonspecific and specific molecular adsorption [43]. Nonspecific interactions of NAA-FPIs with glucose were characterized by effective optical thickness changes measured from the interferometric pattern in the PL spectrum of NAA-FPIs. An analysis of these changes as a function of the concentration of glucose established a sensitivity of 0.013% mM^{-1} and *LLoD* of 0.01 M. The proposed sensor was also used to detect L-cysteine under specific adsorption conditions. The binding of L-cysteine, a model peptide, to silane-modified NAA-FPIs were monitored by ΔOT_{eff} quantified from the characteristic PL spectrum as a function of the concentration of L-cysteine. Under specific adsorption conditions, the proposed PL sensor had a sensitivity of 0.029% mM^{-1} and *LLoD* of 5 mM for L-cysteine. Ferro et al. combined NAA-FPIs with PL spectroscopy for glucose sensing, where the characteristic PL spectra of NAA-FPIs was monitored after immersion in solutions containing different concentrations of glucose [248]. A multivariate analysis was used to derive a quantitative model for glucose concentration determination and the *LLoD* of the sensing system was 0.01 mol L^{-1}. Trivinho-Strixino et al. developed a PL-based sensor using NAA-FPIs to detect commercial pesticide molecules [249]. NAA-PFIs were infiltrated with different concentrations of chloropyriphos pesticide and shifts in the characteristic PL spectra of these PC platforms were quantified. This analysis established a linear red shift of the characteristic PL band with increasing pesticide concentration, enabling the qualitative determination of pesticide.

4.5. Other Nanoporous Anodic Alumina Photonic Crystal Sensing Platforms

Law et al. combined NAA-PC platforms with RIfS to develop a sensing system able to monitor in real-time the formation of self-assembled monolayers of thiol molecules (Figure 14a,b) [123]. NAA-PCs with effective medium modulated in a sawtooth-like fashion were coated with gold and exposed to different concentrations of 11-mercaptoundecanoic acid (11-MUA). The gold–thiol interaction resulted in a shift in the characteristic PSB of these PCs the in RIfS spectra, which was found to red-shift with the concentration of 11-MUA. An analysis of this interaction revealed that it follows a Langmuir isotherm binding model.

The working range of this sensor was from 0.3125 to 1.25 mM: S = 8.88 nm mM^{-1}, *LLoD* = 0.3125 mM, and R^2 = 0.90. Yan et al. fabricated NAA-PCs with sinusoidally modulated nanopores, the sensitivity of which was assessed by infiltrating their nanoporous structure with analytes of different refractive index such as water, ethyl alcohol, ethylene glycol, and glycerol [250]. The sensitivity of these NAA-PCs was assessed using shifts in the position of the characteristic PSB upon infiltration. Shifts in the position of the PSB were found to follow a linear trend with increasing refractive index of the media filling the nanopores, with a sensitivity of 108.5 nm RIU^{-1}. Shang et al. developed NAA-PCs with narrow photonic stopbands produced by a modified two-step anodization process incorporating a step voltage compensation. The application of these PCs as sensing platforms for gas sensing was demonstrated [251]. When NAA-PCs were exposed to an increasing concentration of anhydrous ethanol gas, from 0 to 13.72 mmol L^{-1}, the PSB's position in the transmission spectra underwent a red shift of 66 nm. This red shift was also observed when NAA-PCs were exposed to a saturated ethanol gas environment for longer time. Using the same anodization approach, Shang et al. used these NAA-PCs to monitor the adsorption of organic molecules via capillary condensation [252].

The adsorption of ethanol, methanol, acetone, and toluene in both gas and liquid forms were monitored through shifts in the characteristic PSB of these PC structures. Their observations indicate that, upon saturation of condensed analyte molecules in the nanopores of NAA-PCs, the position of the PSB red-shifts whereas the transmission intensity is reduced.

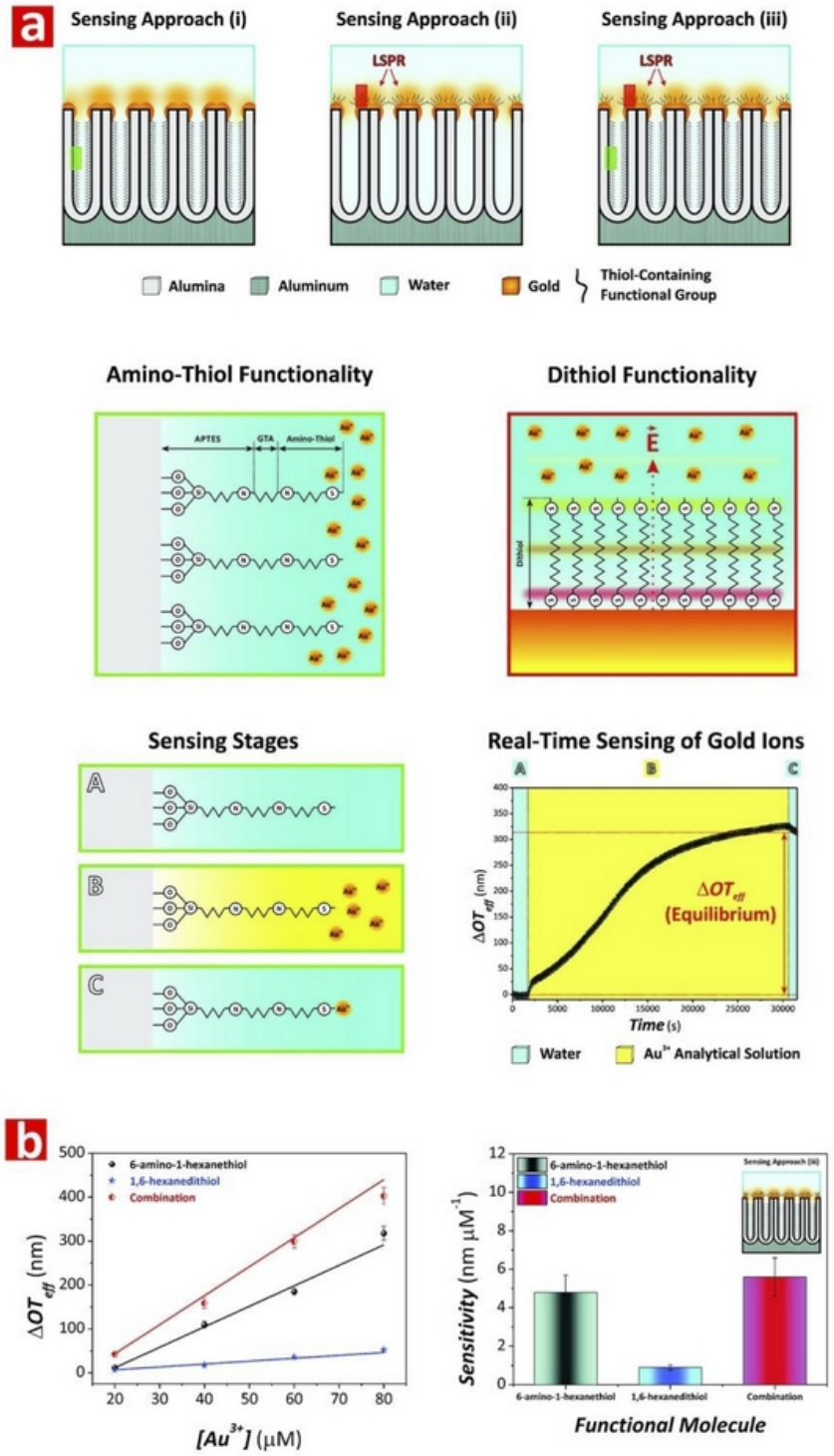

Figure 14. Examples of applicability of NAA-PCs in chemo- and biosensing applications. (**a**) Schematics showing the surface chemistry architecture and sensing concept of gold-modified NAA-FPIs for real-time sensing of gold ions. (**b**) Sensitivity as a function of the surface chemistry architecture in NAA-FPIs. Reproduced from [123], with copyright permission from American Chemical Society, 2017.

Table 3 collates the most representative systems combining NAA-PCs with different optical techniques, summarizing the sensing performances of these systems. These studies demonstrate that NAA-PCs are excellent sensing platforms due to their highly controllable and tunable effective medium and versatile surface chemistry, which can be precisely engineered to achieve outstanding performances for a broad range of chemo- and biosensing applications.

Table 3. Comparison of the sensing performance for representative optical sensing system using NAA-PCs.

Ref.	NAA-PC	Analyte	Sensing Technique *	*S*	*LLoD*
[231]	NAA-DBR	Au^{3+}	RIfS	22.2 nm μM^{-1}	0.16 µM
[232]	NAA-DBR	Vitamin C	RIfS	227 nm μM^{-1}	0.02 µM
[111]	NAA-DBR	Hg^{2+}	RIfS	0.0115 nm μM^{-1}	4.20 µM
[234]	NAA-DBR	Alkanes	TS	71.4 nm RIU^{-1}	-
[234]	NAA-DBR	Alcohols	TS	61.9 nm RIU^{-1}	-
[238]	NAA-GIF	D-glucose	RIfS	4.93 nm M^{-1}	0.01 M
[153]	NAA-GIF	Indomethacin	RIfS	0.63 nm mM^{-1}	65 µM
[172]	NAA-GIF	Indomethacin	RIfS	89.8 nm mM^{-1}	
[172]	NAA-GIF	Sulfadymethoxine	RIfS	5.50 nm mM^{-1}	-
[172]	NAA-GIF	Warfarin	RIfS	18.4 nm mM^{-1}	-
[172]	NAA-GIF	Coumarin	RIfS	8.30 nm mM^{-1}	-
[172]	NAA-GIF	Salicylic acid	RIfS	4.90 nm mM^{-1}	-
[112]	NAA-GIF	Hg^{2+}	RIfS	0.072 nm μM^{-1}	1 µM
[81]	NAA-GIF	Polar and nonpolar analytes	RS	441 nm RIU^{-1}	-
[83]	NAA-µCVs	Au^{3+}	RIfS	8.88 nm mM^{-1}	0.3125 mM
[111]	NAA-FPI	Glucose	RIfS	18.42% RIU^{-1}	0.084 RIU
[111]	NAA-FPI	Hg^{2+}	RIfS	0.0009% μM^{-1}	22.82 RIU
[123]	NAA-FPI	Au^{3+}	RIfS	5.6 nm μM^{-1}	
[240]	NAA-FPI	TNF-α	RIfS	22.384 nm $(ng\ mL^{-1})^{-1}$	0.13 µg mL^{-1}
[241]	NAA-FPI	Circulating tumour cells	RIfS	-	1000 cells mL^{-1}
[232]	NAA-FPI	D-glucose	RIfS	0.007% mM^{-1}	100 mM
[43]	NAA-FPI	L-cysteine	RIfS	0.026% mM^{-1}	5 mM
[113]	NAA-FPI	Au^{3+}	RIfS	1.09 nm μM^{-1}	0.1 µM
[244]	NAA-FPI	Tyrypsin	RIfS	−106.9 nm $(mg\ mL^{-1})^{-1}$	0.025 mg mL^{-1}
[142]	NAA-FPI	Proteinase K	RIfS	12.311 nm $(mg\ mL^{-1})^{-1}$	0.06 mg mL^{-1}
[245]	NAA-FPI	β-galactosidase	RIfS	39.04 nm $(unit\ mL^{-1})^{-1}$	0.05 units enzyme mL^{-1}
[43]	NAA-FPI	D-glucose	PL	0.013% mM^{-1}	0.01 M
[43]	NAA-FPI	L-cysteine	PL	0.029% mM^{-1}	5 mM

* RIfS = reflectometric interference spectroscopy, TS = transmission spectroscopy, RS = reflection spectroscopy, and PL = photoluminescence spectroscopy.

5. Conclusions

This review provides a comprehensive and up-to-date collation of fundamental and applied developments of nanoporous anodic alumina photonic crystals as optical platforms for chemo- and biosensing applications. Pioneering studies over the past two decades have demonstrated the potential of this nanoporous material to be integrated with different optical techniques to develop sensing systems with unique properties and capabilities. NAA provides an excellent PC platform due to its self-organized and highly controllable nanoporous structure, the optical properties of which can be precisely engineered by the fabrication conditions. The effective medium of NAA-PCs can be modulated in a multidimensional fashion to control light in different ways and utilize light–matter interactions at the nanoscale to achieve high sensitivity for different sensing applications. Furthermore, a broad range of chemical and physical methods can be used to engineer the surface chemistry of NAA-PCs to achieve chemical selectivity toward analytes and molecules of interest. Pioneering studies demonstrated the potential of NAA-PCs for optical applications and recent developments of rationally designed pulse-like anodization strategies have boosted the applicability of multidimensional NAA-PCs for chemo- and biosensing applications, providing new opportunities to develop optical systems based on different sensing principles (e.g., colorimetry, reflection, transmission, photoluminescence, etc.).

Anodization is a cost-competitive, simple, and fully scalable nanofabrication approach that enables the generation of NAA-PCs with finely tuned optical properties across the spectral regions, from UV to IR. However, more systematic theoretical and experimental investigations will be needed to fully develop the potential of this technology. NAA has intrinsic limitations such as its relatively low refractive index and its limited range of lattice constants. The design of novel anodization strategies and new NAA-PC architectures could overcome these intrinsic limitations and enable the development of PC platforms with unprecedented optical properties for sensing applications. Proof-of-concept studies have demonstrated the integration of NAA-PCs into fully functional optical sensing devices and lab-on-a-chip systems. However, more fundamental and applied research will be required to harness the potential of NAA-PC technology and utilize its unique properties to create practical devices and systems with optimal performances for real-world chemo- and biosensing applications. These systems will require the integration of NAA-PCs with other technologies such as microfabrication and microfluidics as well as new functionalization approaches to achieve high chemical selectivity toward analytes of interest.

As this review demonstrates, NAA-PC technology has huge potential and broad applicability for sensing applications. These photonic platform materials are an attractive technology to realize unique sensing concepts and devices that are distinctly different from and complementary to existing technologies such as porous silicon or inverted opals. It is thus expected that this highly dynamic and exciting field will continue to grow and spread toward more sophisticated PC structures, sensing concepts and applications.

Funding: This research was funded by the Australian Research Council (ARC) through the grant number CE140100003.

Acknowledgments: The authors would like to thank the following institutions for their support, the Australian Research Council (ARC), the School of Chemical Engineering, the University of Adelaide (DVCR 'Research for Impact' initiative), the Institute for Photonics and Advanced Sensing (IPAS), and the ARC Centre of Excellence for Nanoscale BioPhotonics (CNBP).

Conflicts of Interest: The authors declare no conflicts of interest.

References

1. Homola, J.; Yee, S.S.; Gauglitz, G. Surface plasmon resonance sensors: Review. *Sens. Actuators B Chem.* **1999**, *54*, 3–15. [CrossRef]
2. Holtz, J.H.; Asher, S.A. Polymerized colloidal crystal hydrogel films as intelligent chemical sensing materials. *Nature* **1997**, *389*, 829–832. [CrossRef]

3. Dickinson, T.A.; White, J.; Kauer, J.S.; Walt, D.R. A chemical-detecting system based on a cross-reactive optical sensor array. *Nature* **1996**, *382*, 697–700. [CrossRef] [PubMed]
4. Rosenstein, J.K.; Wanunu, M.; Merchant, C.A.; Drndic, M.; Shepard, K.L. Integrated nanopore sensing platform with sub-microsecond temporal resolution. *Nat. Methods* **2012**, *9*, 487–492. [CrossRef] [PubMed]
5. Miles, B.N.; Ivanov, A.P.; Wilson, K.A.; Dogan, F.; Japrung, D.; Edel, J.B. Single molecule sensing with solid-state nanopores: Novel materials, methods, and applications. *Chem. Soc. Rev.* **2013**, *42*, 15–28. [CrossRef] [PubMed]
6. Hotta, K.; Yamaguchi, A.; Teramae, N. Nanoporous waveguide sensor with optimized nanoarchitectures for highly sensitive label-free biosensing. *ACS Nano* **2012**, *6*, 1541–1547. [CrossRef] [PubMed]
7. Dhathathreyan, A. Real-time monitoring of invertase activity immobilized in nanoporous aluminum oxide. *J. Phys. Chem. B* **2011**, *115*, 6678–6682. [CrossRef] [PubMed]
8. Yeom, S.H.; Kim, O.G.; Kang, B.H.; Kim, K.J.; Yuan, H.; Kwon, D.H.; Kim, H.R.; Kang, S.W. Highly sensitive nano-porous lattice biosensor based on localized surface plasmon resonance and interference. *Opt. Express* **2011**, *19*, 22882–22891. [CrossRef] [PubMed]
9. Kim, D.K.; Kerman, K.; Saito, M.; Sathuluri, R.R.; Endo, T.; Yamamura, S.; Kwon, Y.S.; Tamiya, E. Label-free DNA biosensor based on localized surface plasmon resonance coupled with interferometry. *Anal. Chem.* **2007**, *79*, 1855–1864. [CrossRef] [PubMed]
10. Ko, H.; Tsukruk, V.V. Nanoparticle-decorated nanocanals for surface-enhanced Raman scattering. *Small* **2008**, *4*, 1980–1984. [CrossRef] [PubMed]
11. Lu, Z.; Ruan, W.; Yang, J.; Xu, W.; Zhao, C.; Zhao, B. Deposition of Ag nanoparticles on porous anodic alumna for surface enhanced Raman scattering substrate. *J. Raman Spectrosc.* **2009**, *40*, 112–116. [CrossRef]
12. Feng, C.L.; Zhong, X.; Steinhart, M.; Caminade, A.M.; Majoral, J.P.; Knoll, W. Graded-bandgap quantum-dot-modified nanotubes: A sensitive biosensor for enhanced detection of DNA hybridization. *Adv. Mater.* **2007**, *19*, 1933–1936. [CrossRef]
13. Santos, A.; Balderrama, V.S.; Alba, M.; Formentín, P.; Ferré-Borrull, J.; Pallarès, J.; Marsal, L.F. Nanoporous anodic alumina barcodes: Toward Smart optical biosensors. *Adv. Mater.* **2012**, *24*, 1050–1054. [CrossRef] [PubMed]
14. Dronov, R.; Jane, A.; Shapter, J.G.; Hodges, A.; Voelcker, N.H. Nanoporous alumina-based interferometric transducers ennobled. *Nanoscale* **2011**, *3*, 3109–3114. [CrossRef] [PubMed]
15. Alvarez, S.D.; Li, C.P.; Chiang, C.E.; Schuller, I.K.; Sailor, M.J. A label-free porous alumina interferometric immunosensor. *ACS Nano* **2009**, *3*, 3301–3307. [CrossRef] [PubMed]
16. López, C. Materials aspects of photonic crystals. *Adv. Mater.* **2003**, *15*, 1680–1704. [CrossRef]
17. Yablonovitch, E. Inhibited spontaneous emission in solid-state physics and electronics. *Phys. Rev. Lett.* **1987**, *58*, 2059. [CrossRef] [PubMed]
18. John, S. Strong localization of photons in certain disordered dielectric superlattices. *Phys. Rev. Lett.* **1987**, *58*, 2486. [CrossRef] [PubMed]
19. Xia, Y.; Gates, B.; Li, Z.-Y. Self-assembly approaches to three-dimensional photonic crystals. *Adv. Mater.* **2001**, *13*, 409–413. [CrossRef]
20. Von Freymann, G.; John, S.; Schulz-Dobrick, M.; Vekris, E.; Tétreault, N.; Wong, S.; Kitaev, V.; Ozin, G.A. Tungsten inverse opals: The influence of absorption on the photonic band structure in the visible spectral region. *Appl. Phys. Lett.* **2004**, *84*, 224–226. [CrossRef]
21. Chen, J.I.; Ozin, G.A. Heterogeneous photocatalysis with inverse titania opals: Probing structural and photonic effects. *J. Mater. Chem.* **2009**, *19*, 2675–2678. [CrossRef]
22. Curti, M.; Schneider, J.; Bahnemann, D.W.; Mendive, C.B. Inverse opal photonic crystals as a strategy to improve photocatalysis: Underexplored questions. *J. Phys. Chem. Lett.* **2015**, *6*, 3903–3910. [CrossRef] [PubMed]
23. Pace, S.; Vasani, R.B.; Zhao, W.; Perrier, S.; Voelcker, N.H. Photonic porous silicon as a pH sensor. *Nanoscale Res. Lett.* **2014**, *9*, 420. [CrossRef] [PubMed]
24. Aisyiyah Jenie, S.N.; Plush, S.E.; Voelcker, N.H. Singlet oxygen detection on a nanostructured porous silicon thin film via photonic luminescence enhancements. *Langmuir* **2017**, *33*, 8606–8613. [CrossRef] [PubMed]
25. Kilian, K.A.; Lai, L.M.H.; Magenau, A.; Cartland, S.; Böcking, T.; Di Girolamo, N.; Gal, M.; Gauss, K.; Gooding, J.J. Smart tissue culture: In situ monitoring of the activity of protease enzymes secreted from live cells using nanostructured photonic crystals. *Nano Lett.* **2009**, *9*, 2021–2025. [CrossRef] [PubMed]

26. Lin, V.S.-Y.; Motesharei, K.; Dancil, K.-P.S.; Sailor, M.J.; Ghadiri, M.R. A Porous Silicon-Based Optical Interferometric Biosensor. *Science* **1997**, *278*, 840–843. [CrossRef] [PubMed]
27. Janshoff, A.; Dancil, K.-P.S.; Steinem, C.; Greiner, D.P.; Lin, V.S.-Y.; Gurtner, C.; Motesharei, K.; Sailor, M.J.; Ghadiri, M.R. Macroporous p-Type Silicon Fabry–Perot Layers. Fabrication, Characterization, and Applications in Biosensing. *J. Am. Chem. Soc.* **1998**, *120*, 12108–12116. [CrossRef]
28. Lee, W.; Park, S.-J. Porous anodic aluminum oxide: Anodization and templated synthesis of functional nanostructures. *Chem. Rev.* **2014**, *114*, 7487–7556. [CrossRef] [PubMed]
29. Santos, A. Nanoporous anodic alumina photonic crystals: Fundamentals, developments and perspectives. *J. Mater. Chem. C* **2017**, *5*, 5581–5599. [CrossRef]
30. Masuda, H.; Fukuda, K. Ordered metal nanohole arrays made by a two-step replication of honeycomb structures of anodic alumina. *Science* **1995**, *268*, 1466–1468. [CrossRef] [PubMed]
31. Masuda, H.; Hasegwa, F. Self-ordering of cell arrangement of anodic porous alumina formed in sulfuric acid solution. *J. Electrochem. Soc.* **1997**, *144*, L127–L130. [CrossRef]
32. Masuda, H.; Yada, K.; Osaka, A. Self-ordering of cell configuration of anodic porous alumina with large-size pores in phosphoric acid solution. *Jpn. J. Appl. Phys.* **1998**, *37*, L1340–L1342. [CrossRef]
33. Lee, W.; Ji, R.; Gösele, U.; Nielsch, K. Fast fabrication of long-range ordered porous alumina membranes by hard anodization. *Nat. Mater.* **2006**, *5*, 741–747. [CrossRef] [PubMed]
34. Santos, A.; Kumeria, T.; Losic, D. Nanoporous anodic alumina: A versatile platform for optical biosensors. *Materials* **2014**, *7*, 4297–4320. [CrossRef] [PubMed]
35. Jani, A.M.M.; Losic, D.; Voelcker, N.H. Nanoporous anodic aluminium oxide: Advances in surface engineering and emerging applications. *Prog. Mater. Sci.* **2013**, *58*, 636–704. [CrossRef]
36. Marsal, L.F.; Vojkuvka, L.; Formentin, P.; Pallarés, J.; Ferré-Borrull, J. Fabrication and optical characterization of nanoporous alumina films annealed at different temperatures. *Opt. Mater.* **2009**, *31*, 860–864. [CrossRef]
37. Vrublevsky, I.; Jagminas, A.; Hemeltjen, S.; Goedel, W. Photoluminescence behavior of heat-treated porous alumina films formed in malonic acid. *Appl. Surf. Sci.* **2010**, *256*, 2013–2017. [CrossRef]
38. Stojadinovic, S.; Nedic, Z.; Belca, I.; Vasilic, R.; Kasalica, B.; Petkovic, M.; Zekovic, L.J. The effect of annealing on the photoluminescence and optical properties of porous anodic alumina films formed in sulfamic acid. *Appl. Surf. Sci.* **2009**, *256*, 763–767. [CrossRef]
39. Santos, A.; Alba, M.; Rahman, M.M.; Formentín, P.; Ferré-Borrull, J.; Pallarès, J.; Marsal, L.F. Structural tuning of photoluminescence in nanoporous anodic alumina by hard anodization in oxalic and malonic acids. *Nanoscale Res. Lett.* **2012**, *7*, 228. [CrossRef] [PubMed]
40. Gardelis, S.; Nassiopoulou, A.G.; Gianneta, V.; Theodoropoulou, M. Photoluminescence-induced oscillations in porous anodic aluminum oxide films grown on Si: Effect of the interface and porosity. *J. Appl. Phys.* **2010**, *107*, 113104. [CrossRef]
41. Huang, K.; Pu, L.; Shi, Y.; Han, P.; Zhang, R.; Zheng, Y.D. Photoluminescence oscillations in porous alumina films. *Appl. Phys. Lett.* **2006**, *89*, 201118. [CrossRef]
42. Cantelli, L.; Santos, J.S.; Trivinho-Strixino, F. The effect of anodization temperature on optical properties of nanoporous anodic alumina (NAA) films. *J. Electroanal. Chem.* **2016**, *780*, 386–390. [CrossRef]
43. Santos, A.; Kumeria, T.; Losic, D. Optically optimized photoluminescent and interferometric biosensors based on nanoporous anodic alumina: A comparison. *Anal. Chem.* **2013**, *85*, 7904–7911. [CrossRef] [PubMed]
44. Theiβ, W.; Henkel, S.; Arntzen, M. Connecting microscopic and macroscopic properties of porous media: Choosing appropriate effective medium concepts. *Thin Solid Films* **1995**, *255*, 177–180. [CrossRef]
45. Yao, J.; Liu, Z.; Liu, Y.; Wang, Y.; Sun, C.; Bartal, G.; Stacy, A.M.; Zhang, X. Optical negative refraction in bulk metamaterials of nanowires. *Science* **2008**, *321*, 930. [CrossRef] [PubMed]
46. Masuda, H.; Ohya, M.; Asoh, H.; Nakao, M.; Nohtomi, M.; Tamamura, T. Photonic cristal using anodic porous alumina. *Jpn. J. Appl. Phys.* **1999**, *38*, L1403–L1405. [CrossRef]
47. Masuda, H.; Ohya, M.; Nishio, K.; Asoh, H.; Nakao, M.; Nohtomi, M.; Yokoo, A.; Tamamura, T. Photonic band gap in anodic porous alumina with extremely high aspect ratio formed in phosphoric acid solution. *Jpn. J. Appl. Phys.* **2000**, *39*, L1039–L1041. [CrossRef]
48. Masuda, H.; Ohya, M.; Asoh, H.; Nishio, K. Photonic band gap in naturally occurring ordered anodic porous alumina. *Jpn. J. Appl. Phys.* **2001**, *40*, L1217–L1219. [CrossRef]
49. Choi, J.; Luo, Y.; Wehrspohn, R.B.; Hillebrand, R.; Schilling, J.; Gösele, U. Perfect two-dimensional porous anodic alumina photonic crystal with duplex oxide layers. *J. Appl. Phys.* **2003**, *8*, 4757–4762. [CrossRef]

50. Kondo, R.; Kikuchi, T.; Natsui, S.; Suzuki, R.O. Fabrication of self-ordered porous alumina via anodizing in sulfate solutions. *Mater. Lett.* **2016**, *183*, 285–289. [CrossRef]
51. Nishinaga, O.; Kikuchi, T.; Natsui, S.; Suzuki, R.O. Rapid fabrication of self-ordered porous alumina with 10-/ sub-10-nm-scale nanostructures by selenic acid anodizing. *Sci. Rep.* **2013**, *3*, 2748. [CrossRef] [PubMed]
52. Takenaga, A.; Kikuchi, T.; Natsui, S.; Suzuki, R.O. Exploration for the self-ordering of porous alumina fabricated via anodizing in etidronic acid. *Electrochim. Acta* **2016**, *211*, 515–523. [CrossRef]
53. Kikuchi, T.; Yamamoto, T.; Suzuki, R.O. Growth behavior of anodic porous alumina formed in malic acid solution. *Appl. Surf. Sci.* **2013**, *284*, 907–913. [CrossRef]
54. Akiya, S.; Kikuchi, T.; Natsui, S.; Sakaguchi, N.; Suzuki, R.O. Self-ordered porous alumina fabricated via phosphonic acid anodizing. *Electrochim. Acta* **2016**, *190*, 471–479. [CrossRef]
55. Akiya, S.; Kikuchi, T.; Natsui, S.; Suzuki, R.O. Optimum exploration for the self-ordering of anodic porous alumina formed via selenic acid anodizing. *J. Electrochem. Soc.* **2015**, *162*, E244–E250. [CrossRef]
56. Takenaga, A.; Kikuchi, T.; Natsui, S.; Suzuki, R.O. Self-ordered aluminum anodizing in phosphonoacetic acid and its structural coloration. *ECS Solid State Lett.* **2015**, *4*, P55–P58. [CrossRef]
57. Kikuchi, T.; Nishinaga, O.; Natsui, S.; Suzuki, R.O. Fabrication of self-ordered porous alumina via etidronic acid anodizing and structural color generation from submicrometer-scale dimple array. *Electrochim. Acta* **2015**, *156*, 235–243. [CrossRef]
58. Nakajima, D.; Kikuchi, T.; Natsui, S.; Suzuki, R.O. Growth behavior of anodic oxide formed by aluminum anodizing in glutaric and its derivative acid electrolytes. *Appl. Surf. Sci.* **2014**, *321*, 364–370. [CrossRef]
59. Kikuchi, T.; Nishinaga, O.; Natsui, S.; Suzuki, R.O. Self-ordering behavior of anodic porous alumina via selenic acid anodizing. *Electrochim. Acta* **2014**, *137*, 728–735. [CrossRef]
60. Kikuchi, T.; Nakajima, D.; Kawashima, J.; Natsui, S.; Suzuki, R.O. Fabrication of anodic porous alumina via anodizing in cyclic oxocarbon acids. *Appl. Surf. Sci.* **2014**, *313*, 276–285. [CrossRef]
61. Kikuchi, T.; Yamamoto, T.; Natsui, S.; Suzuki, R.O. Fabrication of anodic porous alumina by squaric acid anodizing. *Electrochim. Acta* **2014**, *123*, 14–22. [CrossRef]
62. Jessensky, O.; Müller, F.; Gösele, U. Self-organized formation of hexagonal pore arrays in anodic alumina. *Appl. Phys. Lett.* **1998**, *72*, 1173–1175. [CrossRef]
63. Lee, W.; Nielsch, K.; Gösele, U. Self-ordering behavior of nanoporous anodic aluminum oxide (AAO) in malonic acid anodization. *Nanotechnology* **2007**, *18*, 475713. [CrossRef]
64. Vega, V.; García, J.; Montero-Moreno, J.M.; Hernando, B.; Bachmann, J.; Prida, V.M.; Nielsh, K. Unveiling the hard anodization regime of aluminum: Insight into nanopores self-organization and growth mechanism. *ACS Appl. Mater. Interfaces* **2015**, *7*, 28682–28692. [CrossRef] [PubMed]
65. O'Sullivan, J.P.; Wood, G.C. The morphology and mechanism of formation of porous anodic films on aluminium. *Proc. R. Soc. Lond. Ser. A* **1970**, *317*, 511–543. [CrossRef]
66. Sulka, G.D.; Parkoła, K.G. Temperature influence on well-ordered nanopore structures grown by anodization of aluminium in sulphuric acid. *Electrochim. Acta* **2007**, *52*, 1880–1888. [CrossRef]
67. Vrublevsky, I.; Parkoun, V.; Schreckenbach, J. Analysis of porous oxide film growth on aluminum in phosphoric acid using re-anodizing. *Appl. Surf. Sci.* **2005**, *242*, 333–338. [CrossRef]
68. Furneaux, R.C.; Rigby, W.R.; Davidson, A.P. The formation of controlled-porosity membranes from anodically oxidized aluminium. *Nature* **1989**, *337*, 147–149. [CrossRef]
69. Cheng, W.; Steinhart, M.; Gösele, U.; Wehrspohn, R.B. Tree-like alumina nanopores generated in a non-steady-state anodization. *J. Mater. Chem.* **2007**, *17*, 3493–3495. [CrossRef]
70. Montero-Moreno, J.M.; Belenguer, M.; Sarret, M.; Müller, C.M. Production of alumina templates suitable for electrodeposition of nanostructures using stepped techniques. *Electrochim. Acta* **2009**, *54*, 2529–2535. [CrossRef]
71. Lee, W.; Kim, J.-C. Highly ordered porous alumina with tailor-made pore structures fabricated by pulse anodization. *Nanotechnology* **2010**, *21*, 485304. [CrossRef] [PubMed]
72. Lee, W.; Schwirn, K.; Steinhart, M.; Pippel, E.; Scholz, R.; Gösele, U. Structural engineering of nanoporous anodic aluminium oxide by pulse anodization of aluminium. *Nat. Nanotechnol.* **2008**, *3*, 234–239. [CrossRef] [PubMed]
73. Lee, W.; Scholz, R.; Gösele, U. A continuous process for structurally well-defined AlO nanotubes based on pulse anodization of aluminum. *Nano Lett.* **2008**, *8*, 2155–2160. [CrossRef] [PubMed]

74. Lee, W.; Kim, J.C.; Gösele, U. Spontaneous current oscillations during hard anodization of aluminum under potentiostatic conditions. *Adv. Funct. Mater.* **2009**, *19*, 1–7. [CrossRef]
75. Sulka, G.D.; Hnida, K. Distributed Bragg reflector based on porous anodic alumina fabricated by pulse anodization. *Nanotechnology* **2012**, *23*, 075303. [CrossRef] [PubMed]
76. Martín, J.; Martín-González, M.; Fernández, J.F.; Caballero-Calero, O. Ordered three-dimensional interconnected nanoarchitectures in anodic porous alumina. *Nat. Commun.* **2014**, *5*, 5130. [CrossRef] [PubMed]
77. Santos, A.; Yoo, J.H.; Rohatgi, C.V.; Kumeria, T.; Wang., Y.; Losic, D. Realisation and advanced engineering of true optical rugate filters based on nanoporous anodic alumina by sinusoidal pulse anodization. *Nanoscale* **2016**, *8*, 1360–1373. [CrossRef] [PubMed]
78. Santos, A.; Law, C.S.; Lei, D.W.C.; Pereira, T.; Losic, D. Fine tuning of optical signals in nanoporous anodic alumina photonic crystals by apodized sinusoidal pulse anodization. *Nanoscale* **2016**, *8*, 18360–18375. [CrossRef] [PubMed]
79. Lim, S.Y.; Law, C.S.; Marsal, L.F.; Santos, A. Engineering of hybrid nanoporous anodic alumina photonic crystals by heterogeneous pulse anodization. *Sci. Rep.* **2018**, *8*, 9455. [CrossRef] [PubMed]
80. Law, C.S.; Lim, S.Y.; Santos, A. Fine tuning of transmission features in nanoporous anodic alumina distributed Bragg reflectors. *Proc. SPIE Nanophotonics Australas.* **2018**, *10456*, 1045659.
81. Macias, G.; Ferré-Borrull, J.; Pallarès, J.; Marsal, L.F. 1-D nanoporous anodic alumina rugate filters by means of small current variations for real-time sensing applications. *Nanoscale Res. Lett.* **2014**, *9*, 315. [CrossRef] [PubMed]
82. Lee, J.; Bae, K.; Kang, G.; Choi, M.; Baek, S.; Yoo, D.-S.; Lee, C.-W.; Kim, K. Graded-lattice AAO photonic crystal heterostructure for high *Q* refractive index sensing. *RSC Adv.* **2015**, *5*, 71770–71777. [CrossRef]
83. Wang, Y.; Chen, Y.; Kumeria, T.; Ding, F.; Evdokiou, A.; Losic, D.; Santos, A. Facile synthesis of optical microcavities by a rationally designed anodization approach: tailoring photonic signals by nanopore structure. *ACS Appl. Mater. Interfaces* **2015**, *7*, 9879–9888. [CrossRef] [PubMed]
84. Yan, P.; Fei, G.-T.; Li, H.; Shang, G.-L.; Wu, B.; Zhang, L.-D. Alumina photonic crystals with defect modes for sensor application. *Chin. J. Chem. Phys.* **2014**, *27*, 121–124. [CrossRef]
85. Law, C.S.; Lim, S.Y.; Macalincag, R.M.; Abell, A.D.; Santos, A. Light-confining nanoporous anodic alumina microcavities by apodized stepwise pulse anodization. *ACS Appl. Nano Mater.* **2018**, *1*, 4418–4434. [CrossRef]
86. Santos, A.; Pereira, T.; Law, C.S.; Losic, D. Rational engineering of nanoporous anodic alumina optical bandpass filters. *Nanoscale* **2016**, *8*, 14846–14857. [CrossRef] [PubMed]
87. Sukarno; Law, C.S.; Santos, A. Realisation and optical engineering of linear variable bandpass filters in nanoporous anodic alumina photonic crystals. *Nanoscale* **2017**, *9*, 7541–7550. [CrossRef] [PubMed]
88. Santos, A.; Kumeria, T.; Losic, D. Nanoporous anodic aluminum oxide for chemical sensing and biosensors. *TrAC Trend. Anal. Chem.* **2013**, *44*, 25–38. [CrossRef]
89. Yamamoto, Y.; Baba, N.; Tajima, S. Coloured materials and photoluminescence centres in anodic film on aluminium. *Nature* **1981**, *289*, 572. [CrossRef]
90. Santos, A.; Kumeria, T.; Wang, Y.; Losic, D. In situ monitored engineering of inverted nanoporous anodic alumina funnels: On the precise generation of 3D optical nanostructures. *Nanoscale* **2014**, *6*, 9991–9999. [CrossRef] [PubMed]
91. Jani, A.M.M.; Yazid, H.; Habiballah, A.S.; Mahmud, A.H.; Losic, D. Soft and hard surface manipulation of nanoporous anodic aluminum oxide (AAO). In *Nanoporous Alumina: Fabrication, Structure, Properties and Applications*; Losic, D., Santos, A., Eds.; Springer International Publishing: Cham, Switzerland, 2015; pp. 155–184. ISBN 978-3-319-20334-8.
92. Xifre-Perez, E.; Ferre-Borrull, J.; Pallares, J.; Marsal, L.F. Mesoporous alumina as a biomaterial for biomedical applications. *Mesoporous Biomater.* **2015**, *2*, 13–32. [CrossRef]
93. Chaki, N.K.; Vijayamohanan, K. Self-assembled monolayers as a tunable platform for biosensor applications. *Biosens. Bioelectron.* **2002**, *17*, 1–12. [CrossRef]
94. Tao, Y.T. Structural comparison of self-assembled monolayers of n-alkanoic acids on the surfaces of silver, copper, and aluminum. *J. Am. Chem. Soc.* **1993**, *115*, 4350–4358. [CrossRef]
95. Lang, P.; Mottaghi, D.; Lacaze, P.C. On the relationship between the structure of self-assembled carboxylic acid monolayers on alumina and the organization and electrical properties of a pentacene thin film. *Appl. Surf. Sci.* **2016**, *365*, 364–375. [CrossRef]

96. Alexander, S.; Morrow, L.; Lord, A.M.; Dunnill, C.W.; Barron, A.R. pH-responsive octylamine coupling modification of carboxylated aluminium oxide surfaces. *J. Mater. Chem. A* **2015**, *3*, 10052–10059. [CrossRef]
97. Debrassi, A.; Ribbera, A.; de Vos, W.M.; Wennekes, T.; Zuilhof, H. Stability of (bio) functionalized porous aluminum oxide. *Langmuir* **2014**, *30*, 1311–1320. [CrossRef] [PubMed]
98. Cheow, P.S.; Liu, L.; Toh, C.S. Grafting of nanoporous alumina membranes and films with organic acids. *Surf. Interface Anal.* **2007**, *39*, 601–610. [CrossRef]
99. Cichomski, M.; Kośla, K.; Grobelny, J.; Kozłowski, W.; Szmaja, W. Tribological and stability investigations of alkylphosphonic acids on alumina surface. *Appl. Surf. Sci.* **2013**, *273*, 570–577. [CrossRef]
100. Gao, W.; Dickinson, L.; Grozinger, C.; Morin, F.G.; Reven, L. Self-assembled monolayers of alkylphosphonic acids on metal oxides. *Langmuir* **1996**, *12*, 6429–6435. [CrossRef]
101. Zhao, R.; Rupper, P.; Gaan, S. Recent development in phosphonic acid-based organic coatings on aluminum. *Coatings* **2017**, *7*, 133. [CrossRef]
102. Lee, J.; Bong, J.; Ha, Y.G.; Park, S.; Ju, S. Durability of self-assembled monolayers on aluminum oxide surface for determining surface wettability. *Appl. Surf. Sci.* **2015**, *330*, 445–448. [CrossRef]
103. Phung, L.; Kleinert, H.; Füssel, U.; Duc, L.; Rammelt, U.; Plieth, W. Influence of self-assembling adhesion promoter on the properties of the epoxy/aluminium interphase. *Int. J. Adhes. Adhes.* **2005**, *25*, 239–245. [CrossRef]
104. Jaehne, E.; Oberoi, S.; Adler, H.J.P. Ultra thin layers as new concepts for corrosion inhibition and adhesion promotion. *Prog. Org. Coat.* **2008**, *61*, 211–223. [CrossRef]
105. Kant, K.; Yu, J.; Priest, C.; Shapter, J.G.; Losic, D. Impedance nanopore biosensor: Influence of pore dimensions on biosensing performance. *Analyst* **2014**, *139*, 1134–1140. [CrossRef] [PubMed]
106. Kumeria, T.; Santos, A.; Losic, D. Nanoporous anodic alumina platforms: Engineered surface chemistry and structure for optical sensing applications. *Sensors* **2014**, *14*, 11878–11918. [CrossRef] [PubMed]
107. Norek, M.; Krasiński, A. Controlling of water wettability by structural and chemical modification of porous anodic alumina (PAA): Towards super-hydrophobic surfaces. *Surf. Coat. Tech.* **2015**, *276*, 464–470. [CrossRef]
108. Velleman, L.; Triani, G.; Evans, P.J.; Shapter, J.G.; Losic, D. Structural and chemical modification of porous alumina membranes. *Microporous Mesoporous Mater.* **2009**, *126*, 87–94. [CrossRef]
109. Tian, F.; Lyu, J.; Shi, J.; Tan, F.; Yang, M. A polymeric microfluidic device integrated with nanoporous alumina membranes for simultaneous detection of multiple foodborne pathogens. *Sens. Actuators B Chem.* **2016**, *225*, 312–318. [CrossRef]
110. Chen, Y.; Santos, A.; Wang, Y.; Kumeria, T.; Ho, D.; Li, J.; Wang, C.; Losic, D. Rational design of photonic dust from nanoporous anodic alumina films: A versatile photonic nanotool for visual sensing. *Sci. Rep.* **2015**, *5*, 12893. [CrossRef] [PubMed]
111. Kumeria, T.; Santos, A.; Rahman, M.M.; Ferré-Borrull, J.; Marsal, L.F.; Losic, D. Advanced structural engineering of nanoporous photonic structures: Tailoring nanopore architecture to enhance sensing properties. *ACS Photonics* **2014**, *1*, 1298–1306. [CrossRef]
112. Kumeria, T.; Rahman, M.M.; Santos, A.; Ferré-Borrull, J.; Marsal, L.F.; Losic, D. Nanoporous anodic alumina rugate filters for sensing of ionic mercury: Toward environmental point-of-analysis systems. *ACS Appl. Mater Inter.* **2014**, *6*, 12971–12978. [CrossRef] [PubMed]
113. Kumeria, T.; Santos, A.; Losic, D. Ultrasensitive nanoporous interferometric sensor for label-free detection of gold (III) ions. *ACS Appl. Mater. Interfaces* **2013**, *5*, 11783–11790. [CrossRef] [PubMed]
114. De la Escosura-Muñiz, A.; Espinoza-Castañeda, M.; Chamorro-Garcia, A.; Rodríguez-Hernández, C.J.; de Torres, C.; Merkoçi, A. In situ monitoring of PTHLH secretion in neuroblastoma cells cultured onto nanoporous membranes. *Biosens. Bioelectron.* **2018**, *107*, 62–68. [CrossRef] [PubMed]
115. Pla, L.; Xifré-Pérez, E.; Ribes, À.; Aznar, E.; Marcos, M.D.; Marsal, L.F.; Martínez-Máñez, R.; Sancenón, F. A mycoplasma genomic DNA probe using gated nanoporous anodic alumina. *Chempluschem* **2017**, *82*, 337–341. [CrossRef]
116. Li, P.-F.; Xie, R.; Jiang, J.-C.; Meng, T.; Yang, M.; Ju, X.-J.; Yang, L.; Chu, L.-Y. Thermo-responsive gating membranes with controllable length and density of poly (n-isopropylacrylamide) chains grafted by ATRP method. *J. Membr. Sci.* **2009**, *337*, 310–317. [CrossRef]
117. Huo, X.-L.; Yang, H.; Zhao, W.; Xu, J.-J.; Chen, H.-Y. Nanopore-based electrochemiluminescence for detection of microRNAs via duplex-specific nuclease-assisted target recycling. *ACS Appl. Mater. Interfaces* **2017**, *9*, 33360–33367. [CrossRef] [PubMed]

118. Jani, A.M.M.; Anglin, E.J.; McInnes, S.J.; Losic, D.; Shapter, J.G.; Voelcker, N.H. Nanoporous anodic aluminium oxide membranes with layered surface chemistry. *Chem. Commun.* **2009**, 3062–3064. [CrossRef] [PubMed]
119. Jani, A.M.M.; Kempson, I.M.; Losic, D.; Voelcker, N.H. Dressing in layers: Layering surface functionalities in nanoporous aluminum oxide membranes. *Angew. Chem. Int. Ed.* **2010**, *49*, 7933–7937. [CrossRef] [PubMed]
120. Law, C.S.; Santos, A.; Nemati, M.; Losic, D. Structural engineering of nanoporous anodic alumina photonic crystals by sawtooth-like pulse anodization. *ACS Appl. Mater. Interfaces* **2016**, *8*, 13542–13554. [CrossRef] [PubMed]
121. Lim, L.; Ng, B.; Fu, C.; Tobing, L.Y.; Zhang, D. Highly sensitive and scalable AAO-based nano-fibre SERS substrate for sensing application. *Nanotechnology* **2017**, *28*, 235302. [CrossRef] [PubMed]
122. Proux-Delrouyre, V.; Elie, C.; Laval, J.-M.; Moiroux, J.; Bourdillon, C. Formation of tethered and streptavidin-supported lipid bilayers on a microporous electrode for the reconstitution of membranes of large surface area. *Langmuir* **2002**, *18*, 3263–3272. [CrossRef]
123. Law, C.S.; Sylvia, G.M.; Nemati, M.; Yu, J.; Losic, D.; Abell, A.D.; Santos, A. Engineering of surface chemistry for enhanced sensitivity in nanoporous interferometric sensing platforms. *ACS Appl. Mater. Interfaces* **2017**, *9*, 8929–8940. [CrossRef] [PubMed]
124. Bhairamadgi, N.S.; Pujari, S.P.; Trovela, F.G.; Debrassi, A.; Khamis, A.A.; Alonso, J.M.; Al Zahrani, A.A.; Wennekes, T.; Al-Turaif, H.A.; van Rijn, C. Hydrolytic and thermal stability of organic monolayers on various inorganic substrates. *Langmuir* **2014**, *30*, 5829–5839. [CrossRef] [PubMed]
125. Ter Maat, J.; Regeling, R.; Ingham, C.J.; Weijers, C.A.; Giesbers, M.; de Vos, W.M.; Zuilhof, H. Organic modification and subsequent biofunctionalization of porous anodic alumina using terminal alkynes. *Langmuir* **2011**, *27*, 13606–13617. [CrossRef] [PubMed]
126. Queffélec, C.; Petit, M.; Janvier, P.; Knight, D.A.; Bujoli, B. Surface modification using phosphonic acids and esters. *Chem. Rev.* **2012**, *112*, 3777–3807. [CrossRef] [PubMed]
127. Chinwangso, P.; Jamison, A.C.; Lee, T.R. Multidentate adsorbates for self-assembled monolayer films. *Accounts Chem. Res.* **2011**, *44*, 511–519. [CrossRef] [PubMed]
128. Largueze, J.-B.; El Kirat, K.; Morandat, S. Preparation of an electrochemical biosensor based on lipid membranes in nanoporous alumina. *Colloids Surf. B* **2010**, *79*, 33–40. [CrossRef] [PubMed]
129. Marek, A.; Tang, W.; Milikisiyants, S.; Nevzorov, A.A.; Smirnov, A.I. Nanotube array method for studying lipid-induced conformational changes of a membrane protein by solid-state NMR. *Biophys. J.* **2015**, *108*, 5–9. [CrossRef] [PubMed]
130. Banerjee, A.; Perez-Castillejos, R.; Hahn, D.; Smirnov, A.I.; Grebel, H. Micro-fluidic channels on nanopatterned substrates: Monitoring protein binding to lipid bilayers with surface-enhanced Raman spectroscopy. *Chem. Phys. Lett.* **2010**, *489*, 121–126. [CrossRef] [PubMed]
131. Römer, W.; Steinem, C. Impedance analysis and single-channel recordings on nano-black lipid membranes based on porous alumina. *Biophys. J.* **2004**, *86*, 955–965. [CrossRef]
132. Demé, B.; Marchal, D. Polymer-cushioned lipid bilayers in porous alumina. *Eur. Biophys. J.* **2005**, *34*, 170–179. [CrossRef] [PubMed]
133. Wattraint, O.; Warschawski, D.E.; Sarazin, C. Tethered or adsorbed supported lipid bilayers in nanotubes characterized by deuterium magic angle spinning NMR spectroscopy. *Langmuir* **2005**, *21*, 3226–3228. [CrossRef] [PubMed]
134. Lau, K.H.A.; Tan, L.-S.; Tamada, K.; Sander, M.S.; Knoll, W. Highly sensitive detection of processes occurring inside nanoporous anodic alumina templates: A waveguide optical study. *J. Phys. Chem. B* **2004**, *108*, 10812–10818. [CrossRef]
135. Eckstein, C.; Acosta, L.K.; Pol, L.; Xifré-Pérez, E.; Pallares, J.; Ferré-Borrull, J.; Marsal, L.F. Nanoporous anodic alumina surface modification by electrostatic, covalent, and immune complexation binding investigated by capillary filling. *ACS Appl. Mater. Interfaces* **2018**, *10*, 10571–10579. [CrossRef] [PubMed]
136. Macias, G.; Ferré-Borrull, J.; Pallarès, J.; Marsal, L. Effect of pore diameter in nanoporous anodic alumina optical biosensors. *Analyst* **2015**, *140*, 4848–4854. [CrossRef] [PubMed]
137. Yang, Z.; Si, S.; Zhang, C. Study on the activity and stability of urease immobilized onto nanoporous alumina membranes. *Microporous Mesoporous Mater.* **2008**, *111*, 359–366. [CrossRef]

138. Michel, M.; Toniazzo, V.; Ruch, D.; Ball, V. Deposition mechanisms in layer-by-layer or step-by-step deposition methods: From elastic and impermeable films to soft membranes with ion exchange properties. *ISRN Mater. Sci.* **2012**, 1–13. [CrossRef]
139. Joseph, N.; Ahmadiannamini, P.; Hoogenboom, R.; Vankelecom, I.F. Layer-by-layer preparation of polyelectrolyte multilayer membranes for separation. *Polym. Chem.* **2014**, *5*, 1817–1831. [CrossRef]
140. Ariga, K.; Hill, J.P.; Ji, Q. Layer-by-layer assembly as a versatile bottom-up nanofabrication technique for exploratory research and realistic application. *Phys. Chem. Chem. Phys.* **2007**, *9*, 2319–2340. [CrossRef] [PubMed]
141. Tang, Z.; Wang, Y.; Podsiadlo, P.; Kotov, N.A. Biomedical applications of layer-by-layer assembly: From biomimetics to tissue engineering. *Adv. Mater.* **2006**, *18*, 3203–3224. [CrossRef]
142. Krismastuti, F.S.H.; Bayat, H.; Voelcker, N.H.; Schönherr, H. Real time monitoring of layer-by-layer polyelectrolyte deposition and bacterial enzyme detection in nanoporous anodized aluminum oxide. *Anal. Chem.* **2015**, *87*, 3856–3863. [CrossRef] [PubMed]
143. Sheng, C.; Wijeratne, S.; Cheng, C.; Baker, G.L.; Bruening, M.L. Facilitated ion transport through polyelectrolyte multilayer films containing metal-binding ligands. *J. Membr. Sci.* **2014**, *459*, 169–176. [CrossRef]
144. Liu, Y.; Wang, H.; Indacochea, J.; Wang, M. A colorimetric sensor based on anodized aluminum oxide (AAO) substrate for the detection of nitroaromatics. *Sens. Actuators B Chem.* **2011**, *160*, 1149–1158. [CrossRef]
145. Balachandra, A.M.; Dai, J.; Bruening, M.L. Enhancing the anion-transport selectivity of multilayer polyelectrolyte membranes by templating with Cu^{2+}. *Macromolecules* **2002**, *35*, 3171–3178. [CrossRef]
146. Lazzara, T.D.; Lau, K.A.; Abou-Kandil, A.I.; Caminade, A.-M.; Majoral, J.-P.; Knoll, W. Polyelectrolyte layer-by-layer deposition in cylindrical nanopores. *Acs Nano* **2010**, *4*, 3909–3920. [CrossRef] [PubMed]
147. Kodiyath, R.; Malak, S.T.; Combs, Z.A.; Koenig, T.; Mahmoud, M.A.; El-Sayed, M.A.; Tsukruk, V.V. Assemblies of silver nanocubes for highly sensitive SERS chemical vapor detection. *J. Mater. Chem. A* **2013**, *1*, 2777–2788. [CrossRef]
148. Porta-i-Batalla, M.; Eckstein, C.; Xifré-Pérez, E.; Formentín, P.; Ferré-Borrull, J.; Marsal, L.F. Sustained, controlled and stimuli-responsive drug release systems based on nanoporous anodic alumina with layer-by-layer polyelectrolyte. *Nanoscale Res. Lett.* **2016**, *11*, 372. [CrossRef] [PubMed]
149. Dai, J.; Baker, G.L.; Bruening, M.L. Use of porous membranes modified with polyelectrolyte multilayers as substrates for protein arrays with low nonspecific adsorption. *Anal. Chem.* **2006**, *78*, 135–140. [CrossRef] [PubMed]
150. Matsumoto, F.; Nishio, K.; Masuda, H. Flow-through-type DNA array based on ideally ordered anodic porous alumina substrate. *Adv. Mater.* **2004**, *16*, 2105–2108. [CrossRef]
151. Sada, T.; Fujigaya, T.; Nakashima, N. Layer-by-layer assembly of trivalent metal cation and anionic polymer in nanoporous anodic aluminum oxide with 35 nm pore. *Chem. Lett.* **2014**, *43*, 1478–1480. [CrossRef]
152. Hou, S.; Wang, J.; Martin, C.R. Template-synthesized DNA nanotubes. *J. Am. Chem. Soc.* **2005**, *127*, 8586–8587. [CrossRef] [PubMed]
153. Hou, S.; Wang, J.; Martin, C.R. Template-synthesized protein nanotubes. *Nano Lett.* **2005**, *5*, 231–234. [CrossRef] [PubMed]
154. Krishnamoorthy, M.; Hakobyan, S.; Ramstedt, M.; Gautrot, J.E. Surface-initiated polymer brushes in the biomedical field: Applications in membrane science, biosensing, cell culture, regenerative medicine and antibacterial coatings. *Chem. Rev.* **2014**, *114*, 10976–11026. [CrossRef] [PubMed]
155. Zoppe, J.O.; Ataman, N.C.; Mocny, P.; Wang, J.; Moraes, J.; Klok, H.-A. Surface-initiated controlled radical polymerization: State-of-the-art, opportunities, and challenges in surface and interface engineering with polymer brushes. *Chem. Rev.* **2017**, *117*, 1105–1318. [CrossRef] [PubMed]
156. Bruening, M.L.; Dotzauer, D.M.; Jain, P.; Ouyang, L.; Baker, G.L. Creation of functional membranes using polyelectrolyte multilayers and polymer brushes. *Langmuir* **2008**, *24*, 7663–7673. [CrossRef] [PubMed]
157. Tian, Y.; He, Q.; Cui, Y.; Li, J. Fabrication of protein nanotubes based on layer-by-layer assembly. *Biomacromolecules* **2006**, *7*, 2539–2542. [CrossRef] [PubMed]
158. Wu, H.; Higaki, Y.; Takahara, A. Molecular self-assembly of one-dimensional polymer nanostructures in nanopores of anodic alumina oxide templates. *Prog. Polym. Sci.* **2018**, *77*, 95–117. [CrossRef]

159. Chu, C.-W.; Higaki, Y.; Cheng, C.-H.; Cheng, M.-H.; Chang, C.-W.; Chen, J.-T.; Takahara, A. Zwitterionic polymer brush grafting on anodic aluminum oxide membranes by surface-initiated atom transfer radical polymerization. *Polym. Chem.* **2017**, *8*, 2309–2316. [CrossRef]
160. Du, T.; Ma, S.; Pei, X.; Wang, S.; Zhou, F. Bio-inspired design and fabrication of micro/nano-brush dual structural surfaces for switchable oil adhesion and antifouling. *Small* **2017**, *13*, 1602020. [CrossRef] [PubMed]
161. Oliveira, G.B.; Lima Filho, J.L.; Chaves, M.E.C.; Azevedo, W.M.; Carvalho Jr, L.B. Enzyme immobilization on anodic aluminum oxide/polyethyleneimine or polyaniline composites. *React. Funct. Polym.* **2008**, *68*, 27–32. [CrossRef]
162. Liu, J.; Ma, S.; Wei, Q.; Jia, L.; Yu, B.; Wang, D.; Zhou, F. Parallel array of nanochannels grafted with polymer-brushes-stabilized Au nanoparticles for flow-through catalysis. *Nanoscale* **2013**, *5*, 11894–11901. [CrossRef] [PubMed]
163. Qiu, X.; Xu, X.-Y.; Liang, Y.; Hua, Y.; Guo, H. Fabrication of a molecularly imprinted polymer immobilized membrane with nanopores and its application in determination of β_2-agonists in pork samples. *J. Chromatogr. A* **2016**, *1429*, 79–85. [CrossRef] [PubMed]
164. Ma, S.; Liu, J.; Ye, Q.; Wang, D.; Liang, Y.; Zhou, F. A general approach for construction of asymmetric modification membranes for gated flow nanochannels. *J. Mater. Chem. A* **2014**, *2*, 8804–8814. [CrossRef]
165. Balachandra, A.M.; Baker, G.L.; Bruening, M.L. Preparation of composite membranes by atom transfer radical polymerization initiated from a porous support. *J. Membr. Sci.* **2003**, *227*, 1–14. [CrossRef]
166. Choy, K. Chemical vapour deposition of coatings. *Prog. Mater. Sci.* **2003**, *48*, 57–170. [CrossRef]
167. Xue, T.; Xu, Q.; Li, Y.-X.; Qi, H.-Y.; Wang, Z.-B.; Yang, Y.; Ren, T.-L. A method of controlling the hole size of nanopores array on anodic aluminum oxide. *Mater. Lett.* **2018**, *215*, 183–186. [CrossRef]
168. Entani, S.; Honda, M.; Shimoyama, I.; Li, S.; Naramoto, H.; Yaita, T.; Sakai, S. Effective adsorption and collection of cesium from aqueous solution using graphene oxide grown on porous alumina. *Jpn. J. Appl. Phys.* **2018**, *57*, 04FP04. [CrossRef]
169. Bindra, H.S.; John, S.; Roy, S.C.; Sinha, O.P.; Islam, S.; Nayak, R. Controlled and selective growth of 1D and 3D CdTe nanostructures through a structurally engineered porous alumina template for enhanced optical applications. *J. Electrochem. Soc.* **2018**, *165*, H3061–H3068. [CrossRef]
170. Ince, G.O.; Armagan, E.; Erdogan, H.; Buyukserin, F.; Uzun, L.; Demirel, G. One-dimensional surface-imprinted polymeric nanotubes for specific biorecognition by initiated chemical vapor deposition (iCVD). *ACS Appl. Mater. Interfaces* **2013**, *5*, 6447–6452. [CrossRef] [PubMed]
171. Pujari, S.P.; Scheres, L.; Marcelis, A.T.; Zuilhof, H. Covalent surface modification of oxide surfaces. *Angew. Chem. Int. Ed.* **2014**, *53*, 6322–6356. [CrossRef] [PubMed]
172. Nemati, M.; Santos, A.; Law, C.S.; Losic, D. Assessment of binding affinity between drugs and human serum albumin using nanoporous anodic alumina photonic crystals. *Anal. Chem.* **2016**, *88*, 5971–5980. [CrossRef] [PubMed]
173. Zhao, Q.; Wen, G.; Liu, Z.; Fan, Y.; Zou, G.; Li, L.; Zheng, R.; Ringer, S.P.; Mao, H.-K. Synthesis of dense, single-crystalline CrO_2 nanowire arrays using AAO template-assisted chemical vapor deposition. *Nanotechnology* **2011**, *22*, 125603. [CrossRef] [PubMed]
174. Mezni, A.; Saber, N.B.; Almalki, A.; Gobouri, A.; Basiuk, E.V.; Rizo, J.; Basiuk, V.A.; Kumeria, T.; Santos, A.; Losic, D. Chemical functionalization of inner walls of carbon nanotubes with long-chain aliphatic amines. *Nanosci. Nanotechnol. Lett.* **2017**, *9*, 712–718. [CrossRef]
175. Mattox, D.M. *Handbook of Physical Vapor Deposition (PVD) Processing*, 2nd ed.; William Andrew: Burlington, MA, USA, 2010; pp. 1–24. ISBN 978-0-8155-2037-5.
176. Reichelt, K.; Jiang, X. The preparation of thin films by physical vapour deposition methods. *Thin Solid Films* **1990**, *191*, 91–126. [CrossRef]
177. Kumar, A.; Sanger, A.; Kumar, A.; Chandra, R. Highly sensitive and selective CO gas sensor based on a hydrophobic SnO_2/CuO bilayer. *RSC Adv.* **2016**, *6*, 47178–47184. [CrossRef]
178. Pereira, A.; Laplante, F.; Chaker, M.; Guay, D. Functionally modified macroporous membrane prepared by using pulsed laser deposition. *Adv. Funct. Mater.* **2007**, *17*, 443–450. [CrossRef]
179. Salerno, M.; Shayganpour, A.; Salis, B.; Dante, S. Surface-enhanced Raman scattering of self-assembled thiol monolayers and supported lipid membranes on thin anodic porous alumina. *Beilstein J. Nanotechnol.* **2017**, *8*, 74–81. [CrossRef] [PubMed]

180. Kim, S.-W.; Lee, J.-S.; Lee, S.-W.; Kang, B.-H.; Kwon, J.-B.; Kim, O.-S.; Kim, J.-S.; Kim, E.-S.; Kwon, D.-H.; Kang, S.-W. Easy-to-fabricate and high-sensitivity LSPR type specific protein detection sensor using AAO nano-pore size control. *Sensors* **2017**, *17*, 856. [CrossRef] [PubMed]
181. Muneshwar, T.; Miao, M.; Borujeny, E.R.; Cadien, K. Atomic layer deposition: Fundamentals, practice and challenges. In *Handbook of Thin Film Deposition*, 4th ed.; Seshan, K., Schepis, D., Eds.; William Andrew: Burlington, MA, USA, 2018; pp. 359–373. ISBN 978-0-12-812311-9.
182. Elam, J.; Routkevitch, D.; Mardilovich, P.; George, S. Conformal coating on ultrahigh-aspect-ratio nanopores of anodic alumina by atomic layer deposition. *Chem. Mater.* **2003**, *15*, 3507–3517. [CrossRef]
183. Johnson, R.W.; Hultqvist, A.; Bent, S.F. A brief review of atomic layer deposition: From fundamentals to applications. *Mater. Today* **2014**, *17*, 236–246. [CrossRef]
184. Leskelä, M.; Ritala, M. Atomic layer deposition chemistry: Recent developments and future challenges. *Angew. Chem. Int. Ed.* **2003**, *42*, 5548–5554. [CrossRef] [PubMed]
185. Comstock, D.J.; Christensen, S.T.; Elam, J.W.; Pellin, M.J.; Hersam, M.C. Tuning the composition and nanostructure of Pt/Ir films via anodized aluminum oxide templated atomic layer deposition. *Adv. Funct. Mater.* **2010**, *20*, 3099–3105. [CrossRef]
186. Vega, V.; Gelde, L.; González, A.; Prida, V.; Hernando, B.; Benavente, J. Diffusive transport through surface functionalized nanoporous alumina membranes by atomic layer deposition of metal oxides. *J. Ind. Eng. Chem.* **2017**, *52*, 66–72. [CrossRef]
187. Norek, M.; Putkonen, M.; Zaleszczyk, W.; Budner, B.; Bojar, Z. Morphological, structural and optical characterization of SnO_2 nanotube arrays fabricated using anodic alumina (AAO) template-assisted atomic layer deposition. *Mater. Charact.* **2018**, *136*, 52–59. [CrossRef]
188. Lee, J.; Kim, D.H.; Hong, S.-H.; Jho, J.Y. A hydrogen gas sensor employing vertically aligned TiO_2 nanotube arrays prepared by template-assisted method. *Sens. Actuators B Chem.* **2011**, *160*, 1494–1498. [CrossRef]
189. Tan, L.K.; Kumar, M.K.; An, W.W.; Gao, H. Transparent, well-aligned TiO_2 nanotube arrays with controllable dimensions on glass substrates for photocatalytic applications. *ACS Appl. Mater. Interfaces* **2010**, *2*, 498–503. [CrossRef] [PubMed]
190. Gelde, L.; Cuevas, A.L.; Martínez de Yuso, M.d.V.; Benavente, J.; Vega, V.; González, A.S.; Prida, V.M.; Hernando, B. Influence of TiO_2-coating layer on nanoporous alumina membranes by ALD technique. *Coatings* **2018**, *8*, 60. [CrossRef]
191. Wang, H.; Wei, M.; Zhong, Z.; Wang, Y. Atomic-layer-deposition-enabled thin-film composite membranes of polyimide supported on nanoporous anodized alumina. *J. Membr. Sci.* **2017**, *535*, 56–62. [CrossRef]
192. Vaish, A.; Krueger, S.; Dimitriou, M.; Majkrzak, C.; Vanderah, D.J.; Chen, L.; Gawrisch, K. Enhancing the platinum atomic layer deposition infiltration depth inside anodic alumina nanoporous membrane. *J. Vac. Sci. Technol. A* **2015**, *33*, 01A148. [CrossRef]
193. Nasirpouri, F. Fundamentals and principles of electrode-position. In *Electrodeposition of Nanostructured Materials*; Springer International Publishing: Cham, Switzerland, 2017; Volume 62, pp. 75–121. ISBN 978-3-319-44920-3.
194. Kondo, T.; Kitagishi, N.; Yanagishita, T.; Masuda, H. Surface-enhanced Raman scattering on gold nanowire array formed by mechanical deformation using anodic porous alumina molds. *Appl. Phys. Express* **2015**, *8*, 062002. [CrossRef]
195. Bicelli, L.P.; Bozzini, B.; Mele, C.; D'Urzo, L. A review of nanostructural aspects of metal electrodeposition. *Int. J. Electrochem. Sci* **2008**, *3*, 356–408.
196. Stepniowski, W.J.; Moneta, M.; Karczewski, K.; Michalska-Domanska, M.; Czujko, T.; Mol, J.M.; Buijnsters, J.G. Fabrication of copper nanowires via electrodeposition in anodic aluminum oxide templates formed by combined hard anodizing and electrochemical barrier layer thinning. *J. Electroanal. Chem.* **2018**, *809*, 59–66. [CrossRef]
197. Guiliani, J.; Cadena, J.; Monton, C. Template-assisted electrodeposition of Ni and Ni/Au nanowires on planar and curved substrates. *Nanotechnology* **2018**, *29*, 075301. [CrossRef] [PubMed]
198. Zaraska, L.; Kurowska, E.; Sulka, G.D.; Jaskuła, M. Template-assisted fabrication of tin and antimony based nanowire arrays. *Appl. Surf. Sci.* **2012**, *258*, 9718–9722. [CrossRef]
199. Xu, Q.; Meng, G.; Han, F. Porous AAO template-assisted rational synthesis of large-scale 1D hybrid and hierarchically branched nanoarchitectures. *Prog. Mater. Sci.* **2018**, *95*, 243–285. [CrossRef]

200. Khan, B.S.; Saeed, A.; Hayat, S.S.; Mukhtar, A.; Mehmood, T. Mechanism for the formation of cuprous oxide nanowires in AAO template by electrodeposition. *Int. J. Electrochem. Sci.* **2017**, *12*, 890–897. [CrossRef]
201. Ahmad, N.; Awais, M.; Shah, S.A.; Ahmed, I.; Jabeen, N.; Majid, A.; Iqbal, J. Influence of voltage variation on structure and magnetic properties of $Co_{1-x}Sn_x$ (X = 0.3–0.7) nanowire alloys in alumina by electrochemical deposition. *Appl. Phys. A Mater.* **2017**, *123*, 65. [CrossRef]
202. Agarwal, S.; Hashmi, S.; Nandan, B.; Patra, A.K.; Singh, R.P.; Chelvane, J.A.; Khatri, M.S. Structure and magnetic properties of electrodeposited CoPtP/Pt multilayer nanowires. *Chem. Phys. Lett.* **2017**, *684*, 378–382. [CrossRef]
203. Kondo, T.; Nishio, K.; Masuda, H. Surface-enhanced Raman scattering in multilayered Au nanoparticles in anodic porous alumina matrix. *Appl. Phys. Express* **2009**, *2*, 032001. [CrossRef]
204. Park, S.; Son, Y.J.; Leong, K.W.; Yoo, H.S. Therapeutic nanorods with metallic multi-segments: Thermally inducible encapsulation of doxorubicin for anti-cancer therapy. *Nano Today* **2012**, *7*, 76–84. [CrossRef]
205. Fond, A.M.; Birenbaum, N.S.; Felton, E.J.; Reich, D.H.; Meyer, G.J. Preferential noncovalent immunoglobulin G adsorption onto hydrophobic segments of multi-functional metallic nanowires. *J. Photochem. Photobiol. A Chem.* **2007**, *186*, 57–64. [CrossRef]
206. Hernández, R.M.; Richter, L.; Semancik, S.; Stranick, S.; Mallouk, T.E. Template fabrication of protein-functionalized gold-polypyrrole-gold segmented nanowires. *Chem. Mater.* **2004**, *16*, 3431–3438. [CrossRef]
207. Djokić, S.S.; Cavallotti, P.L. Electroless deposition: Theory and applications. In *Electrodeposition: Theory and Practice*; Djokić, S.S., Ed.; Springer Science + Business Media: New York, NY, USA, 2010; Volume 48, pp. 251–291. ISBN 978-1-4419-5589-0.
208. Wang, W.; Li, N.; Li, X.; Geng, W.; Qiu, S. Synthesis of metallic nanotube arrays in porous anodic aluminum oxide template through electroless deposition. *Mater. Res. Bull.* **2006**, *41*, 1417–1423. [CrossRef]
209. Wang, G.; Shi, C.; Zhao, N.; Du, X. Synthesis and characterization of Ag nanoparticles assembled in ordered array pores of porous anodic alumina by chemical deposition. *Mater. Lett.* **2007**, *61*, 3795–3797. [CrossRef]
210. Yu, Y.; Kant, K.; Shapter, J.G.; Addai-Mensah, J.; Losic, D. Gold nanotube membranes have catalytic properties. *Microporous Mesoporous Mater.* **2012**, *153*, 131–136. [CrossRef]
211. Velleman, L.; Bruneel, J.-L.; Guillaume, F.; Losic, D.; Shapter, J.G. Raman spectroscopy probing of self-assembled monolayers inside the pores of gold nanotube membranes. *Phys. Chem. Chem. Phys.* **2011**, *13*, 19587–19593. [CrossRef] [PubMed]
212. Silina, Y.E.; Kychmenko, T.A.; Koch, M. Nanoporous anodic aluminum oxide films for UV/vis detection of noble and non-noble metals. *Anal. Methods* **2016**, *8*, 45–51. [CrossRef]
213. Li, X.; Wang, M.; Ye, Y.; Wu, K. Boron-doping Ni@Au nanotubes: Facile synthesis, magnetic property, and in vitro cytotoxicity on Molt-4 cells. *Mater. Lett.* **2013**, *108*, 222–224. [CrossRef]
214. Kumar, A.; Grant, D.; Alancherry, S.; Al-Jumaili, A.; Bazaka, K.; Jacob, M.V. Plasma polymerization: Electronics and biomedical application. In *Plasma Science and Technology for Emerging Economies: An AAAPT Experience*; Rawat, R.S., Ed.; Springer: Singapore, 2017; pp. 593–657. ISBN 978-981-10-4217-1.
215. Brevnov, D.A.; Barela, M.J.; Brooks, M.J.; López, G.P.; Atanassov, P.B. Fabrication of anisotropic super hydrophobic/hydrophilic nanoporous membranes by plasma polymerization of C_4F_8 on anodic aluminum oxide. *J. Electrochem. Soc.* **2004**, *151*, B484–B489. [CrossRef]
216. Simovic, S.; Losic, D.; Vasilev, K. Controlled drug release from porous materials by plasma polymer deposition. *Chem. Commun.* **2010**, *46*, 1317–1319. [CrossRef] [PubMed]
217. Simovic, S.; Diener, K.; Bachhuka, A.; Kant, K.; Losic, D.; Hayball, J.; Brownc, M.; Vasilev, K. Controlled release and bioactivity of the monoclonal antibody rituximab from a porous matrix: A potential in situ therapeutic device. *Mater. Lett.* **2014**, *130*, 210–214. [CrossRef]
218. Losic, D.; Cole, M.A.; Dollmann, B.; Vasilev, K.; Griesser, H.J. Surface modification of nanoporous alumina membranes by plasma polymerization. *Nanotechnology* **2008**, *19*, 245704. [CrossRef] [PubMed]
219. Danks, A.; Hall, S.; Schnepp, Z. The evolution of 'sol-gel'chemistry as a technique for materials synthesis. *Mater. Horiz.* **2016**, *3*, 91–112. [CrossRef]
220. Owens, G.J.; Singh, R.K.; Foroutan, F.; Alqaysi, M.; Han, C.-M.; Mahapatra, C.; Kim, H.-W.; Knowles, J.C. Sol-gel based materials for biomedical applications. *Prog. Mater. Sci.* **2016**, *77*, 1–79. [CrossRef]
221. Figueira, R.; Silva, C.J.; Pereira, E. Organic-inorganic hybrid sol-gel coatings for metal corrosion protection: A review of recent progress. *J. Coat. Technol. Res.* **2015**, *12*, 1–35. [CrossRef]

222. Clark Wooten, M.K.; Koganti, V.R.; Zhou, S.; Rankin, S.E.; Knutson, B.L. Synthesis and nanofiltration membrane performance of oriented mesoporous silica thin films on macroporous supports. *ACS Appl. Mater. Interfaces* **2016**, *8*, 21806–21815. [CrossRef] [PubMed]
223. Lim, S.Y.; Law, C.S.; Markovic, M.; Kirby, J.K.; Abell, A.D.; Santos, A. Engineering the slow photon effect in photoactive nanoporous anodic alumina gradient-index filters for photocatalysis. *ACS Appl. Mater. Interfaces* **2018**, *10*, 24124–24136. [CrossRef] [PubMed]
224. Karak, N.; Pal, B.; Sarkar, D.; Kundu, T.K. Growth of Co-doped ZnO nanoparticles by porous alumina assisted sol-gel route: Structural optical and magnetic properties. *J. Alloy. Compd.* **2015**, *647*, 252–258. [CrossRef]
225. Ni, S.; Li, X.; Yang, P.; Ni, S.; Hong, F.; Webster, T.J. Enhanced apatite-forming ability and antibacterial activity of porous anodic alumina embedded with CaO-SiO_2-Ag_2O bioactive materials. *Mater. Sci. Eng. C* **2016**, *58*, 700–708. [CrossRef] [PubMed]
226. Ebrahimi, F.; Ashrafizadeh, F.; Bakhshi, S.; Farle, M. Synthesis and structure of strontium ferrite nanowires and nanotubes of high aspect ratio. *J. Sol-Gel Sci. Technol.* **2016**, *77*, 708–717. [CrossRef]
227. He, B.; Kim, S.K.; Son, S.J.; Lee, S.B. Shape-coded silica nanotubes for multiplexed bioassay: Rapid and reliable magnetic decoding protocols. *Nanomedicine* **2010**, *5*, 77–88. [CrossRef] [PubMed]
228. Wang, L.; Kim, M.; Fang, Q.; Min, J.; Jeon, W.I.; Lee, S.Y.; Son, S.J.; Joo, S.-W.; Lee, S.B. Hydrophobic end-gated silica nanotubes for intracellular glutathione-stimulated drug delivery in drug-resistant cancer cells. *Chem. Commun.* **2013**, *49*, 3194–3196. [CrossRef] [PubMed]
229. Ateş, S.; Baran, E. Fabrication of Al_2O_3 nanopores/SnO_2 and its application in photocatalytic degradation under UV irradiation. *Mater. Chem. Phys.* **2018**, *214*, 17–27. [CrossRef]
230. Pacholski, C. Photonic crystal sensors based on porous silicon. *Sensors* **2013**, *13*, 4694–4713. [CrossRef] [PubMed]
231. Chen, Y.; Santos, A.; Wang, Y.; Kumeria, T.; Wang, C.; Li, J.; Losic, D. Interferometric nanoporous anodic alumina photonic coatings for optical sensing. *Nanoscale* **2015**, *7*, 7770–7779. [CrossRef] [PubMed]
232. Chen, Y.; Santos, A.; Wang, Y.; Kumeria, T.; Li, J.; Wang, C.; Losic, D. Biomimetic nanoporous anodic alumina distributed Bragg reflectors in the form of films and microsized particles for sensing applications. *ACS Appl. Mater. Interfaces* **2015**, *7*, 19816–19824. [CrossRef] [PubMed]
233. Law, C.S.; Lim, S.Y.; Santos, A. On the precise tuning of optical filtering features in nanoporous anodic alumina distributed Bragg reflectors. *Sci. Rep.* **2018**, *8*, 4642. [CrossRef] [PubMed]
234. Guo, D.-L.; Fan, L.-X.; Wang, F.-H.; Huang, S.-Y.; Zou, X.-W. Porous anodic aluminum oxide Bragg stacks as chemical sensors. *J. Phys. Chem. C* **2008**, *112*, 17952–17956. [CrossRef]
235. Ruiz-Clavijo, A.; Tsurimaki, Y.; Caballero-Calero, O.; Ni, G.; Chen, G.; Boriskina, S.V.; Martín-González, M. Engineering a full gamut of structural colors in all-dielectric mesoporous network metamaterials. *ACS Photonics* **2018**, *5*, 2120–2128. [CrossRef]
236. Ilyas, S.; Böcking, T.; Kilian, K.; Reece, P.; Gooding, J.; Gaus, K.; Gal, M. Porous silicon based narrow line-width rugate filters. *Opt. Mater.* **2007**, *29*, 619–622. [CrossRef]
237. Lorenzo, E.; Oton, C.J.; Capuj, N.E.; Ghulinyan, M.; Navarro-Urrios, D.; Gaburro, Z.; Pavesi, L. Porous silicon-based rugate filters. *Appl. Opt.* **2005**, *44*, 5415–5421. [CrossRef]
238. Kumeria, T.; Rahman, M.M.; Santos, A.; Ferré-Borrull, J.; Marsal, L.F.; Losic, D. Structural and optical nanoengineering of nanoporous anodic alumina rugate filters for real-time and label-free biosensing applications. *Anal. Chem.* **2014**, *86*, 1837–1844. [CrossRef] [PubMed]
239. An, Y.-Y.; Wang, J.; Zhou, W.-M.; Jin, H.-X.; Li, J.-F.; Wang, C.-W. The preparation of high quality alumina defective photonic crystals and their application of photoluminescence enhancement. *Superlattices Microstruct.* **2018**, *119*, 1–8. [CrossRef]
240. Rajeev, G.; Xifre-Perez, E.; Simon, B.P.; Cowin, A.J.; Marsal, L.F.; Voelcker, N.H. A label-free optical biosensor based on nanoporous anodic alumina for tumour necrosis factor-alpha detection in chronic wounds. *Sens. Actuators B Chem.* **2018**, *257*, 116–123. [CrossRef]
241. Kumeria, T.; Kurkuri, M.D.; Diener, K.R.; Parkinson, L.; Losic, D. Label-free reflectometric interference microchip biosensor based on nanoporous alumina for detection of circulating tumour cells. *Biosens. Bioelectron.* **2012**, *35*, 167–173. [CrossRef] [PubMed]
242. Kumeria, T.; Parkinson, L.; Losic, D. A nanoporous interferometric micro-sensor for biomedical detection of volatile sulphur compounds. *Nanoscale Res. Lett.* **2011**, *6*, 634. [CrossRef] [PubMed]

243. Casanova, F.; Chiang, C.; Li, C.-P.; Roshchin, I.; Ruminski, A.; Sailor, M.; Schuller, I. Effect of surface interactions on the hysteresis of capillary condensation in nanopores. *Europhys. Lett.* **2007**, *81*, 26003. [CrossRef]
244. Nemati, M.; Santos, A.; Kumeria, T.; Losic, D. Label-free real-time quantification of enzyme levels by interferometric spectroscopy combined with gelatin-modified nanoporous anodic alumina photonic films. *Anal. Chem.* **2015**, *87*, 9016–9024. [CrossRef] [PubMed]
245. Lee, J.C.; An, J.Y.; Kim, B.W. Application of anodized aluminium oxide as a biochip substrate for a Fabry-Perot interferometer. *J. Chem. Technol. Biotechnol.* **2007**, *82*, 1045–1052. [CrossRef]
246. Bae, K.; Lee, J.; Kang, G.; Yoo, D.-S.; Lee, C.-W.; Kim, K. Refractometric and colorimetric index sensing by a plasmon-coupled hybrid AAO nanotemplate. *RSC Adv.* **2015**, *5*, 103052–103059. [CrossRef]
247. Santos, A.; Macías, G.; Ferré-Borrull, J.; Pallarès, J.; Marsal, L.F. Photoluminescent enzymatic sensor based on nanoporous anodic alumina. *ACS Appl. Mater. Interfaces* **2012**, *4*, 3584–3588. [CrossRef] [PubMed]
248. Ferro, L.M.; Lemos, S.G.; Ferreira, M.; Trivinho-Strixino, F. Use of multivariate analysis on Fabry–Pérot interference spectra of nanoporous anodic alumina (NAA) for optical sensors purposes. *Sens. Actuators B Chem.* **2017**, *248*, 718–723. [CrossRef]
249. Trivinho-Strixino, F.; Guerreiro, H.; Gomes, C.; Pereira, E.; Guimarães, F.E.G. Active waveguide effects from porous anodic alumina: An optical sensor proposition. *Appl. Phys. Lett.* **2010**, *97*, 011902. [CrossRef]
250. Yan, P.; Fei, G.T.; Shang, G.L.; Wu, B.; De Zhang, L. Fabrication of one-dimensional alumina photonic crystals with a narrow band gap and their application to high-sensitivity sensors. *J. Mater. Chem. C* **2013**, *1*, 1659–1664. [CrossRef]
251. Shang, G.L.; Fei, G.T.; Zhang, Y.; Yan, P.; Xu, S.H.; De Zhang, L. Preparation of narrow photonic bandgaps located in the near infrared region and their applications in ethanol gas sensing. *J. Mater. Chem. C* **2013**, *1*, 5285–5291. [CrossRef]
252. Shang, G.; Fei, G.; Li, Y.; Zhang, L. Influence of dielectrics with light absorption on the photonic bandgap of porous alumina photonic crystals. *Nano Res.* **2016**, *9*, 703–712. [CrossRef]

Chapter 3

Structural Engineering of Nanoporous Anodic Alumina Photonic Crystals by Sawtooth-like Pulse Anodisation

Statement of Authorship

Title of Paper	Structural Engineering of Nanoporous Anodic Alumina Photonic Crystals by Sawtooth-like Pulse Anodization.
Publication Status	☑ Published ☐ Accepted for Publication ☐ Submitted for Publication ☐ Unpublished and Unsubmitted w ork w ritten in manuscript style
Publication Details	Law, C.S., A. Santos, N. Mahdieh, and D. Losic, *Structural engineering of nanoporous anodic alumina photonic crystals by sawtooth-like pulse anodization*. ACS Applied Materials & Interfaces, 2016. **8**(21): p. 13542-13554.

Principal Author

Name of Principal Author (Candidate)	Cheryl Suwen Law		
Contribution to the Paper	Under the supervision of A. Santos and A. D. Abell, I performed the experiments, interpreted and processed the data and wrote the manuscript for submission.		
Overall percentage (%)	60		
Certification:	This paper reports on original research I conducted during the period of my Higher Degree by Research candidature and is not subject to any obligations or contractual agreements with a third party that would constrain its inclusion in this thesis. I am the primary author of this paper.		
Signature		Date	23/11/2018

Co-Author Contributions

By signing the Statement of Authorship, each author certifies that:

i. the candidate's stated contribution to the publication is accurate (as detailed above);
ii. permission is granted for the candidate in include the publication in the thesis; and
iii. the sum of all co-author contributions is equal to 100% less the candidate's stated contribution.

Name of Co-Author	Abel Santos		
Contribution to the Paper	I acted as primary supervisor for the candidate, aided in developing of the experiments, revising the manuscript and evaluating the final version of the manuscript. I give consent for Cheryl Suwen Law to present this paper for examination towards the Doctorate of Philosophy.		
Signature		Date	23/11/2018

Name of Co-Author	Mahdieh Nemati		
Contribution to the Paper	I aided in performing the experiments. I give consent for Cheryl Suwen Law to present this paper for examination towards the Doctorate of Philosophy.		
Signature		Date	18/11/2018

Name of Co-Author	Dusan Losic		
Contribution to the Paper	I aided in the evaluation of final version of manuscript. I give consent for Cheryl Suwen Law to present this paper for examination towards the Doctorate of Philosophy.		
Signature		Date	19/11/2018

3. Structural Engineering of Nanoporous Anodic Alumina Photonic Crystals by Sawtooth-like Pulse Anodisation

3.1 Introduction, Significance and Commentary

The application of pulse-like anodisation strategies has paved the way for designing nanoporous anodic alumina photonic crystals (NAA-PCs) with advanced nanostructures to control light–matter interactions at the nanoscale for sensing applications. This study explores a galvanostatic pulse-like anodisation strategy based on sawtooth-like waves to fabricate a novel type of NAA-PCs, with tuneable photonic properties and optimally engineered effective medium, which is suitable for advanced sensing applications.

3.2 Publication

This section is presented as published research paper by **Law, C.S.**, A. Santos, N. Mahdieh, and D. Losic, *Structural engineering of nanoporous anodic alumina photonic crystals by sawtooth-like pulse anodization*. ACS Applied Materials & Interfaces, 2016. **8**(21): p. 13542-13554.

ACS APPLIED MATERIALS & INTERFACES

Research Article

www.acsami.org

Structural Engineering of Nanoporous Anodic Alumina Photonic Crystals by Sawtooth-like Pulse Anodization

Cheryl Suwen Law,[†] Abel Santos,[*,†,‡,§] Mahdieh Nemati,[†] and Dusan Losic[*,†]

[†]School of Chemical Engineering, The University of Adelaide, Engineering North Building, 5005 Adelaide, Australia

[‡]Institute for Photonics and Advanced Sensing (IPAS), The University of Adelaide, 5005 Adelaide, Australia

[§]ARC Centre of Excellence for Nanoscale BioPhotonics (CNBP), The University of Adelaide, 5005 Adelaide, Australia

Supporting Information

ABSTRACT: This study presents a sawtooth-like pulse anodization approach aiming to create a new type of photonic crystal structure based on nanoporous anodic alumina. This nanofabrication approach enables the engineering of the effective medium of nanoporous anodic alumina in a sawtooth-like manner with precision. The manipulation of various anodization parameters such as anodization period, anodization amplitude, number of anodization pulses, ramp ratio and pore widening time allows a precise control and fine-tuning of the optical properties (i.e., characteristic transmission peaks and interferometric colors) exhibited by nanoporous anodic alumina photonic crystals (NAA-PCs). The effect of these anodization parameters on the photonic properties of NAA-PCs is systematically evaluated for the establishment of a fabrication methodology toward NAA-PCs with tunable optical properties. The effective medium of the resulting NAA-PCs is demonstrated to be optimal for the development of optical sensing platforms in combination with reflectometric interference spectroscopy (RIfS). This application is demonstrated by monitoring in real-time the formation of monolayers of thiol molecules (11-mercaptoundecanoic acid) on the surface of gold-coated NAA-PCs. The obtained results reveal that the adsorption mechanism between thiol molecules and gold-coated NAA-PCs follows a Langmuir isotherm model, indicating a monolayer sorption mechanism.

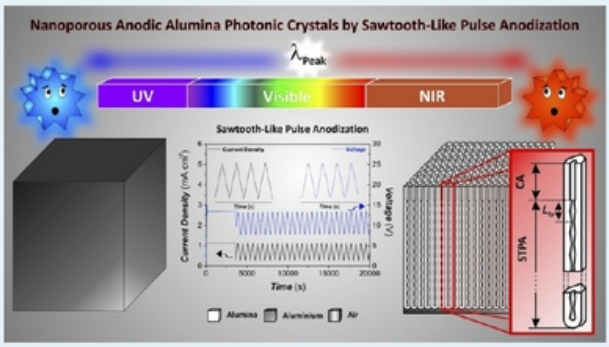

KEYWORDS: *sawtooth-like pulse anodization, structural engineering, nanoporous anodic alumina, photonic crystals, reflectometric interference spectroscopy*

INTRODUCTION

Photonic crystals are optical structures that feature a periodical variation of refractive index, which is spatially distributed in one, two or three orthogonal directions.[1,2] Photonic crystals can be fabricated through a variety of methods such as lithography and dry etching,[3−7] vertical selective oxidation,[8] wet chemical etching,[9,10] fiber-pulling,[11] embossing,[12] self-organization[13,14] and electrochemical etching.[15−18] Among these micro/nano-fabrication techniques, electrochemical etching is a top-down approach that has been demonstrated as a cost-effective and precise method to fabricate photonic crystal structures based on nanoporous materials. Electrochemical fabrication makes it possible to produce photonic crystals with high degree of regularity, optimal resolution and high aspect ratio as compared to other fabrication techniques.[19] Porous silicon (pSi)-based photonic crystals produced by electrochemical etching of silicon are outstanding examples of that and have been extensively used in many research fields and applications due to their superior optoelectronic properties.[2] The porosity of porous silicon can be engineered in depth by alternating the current density applied during the electrochemical etching process, which is typically performed in hydrofluoric acid (HF)-based electrolytes.[20−26] The relationship between the porosity of pSi and its effective refractive index makes it achievable to tune the photonic stop band of pSi through its porosity. This enables a precise and versatile means for engineering the interaction between light and matter in the form of a broad range of photonic nanostructures such as microcavities, distributed Bragg reflectors, waveguides, omnidirectional mirrors and rugate filters.[27−32] Despite the numerous advantages of pSi-based photonic structures, this material presents some inherent limitations such as poor chemical stability and weak mechanical strength. Furthermore, the use of HF-based electrolytes makes the production of pSi a life-threatening fabrication process that, apart from standard laboratory equipment (e.g., fumehood with ventilation), requires high level personal protective equipment such as HF gas monitor with audible alarm, safety sensor for liquids, safety

Received: April 1, 2016
Accepted: May 12, 2016
Published: May 12, 2016

DOI: 10.1021/acsami.6b03900
ACS Appl. Mater. Interfaces 2016, 8, 13542−13554

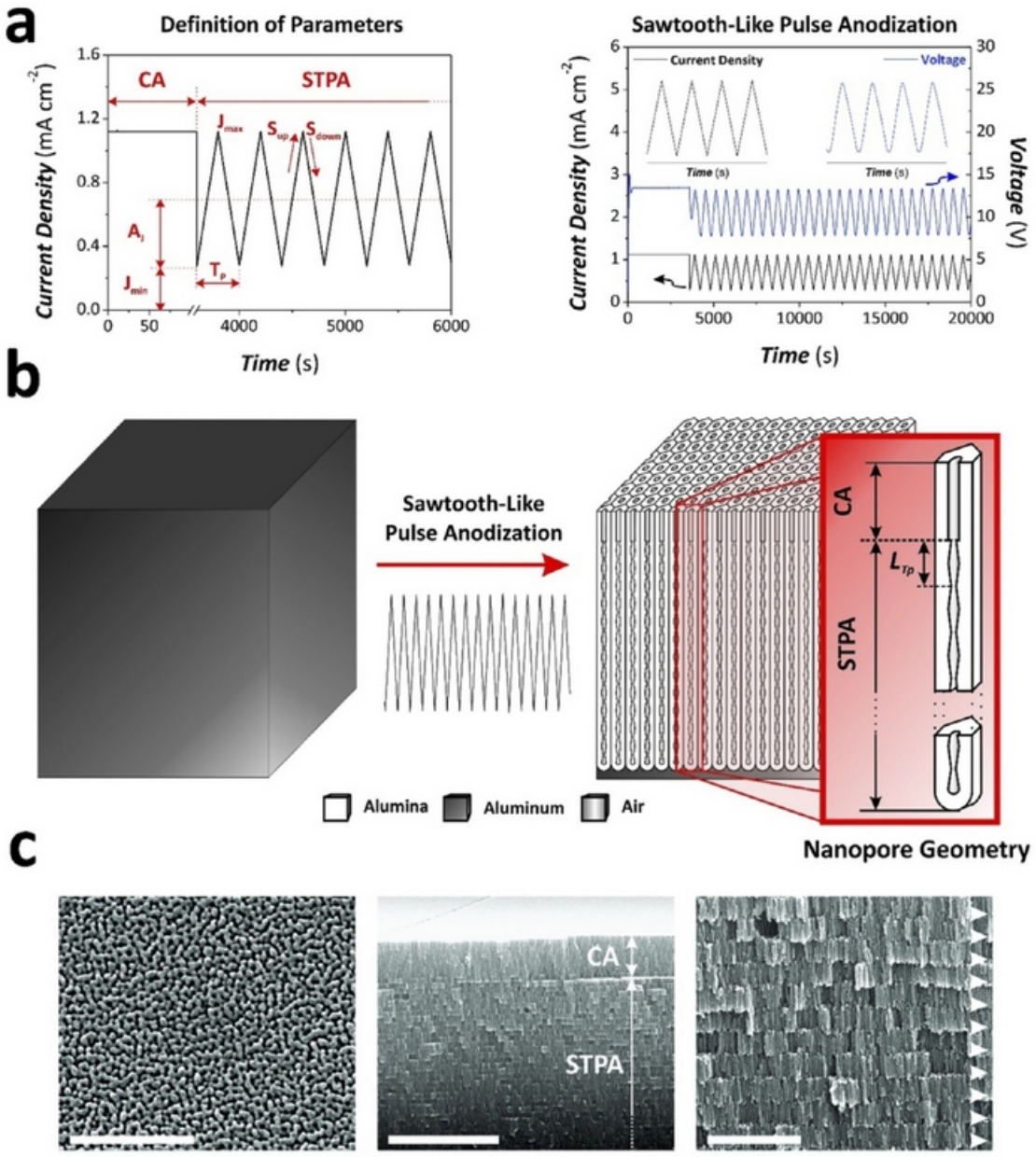

Figure 1. Fabrication of nanoporous anodic alumina photonic crystals (NAA-PCs) by sawtooth-like pulse anodization (STPA). (a, left) Graphical definition of the different parameters defining a current density pulse (i.e., T_P, A_J, J_{min}, J_{max}, S_{up} and S_{down}) in STPA and (right) example of actual anodization profile used to produce a NAA-PCs with T_P = 600 s, A_J = 0.42 mA cm^{-2}, ramp ratio (S_{up}/S_{down}) = 1, number of anodization pulses (N_P) = 124 and time of pore widening (t_{pw}) = 0 min. (b) Schematic illustration describing the fabrication of NAA-PCs from aluminum substrates by SPTA. (c) SEM images showing the nanoporous structure of a NAA-PC produced by STPA with T_P = 900 s, A_J = 0.42 mA cm^{-2}, S_{up}/S_{down} = 1, N_P = 124 and t_{pw} = 6 min (left, general top view SEM image (scale bar = 500 nm); center, cross-sectional view (scale bar = 5 μm); right, magnified cross-sectional view (scale bar = 1 μm)) (NB: white arrowheads denote layers of NAA in the structure of NAA-PCs).

goggles, face shield, chemically resistant butyl rubber gloves and apron and so on.[33] Recently, nanoporous anodic alumina (NAA) produced by electrochemical oxidation (i.e., anodization) of aluminum has been envisaged as an alternative platform to overcome the drawbacks of pSi photonic crystal structures.[34−36] NAA has superior intrinsic properties than those of pSi in terms of mechanical robustness, thermal stability and chemical inertness as well as controllable and versatile nanopore geometry.[37] Moreover, the effective medium of this nanomaterial can also be engineered with precision by means of the anodization parameters. Anodization of aluminum is an industrial process that can be performed in mild aqueous solutions of acid electrolytes such as sulfuric, oxalic and phosphoric and does not require special safety measures. However, it is worthwhile noting that anodization of aluminum presents some challenges given that, in contrast to pSi, abrupt modifications of the anodization current density or voltage are not directly translated into porosity changes due to the presence of the oxide barrier layer located at the nanopore bottom tips. In the course of anodization, the electric field is the

DOI: 10.1021/acsami.6b03900
ACS Appl. Mater. Interfaces 2016, 8, 13542−13554

driving force that allows the flow of ionic species from and to the bulk electrolyte along the nanopores and across the oxide barrier layer located at the nanopores tips for the formation and dissolution of alumina at the metal/oxide and oxide/electrolyte interfaces, respectively.[38−41] Therefore, the anodization conditions must be carefully selected in order to achieve a correct control over the porosity and enable a precise engineering of the effective medium of NAA in depth. Pioneering studies aimed at shaping the nanoporous structure of NAA by pulse anodization approaches, where the anodization voltage or current density where switched between mild and hard regimes.[42−49] Although these strategies make it achievable to modulate the nanopore geometry with precision, the generation of photonic structures by mild-hard pulse anodization still remains challenging due to the limited controllability of anodization under hard conditions (i.e., fast growth rate of the oxide layer, dependence of growth rate on the nanopore length, heat generation, low porosity level, etc.). Recent studies have demonstrated that a pulse anodization approach under mild conditions can be readily used to create a set of NAA-based photonic crystal structures (NAA-PCs) with outstanding optical properties for numerous applications.[50−59] These rationally designed electrochemical approaches are demonstrated not only to be able to dodge the limitations of anodization of aluminum but also enable effective means to engineer the photonic stop band of NAA through different anodization profiles.

In this context, this study aims for the first time to produce a new type of NAA-PCs by means of a sawtooth-like pulse anodization (STPA) approach (Figure 1). To achieve a better control over the oxide growth rate and porosity of NAA, this process is carried out under mild anodization conditions. Our study also establishes a rationale for a better understanding of the effect that the different anodization parameters (i.e., anodization period, anodization amplitude, number of anodization pulses, ramp ratio and pore widening time) have on the optical properties of NAA-PCs such as their characteristic transmission peaks and the interferometric colors displayed across the UV−visible-NIR spectrum. The effective medium of the resulting photonic crystal structures is demonstrated to be optimal for the development of optical sensing platforms. Finally, as a proof-of-concept, NAA-PCs are used as selective optical sensing platforms in combination with reflectometric interference spectroscopy (RIfS) in order to monitor the formation of monolayers of thiol molecules onto gold-coated NAA-PCs.

■ EXPERIMENTAL SECTION

2.1. Materials. High purity (99.9997%) aluminum foils 0.32 mm thick supplied by Goodfellow Cambridge Ltd. (UK) were used to produce NAA-PCs by sawtooth-like pulse anodization. Sulfuric acid (H_2SO_4), perchloric acid ($HClO_4$), hydrochloric acid (HCl), copper-(II) chloride ($CuCl_2$), sodium chloride (NaCl), ethanol (EtOH-C_2H_5OH) and 11-mercaptoundecanoic acid (11-MUA) were purchased from Sigma-Aldrich (Australia) and used as received, without additional purification steps. Ultrapure water (18.2 Ω·m) Option Q-Purelabs (Australia) was used to prepare the aqueous solutions used in this study.

2.2. Fabrication of NAA-Based Photonic Crystals (NAA-PCs). NAA-based photonic crystals were fabricated through a sawtooth-like anodization approach under mild conditions and current density control in sulfuric acid electrolyte. In this process, 2.25 cm^2 square aluminum (Al) chips were first cleaned under sonication in EtOH and distilled water for 15 min each in order to remove organic residues from the surface of aluminum. Cleaned Al chips were electropolished in a mixture of EtOH and $HClO_4$ 4:1 (v:v) at 20 V and 5 °C for 3 min to obtain a smooth surface with a mirror-like finishing. The electropolished Al substrates were anodized in an aqueous solution 1.1 M of sulfuric acid, with 25 vol % of EtOH to lower the freezing point of the electrolyte solution, the temperature of which was kept constant at −1 °C throughout the whole anodization process.[60,61] The anodization process started with a constant current density of 1.12 mA cm^{-2} for 1 h to form a thin layer of nanoporous oxide, which acted as a shuttle for achieving a homogeneous pore growth before sawtooth-like pulse anodization. The anodization profile was subsequently set to sawtooth-like pulse mode. In the course of this process, the anodization current density was pulsed between high and low current density values (i.e., J_{max} and J_{min}) following a sawtooth-like fashion with up and down linear ramps and an anodization period calculated by eq 1:

$$T_P = \frac{(J_{max} - J_{min})}{S_{up}} + \frac{(J_{max} - J_{min})}{S_{down}} \quad (1)$$

where T_P is the anodization period, J_{max} is the maximum current density, J_{min} is the minimum current density and S_{up} and S_{down} are the rates of the current density ramps up and down, respectively. Note that the anodization amplitude (A_J) of the anodization waveform is here defined by eq 2.

$$A_J = \frac{(J_{max} - J_{min})}{2} \quad (2)$$

A graphical definition of these parameters used to create sawtooth-like anodization profiles is illustrated in Figure 1a. The different anodization parameters defining the STPA waveforms were systematically modified in order to investigate their effect on the optical properties of NAA-PCs (Figure 1b). To this end, taking as a reference a NAA-PC fabricated with T_P = 700 s, A_J = 0.42 mA cm^{-2}, ramp ratio (S_{up}/S_{down}) = 1, number of anodization pulses (N_P) = 124 and time of pore widening (t_{pw}) = 0 min, the anodization parameters were modified from 400 to 1100 s for T_P with ΔT_P = 100 s, from 0.21 to 0.63 mA cm^{-2} for A_J with ΔA_J = 0.105 mA cm^{-2}, from 62 (12 h) to 310 (60 h) pulses for N_P, with ΔN_P = 62 pulses (12 h), from 0.5 to 2 for S_{up}/S_{down} with $\Delta S_{up}/S_{down}$ = 0.5 and from 0 to 6 min for t_{pw} with Δt_{pw} = 2 min.

This set of experiments aimed to create a better understanding of how the optical properties (i.e., characteristic transmission peaks and interferometric color) of NAA-PCs produced by a sawtooth-like pulse anodization approach can be engineered by means of these fabrication parameters.

2.3. Optical Characterization. The transmission spectra of NAA-based photonic crystals fabricated by STPA under different conditions were acquired across UV−visible-NIR spectrum, ranging from 200 to 1000 nm, at normal incidence (i.e., $\theta = 0°$) using a UV−visible-NIR spectrometer (Cary 60, Agilent, USA). Note that the remaining aluminum substrate was selectively removed from the backside of NAA-PCs by wet chemical etching in a saturated solution of HCl−$CuCl_2$, using an etching mask with a circular window of 5 mm in diameter. Digital images of NAA-PCs displaying interferometric colors were obtained using a Sony HX90 V Compact Camera with 18.2 MP and 30× optical zoom and autofocus feature under natural illumination.

2.4. Assessment of the Effective Medium of NAA-Based Photonic Crystals. The effective medium of a reference NAA-based photonic crystal (i.e., T_P = 700 s, A_J = 0.42 mA cm^{-2}, S_{up}/S_{down} = 1, N_P = 124 pulses and t_{pw} = 0 min) was assessed by measuring the shifts in the position of characteristic reflection peak (λ_{Peak}) after selective infiltration of its nanopores with aqueous solutions of sodium chloride of different concentrations (i.e., from 0 to 1 M) in order to provide different refractive index values of the medium filling the nanopores (i.e., from 1.333 to 1.340 RIU). The position of λ_{Peak} was measured by reflectometric interference spectroscopy (RIfS) in a custom-made flow cell. In this system, white light from a tungsten source (LS-1LL, Ocean Optics, USA) is focused by a bifurcated optical probe on the surface of

DOI: 10.1021/acsami.6b03900
ACS Appl. Mater. Interfaces 2016, 8, 13542−13554

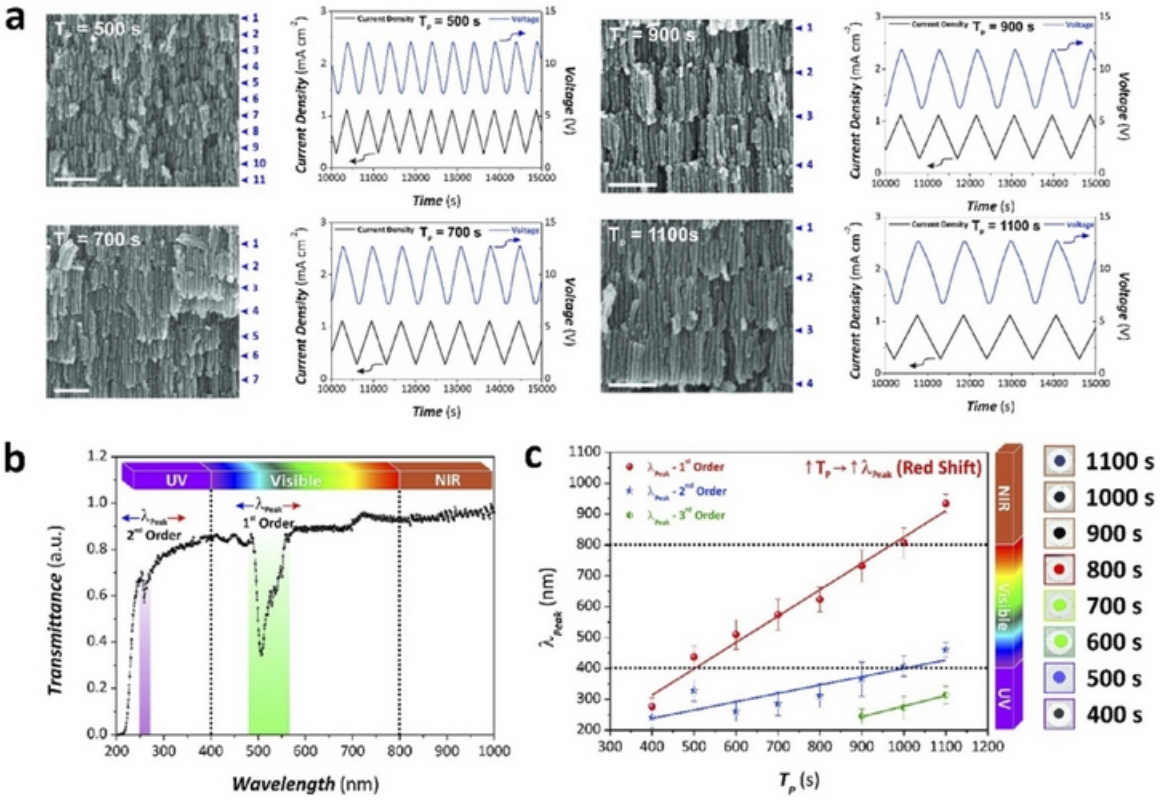

Figure 2. Characteristic transmission peaks tuneability by modifying the anodization period (T_P). (a) Cross-sectional view SEM images of NAA-PCs produced by STPA with T_P = 500, 700, 900 and 1100 s, A_J = 0.42 mA cm^{-2}, S_{up}/S_{down} = 1 and t_{pw} = 6 min (scale bars = 250 nm) (left) and STPA anodization profiles used to produce these NAA-PCs (right) (NB: blue arrowheads denote the interfaces between anodization periods, L_{T_P}). (b) Representative of transmission spectrum of a reference NAA-PC (i.e., T_P = 600 s, A_J = 0.42 mA cm^{-2}, S_{up}/S_{down} = 1 and t_{pw} = 0 min) showing the characteristic transmission peaks of these photonic crystal structures. (c) Position of the 1st, 2nd and 3rd characteristic transmission peaks of NAA-PCs as a function of T_P (left) and digital pictures of NAA-PCs from 400 to 1100 s showing the interferometric color displayed by these photonic crystal structures (right) (NB: the underlying aluminum substrate was chemically etched away through a circular etching mask with a diameter of 5 mm using a saturated solution of HCl/$CuCl_2$).

NAA-PCs with an illumination spot of 2 mm in diameter, the size of which is adjusted by a lens system (VIS Collimating Lens, 350−2000 nm, Ocean Optics, USA). The light reflected from this spot is collected by the collection fiber assembled in the same optical probe and directly transferred to a miniature spectrometer (USB 4000+VIS-NIR-ES, Ocean Optics, USA). In this study, the optical spectra were acquired in the range of 400−1000 nm wavelength and saved at intervals of 30 s, with an integration time of 10 ms and 50 average measurements. The RIfS spectra were processed using Igor Pro library (Wavemetrics, USA) to determine the shifts in λ_{Peak} of NAA-based photonic crystals. Note that the surface of the NAA-PCs was coated with an ultrathin layer of gold (Au) using a sputter coater equipped with film thickness monitor (sputter coater 108 Auto, Cressington, USA) in order to improve the interference effect.[62,63] The reference NAA-PC was packed in a custom-made flow cell through which the different analytical solutions of NaCl were flowed at constant flow rate. A stable baseline with ultrapure water was first established for 10 min prior to injection of the different analytical solutions into the flow cell. Different concentrations of sodium chloride solution (i.e., 0.0625, 0.125, 0.25, 0.5 and 1 M) were prepared in ultrapure water and flowed through the flow cell at a constant flow rate of 100 μL min^{-1} using a syringe pump (Fusion touch, Chemyx, USA). The filling of the nanopores of NAA-PCs with different concentrations of sodium chloride solution induced changes in the effective refractive index of the photonic structure, resulting in shifts in the position of λ_{Peak}, denoted as $\Delta\lambda_{Peak}$.

2.5. Real-Time Monitoring of Monolayer Formation on the Surface of Gold-Coated NAA-Based Photonic Crystals. The formation of monolayers of thiol-containing molecules on the surface of gold-coated NAA-PCs was monitored in real-time by RIfS using the system described in the previous section (*vide supra*). A set of reference Au-coated NAA-PCs (i.e., T_P = 700 s, A_J = 0.42 mA cm^{-2}, S_{up}/S_{down} = 1, N_P = 124 and t_{pw} = 0 min) was used in this experiment as optical sensing platforms. Analytical solutions of 11-mercaptoundecanoic acid (11-MUA), a thiol model molecule, with different concentrations (i.e., 0.3125, 0.625, 1.25, 2.5 and 5 mM) were prepared in ethanol. A stable baseline with ethanol was first established for 10 min prior to injection of the different 11-MUA analytical solutions into the flow cell by a syringe pump at a constant flow rate of 100 μL min^{-1}. The formation of 11-MUA monolayers on the surface of Au-coated NAA-PCs was monitored through shifts in the characteristic reflection peak ($\Delta\lambda_{Peak}$) measured by RIfS. Fresh ethanol was flowed through the cell after the binding equilibrium was achieved in order to establish the total shift in the characteristic peak position associated with the corresponding concentration of 11-MUA. Langmuir and Freundlich isotherm models were adapted to this system to determine the kinetics binding mechanism of 11-MUA onto the gold-coated surface of NAA-PCs.

2.6. Structural Characterization. The geometric features of the different NAA-PCs produced in this study were characterized by field emission gun scanning electron microscopy (FEG-SEM FEI Quanta 450). ImageJ (public domain program developed at the RSB of the NIH) was used for SEM image analysis.[64]

DOI: 10.1021/acsami.6b03900
ACS Appl. Mater. Interfaces 2016, 8, 13542−13554

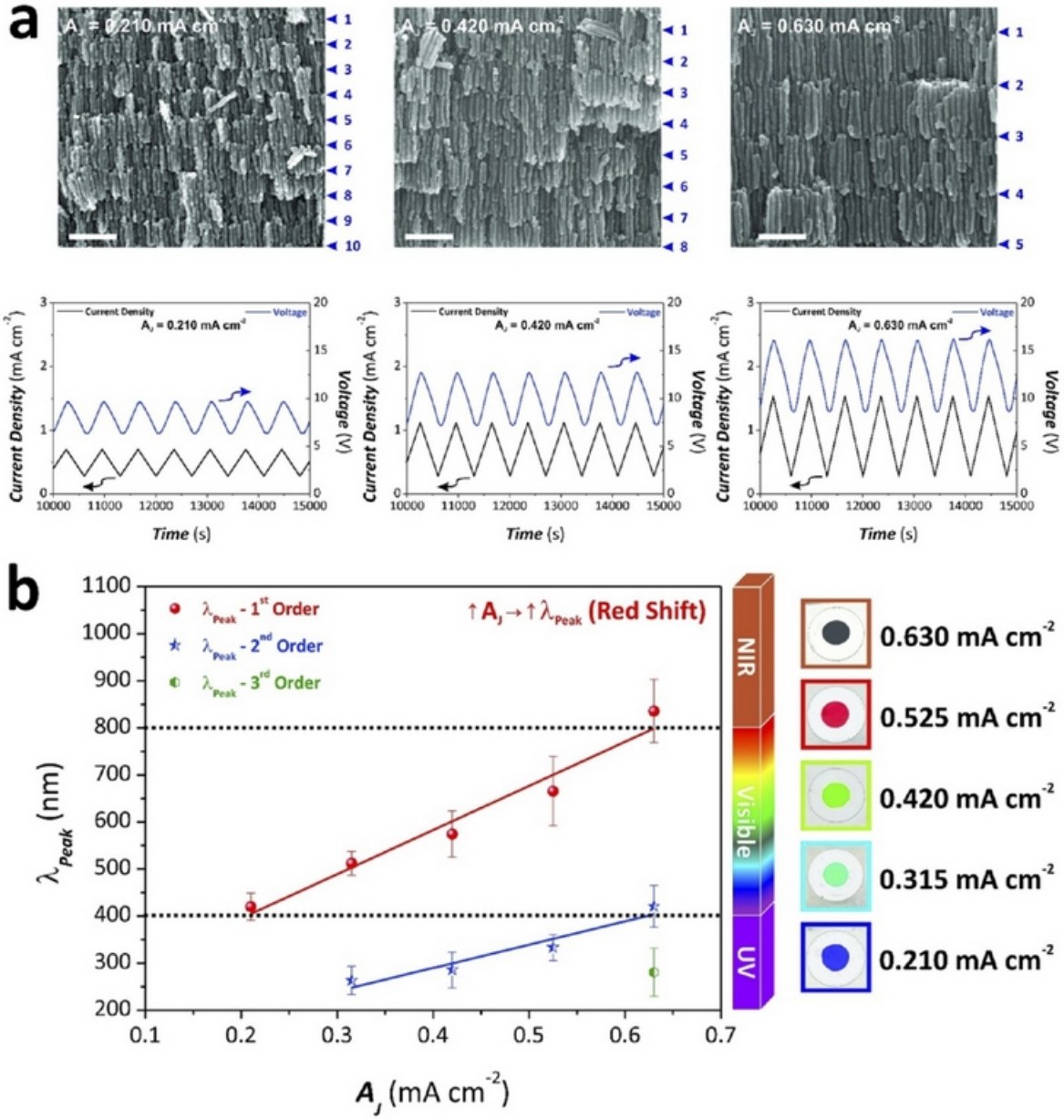

Figure 3. Characteristic transmission peaks tuneability by modifying the anodization amplitude (A_J). (a) Cross-sectional view SEM images of NAA-PCs fabricated by STPA with A_J = 0.210, 0.420 and 0.630 mA cm^{-2}, T_p = 700 s, S_{up}/S_{down} = 1 and t_{pw} = 6 min (scale bars = 250 nm) (up) and corresponding STPA anodization waveforms used to produce these NAA-PCs (down) (NB: blue arrowheads denote the interfaces between anodization periods, L_{T_p}). (b) Position of the 1st, 2nd and 3rd characteristic transmission peaks of NAA-PCs as a function of A_J (left) and digital pictures of NAA-PCs from 0.210 to 0.630 mA cm^{-2} revealing the interferometric color displayed by these photonic crystal structures (right) (NB: the underlying aluminum substrate was chemically etched away through a circular etching mask with a diameter of 5 mm using a saturated solution of HCl/$CuCl_2$).

■ RESULTS AND DISCUSSION

3.1. Structural Characteristics of NAA-PCs. Figure 1c illustrates a set of SEM images showing the structure of NAA-based photonic crystals fabricated by sawtooth-like pulse anodization. A top view SEM image reveals that, under the fabrication conditions used in our study, NAA-PCs feature a random but homogeneous distribution of nanopores across their surface (Figure 1c, right). As commented above, the STPA process starts with a short step at constant anodization current density (Figure 1a), which yields a layer of nanoporous oxide with straight pores as shown in Figure 1c, center. A magnified cross-sectional SEM image of the STPA section shows that NAA-PCs fabricated by this anodization approach can be described as nanoporous structures composed of stacks of layers of NAA with modulated porosity in depth following a sawtooth-like fashion, where the level of porosity is directly proportional to the current density applied during the STPA process (Figure 1c, left). The period length (L_{T_p}), defined as the length of NAA layers corresponding to each sawtooth pulse, is established by the anodization period (T_p) and each STPA

DOI: 10.1021/acsami.6b03900
ACS Appl. Mater. Interfaces 2016, 8, 13542−13554

pulse can be identified by physical interfaces between consecutive layers in the structure of NAA-PCs (white arrowheads shown in Figure 1c, left).

3.2. Effect of Anodization Parameters on the Optical Properties of NAA-Based Photonic Crystals. The effect of the different anodization parameters (i.e., anodization period, anodization amplitude, ramp ratio, number of anodization pulses and time of pore widening) over the optical properties of NAA-PCs was evaluated in order to establish a methodology toward the precise engineering of this type of photonic nanostructures.

3.2.1. Effect of Anodization Period (T_P). To study the effect of T_P on the photonic features of NAA-PCs, the anodization period was varied from 400 to 1100 s with an interval (ΔT_P) of 100 s. Figure 2a shows representative cross-sectional SEM images and the corresponding anodization profiles of NAA-based photonic crystals fabricated by STPA with different anodization periods (i.e., 500, 700, 900 and 1100 s). These anodization profiles denote that the anodization voltage (i.e., output) follows closely the current density (i.e., input) applied during the anodization process with a slight time delay, as expected by the insulating effect of the oxide barrier layer. However, as compared to other anodization processes,[65] the conditions used in our study make it possible to minimize the voltage recovery stage as so the anodization current density can be efficiently translated into modifications of porosity in depth. These conditions enable the precise engineering of the effective medium of NAA in order to create photonic crystal structures. SEM image analysis also reveals that L_{T_P} increases linearly with T_P, where L_{TP} was found to be 116 ± 7, 169 ± 6, 213 ± 9 and 268 ± 13 nm for NAA-PCs produced with anodization periods of 500, 700, 900 and 1100 s, respectively (Figure S1 of the Supporting Information). The transmission spectrum of NAA-PCs as a function of T_P (Figure 2b) also reveals that the position of the characteristic transmission peaks of NAA-PCs (λ_{Peak}) is red-shifted with T_P (Figure 2c). In other words, the wavelength at which NAA-PCs reflect light more efficiently increases as the anodization period becomes longer. The analysis of the transmission spectra establishes a linear relationship between T_P and λ_{Peak}, as denoted in Figure 2c. Nevertheless, this dependence is distinct for the different transmission orders (i.e., first, second and third order) as revealed by the slopes of the linear fittings shown in Figure 2c. The slopes for the first, second and third order peaks were found to be 0.85 ± 0.05, 0.27 ± 0.06 and 0.34 ± 0.03 nm s^{-1}, respectively, showing a strong dependence of λ_{Peak} on T_P for the first order peak, which becomes less marked for the second and third order peaks. Furthermore, it is worthwhile noting that, whereas the first order peak can be tuned across the UV−visible-NIR spectrum (i.e., from 200 to 1000 nm), the second order peak can only be shifted through the UV range and the lower part of the visible spectrum. Only NAA-PCs fabricated with an anodization period of 900, 1000 and 1100 s exhibit third order peak, which is limited within the UV range. Therefore, the characteristic transmission peaks of NAA-PCs produced by STPA can be tuned across the entire UV−visible-NIR spectrum by manipulating the anodization period. Note that the position of the characteristic transmission peak in the UV−visible-NIR spectrum establishes the interferometric color of NAA-PCs. Those NAA-PC structures with the first order peak located within the visible spectrum (i.e., from 400 to 800 nm) display vivid interferometric colors (i.e., purple, cyan, green and red) as they reflect light at wavelengths that correspond to the position of the first order peak (Figure 2c). In contrast, NAA-PCs produced with T_P 400 s (UV), 900 s (NIR), 1000 s (NIR) and 1100 s (NIR) were transparent, as these samples reflect light of wavelength within the UV or NIR ranges. This suggests that the first order peak plays a more significant role in determining the interferometric color of NAA-PCs fabricated by STPA as compared to the weight of the second and third order peaks.

3.2.2. Effect of Anodization Amplitude (A_J). The effect of the anodization amplitude (A_J) on the optical properties of NAA-PCs produced by STPA was studied by varying A_J from 0.21 to 0.63 mA cm^{-2} with an interval of 0.105 mA cm^{-2} while keeping the minimum current density constant (i.e., J_{min} = 0.28 mA cm^{-2}). Cross-sectional SEM images of NAA-PCs produced with A_J = 0.21, 0.42 and 0.63 mA cm^{-2} (Figure 3a) reveal that L_{T_P} increases linearly with A_J and the period length was found to be 135 ± 6, 173 ± 16 and 261 ± 15 nm, respectively (Figure S1 of the Supporting Information). As far as the characteristic transmission peaks is concerned, only NAA-PCs produced with A_J = 0.63 mA cm^{-2} exhibit first, second and third order characteristic peaks in the transmission spectrum (Figure 3b). NAA photonic crystals produced with A_J from 0.315 to 0.525 mA cm^{-2} show first and second order peaks whereas NAA-PCs fabricated with A_J = 0.21 mA cm^{-2} present only first order characteristic peak. It was observed that the first order peaks are more well-resolved and intense than those corresponding to the second and third orders. Furthermore, the position of the characteristic transmission peaks (λ_{Peak}) undergoes a red shift (i.e., shift toward the NIR range) as A_J increases. Figure 3b shows that all the first order peaks are located within the visible range except that of NAA-PCs produced with A_J = 0.63 mA cm^{-2}, which is located in the NIR region. Contrarily, all the second and third order peaks are located within the UV region for any NAA-PC. These results demonstrate that the transmission peaks across the UV−visible-NIR spectrum of NAA-PCs produced by STPA waveforms can be tuned by A_J.

A more detailed analysis of the dependence of the positon of the characteristic transmission peaks on the anodization amplitude can be obtained from the fitting lines shown in Figure 3b. The slope of the fitting lines for the first and second order peaks was found to be 938 ± 47 and 495 ± 98 nm (mA cm^{-2})$^{-1}$, respectively. This result reveals that the effect of A_J on λ_{Peak} is almost 2-fold stronger for the first than for the second order peak (note that only one sample displayed third order peak, A_J = 0.63 mA cm^{-2}). Analogously to the case of T_P, only NAA-PCs with the first order characteristic peak located within the visible range of the spectrum feature interferometric colors. NAA-PCs produced with different values of A_J displayed vivid colors, which ranged from purple, green, chartreuse to red. Only NAA-PCs fabricated with A_J = 0.63 mA cm^{-2} were found to be transparent, as these photonic crystal structures reflect light in the NIR range (Figure 3b).

3.2.3. Effect of Number of Anodization Pulses (N_P). The effect of the number of STPA pulses (N_P) on the optical properties of NAA-PCs was analyzed by modifying N_P from 62 (12 h) to 310 pulses (60 h) with an interval of 62 (12 h) pulses. Note that the rest of anodization parameters were kept constant (i.e., T_P = 700 s, A_J = 0.42 mA cm^{-2}, S_{up}/S_{down} = 1 and t_{pw} = 0 min). Figure 4a illustrates the effect of N_P on the position of the characteristic transmission peaks of NAA-PCs. All the NAA-PCs show first and second order transmission

DOI: 10.1021/acsami.6b03900
ACS Appl. Mater. Interfaces 2016, 8, 13542−13554

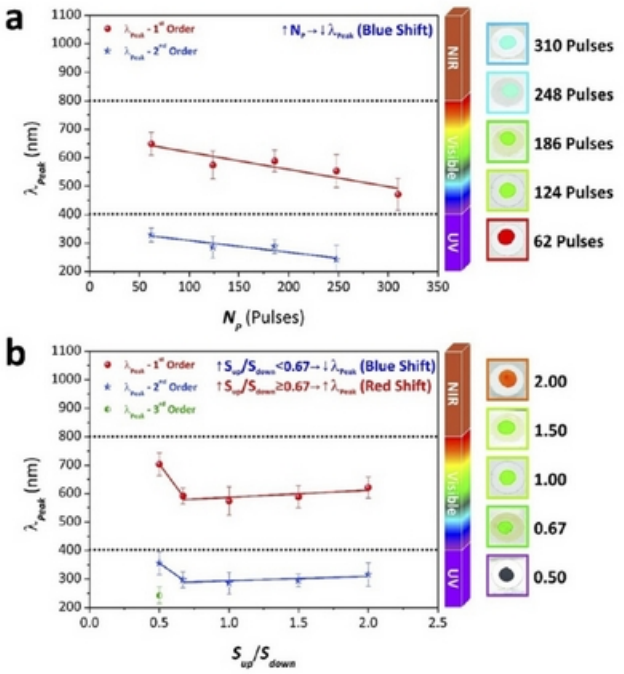

Figure 4. Characteristic transmission peaks tuneability by modifying the number of anodization pulses (N_p) and the ramp ratio (S_{up}/S_{down}). (a) Position of the 1st and 2nd characteristic transmission peaks of NAA-PCs with N_p (NB: T_p = 700 s, A_j = 0.42 mA cm^{-2}, S_{up}/S_{down} = 1 and t_{pw} = 0 min) (left) and digital pictures of NAA-PCs from 62 to 310 pulses denoting the interferometric color displayed by these photonic crystal structures (right). (b) Position of the 1st, 2nd and 3rd characteristic transmission peaks of NAA-PCs as a function of S_{up}/S_{down} (NB: T_p = 700 s, A_j = 0.42 mA cm^{-2}, N_p = 124 pulses and t_{pw} = 0 min) (left) and digital pictures of NAA-PCs from 0.50 to 2.00 revealing the interferometric color displayed by these photonic crystal structures (right).

peaks but those NAA-PCs produced with N_p = 310 pulses only displayed the first order peak. No third order peak was observed for any of the NAA-PCs and the position of the first and second transmission peaks undergoes a blue shift as the number of anodization pulses increases. It is worthwhile to stress that the total thickness of NAA-PCs is directly proportional to the number of pulses (i.e., anodization time). So, the higher the number of pulses the thicker the total thickness of NAA-PCs. Figure 4a shows a linear relationship between N_p and λ_{Peak}, denoting that the first order peaks are located within the visible spectrum whereas the second order peaks are in the UV range for the whole range of N_p studied. The dependence of λ_{Peak} on N_p obtained from the slope of the fitting lines shown in Figure 4a was found to be −0.6 ± 0.1 and −0.4 ± 0.1 nm pulse^{-1}, for the first and second order peaks, respectively, suggesting a fairly stronger effect of N_p on λ_{Peak} for the first order peaks. However, when compared with the effect of T_p and A_j, the dependency of λ_{Peak} on N_p is less significant. Furthermore, it was found that NAA-PCs produced with different N_p also display distinctive interferometric colors, which are established by the position of the first order peak. NAA-PCs produced with different number of anodization pulses feature blue, green and red color, which is blue-shifted with N_p (Figure 4a).

3.2.4. Effect of Ramp Ratio (S_{up}/S_{down}). Anodization pulses in STPA consist of linear increments and decrements of current density from a minimum to a maximum value and vice versa denoted by increasing and decreasing current density ramps (i.e., S_{up} and S_{down}) (see graphic definition in Figure 1a). The ramp ratio, defined as S_{up}/S_{down}, was systematically modified from 0.5 to 2 in order to study the effect of this anodization parameter on the optical properties of NAA-PCs. The values of S_{up} and S_{down} for the different ratios estimated by eq 1 were 0.0018 and 0.0036 mA cm^{-2} s^{-1} for S_{up}/S_{down} = 0.5, 0.0020 and 0.0030 mA cm^{-2} s^{-1} for S_{up}/S_{down} = 0.67, 0.0024 and 0.0024 mA cm^{-2} s^{-1} for S_{up}/S_{down} = 1, 0.0030 and 0.0020 mA cm^{-2} s^{-1} for S_{up}/S_{down} = 1.5 and 0.0036 and 0.0018 mA cm^{-2} s^{-1} for S_{up}/S_{down} = 2, respectively. Figure 4b depicts the position of the characteristic transmission peak of NAA-PCs produced by STPA with different S_{up}/S_{down}, where all the samples exhibit both first and second order characteristic peaks and only NAA-PCs produced with S_{up}/S_{down} = 0.5 feature third order peak. Both the first and second order peaks follow the same trend with the ramp ratio, where a blue shift in their position takes place from 0.5 to 0.67. Nonetheless, further increase in S_{up}/S_{down} up to 2 leads to a slight red shift in λ_{Peak} for both orders (Figure 4b). As determined by the slopes of the fitting lines, the first order peak has a dependence of −230 ± 150 nm per ramp ratio unit from S_{up}/S_{down} = 0.5 to S_{up}/S_{down} = 0.67, and 47 ± 10 nm per ramp ratio unit from S_{up}/S_{down} = 0.67 to S_{up}/S_{down} = 2. The second order peak, however, presents a dependence of −127 ± 78 nm per ramp ratio unit from S_{up}/S_{down} = 0.5 to S_{up}/S_{down} = 0.67, and 30 ± 7 nm per ramp ratio unit from S_{up}/S_{down} = 0.67 to S_{up}/S_{down} = 2. These results denote that S_{up}/S_{down} has a stronger influence on the first order peak as compared to that shown by the second order peak. In addition, the position of the first and second order peaks are found to be in the visible and UV part of the spectrum and the only third order peak is located within the UV region of the spectrum. These NAA-PCs also displayed interferometric colors established by the position of the first order characteristic peak (Figure 4b).

3.2.5. Effect of Pore Widening Time (t_{pw}). To widen the pore size of NAA photonic structures has been demonstrated as an optimal means of enhancing the contrast of porosity between consecutive layers due to the gradient in dissolution rate shown by these layers produced at different current density values.[66] In our study, the pore size of NAA-PCs produced by STPA was widened by wet chemical etching in an aqueous solution 5 vol % H_3PO_4 at 35 °C. NAA-PCs were etched in this solution from 0 to 6 min with an interval of 2 min. Figure 5a shows representative top and cross-sectional SEM images of NAA-PCs before and after the aforementioned pore widening treatment. Top view SEM images of NAA-PCs reveal that these structures feature a pore size in the top layer of 8 ± 2 and 18 ± 4 nm before (t_{pw} = 0 min) and after etching (t_{pw} = 6 min), respectively. Figure 5b–e shows the transmission spectrum of representative NAA-PCs produced by STPA with T_p = 500, 700, 900 and 1100 s at different etching times. The transmission spectrum of NAA-PCs produced with T_p = 500 and 1100 s show first, second, third and fourth order peaks, NAA-PCs fabricated with T_p = 700 s only show first and second order characteristic peaks and NAA-PCs with T_p = 900 show first, second and third order transmission peaks. In all the cases, the position and relative intensity of the characteristic transmission peaks decreases with the order and it is also observed that all the peaks undergo a linear blue shift with the pore widening time, which is in good agreement with previous studies.[67−69] For example, the slope of the fitting lines for the first, second and third order peaks in NAA-PCs produced were

DOI: 10.1021/acsami.6b03900
ACS Appl. Mater. Interfaces 2016, 8, 13542−13554

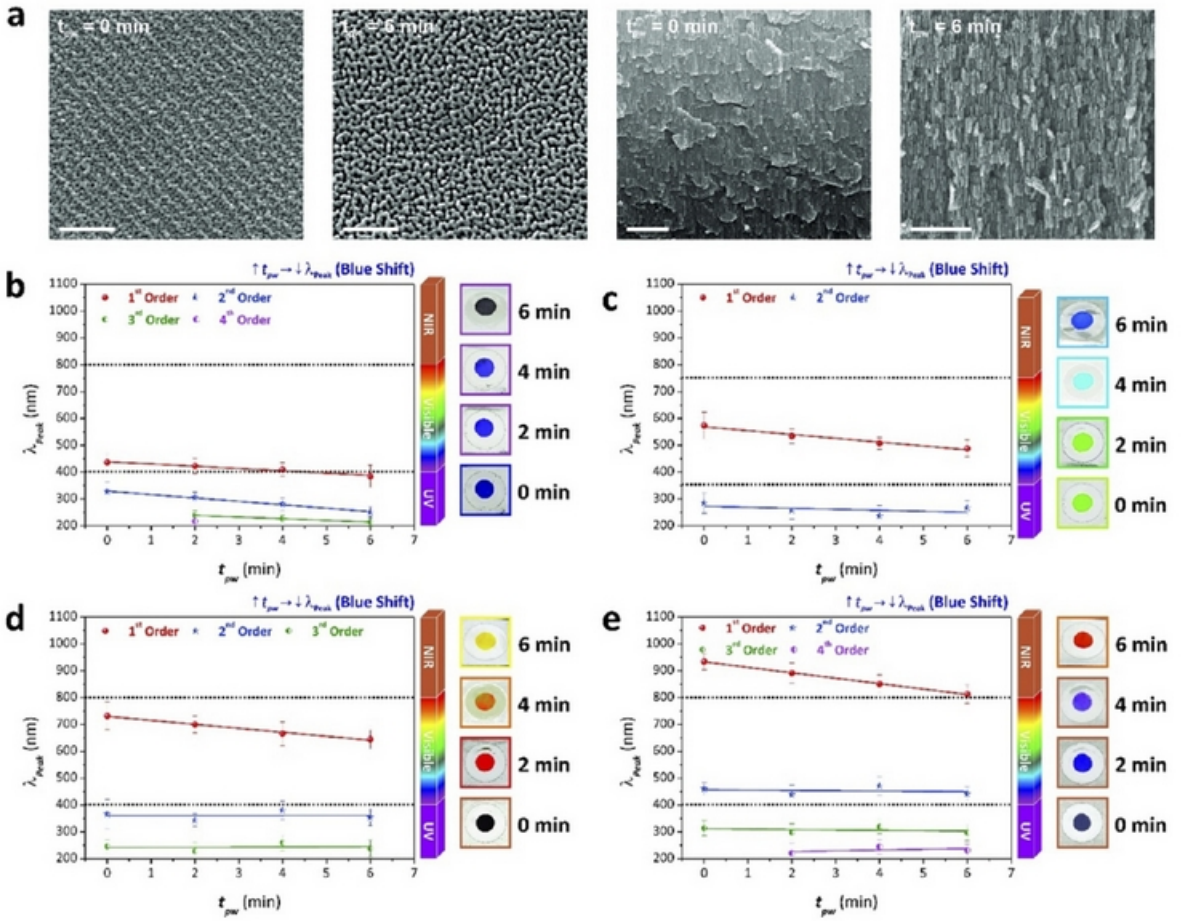

Figure 5. Characteristic transmission peaks tuneability by modifying the pore widening time (t_{pw}). (a) Top and cross-sectional SEM views of a representative NAA-PCs before and after pore widening treatment (T_P = 500 s, A_J = 0.42 mA cm^{-2}, S_{up}/S_{down} = 1 and N_P = 124 pulses) (scale bar (top) = 250 nm and scale bar (cross section) = 500 nm). (b–e) Position of the 1st, 2nd, 3rd and 4th characteristic transmission peaks of NAA-PCs as a function of t_{pw} for NAA-PCs produced with T_P = 500 s (b), 700 s (c) 900 s (d) and 1100 s (e) (left) and digital pictures of NAA-PCs from 0 to 6 min of pore widening treatment showing the interferometric color displayed by these photonic crystal structures (right).

found to be −8.0 ± 1.0, −12.0 ± 0.7 and −6.0 ± 0.2 nm min^{-1}, respectively. Furthermore, we also observed that the relative distance between the different transmission peaks increases with the anodization period (Figure 5b–e). As far as the position of the different characteristic transmission peaks is concerned, whereas the first order peaks are located within the visible range for all the pore widening times and all the anodization periods studied, the second, third and fourth order peaks are positioned in the UV region of the spectrum (except for the second order peak of NAA-PCs produced with T_P = 1100 s, which is entirely located in the visible range) within the period of pore widening time studied. Another interesting characteristic that a pore widening treatment enables is the tuneability of the original interferometric color of NAA-PCs. The chemical etching treatment leads to a modification of the nanoporous structure of NAA-PCs, the effective medium of which is altered. This in turn induces a change in the photonic stop band of these photonic crystal structures. Therefore, the interferometric color displayed by NAA-PCs can be precisely tuned across the whole UV–visible-NIR spectrum through the alteration of their photonic stop band induced by a pore widening treatment (Figure 5b–e).

Table S1 (Supporting Information) provides a detailed summary of the effect of each of these factors on the position of the characteristic transmission peaks of NAA-PCs. These parameters allow a precise and fine-tuning of the photonic features of NAA-PCs such as the position of the characteristic reflection peaks across UV–vis-NIR spectrum and their interferometric color. A red shift in the position of the characteristic transmission peaks can be achieved by increasing T_P and A_J, whereas a blue shift can be accomplished by increasing N_P and t_{pw}. S_{up}/S_{down} induces a blue shift and a slight red shift for values of the ramp ratio below and above 0.67, respectively. This analysis has also revealed that the first order peak of NAA-PCs produced by STPA exhibit a strong dependence on T_P as compared to other factors, and its position can be finely positioned across the entire UV–visible-NIR spectrum by modifying T_P. Therefore, T_P can be considered as the most effective anodization parameter to tune the photonic properties of NAA-PCs across the light spectrum.

It is worthwhile noting that, as our study demonstrates, the above-mentioned anodization parameters have a direct impact on the period length (L_{T_P}), which is the key structural feature stablishing the optical properties of NAA-PCs. We found that L_{T_P} increases proportionally with T_P and A_J (see Figure S1 of the Supporting Information) and these anodization parameters

DOI: 10.1021/acsami.6b03900
ACS Appl. Mater. Interfaces 2016, 8, 13542–13554

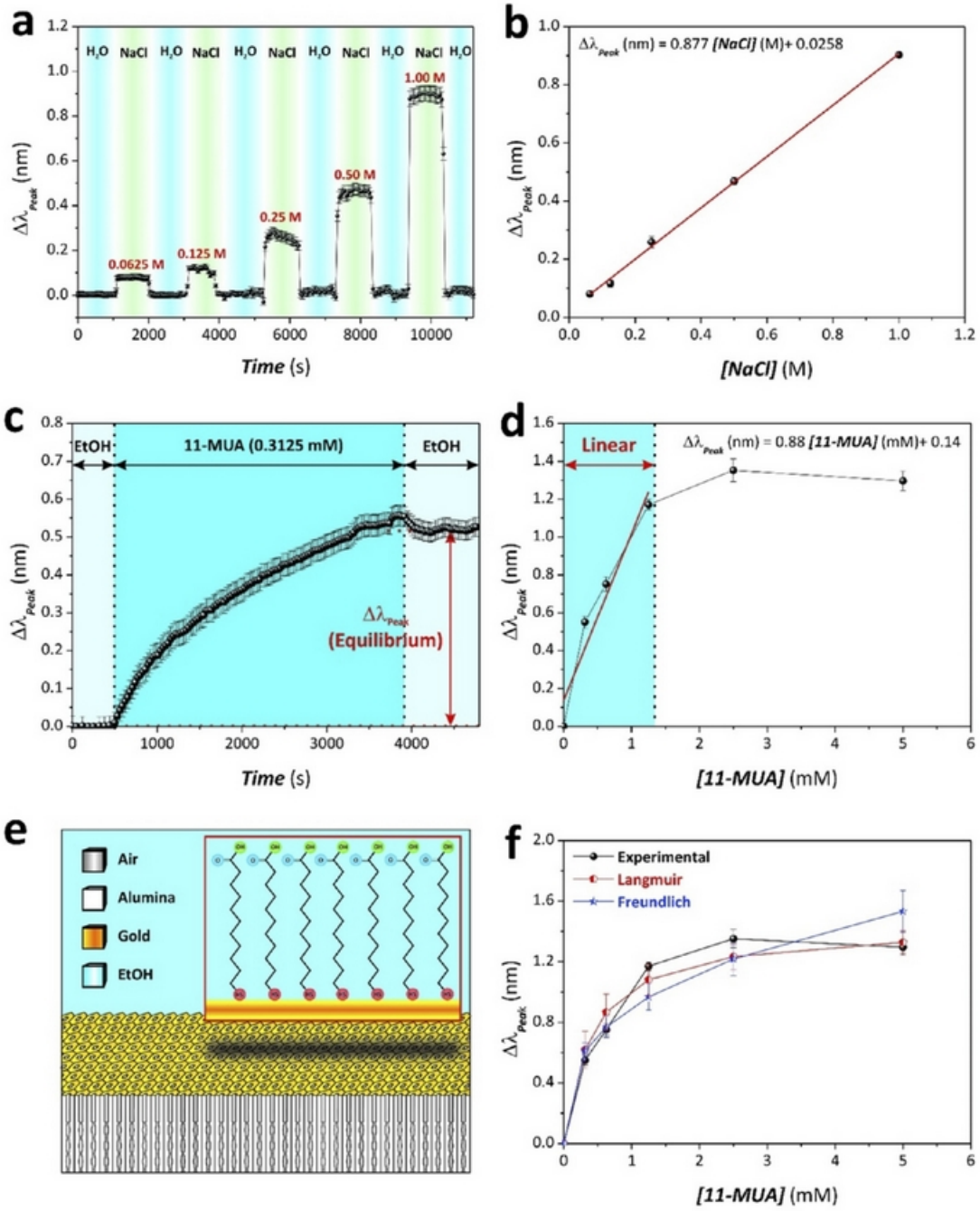

Figure 6. Assessment of NAA-PCs produced by STPA as optical sensing platforms combined with RIfS (NB: NAA-RFs produced with T_p = 700 s, A_j = 0.420 mA cm^{-2}, N_p = 124 pulses, S_{up}/S_{down} = 1 and t_{pw} = 0 min). (a) Real-time monitoring of $\Delta\lambda_{Peak}$ by RIfS as a function of the concentration of NaCl in water. (b) Linear correlation between $\Delta\lambda_{Peak}$ and [NaCl]. (c) Representative real-time monitoring of $\Delta\lambda_{Peak}$ by RIfS as a function of concentration of 11-MUA (i.e., 0.625 mM) in ethanol for the establishment of $\Delta\lambda_{Peak}$ at equilibrium. (d) $\Delta\lambda_{Peak}$ as a function of concentration of 11-MUA in ethanol for the whole range of concentrations studied (i.e., from 0.3125 to 5 mM) (NB: blue area denotes the linear working range). (e) Schematic diagram showing the formation of 11-MUA SAMs on the surface of gold-coated NAA-PCs. (f) Langmuir and Freundlich binding isotherms and experimental values.

have been demonstrated to have the most significant impact on the position of the characteristic transmission peaks. We also established that an increment of the number of pulses (i.e., total anodization time) results in a slight blue shift in the position of the characteristic transmission peaks of NAA-PCs due to the increment in the total thickness of the NAA-PC. Note that the transmission spectrum of NAA-PCs is also dependent on the total thickness of the film and two effects must be considered in this phenomenon: namely; (i) the interference of light from all layers of the multilayered NAA-PC structure and (ii) the light interference produced by the reflections of light at the interfaces bordering the NAA-PC film. However, we observed that this shift is significantly small as compared to that occurring when the anodization period and the anodization

DOI: 10.1021/acsami.6b03900
ACS Appl. Mater. Interfaces 2016, 8, 13542−13554

amplitude are modified. As far as the effect of the pore widening time is concerned (t_{pw}), the position of the characteristic transmission peaks undergoes a relatively marked blue shift with the pore widening time as a result of the modification of the effective medium of NAA. The effective refractive index of NAA-PCs decreases when their nanoporous structure is etched (i.e., increment of porosity) and this is translated into a blue shift in the transmission peaks of the photonic crystal structure. We also established that this shift is directly dependent on the anodization period and different NAA-PC structures present different shifts for the same pore widening treatment. Finally, we established that an increment in the ramp ratio (S_{up}/S_{down}) results in a slight red shift for values of the ramp ratio above 0.67, indicating that S_{up} increases the period length in the NAA-PC structure. The effect of these parameters on the characteristic transmission peaks of NAA-PCs produced by sawtooth-like pulse anodization are similar to and in good agreement with those observed in NAA-PC structures by other electrochemical approaches such as sinusoidal pulse anodization.[69]

To conclude, our analysis on the effect of the different anodization parameters on the photonic properties of NAA-PCs produced by sawtooth-like pulse anodization provides a fundamental understanding and a solid rationale toward a precise engineering and design of this type of photonic crystal structures.

3.3. Assessment of the Effective Medium of NAA-PCs Produced by STPA and their Use as Optical Sensing Platforms. The fabrication process of NAA-PCs using sawtooth-like pulse anodization profile produces photonic crystal nanostructures based on air and layers of NAA with sawtooth-like modulated porosity in depth. By using the effective medium approximation, the optical properties of NAA-PCs, which are considered a composite material, can be described based on the average properties of the individual compounds (i.e., air and alumina).[70] To assess the effective medium of these photonic structures, the nanopores of a reference NAA-PC (i.e., T_P = 700 s, A_J = 0.42 mA cm^{-2}, S_{up}/S_{down} = 1, N_P = 124 and t_{pw} = 0 min) were infiltrated with different analytical solutions of NaCl with concentrations ranging from 0 to 1 M in order to change the refractive index of the medium filling the nanopores, which ranged from 1.3338 (0 M) to 1.3433 (1 M) RIU, respectively. The correlation between the position of the characteristic reflection peak (λ_{Peak}) and the concentration of NaCl solution filling the nanopores ([NaCl]) was estimated in real-time by RIfS in a flow cell, where the different analytical solutions of NaCl where sequentially injected into the system by a syringe pump (see the Experimental Section). Figure 6a shows that the position of the characteristic reflection peak of NAA-PCs undergoes red shifts with the infiltration of their nanopores with solutions of higher refractive index. The magnitude of shift in the characteristic reflection peak ($\Delta\lambda_{Peak}$) from the water baseline (i.e., n_{water} = 1.3338 RIU) was found to be linear with the concentration of NaCl, which makes this photonic crystal structures optimal for the development of optical sensing platforms (Figure 6b).[67,69] Given that there is no chemical interaction between NaCl molecules and the surface of alumina, the shifts in the position of λ_{Peak} were reversible and the baseline level was achieve after water was flowed through the system (Figure 6a).

Finally, to demonstrate the potential applicability of NAA-PCs produced by STPA as sensing platforms, these photonic crystal structures were combined with RIfS to monitor the formation of self-assembled monolayers (SAMs) of 11-mercaptoundecanoic acid (11-MUA) molecules onto the surface of gold-coated NAA-PCs in real-time. A set of reference NAA-PCs (i.e., T_P = 700 s, A_J = 0.42 mA cm^{-2}, S_{up}/S_{down} = 1, N_P = 124 and t_{pw} = 0 min) were coated with a thin layer of gold on the top by sputter coating technique (*vide supra*). Each of these NAA-PCs was exposed to the different analyte solutions of 11-MUA in the flow cell. Our RIfS system makes it possible to monitor the formation of 11-MUA SAMs by monitoring shifts in the characteristic reflection peaks of NAA-PCs ($\Delta\lambda_{Peak}$). The formation of monolayers of thiolate molecules onto gold surfaces follow the mechanism shown in eq 3.

$$2\text{–RSH} + 2\text{Au}_{(s)} \rightarrow 2\text{RS–Au}_{(s)} + \text{H}_2 \quad (3)$$

Figure 6c shows a representative example of real-time monitoring of the formation of 11-MUA SAMs onto the surface of gold-coated NAA-PCs by RIfS. In this experiment, ethanol was flowed first through the cell in order to obtain a stable baseline. Next, analytical solutions of 11-MUA of different concentrations (i.e., from 0.3125 to 5 mM) were injected into the flow cell. The chemical interaction between thiol groups present in 11-MUA molecules and the gold-coated surface of NAA-PCs results in a red shift in λ_{Peak} (Figure 6c). After λ_{Peak} reaches its maximum value, fresh ethanol solution is flowed again through the flow cell. During this process, λ_{Peak} decreases slightly due to the removal of physisorbed thiol molecules form the surface of NAA-PCs. Following this procedure and using λ_{Peak} as the sensing parameter, different analytical solutions of 11-MUA were flowed through the cell using fresh gold-coated NAA-PCs. As shown in Figure 6d, $\Delta\lambda_{Peak}$ increases with the concentration of 11-MUA, establishing a linear relationship for the concentration range from 0.3125 to 1.25 mM. However, $\Delta\lambda_{Peak}$ saturates at concentrations above 1.25 mM and a plateau in $\Delta\lambda_{Peak}$ is achieved due to the saturation of binding sites on the gold-coated surface of NAA-PCs with 11-MUA molecules above that concentration (Figure 6e). A linear fitting within the linear range (i.e., working range) establishes a sensitivity (S) of 8.88 nm mM^{-1}, a low limit of detection (LLoD) of 0.3125 mM and a linearity (R^2) of 0.90.

The obtained results were fitted into Langmuir and Fruendlich binding isotherm models in order to establish the kinetics binding mechanism of 11-MUA molecules onto gold-coated NAA-PCs.[52,70] eq 4 establishes the Langmuir isotherm model for the binding of thiol molecules to gold surfaces.

$$\frac{[\text{R–SH}]}{\Delta\lambda^{e}_{Peak}} = \frac{1}{K_L \Delta\lambda^{m}_{Peak}} + \frac{[\text{R–SH}]}{\Delta\lambda^{m}_{Peak}} \quad (4)$$

where $\Delta\lambda^{e}_{Peak}$ is the shift in the reflection peak positon at equilibrium and K_L and $\Delta\lambda^{m}_{Peak}$ characteristic constants of the Langmuir model.

The Langmuir isotherm model describes the binding of molecules to flat/smooth surfaces. This model considers the number of binding sites to be independent of the concentration of analyte molecules and constant throughout the reaction.[70] The characteristic Langmuir's constants can be estimated form a linear fitting between $\Delta\lambda^{e}_{Peak}$ and [11-MUA].

The Freundlich isotherm model adapted to the binding of thiol molecules to gold surfaces is given by eq 5.

$$\log \Delta\lambda^{e}_{Peak} = \log(K_F) + \frac{1}{n}\log[\text{R–SH}] \quad (5)$$

DOI: 10.1021/acsami.6b03900
ACS Appl. Mater. Interfaces 2016, 8, 13542–13554

Table 1. Langmuir and Freundlich Isotherm Model Constants Obtained from the Experimental Results Shown in Figure 6f

Langmuir model			Freundlich model		
$\Delta\lambda^{m}_{Peak}$ (nm)	K_L (mM^{-1})	R^2	K_F	n	R^2
1.44 ± 0.08	0.41 ± 0.10	0.99	0.90 ± 0.01	3.02 ± 0.71	0.81

where K_F and n are the characteristic Freundlich constants.

The Freundlich isotherm model describes the binding of molecules to rough surfaces with the assumption that the number of binding sites increases with the concentration of analyte molecules (i.e., [R−SH]). The Freundlich characteristic constants can be obtained by the intercept and slope of the linear fitting between log $\Delta\lambda^{e}_{Peak}$ against log[11-MUA].

The experimental data were fitted to both isotherm models and the characteristic constants for each model were calculated. The calculated characteristic parameters and correlation factors for both models are summarized in Table 1. These results reveal that the Langmuir isotherm model describes the experimental data better than the Freundlich model, according to R^2 values. This denotes that the binding mechanism of 11-MUA molecules to the gold-coated surface of NAA-PCs follows a Langmuir isotherm model. Figure 6f also shows that the experimental data fit closely to the Langmuir isotherm model. This indicates that the binding between thiol molecules and gold-coated NAA-PCs follows a monolayer sorption mechanism, which is expected as the number of binding sites on the surface of NAA-PCs remains constant during the process and the surface of that thin film is fairly flat and smooth.

CONCLUSIONS

In summary, this study has presented a new anodization approach, so-called sawtooth-like pulse anodization, aiming to engineer the effective medium of nanoporous anodic alumina following a sawtooth fashion in depth. The resulting photonic crystal structures feature optical properties (i.e., characteristic transmission peaks and interferometric colors), which can be precisely tuned by different anodization parameters. The effects of the anodization period, the anodization amplitude, the number of anodization pulses, the ramp ratio and the pore widening time over the optical properties of NAA-PCs have been established by a systematic modification of these parameters and subsequent analysis of the optical properties of these photonic crystal structures. These fabrication parameters make it possible to engineer the nanoporous structure of NAA with precision and modify the photonic stop band of NAA in order to create a set of unique photonic crystal structures. This study has also verified that the characteristic reflection peak of NAA-PCs produced by STPA changes linearly with the concentration of the medium filling the nanopores, making these photonic crystal structure excellent candidates for the development of optical sensing platforms. Furthermore, the applicability of NAA-based photonic crystals as optical sensing platforms has been demonstrated by monitoring the formation of monolayers of thiol molecules on the surface of gold-coated NAA photonic crystals in real-time. The binding mechanism between thiol molecules and gold-coated NAA photonic crystals was shown to follow a Langmuir isotherm model.

In conclusion, this study provides a foundation on the structural engineering and sensing applicability of NAA photonic crystals produced by sawtooth-like pulse anodization approach, which could open new opportunities for the future development and application of these photonic structures.

ASSOCIATED CONTENT

Supporting Information

The Supporting Information is available free of charge on the ACS Publications website at DOI: 10.1021/acsami.6b03900.

Further information about the relationship between the period length (L_{T_p}) and the anodization period (T_p) and the anodization amplitude (A_J); this file also contains a comprehensive table summarizing the effect of each anodization parameter on the position of the characteristic transmission peaks of NAA-PCs produced by STPA (PDF).

AUTHOR INFORMATION

Corresponding Authors

*Doctor Abel Santos. Phone: +61 8 8313 1535. Fax: +61 8 8303 4373. Email: abel.santos@adelaide.edu.au. Web page: http://www.adelaide.edu.au/directory/abel.santos.

*Professor Dusan Losic. Phone: + 61 8 8313 4648. Fax: +61 8 8303 4373. Email: dusan.losic@adelaide.edu.au. Web page: http://www.adelaide.edu.au/directory/dusan.losic.

Author Contributions

Ms. Cheryl Suwen Law carried out the experimental part of this work assisted by Dr. Abel Santos and Ms. Mahdieh Nemati. Dr. Abel Santos conceived the idea and designed the experimental part of this work. The obtained results were discussed and analyzed by all the authors. The final version of the paper was written through contributions of all the authors. All the authors have given approval to the final version of the paper.

Notes

The authors declare no competing financial interest.

ACKNOWLEDGMENTS

Authors thank the support provided by the Australian Research Council (ARC) through the grants number DE140100549, DP120101680 and FT110100711 and the School of Chemical Engineering (UoA). Authors thank the Adelaide Microscopy (AM) centre for FEG-SEM characterization.

REFERENCES

(1) Krauss, T. F.; Richard, M. Photonic Crystals in the Optical Regime - Past, Present and Future. *Prog. Quantum Electron.* **1999**, *23* (2), 51−96.

(2) *Electrochemically Engineered Nanoporous Materials: Methods, Properties and Applications*; Losic, D.; Santos, A., Eds.; Springer International Publishing: Cham, Switzerland, 2015.

(3) Charlton, M. D. B.; Roberts, S. W.; Parker, G. J. Guided Mode Analysis, and Fabrication of a 2-Dimensional Visible Photonic Band Structure Confined within a Planar Semiconductor Waveguide. *Mater. Sci. Eng., B* **1997**, *49* (2), 155−165.

(4) Gerard, J. M.; Izrael, A.; Marzin, J. Y.; Padjen, R.; Ladan, F. R. Photonic Bandgap of Two-Dimensional Dielectric Crystals. *Solid-State Electron.* **1994**, *37* (4), 1341−1344.

(5) Berger, V.; Gauthier-Lafaye, O.; Costard, E. Costard, E. Fabrication of a 2D Photonic Bandgap by a Holographic Method. *Electron. Lett.* **1997**, *33* (5), 425−426.

(6) Yi-Yan, A.; Wilkinson, C. D.; Laybourn, P. J. Two-Dimensional Grating Unit Cell Demultiplexer for Thin-Film Optical Waveguides. *IEEE J. Quantum Electron.* **1980**, *16*, 1089−1092.
(7) Zengerle, R. Light Propagation in Singly and Doubly Periodic Planar Waveguides. *J. Mod. Opt.* **1987**, *34* (12), 1589−1617.
(8) Dallesasse, J. M.; Holonyak, N., Jr.; Sugg, A. R.; Richard, T. A.; El-Zein, N. Hydrolyzation Oxidation of AlxGa1− xAs-AlAs-GaAs Quantum Well Heterostructures and Superlattices. *Appl. Phys. Lett.* **1990**, *57* (26), 2844−2846.
(9) Little, B. E.; Foresi, J. S.; Steinmeyer, G.; Thoen, E. R.; Chu, S. T.; Haus, H. A.; Ippen, E. P.; Kimerling, L. C.; Greene, W. Ultra-Compact Si-SiO_2 Microring Resonator Optical Channel Dropping Filters. *IEEE Photonics Technol. Lett.* **1998**, *10* (4), 549−551.
(10) Scherer, A.; Painter, O.; d'Urso, B.; Lee, R.; Yariv, A. InGaAsP Photonic Band Gap Crystal Membrane Microresonators. *J. Vac. Sci. Technol., B* **1998**, *16* (6), 3906−3910.
(11) Tonucci, R. J.; Justus, B. L.; Campillo, A. J.; Ford, C. E. Nanochannel Glass Arrays. *Science* **1992**, *258*, 783−785.
(12) Brittain, S.; Paul, K.; Zhao, X. M.; Whitesides, G. Soft Lithography and Microfabrication. *Phys. World* **1998**, *11* (5), 31−36.
(13) Lawandy, N. M.; Balachandran, R. M.; Gomes, A. S. L.; Sauvain, E. Laser Action in Strongly Scattering Media. *Nature* **1994**, *368* (6470), 436−438.
(14) Holland, B. T.; Blanford, C. F.; Stein, A. Synthesis of Macroporous Minerals with Highly Ordered Three-Dimensional Arrays of Spheroidal Voids. *Science* **1998**, *281* (5376), 538−540.
(15) Grüning, U.; Lehmann, V.; Engelhardt, C. M. Two-Dimensional Infrared Photonic Band Gap Structure Based on Porous Silicon. *Appl. Phys. Lett.* **1995**, *66* (24), 3254−3256.
(16) Rowson, S.; Chelnokov, A.; Cuisin, C.; Lourtioz, J. M.; December. Three-Dimensional Characterisation of a Two-Dimensional Photonic Bandgap Reflector at Midinfrared Wavelengths. *IEE Proc.: Optoelectron.* **1998**, *145* (6), 403−408.
(17) Grüning, U.; Lehmann, V.; Ottow, S.; Busch, K. Macroporous Silicon with a Complete Two-Dimensional Photonic Band Gap Centered at 5 μm. *Appl. Phys. Lett.* **1996**, *68* (6), 747−749.
(18) Lau, H. W.; Parker, G. J.; Greef, R.; Hölling, M. High Aspect Ratio Submicron Silicon Pillars Fabricated by Photoassisted Electrochemical Etching and Oxidation. *Appl. Phys. Lett.* **1995**, *67* (13), 1877−1879.
(19) Wehrspohn, R. B.; Schilling, J.; Choi, J.; Luo, Y.; Matthias, S.; Schweizer, S. L.; Müller, F.; Gösele, U.; Lölkes, S.; Langa, S.; Carstensen, J. Electrochemically-Prepared 2D and 3D Photonic Crystals. In *Photonic Crystals: Advances in Design, Fabrication, and Characterization*; Busch, K.; Lölkes, S.; Wehrspohn, R. B.; Föll, H., Eds.; Wiley-VCH Verlag GmbH & Co. KGaA: Weinheim, Germany, 2004; pp 63−82.
(20) Uhlir, A. Electrolytic Shaping of Germanium and Silicon. *Bell Syst. Tech. J.* **1956**, *35* (2), 333−347.
(21) Lehmann, V.; Föll, H. Formation Mechanism and Properties of Electrochemically Etched Trenches in n-type Silicon. *J. Electrochem. Soc.* **1990**, *137* (2), 653−659.
(22) Canham, L. T. Silicon Quantum Wire Array Fabrication by Electrochemical and Chemical Dissolution of Wafers. *Appl. Phys. Lett.* **1990**, *57* (10), 1046−1048.
(23) Lehmann, V.; Gösele, U. Porous Silicon Formation: A Quantum Wire Effect. *Appl. Phys. Lett.* **1991**, *58* (8), 856−858.
(24) Lehmann, V. The Physics of Macropore Formation in Low Doped n-Type Silicon. *J. Electrochem. Soc.* **1993**, *140* (10), 2836−2843.
(25) Sailor, M. J. *Porous Silicon in Practice: Preparation, Characterization and Applications*; Wiley-VCH Verlag GmbH & Co. KGaA: Weinheim, Germany, 2012.
(26) Estevez, J. O.; Agarwal, V. Porous Silicon Photonic Crystals. In *Handbook of Porous Silicon*; Canham, L. T., Ed.; Springer International Publishing: Cham, Switzerland, 2014; pp 805−814.
(27) Ilyas, S.; Böcking, T.; Kilian, K.; Reece, P. J.; Gooding, J.; Gaus, K.; Gal, M. Porous Silicon Based Narrow Line-Width Rugate Filters. *Opt. Mater.* **2007**, *29* (6), 619−622.
(28) Mulloni, V.; Pavesi, L. Porous Silicon Microcavities as Optical Chemical Sensors. *Appl. Phys. Lett.* **2000**, *76* (18), 2523−2525.
(29) Xifré-Pérez, E.; Marsal, L. F.; Ferré-Borrull, J.; Pallarès, J. Porous Silicon Omnidirectional Mirrors and Distributed Bragg Reflectors for Planar Waveguide Applications. *J. Appl. Phys.* **2007**, *102* (6), 063111.
(30) Meade, S. O.; Yoon, M. S.; Ahn, K. H.; Sailor, M. J. Porous Silicon Photonic Crystals as Encoded Microcarriers. *Adv. Mater.* **2004**, *16* (20), 1811−1814.
(31) Pacholski, C.; Sartor, M.; Sailor, M. J.; Cunin, F.; Miskelly, G. M. Biosensing Using Porous Silicon Double-Layer Interferometers: Reflective Interferometric Fourier Transform Spectroscopy. *J. Am. Chem. Soc.* **2005**, *127* (33), 11636−11645.
(32) Lin, V. S. Y.; Motesharei, K.; Dancil, K. P. S.; Sailor, M. J.; Ghadiri, M. R. A Porous Silicon-Based Optical Interferometric Biosensor. *Science* **1997**, *278* (5339), 840−843.
(33) Lehmann, V. *Electrochemistry of Silicon - Instrumentation, Science, Materials and Applications*; WILEY-VCH Verlag GmbH & Co. KGaA: Weinheim, Germany, 2002.
(34) Santos, A.; Kumeria, T.; Losic, D. Nanoporous Anodic Aluminum Oxide for Chemical Sensing and Biosensors. *TrAC, Trends Anal. Chem.* **2013**, *44*, 25−38.
(35) Santos, A.; Kumeria, T.; Losic, D. Nanoporous Anodic Alumina: A Versatile Platform for Optical Biosensors. *Materials* **2014**, *7*, 4297−4320.
(36) Kumeria, T.; Santos, A.; Losic, D. Nanoporous Anodic Alumina Platforms: Engineered Surface Chemistry and Structure for Optical Sensing Applications. *Sensors* **2014**, *14*, 11878−11918.
(37) Lee, W.; Park, S. J. Porous Anodic Aluminum Oxide: Anodization and Templated Synthesis of Functional Nanostructures. *Chem. Rev.* **2014**, *114*, 7487−7556.
(38) Masuda, H.; Fukuda, K. Ordered Metal Nanohole Arrays Made by a Two-Step Replication of Honeycomb Structures of Anodic Alumina. *Science* **1995**, *268*, 1466−1468.
(39) Masuda, H.; Hasegwa, F. J. Self-Ordering of Cell Arrangement of Anodic Porous Alumina Formed in Sulfuric Acid Solution. *J. Electrochem. Soc.* **1997**, *144*, L127−L130.
(40) Masuda, H.; Yada, K.; Osaka, A. Self-Ordering of Cell Configuration of Anodic Porous Alumina with Large-Size Pores in Phosphoric Acid Solution. *Jpn. J. Appl. Phys.* **1998**, *37*, L1340−L1342.
(41) Nielsch, K.; Choi, J.; Schwirn, K.; Wehrspohn, R. B.; Gösele, U. Self-ordering Regimes of Porous Alumina: The 10% Porosity Rule. *Nano Lett.* **2002**, *2*, 677−680.
(42) Lee, W.; Ji, R.; Gösele, U.; Nielsch, K. Fast Fabrication of Long-Range Ordered Porous Alumina Membranes by Hard Anodization. *Nat. Mater.* **2006**, *5* (9), 741−747.
(43) Schwirn, K.; Lee, W.; Hillebrand, R.; Steinhart, M.; Nielsch, K.; Gösele, U. Self-Ordered Anodic Aluminum Oxide Formed by H_2SO_4 Hard Anodization. *ACS Nano* **2008**, *2* (2), 302−310.
(44) Lee, W.; Schwirn, K.; Steinhart, M.; Pippel, E.; Scholz, R.; Gösele, U. Structural Engineering of Nanoporous Anodic Aluminium Oxide by Pulse Anodization of Aluminium. *Nat. Nanotechnol.* **2008**, *3* (4), 234−239.
(45) Lee, W.; Kim, J. C.; Gösele, U. Spontaneous Current Oscillations during Hard Anodization of Aluminum under Potentiostatic Conditions. *Adv. Funct. Mater.* **2010**, *20*, 21−27.
(46) Lee, W.; Kim, J. C. Highly Ordered Porous Alumina with Tailor-Made Pore Structures Fabricated by Pulse Anodization. *Nanotechnology* **2010**, *21*, 485304.
(47) Losic, D.; Lillo, M.; Losic, D., Jr. Porous Alumina with Shaped Pore Geometries and Complex Pore Architectures Fabricated by Cyclic Anodization. *Small* **2009**, *5* (12), 1392−1397.
(48) Yi, L.; Zhiyuan, L.; Xing, H.; Yisen, L.; Yi, C. Formation and Microstructures of Unique Nanoporous AAO Films Fabricated by High Voltage Anodization. *J. Mater. Chem.* **2011**, *21* (26), 9661−9666.
(49) Losic, D.; Losic, D., Jr. Preparation of Porous Anodic Alumina with Periodically Perforated Pores. *Langmuir* **2009**, *25* (10), 5426−5431.
(50) Kumeria, T.; Santos, A.; Rahman, M. M.; Ferré-Borrull, J.; Marsal, L. F.; Losic, D. Advanced Structural Engineering of

DOI: 10.1021/acsami.6b03900
ACS Appl. Mater. Interfaces 2016, 8, 13542−13554

Nanoporous Photonic Structures: Tailoring Nanopore Architecture to Enhance Sensing Properties. *ACS Photonics* **2014**, *1*, 1298−1306.
(51) Kumeria, T.; Rahman, M. M.; Santos, A.; Ferré-Borrull, J.; Marsal, L. F.; Losic, D. Structural and Optical Nanoengineering of Nanoporous Anodic Alumina Rugate Filters for Real-Time and Label-Free Biosensing Applications. *Anal. Chem.* **2014**, *86*, 1837−1844.
(52) Kumeria, T.; Rahman, M. M.; Santos, A.; Ferré-Borrull, J.; Marsal, L. F.; Losic, D. Nanoporous Anodic Alumina Rugate Filters for Sensing of Ionic Mercury: Toward Environmental Point-of-Analysis Systems. *ACS Appl. Mater. Interfaces* **2014**, *6*, 12971−12978.
(53) Santos, A.; Kumeria, T.; Wang, Y.; Losic, D. *In Situ* Monitored Engineering of Inverted Nanoporous Anodic Alumina Funnels: On The Precise Generation of 3D Optical Nanostructures. *Nanoscale* **2014**, *6*, 9991−9999.
(54) Chen, Y.; Santos, A.; Wang, Y.; Kumeria, T.; Wang, C.; Li, J.; Losic, D. Interferometric Nanoporous Anodic Alumina Photonic Coatings for Optical Sensing. *Nanoscale* **2015**, *7*, 7770−7779.
(55) Chen, Y.; Santos, A.; Ho, D.; Wang, Y.; Kumeria, T.; Li, J.; Wang, C.; Losic, D. On The Generation of Interferometric Colors in High Purity and Technical Grade Aluminum: An Alternative Green Process for Metal Finishing Industry. *Electrochim. Acta* **2015**, *174*, 672−681.
(56) Wang, Y.; Chen, Y.; Kumeria, T.; Ding, F.; Evdokiou, A.; Losic, D.; Santos, A. Facile Synthesis of Optical Microcavities by a Rationally Designed Anodization Approach: Tailoring Photonic Signals by Nanopore Structure. *ACS Appl. Mater. Interfaces* **2015**, *7*, 9879−9888.
(57) Chen, Y.; Santos, A.; Wang, Y.; Kumeria, T.; Ho, D.; Li, J.; Wang, C.; Losic, D. Rational Design of Photonic Dust from Nanoporous Anodic Alumina Films: A Versatile Photonic Nanotool for Visual Sensing. *Sci. Rep.* **2015**, *5*, 12893.
(58) Chen, Y.; Santos, A.; Wang, Y.; Kumeria, T.; Li, J.; Wang, C.; Losic, D. Biomimetic Nanoporous Anodic Alumina Distributed Bragg Reflectors in the Form of Films and Micro-Sized Particles for Sensing Applications. *ACS Appl. Mater. Interfaces* **2015**, *7*, 19816−19824.
(59) Santos, A.; Law, C. S.; Pereira, T.; Losic, D. Nanoporous Hard Data: Optical Encoding of Information within Nanoporous Anodic Alumina Photonic Crystals. *Nanoscale* **2016**, *8*, 8091.
(60) Wang, Y.; Santos, A.; Evdokiou, A.; Losic, D. Rational Design of Ultra-Short Anodic Alumina Nanotubes by Short-Time Pulse Anodization. *Electrochim. Acta* **2015**, *154*, 379−386.
(61) Santos, A.; Formentín, P.; Ferré-Borrull, J.; Pallarès, J.; Marsal, L. F. Nanoporous Anodic Alumina Obtained without Protective Oxide Layer by Hard Anodization. *Mater. Lett.* **2012**, *67*, 296−299.
(62) Dronov, R.; Jane, A.; Shapter, J. G.; Hodges, A.; Voelcker, N. H. Nanoporous Alumina-Based Interferometric Transducers Ennobled. *Nanoscale* **2011**, *3*, 3109−3114.
(63) Macias, G.; Hernández-Eguía, L. P.; Ferré-Borrull, J.; Pallarès, J.; Marsal, L. F. Gold-Coated Ordered Nanoporous Anodic Alumina Bilayers for Future Label-Free Interferometric Biosensors. *ACS Appl. Mater. Interfaces* **2013**, *5*, 8093−8098.
(64) Abràmoff, M. D.; Magalhaes, P. J.; Ram, S. J. Image Processing with ImageJ. *Biophotonics Int.* **2004**, *11*, 36−50.
(65) Santos, A.; Montero-Moreno, J. M.; Bachmann, J.; Nielsch, K.; Formentín, P.; Ferré-Borrull, J.; Pallarès, J.; Marsal, L. F. Understanding Pore Rearrangement during Mild to Hard Transition in Bilayered Porous Anodic Alumina Membranes. *ACS Appl. Mater. Interfaces* **2011**, *3*, 1925−1932.
(66) Han, H.; Park, S.-J.; Jang, J. S.; Ryu, H.; Kim, K. J.; Baik, S.; Lee, W. *In Situ* Determination of the Pore Opening Point during Wet-Chemical Etching of the Barrier Layer of Porous Anodic Aluminum Oxide: Nonuniform Impurity Distribution in Anodic Oxide. *ACS Appl. Mater. Interfaces* **2013**, *5*, 3441−3448.
(67) Santos, A.; Kumeria, T.; Losic, D. Optically Optimized Photoluminescent and Interferometric Biosensors Based on Nanoporous Anodic Alumina: A Comparison. *Anal. Chem.* **2013**, *85*, 7904−7911.
(68) Santos, A.; Balderrama, V. S.; Alba, M.; Formentín, P.; Ferré-Borrull, J.; Pallarès, J.; Marsal, L. F. Nanoporous Anodic Alumina Barcodes: Toward Smart Optical Biosensors. *Adv. Mater.* **2012**, *24*, 1050−1054.
(69) Santos, A.; Yoo, J.; Rohatgi, C.; Kumeria, T.; Wang, Y.; Losic, D. Realisation and Advanced Engineering of True Optical Rugate Filters Based on Nanoporous Anodic Alumina by Sinusoidal Pulse Anodisation. *Nanoscale* **2016**, *8*, 1360−1373.
(70) Kumeria, T.; Santos, A.; Losic, D. Ultrasensitive Nanoporous Interferometric Sensor for Label-Free Detection of Gold(III) Ions. *ACS Appl. Mater. Interfaces* **2013**, *5*, 11783−11790.

DOI: 10.1021/acsami.6b03900
ACS Appl. Mater. Interfaces 2016, 8, 13542−13554

Supporting Information

Structural Engineering of Nanoporous Anodic Alumina Photonic Crystals by Sawtooth-Like Pulse Anodization

Cheryl Suwen Law[1], Abel Santos[1*], Mahdieh Nemati[1] and Dusan Losic[1*]

[1]School of Chemical Engineering, The University of Adelaide, Engineering North Building, 5005 Adelaide, Australia

***E-Mails:** abel.santos@adelaide.edu.au ; dusan.losic@adelaide.edu.au

S1. Linear dependence of the period length on the anodization period and the anodization amplitude.

Figure S1 shows fitting lines between the period length (L_{Tp}) and the anodization period (T_P) and the anodization amplitude (A_J).

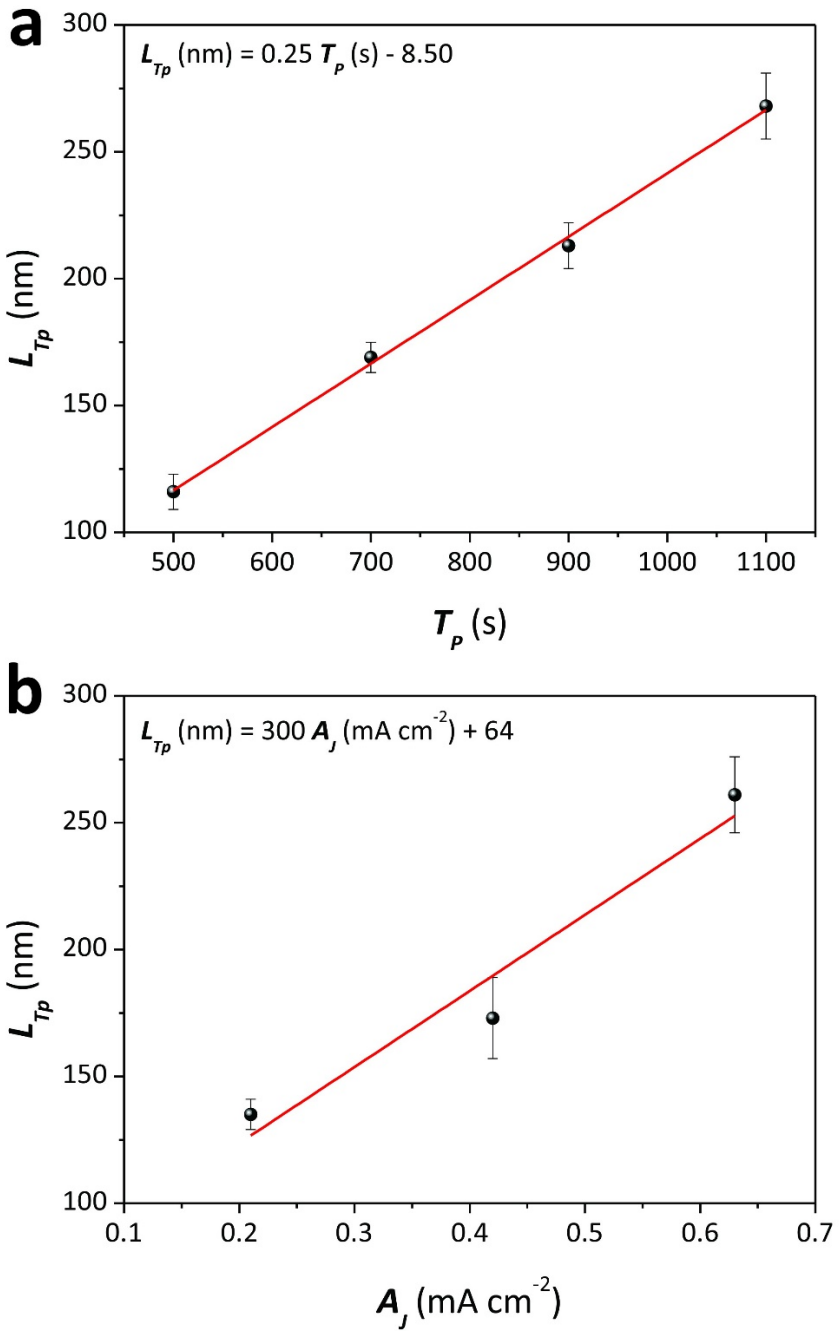

Figure S1. Linear dependence of the period length (L_{Tp}) on the anodization period (T_P) (a) and the anodization amplitude (A_J).

S2. Summary of results

Table S1 compiles a comprehensive summary of the experiments carried out in our study, where the effect of the main anodization parameters on the position of the characteristic transmission peaks of NAA-PCs was systematically analyzed. To this end, a NAA-PC produced with T_p = 700 s, A_J = 0.420 mA cm^{-2}, J_{min} = 0.28 mA cm^{-2}, S_{up}/S_{down} = 1, N_P = 124 pulses and t_{pw} = 0 min was chosen as the reference structure. From this, the anodization period (T_p), the anodization amplitude (A_J), the number of pulses (N_P), the ramp ratio (S_{up}/S_{down}) and the pore widening time (t_{pw}) were systematically modified from 400 to 1100 s (ΔT_P = 100 s), from 0.210 to 0.630 mA cm^{-2} (ΔA_J = 0.105 mA cm^{-2}), from 62 to 310 pulses (ΔN_P = 62 pulses), from 0.5 to 2 ($\Delta S_{up}/S_{down}$ = 0.5 ratio units) and from 0 to 6 min (Δt_{pw} = 2 min), respectively.

Table S1. Comprehensive summary of the effect of the different anodization parameters on the position of the characteristic transmission peaks of NAA-PCs analyzed in this study.

Analyzed Parameter	Range and Step Size	Peaks	Fitting Parameters	Range of λ_{Peak}
Anodization Period – T_P	From 400 to 1100 s ΔT_P = 100 s	1st Order	*Slope* = 0.85 ± 0.05 nm s^{-1} *Intercept* = -28.30 ± 36.38 nm R^2 = 0.9797	277 – 934 nm (Red Shift)
		2nd Order	*Slope = 0.27 ± 0.06 nm* s^{-1} *Intercept = 130.32 ± 45.34 nm* R^2 = 0.9800	242 – 460 nm (Red Shift)
		3rd Order	*Slope = 0.34 ± 0.03 nm* s^{-1} *Intercept = -62.94 ± 34.32 nm* R^2 = 0.9800	278 – 347 nm (Red Shift)
Anodization Amplitude - A_J	From 0.210 to 0.630 mA cm^{-2} ΔA_J = 0.105 mA cm^{-2}	1st Order	*Slope* = 937.58 ± 46.76 nm (mA cm^{-2})$^{-1}$ *Intercept* = 207.83 ± 46.76 nm R^2 = 0.9517	420– 836 nm (Red Shift)
		2nd Order	*Slope* = 494.58 ± 98.00 nm (mA cm^{-2})$^{-1}$ *Intercept* = 82.62 ± 45.64 nm R^2 = 0.9063	263 – 420 nm (Red Shift)
Number of Pulses - N_P	From 62 to 310 pulses ΔN_P = 62 pulses	1st Order	*Slope* = -0.61 ± 0.15 nm $pulse^{-1}$ *Intercept* = 680.09 ± 29.90 nm R^2 = 0.8036	649 – 471 nm (Blue Shift)
		2nd Order	*Slope* = -0.41 ± 0.11 nm $pulse^{-1}$ *Intercept* = 350.72 ± 18.47 nm R^2 = 0.8187	329 – 242 nm (Blue Shift)
Ramp Ratio - S_{up}/S_{down}	From 0.5 to 2 $\Delta S_{up}/S_{down}$ = 0.5	1st Order	*From 0.5 to 0.67* *Slope* = -230.42 ± 150.25 nm Ramp Ratio $Units^{-1}$ *Intercept* = 790.22 ± 113.07 nm R^2 = 0.9597 *From 0.67 to 2* *Slope* = 47.16 ± 10.22 nm Ramp Ratio $Units^{-1}$ *Intercept* = 524.44 ± 15.89 nm R^2 = 0.9103	704 – 575 nm (Blue Shift) 575 – 622 nm (Red Shift)
		2nd Order	*From 0.5 to 0.67* *Slope* = -126.71 ± 78.09 nm Ramp Ratio $Units^{-1}$ *Intercept* = 790.22 ± 113.07 nm R^2 = 0.9597 *From 0.67 to 2* *Slope* = 29.99 ± 6.85 nm Ramp Ratio $Units^{-1}$ *Intercept* = 253.79 ± 10.65 nm R^2 = 0.9008	317 – 286 nm (Blue Shift) 286 – 316 nm (Blue Shift)
Pore Widening Time - t_{pw}	From 0 to 6 min Δt_{pw} = 2 min (T_P = 500s)	1st Order	*Slope* = -8.48 ± 1.07 nm min^{-1} *Intercept* = 439.17 ± 4.01 nm R^2 = 0.9536	437 – 385 nm (Blue Shift)
		2nd Order	*Slope* = -12.70 ± 0.67 nm min^{-1} *Intercept* = 329.72 ± 2.50 nm R^2 = 0.9917	327 – 251 nm (Blue Shift)
		3rd Order	*Slope* = -6.28 ± 0.21 nm min^{-1} *Intercept* = 252.21 ± 0.89 nm R^2 = 0.9978	239 – 214 nm (Blue Shift)

Chapter 4

On the Precise Tuning of Optical Filtering Features in Nanoporous Anodic Alumina Distributed Bragg Reflectors

Statement of Authorship

Title of Paper	On the precise tuning of optical filtering features in nanoporous anodic alumina distributed Bragg reflectors.
Publication Status	☑ Published ☐ Accepted for Publication ☐ Submitted for Publication ☐ Unpublished and Unsubmitted w ork w ritten in manuscript style
Publication Details	Law, C.S., S.Y. Lim, and A. Santos, *On the precise tuning of optical filtering features in nanoporous anodic alumina distributed Bragg reflectors*. Scientific Reports, 2018. **8**(1): p. 4642.

Principal Author

Name of Principal Author (Candidate)	Cheryl Suwen Law		
Contribution to the Paper	Under the supervision of A. Santos and A. D. Abell, I performed the experiments, interpreted and processed the data and wrote the manuscript.		
Overall percentage (%)	70		
Certification:	This paper reports on original research I conducted during the period of my Higher Degree by Research candidature and is not subject to any obligations or contractual agreements with a third party that would constrain its inclusion in this thesis. I am the primary author of this paper.		
Signature		Date	23/11/2018

Co-Author Contributions

By signing the Statement of Authorship, each author certifies that:

i. the candidate's stated contribution to the publication is accurate (as detailed above);
ii. permission is granted for the candidate in include the publication in the thesis; and
iii. the sum of all co-author contributions is equal to 100% less the candidate's stated contribution.

Name of Co-Author	Siew Yee Lim		
Contribution to the Paper	I helped Cheryl Suwen Law with performing the experiments. I give consent for Cheryl Suwen Law to present this paper for examination towards the Doctorate of Philosophy.		
Signature		Date	14/11/2018

Name of Co-Author	Abel Santos		
Contribution to the Paper	I acted as primary supervisor for the candidate, aided in developing of the experiments, revising the manuscript and evaluating the final version of the manuscript. I give consent for Cheryl Suwen Law to present this paper for examination towards the Doctorate of Philosophy.		
Signature		Date	23/11/2018

4. On the Precise Tuning of Optical Filtering Features in Nanoporous Anodic Alumina Distributed Bragg Reflectors

4.1 Introduction, Significance and Commentary

The increasing interest in using nanoporous anodic alumina (NAA)-based sensing platforms in optical sensing requires the development of narrow line-width NAA-PCs that are capable of detecting small changes in refractive index. This chapter presents an apodisation strategy to modulate the effective medium of NAA-PCs in-depth in a stepwise fashion in order to reduce the spectral bandwidth. Apodised NAA-DBRs show a photonic stop band with narrow bandwidth that provides enhanced sensitivity over their non-apodised counterparts. The application of these NAA-PCs as sensing platforms can be extended to a variety of fields such as biomedicine, environmental and industrial monitoring.

4.2 Publication

This section is presented as published research paper by **Law, C.S.**, S.Y. Lim, and A. Santos, *On the precise tuning of optical filtering features in nanoporous anodic alumina distributed Bragg reflectors*. Scientific Reports, 2018. **8**(1): p. 4642.

SCIENTIFIC REPORTS

OPEN

On the Precise Tuning of Optical Filtering Features in Nanoporous Anodic Alumina Distributed Bragg Reflectors

Received: 9 January 2018
Accepted: 1 March 2018
Published online: 15 March 2018

Cheryl Suwen Law[1,2,3], Siew Yee Lim[1,2,3] & Abel Santos[1,2,3]

This study presents a nanofabrication approach that enables the production of nanoporous anodic alumina distributed Bragg reflectors (NAA-DBRs) with finely engineered light filtering features across the spectral regions. The photonic stopband (PSB) of these NAA-based photonic crystal (PC) structures is precisely tuned by an apodization strategy applied during stepwise pulse anodization with the aim of engineering the effective medium of NAA-DBRs in depth. We systematically assess the effect of different fabrication parameters such as apodization function (i.e. linear positive, linear negative, logarithmic positive and logarithmic negative), amplitude difference (from 0.105 to 0.420 mA cm^{-2}), current density offset (from 0.140 to 0.560 mA cm^{-2}), anodization period (from 1100 to 1700 s), and pore widening time (from 0 to 6 min) on the quality and central wavelength of the PSB of NAA-DBRs. The PSB's features these PC structures are demonstrated to be highly tunable with the fabrication parameters, where a logarithmic negative apodization is found to be the most effective function to produce NAA-DBRs with high quality PSBs across the UV-visible-NIR spectrum. Our study establishes that apodized NAA-DBRs are more sensitive to changes in their effective medium than non-apodized NAA-DBRs, making them more suitable sensing platforms to develop advanced optical sensing systems.

Photonic crystals (PCs) in various forms such as optical lenses, fibers, mirrors, resonators, cavities, thin films, and optical filters are key elements in advanced optical devices since these structures enable the precise control over electromagnetic waves by light–matter interactions at the nanoscale. Of all the PC structures, optical filters are vital components for a broad range of applications, including laser mirrors, arc welding, polarizers, solar protection, photography, imaging, astronomy, and complex instrumentation[1,2]. PCs can selectively allow and forbid the pass of light of certain wavelengths or energies when photons travel across the PCs' structure. This property can be precisely designed by engineering the PCs' structure to develop PC-based advanced optical filters with unique light-filtering features[3]. Typically, optical filters are fabricated by chemical vapor deposition[3,4], photolithography[5], and co-evaporation[6], processes through which substrates such as thin glass, plastic, and dielectric materials (e.g. silicon dioxide, titanium dioxide, zinc sulfide, magnesium fluoride) are endowed with selective light-filtering properties[3]. The raise of nanotechnology has enabled multiple opportunities to produce advanced PC-based optical filters using nanomaterials featuring layers of alternating refractive index. Among these, PC structures based on nanoporous materials produced by electrochemical etching of metals have opened new opportunities to develop advanced photonic platforms with applicability in photonics, photocatalysis, optoelectronics, and sensing[7]. The refractive index/dielectric constant of these nanomaterials can be engineered a 1D, 2D, or 3D fashion by modulating their porosity in depth, enabling the generation of a broad range of multi-dimensional PCs such as Bragg reflectors[8,9], microcavities[10,11], waveguides[12,13], and others[14,15].

Of all these PCs, nanoporous anodic alumina photonic crystals (NAA-PCs) produced by electrochemical oxidation (anodization) of aluminum have attracted considerable attention during recent years due to the versatility of the nanoporous structure of NAA[16]. This top-down nanofabrication approach offers industrial scalability (from

[1]School of Chemical Engineering, The University of Adelaide, Adelaide, SA 5005, Australia. [2]Institute for Photonics and Advanced Sensing (IPAS), The University of Adelaide, 5005, Adelaide, Australia. [3]ARC Centre of Excellence for Nanoscale BioPhotonics (CNBP), The University of Adelaide, 5005, Adelaide, Australia. Correspondence and requests for materials should be addressed to A.S. (email: abel.santos@adelaide.edu.au)

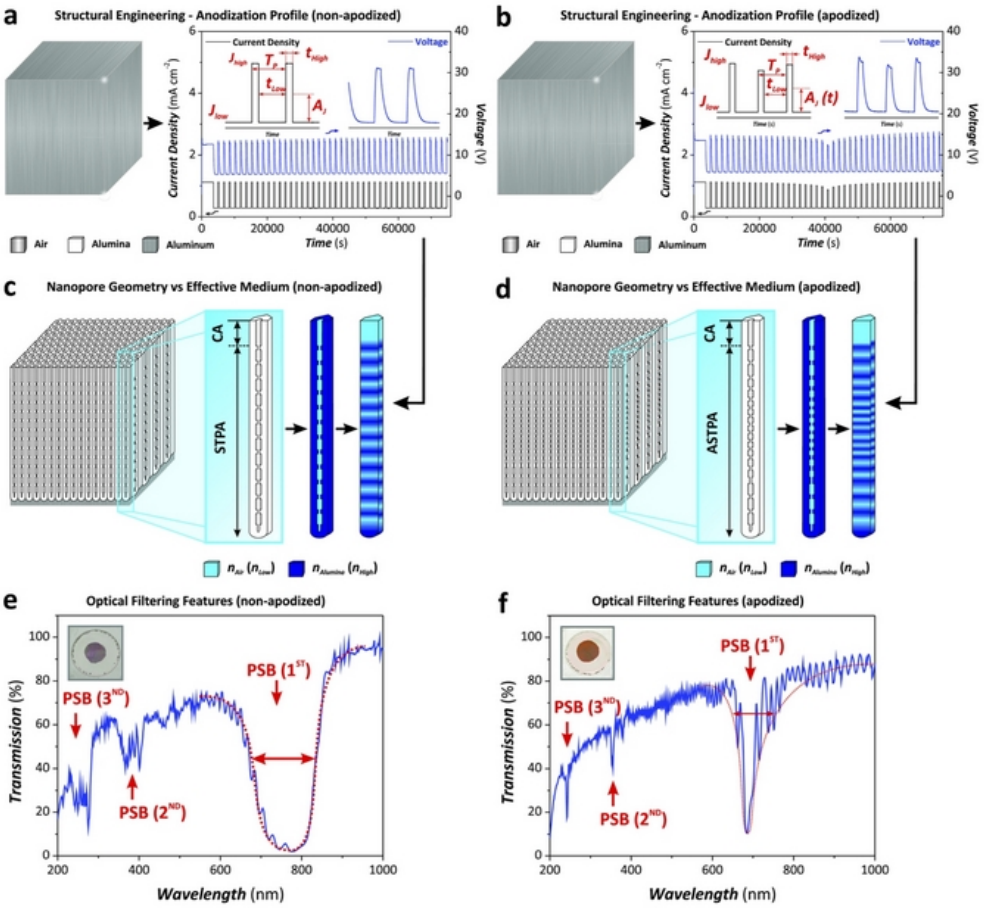

Figure 1. Conceptual illustration showing the generation of nanoporous anodic alumina distributed Bragg reflectors (NAA-DBRs) by stepwise pulse anodization (STPA) and the apodization of optical signals by apodized stepwise pulse anodization (ASTPA). (**a** and **b**) Representative STPA and ASTPA profiles used to fabricate NAA-DBRs (left – aluminum substrates; right – real anodization profiles with insets showing graphical descriptions of the anodization parameters: T_P = anodization period, A_J = anodization amplitude (constant for STPA and time-dependent for ASTPA), J_{High} and J_{Low} = high and low current density values, respectively, t_{High} and t_{Low} = anodization time at J_{High} and J_{Low}, respectively) (Note: CA = constant current anodization step). (**c** and **d**) Scheme describing the correlation between nanopore geometry and distribution of high and low refractive indexes ($n_{Alumina} = n_{High} \sim 1.7$ and $n_{Air} = n_{Low} \sim 1.0$) in depth for non-apodized and apodized NAA-DBRs, respectively. (**e** and **f**) Representative transmission spectra of non-apodized ($T_P = 1700$ s, $A_J = 0.420\ mA\ cm^{-2}$, $J_{min} = J_{offset} = 0.280\ mA\ cm^{-2}$, $t_{STPA} = 20$ h, and $t_{pw} = 0$ min) and apodized (apodization function = logarithmic negative, $T_P = 1700$ s, $\Delta A_J = 0.210\ mA\ cm^{-2}$, $J_{min} = J_{offset} = 0.280\ mA\ cm^{-2}$, $t_{ASTPA} = 20$ h, and $t_{pw} = 0$ min) NAA-DBRs with insets showing digital images of these photonic crystal structures, respectively.

mm^2 to m^2), cost-competitiveness, and versatile control over the features of nanopores, which can be modulated with precision by means of the anodization parameters to generate unique multi-dimensional PC structures able to guide, reflect, modulate, confine, transmit, emit, and enhance incident light selectively across the spectral regions[17,18]. Recent studies have demonstrated that rationally designed pulse-like anodization profiles under suitable conditions enable the precise engineering of the photonic stopband (PSB) of NAA-PCs by creating structures such as gradient index filters[19–22], optical microcavities[23], distributed Bragg reflectors[24–28], bandpass and linear variable bandpass filters[29,30]. These PCs can be used as optical filters for a plethora of applications due to the flexibility and selectively to engineer their light-filtering features across the spectral regions[31,32].

In this study, we demonstrate for the first time that an apodized stepwise pulse anodization (STPA) approach enables the fine tuning of the features of the characteristic PSB of NAA-based distributed Bragg reflectors (DBRs) (Fig. 1). The effect of the fabrication parameters (i.e. apodization function, anodizing current density, amplitude difference, current density offset, anodization period, and pore widening time) on the characteristic PSB of NAA-DBRs is systematically analyzed to attain full controllability over the filtering features of these PCs and to establish the most optimal path for high quality PSBs. We further assess the effective medium of apodized and non-apodized NAA-DBRs after infiltrating their nanopores with mediums of different refractive index. Shifts in

the position of the characteristic PSB of these PCs demonstrate that to apodize the structure of NAA-DBRs can enhance the sensitivity of these PCs, opening new opportunities to develop materials for sensing applications.

Results and Discussion

Apodization of Stepwise Pulse Anodization Profiles. Figure 2 displays the anodization profiles of a set of non-apodized NAA-DBRs produced by STPA at different anodization periods (T_p), from $T_P = 900$ s to 1700 s with $\Delta T_P = 100$ s (Note: displayed only from 900 to 1600 s). These NAA photonic structures were produced by STPA approach under galvanostatic conditions, where the current density (J) is switched between maximum ($J_{Max} = 1.120\,mA\,cm^{-2}$) and minimum ($J_{Min} = 0.280\,mA\,cm^{-2}$) levels to modulate the porosity of NAA in depth[33]. In our study, an apodization strategy was applied to the STPA profile with the aim of tuning the PSB of NAA-DBRs by engineering their effective medium in a stepwise fashion through different apodization windows. Four different apodization functions (i.e. linear positive, linear negative, logarithmic positive, and logarithmic negative) were used to modify the conventional STPA process. Furthermore, we systematically modified the amplitude difference (i.e. current density amplitude difference between the initial (t_0) and half anodization time ($t_{1/2}$) under ASTPA $-\ \Delta A_J = |A_J(t_0) - A_J(t_{1/2})|$), from $\Delta A_J = 0.105\,mA\,cm^{-2}$ to $0.420\,mA\,cm^{-2}$ with a step size of $0.105\,mA\,cm^{-2}$. Figure 3 shows the ASTPA profiles used to produce apodized NAA-DBRs by each apodization function and amplitude difference. These profiles reveal that, under the anodization conditions used in our study (see Methods), modifications of the current density (input) are directly translated into voltage (output) changes, which is a critical factor for the accurate translation of current density profiles into porosity modulation in depth during anodization.

Structural Characterization of NAA-DBRs. Figure 4 compiles a set of representative field-emission gun scanning electron microscopy (FEG-SEM) images of NAA-DBRs produced in our study. As these images reveal, NAA-DBRs feature an even but random distribution of nanopores across their surface, the average diameter (d_p) of which was estimated to be $d_p = 10 \pm 3$ and 19 ± 3 nm, for pore widening times (t_{pw}) 0 and 6 min, respectively (Fig. 4a and b). This range of pore sizes was found to be optimal to obtain well-defined and intense PSBs in the transmission spectra of NAA-DBRs. NAA-based PC structures featuring bigger pore sizes, such as those produced in oxalic and phosphoric acids, scatter and absorb more light when photons travel across the PC structure, resulting in less intense PSBs. The resulting PCs feature a modulation of the pore diameter in depth that follows with precision the stepwise current density profile applied during STPA and ASTPA (Fig. 4c and d). This results in an in-depth modification of the effective refractive index of NAA that enables the generation of 1D NAA-DBRs. We also observed a linear relationship between the anodization period (T_P) and the period length (L_{TP}), defined as the distance between adjacent layers in the stacked structure of NAA-DBRs, where the latter changes at a rate of $0.22\,nm\,s^{-1}$ with the former (Fig. 4e).

Effect of Apodization on Optical Properties of NAA-DBRs. The transmission spectrum of NAA-DBRs displays a characteristically broad PSB with due to discontinuities in the effective refractive index profile[34]. Figure 1e shows the transmission spectra of a NAA-DBR produced with an anodization period of 1700 s. It is well-known that the PSB of DBRs can be engineered through apodization, optical filtering technique used to narrow the bandwidth of PC structures[35]. Figure 1f shows the transmission spectra of a NAA-DBR produced with $T_P = 1700$ s by a ASTPA profile apodized with a logarithmic negative function. It is clearly seen that the PSB of the NAA-DBR is significantly narrowed after apodizing the anodization profile. This effect is also observed for the different transmission orders of the PSB, where the apodized PC structure shows much well resolved and sharper PSBs than its non-apodized counterpart. Therefore, to apply an apodization approach to the STPA profile under the conditions used in our study enables the fine tuning of the light-filtering features of NAA-DBRs for specific applications, such as highly selective optical filters, high quality resonators, and ultrasensitive optical sensors.

Figure 5 shows contour maps summarizing the dependence of the central wavelength (λ_{PSB}) and the quality factor (Q_{PSB} – calculated as the position of the central wavelength divided by the PSB's full width at half maximum ($FWHM_{PSB}$) – Equation 1) of the PSB of NAA-DBRs with the apodization function (i.e. linear positive, linear negative, logarithmic positive, and logarithmic negative), the amplitude difference (ΔA_J), and the pore widening time (t_{pw}). These graphs show how Q_{PSB} and λ_{PSB} vary with the fabrication parameters, enabling optimization paths to precisely tune the filtering features of NAA-DBRs.

$$Q_{PSB} = \frac{\lambda_{PSB}}{FWHM_{PSB}} \tag{1}$$

Figure 5a and b show the effect of ΔA_J and t_{pw} on the filtering features of NAA-DBRs apodized following a linear positive function. Figure 5a denotes three maxima regions where Q_{PSB} presents the highest values, from $\Delta A_J = 0.210$ to $0.420\,mA\,cm^{-2}$ and $t_{pw} = 0$ to 2 min; from $\Delta A_J = 0.105$ to $0.210\,mA\,cm^{-2}$ and $t_{pw} = 0$ to 2 min; and from $\Delta A_J = 0.105$ to $0.210\,mA\,cm^{-2}$ and $t_{pw} = 4$ to 6 min. Linear positive apodized NAA-DBRs achieve the highest quality factor (6.2 ± 0.3) at $\Delta A_J = 0.105\,mA\,cm^{-2}$ and $t_{pw} = 0$ min, as indicated by the red region in the contour plot. In contrast to Q_{PSB}, λ_{PSB} was found to change smoothly with ΔA_J and t_{pw}, as revealed by the homogeneous distance between color fields (Fig. 5b). λ_{PSB} undergoes a blue shift as t_{pw} and ΔA_J increase, although the magnitude of the blue shift produced by t_{pw} is more significant than that of ΔA_J. Figure 5c and d display the effect of ΔA_J and t_{pw} on the central wavelength position and the quality factor of NAA-DBRs produced by a linear negative apodization function. It is observed that Q_{PSB} features a weak correlation with ΔA_J and t_{pw} at higher values of these two fabrication parameters (Fig. 5c). However, the quality factor of these NAA-DBRs increases significantly as ΔA_J and t_{pw} decrease, reaching its maximum value of 14.1 ± 0.7 at $\Delta A_J = 0.105\,mA\,cm^{-2}$ and $t_{pw} = 0$ min. In the case of the position of the central wavelength (Fig. 5d), this is red-shifted as both ΔA_J and t_{pw}

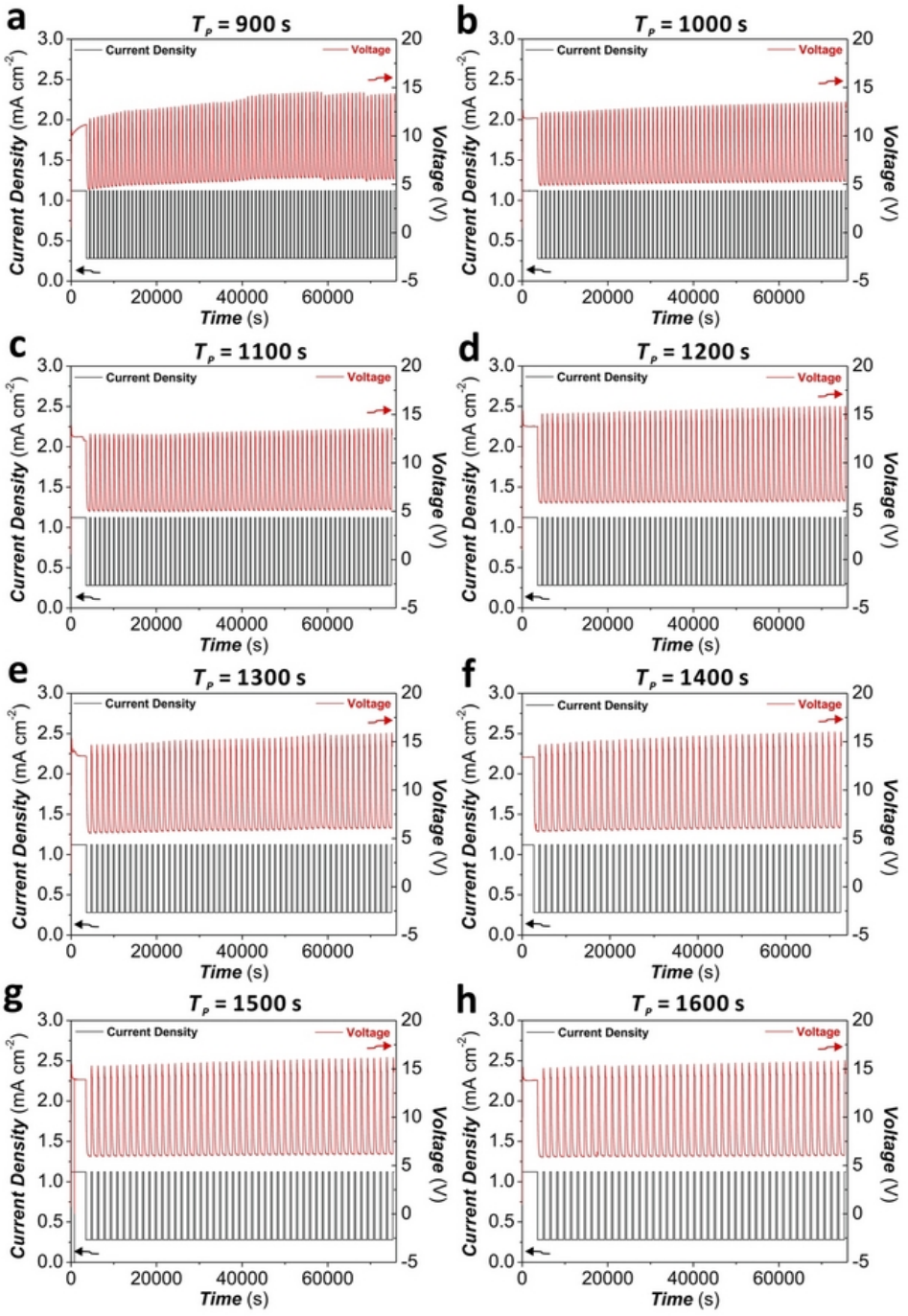

Figure 2. Representative STPA anodization profiles used to produce non-apodized nanoporous anodic alumina distributed Bragg reflectors (NAA-DBRs) by modifying the anodization period from $T_P = 900$ to 1700 s with $\Delta T_P = 100$ s (constant parameters – $A_J = 0.420$ mA cm^{-2}, $J_{Low} = J_{Offset} = 0.280$ mA cm^{-2}, and $t_{STPA} = 20$ h). (**a**) $T_P = 900$ s. (**b**) $T_P = 1000$ s. (**c**) $T_P = 1100$ s. (**d**) $T_P = 1200$ s. (**e**) $T_P = 1300$ s. (**f**) $T_P = 1400$ s. (**g**) $T_P = 1500$ s. (**h**) $T_P = 1600$ s.

decrease. Likewise for a linear positive apodization, this change is smooth and homogeneous as denoted by the even distribution of color fields, although the effect of ΔA_J on λ_{PSB} is less significant than that of t_{pw}. Figure 5e and f show the dependence of Q_{PSB} and λ_{PSB} with ΔA_J and t_{pw} for NAA-DBRs apodized with a logarithmic positive function. Figure 5e reveals that Q_{PSB} evolves homogeneously with ΔA_J and t_{pw}. A reduction of the amplitude

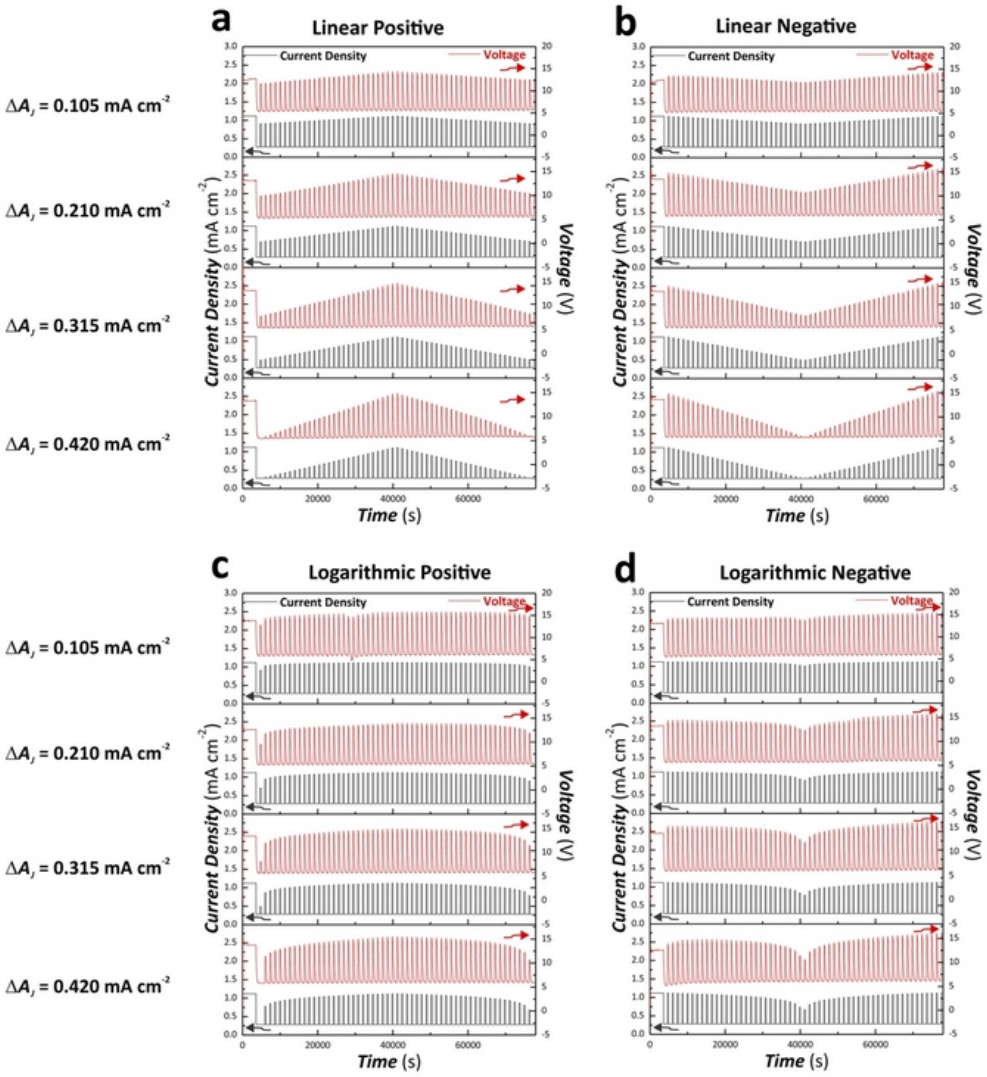

Figure 3. Representative ASTPA anodization profiles used to produce apodized nanoporous anodic alumina distributed Bragg reflectors (NAA-DBRs) by modifying the apodization function (linear positive, linear negative, logarithmic positive, and logarithmic negative) and the anodization amplitude difference from $\Delta A_J = 0.105$ to $0.420\,mA\,cm^{-2}$ (constant parameters – $T_P = 1300\,s$, $J_{Low} = J_{Offset} = 0.280\,mA\,cm^{-2}$, and $t_{ASTPA} = 20\,h$. (**a**) Linear positive apodization. (**b**) Linear negative apodization. (**c**) Logarithmic positive apodization. (**d**) Logarithmic negative apodization.

difference and pore widening time results in an enhancement of the quality factor of these NAA-DBRs, where Q_{PSB} is strongly dependent on these fabrication parameters as its value is nearby the maximum ($Q_{PSB} = 10.5 \pm 0.5$), located at $\Delta A_J = 0.105\,mA\,cm^{-2}$ and $t_{pw} = 0\,min$. A similar trend is observed for the correlation between λ_{PSB} and ΔA_J and t_{pw}, with a marked dependence on the fabrication parameters around its maximum ($\lambda_{PSB} = 716 \pm 1\,nm$), located at $\Delta A_J = 0.105\,mA\,cm^{-2}$ and $t_{pw} = 0\,min$. In good agreement with previous studies[36,37], the position of the central wavelength is blue-shifted with t_{pw} following a linear fashion, as denoted by the equidistant separation between color fields as t_{pw} increases. Finally, Fig. 5g and h depict the relationship between Q_{PSB} and λ_{PSB} with ΔA_J and t_{pw} for NAA-DBRs produced by a logarithmic negative apodization approach. Figure 5g denotes a high concentration of color fields at short pore widening times, where the field lines are closer each other around the maximum. The combination of fabrication parameters that gives the highest Q_{PSB} (21.4 ± 1.0) for these NAA-DBRs is $\Delta A_J = 0.210\,mA\,cm^{-2}$ and $t_{pw} = 0\,min$. As far as λ_{PSB} is concerned, it is observed that the central wavelength undergoes a homogenous variation with ΔA_J and t_{pw}, in a similar way than that of NAA-DBRs produced by a logarithmic positive apodization. However, the maximum value of λ_{PSB} is located at $\Delta A_J = 0.315\,mA\,cm^{-2}$ and $t_{pw} = 0\,min$.

Another interesting property of NAA-DBRs is that these PC structures display vivid interferometric colors when the position of the central wavelength is located within the visible range of the spectrum. Figure 6a compiles

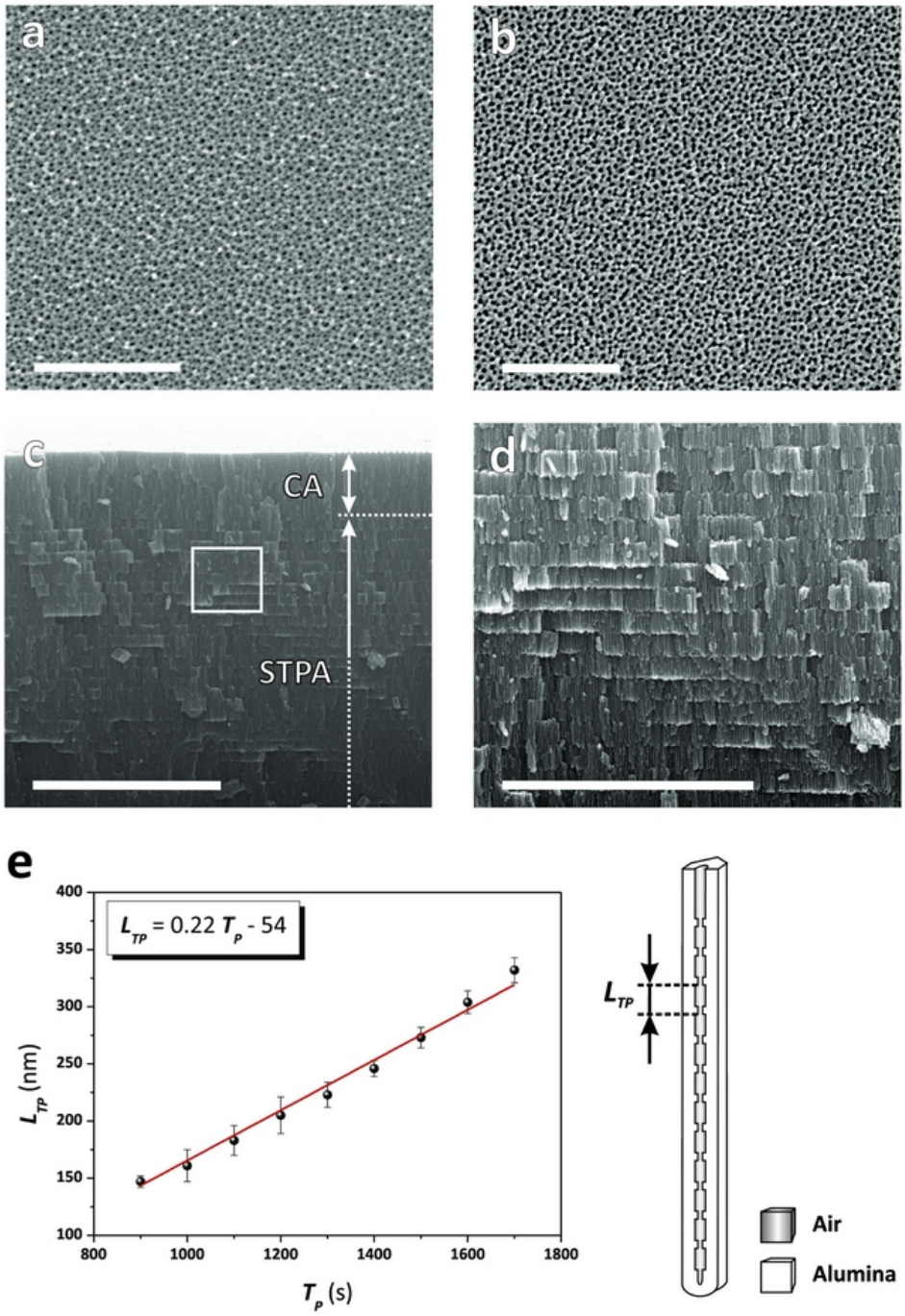

Figure 4. Representative FEG-SEM images of NAA-DBRs produced by STPA (Note; CA = constant current density anodization step). (**a**) Top view SEM image of a NAA-DBR produced with $T_P = 1000$ s, $A_J = 0.420$ mA cm^{-2}, $J_{Offset} = 0.280$ mA cm^{-2}, $t_{STPA} = 20$ h, and $t_{pw} = 0$ min (scale bar = 500 nm). (**b**) Top view SEM image of a NAA-DBR produced with $T_P = 1000$ s, $A_J = 0.420$ mA cm^{-2}, $J_{Offset} = 0.280$ mA cm^{-2}, $t_{STPA} = 20$ h, and $t_{pw} = 6$ min (scale bar = 500 nm). (**c**) General cross-sectional SEM image of a NAA-DBR showing the stacked layered structure with stepwise modulated porosity in depth (scale bar = 5 μm). (**d**) Magnified view of the white square shown in (**c**) (scale bar = 3 μm). (**e**) Linear correlation establishing the dependency of the period length (L_{TP}) with the anodization period (T_P) from $T_P = 900$ to 1700 s and schematic definition of L_{TP} in NAA-DBRs.

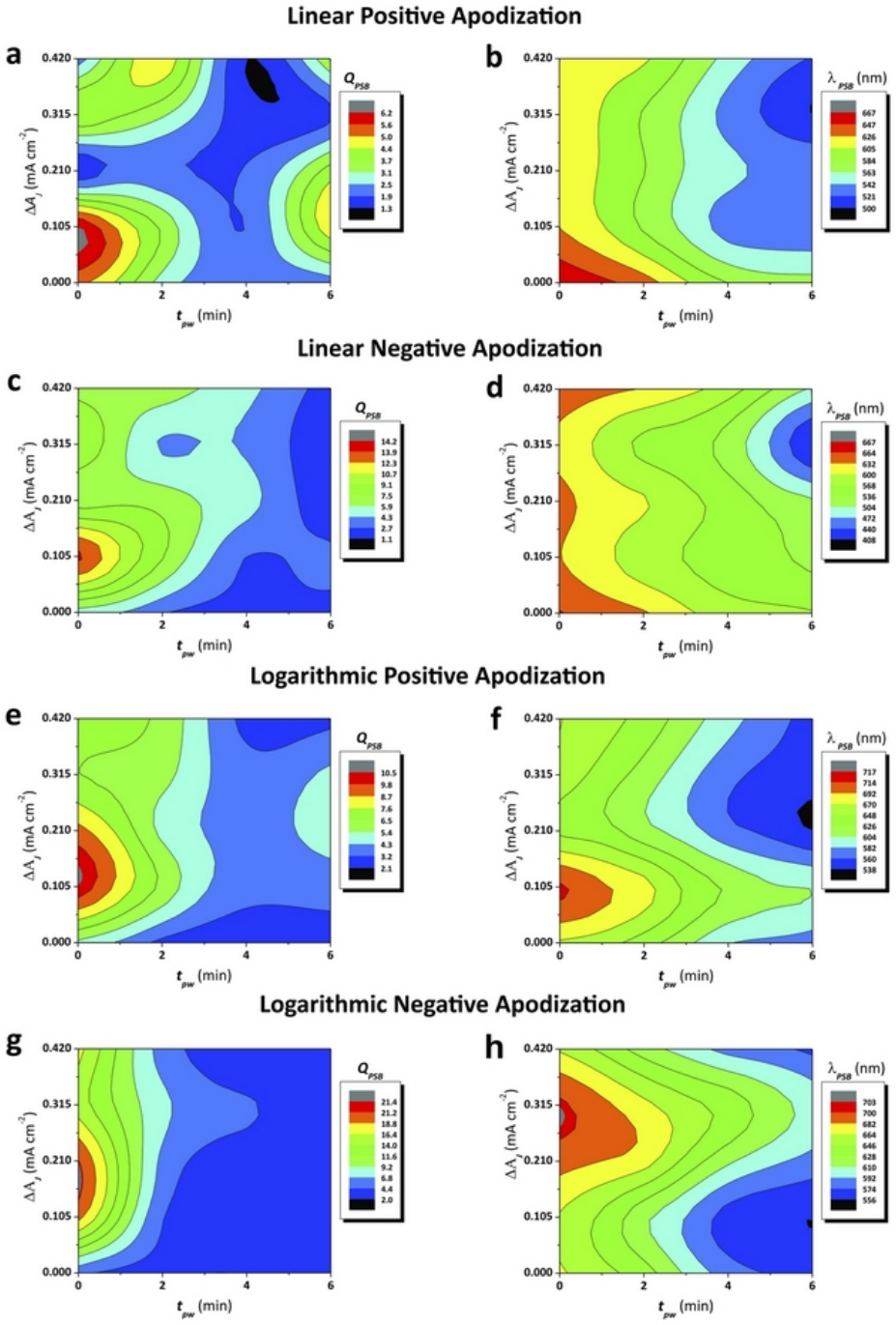

Figure 5. Contour maps showing the dependence of Q_{PSB} and λ_{PSB} of apodized NAA-DBRs as a function of the fabrication parameters ($\Delta A_J = A_{max} - A_{min}$ – amplitude difference and t_{pw} – pore widening time) (Note: $\Delta A_J = 0$ – non-apodized NAA-DBRs). (**a** and **b**) Values of Q_{PSB} and λ_{PSB} as a function of ΔA_J and t_{pw} for linear positive apodization, respectively. (**c** and **d**) Values of Q_{PSB} and λ_{PSB} as a function of ΔA_J and t_{pw} for linear negative apodization, respectively. (**e** and **f**) Values of Q_{PSB} and λ_{PSB} as a function of ΔA_J and t_{pw} for logarithmic positive apodization, respectively. (**g** and **h**) Values of Q_{PSB} and λ_{PSB} as a function of ΔA_J and t_{pw} for logarithmic negative apodization, respectively.

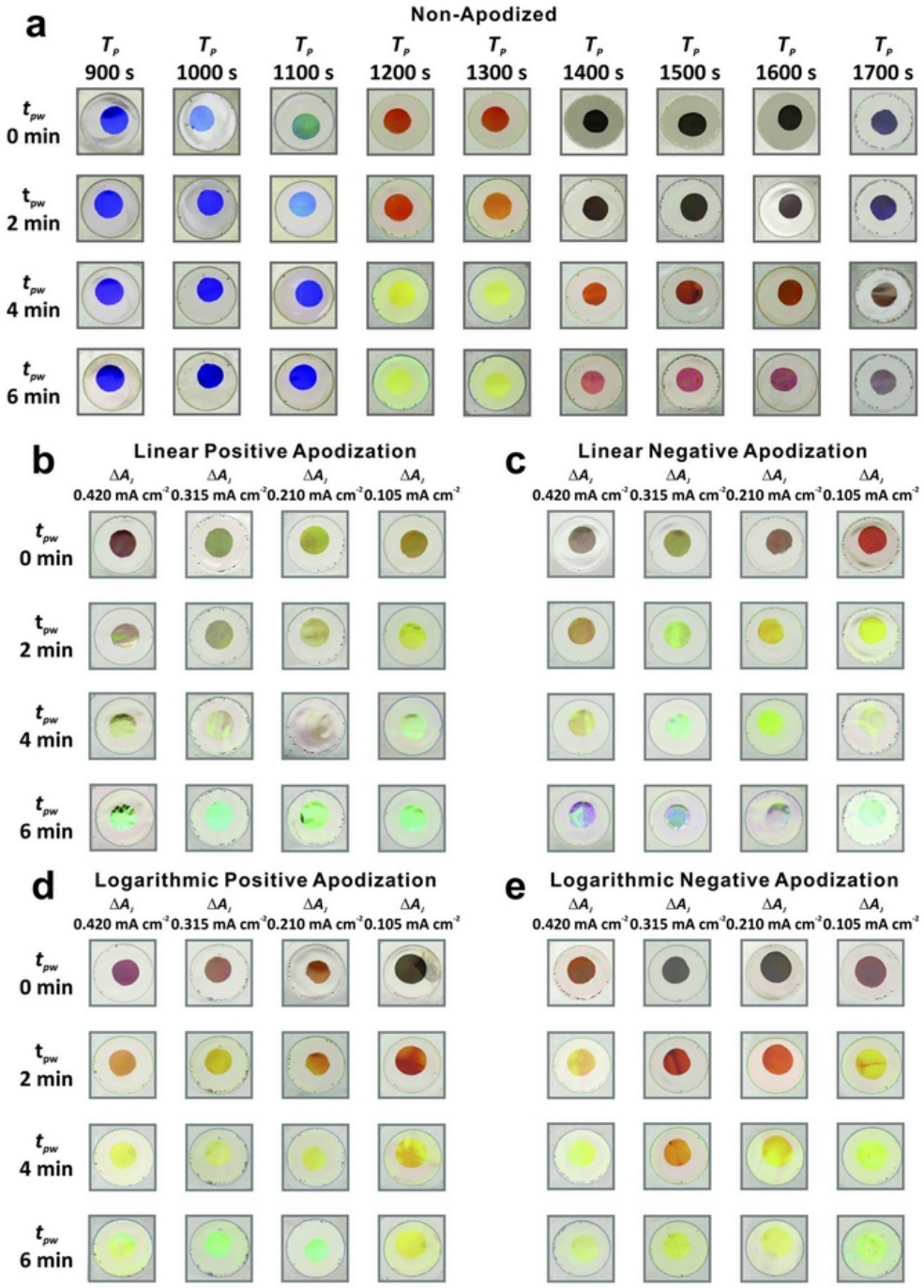

Figure 6. Digital pictures of non-apodized and apodized NAA-DBRs produced by STPA and ASTPA, respectively (diameter = 1 cm). (**a**) Non-apodized NAA-DBRs produced by STPA with T_P from 900 to 1700 s and t_{pw} from 0 min to 6 min (Note: fixed parameters – $A_J = 0.420\,mA\,cm^{-2}$, $J_{Offset} = 0.280\,mA\,cm^{-2}$, and $t_{STPA} = 20\,h$). (**b–e**) Apodized NAA-DBRs produced by ASTPA with ΔA_J from 0.105 to 0.420 mA cm^{-2} and t_{pw} from 0 to 6 min for (**b**) linear positive apodization, (**c**) linear negative apodization, (**d**) logarithmic positive apodization, and (**e**) logarithmic negative apodization (Note: fixed parameters – $T_P = 1300\,s$, $J_{Offset} = 0.280\,mA\,cm^{-2}$, and $t_{ASTPA} = 20\,h$).

a set of digital pictures of non-apodized NAA-DBRs produced at different anodization periods ($T_P = 900$ to 1700 s with $\Delta T_P = 100\,s$) and pore widening times ($t_{pw} = 0$ to 6 min with $\Delta t_{pw} = 2\,min$). Figure 6b–e show digital pictures

of apodized NAA-DBRs produced with an anodization period of 1300 s with four apodization functions (linear positive, linear negative, logarithmic positive, and logarithmic negative) as a function of ΔA_J and t_{pw}. These pictures demonstrate that apodized and non-apodized NAA-DBRs display vivid colors such as orange, yellow, cyan and green, which corresponds to the position of their characteristic PSB within the visible range. This property can be readily engineered by modifying the fabrication parameters. For instance, linear negative apodized NAA-DBR with $\Delta A_J = 0.105\,mA\,cm^{-2}$ and $t_{pw} = 2$ min displays yellow color, which corresponds to the position of its PSB at $\lambda_{PSB} = 580 \pm 1$ nm. On the other hand, NAA-DBRs with their characteristic PSB in the NIR region (e.g. logarithmic negative apodized NAA-DBRs with $\Delta A_J = 0.315\,mA\,cm^{-2}$ and $t_{pw} = 0$ min, where $\lambda_{PSB} = 703 \pm 1$ nm) are transparent in color (black background).

To summarize, different apodization functions were explored to produce NAA-DBRs with optimized optical properties in terms of Q_{PSB} and λ_{PSB}. All four apodization strategies (i.e. linear positive, linear negative, logarithmic positive and logarithmic negative) have shown to improve the quality of PSB as compared to non-apodized NAA-DBRs by certain combinations of fabrication parameters (i.e. ΔA_J and t_{pw}). Among these functions, logarithmic negative apodization was found to be the most effective strategy to enhance the quality of the PSB of NAA-DBRs, as proven by the high value of Q_{PSB} (21.4 ± 1.0).

Effect of Anodization Offset and Period on Optical Properties of NAA-DBRs. To further optimize the optical properties of NAA-DBRs, the combined effect of the current density offset (J_{offset}) and anodization period (T_P) with t_{pw} on the optical properties of NAA-DBRs was systematically investigated by fabricating a set of non-apodized and apodized NAA-DBRs with different J_{offset} (from 0.140 to 0.560 mA cm^{-2} with $\Delta J_{offset} = 0.140\,mA\,cm^{-2}$) (Fig. 7) and T_P (from 1100 to 1700 s with $\Delta T_P = 200$ s) (Fig. 8). Figure 7a and b show representative anodization profiles of logarithmic negative apodized ($J_{offset} = 0.420\,mA\,cm^{-2}$, $T_P = 1300$ s, and $\Delta A_J = 0.210\,mA\,cm^{-2}$) and non-apodized NAA-DBRs ($J_{offset} = 0.420\,mA\,cm^{-2}$, $T_P = 1300$ s, and $A_J = 0.420\,mA\,cm^{-2}$) produced with different J_{Offset}. Figure S1 (Supporting Information) compiles the anodization profiles of all the samples analyzed in our study. A qualitative comparison of the transmission spectra of these NAA-DBRs (Fig. 7c and d, respectively) reveals that a logarithmic negative apodization function significantly enhances the quality of the PSB of NAA-DBRs. Similarly to previous observations, t_{pw} intensifies and broadens the PSB in both apodized and non-apodized NAA-DBRs. The combined effect of J_{offset} and t_{pw} on the Q_{PSB} and λ_{PSB} of non-apodized and apodized NAA-DBRs is summarized in the contour maps shown in Fig. 7e and f, respectively. As Fig. 7e reveals, the color fields and field line distances are broad at longer t_{pw} and higher J_{offset} for non-apodized NAA-DBRs. The dependence of Q_{PSB} on t_{pw} increases as t_{pw} decreases, particularly at $J_{offset} = 0.140$ and 0.560 mA cm^{-2}, as indicated by the denser field lines around the maximum ($Q_{PSB} = 10.9 \pm 0.5$) located at $J_{offset} = 0.560\,mA\,cm^{-2}$ and $t_{pw} = 0$ min. Figure 7f displays the distribution of Q_{PSB} as a function of J_{offset} and t_{pw} for logarithmic negative apodized NAA-DBRs. The field lines from $J_{offset} = 0.420$ to $0.560\,mA\,cm^{-2}$ and from $t_{pw} = 2$ to 6 min are wide apart, indicating that Q_{PSB} in apodized NAA-DBRs has a weak correlation with the pore widening time and the current density offset within the range of fabrication parameters assessed. The maximum of Q_{PSB} (21.4 ± 1.0) is achieved when J_{offset} and t_{pw} are set to $0.280\,mA\,cm^{-2}$ and 0 min, respectively. The color field and field lines concentrate around this maximum, where the dependency of Q_{PSB} on J_{offset} and t_{pw} increases. Both non-apodized and apodized NAA-DBRs have poor quality of PSB when they are over-etched (i.e. long t_{pw}), as revealed by the low values of Q_{PSB} and broad color fields within these regions of the contour maps. The distribution of λ_{PSB} with J_{offset} and t_{pw} for non-apodized and apodized NAA-DBRs is summarized in the contour maps shown in Fig. 7g and h, respectively. As these graphics reveal, λ_{PSB} of non-apodized NAA-DBRs has a stronger dependency with J_{offset} at high values of this fabrication parameter (from 0.420 to 0.560 mA cm^{-2}) (Fig. 7g), while this dependence is stronger at moderate J_{offset} values in the case of apodized NAA-DBRs (from 0.280 to 0.420 mA cm^{-2}) (Fig. 7h). However, in both cases it is observed a similar trend in the shift of λ_{PSB} with J_{offset} and t_{pw}: when J_{offset} increases, λ_{PSB} is red-shifted toward the NIR region of the spectrum. In the case of t_{pw}, the longer t_{pw} is the shorter the wavelength at which both non-apodized and apodized NAA-DBRs reflect light more efficiently (blue shift). The transmission spectra of all the NAA-DBRs analyzed in this study as a function of J_{offset} and t_{pw} are compiled in Figure S2 (Supporting Information).

Likewise in previous cases, these NAA-DBRs also display vibrant interferometric colors, which correspond to the position of the characteristic PSB across the UV-vis-NIR spectrum. Figure S3 (Supporting Information) displays digital pictures of non-apodized and logarithmic negative apodized NAA-DBRs produced at different values of J_{offset} and t_{pw}. It is worthwhile to note that apodized NAA-DBRs have their characteristic PSB located at longer wavelengths as compared to their non-apodized counterparts. This is also denoted by the difference in the interferometric color displayed by these PCs. Furthermore, NAA-DBRs with high J_{offset} show transparent color as there is a red shift in the position of PSB (NIR region) as J_{offset} increases.

To assess the combined effect of the anodization period (T_P) and t_{pw} on the optical filtering features of non-apodized and logarithmic negative apodized NAA-DBRs, T_P and t_{pw} were systematically modified from 1100 to 1700 s with $\Delta T_P = 200$ s, and from 0 to 6 min with $\Delta t_{pw} = 2$ min, respectively. The obtained results showing the dependency of Q_{PSB} and λ_{PSB} with T_P and t_{pw} for these NAA-DBRs are summarized in Fig. 8. Figure 8a and b display representative anodization profiles of non-apodized and apodized NAA-DBRs produced with $T_P = 1500$ s, respectively, whereas Figure S4 (Supporting Information) compiles the anodization profiles of all the NAA-DBRs analyzed in this study. Representative transmission spectra of non-apodized ($T_P = 1500$ s, $A_J = 0.420\,mA\,cm^{-2}$, and $J_{offset} = 0.280\,mA\,cm^{-2}$) and logarithmic negative apodized ($T_P = 1500$ s, $\Delta A_J = 0.210\,mA\,cm^{-2}$, and $J_{offset} = 0.280\,mA\,cm^{-2}$) NAA-DBRs at different t_{pw} are presented in Fig. 8c and d, respectively.

These graphs show that the transmission spectrum of apodized NAA-DBRs features much narrower PSBs than those of non-apodized NAA-DBRs. It is also observed that to widen the nanoporous structure of NAA-DBRs increases the intensity and width of the PSBs, independently on the anodization period (Figure S5 – Supporting Information).

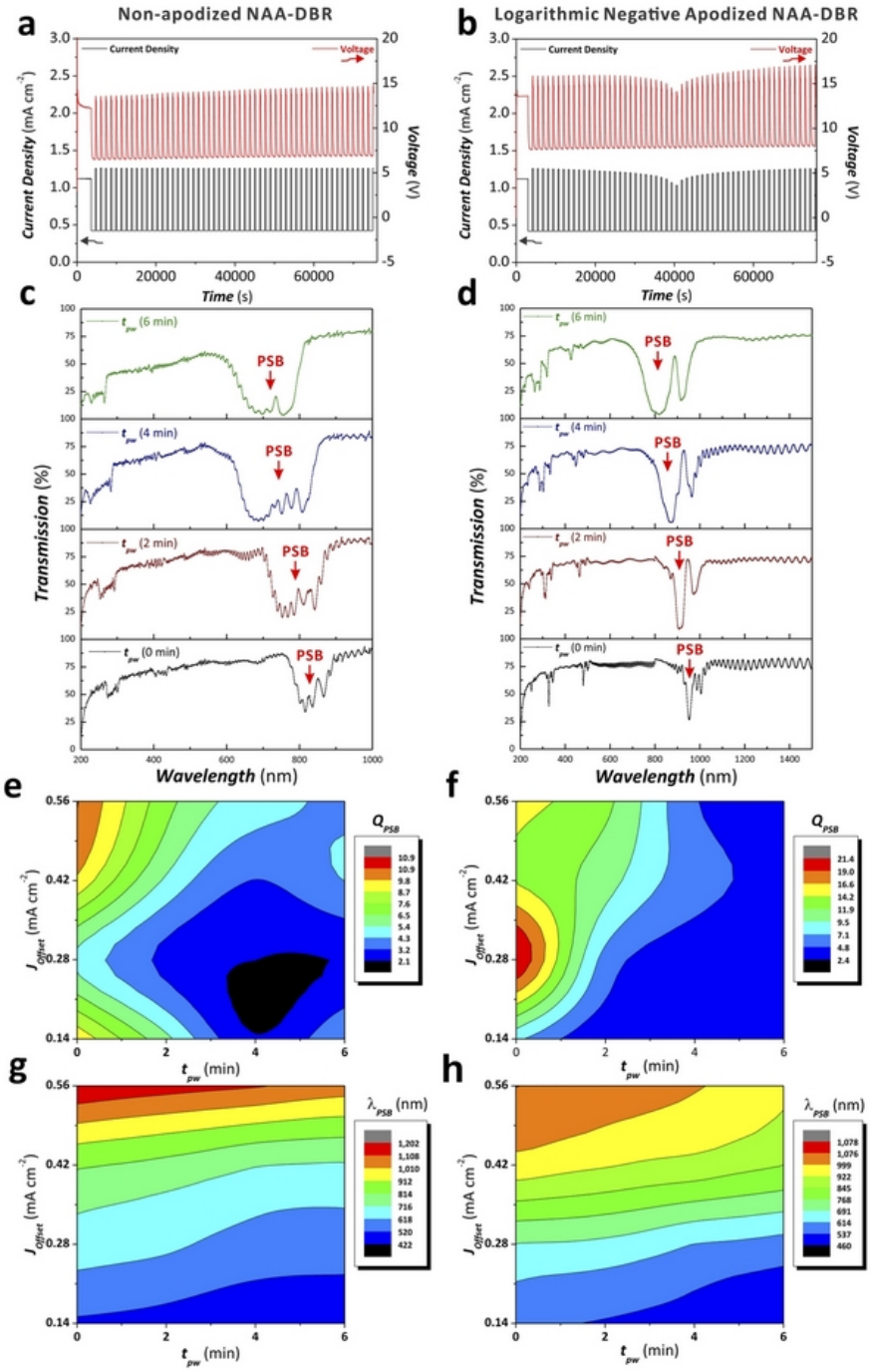

Figure 7. Effect of the current density offset (J_{Offset}) and the pore widening time (t_{pw}) on the Q_{PSB} and λ_{PSB} of non-apodized and logarithmic negative apodized NAA-DBRs. (**a** and **b**) Representative anodization profiles of non-apodized ($T_P = 1500$ s, $A_J = 0.420$ mA cm^{-2}, and $t_{STPA} = 20$ h) and apodized NAA-DBRs (apodization function = logarithmic negative, $T_P = 1500$ s, $\Delta A_J = 0.210$ mA cm^{-2}, and $t_{ASTPA} = 20$ h), respectively. (**c** and **d**) Transmission spectra of non-apodized and apodized NAA-DBRs showing the PSB as a function of the pore widening time, respectively. (**e** and **f**) Contour maps showing the dependency of Q_{PSB} of non-apodized and apodized NAA-DBRs as a function of J_{Offset} and t_{pw}, respectively. (**g** and **h**) Contour maps showing the dependency of λ_{PSB} of non-apodized and apodized NAA-DBRs as a function of J_{Offset} and t_{pw}, respectively.

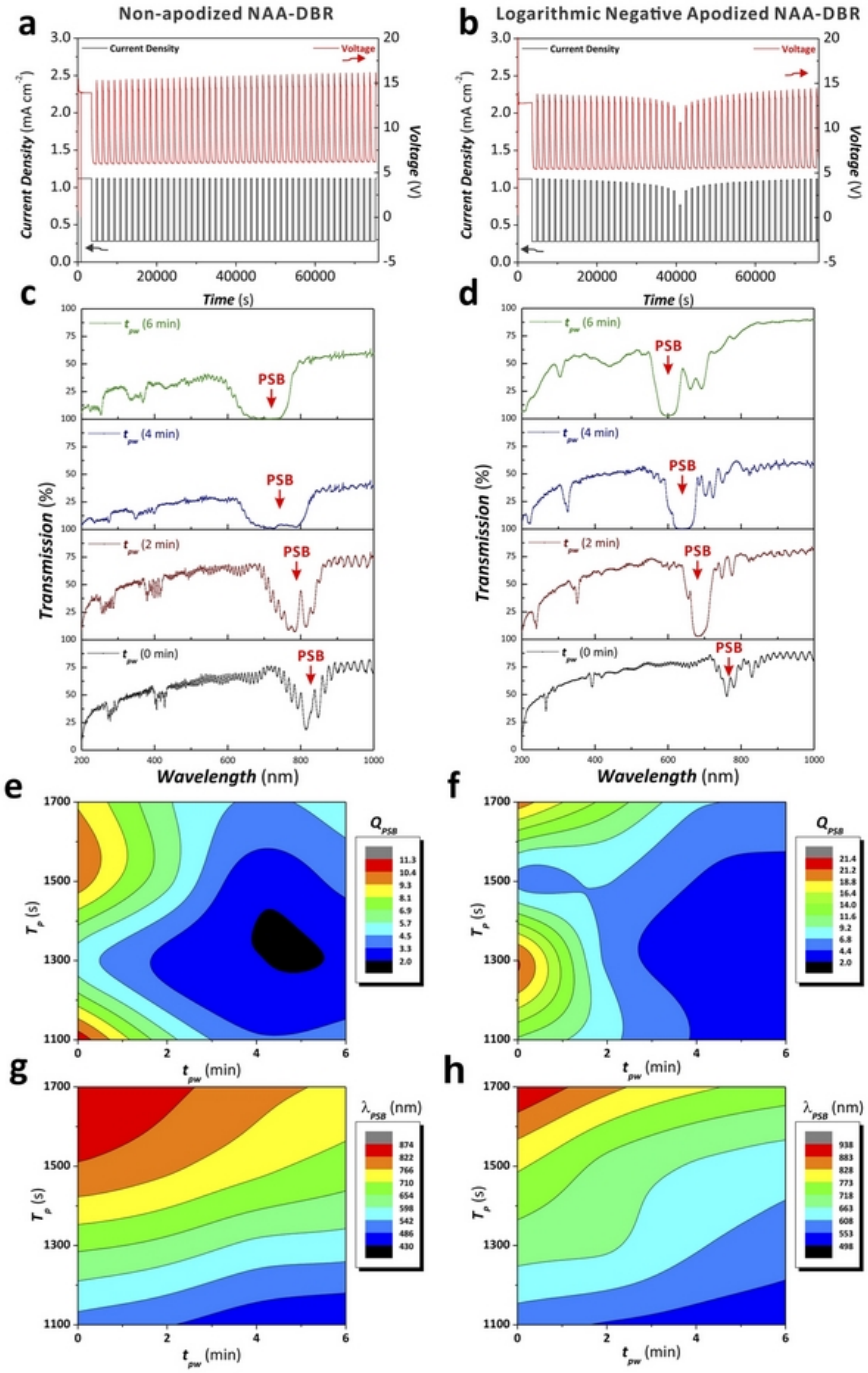

Figure 8. Effect of the anodization period (T_p) and the pore widening time (t_{pw}) on the Q_{PSB} and λ_{PSB} of non-apodized and apodized NAA-DBRs. (**a** and **b**) Representative anodization profiles of non-apodized ($T_p = 1100$ s, $A_J = 0.420$ mA cm^{-2}, $J_{min} = J_{offset} = 0.280$ mA cm^{-2}, and $t_{STPA} = 20$ h) and apodized NAA-DBRs (apodization function = logarithmic negative, $T_p = 1100$ s, $\Delta A_J = 0.210$ mA cm^{-2}, $J_{min} = J_{offset} = 0.280$ mA cm^{-2}, and $t_{ASTPA} = 20$ h), respectively. (**c** and **d**) Transmission spectra of non-apodized and apodized NAA-DBRs showing the PSB as a function of the pore widening time, respectively. (**e** and **f**) Contour maps showing the dependency of Q_{PSB} of non-apodized and apodized NAA-DBRs as a function of T_p and t_{pw}, respectively. (**g** and **h**) Contour maps showing the dependency of λ_{PSB} of non-apodized and apodized NAA-DBRs as a function of T_p and t_{pw}, respectively.

Figure 8e and f show contour maps describing how Q_{PSB} varies with T_P and t_{pw} for non-apodized NAA-DBRs and logarithmic negative apodized NAA-DBRs, respectively. Both graphs exhibit similar Q_{PSB} distribution with broad color fields and field lines at longer t_{pw} and increasing concentration of color fields as t_{pw} decreases. Non-apodized NAA-DBRs display two maxima located at $T_P = 1100$ and 1500 s with $t_{pw} = 0$ min, where the former has the maximum value for Q_{PSB} (11.2 ± 0.6). In the case of apodized NAA-DBRs, the maxima are located at $T_P = 1300$ and 1700 s with $t_{pw} = 0$ min, where the former gives the maximum Q_{PSB} value of 21.3 ± 0.6, which is almost twice higher than that of the non-apodized counterparts. The dependency of Q_{PSB} with T_P increases around the maxima, as indicated by the close field lines and the concentration of color fields around these points. It is worth nothing that the Q_{PSB} of apodized NAA-DBRs has a stronger dependency on T_P as compared to non-apodized NAA-DBRs, denoted by the smaller field line distances in Fig. 8f.

The dependency of λ_{PSB} on T_P and t_{pw} for non-apodized and apodized NAA-DBRs is summarized in Fig. 8g and h, respectively. As shown by the contour map for non-apodized NAA-DBRs (Fig. 8g), the color fields are distributed homogenously throughout the map with equidistant field lines at $T_P < 1500$ s, which suggest a fairly strong dependence of λ_{PSB} on this range of T_P. The distance between field lines increases from $T_P = 1500$ to 1700 s, indicating a weaker dependence of λ_{PSB} on T_P. In contrast, the contour map for apodized NAA-DBRs (Fig. 8h) shows an even distribution of color fields with equidistant field lines at $T_P > 1500$ s and broader color fields with more distant field lines at $T_P < 1500$ s. These results indicates that the dependency of λ_{PSB} on T_P is stronger at longer T_P than that at shorter T_P. Compared to T_P, t_{pw} has a less significant impact on the distribution of λ_{PSB}, with a similar effect in both non-apodized and apodized NAA-DBRs, where an increment in T_P red-shifts the position of λ_{PSB} while an increment in t_{pw} blue-shifts the position of λ_{PSB}. This result is good agreement with previous studies, establishing the behavior of the characteristic PSB of NAA-based photonic structures under the manipulation of T_P and t_{pw}[38].

NAA-DBRs also displayed tunable vivid interferometric colors as the position of the PSB is shifted across spectral regions (Figure S6 – Supporting Information). The difference in the interferometric colors shown by non-apodized and apodized NAA-DBRs is due to the shift in the PSB's position, which is located at longer wavelengths for apodized NAA-DBRs as compared to that of non-apodized NAA-DBRs produced with the same T_P.

Assessment of Effective Medium Sensitivity of Non-apodized and Apodized NAA-PCs. As revealed by the analysis of Q_{PSB}, the implementation of an apodization strategy during anodization is an effective approach to improve the quality of the PSB of NAA-DBRs, which results in better resolved and narrower characteristic PSBs with tunable filtering features across the spectral regions. This feature can be readily used to develop highly sensitive optical sensing platforms to detect analytes of interest based on effective refractive index changes[17]. It is known that PC structures with high quality PSBs are more sensitive to effective medium changes (i.e. larger shifts in the position of PSB upon small effective medium changes), making them optimal platforms to develop advanced sensing system[39].

To verify that apodized NAA-DBRs with better Q_{PSB} are more sensitive toward effective medium changes, we systematically infiltrated the nanoporous network of non-apodized and apodized NAA-DBRs produced with different T_P (i.e. 1100, 1300, 1500, and 1700 s) with media of different refractive index and measured shifts in the PSB ($\Delta\lambda_{PSB}$) using reflectometric interference spectroscopy (RIfS). Figure 9a and b show representative RIfS spectra for non-apodized ($T_P = 1700$ s, $A_J = 0.420$ mA cm^{-2}, $J_{offset} = 0.280$ mA cm^{-2}, and $t_{pw} = 4$ min) and apodized NAA-DBRs ($T_P = 1700$ s, $\Delta A_J = 0.210$ mA cm^{-2}, $J_{offset} = 0.280$ mA cm^{-2}, and $t_{pw} = 4$ min), respectively, infiltrated with different media (air ~1.00 RIU, water ~1.33 RIU, and ethanol ~1.36 RIU). As demonstrated in our previous study[22], the RIfS spectra of NAA-DBRs features two main regions: namely; i) the interference of light from all layers of the multilayered NAA-DBR structure characterized by a relatively narrow and intense PSB, and ii) the Fabry-Pérot interference spectrum (i.e. fast oscillations) produced by the reflections of light at the interfaces bordering the NAA-DBR. In this study, we used the positon of the characteristic PSB in the RIfS spectra of NAA-DBRs as sensing parameter. The sensitivity of these PC structures as a function of T_P and t_{pw} is established by the slope of the linear fitting obtained by correlating $\Delta\lambda_{PSB}$, determined by RIfS, and the refractive index of the medium filling the nanopores. The obtained results for non-apodized and apodized NAA-DBRs are summarized in Fig. 9c and d.

Figure 9c reveals that non-apodized NAA-DBRs produced with $T_P = 1700$ s have the highest sensitivity at $t_{pw} = 0$, 2, and 4 min (i.e. 119 ± 13, 254 ± 39, and 339 ± 60 nm RIU^{-1}, respectively), whereas at $t_{pw} = 6$ min, those NAA-DBRs produced at $T_P = 1300$ s display the highest sensitivity (i.e. 332 ± 51 nm RIU^{-1}, respectively). In contrast, Fig. 9d denotes that logarithmic negative apodized NAA-DBRs produced with $T_P = 1500$ s have the highest sensitivity at $t_{pw} = 0$ (120 ± 13 nm RIU^{-1}, respectively). However, at $t_{pw} = 2$ and 4 min, apodized NAA-DBRs produced at $T_P = 1700$ s have the highest sensitivity (280 ± 43 and 392 ± 65 nm RIU^{-1}, respectively) and, at $t_{pw} = 6$ min, NAA-DBRs fabricated with $T_P = 1300$ s are the most sensitive PC structures (363 ± 64 nm RIU^{-1}).

In general, it is observed that the sensitivity of non-apodized and apodized NAA-DBRs is enhanced by the pore widening treatment for $0 \text{ min} \leq t_{pw} \leq 4$ min. However, as denoted by the Q_{PSB} analysis, further increase in t_{pw} worsens the quality of the PSB due to the over-etching of the nanoporous structure of NAA-DBRs, which broadens the PSB and reduces the sensitivity of these platforms. Interestingly, both non-apodized and apodized NAA-DBRs have exhibited the highest sensitivity (i.e. 339 ± 59 and 392 ± 65 nm RIU^{-1}, respectively) at $t_{pw} = 4$ min and $T_P = 1700$ s, where the latter is revealed to be the most sensitive platform toward changes in the effective medium. The sensitivity of apodized NAA-DBRs was found to be ~ 16% higher than that of their non-apodized counterparts.

To conclude, this study provides new insights into the capability of anodization to engineer and tune the optical properties of NAA-based photonic crystal structures. An apodization strategy applied during stepwise pulse anodization enables the precise control over the features of the photonic stopband of NAA-DBRs by manipulating various anodization parameters (i.e. apodization function, amplitude difference, current density

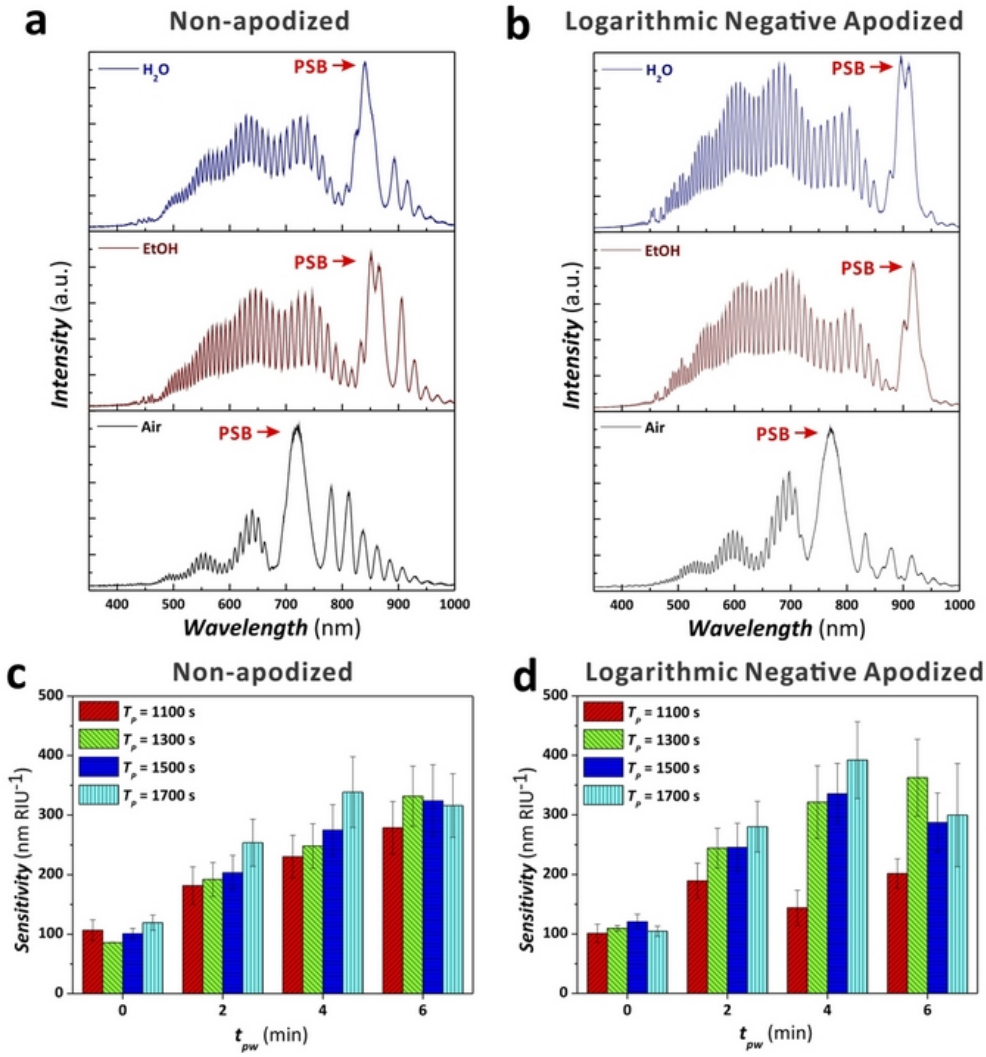

Figure 9. Assessment of sensitivity of NAA-DBRs upon effective medium changes in non-apodized and apodized NAA-DBRs. (**a**) Representative RIfS spectra of a non-apodized NAA-DBR under different nanopores-infiltrating medium (i.e. air, ethanol, and water) ($T_P = 1700$ s, $A_J = 0.420\,mA\,cm^{-2}$, $J_{min} = J_{offset} = 0.280\,mA\,cm^{-2}$, $t_{STPA} = 20$ h, and $t_{pw} = 4$ min). (**b**) Representative RIfS spectra of a logarithmic negative apodized NAA-DBR under different nanopores-infiltrating medium (i.e. air, ethanol, and water) ($T_P = 1700$ s, $\Delta A_J = 0.210\,mA\,cm^{-2}$, $J_{min} = J_{offset} = 0.280\,mA\,cm^{-2}$, $t_{ASTPA} = 20$ h, and $t_{pw} = 4$ min). (**c**) Bar chart showing the sensitivity in nm RIU^{-1} of non-apodized NAA-DBRs produced at different T_P (1100, 1300, 1500, and 1700 s) and t_{pw} (0, 2, 4, and 6 min) ($A_J = 0.420\,mA\,cm^{-2}$, $J_{min} = J_{offset} = 0.280\,mA\,cm^{-2}$, and $t_{STPA} = 20$ h). (**d**) Bar chart showing the sensitivity in nm RIU^{-1} of logarithmic negative apodized NAA-DBRs produced at different T_P (1100, 1300, 1500, and 1700 s) and t_{pw} (0, 2, 4, and 6 min) ($\Delta A_J = 0.210\,mA\,cm^{-2}$, $J_{min} = J_{offset} = 0.280\,mA\,cm^{-2}$, and $t_{ASTPA} = 20$ h).

offset, anodisation period, and pore widening time). The systematic analysis on the effect of each fabrication parameter reveals that a logarithmic negative apodization function provides the highest quality of the photonic stopband ($Q_{PSB} = 21.4 \pm 1.0$). Apodized NAA-DBRs are demonstrated to be a more sensitive sensing platform than non-apodized NAA-DBRs as they have shown higher sensitivity toward effective medium changes (~16% enhancement). Logarithmic negative apodized and non-apodized NAA-DBRs produced with $T_P = 1700$ s and $t_{pw} = 4$ min have a sensitivity of 392 ± 65 and 339 ± 59 nm RIU^{-1}, respectively.

These innovative NAA-based photonic crystal structures with enhanced optical properties pave the way for the development of ultrasensitive optical sensing systems and other photonic elements such as selective optical filters with broad applicability.

Methods

Materials. High purity (99.9997%) aluminum (Al) foils of thickness 0.32 mm were supplied by Goodfellow Cambridge Ltd. (UK). Sulfuric acid (H_2SO_4), perchloric acid ($HClO_4$), copper (II) chloride ($CuCl_2$), hydrochloric

acid (HCl), phosphoric acid (H_3PO_4), and ethanol (EtOH – C_2H_5OH) were supplied by Sigma-Aldrich (Australia) and used as received, without further purification. Aqueous solutions used in this study were prepared with ultrapure Mili-Q® water (18.2 mΩ.cm) (Australia).

Fabrication of NAA Photonic Structures. Non-apodized NAA photonic structures were produced by stepwise pulse anodisation (STPA) approach under current density control conditions. 1.5 × 1.5 cm Al square chips were first washed in ethanol and water under sonification for 15 min each and dried under air stream. These Al substrates were then electropolished in a mixture of EtOH and $HClO_4$ 4:1 *(v:v)* at 20 V and 5 °C for 3 min. After electropolishing, Al chips were anodized in an aqueous solution of 1.1 M H_2SO_4 with 25 *v*% of EtOH at −1 °C. The galvanostatic anodization process started with a constant step at a current density of 1.120 mA cm^{-2} for 1 h to achieve a homogenous pore growth rate prior to stepwise pulse anodization. The anodization profile was subsequently switched to stepwise pulse mode, where the current density was pulsed between high (J_{max} = 1.120 mA cm^{-2}) and low (J_{min} = 0.280 mA cm^{-2}) current density values following a stepwise modulation for a total anodization time (t_{STPA} or t_{ASTPA}) of 20 h. A set of reference non-apodized NAA-DBRs were produced, where the current density amplitude (A_J) and current density offset (J_{offset}) were set at 0.420 mA cm^{-2} and 0.280 mA cm^{-2}, respectively, whereas the anodization period (T_P) (i.e. time between consecutive pulses) was modified from 900 to 1700 s with a step size of 100 s. Note that T_P is given by Equation 2.

$$T_P = t_{max} + t_{min} \tag{2}$$

where t_{max} and t_{min} are the time lengths at J_{max} and J_{min}, respectively, and t_{max} and t_{min} were set at a ratio of 1:4 (i.e. $t_{min} = 4t_{max}$) for T_P = 900 to 1700 s.

To assess the effect of J_{Offset}, another set of non-apodized NAA photonic structures was fabricated based on the following parameters: A_J = 0.420 mA cm^{-2}, T_P = 1300 s, where J_{offset} was adjusted from 0.140 to 0.560 mA cm^{-2} with an interval of 0.140 mA cm^{-2}. The current density during stepwise pulse mode was pulsed between J_{min} and J_{max}, where the these parameters were defined by Equations 3 and 4, respectively.

$$J_{Low} = J_{offset} \tag{3}$$

$$J_{High} = 2A_J + J_{offset} \tag{4}$$

Apodization and Optical Tuning of the PSB of NAA-DBRs. Four different apodization functions: (i) linear positive, (ii) linear negative, (iii) logarithmic positive, and (iv) logarithmic negative, were implemented in a reference STPA profile (i.e. T_P = 1300 s, $J_{min} = J_{offset}$ = 0.280 mA cm^{-2}, J_{High} = 1.120 mA cm^{-2}, A_J = 0.420 mA cm^{-2}, and t_{STPA} = 20 h). The mathematical expressions for each apodization function are listed in Equations S1–S8 (Supporting Information). These ASTPA anodisation profiles were produced by a custom-designed Labview®-based software based on Equation 5:

$$J(t) = 2A_J(t) + J_{offset} \tag{5}$$

where A_J *(t)* is the time-dependent current density amplitude defined for a time between a minimum (A_{min}) and maximum (A_{max}) of amplitude for the corresponding apodization functions (Equations S1–S8 – Supporting Information).

To investigate the effect of ΔA_J on the optical properties of NAA-DBRs, the amplitude difference (ΔA_J) was modified from 0.105 to 0.420 mA cm^{-2} with an interval of 0.105 mA cm^{-2} for each apodization function. Using the most effective apodization function with optimized ΔA_J, which was determined by analyzing the quality factor (Q_{PSB}), other apodization parameters such as J_{Offset} and T_P were systematically modified from 0.140 to 0.560 mA cm^{-2} with a step size of 0.140 cm^{-2}, and from 1100 to 1700 s with a step size of 200 s, respectively, in order to further optimize the optical signals as well as to tune the optical properties of NAA photonic structures.

Optical Characterization. Prior to optical characterization, NAA-DBRs were etched chemically in a saturated solution of $HCl/CuCl_2$ to dissolve the remaining aluminum substrate from the backside. This process was carried out using an etching mask with a circular window of 5 mm in diameter in an etching cell. The optical properties of these etched NAA photonic structures were characterized by analyzing their transmission spectra measured using a UV-visible-NIR spectrophotometer (Cary 300 and Cary 5000, Agilent, USA, for wavelength range of 200–1000 nm and 200–1500 nm respectively). These spectra were obtained at normal incidence (i.e. $\theta = 0°$) with a resolution of 1 nm. To characterize the interferometric color exhibited by these NAA photonic structures, digital images with a black card as background were acquired using a Canon EOS 700D digital camera equipped with a Tamron 90 mm F2.8 VC USD macro mount lens with autofocus function under natural illumination. These NAA photonic crystals were pore widened using an aqueous solution of 5 *wt*% H_3PO_4 at 35 °C for t_{pw} from 0 to 6 min with an interval of 2 min. After each pore widening step, the optical characterization of NAA-DBRs was carried out by recording the transmission spectra and digital images as outlined above.

Assessment of Sensitivity of Non-apodized and Apodized NAA-DBRs. The sensitivity of non-apodized and apodized NAA-DBRs was assessed by correlating the shift in the position of central wavelength (λ_{PSB}) to the refractive index values of the medium filling the nanopores. The spectra of NAA-DBRs with medium-filled nanopores was measured and recorded using a reflectometric interference spectroscopy (RIfS) set-up. White light from a tungsten source (LS-1LL, Ocean Optics, USA) was focused on the surface of NAA-DBRs with an illumination spot of ~2 mm in diameter by a bifurcated optical probe. The collection fiber in

the optical probe collected and transferred the light reflected from the illumination spot to a miniature spectrometer (USB 4000+VIS-NIR-ES, Ocean Optics, USA). The optical spectra acquired in the range of 400–1000 nm wavelength were saved with an integration time of 10 ms and 10 average measurements. Note that NAA-DBRs were coated with an ultra-thin layer of gold by a sputter coater (Sputter coater 108, Cressington, USA) to enhance intereferometric reflection. After recording the optical spectra of NAA-DBRs with air filling the nanopores, a drop of EtOH was placed on the surface and allowed to settle into the nanopores for a few seconds to ensure that the nanopores were infiltrated by EtOH. The spectrum was recorded once the signals were stabilized. Then, a drop of water was placed on the surface of NAA photonic crystals after EtOH had completely evaporated. The RIfS spectrum of NAA-DBRs with H_2O-filled nanopores was recorded and saved. NAA photonic crystals measured were pore widened for $t_{pw} = 0$ to 6 min. After each pore widening step, RIfS spectra were recorded for each NAA-DBRs with different medium filling the nanopores (i.e. air, EtOH, and H_2O). The spectra acquired were then processed using Igor Pro library (Wavemetrics, USA) to determine $\Delta\lambda_{PSB}$ in non-apodized and apodized NAA-DBRs.

Structural Characterization of NAA-DBRs. The morphology and structure of NAA photonic crystals were characterized by FEG-SEM image analysis from images acquired by field emission gun scanning electron microscopy (FEG-SEM FEI Quanta 450). The acquired FEG-SEM images were analyzed using ImageJ (public domain program developed at RSB of the NIH)[40].

References

1. Lee, C.-C. *The current trends of optics and photonics*. Vol. 129 (Springer: 2014)
2. López, C. Materials aspects of photonic crystals. *Adv. Mater.* **15**, 1679–1704 (2003).
3. Philip, J., Jaykumar, T., Kalyanasundaram, P. & Raj, B. A tunable optical filter. *Meas. Sci. Technol.* **14**, 1289 (2003).
4. Bulkin, P. V., Swart, P. L. & Lacquet, B. M. Fourier-transform design and electron cyclotron resonance plasma-enhanced deposition of lossy graded-index optical coatings. *Appl. Opt.* **35**, 4413–4419 (1996).
5. Santos, A., Deen, M. & Marsal, L. Low-cost fabrication technologies for nanostructures: State-of-the-art and potential. *Nanotechnology* **26**, 042001 (2015).
6. Ouellette, M. *et al.* Experimental studies of inhomogeneous coatings for optical applications. *J. Vac. Sci. Technol., A* **9**, 1188–1192 (1991).
7. Wijnhoven, J. E. G. J. & Vos, W. L. Preparation of photonic crystals made of air spheres in titania. *Science* **281**, 802–804 (1998).
8. Agarwal, V. & Del Rio, J. Tailoring the photonic band gap of a porous silicon dielectric mirror. *Appl. Phys. Lett.* **82**, 1512–1514 (2003).
9. Chen, Y. *et al.* Rational design of photonic dust from nanoporous anodic alumina films: A versatile photonic nanotool for visual sensing. *Sci. Rep.* **5**, 12893 (2015).
10. Bisi, O., Ossicini, S. & Pavesi, L. Porous Silicon: A Quantum Sponge Structure for Silicon Based Optoelectronics. *Surf. Sci. Rep.* **38**, 1–126 (2000).
11. Santos, A. *et al.* Tunable Fabry-Pérot interferometer based on nanoporous anodic alumina for optical biosensing purposes. *Nanoscale Res. Lett.* **7**, 370 (2012).
12. Hotta, K., Yamaguchi, A. & Teramae, N. Nanoporous waveguide sensor with optimized nanoarchitectures for highly sensitive label-free biosensing. *ACS Nano* **6**, 1541–1547 (2012).
13. Loni, A. *et al.* Porous silicon multilayer optical waveguides. *Thin Solid Films* **276**, 143–146 (1996).
14. Dal Negro, L. *et al.* Light transport through the band-edge states of Fibonacci quasicrystals. *Phys. Rev. Lett.* **90**, 055501 (2003).
15. Sapienza, R. *et al.* Optical analogue of electronic bloch oscillations. *Phys. Rev. Lett.* **91**, 263902 (2003).
16. Santos, A. Nanoporous anodic alumina photonic crystals: Fundamentals, developments and perspectives. *J. Mater. Chem. C* **5**, 5581–5599 (2017).
17. Ilyas, S. *et al.* Porous silicon based narrow line-width rugate filters. *Opt. Mater.* **29**, 619–622 (2007).
18. Chen, Y. *et al.* On the generation of interferometric colors in high purity and technical grade aluminum: An alternative green process for metal finishing industry. *Electrochim. Acta* **174**, 672–681 (2015).
19. Kumeria, T., Rahman, M. M., Santos, A., Ferré-Borrull, J., Marsal, L. F. & Losic, D. Structural and optical nanoengineering of nanoporous anodic alumina rugate filters for real-time and label-free biosensing applications. *Anal. Chem.* **86**, 1837–1844 (2014).
20. Santos, A. *et al.* Realisation and advanced engineering of true optical rugate filters based on nanoporous anodic alumina by sinusoidal pulse anodisation. *Nanoscale* **8**, 1360–1373 (2016).
21. Kumeria, T., Rahman, M. M., Santos, A., Ferré-Borrull, J., Marsal, L. F. & Losic, D. Nanoporous anodic alumina rugate filters for sensing of ionic mercury: Toward environmental point-of-analysis systems. *ACS Appl. Mater. Interfaces* **6**, 12971–12978 (2014).
22. Nemati, M., Santos, A., Law, C. S. & Losic, D. Assessment of binding affinity between drugs and human serum albumin using nanoporous anodic alumina photonic crystals. *Anal. Chem.* **88**, 5971–5980 (2016).
23. Wang, Y. *et al.* Facile synthesis of optical microcavities by a rationally designed anodization approach: Tailoring photonic signals by nanopore structure. *ACS Appl. Mater. Interfaces* **7**, 9879–9888 (2015).
24. Sulka, G. D. & Hnida, K. Distributed Bragg reflector based on porous anodic alumina fabricated by pulse anodization. *Nanotechnology* **23**, 075303 (2012).
25. Chen, Y. *et al.* Interferometric nanoporous anodic alumina photonic coatings for optical sensing. *Nanoscale* **7**, 7770–7779 (2015).
26. Rahman, M. M., Marsal, L. F., Pallarès, J. & Ferré-Borrull, J. Tuning the photonic stop bands of nanoporous anodic alumina-based distributed Bragg reflectors by pore widening. *ACS Appl. Mater. Interfaces* **5**, 13375-–13381 (2013).
27. Law, C. S., Santos, A., Nemati, M. & Losic, D. Structural engineering of nanoporous anodic alumina photonic crystals by sawtooth-like pulse anodization. *ACS Appl. Mater. Interfaces* **8**, 13542–13554 (2016).
28. Yisen, L., Yi, C., Zhiyuan, L., Xing, H. & Yi, L. Structural coloring of aluminum. *Electrochem. Commun.* **13**, 1336–1339 (2011).
29. Santos, A., Pereira, T., Law, C. S. & Losic, D. Rational engineering of nanoporous anodic alumina optical bandpass filters. *Nanoscale* **8**, 14846–14857 (2016).
30. Sukarno, L. C. S. & Santos, A. Realisation and optical engineering of linear variable bandpass filters in nanoporous anodic alumina photonic crystals. *Nanoscale* **9**, 7541–7550 (2017).
31. Santos, A., Kumeria, T., Wang, Y. & Losic, D. *In situ* monitored engineering of inverted nanoporous anodic alumina funnels: On the precise generation of 3D optical nanostructures. *Nanoscale* **6**, 9991–9999 (2014).
32. Siraji, A. A. & Zhao, Y. High-sensitivity and high-Q-factor glass photonic crystal cavity and its applications as sensors. *Opt. Lett.* **40**, 1508–1511 (2015).
33. Wang, Y., Santos, A., Evdokiou, A. & Losic, D. Rational design of ultra-short anodic alumina nanotubes by short-time pulse anodization. *Electrochim. Acta* **154**, 379–386 (2015).
34. Southwell, W. H. Using apodization functions to reduce sidelobes in rugate filters. *Appl. Opt.* **28**, 5091–5094 (1989).

35. Losic, D. & Santos, A. *Nanoporous alumina: fabrication, structure, properties and applications*. Vol. 219 (Springer: 2015).
36. Shang, G. L., Zhang, Y., Fei, G. T., Su, Y. & Zhang, L. D. Energy-lose induced unidirectional light propagation in porous alumina photonic crystal. *Ann. Phys.* **528**, 288–294 (2016).
37. Ling, Z., Chen, S., Hu, X. & Li, Y. Optical transmission spectra of anodic aluminum oxide membranes with a dual layer-by-layer structure. *Chin. Phys. Lett.* **26**, 054213 (2009).
38. Santos, A., Law, C. S., Lei, D. W. C., Pereira, T. & Losic, D. Fine tuning of optical signals in nanoporous anodic alumina photonic crystals by apodized sinusoidal pulse anodisation. *Nanoscale* **8**, 18360–18375 (2016).
39. Shang, G. L. *et al*. Preparation of narrow photonic bandgaps located in the near infrared region and their applications in ethanol gas sensing. *J. Mater. Chem. C* **1**, 5285–5291 (2013).
40. Abràmoff, M. D., Magalhaes, P. J. & Ram, S. J. Image processing with ImageJ. *Biophotonics Int.* **11**, 36–42 (2004).

Acknowledgements

Authors thank the support provided by the Australian Research Council (ARC) DE140100549, the School of Chemical Engineering (UoA), and The University of Adelaide. Authors thank the Adelaide Microscopy (AM) centre for FEG-SEM characterization.

Author Contributions

Ms. Cheryl Suwen Law carried out the experimental part of this work assisted by Ms. Siew Yee Lim. Dr. Abel Santos conceived the idea and designed the experimental part of this work. The obtained results were discussed and analyzed by all the authors. The final version of the manuscript was written through contributions of all the authors. All the authors have given approval to the final version of the manuscript.

Additional Information

Supplementary information accompanies this paper at https://doi.org/10.1038/s41598-018-22895-5.

Competing Interests: The authors declare no competing interests.

Publisher's note: Springer Nature remains neutral with regard to jurisdictional claims in published maps and institutional affiliations.

Supporting Information

On the Precise Tuning of Optical Filtering Features in Nanoporous Anodic Alumina Distributed Bragg Reflectors

Cheryl Suwen Law[1,2,3], Siew Yee Lim[1,2,3], and Abel Santos[1,2,3]*

[1]School of Chemical Engineering, The University of Adelaide, Adelaide, SA 5005, Australia
[2]Institute for Photonics and Advanced Sensing (IPAS), The University of Adelaide, 5005 Adelaide, Australia
[3]ARC Centre of Excellence for Nanoscale BioPhotonics (CNBP), The University of Adelaide, 5005 Adelaide, Australia

***E-Mail:** abel.santos@adelaide.edu.au

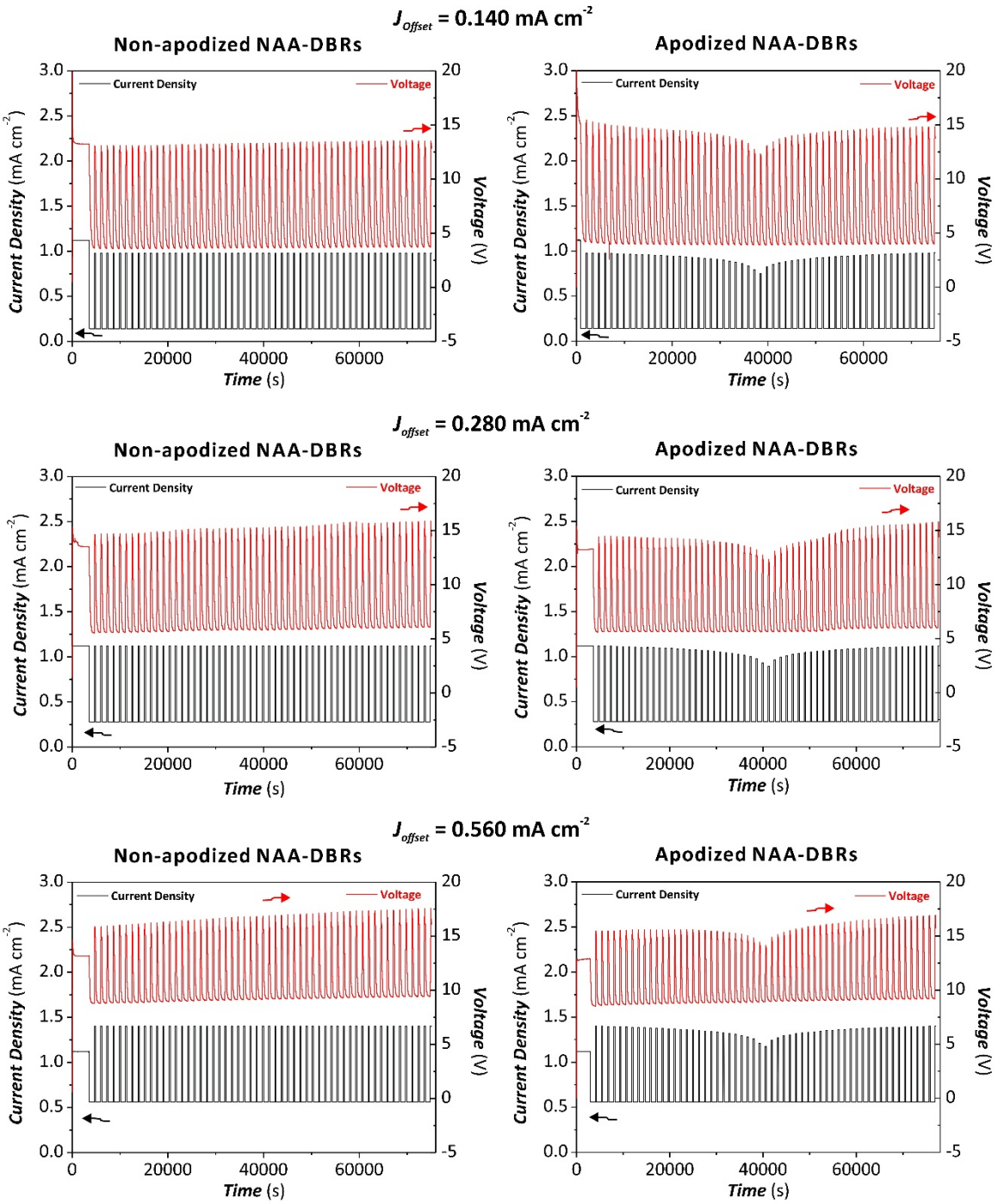

Figure S1. Anodization profiles of non-apodized and logarithmic negative apodized NAA-DBRs as a function of J_{Offset}.

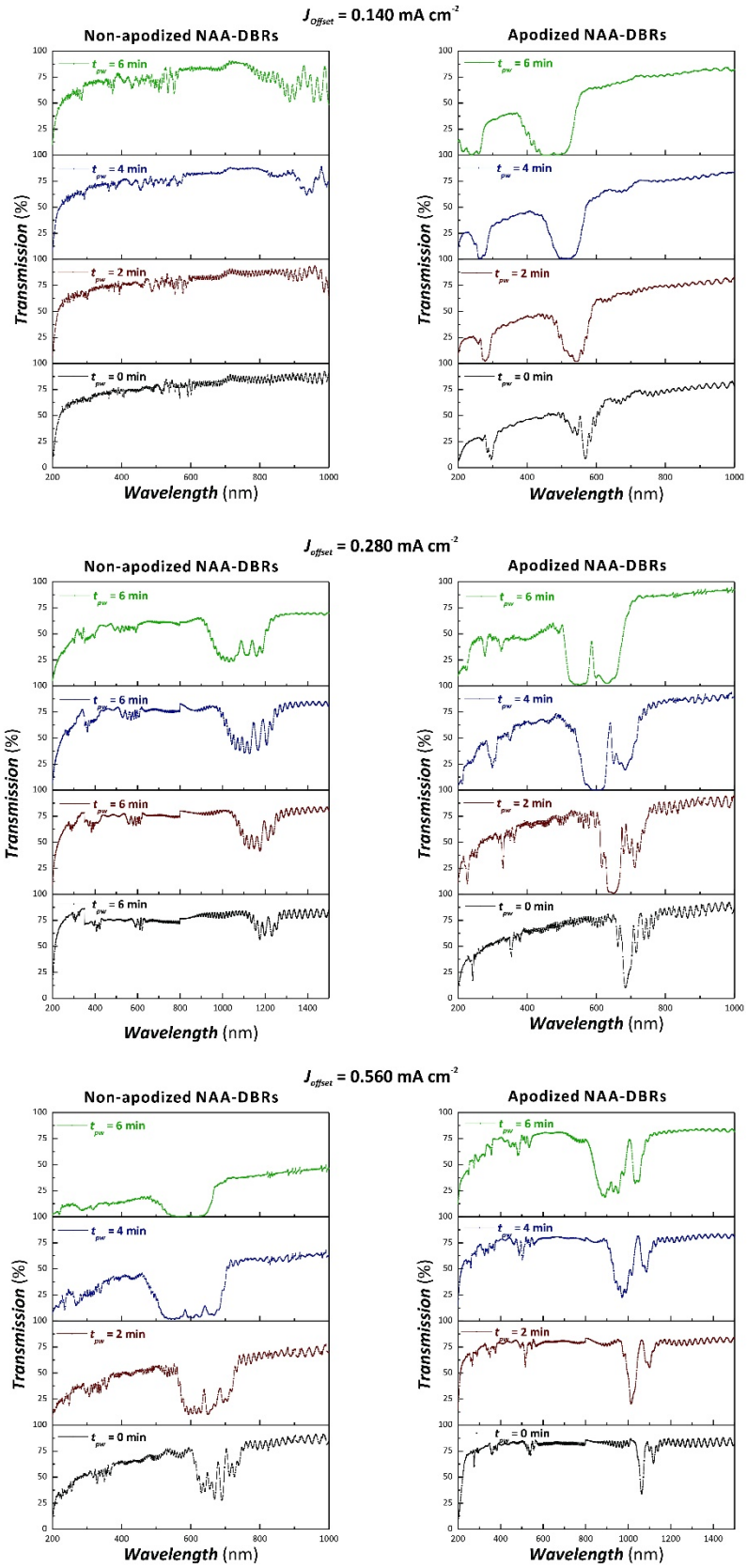

Figure S2. Transmission spectra of non-apodized and logarithmic negative apodized NAA-DBRs as a function of J_{Offset} and t_{pw}.

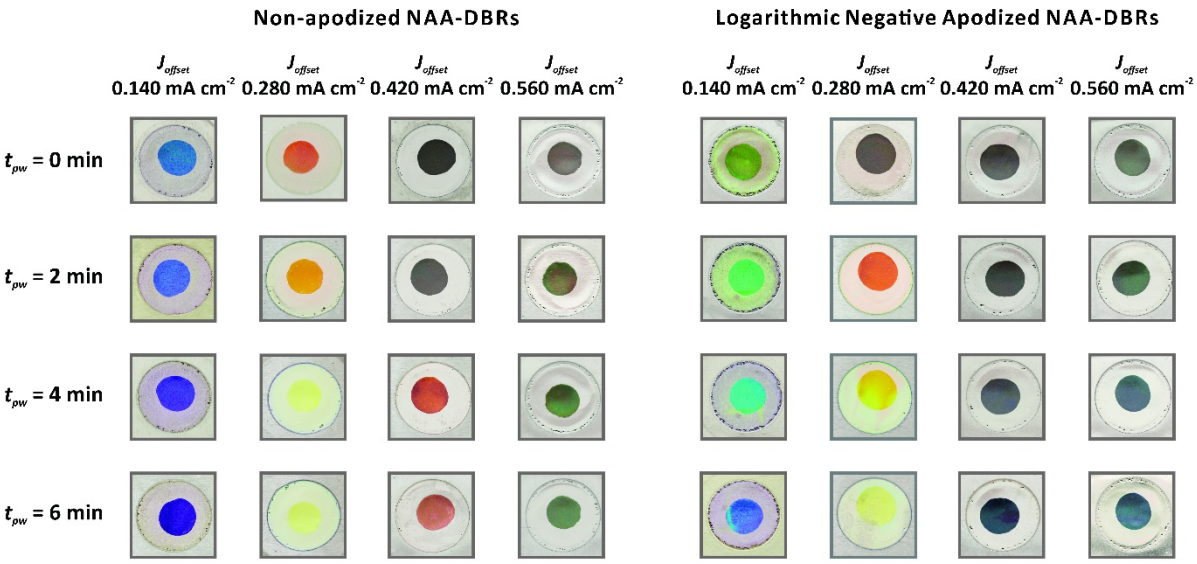

Figure S3. Digital pictures of non-apodized and logarithmic negative apodized NAA-DBRs as a function of J_{Offset} and t_{pw}.

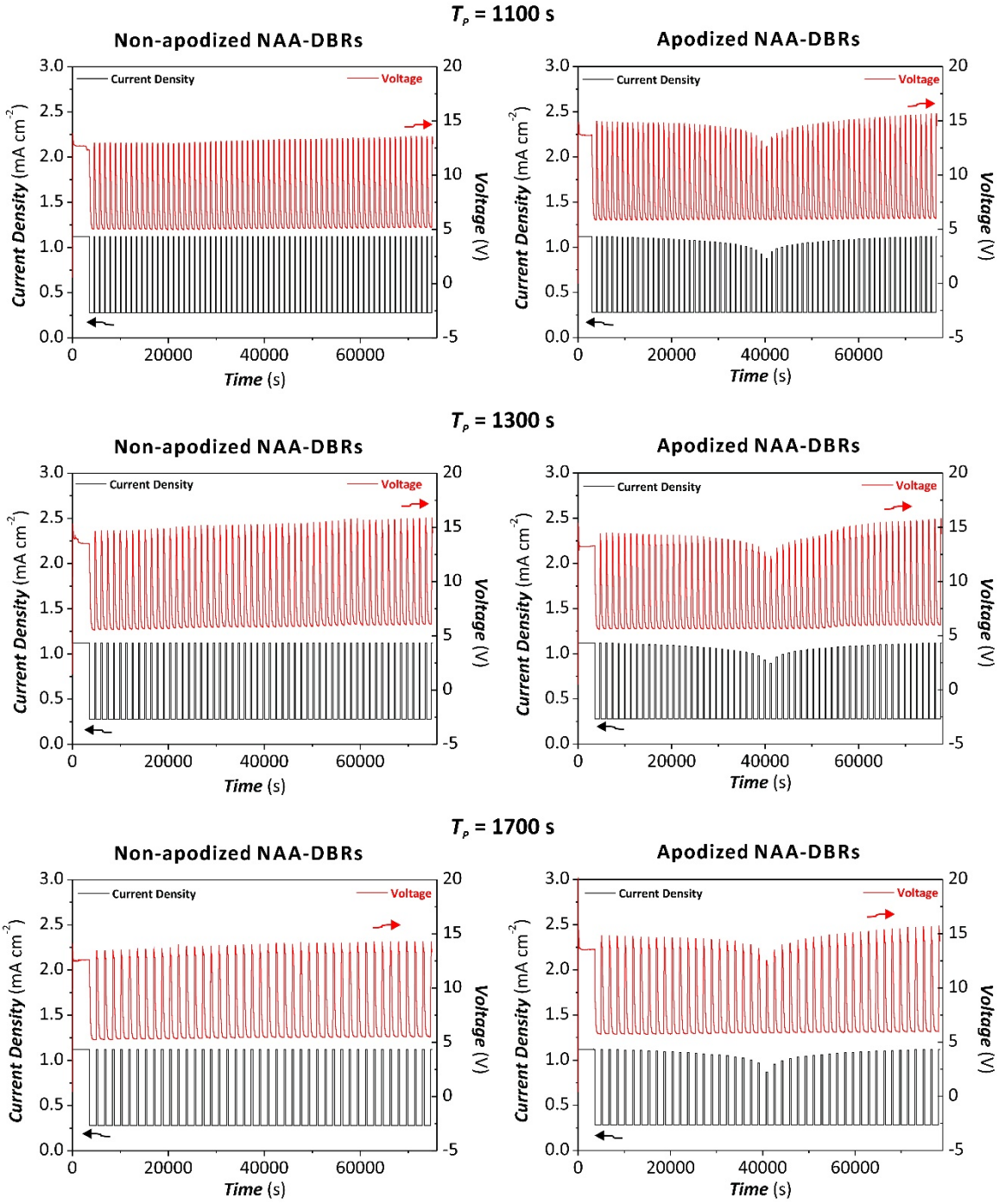

Figure S4. Anodization profiles of non-apodized and logarithmic negative apodized NAA-DBRs as a function of T_P.

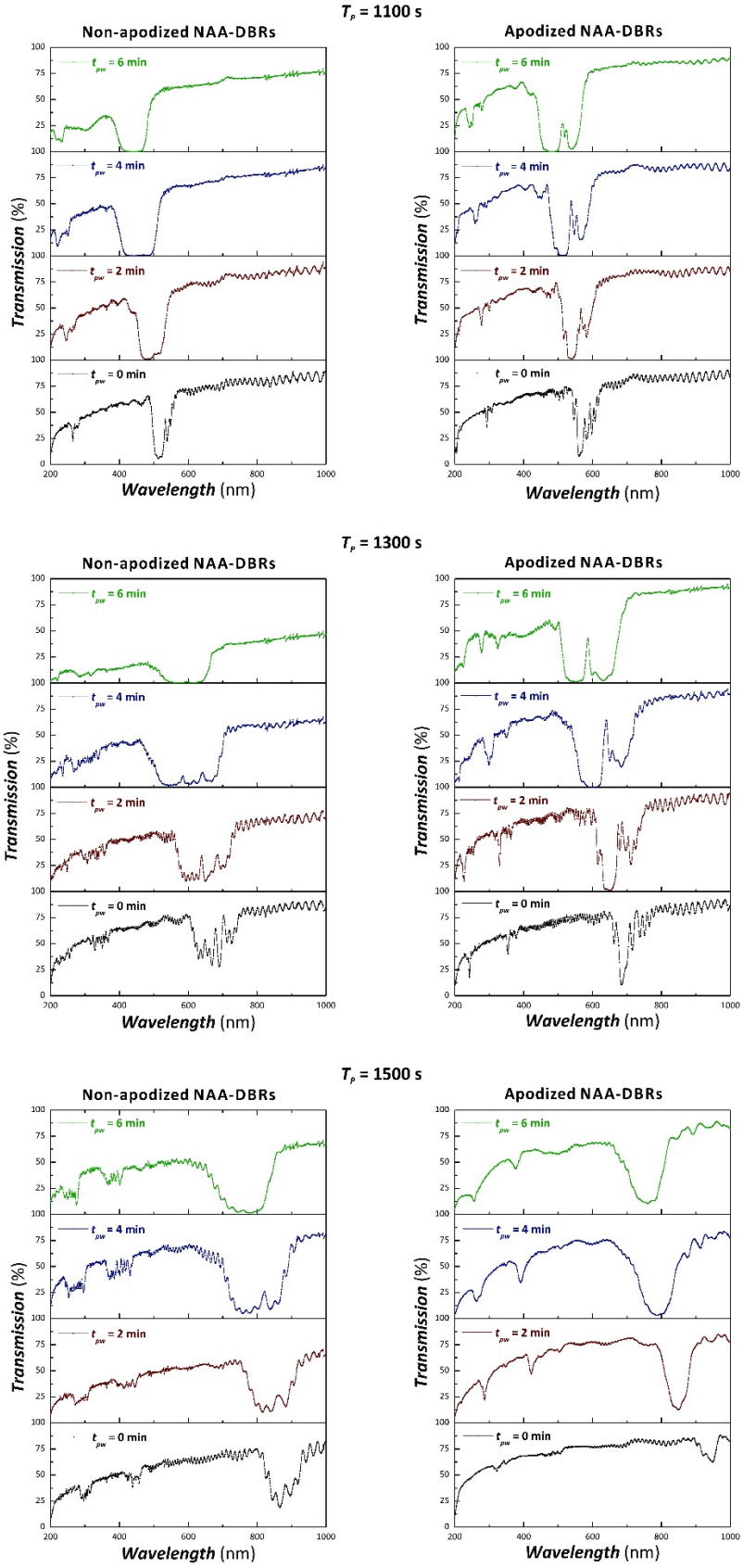

Figure S5. Transmission spectra of non-apodized and logarithmic negative apodized NAA-DBRs as a function of T_P and t_{pw}.

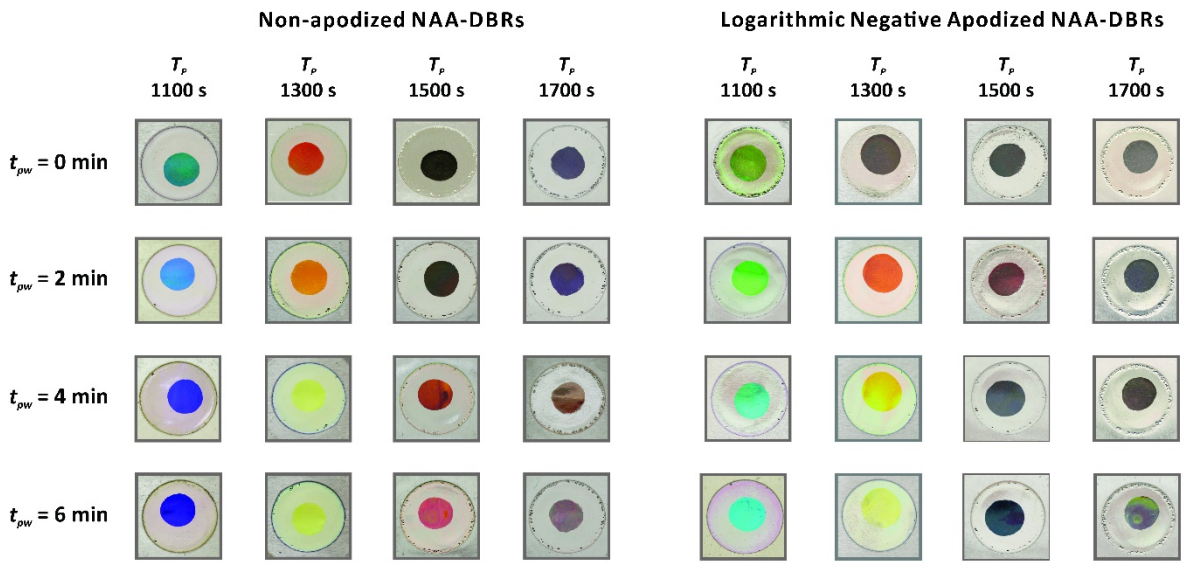

Figure S6. Digital pictures of non-apodized and logarithmic negative apodized NAA-DBRs as a function of T_P and t_{pw}.

The amplitudes as a function of time for the corresponding apodization functions applied in this study are given as **Equations S1 - S8:**

(i) Linear positive apodization

For $t \leqslant t_{an}/2$

$$A(t)_J = A_{min} + \left(\frac{A_{max} - A_{min}}{\frac{t_{an}}{2}}\right).t \qquad \textbf{Eq. S1}$$

For $t > t_{an}/2$

$$A(t)_J = A_{min} + \left(\frac{A_{max} - A_{min}}{t_{an} - \frac{t_{an}}{2}}\right).(t_{an} - t) \qquad \textbf{Eq. S2}$$

(ii) Linear negative apodization

For $t \leqslant t_{an}/2$

$$A(t)_J = A_{max} - \left(\frac{A_{max} - A_{min}}{\frac{t_{an}}{2}}\right).t \qquad \textbf{Eq. S3}$$

For $t > t_{an}/2$

$$A(t)_J = A_{max} + \left(\frac{A_{min} - A_{max}}{t_{an} - \frac{t_{an}}{2}}\right).(t - t_{an}) \qquad \textbf{Eq. S4}$$

(iii) **Logarithmic positive apodization**

For $t \leqslant t_{an}/2$

$$A(t)_J = A_{min} + \left(\frac{A_{max} - A_{min}}{\log\left(\frac{t_{an}}{2} + 10\right) - 1}\right).(\log(t + 10) - 1) \qquad \textbf{Eq. S5}$$

For $t > t_{an}/2$

$$A(t)_J = \left(\frac{A_{min}-A_{max}}{\log(t_{an}+10)-\log\left(\frac{t_{an}}{2}+10\right)}\right).\left(\log(t+10)-\log\left(\frac{t_{an}}{2}+10\right)\right)+A_{max} \quad \textbf{Eq. S6}$$

(iv) Logarithmic negative apodization

For $t \leqslant t_{an}/2$

$$A(t)_J = A_{max}+\left(\frac{A_{min}-A_{max}}{\log\left(\frac{t_{an}}{2}+10\right)-1}\right).(\log(t+10)-1) \quad \textbf{Eq. S7}$$

For $t > t_{an}/2$

$$A(t)_J = \left(\frac{A_{max}-A_{min}}{\log(t_{an}+10)-\log\left(\frac{t_{an}}{2}+10\right)}\right).\left(\log(t+10)-\log\left(\frac{t_{an}}{2}+10\right)\right)+A_{min} \quad \textbf{Eq. S8}$$

Chapter 5

Structural Tailoring of Nanoporous Anodic Alumina Optical Microcavities for Enhanced Resonant Recirculation of Light

Statement of Authorship

Title of Paper	Structural Tailoring of Nanoporous Anodic Alumina Optical Microcavities for Enhanced Resonant Recirculation of Light.
Publication Status	☑ Published ☐ Accepted for Publication ☐ Submitted for Publication ☐ Unpublished and Unsubmitted w ork w ritten in manuscript style
Publication Details	Law, C.S., S.Y. Lim, A.D. Abell, L.F. Marsal, and A. Santos, *Structural tailoring of nanoporous anodic alumina optical microcavities for enhanced resonant recirculation of light*. Nanoscale, 2018. **10**(29): p. 14139-14152.

Principal Author

Name of Principal Author (Candidate)	Cheryl Suwen Law		
Contribution to the Paper	Under the supervision of A. Santos and A. D. Abell, I performed the experiments, interpreted and processed the data and wrote the manuscript.		
Overall percentage (%)	70		
Certification:	This paper reports on original research I conducted during the period of my Higher Degree by Research candidature and is not subject to any obligations or contractual agreements with a third party that would constrain its inclusion in this thesis. I am the primary author of this paper.		
Signature		Date	23/11/2018

Co-Author Contributions

By signing the Statement of Authorship, each author certifies that:

i. the candidate's stated contribution to the publication is accurate (as detailed above);
ii. permission is granted for the candidate in include the publication in the thesis; and
iii. the sum of all co-author contributions is equal to 100% less the candidate's stated contribution.

Name of Co-Author	Siew Yee Lim		
Contribution to the Paper	I aided in performing the experiments. I give consent for Cheryl Suwen Law to present this paper for examination towards the Doctorate of Philosophy.		
Signature		Date	14/11/2018

Name of Co-Author	Andrew D. Abell		
Contribution to the Paper	I acted as secondary supervisor for the candidate, aided in revising the manuscript and evaluating the final version of manuscript. I give consent for Cheryl Suwen Law to present this paper for examination towards the Doctorate of Philosophy.		
Signature		Date	23/11/2018

Name of Co-Author	Lluis F. Marsal		
Contribution to the Paper	I aided in revising the manuscript and evaluating in the final version of manuscript. I give consent for Cheryl Suwen Law to present this paper for examination towards the Doctorate of Philosophy.		
Signature		Date	17/11/2018

Name of Co-Author	Abel Santos		
Contribution to the Paper	I acted as primary supervisor for the candidate, aided in developing of the experiments, revising the manuscript and evaluating the final version of the manuscript. I give consent for Cheryl Suwen Law to present this paper for examination towards the Doctorate of Philosophy.		
Signature		Date	23/11/2018

5. Structural Tailoring of Nanoporous Anodic Alumina Optical Microcavities for Enhanced Resonant Recirculation of Light

5.1 Introduction, Significance and Commentary

Optical microcavities (μCVs) have been long used in optical sensing due to their ability to strongly confine light. However, the quality of nanoporous anodic alumina (NAA)-based μCVs (NAA-μCVs) is much poorer than that of porous silicon – reference nanoporous material in optical sensing. Therefore, this chapter explores galvanostatic stepwise and sinusoidal pulse anodisation to fabricate NAA-μCVs with high quality photonic stop bands that can be spectrally tuned by means of the anodisation parameters. This work has successfully produced NAA-μCVs with high quality factors (i.e. approximately threefold quality enhancement compared to previous studies), which suggests that a rational structural design of NAA-μCVs can significantly enhance light confinement quality within the nanoporous structures, opening new opportunities to NAA-μCVs as ultrasensitive sensing platforms.

5.2 Publication

This section is presented as published research paper by **Law, C.S.**, S.Y. Lim, A.D. Abell, L.F. Marsal, and A. Santos, *Structural tailoring of nanoporous anodic alumina optical microcavities for enhanced resonant recirculation of light*. Nanoscale, 2018. **10**(29): p. 14139-14152.

Nanoscale

PAPER

View Article Online
View Journal | View Issue

Cite this: *Nanoscale*, 2018, **10**, 14139

Structural tailoring of nanoporous anodic alumina optical microcavities for enhanced resonant recirculation of light†

Cheryl Suwen Law, [a,b,c] Siew Yee Lim, [a,b,c] Andrew D. Abell, [*b,c,d] Lluís F. Marsal [*e] and Abel Santos [*a,b,c]

A comprehensive study about the structural engineering of high quality nanoporous anodic alumina optical microcavities (NAA-μCVs) fabricated by rationally designed anodisation strategies to enhance the light-confining capabilities of these photonic crystal (PC) structures is presented. Two types of NAA-μCV architectures are produced: (i) GIF-NAA-μCVs composed of a cavity layer featuring straight nanopores that is sandwiched between two gradient-index filters (GIFs) with sinusoidally modulated porosity in depth, and (ii) DBR-NAA-μCVs formed by sandwiching a cavity layer with straight nanopores between two distributed Bragg reflectors (DBRs), in which the porosity is engineered in a stepwise fashion. The geometric features of GIF-NAA-μCVs and DBR-NAA-μCVs are engineered and optimised through a systematic modification of the anodisation parameters (*i.e.* cavity anodisation time, cavity anodisation current density, anodisation period and number of anodisation pulses, and pore widening time). This methodology enables fine-tuning of the optical properties of GIF-NAA-μCVs and DBR-NAA-μCVs, such as quality factor and position and width of resonance band, to generate NAA-μCVs with unprecedented quality factors (*i.e.* 170 ± 8 and 206 ± 10 for the first and second order resonance bands – threefold and fourfold quality enhancement as compared to previous studies). Our results demonstrate that an optimal design of the geometric features and the nanoporous architecture of NAA-μCVs can significantly enhance resonant recirculation of light within these PC structures, creating new opportunities to develop ultrasensitive optical platforms, highly selective optical filters, and other photonic devices.

Received 26th May 2018,
Accepted 4th July 2018

DOI: 10.1039/c8nr04263b

rsc.li/nanoscale

Introduction

Photonic crystals (PC) are a class of materials that mould the flow of electromagnetic waves by light–matter interactions at the micro/nanoscale.[1,2] In PCs, the propagation of light is driven by multiple interferences between Bragg scattered electromagnetic waves, which are defined by Bloch modes and can be precisely engineered by the structural features of the PC.[3–5] Among others, PCs enable the selective absorption, guiding, reflection, transmission, enhancement, and confinement of light for a plethora of applications, including quantum communication,[6] lasing,[7] imaging,[8] energy harvesting,[9] environmental remediation,[10] and sensing.[11]

Optical microcavities (μCVs) are a class of PCs that confine light to small volumes by resonant recirculation of electromagnetic waves within the PCs' structure. They are indispensable for a broad range of applications, including long-distance transmission of data,[12] novel laser sources,[13] quantum communications,[14] sensing and biosensing.[15] The fast development of advanced micro/nanofabrication technologies has boosted the generation of multiple optical μCVs architectures (*e.g.* Fabry–Pérot micropost and bulk cavities,[16–18] microdisks,[19] add/drop filters,[20,21] 2D photonic slabs,[22] microspheres,[23] microtoroids[24]), which can provide ultra-high quality factors ($\sim 10^9$) and ultra-small mode volumes ($\sim 10^3$ μm^3). However, these highly sophisticated technologies require expensive facilities and equipment that are not accessible to the broad scientific community. Low-cost nanofabrication methods based on self-assembly/organisation are promising alternative/complementary technologies to produce PC structures with

[a]*School of Chemical Engineering, The University of Adelaide, 5005 Adelaide, Australia*
[b]*Institute for Photonics and Advanced Sensing (IPAS), The University of Adelaide, 5005 Adelaide, Australia. E-mail: andrew.abell@adelaide.edu.au, abel.santos@adelaide.edu.au*
[c]*ARC Centre of Excellence for Nanoscale BioPhotonics (CNBP), The University of Adelaide, 5005 Adelaide, Australia*
[d]*Department of Chemistry, The University of Adelaide, 5005 Adelaide, Australia*
[e]*Department of Electronic, Electric, and Automatics Engineering, Universitat Rovira i Virgili, 43007 Tarragona, Spain. E-mail: lluis.marsal@urv.cat*
†Electronic supplementary information (ESI) available. See DOI: 10.1039/c8nr04263b

precisely engineered features at the nanoscale.[25] Some of these techniques include colloidal lithography,[26] self-assembly,[27] soft lithography,[28] chemical and electrochemical etching,[29–32] and anodisation.[33–39]

Of all self-organised materials, nanoporous anodic alumina (NAA) produced by anodisation of aluminium is a highly versatile platform material that can be precisely engineered to create unique PCs.[40,41] NAA is composed of a matrix of aluminium oxide (Al_2O_3) featuring honeycomb-like, self-organised arrays of nanopores, the geometric features of which can be engineered with precision in a multi-dimensional fashion.[42,43] Recent developments in this area have demonstrated that features of the photonic stopband (PSB) of NAA-PCs can be tuned across the spectral regions by rationally designed pulse-like anodisation strategies. The versatile effective medium of NAA provides unique opportunities to create 1D, 2D or 3D NAA-PCs in the form of gradient-index filters (GIFs),[44–47] optical microcavities,[48–50] distributed Bragg reflectors (DBRs),[51,52] bandpass and linear variable bandpass filters,[54,55] heterogeneous PCs,[56] and encoded photonic tags.[57]

However, the development of high quality NAA-PCs that can confine light efficiently remains challenging. To date, only a few studies have reported on the development of NAA-based optical μCVs using four different architectures.[48–50] Wang *et al.* produced and assessed the properties of two types of 1D NAA-μCVs: one formed by a thin layer of constant porosity sandwiched between two highly reflective Bragg mirrors, and another architecture formed by a phase shift in the period of two Bragg mirrors.[48] The maximum quality factor reported in this study was ~24. Lee *et al.* developed a 3D NAA-μCV architecture, in which the optical microcavity structure was formed by a progressive asymmetric modulation of effective refractive index in depth and a final chemical etching.[49] The highest quality factor achieved by this type of NAA-μCV was ~55. Yan *et al.* generated a type of 1D NAA-μCV architecture formed by a layer featuring straight nanopores sandwiched between two mirrors produced by sawtooth pulse anodisation, which achieved a quality factor of ~45.[50] The main drawback of NAA to develop high quality NAA-μCVs is the low refractive index of alumina ($n_{Al_2O_3}$ ~ 1.70 RIU). However, the use of anodisation conditions to maximise the effective refractive index contrast between adjacent layers in the mirrors forming the structure of NAA-μCVs would enhance the light-confining capabilities of these PC structures. We and others have demonstrated that pulse-like anodisation strategies performed in sulphuric acid electrolyte enable the direct translation of complex anodisation profiles into porosity changes.[53,58,59] Other critical factors to consider in the fabrication of high quality NAA-μCVs include the type and features of the mirrors (*e.g.* DBRs, GIFs, number of periods, period length) and the geometric features of the cavity layer (*i.e.* porosity and thickness). Therefore, more comprehensive studies are needed to develop NAA-μCVs with enhanced light-confining capabilities. These PC structures would provide new opportunities to develop cost-competitive optical microcavity platforms for a plethora of applications.

In this study, we demonstrate that an optimal design of the structural features and architecture can enhance significantly the resonant recirculation of light in NAA-μCVs to achieve unprecedented quality factors. The effect of the geometric features of two types of NAA-μCV architectures on the light confinement quality within these PCs is investigated (Fig. 1). The first type (GIF-NAA-μCVs) is composed of two gradient-index filters produced by sinusoidal pulse anodisation (SPA), between which a cavity layer featuring straight nanopores is sandwiched (Fig. 1a). The second type (DBR-NAA-μCVs) is created by sandwiching a cavity layer of constant porosity between two distributed Bragg reflectors produced by stepwise pulse anodisation (STPA) (Fig. 1b). The position and width of the resonance band within the PSBs of these NAA-μCVs (Fig. 1c and d) are engineered by a systematic modification of various anodisation parameters to establish the most optimal design for enhancing the light-confining capabilities of these PC structures.

Experimental section

Materials

Aluminium (Al) foils of thickness 320 μm and purity 99.9997% were supplied by Goodfellow Cambridge Ltd. Sulphuric acid (H_2SO_4), phosphoric acid (H_3PO_4), perchloric acid ($HClO_4$), hydrochloric acid (HCl), copper(II) chloride ($CuCl_2$) and ethanol (EtOH-C_2H_5OH) were purchased from Sigma-Aldrich (Australia) and used as received, without further purification. Ultrapure water (18.2 Ω m) Mili-Q® (Australia) was used to prepare all aqueous solutions used in this study.

Fabrication of GIF-NAA-μCVs and DBR-NAA-μCVs

Prior to anodisation, 1.5 × 1.5 cm square Al substrates were cleaned under sonification in EtOH and ultrapure water for 15 min each, dried under air stream and stored till further use. Cleaned Al substrates were electropolished in a mixture of EtOH and $HClO_4$ 4 : 1 (v : v) at 20 V and 5 °C for 3 min. The electropolished Al substrates were then anodised using a 1.1 M H_2SO_4 aqueous solution as acid electrolyte mixed with 25%v EtOH at a temperature of −1 °C, which was maintained throughout the anodisation process. Note that EtOH was added to lower the freezing point of the electrolyte solution and prevent it from freezing during the fabrication process. The anodisation process was performed in an electrochemical reactor with a platinum wire grid acting as cathode, under constant stirring conditions (~300 rpm), and controlled temperature (−1 °C). The fabrication process of NAA-μCVs began with an anodisation step at constant current density of 1.120 mA cm^{-2} for 1 h to form a thin nanoporous oxide layer and achieve homogenous pore growth. The anodisation profile was then switched to pulse mode (*i.e.* SPA or STPA), where the anodising current density was pulsed between high (J_{max} = 1.120 mA cm^{-2}) and low (J_{min} = 0.280 mA cm^{-2}) values.

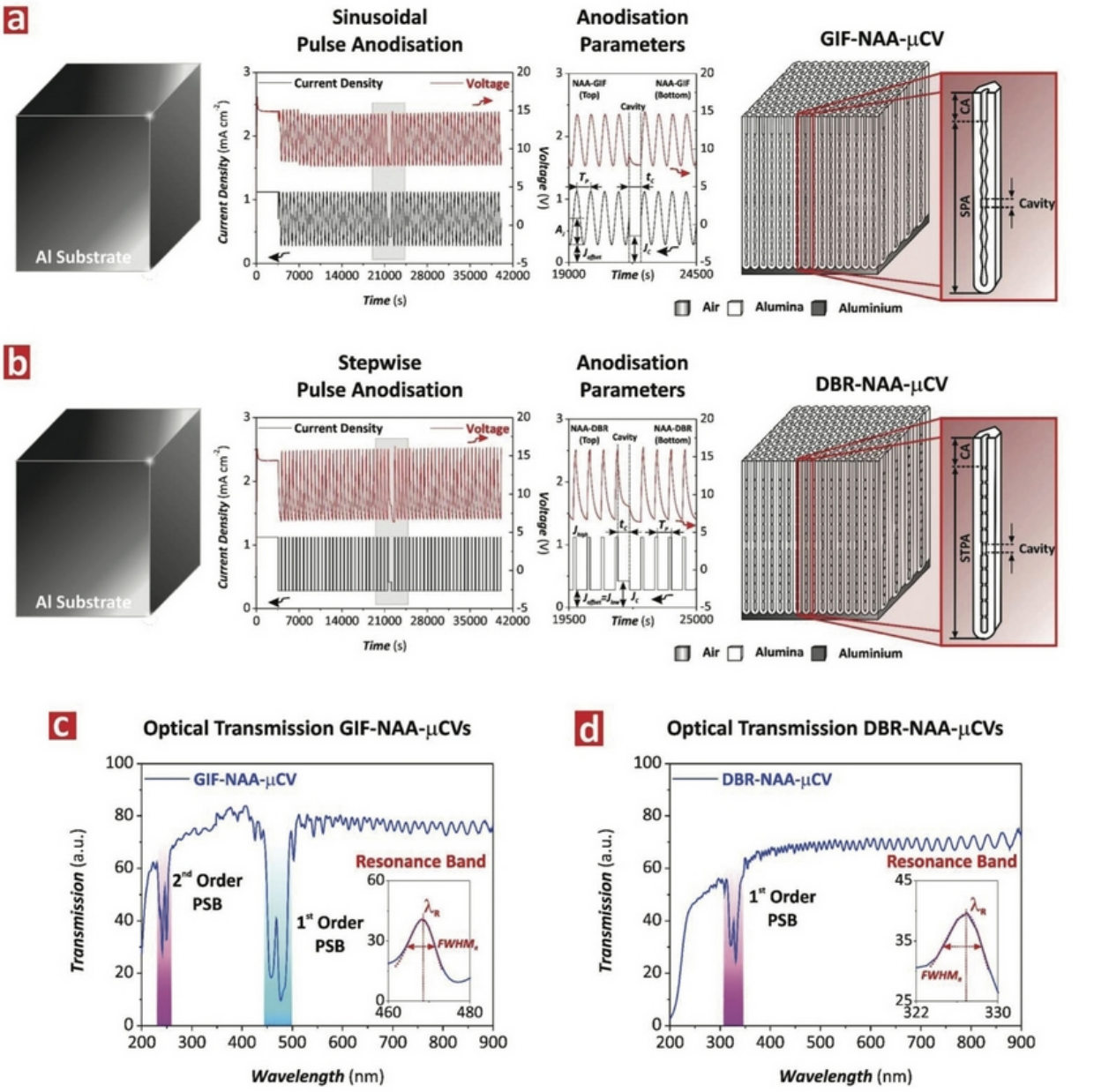

Fig. 1 Fabrication of GIF-NAA-μCVs and DBR-NAA-μCVs by sinusoidal and stepwise pulse anodisation, respectively. (a) and (b) Schematics illustrating the SPA and STPA processes used to fabricate GIF-NAA-μCVs and DBR-NAA-μCVs with representative anodisation profiles describing the fabrication parameters, and nanoporous structure (note: grey rectangle shown in the anodisation profile indicates the step at constant anodisation current density to create the cavity between mirrors). (c) and (d) representative transmission spectra showing the features of the photonic stopband (PSB) and the resonance band (inset) of GIF-NAA-μCVs and DBR-NAA-μCVs with Gaussian fittings, respectively (note: GIF-NAA-μCV produced with T_P = 600 s, A_J = 0.420 mA cm^{-2}, J_{Offset} = 0.280 mA cm^{-2}, N_P = 30 pulses, t_{pw} = 4 min, t_C = 4.5 min, and J_C = 0.420 mA cm^{-2}; DBR-NAA-μCV produced with T_P = 600 s, A_J = 0.420 mA cm^{-2}, J_{Offset} = 0.280 mA cm^{-2}, N_P = 30 pulses, t_{pw} = 0 min, t_C = 4.5 min, and J_C = 0.420 mA cm^{-2}).

GIF-NAA-μCVs were produced by a modified sinusoidal pulse anodisation (SPA) process.[44] This top-down nanofabrication approach started with the generation of a NAA-GIF with a given number of SPA pulses. Then, the process was switched to constant current density anodisation to create a cavity layer featuring straight nanopores, the geometric features of which were systematically modified by the cavity current density (J_C) and the cavity anodisation time (t_C). The anodisation mode was subsequently switched back to SPA to create the underlying NAA-GIF mirror with the same number of pulses as its

top counterpart. The current density-time SPA profiles were produced by a custom-designed Labview®-based software according to eqn (1).

$$J(t) = A_J \times \left[\sin\left(\frac{2\pi}{T_P} \times t\right) + 1\right] + J_{offset} \quad (1)$$

where $J(t)$ is the current density at time t, A_J is the current density amplitude, T_P is the anodisation period, and J_{offset} is the current density offset.

DBR-NAA-μCVs were produced by a modified stepwise pulse anodisation (STPA) approach.[58,60] This process started by generating a NAA-DBR with a given number of STPA pulses. The anodisation mode was then switched to constant current density to create a cavity layer with straight nanopores. The geometry of this cavity layer was systematically modified by varying J_C and t_C. Next, the process continued in STPA mode to generate the bottom NAA-DBR structure featuring the same number of pulses as its top DBR equivalent. The current density-time STPA profiles were generated by a custom-designed Labview®-based software, in which the current density was pulsed between J_{high} = 1.120 mA cm^{-2} and J_{low} = 0.280 mA cm^{-2} in a stepwise fashion, with $J_{offset} = J_{low}$. Note that the anodisation period (T_P) for each STPA pulse was defined as the total time length at maximum and minimum anodisation current density pulses (eqn (2)).

$$T_P = t_{high} + t_{low} \quad (2)$$

where t_{high} and t_{low} are the time duration at high and low current density values, respectively, the ratio of which was set to $t_{high} : t_{low} = 1 : 4$.

To optimise the architecture of both GIF-NAA-μCVs and DBR-NAA-μCVs, the cavity current density (J_C) and cavity anodisation time (t_C) were modified from 0.210 to 0.630 mA cm^{-2}, with a step size of 0.210 mA cm^{-2}, and from 4.5 to 8.5 min, with an interval of 1 min, respectively. The anodisation parameters used to produce the GIF mirrors in GIF-NAA-μCVs such as the anodisation period (T_P), number of pulses (N_P), and pore widening time (t_{pw}) were also systematically modified to assess their effect on the quality of GIF-NAA-μCVs. To gain insight into the combined effect of N_P, T_P, and t_{pw} on the quality of GIF-NAA-μCVs, a set of these PC structures was produced with varied N_P, from 20 to 50 pulses with ΔN_P = 10 pulses at fixed T_P = 600 s. The effect of T_P in the NAA-GIFs forming the structure of GIF-NAA-μCVs was investigated by modifying T_P from 600 to 1200 s, with ΔT_P = 200 s at fixed N_P = 30 pulses.

Optical characterisation

The resonance band of GIF-NAA-μCVs and DBR-NAA-μCVs produced in this study was optically characterised by analysing the transmission spectra of these PC structures. Prior to optical characterisation, a transparent window was created on these NAA-μCVs by selectively dissolving the remaining aluminium substrate through wet chemical etching in a saturated solution of HCl/$CuCl_2$. This process was performed using an etching cell with a Viton® mask with a circular window of 5 mm in diameter. The transmission spectra of NAA-μCV were acquired at normal incidence (*i.e.* θ = 0°) from 200–900 nm and from 200–1500 nm with a resolution of 1 nm in a UV-vis (Cary 60, Agilent, USA) and a UV-vis-NIR spectrometer (UV-3600 Plus, Shimadzu, Japan). The features of the resonance band of these NAA-μCVs were characterised in terms of resonance band position (λ_R) and resonance band full width at half maximum ($FWHM_R$) estimated using OriginPro 8.5®, applying Gaussian fittings over the PSBs and resonance bands shown in the transmission spectra of GIF-NAA-μCVs and DBR-NAA-μCVs. These two parameters were used to estimate the quality factor (Q_R) of these NAA-μCVs according to eqn (3).

$$Q_R = \frac{\lambda_R}{FWHM_R}. \quad (3)$$

The obtained results were summarised in the form of contour maps generated using OriginPro 8.5®, with a contour triangulation algorithm in which the coordinates of the intersection point were computed with linear interpolation.

The interferometric colour of NAA-μCVs was characterised by analysing digital images obtained by a Canon EOS 700D digital camera equipped with a Tamron 90 mm F2.8 VC USD macro mount lens with autofocus function under natural illumination, using a black card as background. NAA-μCVs were chemically etched in an aqueous solution of 5 wt% H_3PO_4 at 35 °C at different etching times (*i.e.* t_{pw} = 0, 2, 4, and 6 min) to widen their nanopores. Transmission spectra and digital images were recorded after each pore widening step to study the effect of porosity increment on the optical properties of NAA-μCVs.

Structural characterisation

The nanoporous structure of GIF-NAA-μCVs and DBR-NAA-μCVs was characterised by field emission gun scanning electron microscopy (FEG-SEM FEI Quanta 450). FEG-SEM images were analysed using ImageJ (public domain programme developed at the RSB of the NIH).[61]

Results and discussion

Fabrication and structural characterisation of GIF-NAA-μCVs and DBR-NAA-μCVs

Fig. 1a and b illustrate the fabrication processes used to produce GIF-NAA-μCVs and DBR-NAA-μCVs by SPA and STPA, respectively. The structure of GIF-NAA-μCVs is composed of two NAA-GIFs, one located at the top and another at the bottom of the PC structure. The porosity within these optical mirrors is modulated in a sinusoidal fashion that follows the SPA profile with precision. NAA-GIFs are characterised by a well-resolved, narrow PSB, the position of which can be tuned across the spectral regions by manipulating T_P.[44] Both NAA-GIFs were produced with the same anodisation period to confine light within a selective range of wavelengths. GIF-NAA-μCVs feature a cavity layer with straight nanopores, which is

created between the top and bottom NAA-GIFs during the SPA process. The geometric features of the cavity layer are critical to create a narrow resonance band within the PSB of GIF-NAA-μCVs, which denotes a strong confinement of light within the structure of NAA-μCVs at that range of wavelengths (Fig. 1a).

DBR-NAA-μCVs are formed by two NAA-DBRs located at the top and bottom of the NAA-μCVs (Fig. 1b). These DBR mirrors feature a stepwise porosity profile in depth, which is generated during the STPA process. The PSB of NAA-DBRs is characteristically broad as compared to that of their NAA-GIFs counterparts and its position can be readily tuned across the spectral regions by modifying T_P.[60] DBR-NAA-μCVs have a cavity layer with straight nanopores that separates the top and bottom NAA-DBRs. This layer is generated by a constant current density step applied during the STPA process. The photonic features of the resonance band in the transmission spectrum of DBR-NAA-μCVs are established by the geometric features of the cavity layer and the NAA-DBRs.

The design of high quality optical μCVs requires precise control over the thickness and effective refractive index of each dielectric stack within the mirrors and the cavity layer. Light reflection by the GIF and DBR mirrors forming the structure of GIF-NAA-μCVs and DBR-NAA-μCVs is maximum at those wavelengths where these PCs interfere light in a constructive fashion. These spectral regions are denoted by the characteristic PSB in the transmission spectra of NAA-GIFs and NAA-DBRs (*i.e.* minimum transmission of light). The introduction of a cavity layer between the mirrors forming the structure of GIF-NAA-μCVs and DBR-NAA-μCVs creates destructive interferences that lead to the generation of a resonance band within the characteristic PSB of the NAA-GIF and NAA-DBR mirrors. Therefore, the characteristics of the cavity layer and the mirrors establish the conditions where light reflection is at a maximum. For this, the optical thickness of the cavity layer must be half the wavelength at which the NAA-GIF and NAA-DBR mirrors reflect light.[62] The quality factor (Q_R), defined by eqn (3), indicates how strong is the resonant recirculation of light within a given NAA-μCV. Therefore, this parameter can be used as a reference to optimise the structure of NAA-μCVs for enhanced confinement of light.

Fig. 2a–c show representative FEG-SEM images of GIF-NAA-μCVs produced by SPA process. Top view FEG-SEM images reveal that the nanopores are evenly distributed across the surface of these NAA-PCs. The average nanopore diameter (d_P) in these NAA-μCV after 6 min of pore widening established by FEG-SEM image analysis was 16 ± 2 nm (Fig. 2a). Fig. 2b shows a general cross-sectional view of a GIF-NAA-μCV produced by SPA, where the NAA-GIFs were fabricated with T_P = 600 s, J_{offset} = 0.280 mA cm^{-2}, A_J = 0.420 mA cm^{-2}, N_P = 20 pulses, and t_{pw} = 6 min and the cavity layer with t_C = 6.5 min and J_C = 0.420 mA cm^{-2}. This image reveals that the structure of GIF-NAA-μCVs is composed of two main sections. The top section is a layer with straight nanopores and thickness of 1.5 ± 0.1 μm, which results from the first anodisation stage at constant anodising current density (CA). The bottom section is much thicker (*i.e.* 5.6 ± 0.3 μm) and corresponds to the NAA-μCV structure (*i.e.* in this case, a GIF-NAA-μCV), which is composed of two NAA-GIFs, each featuring 20 stacked layers of NAA with a sinusoidal modulation of porosity in depth, and a cavity layer featuring straight nanopores in between generated during the SPA process. Fig. 2c shows a magnified cross-sectional view of a NAA-GIF embedded in the GIF-NAA-μCV structure. It is apparent that these NAA-GIFs are composed of stacked layers of NAA, which correspond to each pulse in the SPA profile. FEG-SEM image analysis established an average period length (L_{TP}) –distance between adjacent layers in the NAA-GIFs of the GIF-NAA-μCV– of 148 ± 5 nm.

Fig. 2d and e show representative transmission spectra of GIF-NAA-μCVs and DBR-NAA-μCVs. At first sight, it is observed that the PSB of GIF-NAA-μCVs (Fig. 2d) is red-shifted as compared to their DBR-NAA-μCVs counterparts (Fig. 2e) produced with the same anodisation period (T_P = 600 s), number of pulses (N_P = 30 pulses), and cavity layer features (t_C = 4.5 min and J_C = 0.630 mA cm^{-2}). The transmission spectra also reveal that, under these fabrication conditions and within the spectral range of study (*i.e.* 200–900 nm), GIF-NAA-μCVs display first and second order characteristic PSB, while DBR-NAA-μCVs only show the first order PSB. Another spectral difference is the sidelobes associated with the Fabry–Pérot interferences by the whole PC structure, which are slightly more pronounced in the case of GIF-NAA-μCVs. Note that in GIF-NAA-μCVs, the intensity of the first order PSB is always greater than that of the second order PSB. Resonance bands can be observed within both first and second order PSBs, denoting light confinement by these PCs at these wavelengths.

The transmission spectra of GIF-NAA-μCVs and DBR-NAA-μCVs at different pore widening times (*i.e.* t_{pw} = 0, 2, 4, and 6 min) reveal that an increment of t_{pw} leads to: (i) a gradual reduction of the sidelobes associated with Fabry–Pérot interferences by the overall film; (ii) an increment of the intensity of the PSBs; (iii) a shift towards shorter wavelength spectral regions (*i.e.* blue shift) of the positions of both first and second order PSBs and their respective resonance bands; and (iv) an enlargement of the width of the first and second order PSBs. This qualitative analysis indicates that an optimum t_{pw} can improve the intensity and resolution of the resonance bands within the PSBs due to enhanced porosity contrast between NAA stacks within the NAA-GIF and NAA-DBR mirrors composing the structure of GIF-NAA-μCVs and DBR-NAA-μCVs, respectively. Fig. S1 (ESI†) shows representative FEG-SEM images of NAA-μCVs showing the effect of pore widening on the porosity contrast between adjacent layers in these NAA-PCs. However, an over-etching of these NAA-PCs (*i.e.* prolonged t_{pw}) broadens both the PSBs and the resonance band, while also reducing intensity, and worsening the confinement of light due to the partial collapse of the nanoporous structure and undesired light scattering (Fig. S2 – ESI†).[44]

Fig. 2f and g display representative digital images of a set of GIF-NAA-μCVs and DBR-NAA-μCVs produced with different cavity geometries at t_C from 4.5 to 8.5 min and J_C from 0.210 to 0.630 mA cm^{-2}. As these images reveal, GIF-NAA-μCVs display vivid interferometric colour in most of cases, which is

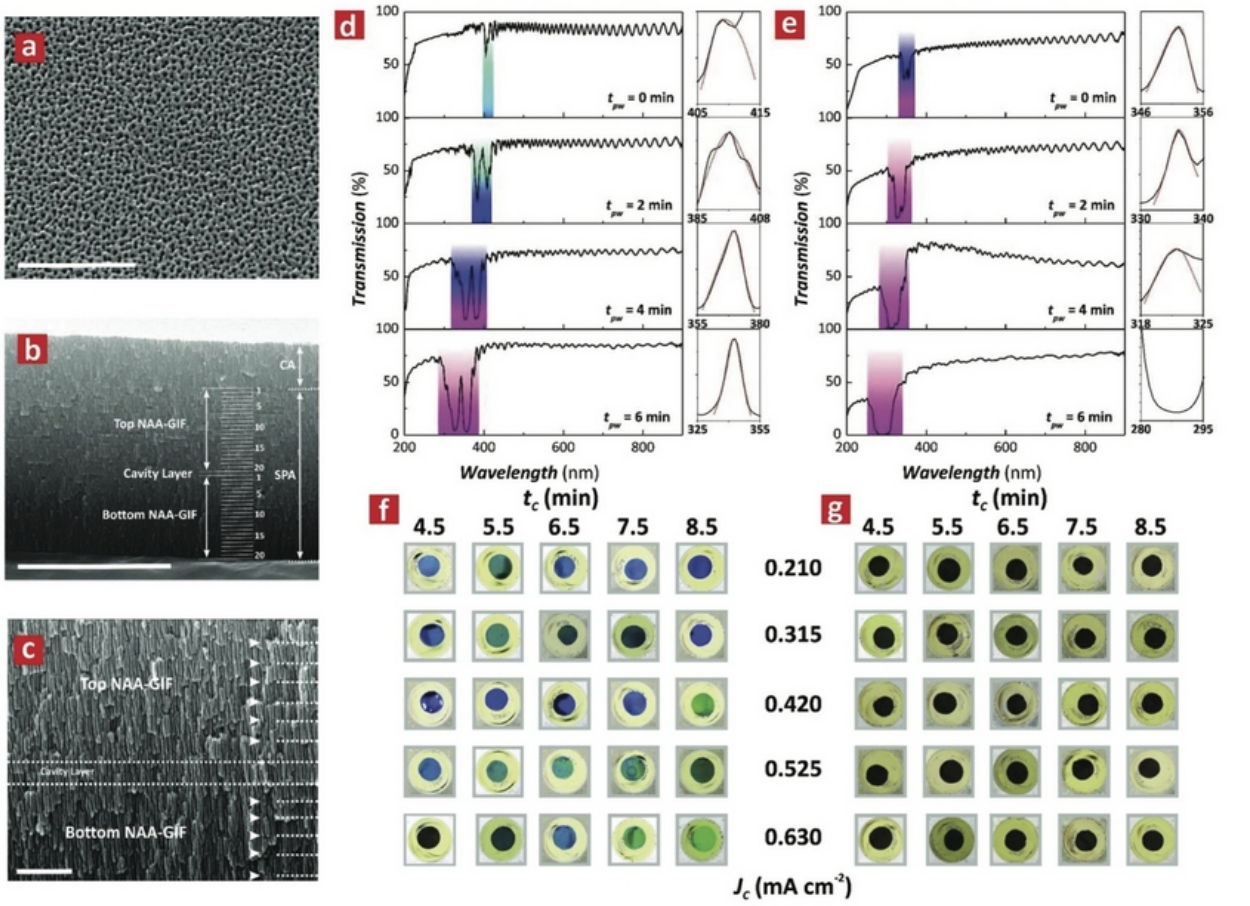

Fig. 2 Characterisation of the nanoporous structure of NAA-μCVs. (a) Representative top view FEG-SEM image of a GIF-NAA-μCV showing a random distribution of nanopores with d_P = 16 ± 2 nm (scale bar = 500 nm). (b) General cross-sectional view FEG-SEM image of a GIF-NAA-μCV showing a top layer with straight nanopore diameter (constant anodization = CA – thickness = 1.5 ± 0.1 μm), the optical microcavity layer formed by two NAA-GIFs (top and bottom) with a sinusoidal nanopore diameter modulation in depth (SPA – thickness = 5.6 ± 0.3 μm, 20 layers each NAA-GIF), and the cavity layer in between (scale bar = 5 μm). (c) Magnified cross-sectional view FEG-SEM image showing details the porosity modulation in the NAA-GIFs with a period length (L_{TP}) of 148 ± 5 nm (scale bar = 500 nm) and the cavity layer (note: GIF-NAA-μCV produced with T_P = 600 s, A_J = 0.420 mA cm^{-2}, J_{Offset} = 0.280 mA cm^{-2}, N_P = 20 pulses, t_{pw} = 6 min, t_C = 6.5 min, and J_C = 0.420 mA cm^{-2}). (d) and (e) Representative transmission spectra of GIF-NAA-μCVs and DBR-NAA-μCVs at different pore widening times, from 0 to 6 min with Δt_{pw} = 2 min, respectively, with details of the Gaussian fittings used to estimate λ_R and $FWHM_R$ (note: GIF-NAA-μCV and DBR-NAA-μCV produced with T_P = 600 s, A_J = 0.420 mA cm^{-2}, J_{Offset} = 0.280 mA cm^{-2}, N_P = 30 pulses, t_C = 4.5 min, and J_C = 0.630 mA cm^{-2}). (f) and (g) digital pictures of GIF-NAA-μCVs and DBR-NAA-μCVs produced with different t_C and J_C values, respectively.

associated with the position of the first order PSB within the visible range of the spectrum.[58,59] In contrast, under the same fabrication conditions, DBR-NAA-μCVs are transparent (*i.e.* black background) since the PSB of these PCs is located within the UV spectral range. In the case of GIF-NAA-μCVs, it can be observed that an increment of t_C red-shifts the interferometric colour of these PCs, from transparent/blue to cyan/green. These images also reveal that an increment in J_C leads to a slight red shift in the interferometric colour of GIF-NAA-μCVs.

In summary, this qualitative analysis reveals distinctive differences between the photonic features of GIF-NAA-μCVs and DBR-NAA-μCVs. GIF-NAA-μCVs display both first and second order PSBs. However, for the same fabrication conditions and cavity features, DBR-NAA-μCVs only have first order PSB. The resonance bands shown within the PSBs of GIF-NAA-μCVs are better resolved and more intense than those of their equivalent DBR-NAA-μCVs. Another distinctive contrast between GIF-NAA-μCVs and DBR-NAA-μCVs is that in the former type of NAA-PC the sidelobes in the transmission spectrum generated from interference oscillations are slightly more intense. Finally, it was observed that, under the same fabrication conditions, the PSB and resonance band of GIF-NAA-μCVs is located within the visible range, while these are positioned in the UV spectral regions for DBR-NAA-μCVs.

Optimisation of light confinement quality in GIF-NAA-μCVs

As Fig. 1c and d show, the resonance band located at the centre of the characteristic PSB of GIF-NAA-μCVs can be approximated to a Gaussian bell. The quality factor (Q_R) of the GIF-NAA-μCVs fabricated in this study was estimated by measuring the position of the resonance band (λ_R) and its full width at half maximum ($FWHM_R$) obtained from Gaussian fittings applied to the resonance band (eqn (3)). A systematic modification of the anodisation cavity time (t_C – from 4.5 to 8.5 min with Δt_C = 1 min), the cavity current density (J_C – from 0.210 to 0.630 mA cm^{-2} with ΔJ_C = 0.105 mA cm^{-2}), and the pore widening time (t_{pw} – from 0 to 6 min with Δt_{pw} = 2 min) was performed to optimise the Q_R of these NAA-μCVs. Note that the rest of anodisation parameters were kept constant (*i.e.* T_P = 600 s, J_{Offset} = 0.280 mA cm^{-2}, A_J = 0.420 mA cm^{-2}, and N_P = 30 pulses). The transmission spectra of GIF-NAA-μCVs produced with various combinations of t_C, J_C, and t_{pw} and their corresponding digital pictures are shown in Fig. S1–S5 (ESI†).

Fig. 3 shows contour maps summarising the combined effect of t_C, J_C, and t_{pw} on the quality of the first order resonance band ($Q_{R\text{-}1^{st}}$) of GIF-NAA-μCVs produced with T_P = 600 s, J_{offset} = 0.280 mA cm^{-2}, A_J = 0.420 mA cm^{-2}, and N_P = 30 pulses. Fig. 3a shows the correlation of $Q_{R\text{-}1^{st}}$ with t_C and J_C for as-produced GIF-NAA-μCVs (*i.e.* t_{pw} = 0 min). The black-blue region located at the top region of the graph indicates that a combination of long t_C and high J_C worsens significantly $Q_{R\text{-}1^{st}}$. Note that the black colour field denotes the absence of resonance band. The high concentration of field lines at the diagonal band of the contour map (*i.e.* from the top-left to bottom-right corner) indicates a strong dependency of $Q_{R\text{-}1^{st}}$ with t_C and J_C as the former parameter is shorten and the latter reduced. These GIF-NAA-μCVs achieve their maximum quality ($Q_{R\text{-}1^{st}}$ = 170 ± 8) at t_C = 5.5 min and J_C = 0.210 mA cm^{-2}.

The relationship between $Q_{R\text{-}1^{st}}$ and t_C and J_C for GIF-NAA-μCVs produced with t_{pw} = 2 min is shown in Fig. 3b. The colour field and field lines across the contour map are relatively broad and wide, denoting a weak correlation of $Q_{R\text{-}1^{st}}$ with t_C and J_C at this pore widening time. Two local maxima of $Q_{R\text{-}1^{st}}$ can be identified at t_C = 4.5 min and J_C = 0.210 mA cm^{-2} ($Q_{R\text{-}1^{st}}$ = 106 ± 5) and at t_C = 7.5 min and J_C = 0.420 mA cm^{-2} ($Q_{R\text{-}1^{st}}$ = 105 ± 5). The dependency of $Q_{R\text{-}1^{st}}$ with t_C and J_C is stronger at those regions around the maxima, as indicated by the more concentrated colour fields and closer field lines. This

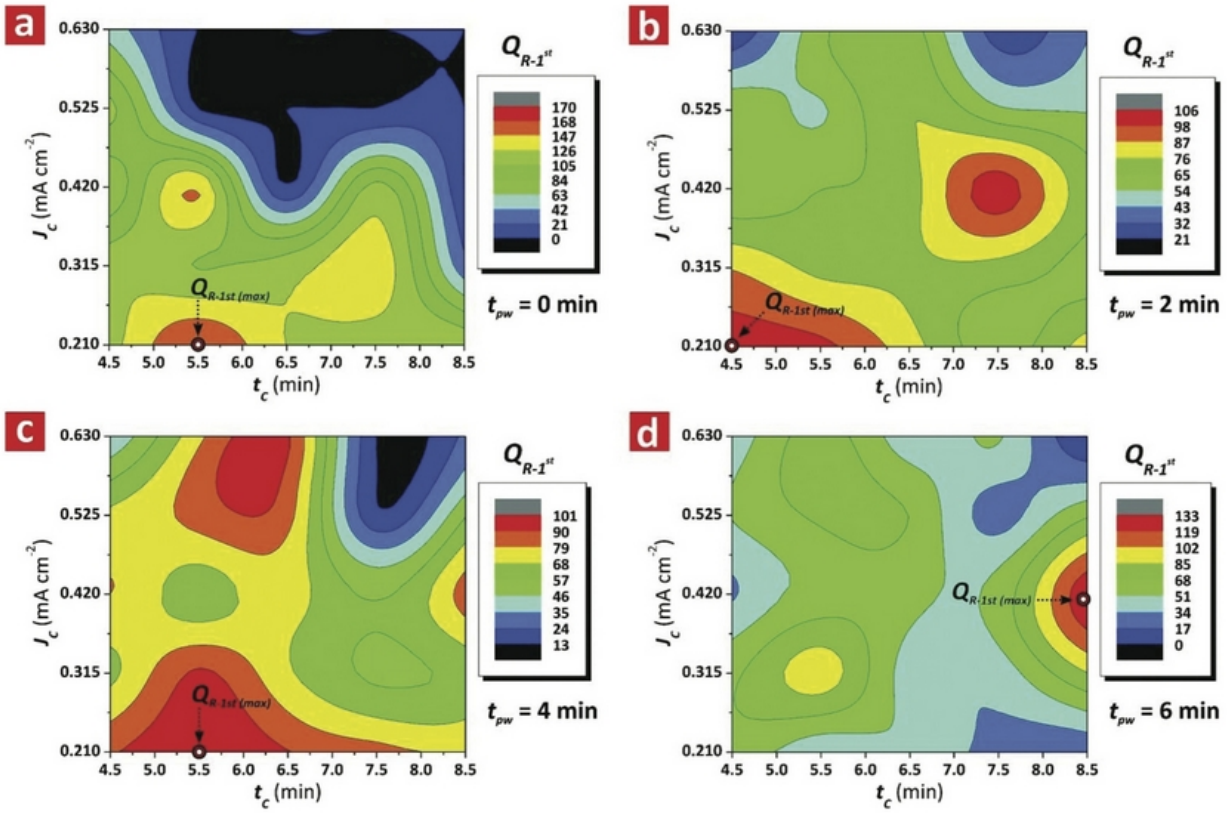

Fig. 3 Contour maps showing the combined effect of cavity fabrication parameters (*i.e.* anodisation time – t_C and current density – J_C) on the quality factor of the first order resonance band ($Q_{R\text{-}1^{st}}$) of GIF-NAA-μCVs produced by SPA at different pore widening times (t_{pw}). (a) t_{pw} = 0 min (b) t_{pw} = 2 min (c) t_{pw} = 4 min (c) t_{pw} = 6 min (note: GIF-NAA-μCVs produced with T_P = 600 s, A_J = 0.420 mA cm^{-2}, J_{Offset} = 0.280 mA cm^{-2}, and N_P = 30 pulses).

graph further confirms that a combination of long t_C and high J_C values is not favourable for achieving high $Q_{R\text{-}1^{st}}$ values.

Fig. 3c shows a contour map that describes how $Q_{R\text{-}1^{st}}$ evolves with t_C and J_C for GIF-NAA-μCVs produced with t_{pw} = 4 min. An area where the resonance band completely vanishes from the PSB of GIF-NAA-μCVs (*i.e.* black colour field) is apparent at the top-right corner of the contour map (t_C = 7.5 min and J_C = 0.525 and 0.630 mA cm^{-2}). This graph also reveals two areas where $Q_{R\text{-}1^{st}}$ is maximum (*i.e.* red fields), with $Q_{R\text{-}1^{st}}$ maxima located at t_C = 6.5 min and J_C = 0.630 mA cm^{-2} ($Q_{R\text{-}1^{st}}$ = 91 ± 3) and t_C = 5.5 min and J_C = 0.210 mA cm^{-2} ($Q_{R\text{-}1^{st}}$ = 101 ± 4). The distribution of colour fields is predominantly more concentrated around the area where the quality factor is minimum (*i.e.* black field), indicating a strong dependency of $Q_{R\text{-}1^{st}}$ with t_C and J_C in these regions.

Finally, Fig. 3d illustrates the dependency of $Q_{R\text{-}1^{st}}$ with t_C and J_C for GIF-NAA-μCVs after 6 min of pore widening treatment. The homogeneous and wide distribution of colour fields across most of this graph suggests a weak effect of t_C and J_C on $Q_{R\text{-}1^{st}}$. However, a local maximum can be observed at t_C = 8.5 min and J_C = 0.420 mA cm^{-2}, where $Q_{R\text{-}1^{st}}$ was estimated to be 132 ± 6. The concentration of colour fields around this maximum is high, with close field lines that indicate that $Q_{R\text{-}1^{st}}$ relies strongly upon t_C and J_C under such fabrication conditions.

To summarise, the analysis on the dependency of $Q_{R\text{-}1^{st}}$ with t_C and J_C at different t_{pw} establishes that GIF-NAA-μCVs achieve the highest quality factor ($Q_{R\text{-}1^{st}}$ = 170 ± 8) when the cavity structure is produced with t_C = 5.5 min, J_C = 0.210 mA cm^{-2}, and t_{pw} = 0 min. Our assessment establishes that J_C = 0.210 mA cm^{-2} is the optimum cavity current density value for producing high quality NAA-μCVs at t_{pw} = 0, 2, and 4 min. In general, an extensive pore widening process (*i.e.* t_{pw} > 4 min) worsens the quality of light confinement in GIF-NAA-μCVs due to light scattering associated with the over-etched nanoporous structure. However, under these conditions, the combination of longer t_C (*i.e.* 8.5 min) and moderate J_C (*i.e.* 0.420 mA cm^{-2}) at t_{pw} = 6 min results in GIF-NAA-μCVs with enhanced quality ($Q_{R\text{-}1^{st}}$ = 132 ± 6). Fig. S1–S5 (ESI†) compile digital pictures of the GIF-NAA-μCVs assessed in Fig. 3. These images reveal that the interferometric colour of these PC structures ranges from transparent (UV), blue, cyan, to green. This is good agreement with the transmission spectra of these GIF-NAA-μCVs, in which the position of the PSB is always located within the UV-visible spectral range under the fabrication conditions used in this study.

As mentioned above, the transmission spectra of GIF-NAA-μCVs showed a second order PSB located within the UV-low visible spectral range (*i.e.* 200–900 nm) (Fig. S1–S5†). Following the protocol used in the first order PSB, we analysed the effect of t_C, J_C, and t_{pw} on the quality factor of the second order resonance band located within the second order PSB ($Q_{R\text{-}2^{nd}}$) of GIF-NAA-μCVs. The obtained results, summarised in the form of contour maps, are shown in Fig. S6 (ESI†). The second order resonance band was found to have a narrower bandwidth than that of its first order equivalent but with lower intensity. Fig. S6a† shows the dependency of $Q_{R\text{-}2^{nd}}$ with t_C and J_C for GIF-NAA-μCVs at t_{pw} = 0 min. This graph presents several large black colour fields located at the top-right corner of the map, which denote the absence of second order resonance band at long t_C and high J_C. Two local maxima can be identified, one located at t_C = 4.5 min and J_C = 0.525 mA cm^{-2}, with $Q_{R\text{-}2^{nd}}$ = 198 ± 10, another at t_C = 6.5 min and J_C = 0.315 mA cm^{-2}, with $Q_{R\text{-}2^{nd}}$ = 173 ± 9. A high concentration of colour fields with close field lines can be observed around the two local maxima, indicating a strong dependency of $Q_{R\text{-}2^{nd}}$ with t_C and J_C in these regions. Fig. S6b† illustrates how t_C and J_C affect $Q_{R\text{-}2^{nd}}$ for GIF-NAA-μCVs produced with t_{pw} = 2 min. The contour map also shows a big black colour field located at the central-right region of the graph, which corresponds to the region t_C > 5.5 min and 0.315 mA cm^{-2} < J_C < 0.525 mA cm^{-2}. Two local maxima are located at t_C = 4.5 min and J_C = 0.420 mA cm^{-2} ($Q_{R\text{-}2^{nd}}$ = 206 ± 10) and at t_C = 5.5 min and J_C = 0.630 mA cm^{-2} ($Q_{R\text{-}2^{nd}}$ = 178 ± 5). Again, a high concentration of colour fields with a high density of field lines can be observed at those regions close to the local maxima, denoting that $Q_{R\text{-}2^{nd}}$ relies strongly on t_C and J_C at these values. The effect of t_C and J_C on $Q_{R\text{-}2^{nd}}$ for GIF-NAA-μCVs produced with t_{pw} = 4 min is shown in Fig. S6c.† This graphs also reveals two local maxima at t_C = 6.5 min and J_C = 0.630 mA cm^{-2}, with $Q_{R\text{-}2^{nd}}$ = 118 ± 6, and at t_C = 8.5 min and J_C = 0.420 mA cm^{-2}, with $Q_{R\text{-}2^{nd}}$ = 119 ± 5. The broad colour fields across most of the areas of the map indicate that the dependency of $Q_{R\text{-}2^{nd}}$ with t_C and J_C is weak. However, the high density of colour fields around the local maxima denotes a strong dependency of $Q_{R\text{-}2^{nd}}$ at these regions. Fig. S6d† depicts the values of $Q_{R\text{-}2^{nd}}$ as a function of t_C and J_C for GIF-NAA-μCVs fabricated with t_{pw} = 6 min. The broad and homogenous colour fields across the map indicate a weak dependency with the cavity parameters in most of the contour map. Although a local maximum is observed at t_C = 5.5 min and J_C = 0.630 mA cm^{-2}, the quality of this resonance band ($Q_{R\text{-}2^{nd}}$ = 94 ± 5) is significantly smaller than that observed at other pore widening times. This result further verifies that over-etching the nanoporous structure of GIF-NAA-μCVs (*i.e.* t_{pw} > 4 min) worsens the quality of the resonance band.

To summarise, the broad black colour fields in the contour maps shown in Fig. S6† indicate that the second order resonance band vanishes from the 2nd order PSB for many combinations of t_C and J_C. However, the analysis of the quality of the second order resonance band in GIF-NAA-μCVs indicates a strong confinement of light at some fabrication conditions, with higher quality factor than that of their 1st order counterparts (*i.e.* $Q_{R\text{-}2^{nd}}$ = 206 ± 10 at t_C = 4.5 min and J_C = 0.420 mA cm^{-2}). Interestingly, the highest $Q_{R\text{-}1^{st}}$ and $Q_{R\text{-}2^{nd}}$ values are obtained at different cavity fabrication conditions in terms of t_C, J_C and t_{pw}.

Optimisation of light confinement quality in DBR-NAA-μCVs

The quality factor in DBR-NAA-μCVs was assessed using the same protocol than in the case of GIF-NAA-μCVs, *i.e.* by systematically modifying t_C from 4.5 to 8.5 min with Δt_C = 1 min and

J_C from 0.210 to 0.630 mA cm^{-2} with ΔJ_C = 0.105 mA cm^{-2}. Transmission spectra of DBR-NAA-μCVs fabricated with different combinations of t_C, J_C, and t_{pw} and digital pictures of these PCs are shown in Fig. S7–11 (ESI†). Fig. 4 contains contour maps that illustrate the effect of t_C and J_C on $Q_{R\text{-}1^{st}}$ for DBR-NAA-μCVs produced with T_P = 600 s, J_{offset} = 0.280 mA cm^{-2}, A_J = 0.420 mA cm^{-2}, and N_P = 30 pulses at t_{pw} = 0, 2, 4, and 6 min. Note that, in contrasts to GIF-NAA-μCVs and under the same fabrication conditions, DBR-NAA-μCVs did not show second order PSB within the spectral range of study (*i.e.* 200–900 nm). Furthermore, at first sight it can be observed that the distribution of $Q_{R\text{-}1^{st}}$ with t_C and J_C is much more heterogeneous than that of their equivalent GIF-NAA-μCVs. Correlation of $Q_{R\text{-}1^{st}}$ with t_C and J_C for DBR-NAA-μCVs without pore widening treatment (*i.e.* t_{pw} = 0 min) is shown in Fig. 4a. This reveals three local maxima, around which the colour fields distribute in a heterogeneous fashion with a high concentration of colour fields, indicating a high dependency of $Q_{R\text{-}1^{st}}$ with t_C and J_C in these regions. The black area located at the top-right of the graph (*i.e.* long t_C and high J_C values) indicates the absence of resonance band at these combinations of cavity fabrication parameters. The maximum $Q_{R\text{-}1^{st}}$ = 168 ± 8 is achieved at t_C = 4.5 min and J_C = 0.315 mA cm^{-2}. Therefore, short cavity times and low cavity current density values are more suitable to enhance light confinement in as-produced DBR-NAA-μCVs. Fig. 4b shows the distribution of $Q_{R\text{-}1^{st}}$ with t_C and J_C for DBR-NAA-μCVs produced with t_{pw} = 2 min. The black colour field at the top-right corner of the graph indicates that the combination of long t_C and high J_C values destroys the light confining capabilities of these PC structures, since the resonance band completely vanishes from the characteristic PSB. Two main local maxima are clearly observed, where the maximum $Q_{R\text{-}1^{st}}$ = 125 ± 6 is achieved at t_C = 5.5 min and J_C = 0.525 mA cm^{-2}. This result indicates that short t_C with moderate J_C are a more optimal combination to produce DBR-NAA-μCVs at t_{pw} = 2 min. The dependency of $Q_{R\text{-}1^{st}}$ with t_C and J_C for DBR-NAA-μCVs after 4 min of pore widening treatment is shown in Fig. 4c. Following the trend shown in Fig. 4a and b, the black colour field located at the top-right corner of the graph confirms that long t_C and high J_C destroy the light-confining capabilities of DBR-NAA-μCVs. A local maximum of $Q_{R\text{-}1^{st}}$ = 98 ± 5 is located at t_C = 8.5 min and J_C = 0. 315 mA cm^{-2}, indicating that long t_C and low J_C is a more suitable combination of cavity fabrication parameters to enhance the

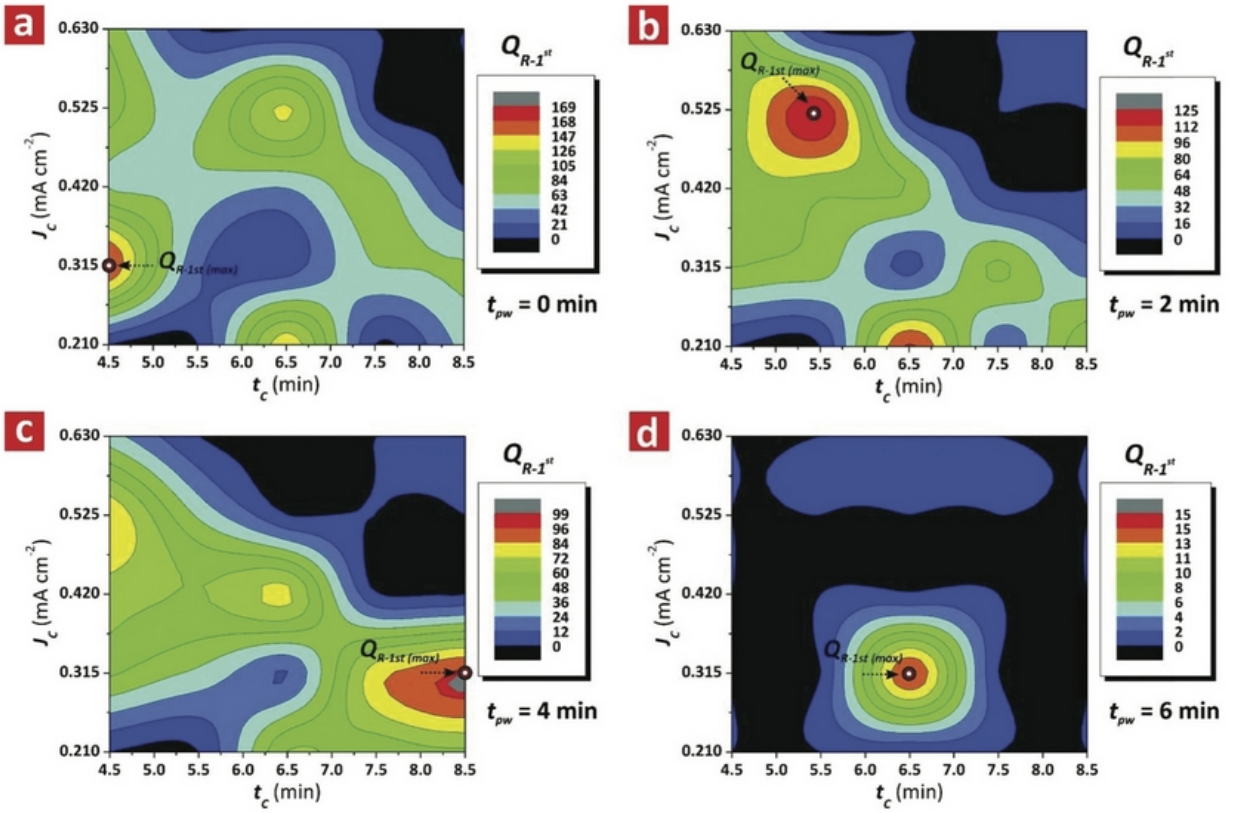

Fig. 4 Contour maps showing the combined effect of cavity fabrication parameters (*i.e.* anodisation time – t_C and current density – J_C) on the quality factor of the first order resonance band ($Q_{R\text{-}1^{st}}$) of DBR-NAA-μCVs produced by STPA at different pore widening times (t_{pw}). (a) t_{pw} = 0 min (b) t_{pw} = 2 min (c) t_{pw} = 4 min (c) t_{pw} = 6 min (note: DBR-NAA-μCVs produced with T_P = 600 s, A_J = 0.420 mA cm^{-2}, J_{Offset} = 0.280 mA cm^{-2}, and N_P = 30 pulses).

quality of DBR-NAA-μCVs at t_{pw} = 4 min. The distribution of colour fields around this maximum is of high density, indicating that $Q_{R\text{-}1^{st}}$ relies strongly on t_C and J_C in that region. Finally, Fig. 4d illustrates how $Q_{R\text{-}1^{st}}$ is affected by t_C and J_C for DBR-NAA-μCVs produced with t_{pw} = 6 min. The large black colour field spread across this graph reveals that an over-etching of the nanoporous structure of DBR-NAA-μCVs has a dramatic effect on the capacity of these PCs to confine light. An excessive pore widening treatment vanishes almost completely the resonance band located within the characteristic PSB of DBR-NAA-μCVs. Under these fabrication conditions, DBR-NAA-μCVs produced with t_C = 6.5 min and J_C = 0.315 mA cm^{-2} present the resonance band with the highest $Q_{R\text{-}1^{st}}$ = 15 ± 1, which is ~10 times smaller than the quality factors obtained at t_{pw} = 0, 2, and 4 min.

A comparative analysis of the graphs shown in Fig. 3 and 4 demonstrates that, under the same fabrication conditions, the quality factor of the first order resonance band in GIF-NAA-μCVs and DBR-NAA-μCVs is statistically the same (*i.e.* $Q_{R\text{-}1^{st}}$ = 170 ± 8 and $Q_{R\text{-}1^{st}}$ = 168 ± 8, respectively). However, the overall $Q_{R\text{-}1^{st}}$ of GIF-NAA-μCVs is higher than that of the equivalent DBR-NAA-μCVs. Furthermore, the quality factor of the second order resonance band of GIF-NAA-μCVs gives the highest quality value reported for NAA-μCVs so far ($Q_{R\text{-}2^{nd}}$ = 206 ± 10), which is almost fourfold higher than that achieved by other NAA-μCV architectures.[48–50] On this basis, it can be inferred that the sinusoidal modulation of porosity in the mirrors forming the structure of GIF-NAA-μCVs couples better with the cavity features generated in this study. NAA-GIFs feature a narrower PSB in their transmission spectra, which enables a much more selective reflection of light at those spectral regions where light is confined within the microcavity structure. The transmission spectra of GIF-NAA-μCVs and DBR-NAA-μCVs demonstrate that, under the same fabrication conditions (*i.e.* T_P, J_{Offset}, A_J, N_P, t_C, J_C, and t_{pw}), the 1st order PSB of the former type of NAA-μCVs is mainly located in the visible range of the spectrum, while the PSB of DBR-NAA-μCVs is in the UV range. This property is further demonstrated by digital images of GIF-NAA-μCVs and DBR-NAA-μCVs (Fig. S1–S5 and S7–S11†), in which GIF-NAA-μCVs display vivid interferometric colours while DBR-NAA-μCVs are transparent (*i.e.* light reflection in the UV). The misalignment between the light reflection in the mirrors composing the structure of DBR-NAA-μCVs, mostly located in the UV-low visible spectral range, and the features of the cavity layer worsens the confinement of light in these NAA-PC structures. Another contributing factor to consider is the partial absorption of light by NAA in the UV range, which is denoted by the curvature shown in the transmission spectra of NAA-PCs. This residual absorption of light could minimise the confinement of light at these spectral regions.

Effect of N_P and T_P on the light confinement quality of GIF-NAA-μCVs

To further understand how the architecture of NAA-μCVs affects the confinement of light, we studied the effect of the number of anodisation pulses (N_P) and the anodisation period (T_P) on the quality factor of GIF-NAA-μCVs produced by SPA. N_P establishes the number of layers in the mirrors forming the structure of GIF-NAA-μCVs (*i.e.* number of sinusoidal pulses in the SPA profile). This fabrication parameter was modified from 20 to 50 pulses with ΔN_P = 10 pulses to assess the effect of this geometric feature of the NAA mirrors on the quality of these NAA-μCVs. Note that other anodisation parameters were kept constant (*i.e.* T_P = 600 s, J_{offset} = 0.280 mA cm^{-2}, A_J = 0.420 mA cm^{-2}, t_C = 6.5 min, and J_C = 0.420 mA cm^{-2}) but t_{pw}, which was modified from 0 to 6 min with Δt_{pw} = 2 min.

Fig. 5a shows representative anodisation profiles used to produce these GIF-NAA-μCVs by SPA. These graphs demonstrate that the sinusoidal current density profile (input) is precisely translated into sinusoidal voltage pulses (output) under the anodisation conditions utilised in our study. Fig. 5b compiles a set of digital pictures of these GIF-NAA-μCVs at different pore widening times. These images indicate that the interferometric colour of these GIF-NAA-μCVs undergoes a significant blue shift with t_{pw}. For example, the interferometric colour of GIF-NAA-μCVs produced with N_P = 20 pulses is dark green, clear green, cyan, and blue after 0, 2, 4, and 6 min of pore widening time, respectively. The interferometric colour of these GIF-NAA-μCVs is associated with the position of the first order characteristic PSB of these PCs is within the visible range of the spectrum (Fig. S12 – ESI†). In contrast, the increment of the number of anodisation pulses in the NAA-GIF mirrors slightly blue-shifts the position of the PSB, as indicated by the digital pictures (Fig. 5b) and the transmission spectra (Fig. S12†) of these GIF-NAA-μCVs. This result is in good agreement with previous studies,[44–47] and is associated with the increment of the overall thickness of the PC structure and a slight reduction of the period length due to the limited diffusion of ionic species along the pores as the thickness increases. The overall thickness of GIF-NAA-μCVs produced with N_P = 20, 30, and 40 pulses estimated by FEG-SEM images analysis was 7.1 ± 0.1 μm, 9.7 ± 0.1 μm, 11.9 ± 0.1 μm, and 14.0 ± 0.1 μm, respectively. FEG-SEM image analysis also confirmed an average L_{TP} of 150 ± 2 nm for these GIF-NAA-μCVs.

The quality of the resonance band located within the first and second order PSBs of these GIF-NAA-μCVs was estimated following the protocol described in the previous sections. Fig. 5c summarises the obtained results for the combined effect of N_P and t_{pw} on $Q_{R\text{-}1^{st}}$. This contour map reveals a maximum for $Q_{R\text{-}1^{st}}$ of 135 ± 7 located at N_P = 40 pulses and t_{pw} = 0 min. The distribution of colour fields along the *x*-axis (*i.e* t_{pw}) is homogeneous, with an increasing distance between colour fields with t_{pw}. Therefore, the effect of t_{pw} on the quality of the resonance band is stronger at short pore widening times. The high density of colour fields and short distance between field lines around the $Q_{R\text{-}1^{st}}$ maximum along the *y*-axis reveals a strong dependency of $Q_{R\text{-}1^{st}}$ on N_P at moderate pore widening times (*i.e.* $t_{pw} \leq 2$ min). The minimum located at N_P = 20 and t_{pw} = 0 min (*i.e.* black colour field – lack of resonance band within the PSB) indicates that, for the combination of fabrication parameters used (*i.e.* T_P = 600 s, J_{offset} = 0.280

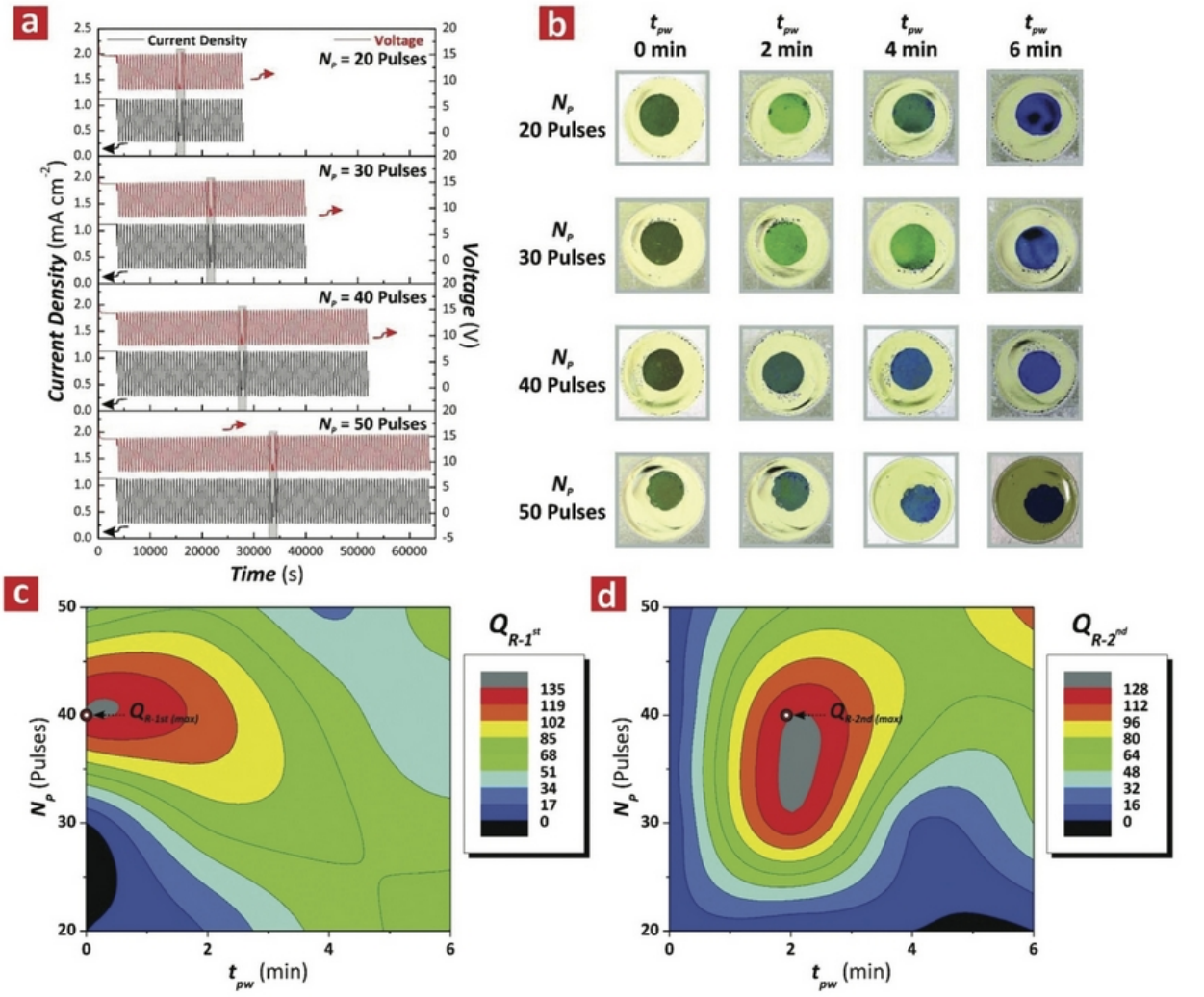

Fig. 5 Combined effect of number of pulses (N_P) and pore widening time (t_{pw}) on the quality factor of the first and second order resonance bands ($Q_{R\text{-}1^{st}}$ and $Q_{R\text{-}2^{nd}}$) of GIF-NAA-μCVs produced by SPA. (a) Representative anodisation profiles used to produce GIF-NAA-μCVs with top and bottom NAA-GIFs featuring 20, 30, 40, and 50 stacked layers of NAA with sinusoidally modulated porosity in depth (note: the grey rectangle indicates the cavity layer step in the SPA profile). (b) Digital pictures of GIF-NAA-μCVs produced with different N_P and t_{pw} values. (c) and (d) contour maps showing the combined effect of N_P and t_{pw} on the quality factor of the first and second order resonance bands GIF-NAA-μCVs fabricated by SPA (note: GIF-NAA-μCVs produced with T_P = 600 s, A_J = 0.420 mA cm^{-2}, J_{Offset} = 0.280 mA cm^{-2}, t_C = 6.5 min, and J_C = 0.420 mA cm^{-2}).

mA cm^{-2}, A_J = 0.420 mA cm^{-2}, t_C = 6.5 min, and J_C = 0.420 mA cm^{-2}), a low number of anodisation pulses and short pore widening times worsens the light-confining capabilities of GIF-NAA-μCVs. These results demonstrate that NAA-GIFs produced with 40 SPA pulses (*i.e.* 40 NAA layers with sinusoidally modulated porosity) provide the most optimal configuration to be coupled with the features of a cavity layer produced with t_C = 6.5 min and J_C = 0.420 mA cm^{-2}. Fig. 5d shows the dependency of $Q_{R\text{-}2^{nd}}$ with N_P and t_{pw} for these GIF-NAA-μCVs. This graph shows a $Q_{R\text{-}2^{nd}}$ maximum of 127 ± 6 located at N_P = 40 pulses and t_{pw} = 2 min. The wider distribution of colour fields and field lines with increasing N_P and t_{pw} denotes a weaker dependency of $Q_{R\text{-}2^{nd}}$ with these fabrication parameters. A local minimum is located at N_P = 20 pulses and t_{pw} = 0 min (*i.e.* black colour field), indicating that the combination of short pore widening times with a low number of pulses worsens the capability of these PC structures to confine light. Therefore, these results demonstrate that, under the fabrication conditions used in this study, GIF-NAA-μCVs confine light more efficiently when the NAA-GIF mirrors are produced with 40 pulses and short pore widening time (*i.e.* $t_{pw} \leq 2$ min).

A set of these PC structures with systematically modified anodisation period (T_P) from 600 to 1200 s with ΔT_P = 200 s was produced in order to gain a better understanding on the effect of the fabrication parameters on the quality of GIF-NAA-μCVs. The rest of anodisation parameters was fixed at J_{offset} =

0.280 mA cm^{-2}, A_J = 0.420 mA cm^{-2}, N_P = 30 pulses, and J_C = 0.420 mA cm^{-2}, but t_{pw}, which was modified from 0 to 6 min with Δt_{pw} = 2 min. Representative anodisation profiles used to produce these GIF-NAA-μCVs are shown in Fig. 6a. Note that the total anodisation time was longer with increasing T_P for a fixed number of pulses (*i.e.* 30 pulses) and t_C was modified according to T_P following the existing linear relationship between T_P and the characteristic PSB of NAA-GIFs. To match the geometric features of the cavity layer with the reflection of the NAA-GIF mirrors, t_C was set to 6.5, 8.8, 10.4, and 12.0 min for T_P = 600, 800, 1000, and 1200 s, respectively. Fig. 6b shows digital images of these GIF-NAA-μCVs as a function of T_P and t_{pw}, where it can be observed that these PCs produced with T_P = 600 and 800 s display vivid interferometric colours that blue-shift with t_{pw}. However, GIF-NAA-μCVs produced with T_P = 1000 and 1200 s are transparent, which indicates that the PSB of these PCs is in the NIR region of the spectrum. As demonstrated in previous studies, increasing T_P red-shifts of the characteristic PSB of NAA-GIFs.[44–47]

This is further confirmed by the transmission spectra of these GIF-NAA-μCVs, which show that the characteristic PSB with a resonance band located at approximately its centre is within the NIR spectral region (Fig. S13 – ESI†). We estimated $Q_{R\text{-}1^{st}}$ and $Q_{R\text{-}2^{nd}}$ from these spectra and assessed the combined effect of T_P and t_{pw} on the quality factor of these GIF-NAA-μCVs. Fig. 6c shows a contour map describing the impact of T_P and t_{pw} on $Q_{R\text{-}1^{st}}$, where the quality factor becomes maximum at T_P = 800 s and t_{pw} = 4 min ($Q_{R\text{-}1^{st}}$ = 159 ± 8). A high density distribution of colour fields with denser field lines is apparent around this maximum, which indicates a strong dependency

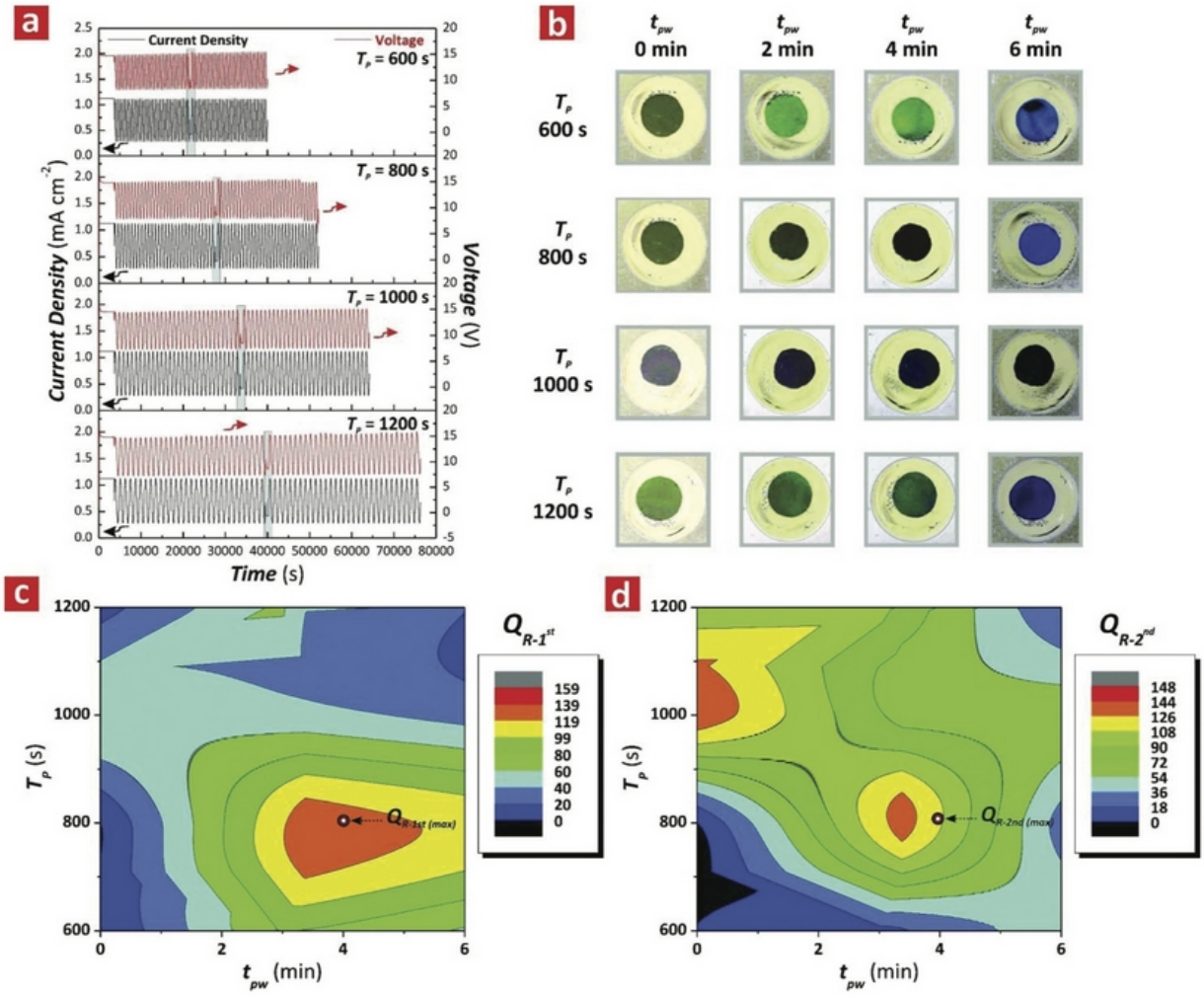

Fig. 6 Combined effect of anodisation period (T_P) and pore widening time (t_{pw}) on the quality factor of the first and second order resonance bands ($Q_{R\text{-}1^{st}}$ and $Q_{R\text{-}2^{nd}}$) of GIF-NAA-μCVs produced by SPA. (a) Representative anodisation profiles used to produce GIF-NAA-μCVs (note: the grey rectangle indicates the cavity layer step in the SPA profile). (b) Digital pictures of GIF-NAA-μCVs produced with different T_P and t_{pw} values. (c) and (d) Contour maps showing the combined effect of T_P and t_{pw} on the quality factor of the first and second order resonance bands GIF-NAA-μCVs produced by SPA (note: GIF-NAA-μCVs produced with A_J = 0.420 mA cm^{-2}, J_{Offset} = 0.280 mA cm^{-2}, N_P = 30 pulses, and J_C = 0.420 mA cm^{-2}).

of $Q_{R\text{-}1st}$ with T_P and t_{pw} in these regions with short T_P (≤800 s) and long t_{pw} (≥4 min). The increment in T_P worsens the quality of the light confinement within the structure of GIF-NAA-μCVs. The transmission spectra of GIF-NAA-μCVs produced with T_P = 600, 800, 1000, and 1200 s features a second order PSB with a resonance band at approximately its central position (Fig. S13 – ESI†). Fig. 6d summarises the combined effect of T_P and t_{pw} on $Q_{R\text{-}2nd}$. This graph reveals two local maxima at T_P = 800 s and t_{pw} = 4 min ($Q_{R\text{-}2nd}$ = 148 ± 7) and at T_P = 1000 s and t_{pw} = 0 min ($Q_{R\text{-}2nd}$ = 140 ± 4). The higher density of colour fields around these local maxima denote that the quality factor relies strongly upon these fabrication parameters at these regions. However, GIF-NAA-μCVs produced with short T_P and t_{pw} do not feature second order resonance band due to the poor effective refractive index contrast. Although a slight increment of T_P and t_{pw} significantly enhances the light confining capabilities of GIF-NAA-μCVs, a combination of long T_P and t_{pw} worsens the confinement of light within these PCs, as indicated by the regions of low $Q_{R\text{-}2nd}$ located at the top-right corner of the contour map.

To summarise, our analysis on the effect of N_P, T_P, and t_{pw} on the quality factor of the characteristic PSBs of GIF-NAA-μCVs clearly establishes that a combination of a moderate number of pulses (~40 pulses) with short t_{pw} (≤2 min) enhances the light-confining properties of GIF-NAA-μCVs. This analysis also indicates that short T_P (≤800 s) and moderate pore widening time (≤4 min) is a more favourable approach to create GIF-NAA-μCVs with high quality factors.

Conclusions

This study demonstrates that a rational design of the architecture of nanoporous anodic alumina optical microcavities can significantly enhance the light-confining performance of these photonic crystal structures. Two types of 1D NAA-μCV architectures have been developed, one formed by a cavity layer featuring straight nanopores sandwiched between two gradient-index filters with sinusoidal modulation of porosity (GIF-NAA-μCVs), and the other type composed of two highly reflective distributed Bragg reflectors with stepwise modulation of porosity sandwiching a cavity layer of constant porosity (DBR-NAA-μCVs). The optimal geometric features for each NAA-μCV architecture were established by a systematic modification of the fabrication parameters (*i.e.* number of anodisation pulses, anodisation period, cavity anodisation time and current density, and pore widening time), using the quality factor as a reference parameter to quantify the light-confining performance in these PCs. Our results demonstrate that, although the best quality of the resonance band achieved in the first order PSB of GIF-NAA-μCVs and DBR-NAA-μCVs is statistically comparable (*i.e.* 170 ± 8 and 168 ± 8, respectively), the second order resonance band in GIF-NAA-μCVs provides the highest quality factor reported to date for a NAA-based PC structure (*i.e.* 206 ± 10 ~fourfold higher than that reported in previous studies using other NAA architectures).

The results presented in this study provide a strong foundation to further develop innovative NAA-based photonic crystal with precisely engineered properties to modulate light. This will generate new opportunities to spread the applicability of these nanoporous PC structures across disciplines such as photonics, optical sensing and biosensing, energy harvesting, and optoelectronics.

Conflicts of interest

There are no conflicts to declare.

Acknowledgements

Authors thank the support provided by the Australian Research Council (ARC) through the grant numbers DE140100549 and CE140100003, the School of Chemical Engineering, the University of Adelaide (DVCR 'Research for Impact' initiative) (13120250), the Institute for Photonics and Advanced Sensing (IPAS), the ARC Centre of Excellence for Nanoscale BioPhotonics (CNBP), the Spanish Ministry of Economy and competitiveness TEC2015-71324-R (MINECO/FEDER), the Catalan authority AGAUR 2017SGR1527, and ICREA under the ICREA Academia Award.

References

1 S. Ogawa, M. Imada, S. Yoshimoto, M. Okano and S. Noda, *Science*, 2004, **305**, 227–229.
2 S. Noda, K. Tomoda, N. Yamamoto and A. Chutinan, *Science*, 2000, **289**, 604–606.
3 E. Yablonovitch, *Phys. Rev. Lett.*, 1987, **58**, 2059–2062.
4 S. John, *Phys. Rev. Lett.*, 1987, **58**, 2486–2489.
5 C. López, *Adv. Mater.*, 2003, **15**, 1680–1704.
6 A. Goban, C.-L. Hung, S.-P. Yu, J. D. Hood, J. A. Muniz, J. H. Lee, M. J. Martin, A. C. McClung, K. S. Choi, D. E. Chang, O. Painter and H. J. Kimble, *Nat. Commun.*, 2014, **5**, 3808.
7 A. Tandaechanurat, S. Ishida, D. Guimard, M. Nomura, S. Iwamoto and Y. Arakawa, *Nat. Photonics*, 2011, **5**, 91.
8 P. V. Parimi, W. T. Lu, P. Vodo and S. Sridhar, *Nature*, 2003, **426**, 404.
9 S. Nishimura, N. Abrams, B. A. Lewis, L. I. Halaoui, T. E. Mallouk, K. D. Benkstein, J. van de Lagemaat and A. J. Frank, *J. Am. Chem. Soc.*, 2003, **125**, 6306–6310.
10 Z. Zhang, L. Zhang, M. N. Hedhili, H. Zhang and P. Wang, *Nano Lett.*, 2013, **13**, 14–20.
11 C. Fenzl, T. Hirsch and O. S. Wolfbeis, *Angew. Chem., Int. Ed.*, 2014, **53**, 3318–3335.
12 D. Englund, A. Faraon, B. Zhang, Y. Yamamoto and J. Vuckovic, *Opt. Express*, 2007, **15**, 5550–5558.
13 O. Painter, R. K. Lee, A. Scherer, A. Yariv, J. D. O'Brien, P. D. Dapkus and I. Kim, *Science*, 1999, **284**, 1819–1821.

Supporting Information

Structural Tailoring of Nanoporous Anodic Alumina Optical Microcavities for Enhanced Resonant Recirculation of Light

Cheryl Suwen Law[a,b,c], Siew Yee Lim[a,b,c], Andrew D. Abell[*b,c,d], Lluís F. Marsal[*e], and Abel Santos[*a,b,c]

[a]School of Chemical Engineering, The University of Adelaide, Adelaide, SA 5005, Australia
[b]Institute for Photonics and Advanced Sensing (IPAS), The University of Adelaide, 5005 Adelaide, Australia
[c]ARC Centre of Excellence for Nanoscale BioPhotonics (CNBP), The University of Adelaide, 5005 Adelaide, Australia
[d]Department of Chemistry, The University of Adelaide, Engineering North Building, 5005 Adelaide, Australia.
[e]Department of Electronic, Electric, and Automatics Engineering, Universitat Rovira i Virgili, 43007 Tarragona, Spain

***E-Mails:** andrew.abell@adelaide.edu.au ; lluis.marsal@urv.cat ; abel.santos@adelaide.edu.au

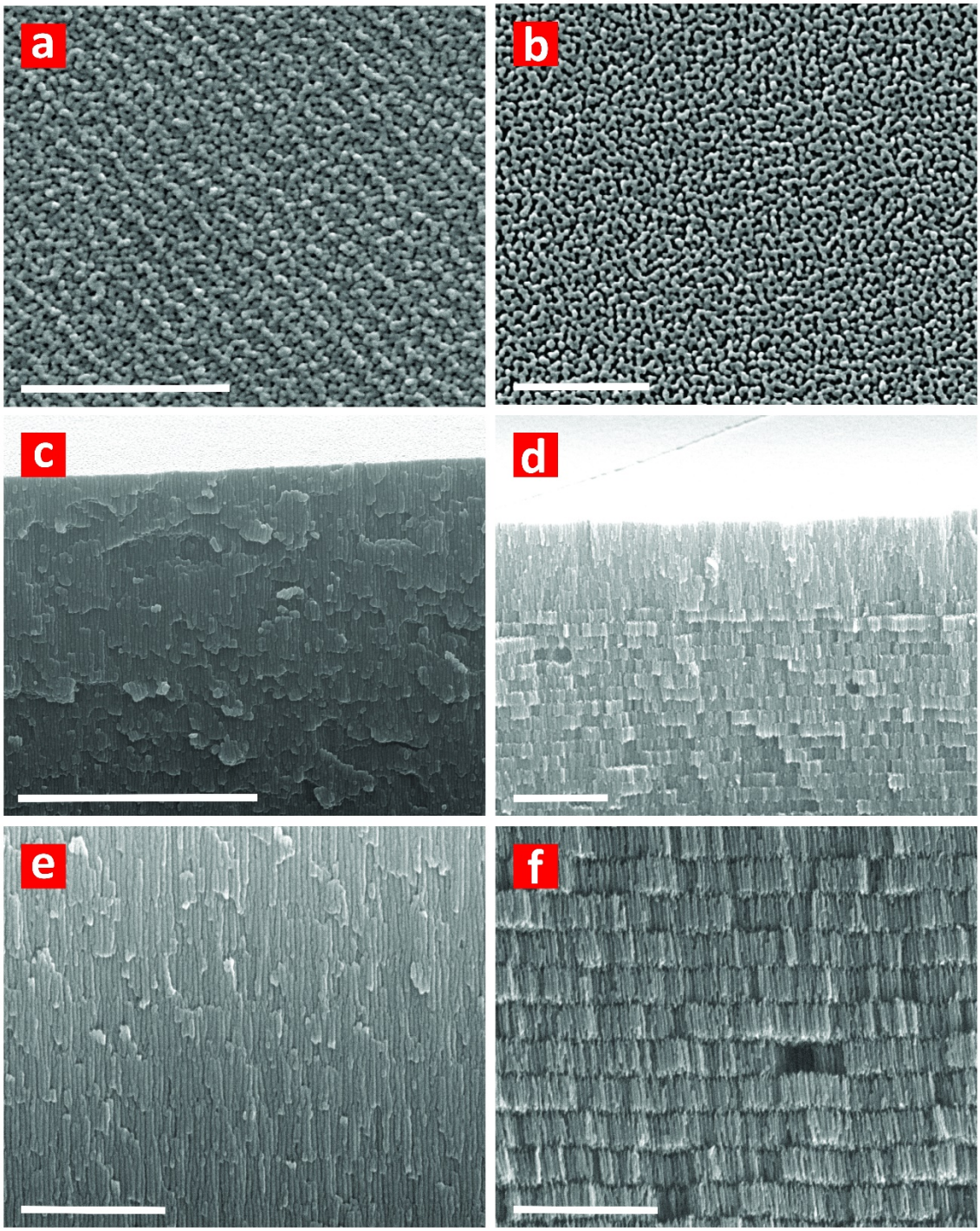

Figure S1. Effect of pore widening time on the structure of NAA-μCVs. a and b) Representative top view FEG-SEM images of a GIF-NAA-μCV at t_{pw} = 0 and 6 min, respectively (scale bars = 500 nm). c and d) General cross-sectional view FEG-SEM images of a GIF-NAA-μCV at t_{pw} = 0 and 6 min (scale bars = 2 μm). e and f) Magnified cross-sectional view FEG-SEM images showing details of the porosity contrast between layers in a GIF-NAA-μCV at t_{pw} = 0 and 6 min, respectively (scale bars = 5 μm).

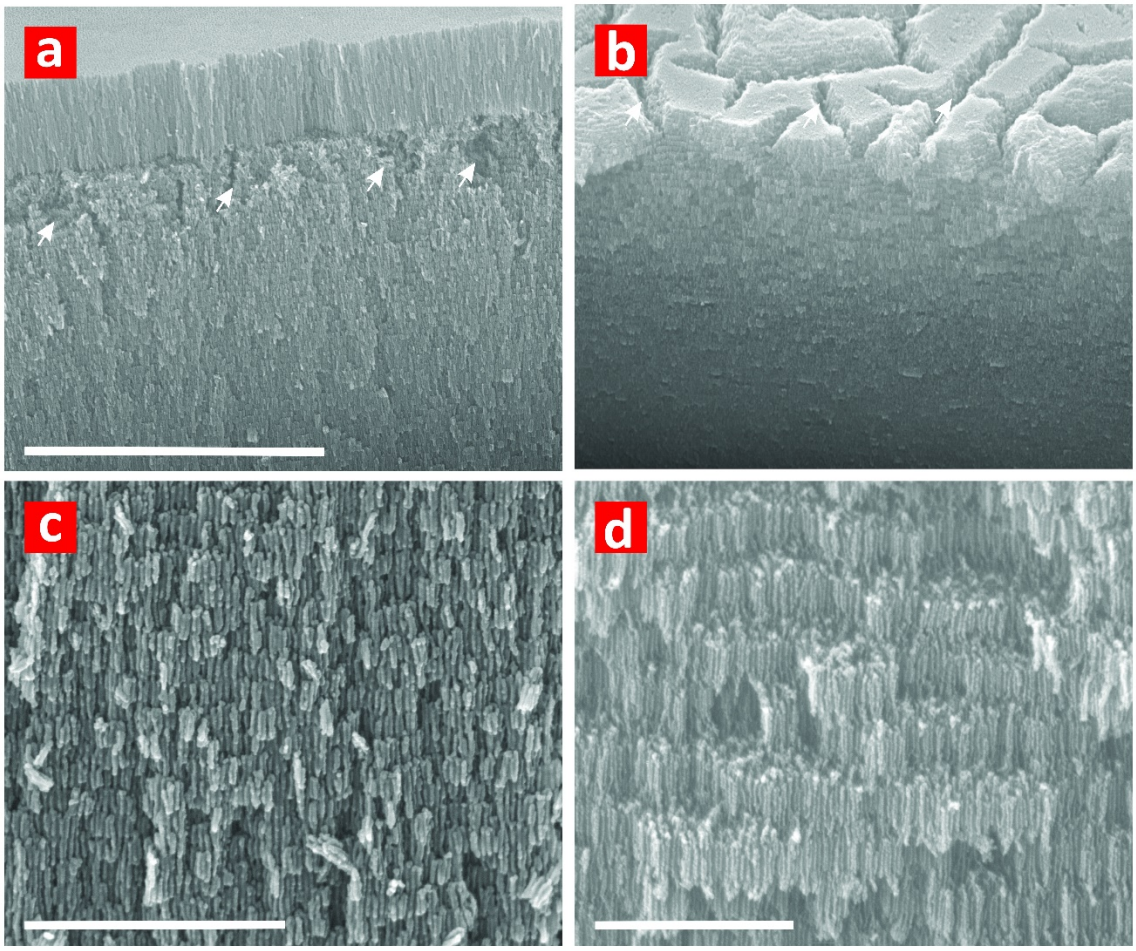

Figure S2. Effect of excessive pore widening time on the structure of NAA-μCVs. a and b) Representative general cross-sectional view FEG-SEM images of a GIF-NAA-μCV at t_{pw} = 6 and 8 min, respectively (scale bars = 5 μm) (note: white arrows indicate regions that partially collapse due to excessive pore widening treatment). c and d) Magnified cross-sectional view FEG-SEM images showing details of the porosity between layers in a GIF-NAA-μCV at t_{pw} = 6 and 8 min, respectively (scale bars = 1 μm).

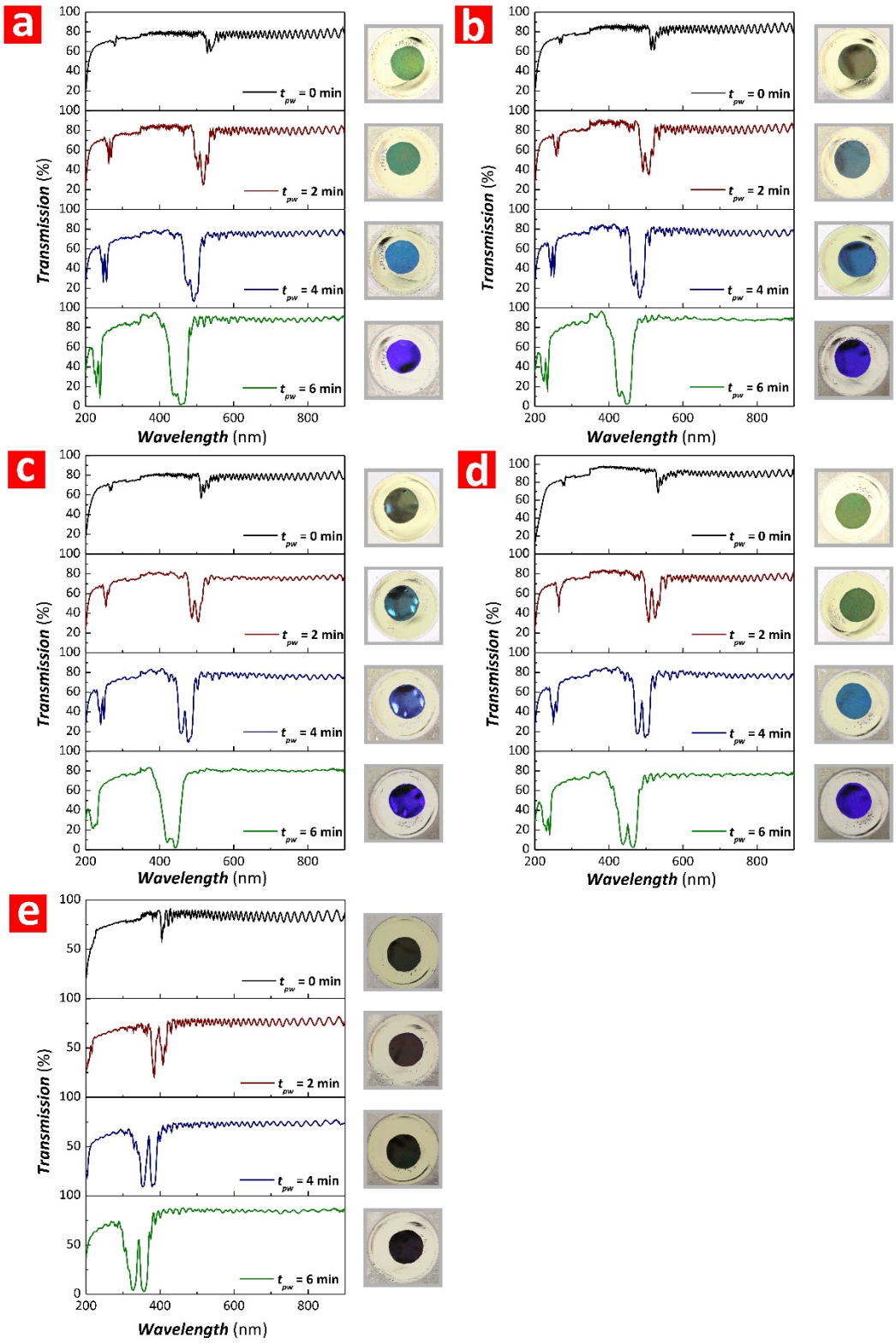

Figure S3. Representative transmission spectra for GIF-NAA-μCVs produced by SPA at t_C = 4.5 min and variable J_C and t_{pw} (note: T_P = 600 s, A_J = 0.420 mA cm^{-2}, J_{Offset} = 0.280 mA cm^{-2}, and N_P = 30 pulses). a) J_C = 0.210 mA cm^{-2}. b) J_C = 0.420 mA cm^{-2}. c) J_C = 0.315 mA cm^{-2}. d) J_C = 0.525 mA cm^{-2}. e) J_C = 0.630 mA cm^{-2}.

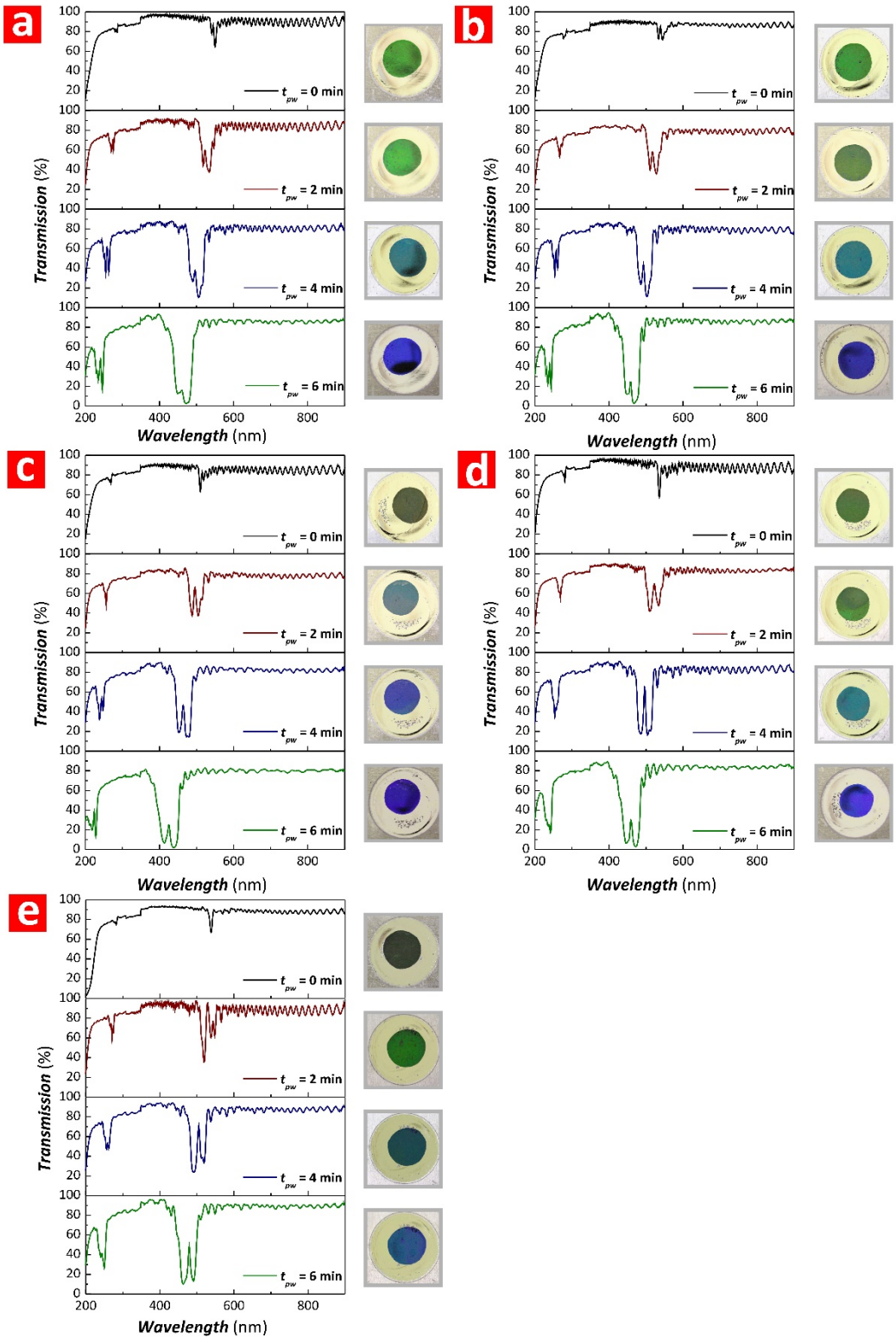

Figure S4. Representative transmission spectra for GIF-NAA-μCVs produced by SPA at t_C = 5.5 min and variable J_C and t_{pw} (note: T_P = 600 s, A_J = 0.420 mA cm^{-2}, J_{Offset} = 0.280 mA cm^{-2}, and N_P = 30 pulses). a) J_C = 0.210 mA cm^{-2}. b) J_C = 0.420 mA cm^{-2}. c) J_C = 0.315 mA cm^{-2}. d) J_C = 0.525 mA cm^{-2}. e) J_C = 0.630 mA cm^{-2}.

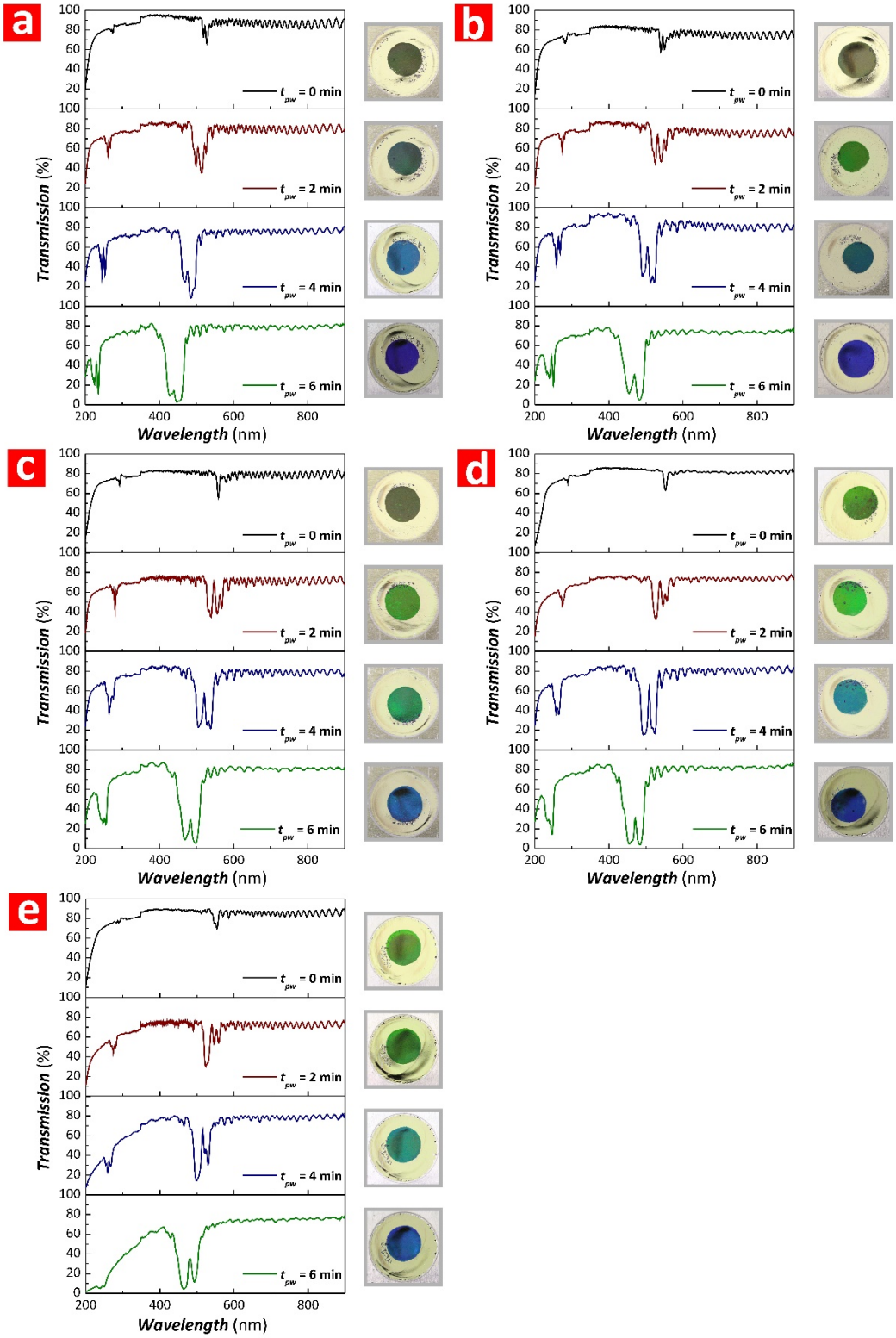

Figure S5. Representative transmission spectra for GIF-NAA-μCVs produced by SPA at t_C = 6.5 min and variable J_C and t_{pw} (note: T_P = 600 s, A_J = 0.420 mA cm^{-2}, J_{Offset} = 0.280 mA cm^{-2}, and N_P = 30 pulses). a) J_C = 0.210 mA cm^{-2}. b) J_C = 0.420 mA cm^{-2}. c) J_C = 0.315 mA cm^{-2}. d) J_C = 0.525 mA cm^{-2}. e) J_C = 0.630 mA cm^{-2}.

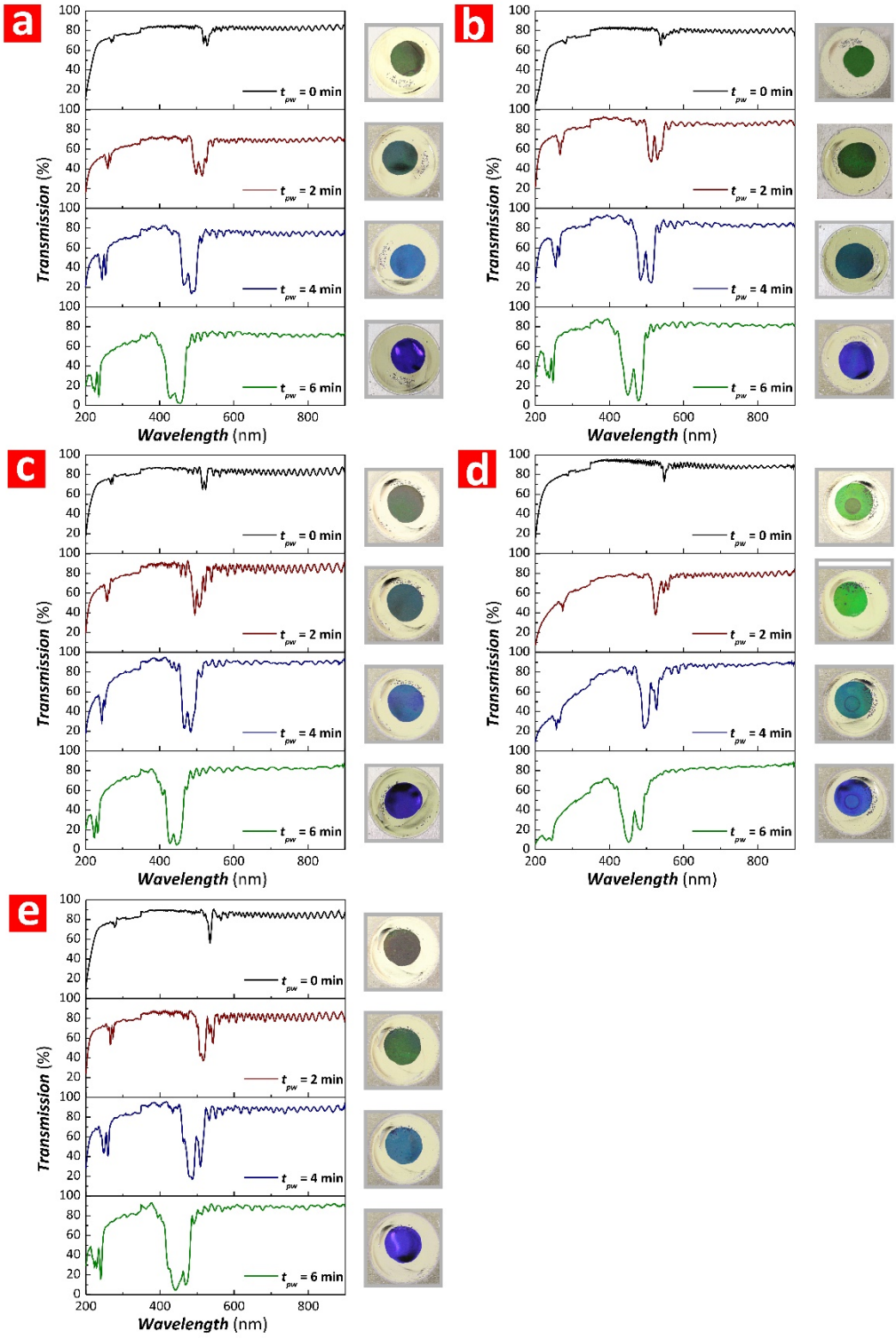

Figure S6. Representative transmission spectra for GIF-NAA-μCVs produced by SPA at t_C = 7.5 min and variable J_C and t_{pw} (note: T_P = 600 s, A_J = 0.420 mA cm^{-2}, J_{Offset} = 0.280 mA cm^{-2}, and N_P = 30 pulses). a) J_C = 0.210 mA cm^{-2}. b) J_C = 0.420 mA cm^{-2}. c) J_C = 0.315 mA cm^{-2}. d) J_C = 0.525 mA cm^{-2}. e) J_C = 0.630 mA cm^{-2}.

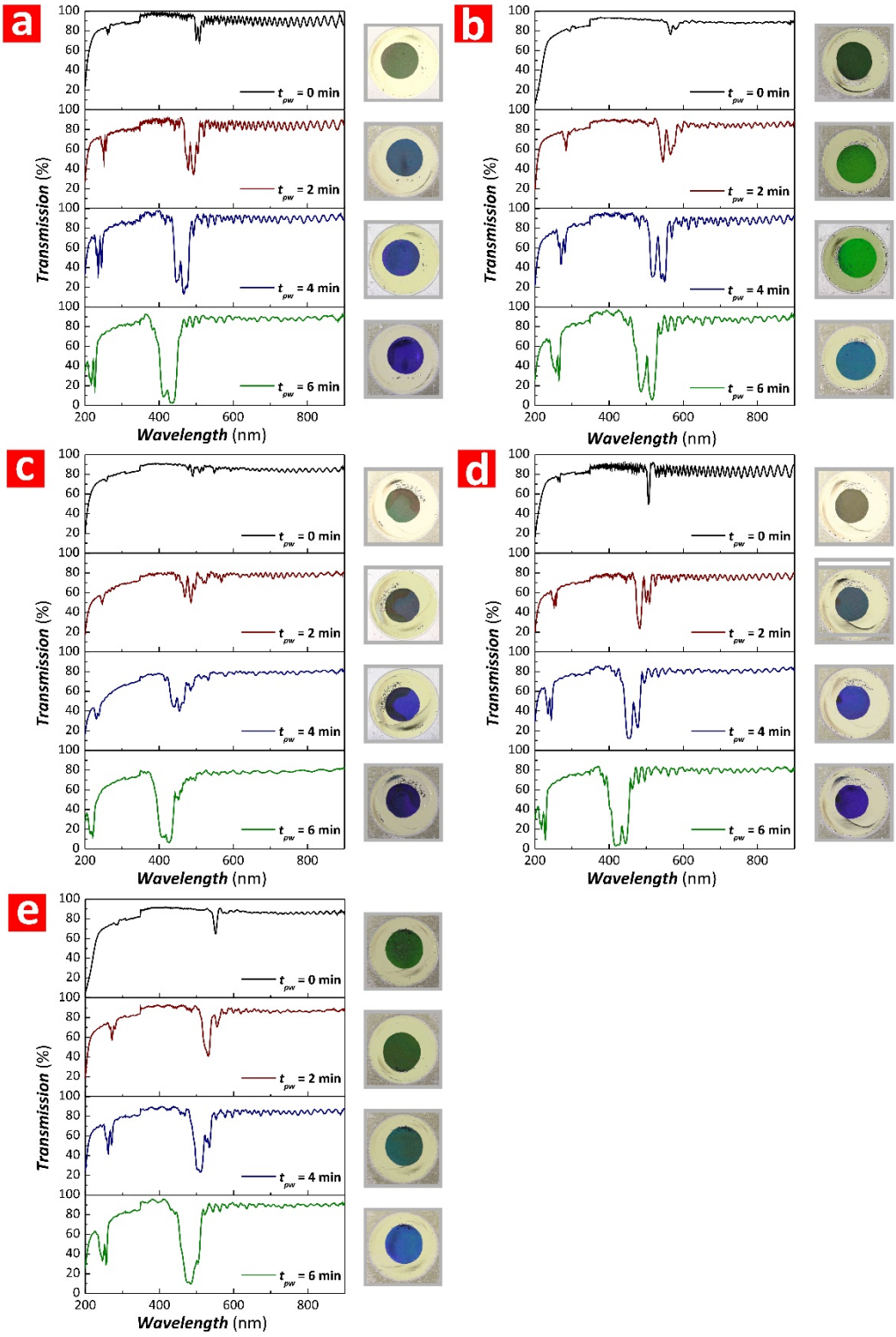

Figure S7. Representative transmission spectra for GIF-NAA-μCVs produced by SPA at t_C = 8.5 min and variable J_C and t_{pw} (note: T_P = 600 s, A_J = 0.420 mA cm^{-2}, J_{Offset} = 0.280 mA cm^{-2}, and N_P = 30 pulses). a) J_C = 0.210 mA cm^{-2}. b) J_C = 0.420 mA cm^{-2}. c) J_C = 0.315 mA cm^{-2}. d) J_C = 0.525 mA cm^{-2}. e) J_C = 0.630 mA cm^{-2}.

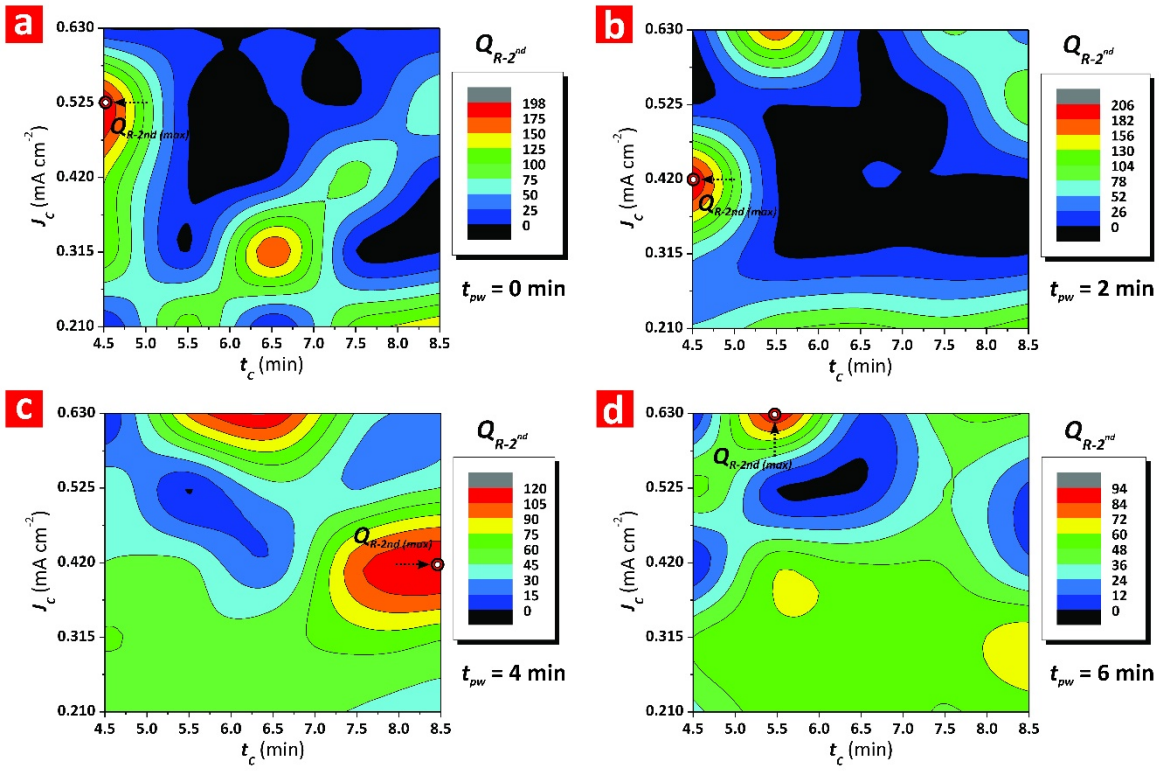

Figure S8. Contour maps showing the combined effect of cavity fabrication parameters (i.e. anodisation time – t_C and current density – J_C) on the quality factor of the secon order resonance band ($Q_{R\text{-}2nd}$) of GIF-NAA-μCVs produced by SPA at different pore widening times (t_{pw}). a) t_{pw} = 0 min. b) t_{pw} = 2 min. c) t_{pw} = 4 min. c) t_{pw} = 6 min. (note: GIF-NAA-μCVs produced with T_P = 600 s, A_J = 0.420 mA cm^{-2}, J_{Offset} = 0.280 mA cm^{-2}, and N_P = 30 pulses).

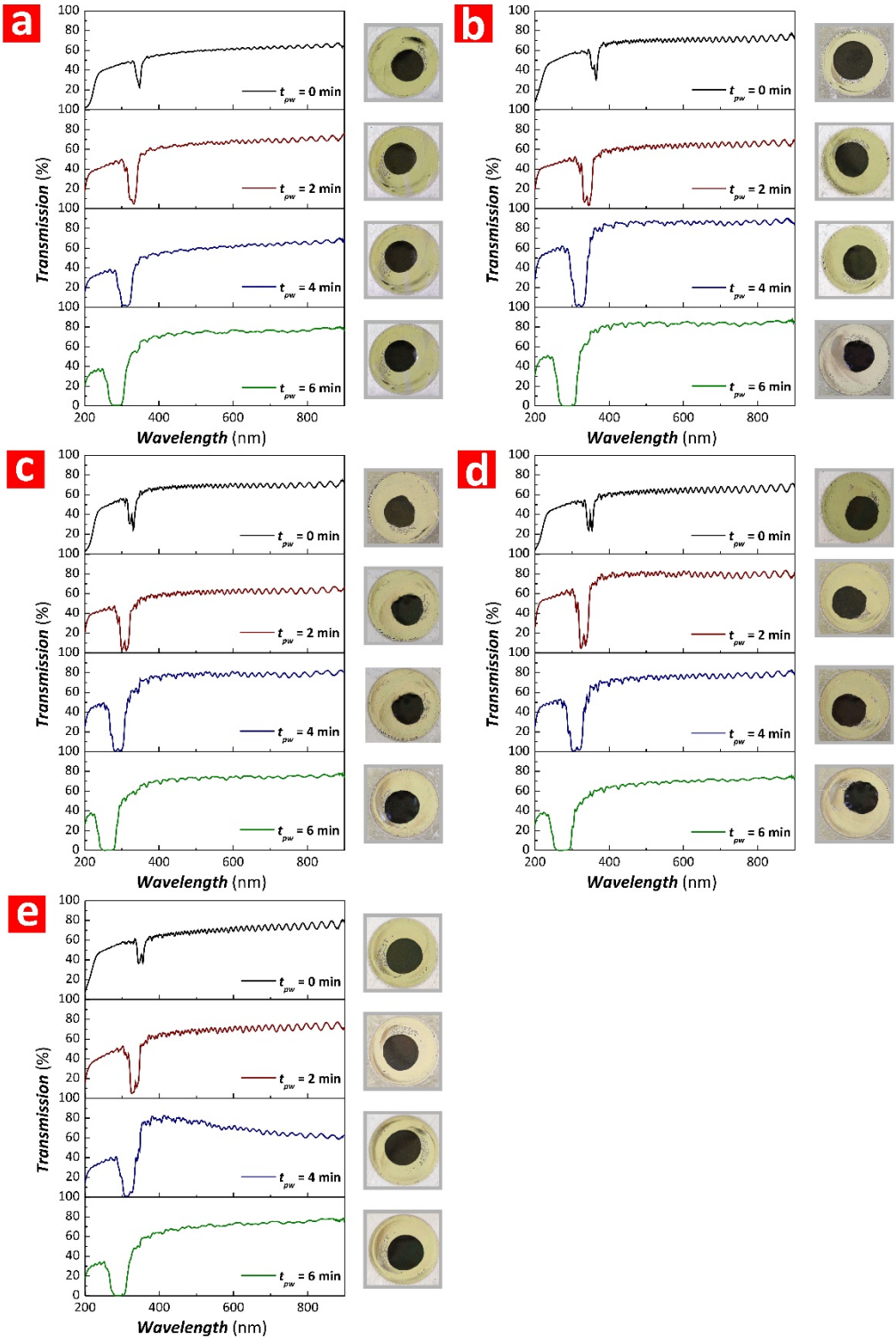

Figure S9. Representative transmission spectra for DBR-NAA-μCVs produced by STPA at t_C = 4.5 min and variable J_C and t_{pw} (note: T_P = 600 s, A_J = 0.420 mA cm^{-2}, J_{Offset} = 0.280 mA cm^{-2}, and N_P = 30 pulses). a) J_C = 0.210 mA cm^{-2}. b) J_C = 0.420 mA cm^{-2}. c) J_C = 0.315 mA cm^{-2}. d) J_C = 0.525 mA cm^{-2}. e) J_C = 0.630 mA cm^{-2}.

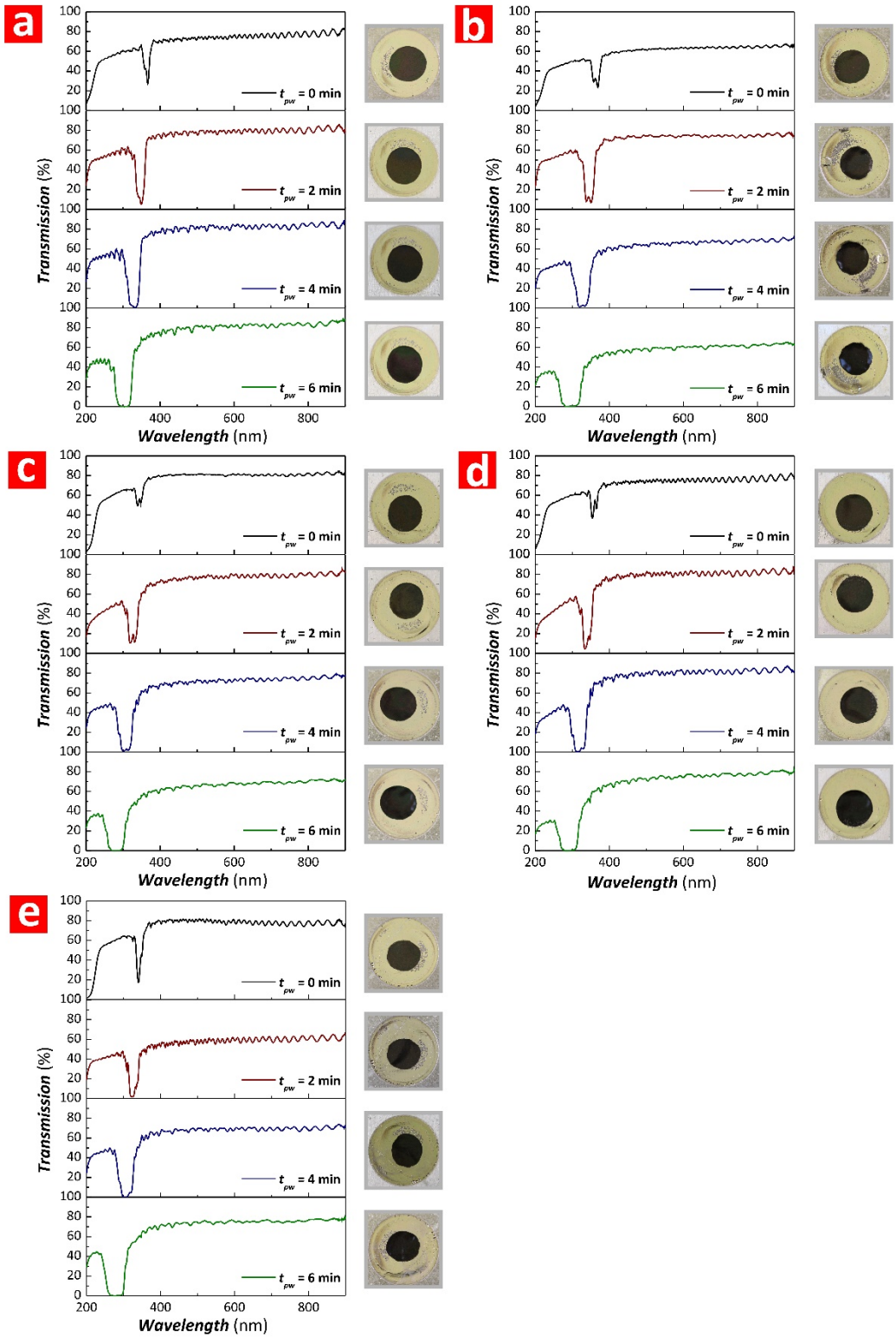

Figure S10. Representative transmission spectra for DBR-NAA-μCVs produced by STPA at t_C = 5.5 min and variable J_C and t_{pw} (note: T_P = 600 s, A_J = 0.420 mA cm^{-2}, J_{Offset} = 0.280 mA cm^{-2}, and N_P = 30 pulses). a) J_C = 0.210 mA cm^{-2}. b) J_C = 0.420 mA cm^{-2}. c) J_C = 0.315 mA cm^{-2}. d) J_C = 0.525 mA cm^{-2}. e) J_C = 0.630 mA cm^{-2}.

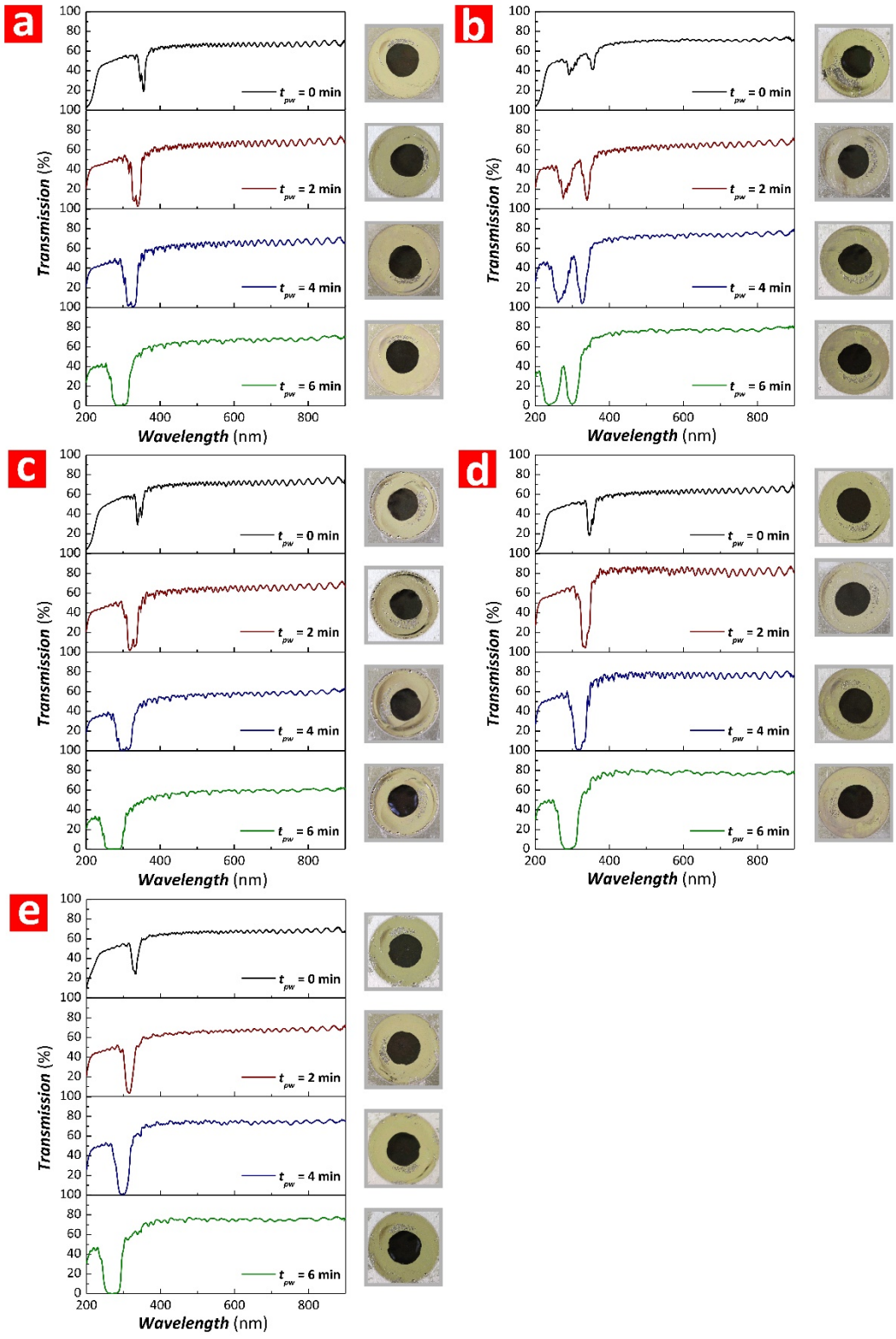

Figure S11. Representative transmission spectra for DBR-NAA-μCVs produced by STPA at t_C = 6.5 min and variable J_C and t_{pw} (note: T_P = 600 s, A_J = 0.420 mA cm^{-2}, J_{Offset} = 0.280 mA cm^{-2}, and N_P = 30 pulses). a) J_C = 0.210 mA cm^{-2}. b) J_C = 0.420 mA cm^{-2}. c) J_C = 0.315 mA cm^{-2}. d) J_C = 0.525 mA cm^{-2}. e) J_C = 0.630 mA cm^{-2}.

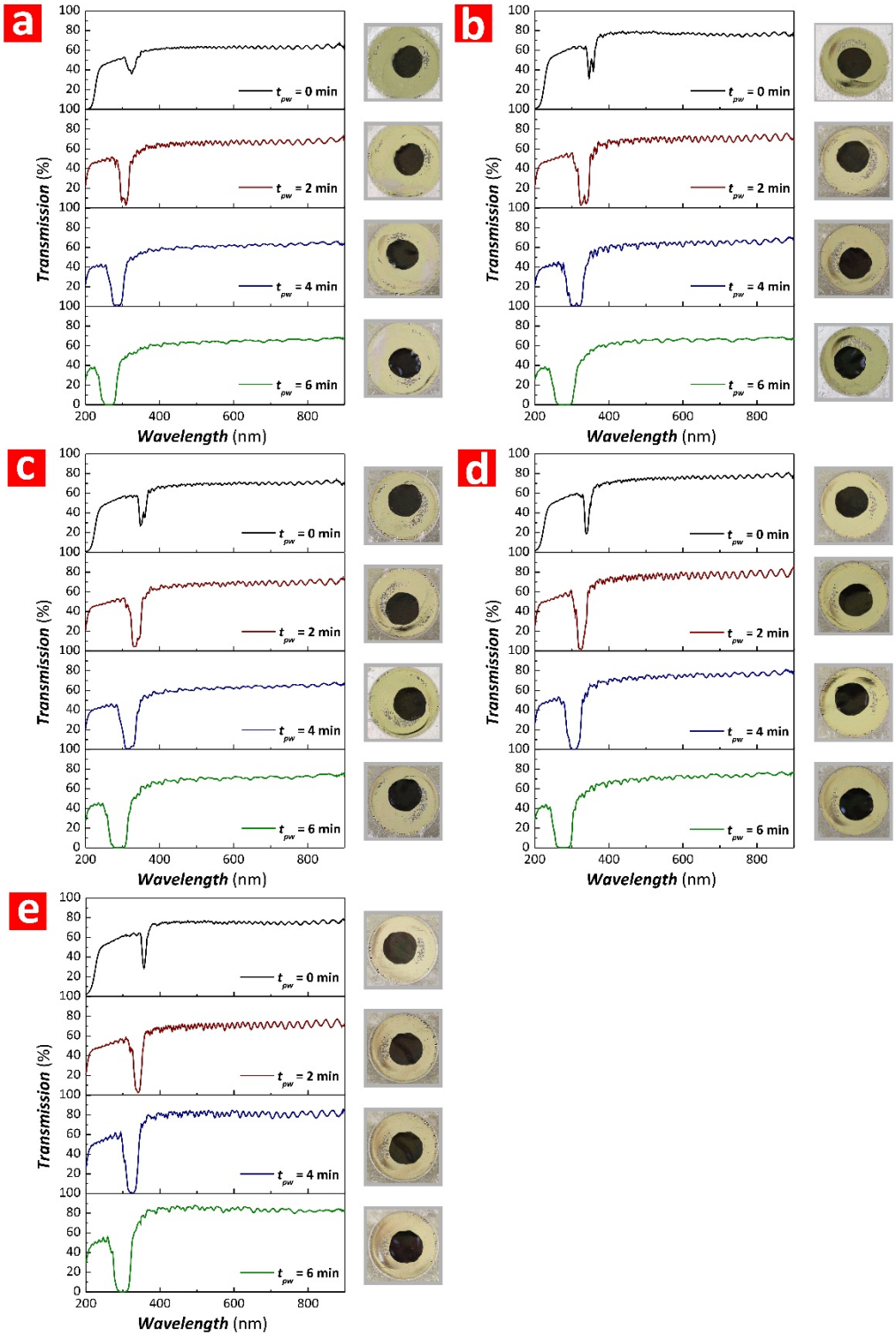

Figure S12. Representative transmission spectra for DBR-NAA-μCVs produced by STPA at t_C = 7.5 min and variable J_C and t_{pw} (note: T_P = 600 s, A_J = 0.420 mA cm^{-2}, J_{Offset} = 0.280 mA cm^{-2}, and N_P = 30 pulses). a) J_C = 0.210 mA cm^{-2}. b) J_C = 0.420 mA cm^{-2}. c) J_C = 0.315 mA cm^{-2}. d) J_C = 0.525 mA cm^{-2}. e) J_C = 0.630 mA cm^{-2}.

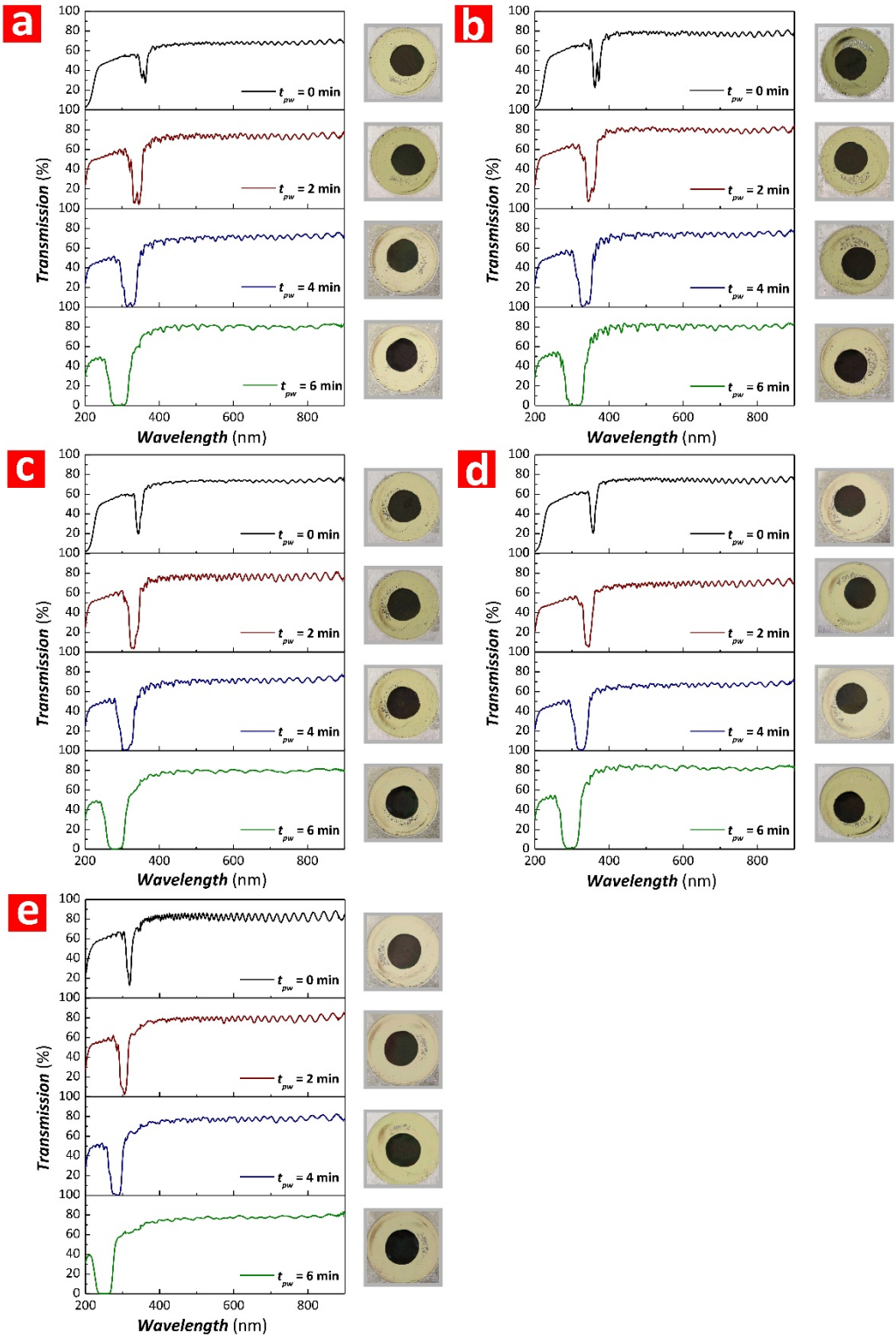

Figure S13. Representative transmission spectra for DBR-NAA-μCVs produced by STPA at t_C = 8.5 min and variable J_C and t_{pw} (note: T_P = 600 s, A_J = 0.420 mA cm^{-2}, J_{Offset} = 0.280 mA cm^{-2}, and N_P = 30 pulses). a) J_C = 0.210 mA cm^{-2}. b) J_C = 0.420 mA cm^{-2}. c) J_C = 0.315 mA cm^{-2}. d) J_C = 0.525 mA cm^{-2}. e) J_C = 0.630 mA cm^{-2}.

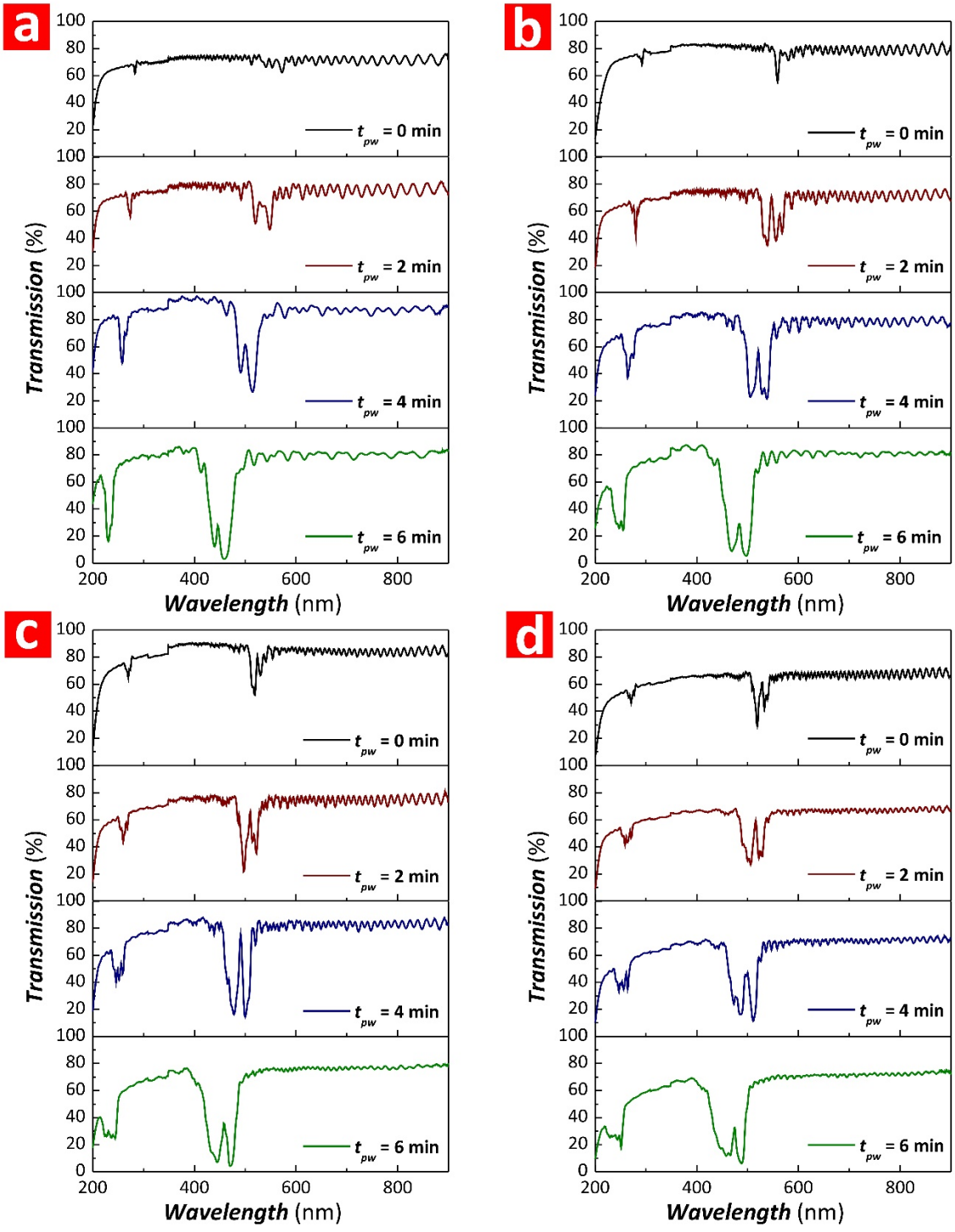

Figure S14. Representative transmission spectra for GIF-NAA-μCVs produced by SPA with variable N_P (note: T_P = 600 s, A_J = 0.420 mA cm^{-2}, J_{Offset} = 0.280 mA cm^{-2}, t_C = 6.5 min, and J_C = 0.420 mA cm^{-2}). a) N_P = 20 pulses. b) N_P = 30 pulses. c) N_P = 40 pulses. d) N_P = 50 pulses.

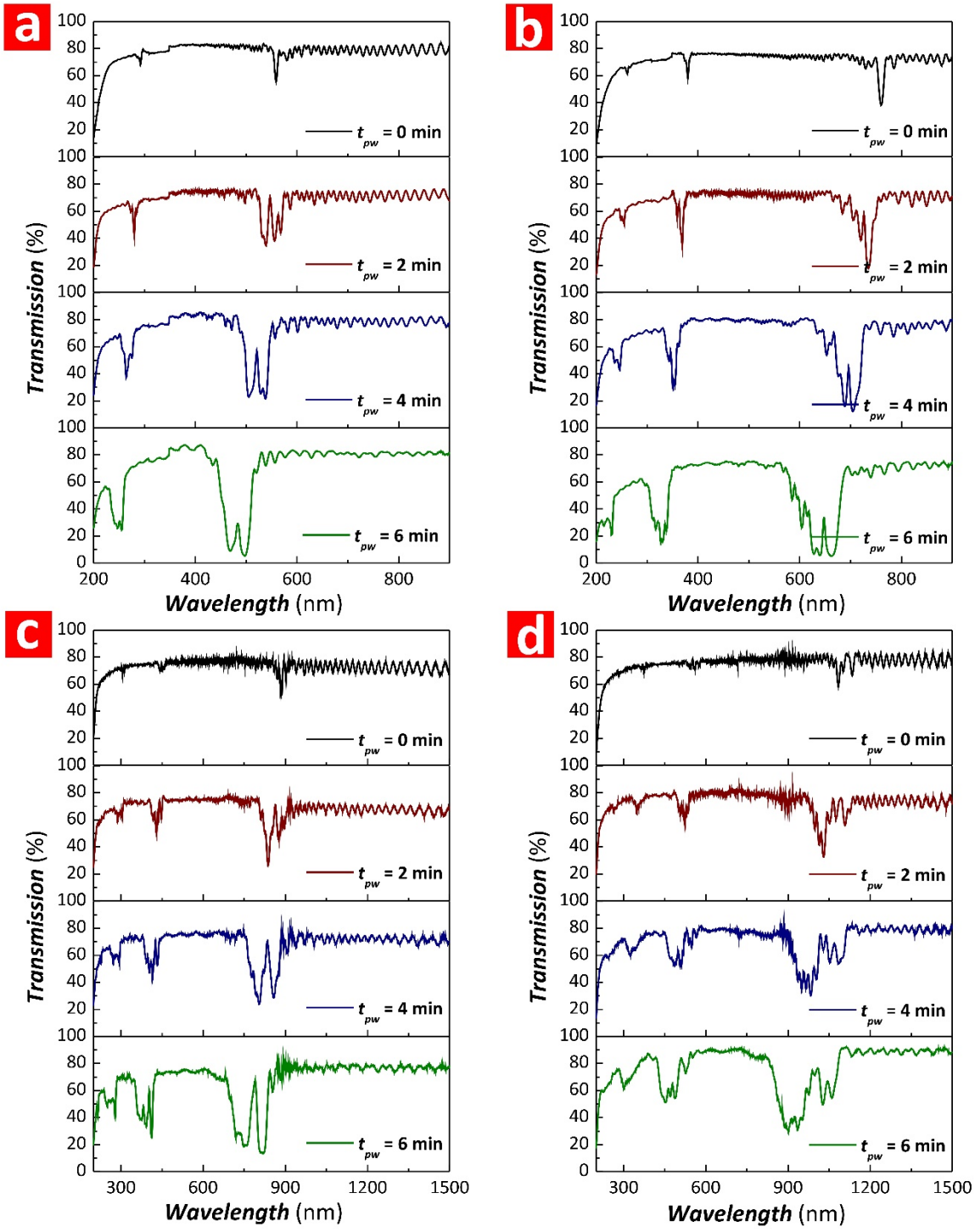

Figure S15. Representative transmission spectra for GIF-NAA-μCVs produced by SPA with variable T_P (note: A_J = 0.420 mA cm^{-2}, J_{Offset} = 0.280 mA cm^{-2}, N_P = 30 pulses, t_C = 6.5 min, and J_C = 0.420 mA cm^{-2}). a) T_P = 600 s. b) T_P = 800 s. c) T_P = 1000 s. d) T_P = 1200 s.

Chapter 6

Light-Confining Nanoporous Anodic Alumina Microcavities by Apodised Stepwise Pulse Anodisation

Statement of Authorship

Title of Paper	Light-Confining Nanoporous Anodic Alumina Microcavities by Apodised Stepwise Pulse Anodization.
Publication Status	☑ Published ☐ Accepted for Publication ☐ Submitted for Publication ☐ Unpublished and Unsubmitted w ork w ritten in manuscript style
Publication Details	Law, C.S., S.Y. Lim, R.M. Macalincag, A.D. Abell, and A. Santos, *Light-confining nanoporous anodic alumina microcavities by apodised stepwise pulse anodization*. ACS Applied Nano Materials, 2018. **1**(9): p. 4418-4434.

Principal Author

Name of Principal Author (Candidate)	Cheryl Suwen Law		
Contribution to the Paper	Under the supervision of A. Santos and A. D. Abell, I performed the experiments, interpreted and processed the data and wrote the manuscript.		
Overall percentage (%)	70		
Certification:	This paper reports on original research I conducted during the period of my Higher Degree by Research candidature and is not subject to any obligations or contractual agreements with a third party that would constrain its inclusion in this thesis. I am the primary author of this paper.		
Signature		Date	23/11/2018

Co-Author Contributions

By signing the Statement of Authorship, each author certifies that:

i. the candidate's stated contribution to the publication is accurate (as detailed above);
ii. permission is granted for the candidate in include the publication in the thesis; and
iii. the sum of all co-author contributions is equal to 100% less the candidate's stated contribution.

Name of Co-Author	Siew Yee Lim		
Contribution to the Paper	I helped Cheryl Suwen Law with performing the experiments. I give consent for Cheryl Suwen Law to present this paper for examination towards the Doctorate of Philosophy.		
Signature		Date	14/11/2018

Name of Co-Author	Raeanne M. Macalincag		
Contribution to the Paper	I helped Cheryl Suwen Law with performing the experiments. I give consent for Cheryl Suwen Law to present this paper for examination towards the Doctorate of Philosophy.		
Signature		Date	14/11/2018

Name of Co-Author	Andrew D. Abell		
Contribution to the Paper	I acted as secondary supervisor for the candidate, aided in revising the manuscript and evaluating in the final version of manuscript. I give consent for Cheryl Suwen Law to present this paper for examination towards the Doctorate of Philosophy.		
Signature		Date	23/11/2018

Name of Co-Author	Abel Santos		
Contribution to the Paper	I acted as primary supervisor for the candidate, aided in developing of the experiments, revising the manuscript and evaluating the final version of the manuscript. I give consent for Cheryl Suwen Law to present this paper for examination towards the Doctorate of Philosophy.		
Signature		Date	23/11/2018

6. Light-Confining Nanoporous Anodic Alumina Microcavities by Apodised Stepwise Pulse Anodisation

6.1 Introduction, Significance and Commentary

Chapter 4 has introduced the concept of apodisation that have successfully narrowed the bandwidth of photonic band gap of NAA-PCs. This has led to an innovative approach to produce high quality NAA-μCVs with narrow and well-resolved resonance bands across the spectral regions. The unprecedented high quality factor achieved (i.e. approximately fourfold enhancement than previous studies) endows NAA-μCVs with promising sensing properties, advancing their applications as ultrasensitive optical platforms.

6.2 Publication

This section is presented as published research paper by **Law, C.S.**, S.Y. Lim, R.M. Macalincag, A.D. Abell, and A. Santos, *Light-confining nanoporous anodic alumina microcavities by apodised stepwise pulse anodization*. ACS Applied Nano Materials, 2018. **1**(9): p. 4418-4434.

ACS APPLIED NANO MATERIALS
Cite This: ACS Appl. Nano Mater. 2018, 1, 4418−4434
Article
www.acsanm.org

Light-Confining Nanoporous Anodic Alumina Microcavities by Apodized Stepwise Pulse Anodization

Cheryl Suwen Law,[†,‡,§] Siew Yee Lim,[†,‡,§] Raeanne M. Macalincag,[†] Andrew D. Abell,[*,‡,§,∥] and Abel Santos[*,†,‡,§]

[†]School of Chemical Engineering, [‡]Institute for Photonics and Advanced Sensing (IPAS), [§]ARC Centre of Excellence for Nanoscale BioPhotonics (CNBP), and [∥]Department of Chemistry, The University of Adelaide, Adelaide SA 5005, Australia

Supporting Information

ABSTRACT: This study presents an innovative approach to fabricate nanoporous anodic alumina optical microcavities (NAA-μCVs) with enhanced quality factor and versatile optical properties. An apodization strategy using a logarithmic negative function is applied to a stepwise pulse anodization process in order to engineer the effective medium of NAA so that it confines light efficiently. The architecture of these light-trapping photonic crystals is composed of two highly reflecting mirrors with an asymmetrically apodized effective medium. Various anodization parameters such as the anodization time, anodization period, current density offset, and pore-widening time are systematically modified to assess their effect on the optical properties of NAA-μCVs in terms of the quality factor and position of the resonance band. We demonstrate that this fabrication approach enables the generation of NAA-μCVs with a high quality factor (~113) and well-resolved and tunable resonance bands across the spectral regions, from UV to near-IR, through manipulation of the anodization parameters. These results represent a comprehensive rationale for the development of high-quality NAA-μCVs with enhanced light-confining capabilities, providing new opportunities for further fundamental and applied research across a broad range of fields and disciplines such as photonics and optical sensing.

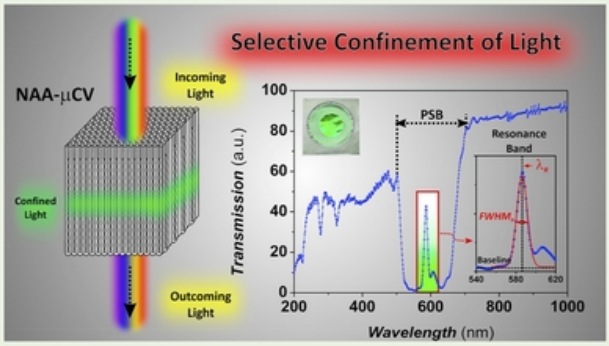

KEYWORDS: *nanoporous anodic alumina, optical microcavity, light confinement, apodized anodization, quality factor*

1. INTRODUCTION

New materials and structures that effectively confine light to small volumes are central for the development and advancement of nanophotonic applications such as quantum communication and computing,[1] nanolasers,[2] ultrasmall photonic filters,[3] and optical sensing.[4] Photons possess no charge or rest mass and are prone to escaping when trapped in photonic structures.[5,6] The confinement of light within small volumes comparable to the wavelength of light is challenging. However, high-quality optical microcavities (μCVs) with strong light-confinement capabilities to attain precise control of light emission and propagation have been realized.[7,8] Photonic crystals (PCs) have emerged as the most promising platforms to develop efficient optical μCVs with high-quality factors and small cavity volume.[9,10] Optical μCVs are PC structures that can guide and build up optical signals by light confinement.[6] Typically, μCVs consist of two plane-parallel mirrors positioned at a fixed distance apart with the objective of capturing and storing light indefinitely, until the system is triggered to release the confined light from the cavity in a controlled fashion.[6,11,12] μCVs can be produced in different materials, including polymers,[13] semiconductors such as GaAs, InP, GaInAsP, and GaN,[14−17] and silicon.[4,18,19] Usually, μCVs are fabricated by a combination of lithographic and etching techniques and chemical or physical vapor deposition.[17] However, alternative materials such as porous silicon produced by the electrochemical etching of silicon opened new opportunities to develop nanoporous μCVs with tunable optical properties and nanoporous architectures for different applications, including light-emitting devices, solar cells, optical filters, biosensors, drug delivery, and theranostics.[20−22] Modulation of the porosity in depth by the anodizing current allows effective engineering of the optical properties of porous silicon μCVs, the composite air−silicon matrix of which acts as a versatile effective medium.[23−27] Porous silicon has outstanding optoelectronic properties; however, it has poor chemical stability and mechanical strength, and its fabrication process requires the use of extremely hazardous HF-based electrolytes.[28,29] To date, different alternative/complementary nanoporous materials have been explored to overcome the intrinsic limitations of porous silicon. Of these, nanoporous anodic alumina (NAA) produced by the anodization of aluminum has properties superior to those of porous silicon with respect to the mechanical, thermal, and chemical

Received: March 26, 2018
Accepted: August 28, 2018
Published: August 28, 2018

DOI: 10.1021/acsanm.8b00494
ACS Appl. Nano Mater. 2018, 1, 4418−4434

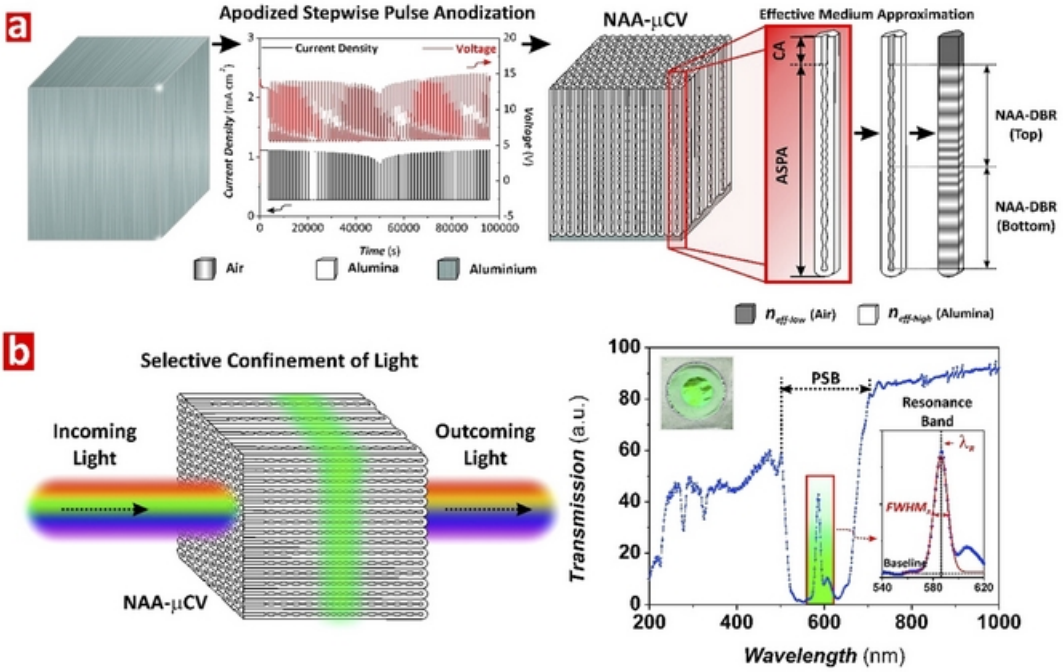

Figure 1. Fabrication of NAA-μCVs by ASPA. (a) Representative ASPA profile (left) and structure of NAA-μCVs (right) showing details of the existing relationship between the nanopore geometry and effective refractive index (n_{eff}) distribution between high (alumina) and low (air) values along the nanopore depth. (b) Schematic showing the confinement of light within the structure of NAA-μCVs (left) and representative transmission spectra showing the characteristic PSB and the resonance band at its center in NAA-μCVs. The insets show a digital picture of the NAA-μCVs, with the characteristic green interferometric color denoting the position of the PSB and a magnified view of the red rectangle showing details of the resonance band (note: NAA-μCV produced with T_P = 1300 s, ΔA_j = 0.210 mA cm^{-2}, J_{offset} = 0.280 mA cm^{-2}, t_{An} = 25 h, and t_{pw} = 6 min).

stabilities as well as versatile nanopore geometry. Furthermore, the anodization of aluminum is a well-established electrochemical process performed in mild acid electrolyte solutions that is an economical and fully scalable process and requires minimum safety measures.[30−36]

Recent studies have demonstrated that the effective refractive index of NAA can be precisely modulated in a multidimensional fashion to create a broad range of PC structures with finely tuned optical properties [e.g., distributed Bragg reflectors (DFRs), gradient-index filters, bandpass and linear variable bandpass filters, encoded photonic tags, etc.]. The realization of NAA-based μCVs (NAA-μCVs) has been demonstrated in a few pioneering studies.[37−40] The fabrication of NAA-μCVs involves the introduction of defect modes in the PC structure, which can be achieved by various approaches such as the insertion of a thin layer of nanopores with constant effective refractive index between two highly reflective Bragg mirrors, a phase shift of the effective refractive index between Bragg mirrors, or a progressive asymmetric modulation of the effective medium in depth.[37,38,41] However, the maximum quality factors of NAA-μCVs reported by Wang et al. (~24),[38] Lee et al. (~55),[37] and Yan et al. (~45)[41] were found to be significantly lower than those of porous silicon-based μCVs (~1500−3400)[19,42,43] because of the low refractive index of alumina (Al_2O_3; $n_{Alumina}$ ~ 1.70).[37−40] Despite this limitation, the development of new pulse-like anodization strategies and novel NAA-PC architectures provides new opportunities to improve the quality of NAA-μCVs and explore new strategies to attain strong light confinements by precise control of light−matter interactions at the nanoscale.[37−59] Recently, we identified sharp resonance bands within the photonic stopband (PSB) of NAA-PCs produced by stepwise pulse anodization when a logarithmic negative apodization function was applied under certain conditions.[60] Motivated by these results, we decided to explore this nanofabrication approach to develop high-quality NAA-μCVs.

In this study, a new architecture of NAA-μCVs that enables high-quality confinement of light by means of a rationally designed apodized stepwise pulse anodization (ASPA) approach is presented. A negative apodization function is implemented in the stepwise pulse anodization profile with the aim of modulating the effective refractive index of NAA in depth and engineering the PSB of the Bragg mirrors (Figure 1).[61,62] Various anodization parameters including the anodization time, anodization period, current density offset, and pore-widening time are systematically modified in order to maximize and tune the resonance band of NAA-μCVs across the spectral regions. Our study establishes a comprehensive rationale toward the fabrication of NAA-μCVs with a high-quality factor and optimized optical properties. These PCs will enable new opportunities to expand the applicability of NAA-μCVs across disciplines such as ultrasensitive sensors, light-harvesting/emitting devices, and optical filters.

2. EXPERIMENTAL SECTION

2.1. Materials. High-purity (99.9997%) aluminum (Al) foils of thickness 0.32 mm were supplied by Goodfellow Cambridge Ltd. (U.K.). Sulfuric acid (H_2SO_4), perchloric acid ($HClO_4$), copper(II) chloride ($CuCl_2$), hydrochloric acid (HCl), phosphoric acid (H_3PO_4), and ethanol (EtOH or C_2H_5OH) were supplied by Sigma-Aldrich (Australia) and used as received, without further purification steps. Aqueous solutions used in this study were prepared with Milli-Q water (18.2 mΩ cm).

DOI: 10.1021/acsanm.8b00494
ACS Appl. Nano Mater. 2018, 1, 4418−4434

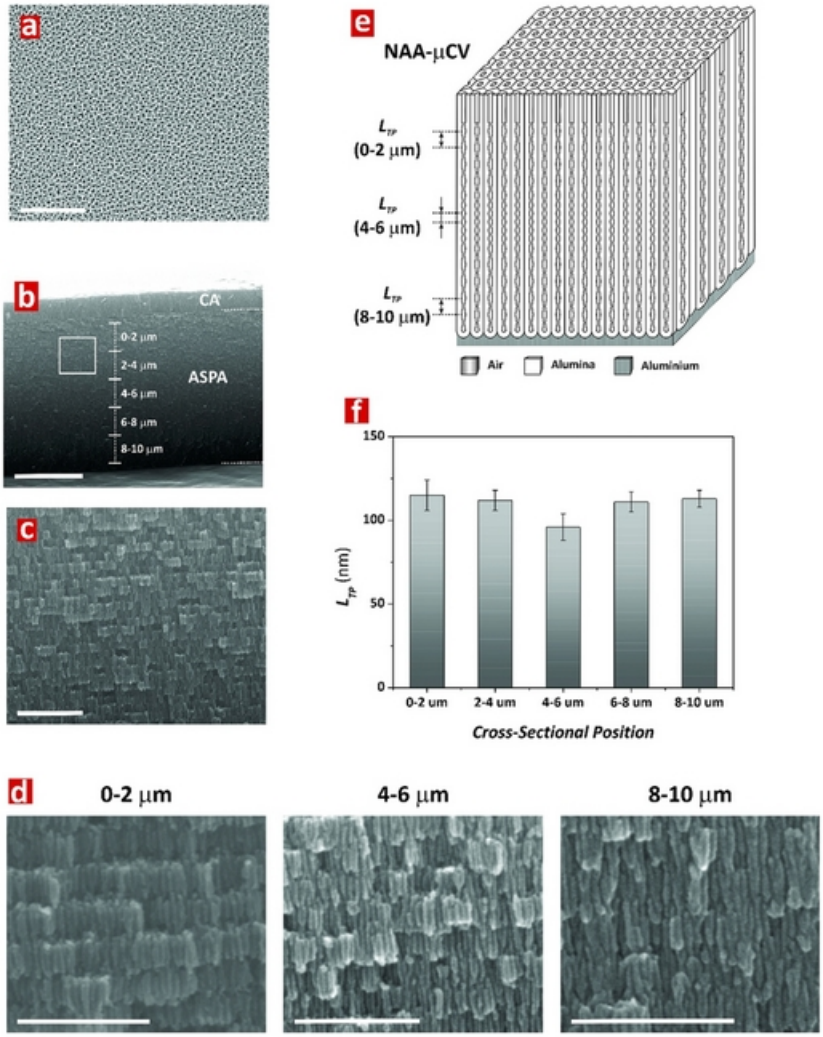

Figure 2. Nanoporous structure of NAA-μCVs produced by ASPA. (a) Representative top-view FEG-SEM image of a NAA-μCV showing a random distribution of nanopores with d_p = 15 ± 2 nm (scale bar = 500 nm). (b) General cross-sectional-view FEG-SEM image of a NAA-μCV showing a top layer of straight nanopore diameter (constant anodization = CA − thickness = 1.4 ± 0.1 μm) and the PC-μCV layer with nanopore diameter modulation (ASPA − thickness = 11.0 ± 0.1 μm) with details showing the areas where the period length (L_{TP}) was estimated (i.e., from 0 to 2 to 8−10 μm; scale bar = 5 μm). (c) Magnified view of the white rectangle shown in part b, revealing the porosity modulation in depth in NAA-μCVs (scale bar = 1 μm). (d) Magnified views at different cross-sectional positions (i.e., 0−2, 4−6, and 8−10 μm) showing details of the period-length modulation (scale bar = 500 nm). (e) Illustration representing the idealized nanoporous structure of NAA-μCVs, where the period length (L_{TP}) is modified in depth to create an optical μCV structure with a logarithmically modulated effective refractive index composed of two NAA-DBRs with an asymmetrically modulated effective refractive index. (f) Bar chart showing the period-length distribution in NAA-μCVs produced by ASPA along the nanopore depth (note: NAA-μCV produced with T_P = 800 s, ΔA_J = 0.210 mA cm^{-2}, J_{offset} = 0.280 mA cm^{-2}, t_{An} = 20 h, and t_{pw} = 6 min).

2.2. Fabrication of NAA-Based Microcavities (NAA-μCVs). NAA-μCVs were produced by ASPA under the current density control conditions. Aluminum square chips of 1.5 × 1.5 cm were cleaned under sonification in EtOH and Milli-Q water for 15 min each and then dried under an air stream. Prior to anodization, these aluminum substrates were electropolished in a mixture of 4:1 (v/v) EtOH/$HClO_4$ at 20 V and 5 °C for 3 min. The anodization process of aluminum substrates was carried out in an electrochemical reactor at a constant temperature of −1 °C, using an aqueous solution of 1.1 M H_2SO_4 with 25 vol % of EtOH as the electrolyte. The galvanostatic anodization process started with a constant current density step at 1.120 mA cm^{-2} for 1 h to create a starting nanoporous oxide layer that acts as a shuttle for achieving a homogeneous pore growth rate preceding the ASPA step. The anodization profile was subsequently set to apodized stepwise pulse mode. A logarithmic negative apodization function was implemented into conventional stepwise pulse anodization. The current density−time ASPA profiles were produced by a custom-designed *Labview*-based software according to eq 1.

$$J(t) = 2A_J(t) + J_{offset} \quad (1)$$

where A_J (t) is the time-dependent current density amplitude, which follows a logarithmic negative apodization function as defined in eqs 2 and 3.

For $t \leq t_{An}/2$,

$$A(t)_J = A_{max} + \left[\frac{A_{min} - A_{max}}{\log\left(\frac{t_{An}}{2} + 10\right) - 1}\right][\log(t + 10) - 1] \quad (2)$$

For $t > t_{An}/2$,

DOI: 10.1021/acsanm.8b00494
ACS Appl. Nano Mater. 2018, 1, 4418−4434

$$A(t)_J = \left[\frac{A_{max} - A_{min}}{\log(t_{An} + 10) - \log\left(\frac{t_{An}}{2} + 10\right)}\right] \left[\log(t + 10) - \log\left(\frac{t_{An}}{2} + 10\right)\right] + A_{min} \quad (3)$$

where A_{max} and A_{min} are the maximum and minimum amplitudes and t_{An} is the total anodization time at ASPA.

Note that T_P in the ASPA profile was defined as the total time length of the high and low anodization current density pulses (eq 4):

$$T_P = t_{high} + t_{low} \quad (4)$$

where t_{high} and t_{low} are the time durations at high and low current density values, respectively. The ratio between t_{high} and t_{low} was set to t_{high}:t_{low} = 1:4.

To gain a better understanding of the light-confining capabilities of NAA-μCVs produced by ASPA, different anodization parameters (i.e., anodization time, t_{An}; anodization period, T_P; current density offset, J_{offset}; pore-widening time, t_{pw}) were systematically manipulated to assess their effects on the optical characteristics of NAA-μCVs, such as the interferometric color, position of the resonance band (λ_R), full width at half-maximum of the resonance band (fwhm$_R$), and quality factor of cavity (Q_C), as defined by eq 5.

$$Q_C = \frac{\lambda_R}{\text{fwhm}_R} \quad (5)$$

2.3. Optical Characterization. Prior to optical characterization, the remaining aluminum substrate was selectively dissolved from the backside of these aluminum chips by wet chemical etching in a saturated solution of HCl/$CuCl_2$, using an etching cell with a Viton mask with a circular window of 5 mm diameter. These etched NAA-μCVs were then optically characterized. The optical transmission spectra of NAA-μCVs fabricated at various conditions were obtained at normal incidence (i.e., θ = 0°) from 200−1000 nm with a resolution of 1 nm and a 5 mm slit using a UV−vis−near-IR (NIR) spectrophotometer (Cary 60, Agilent, USA) and from 200−1500 nm with a resolution of 1 nm in a UV−vis−NIR spectrometer (UV-3600 Plus, Shimadzu, Japan). The interferometric color displayed by these NAA-μCVs as a function of the different fabrication parameters was characterized through digital images acquired by a Canon EOS 700D digital camera equipped with a Tamron 90 mm F2.8 VC USD macro mount lens with an autofocus function under natural illumination. A black card was used as the background for the digital image acquisition. The pore size of NAA-μCVs was widened by isotropic chemical etching in an aqueous solution of 5 wt % H_3PO_4 at 35 °C at different pore-widening times (i.e., t_{pw} = 0, 2, 4, and 6 min), and their transmission spectra and digital images were recorded after each pore-widening step. Note that the features of the resonance band of these NAA-μCVs (i.e., position of the resonance band, λ_R; full width at half-maximum of the resonance band, fwhm$_R$; baseline of the resonance band, y_0) were estimated using *OriginPro 8.5*, applying Gaussian fittings over the resonance bands shown in the transmission spectra of NAA-μCVs, and using as a baseline the lower lobe of the PSB, as illustrated in Figure 1. The obtained results were summarized in contour maps generated using *OriginPro 8.5*, using a triangulation algorithm in which the coordinates of the intersection point were computed with linear interpolation.

2.4. Structural Characterization. The nanoporous structure of NAA-μCVs was characterized by field-emission-gun scanning electron microscopy (FEG-SEM; FEI Quanta 450). The obtained FEG-SEM images were analyzed using *ImageJ* (public domain program developed at the Reproductive Sciences Branch of the National Institutes of Health).[63]

3. RESULTS AND DISCUSSION

3.1. Fabrication and Structural Characterization of NAA-μCVs. Figure 1a illustrates the fabrication process of NAA-μCVs by ASPA. The structure of these PC structures is composed of two highly reflective DBR mirrors with an asymmetrically modulated effective refractive index in a stepwise fashion in depth following a logarithmic negative window. The amplitude of the current density pulse is logarithmically reduced during the fabrication process of the first half of the NAA-μCV (i.e., from t = 0 to $t_{An}/2$; eq 2). At t = $t_{An}/2$, the current density amplitude is progressively increased according to the mathematical expression shown in eq 3. The transmission spectrum of these PC structures is characterized by a relatively broad PSB with a strong and narrow resonance band at approximately its central position (Figure 1b). This resonance band denotes a strong confinement of light within the NAA-μCV at that narrow range of wavelengths, which is established by the geometric features of the NAA-DBR mirrors. Parts a−c of Figure 2 show a set of representative FEG-SEM images of NAA-μCVs produced by ASPA. These images reveal that the structures of these PCs are composed of stacked layers of NAA with a porosity modulation in depth that follows the ASPA current density profile applied during the anodization process. Figure 2a depicts a representative top-view FEG-SEM image of a NAA-μCV, revealing nanopores with an average pore diameter (d_p) of 15 ± 2 nm that are randomly distributed across the surface.

Figure 2b shows a general cross-sectional view of a NAA-μCV produced with T_P = 800 s, J_{offset} = 0.280 mA cm^{-2}, ΔA_J = 0.210 mA cm^{-2}, t_{An} = 10 h, and t_{pw} = 6 min. That image reveals that the structure of these NAA-μCVs is composed of a top layer of 1.4 ± 0.1 μm thickness with a constant nanopore diameter, which results from the first anodization stage at constant anodizing current density (CA − J = 1.120 mA cm^{-2} for 1 h), and a much thicker layer (i.e., 11.0 ± 0.1 μm) with nanopore diameter modulation in depth corresponding to the ASPA stage (Figure 2c,d). A pore branching effect can be observed at the bottom part of the NAA-μCV structure (Figure 2d; 8−10 μm), which can be associated with the non-self-organization conditions used in our study. A closer analysis of the period length (i.e., L_{TP} = distance between adjacent layers in the ASPA section of the NAA-μCVs) reveals a direct dependence with the anodization amplitude (ΔA_J; Figure 2e). For instance, we estimated the average L_{TP} along the ASPA cross section of a NAA-μCV produced with T_P = 800 s, J_{offset} = 0.280 mA cm^{-2}, ΔA_J = 0.210 mA cm^{-2}, t_{An} = 10 h, and t_{pw} = 6 min every 2 μm by FEG-SEM image analysis. Our results indicate that L_{TP} varies along the nanopore depth following the apodization function applied during anodization, with an estimation of 115 ± 9 nm at 0−2 μm, 112 ± 6 nm at 2−4 μm, 96 ± 8 nm at 4−6 μm, 111 ± 6 nm at 6−8 μm, and 113 ± 5 nm at 8−10 μm (Figure 2f). From this analysis, it is apparent that L_{TP} is reduced at the center of the ASPA section of the NAA-μCVs (i.e., $t \sim t_{An}/2$), which is expected because of the significant reduction of the anodization amplitude at $t = t_{An}/2$. Furthermore, the FEG-SEM image analysis denotes a modulation of the porosity in depth with the pulse-anodizing current density. For instance, the porosity at J = 0.280 and 1.120 mA cm^{-2} (i.e., minimum and maximum values of the current density) was estimated to be 18 ± 9 and 32 ± 13%, respectively.[48] Apodization is a filtering technique broadly used in optics to narrow the PSB of photonic structures. The direct relationship between the geometric features of NAA-μCVs and the anodization parameters enables the apodization of the optical signals of these PCs by structural engineering of their effective medium (i.e., effective refractive index modulation).

DOI: 10.1021/acsanm.8b00494
ACS Appl. Nano Mater. 2018, 1, 4418−4434

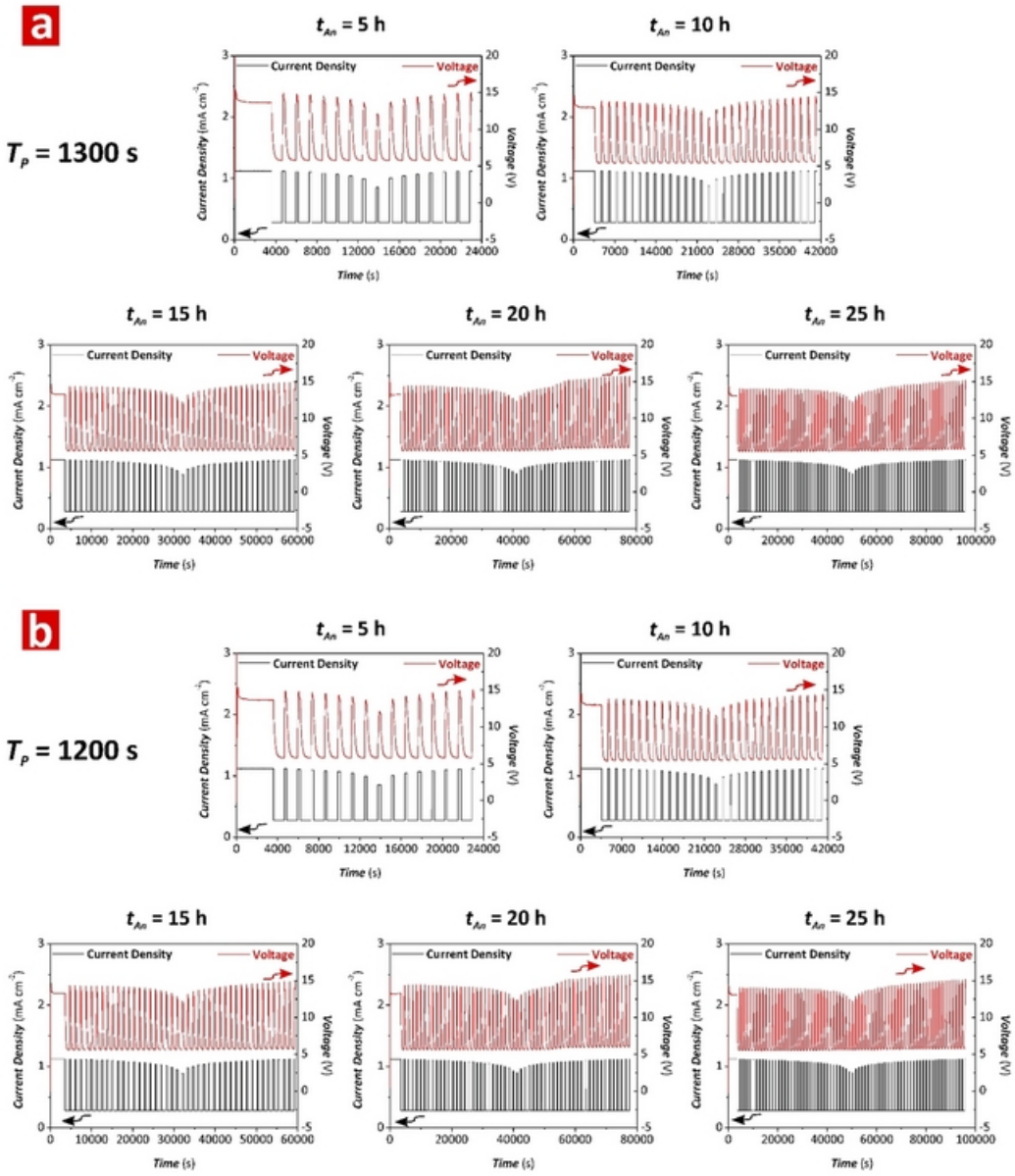

Figure 3. Representative anodization profiles of NAA-μCVs produced by ASPA at different anodization times and anodization periods (note: NAA-μCVs produced with T_P = 1200 and 1300 s, ΔA_J = 0.210 mA cm^{-2}, and J_{offset} = 0.280 mA cm^{-2}). (a) Anodization profiles of NAA-μCVs produced with T_P = 1300 at t_{An} = 5, 10, 15, 20, and 25 h. (b) Anodization profiles of NAA-μCVs produced with T_P = 1200 at t_{An} = 5, 10, 15, 20, and 25 h.

3.2. Effect of the Anodization Time (t_{An}) on the Optical Properties of NAA-μCVs. To understand the effect of t_{An} on the optical characteristics of NAA-μCVs, a set of NAA-μCVs was fabricated using logarithmic negative ASPA with varying t_{An} from 5 to 25 h at an interval of 5 h. Other anodization parameters such as the anodization period (T_P), current density offset (J_{offset}), and amplitude difference (ΔA_J) were fixed at 1200 and 1300 s, 0.280 mA cm^{-2}, and 0.210 mA cm^{-2}, respectively. Parts a and b of Figure 3 show representative anodization profiles for NAA-μCVs fabricated at different t_{An} values (i.e., 5, 10, 15, 20, and 25 h) for T_P = 1200 and 1300 s, respectively. These ASPA profiles denote that, under the anodization conditions used in our study, the anodizing current density profile is precisely translated into modulations of voltage throughout the whole process, resulting in an internal modulation of d_p in depth. The transmission spectra of NAA-μCVs produced at T_P = 1300 s as a function of t_{An} and the pore-widening time (t_{pw}) are displayed in Figure 4a–e. The optical properties of these NAA-μCVs were characterized in terms of λ_R, fwhm$_R$, Q_C, and the interferometric color. Figure 4 shows that the PSB of these NAA-μCVs is located within the vis–NIR range, and it undergoes a blue shift and increases its intensity and width with t_{pw}, from 0 to 6 min. The interferometric color is a result of the selective and constructive reflection of light by the NAA-μCV structure and denotes the position of the PSB within the UV (transparent), visible (color), or NIR (transparent) spectral regions. The transmission spectra of these NAA-μCVs shows a resonance band located at approximately the center of the PSB, which indicates the presence of an optical μCV within the structure of these PCs.

DOI: 10.1021/acsanm.8b00494
ACS Appl. Nano Mater. 2018, 1, 4418–4434

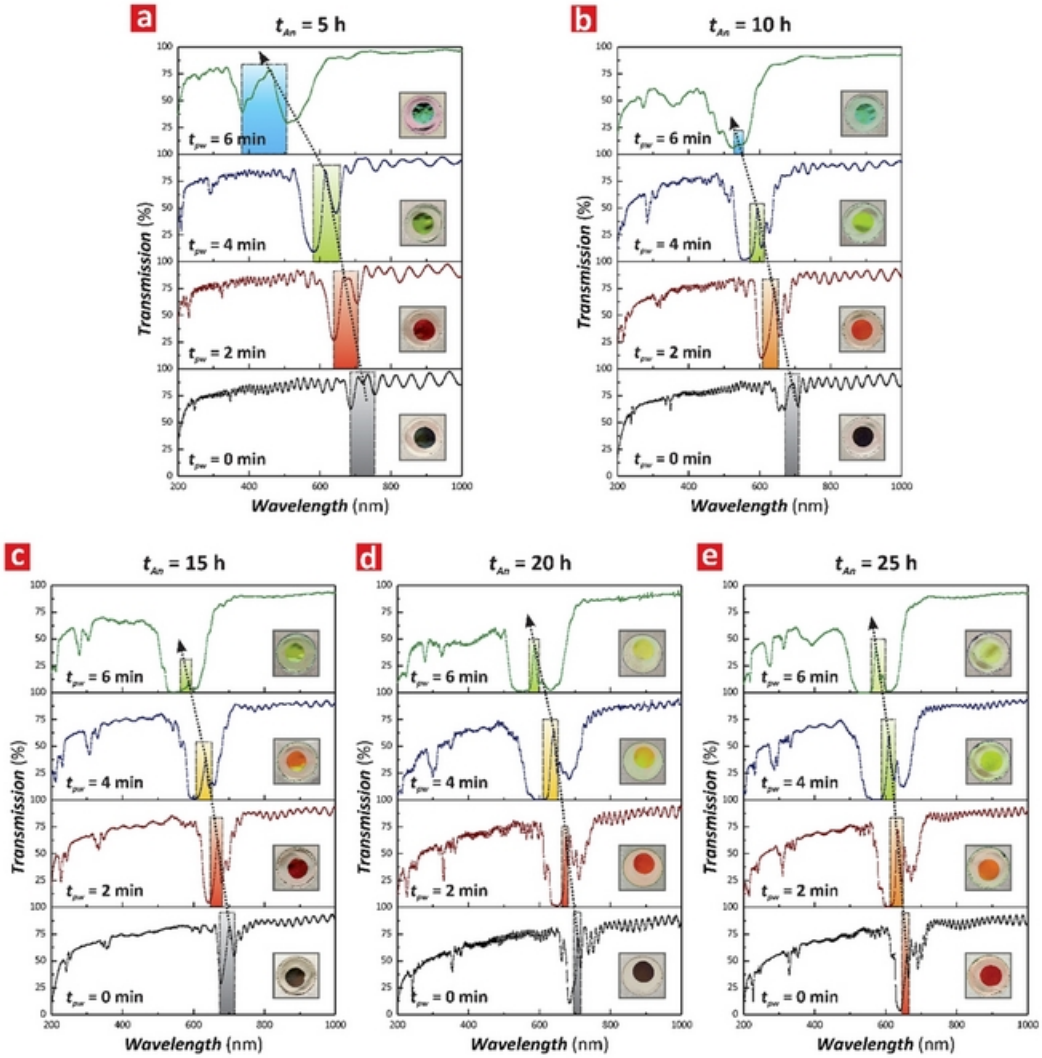

Figure 4. Combinational effect of the anodization time (t_{An}) and pore-widening time (t_{pw}) on the transmission spectrum of NAA-μCVs produced by ASPA at T_P = 1300 s (note: color rectangles denote the approximate position of the resonance band within the PSB, and black dotted arrow lines indicate the blue shift of the resonance bands with t_{pw}): (a) t_{An} = 5; (b) t_{An} = 10; (c) t_{An} = 15; (d) t_{An} = 20; (e) t_{An} = 25 h. The insets in parts a–e display digital pictures of these PC structures showing vivid interferometric colors when the resonance band is located within the visible region and transparent when the band is within the UV or NIR spectral regions.

Parts a–e of Figure 5 show magnified views of the resonance bands observed in the transmission spectra of these NAA-μCVs (Figure 4a–e) with details of the Gaussian fittings used to estimate λ_R, fwhm$_R$, and Q_C. In general, it can be observed that the resonance band of these NAA-μCVs rises as t_{pw} increases, becoming more well-resolved and intense because of the effective refractive index contrast enhancement between adjacent NAA layers.

The stepwise modulation of nanopores within NAA-μCVs is more evident as the nanoporous structure of NAA is chemically etched because the layers produced at lower anodizing current density dissolve at a faster rate than those produced at higher J (Figure S1). However, the overetching of the NAA-μCVs' structure (t_{pw} > 4 min) results in a broadening of the resonance band and a decrement of its intensity due to light scattering by the overall PC structure (Figure S2). So, for NAA-μCVs produced at t_{An} = 5, 10, and 15 h, the resonance band is almost vanished from the transmission spectrum at t_{pw} = 6 min. To further extend the analysis on the effect of t_{An} on the optical properties of NAA-μCVs produced by ASPA, we fabricated another set of NAA-μCVs under the same conditions (i.e., J_{offset} = 0.280 mA cm^{-2}, ΔA_J = 0.210 mA cm^{-2}, and t_{An} = 5, 10, 15, 20, and 25 h) but setting the anodization period at T_P = 1200 s. Figure 3b shows representative anodization profiles of these NAA-μCVs produced at T_P = 1200 s, showing how the anodizing current density (input) is directly translated into voltage (output) changes in a dynamic fashion, without apparent delay. Parts a–e of Figure 6 show the transmission spectra of NAA-μCVs produced with T_P = 1200 s, which also include digital pictures displaying the characteristic interferometric color of these PC structures. As these graphs indicate, the PSB of these NAA-μCVs is located within the vis–NIR region of the spectrum, although slightly blue-shifted compared to their T_P = 1300 s counterparts. As demonstrated in previous studies, this blue shift is associated with the reduction of the anodization period, which results in a shorter period length (L_{TP}) within the nanoporous structure of NAA-μCVs.[43−59] The transmission

DOI: 10.1021/acsanm.8b00494
ACS Appl. Nano Mater. 2018, 1, 4418−4434

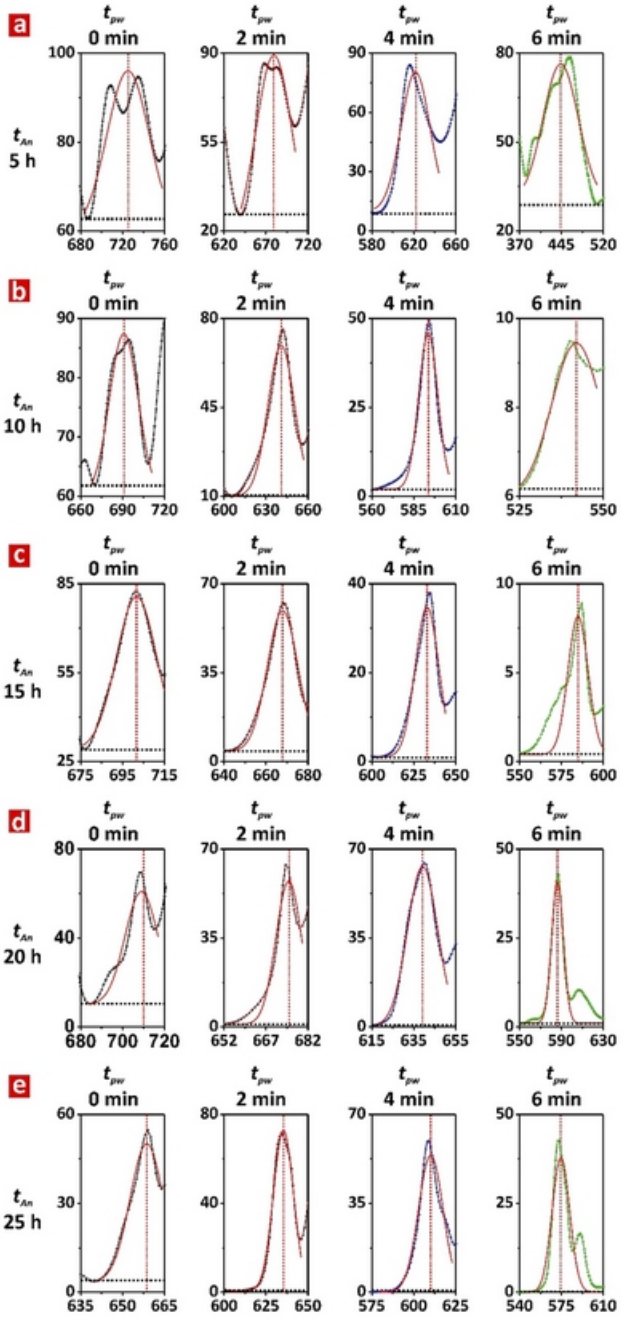

Figure 5. Combinational effect of the anodization time (t_{An}) and pore-widening time (t_{pw}) on the resonance band of NAA-μCVs produced by ASPA at T_P = 1300 s [note: horizontal dotted black lines denote the baseline (y_0) used for the Gaussian fittings, which correspond to the lower lobe of the PSB, and vertical dotted red lines indicate the central wavelength of the resonance band (λ_R) and the symmetry of the Gaussian fitting]: (a) t_{An} = 5; (b) t_{An} = 10; (c) t_{An} = 15; (d) t_{An} = 20; (e) t_{An} = 25 h.

spectra of these NAA-μCVs display a PSB that increases its intensity with t_{pw} and a well-defined resonance band at the center of the PSB. Parts a–e of Figure 7 compile magnified views of the resonance bands observed in the transmission spectra of these NAA-μCVs (Figure 6a–e), with details of the Gaussian fittings used to estimate λ_R, fwhm$_R$, and Q_C.

The quality factor (Q_C), defined as the ratio of the resonance band wavelength (λ_R) to its full width at half-maximum (fwhm$_R$; eq 5), is an important criteria in assessing the strength of photon confinement within optical μCVs.[64,65] The Q_C values of these NAA-μCVs were estimated by fitting the resonance bands shown in Figures 5 and 7 to Gaussian envelopes, using as a baseline the lower lobe of the PSB, as indicated by the horizontal dotted black lines shown in these graphs.

A summary of the estimated values of y_0, λ_R, fwhm$_R$, and Q_C is compiled in Tables S1–S3 along with the quality (R^2) of these Gaussian fittings. Figure 8 shows contour maps summarizing the dependence of Q_C and λ_R with t_{An} and t_{pw} for NAA-μCVs produced with T_P = 1200 and 1300 s, J_{offset} = 0.280 mA cm^{-2}, and ΔA_J = 0.210 mA cm^{-2}. Figure 8a shows the dependence of Q_C on t_{An} and t_{pw} for NAA-μCVs fabricated with T_P = 1300 s. It is apparent that Q_C becomes more dependent on these fabrication parameters at short pore-widening times (i.e., from t_{pw} = 0 to 2 min) and longer anodization times (i.e., from t_{An} = 15 to 25 h). This trend is denoted by a closer and denser concentration of color fields around the Q_C maximum (i.e., Q_C = 63.1 ± 1.2), which is located at t_{pw} = 2 min and t_{An} = 20 h. In general, an increase in t_{An} leads to an enhancement of Q_C of NAA-μCVs, while longer pore-widening times worsen the quality factor of the NAA-μCVs. The relationship between λ_R with t_{An} and t_{pw} for NAA-μCVs produced with T_P = 1300 s is displayed in Figure 8b, where it can be clearly observed that the distance between the color fields gets closer as t_{An} is reduced from 10 to 5 h. This indicates a strong dependence of λ_R with t_{An} at shorter anodization times. Furthermore, it is observed that λ_R is blue-shifted with t_{pw} across the UV–vis spectrum from t_{An} = 5 to 25 h. This analysis also reveals that the effect of t_{An} on the position of the resonance band is not as significant as that of t_{pw} because only a slight red shift is observed as t_{An} increases from 5 to 20 h and a slight blue shift from 20 to 25 h, achieving its maximum value (i.e., 725 ± 1 nm) at t_{An} = 5 h and t_{pw} = 0 min. The distribution of Q_C and λ_R for NAA-μCVs produced at T_P = 1200 s with t_{An} and t_{pw} is presented in parts c and d of Figure 8, respectively. The contour map shown in Figure 8c reveals a concentration of the color fields at the region of longer t_{An} and shorter t_{pw}, achieving a local maximum of Q_C (i.e., 112.6 ± 5.2) at t_{An} = 20 h and t_{pw} = 2 min, which is the highest quality factor reported for a NAA-μCV to date.

The distance between the field lines around the local maximum is shorter, indicating a stronger dependence of Q_C on t_{An} and t_{pw} around that set of fabrication conditions. In contrast, the combination of shorter t_{An} (i.e., 5–15 h) and longer t_{pw} (i.e., 4–6 min) worsens Q_C because the distance between the field lines and color fields is relatively broad at these areas. Figure 8d shows how t_{An} and t_{pw} affect λ_R of NAA-μCVs produced at T_P = 1200 s. This graph denotes a homogeneous but broad distribution of color fields with equidistant field lines throughout, from t_{An} = 5 to 25 h and from t_{pw} = 0 to 4 min, which indicates a weak dependence of λ_R on t_{An} and t_{pw} at these combinations of fabrication parameters. As t_{pw} increases from 4 to 6 min and t_{An} decreases from 10 to 5 h, λ_R shows a stronger dependence with these parameters, as suggested by the closer field lines and high density of the color fields. λ_R is red-shifted as t_{An} increases from 5 to 20 h and slightly blue-shifted when t_{An} increases from 20 to 25 h. The maximum value of λ_R (i.e., 665 ± 1 nm) is achieved at t_{An} = 20 h and t_{pw} = 2 min. Furthermore, this

DOI: 10.1021/acsanm.8b00494
ACS Appl. Nano Mater. 2018, 1, 4418–4434

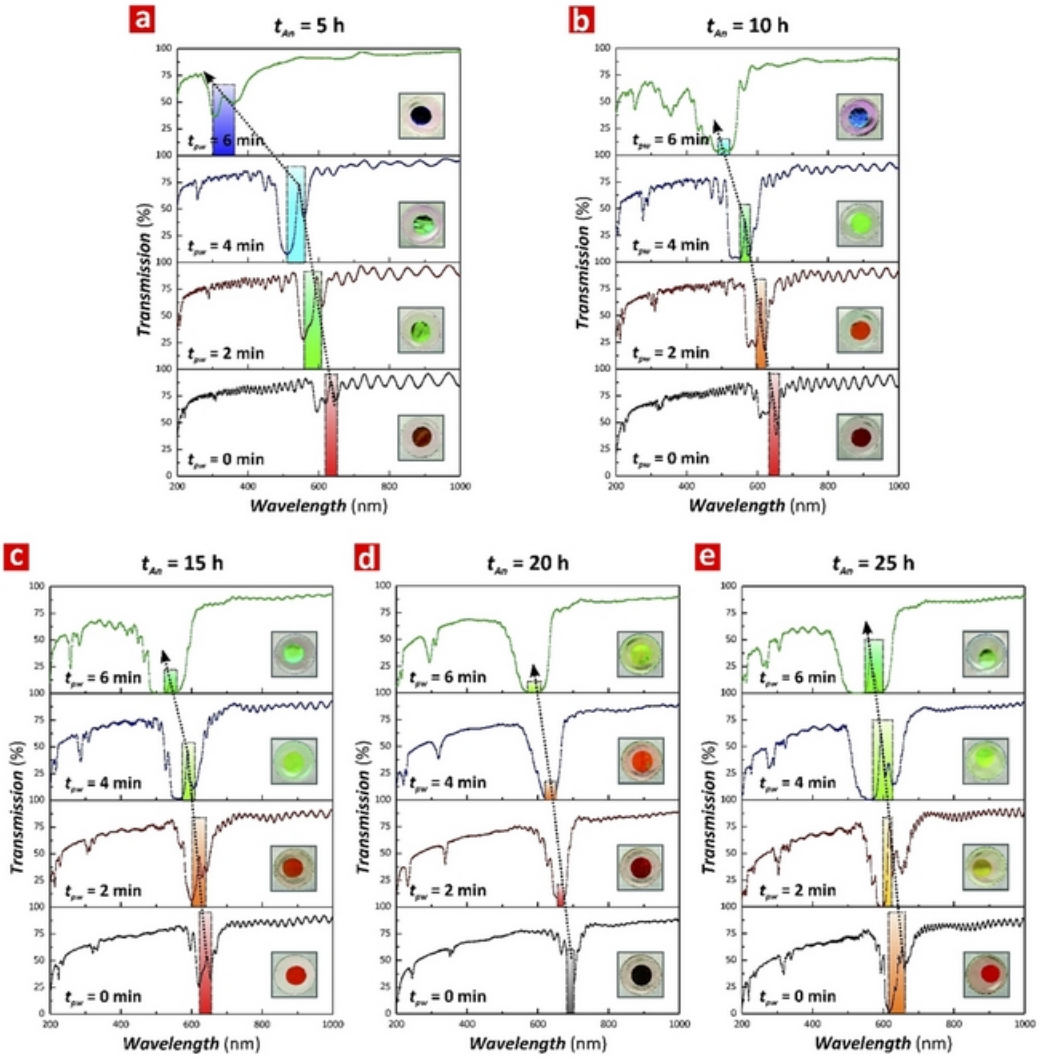

Figure 6. Combinational effect of the anodization time (t_{An}) and pore-widening time (t_{pw}) on the transmission spectrum of NAA-μCVs produced by ASPA at T_P = 1200 s (note: color rectangles denote the approximate position of the resonance band within the PSB, and black dotted arrow lines indicate the blue shift of the resonance bands with t_{pw}): (a) t_{An} = 5; (b) t_{An} = 10; (c) t_{An} = 15; (d) t_{An} = 20; (e) t_{An} = 25 h. The insets in parts a–e display digital pictures of these PC structures showing vivid interferometric colors when the resonance band is located within the visible region and transparent when the band is within the UV or NIR spectral regions.

analysis also reveals that t_{pw} blue-shifts the resonance band of NAA-μCVs produced at T_P = 1200 s as t_{pw} increases. The comparative analysis of Figure 8a,c reveals that a combination of long t_{An} (i.e., from 15 to 25 h) and short t_{pw} (i.e., from 0 to 2 min) results in high-quality NAA-μCVs with narrow and well-resolved resonance bands. The average Q_C values estimated for NAA-μCVs produced with T_P = 1200 and 1300 s were 46.4 ± 24.8 and 33.7 ± 13.8, respectively. It is worthwhile noting that only one of the NAA-μCVs produced at 1300 s showed a light-confining performance superior to those reported in previous studies (i.e., Q_C = 63.1 ± 1.2 for NAA-μCVs produced with T_P = 1300 s, t_{pw} = 2 min, and t_{An} = 20 h; Wang et al. (~24),[38] Lee et al. (~55);[37] and Yan et al. (~45)[41]). However, up to six NAA-μCVs produced with T_P = 1200 s showed superior properties to confine light than previously produced NAA-μCVs (i.e., Q_C = 64.0 ± 1.0 at t_{pw} = 2 min, and t_{An} = 10 h; Q_C = 70.5 ± 2.1 at t_{pw} = 4 min, and t_{An} = 10 h; Q_C = 66.0 ± 1.3 at t_{pw} = 6 min, and t_{An} = 15 h; Q_C = 75.2 ± 3.1 at t_{pw} = 0 min, and t_{An} = 20 h; Q_C = 112.6 ± 5.2 at t_{pw} = 2 min, and t_{An} = 20 h; Q_C = 73.5 ± 2.6 at t_{pw} = 4 min, and t_{An} = 20 h). Although both types of NAA-μCVs have a weak correlation between the shift in λ_R with t_{An}, parts b and d of Figure 8 show that λ_R of NAA-μCVs produced at T_P = 1300 s evolves in a slightly different manner with t_{An} compared to NAA-μCVs fabricated at T_P = 1200 s. This graph also indicates that, as observed in the transmission spectra (Figures 4 and 6), the positions of the PSB and resonance bands of NAA-μCVs produced at T_P = 1200 s are blue-shifted compared to those of their equivalent NAA-μCVs fabricated at T_P = 1300 s. It is also observed that both sets of NAA-μCVs show a stronger dependence of λ_R with t_{pw} than that shown for t_{An}. A pore-widening treatment blue-shifts the positions of the respective resonance bands, and the longer t_{pw} is, the shorter the wavelength where the resonance band is positioned at. It is worthwhile to note that, for a given t_{pw}, the position of the resonance band of NAA-μCVs at T_P = 1300 s is located at longer wavelengths than that of NAA-μCVs produced with T_P = 1200 s due to the red shift associated with the longer anodization period and longer

DOI: 10.1021/acsanm.8b00494
ACS Appl. Nano Mater. 2018, 1, 4418–4434

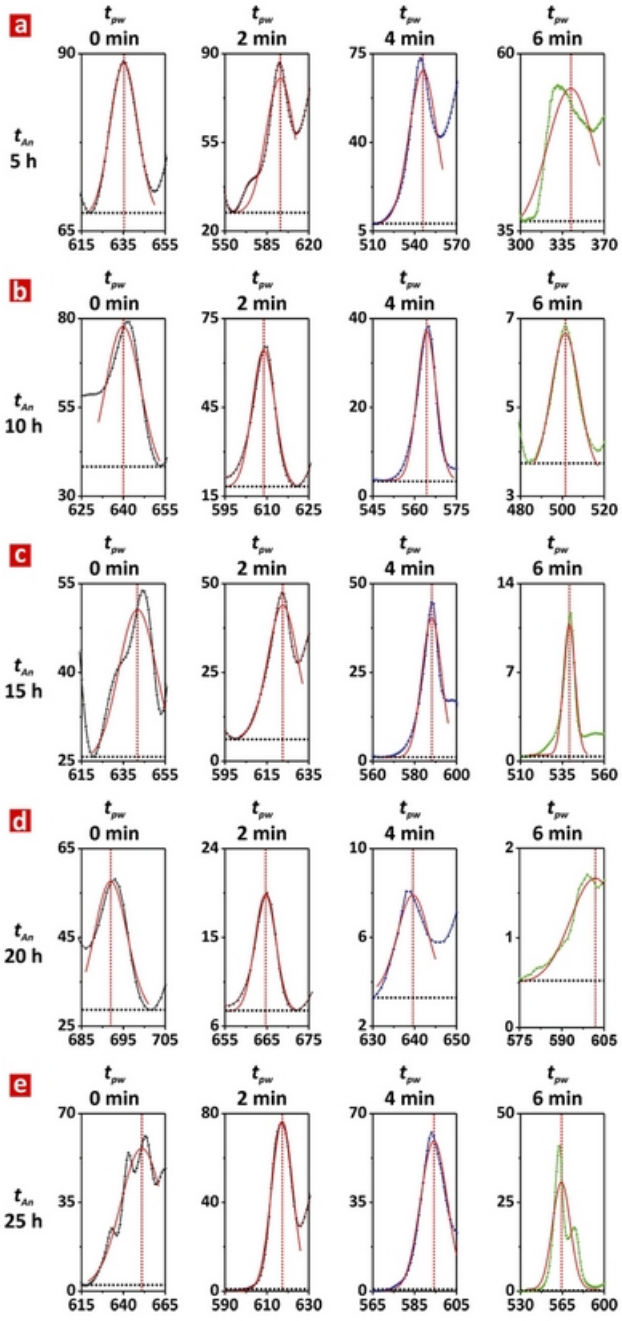

Figure 7. Combinational effect of the anodization time (t_{An}) and pore-widening time (t_{pw}) on the resonance band of NAA-μCVs produced by ASPA at T_P = 1200 s [note: horizontal dotted black lines denote the baseline (y_0) used for the Gaussian fittings, which correspond to the lower lobe of the PSB, and vertical dotted red lines indicate the central wavelength of the resonance band (λ_R) and the symmetry of the Gaussian fitting]: (a) t_{An} = 5; (b) t_{An} = 10; (c) t_{An} = 15; (d) t_{An} = 20; (e) t_{An} = 25 h.

period length. Another interesting optical property of NAA-μCVs is their vivid interferometric colors, which correspond to the wavelengths of their respective PSB and λ_R when these are positioned within the visible range of the spectrum. Parts e and f of Figure 8 compile digital images of NAA-μCVs produced at T_P = 1200 and 1300 s as a function of t_{An} and t_{pw}, respectively. The analysis of these images is in good agreement with the results obtained in Figure 8b,d, where λ_R is blue-shifted with t_{pw}. It is also apparent that λ_R is red-shifted with increasing t_{An} from 5 to 20 h and slightly blue-shifted from t_{An} = 20 to 25 h.

3.3. Effect of the Anodization Period (T_P) on the Optical Properties of NAA-μCVs. To demonstrate the tunability of the position of the resonance band across the spectral regions and to further optimize the quality of NAA-μCVs produced by ASPA, we produced a set of NAA-μCVs with different T_P, where this fabrication parameter was systematically modified from 800 to 1300 s with ΔT_P = 100 s while J_{offset} and ΔA_J remained at 0.280 and 0.210 mA cm^{-2}, respectively. The anodization profiles and transmission spectra of these NAA-μCVs are shown in Figures S3 and 9, respectively. Parts a–d of Figure 9 show the transmission spectra of these NAA-μCVs as a function of T_P and t_{pw} (i.e., from 0 to 6 min), and Figure 10 shows magnified views of the resonance bands and Gaussian fittings used to estimate λ_R, fwhm$_R$, and Q_C. In all of these cases, it is verified that the PSB and resonance band of these NAA-μCVs are red-shifted with T_P and blue-shifted with t_{pw}. Note that the NAA-μCVs produced with T_P > 800 s also showed second- and third-order PSBs. NAA-μCVs fabricated with T_P = 900 s have both first- and second-order PSBs, while NAA-μCVs produced at T_P = 1000, 1100, 1200, and 1300 s show second- and third-order PSBs. However, the first-order PSB plays the primary role in determining the optical properties of NAA-μCVs because this band is much more intense and well-resolved than their higher-order counterparts. At t_{pw} = 0 min (Figure 9a), all NAA-μCVs display a weak resonance band within their first-order PSBs, which is in the range of 400–700 nm and red-shifted with T_P. As T_P increases, the intensity of the resonance band increases and shifts its position (λ_R) toward the NIR spectral region. As the digital pictures shown in Figure 9a–d (insets) indicate, for a given t_{pw}, the interferometric color of these NAA-μCVs is red-shifted with T_P. For instance, at t_{pw} = 0 min, the interferometric color of NAA-μCVs changes from transparent (i.e., UV region) (T_P = 800 s) to blue (T_P = 900 s) to green (T_P = 1000 s) to orange (T_P = 1100 s) to transparent (i.e., NIR region) (T_P = 1200 and 1300 s) as T_P increases. It is also verified that the resonance band increases its intensity, and it is blue-shifted with a pore-widening treatment (i.e., t_{pw} increases), which is in good agreement with our previous observation.

Parts e and f of Figure 10 show contour maps depicting the graphical correlation of Q_C and λ_R of NAA-μCVs with T_P and t_{pw} (Table S2). Figure 10e reveals that the color fields in the region of shorter T_P (i.e., from 800 to 1000 s) are relatively broad across t_{pw}, from 0 to 6 min, which is a visual indication of the weak correlation of Q_C with the fabrication parameters for NAA-μCVs produced at shorter T_P. Therefore, NAA-μCVs produced at T_P = 800, 900, and 1000 s have low Q_C. In contrast, the color fields become denser with closer field lines when T_P increases from 1100 to 1300 s. This suggests that Q_C has a stronger dependence with longer T_P, where the maximum of Q_C (i.e., 112.6 ± 5.2) is achieved at T_P = 1200 s and t_{pw} = 2 min. The average Q_C estimated for NAA-μCVs as a function of T_P, excluding those PCs without resonance bands, was 44.5 ± 23.1. However, seven of these NAA-μCVs showed a light-confining performance superior to those reported in previous studies (i.e., Q_C = 56.8 ± 3.2 at T_P = 900 s and t_{pw} = 4 min, Q_C = 60.2 ± 2.1 at T_P = 1000 s and t_{pw} = 0 min, Q_C = 56.5 ± 1.5 at T_P = 1100 s and t_{pw} = 2 min, Q_C = 75.2 ± 3.3 at T_P = 1200 s and t_{pw} = 0 min, Q_C = 112.6 ± 5.2 at

DOI: 10.1021/acsanm.8b00494
ACS Appl. Nano Mater. 2018, 1, 4418–4434

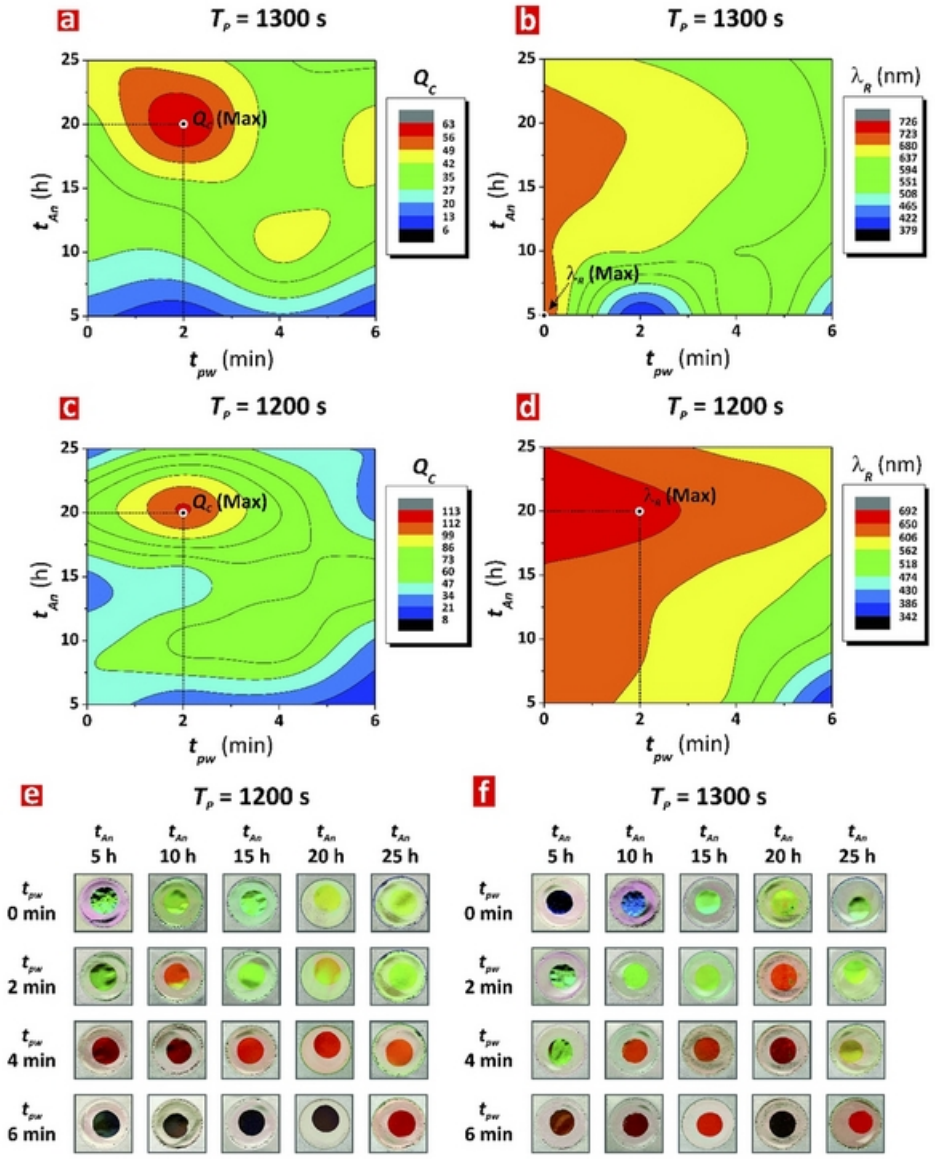

Figure 8. Combinational effect of the anodization time (t_{An}) and pore-widening time (t_{pw}) on the optical properties of NAA-μCVs (i.e., quality factor, Q_C; position of the resonance band, λ_R; interferometric color) produced by ASPA. (a) Contour map showing the dependence of Q_C with t_{An} and t_{pw} for NAA-μCVs produced with T_P = 1300 s. (b) Contour map showing the dependence of λ_R with t_{An} and t_{pw} for NAA-μCVs produced with T_P = 1300 s. (c) Contour map showing the dependency of Q_C with t_{An} and t_{pw} for NAA-μCVs produced with T_P = 1200 s. (d) Contour map showing the dependence of λ_R with t_{An} and t_{pw} for NAA-μCVs produced with T_P = 1200 s. (e) Digital images showing the interferometric color displayed by NAA-μCVs produced with T_P = 1200 s as a function of t_{An} and t_{pw}. (f) Digital images showing the interferometric color displayed by NAA-μCVs produced with T_P = 1300 s as a function of t_{An} and t_{pw}.

T_P = 1200 s and t_{pw} = 2 min, Q_C = 73.5 ± 4.1 at T_P = 1200 s and t_{pw} = 4 min, and Q_C = 63.1 ± 1.2 at T_P = 1300 s and t_{pw} = 2 min). The distribution of λ_R as a function of T_P and t_{pw} is depicted in Figure 10f. This graph shows two local minima in the contour plot due to the absence of resonance bands within the PSB of these NAA-μCVs, which are located at t_{pw} = 0 min for T_P = 1100 s as well as at t_{pw} = 6 min for T_P = 800 s. At t_{pw} = 2 and 4 min, the color distribution reveals a red shift in λ_R resulting from the manipulation of T_P from 800 to 1300 s, where the longest resonance wavelength is achieved at T_P = 1300 s and t_{pw} = 0 min (i.e., 709 ± 1 nm). In general, the longer the anodization period, the longer the wavelength at which NAA-μCVs confine light. This analysis also indicates that an increase in t_{pw} results in a blue shift of λ_R; thus, NAA-μCVs confine light of shorter wavelengths although in a less efficient manner, as indicated by the Q_C analysis shown in Figure 10e, due to a light-scattering effect.

3.4. Effect of the Current Density Offset (J_{offset}) on the Optical Properties of NAA-μCVs. To further understand the effect of the different fabrication parameters on the photonic features of NAA-μCVs produced by ASPA, we investigated how the current density offset (J_{offset}) affects the quality factor and the tuning of resonance bands of NAA-μCVs. To this end, J_{offset} was systematically modified from 0.140 to 0.560 mA cm^{-2} with an interval of 0.140 mA cm^{-2} while the rest of fabrication parameters remained the same (i.e., T_P = 1300 s, J_{offset} = 0.280 mA cm^{-2}, and ΔA_J = 0.210 mA cm^{-2}). The anodization profiles of NAA-μCVs produced at different J_{offset} values are

DOI: 10.1021/acsanm.8b00494
ACS Appl. Nano Mater. 2018, 1, 4418−4434

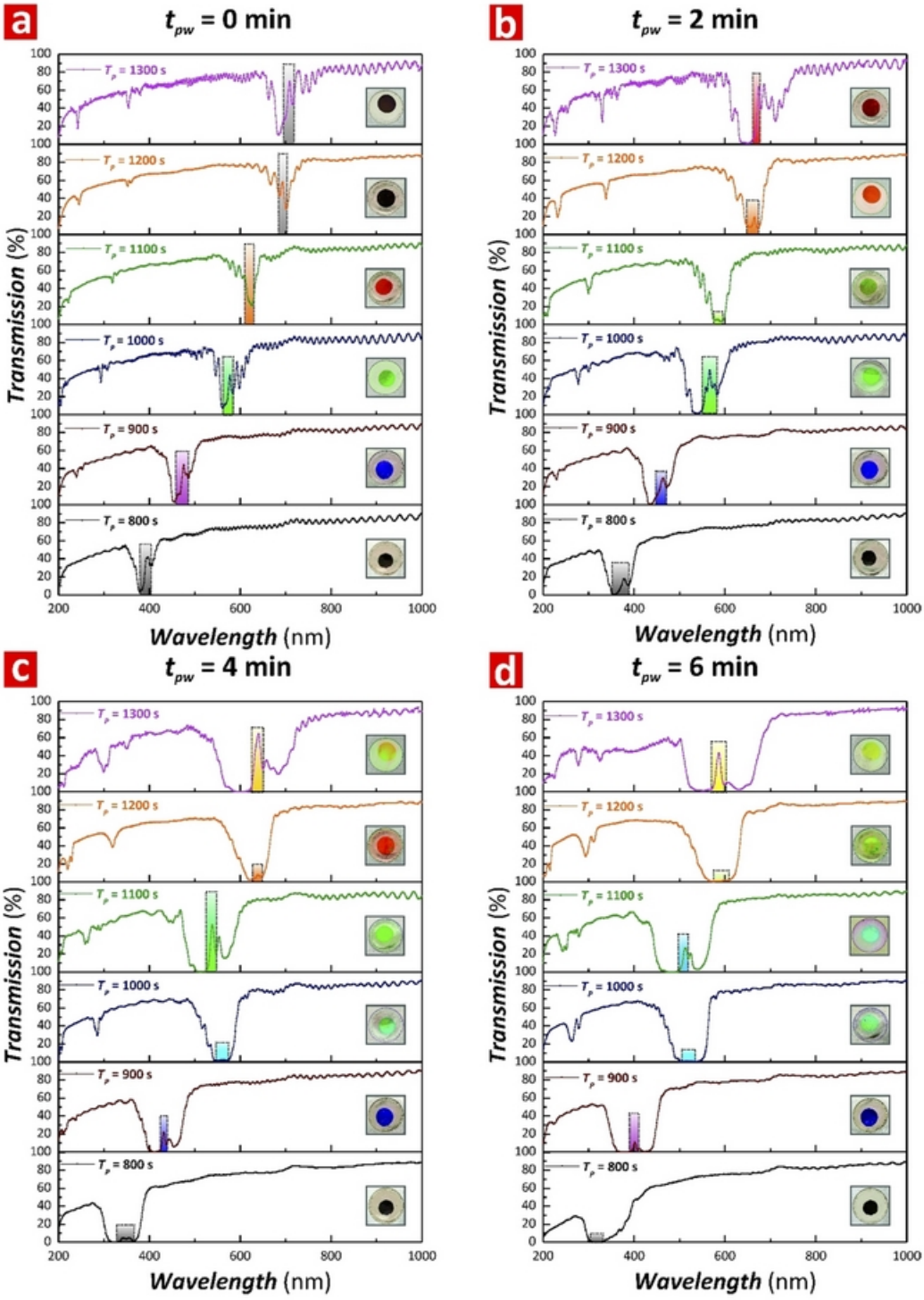

Figure 9. Combinational effect of the anodization period (T_P) and pore-widening time (t_{pw}) on the optical properties of NAA-μCVs (i.e., quality factor Q_C; position of the resonance band λ_R; interferometric color) produced by ASPA. Transmission spectra showing the position of the resonance band (colored rectangles) and digital pictures (insets) of NAA-μCVs for each anodization period (T_P = 800−1300 s) at different pore-widening times [i.e., (a) t_{pw} = 0 min, (b) t_{pw} = 2 min, (c) t_{pw} = 4 min, and (d) t_{pw} = 6 min].

compiled in Figure S4. The transmission spectra of these NAA-μCVs shown in Figure 11a−d were analyzed to establish the effect of this fabrication parameter on Q_C and λ_R. Figure 11a shows the transmission spectra of NAA-μCVs produced at J_{offset} = 0.140 mA cm^{-2} as a function of t_{pw} (i.e., 0 to 6 min). The PSB of this set of NAA-μCVs is located within the visible region, with a very weak resonance band that is almost vanished at long pore-widening times (i.e., t_{pw} > 2 min). The pore-widening treatment blue-shifts the position of the PSB and causes the NAA-μCV to lose its light-confining characteristics. The transmission spectra shown in Figure 11b reveal that the positions of the PSBs of NAA-μCVs produced at J_{offset} =

DOI: 10.1021/acsanm.8b00494
ACS Appl. Nano Mater. 2018, 1, 4418−4434

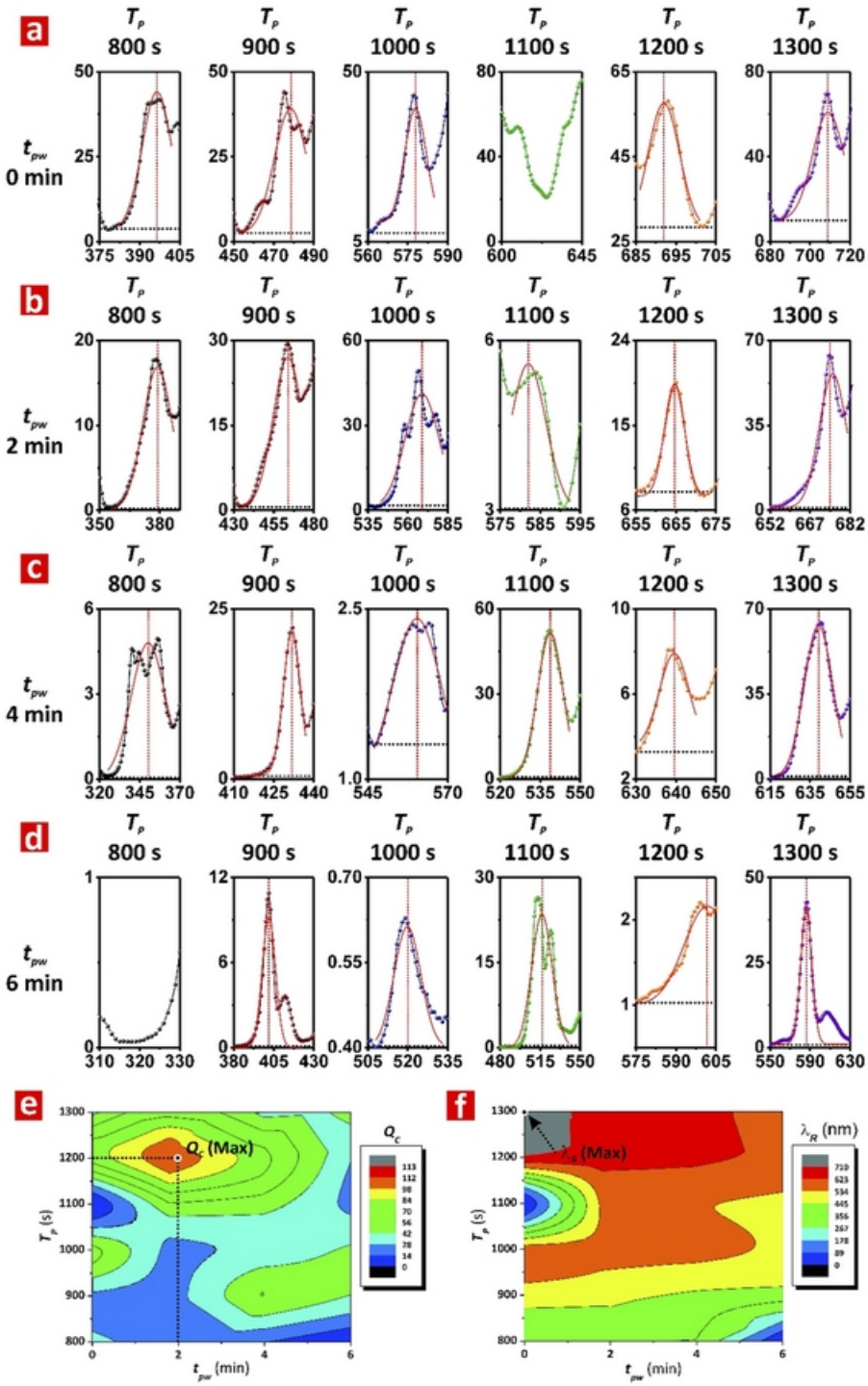

Figure 10. Combinational effect of the anodization period (T_p) and pore-widening time (t_{pw}) on the resonance band of NAA-μCVs produced by ASPA [note: horizontal dotted black lines denote the baseline (y_0) used for the Gaussian fittings, which correspond to the lower lobe of the PSB, and vertical dotted red lines indicate the central wavelength of the resonance band (λ_R) and the symmetry of the Gaussian fitting]: (a) t_{pw} = 0 min; (b) t_{pw} = 2 min; (c) t_{pw} = 4 min; (d) t_{pw} = 6 min. (e) Contour map showing the dependence of Q_C with T_p and t_{pw} for NAA-μCVs produced with T_p = 800−1300 s. (f) Contour map showing the dependence of λ_R with T_p and t_{pw} for NAA-μCVs produced with T_p = 800−1300 s.

0.280 mA cm^{-2} are located within the upper range of the visible spectrum (i.e., 600−800 nm). Unlike NAA-μCVs produced at J_{offset} = 0.140 mA cm^{-2}, the resonance bands of these NAA-μCVs (J_{offset} = 0.280 mA cm^{-2}) remain well-resolved and sharp after pore widening from 0 to 6 min. On the other hand, both sets of NAA-μCVs produced at J_{offset} = 0.420 and 0.560 mA cm^{-2} have their PSBs located in the NIR range (i.e., 900−1100 nm; Figure 11c,d). These NAA-μCVs also show the presence of an intense resonance band within their PSB, which is slightly widened and blue-shifted with the pore-widening treatment, from 0 to 6 min.

DOI: 10.1021/acsanm.8b00494
ACS Appl. Nano Mater. 2018, 1, 4418−4434

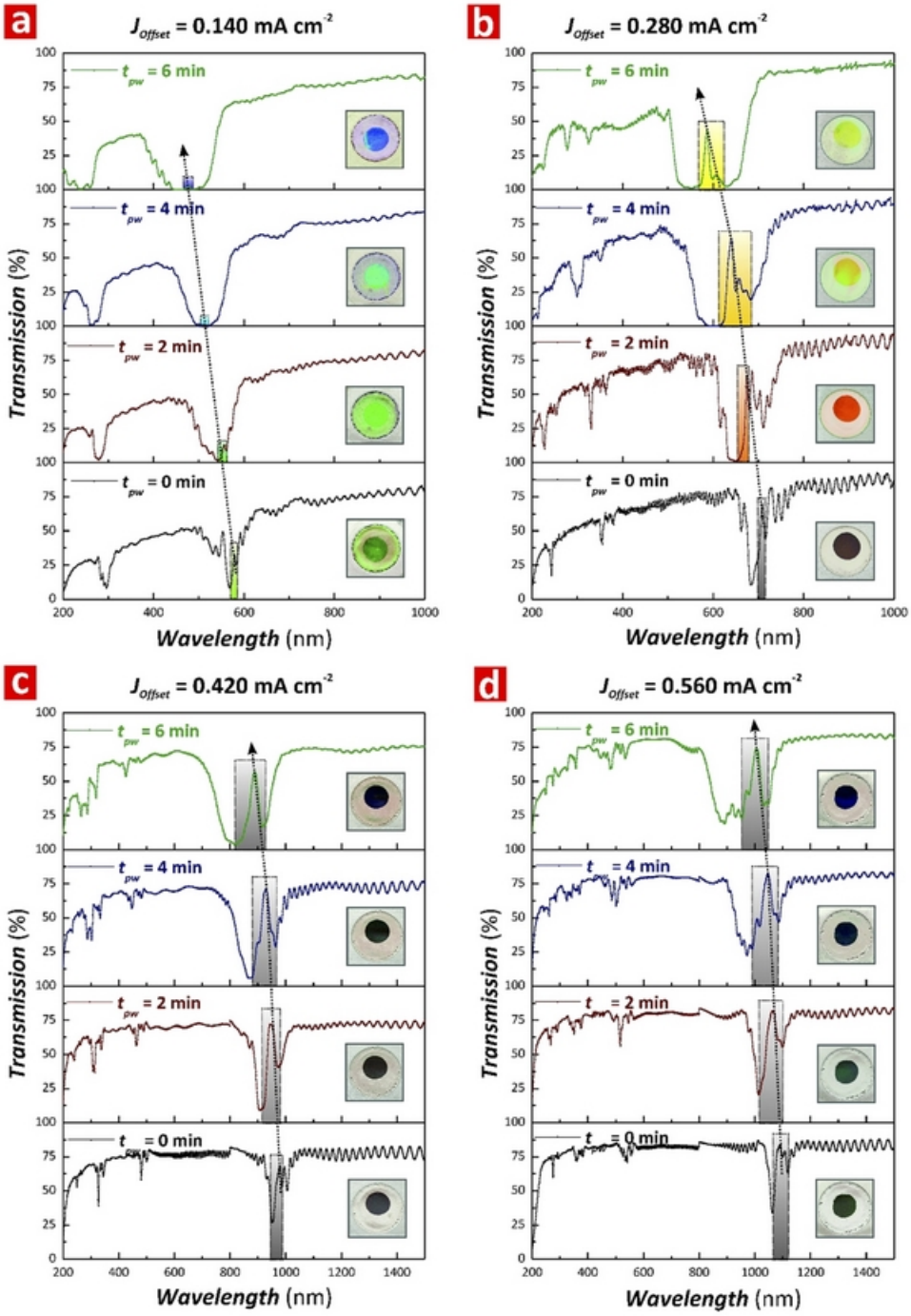

Figure 11. Combinational effect of the anodization offset (J_{offset}) and pore-widening time (t_{pw}) on the optical properties of NAA-μCVs (i.e., quality factor, Q_C; position of the resonance band, λ_R; interferometric color) produced by ASPA. Transmission spectra showing the position of the resonance band, digital pictures (insets) of NAA-μCVs for each anodization offset (J_{offset} = 0.140–0.560 mA cm^{-2}) at different pore-widening times (from 0 to 6 min) [i.e., (a) J_{offset} = 0.140 mA cm^{-2}, (b) J_{offset} = 0.280 mA cm^{-2}, (c) J_{offset} = 0.420 mA cm^{-2}, and (d) J_{offset} = 0.560 mA cm^{-2}] (note: color rectangles denote the approximate position of the resonance band within the PSB, and black dotted arrow lines indicate the blue shift of the resonance bands with t_{pw}).

By a comparison of the transmission spectra at different J_{offset} values, it is apparent that an increase in J_{offset} causes a red shift in the position of the resonance band. As the digital images shown in the insets in Figure 11a–d demonstrate, these NAA-μCVs display vivid interferometric colors, which are affected by the fabrication parameters: J_{offset} and t_{pw}. Although these NAA-μCVs show second- and third-order PSBs, the color displayed by these PCs corresponds to the wavelength at which the first-order PSB is located, denoting a more efficient reflection of light within these spectral regions. In this case, NAA-μCVs produced at lower J_{offset} (i.e., 0.140 and 0.280 mA cm^{-2}) display vivid colors, corresponding to the positions of their PSBs in the visible spectral range. In contrast, the PSBs of NAA-μCVs produced with high J_{offset} (i.e., 0.420 and 0.560 mA

DOI: 10.1021/acsanm.8b00494
ACS Appl. Nano Mater. 2018, 1, 4418–4434

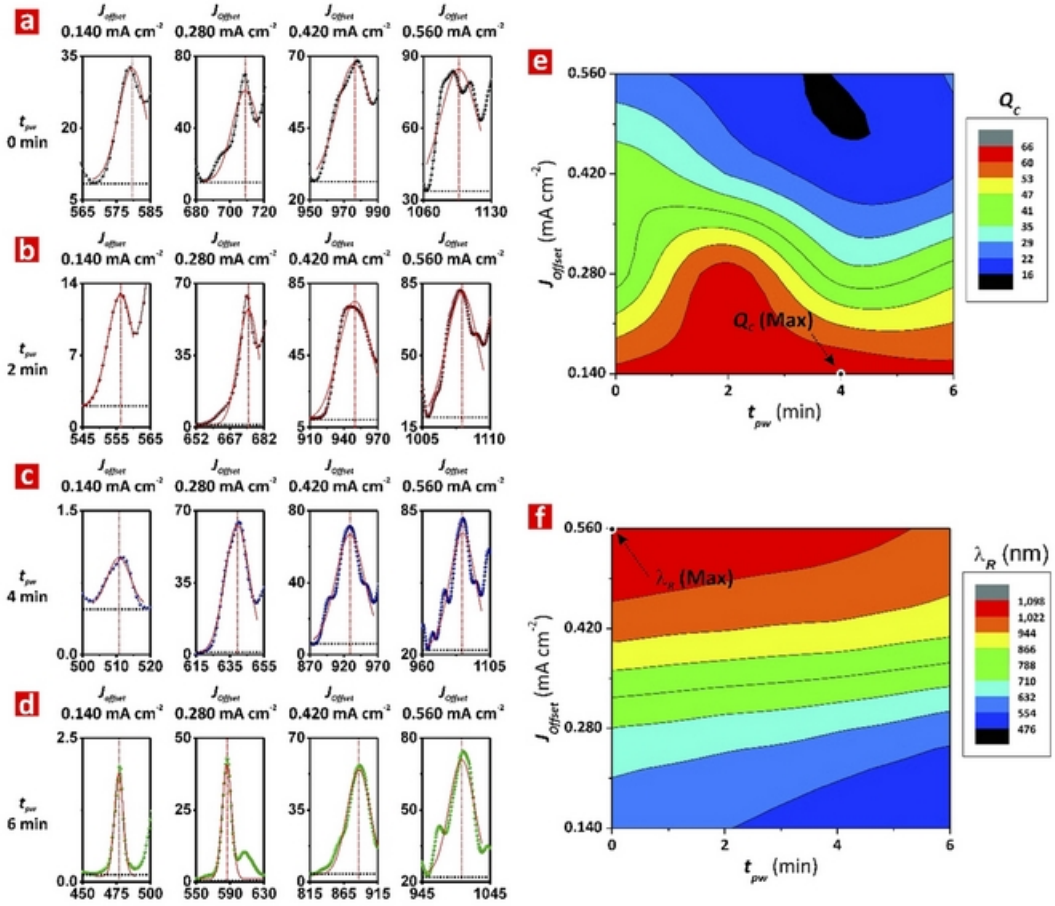

Figure 12. Combinational effect of the current density offset (J_{offset}) and pore-widening time (t_{pw}) on the resonance band of NAA-μCVs produced by ASPA [note: horizontal dotted black lines denote the baseline (y_0) used for the Gaussian fittings, which correspond to the lower lobe of the PSB, and vertical dotted red lines indicate the central wavelength of the resonance band (λ_R) and the symmetry of the Gaussian fitting]: (a) J_{offset} = 0.140 mA cm^{-2}; (b) J_{offset} = 0.280 mA cm^{-2}; (c) J_{offset} = 0.420 mA cm^{-2}; (d) J_{offset} = 0.560 mA cm^{-2}. (e) Contour map showing the dependence of Q_C with J_{offset} and t_{pw} for NAA-μCVs produced with J_{offset} = 0.140−0.560 mA cm^{-2}. (f) Contour map showing the dependence of λ_R with J_{offset} and t_{pw} for NAA-μCVs produced with J_{offset} = 0.140−0.560 mA cm^{-2}.

cm^{-2}) are within the NIR range; thus, no color is observed (i.e., transparent, black). Parts a−d of Figure 12 show magnified views of the resonance bands and Gaussian fittings used to estimate λ_R, fwhm$_R$, and Q_C for these NAA-μCVs, and parts e and f of Figure 12 compile a summary of the estimated values for Q_C and λ_R in the form of contour maps. The visual analysis of the magnified resonance bands shown in Figure 12a−d reveals that, in general, the intensity of the resonance band increases with J_{offset} and decreases with t_{pw}. A closer analysis of the values of Q_C, visually shown in Figure 12e and compiled in Table S3, reveals that the combination of low values of J_{offset} (e.g., 0.140−0.280 mA cm^{-2}) and moderate pore-widening times (i.e., 2−4 min) is favorable in the production of NAA-μCVs with high-quality resonance bands. The Q_C maximum is achieved by NAA-μCVs produced with J_{offset} = 0.140 mA cm^{-2} and t_{pw} = 4 min (i.e., 65.5 ± 2.3), although these PC structures show considerably weaker resonance bands compared to their counterparts produced at higher J_{offset} (i.e., >0.140 mA cm^{-2}). The dependence of Q_C on J_{offset} increases within the range of 0.140−0.420 mA cm^{-2}, as denoted by the denser color fields with a short distance between the adjacent field lines.

The broad color fields and more separated field lines at the region of high J_{offset} and long t_{pw} suggest a weak dependence of Q_C with these combinations of fabrication parameters, which worsens the quality of the μCV structure. The average Q_C estimated for NAA-μCVs as a function of J_{offset} was 39.1 ± 18.4, and five of these NAA-μCVs showed a light-confining performance slightly superior to those reported in previous studies (i.e., Q_C = 61.7 ± 2.2 at J_{offset} = 0.140 mA cm^{-2} and t_{pw} = 0 min, Q_C = 62.5 ± 3.4 at J_{offset} = 0.140 mA cm^{-2} and t_{pw} = 2 min, Q_C = 65.5 ± 3.6 at J_{offset} = 0.140 mA cm^{-2} and t_{pw} = 4 min, Q_C = 61.9 ± 2.4 at J_{offset} = 0.140 mA cm^{-2} and t_{pw} = 6 min, and Q_C = 63.1 ± 1.2 at J_{offset} = 0.280 mA cm^{-2} and t_{pw} = 2 min). The effect of J_{offset} and t_{pw} on the position of the resonance band of NAA-μCVs is summarized in the contour map shown in Figure 12f. This contour map shows that the field-line distances at low J_{offset} (i.e., J_{offset} < 0.280 mA cm^{-2}) and high J_{offset} (i.e., J_{offset} > 0.420 mA cm^{-2}) are relatively wide. However, the color fields become closer with shorter equidistant field lines for J_{offset} between 0.280 and 0.420 mA cm^{-2}, which indicates a stronger dependence of λ_R with J_{offset} within that range of fabrication parameters. It is verified that λ_R is red-shifted toward the NIR region by increasing J_{offset}. The higher J_{offset} is, the longer the wavelength at which light is confined within the structure of NAA-μCVs produced by ASPA. The maximum value of λ_R (i.e., 1096 ± 1 nm) is located at J_{offset} = 0.560 mA cm^{-2} and t_{pw} = 0 min. An increase in t_{pw}

DOI: 10.1021/acsanm.8b00494
ACS Appl. Nano Mater. 2018, 1, 4418−4434

has an effect opposite to that of J_{offset} on the shifting of λ_R. However, J_{offset} has a more significant effect on the position of the resonance band as denoted by the color-field distribution.

4. CONCLUSIONS

In summary, this study has demonstrated that a rational design of the nanoporous structure of NAA-μCVs using ASPA can lead to an enhancement of the light-confining capabilities of these PCs. The structure of these optical μCVs is composed of two apodized NAA-DBRs, which can confine light efficiently (i.e., $Q_C = 112.6 \pm 5.2$). Furthermore, this nanofabrication approach enables the fine-tuning of the optical properties of the two highly reflective mirrors so that light can be confined within the PC structure more efficiently across the spectral regions. The optical properties of NAA-μCVs were assessed in terms of the quality factor, position of the resonance band, and interferometric colors. The anodization parameters investigated were the anodization period, anodization time, current density offset, and pore-widening time. A systematic modification of these parameters allowed one to establish optimization paths toward more efficient light-confining NAA-based PC structures.

In general, our study established that a combination of longer anodization time, longer anodization period, short pore-widening time, and moderate current density offset generates optical μCVs with a high-quality factor, where the most optimal NAA-μCV was that produced with a 20 h anodization time, a 1200 s anodization period, 2 min of pore widening, and 0.280 mA cm^{-2} of current density offset. Our results provide a better understanding and solid foundation to further enhance the light-confining capabilities of NAA-μCVs, opening new opportunities for further fundamental and applied research for these nanoporous PC structures in optical sensing, photonics, and optoelectronics.

■ ASSOCIATED CONTENT

Supporting Information

The Supporting Information is available free of charge on the ACS Publications website at DOI: 10.1021/acsanm.8b00494.

Information about the structure of NAA-μCVs at different pore-widening times, anodization profiles of NAA-μCVs produced by ASPA at different anodization periods, from 800 to 1300 s, and current density offsets, from 0.140 to 0.560 mA cm^{-2}, and a compilation of the values of y_0, λ_R, fwhm$_R$, Q_C, and R^2 (PDF)

■ AUTHOR INFORMATION

Corresponding Authors

*E-mail: andrew.abell@adelaide.edu.au (A.D.A.). Phone: + 61 8 8313 5652. Web page: http://researchers.adelaide.edu.au/profile/andrew.abell#contact-details.

*E-mail: abel.santos@adelaide.edu.au (A.S.). Phone: +61 8 8313 1535. Web page: http://www.adelaide.edu.au/directory/abel.santos.

ORCID

Andrew D. Abell: 0000-0002-0604-2629

Abel Santos: 0000-0002-5081-5684

Notes

The authors declare no competing financial interest.

■ ACKNOWLEDGMENTS

The authors are thankful for support provided by the Australian Research Council (ARC) through Grants DE140100549 and CE140100003, the School of Chemical Engineering, University of Adelaide (DVCR initiative "Research for Impact"), the IPAS, and the CNBP.

■ REFERENCES

(1) Michler, P.; Kiraz, A.; Becher, C.; Schoenfeld, W.; Petroff, P.; Zhang, L.; Hu, E.; Imamoglu, A. A quantum dot single-photon turnstile device. *Science* **2000**, *290*, 2282−2285.

(2) Ogawa, S.; Imada, M.; Yoshimoto, S.; Okano, M.; Noda, S. Control of light emission by 3D photonic crystals. *Science* **2004**, *305*, 227−229.

(3) Noda, S.; Chutinan, A.; Imada, M. Trapping and emission of photons by a single defect in a photonic bandgap structure. *Nature* **2000**, *407*, 608−610.

(4) Song, B.-S.; Asano, T.; Noda, S. Physical origin of the small modal volume of ultra-high-Q photonic double-heterostructure nanocavities. *New J. Phys.* **2006**, *8*, 209.

(5) Notomi, M. Manipulating light with strongly modulated photonic crystals. *Rep. Prog. Phys.* **2010**, *73*, 096501.

(6) Lee, H.; Chen, T.; Li, J.; Yang, K. Y.; Jeon, S.; Painter, O.; Vahala, K. J. Chemically etched ultrahigh-Q wedge-resonator on a silicon chip. *Nat. Photonics* **2012**, *6*, 369−373.

(7) Vahala, K. J. Optical microcavities. *Nature* **2003**, *424*, 839−846.

(8) Matsko, A. B. *Practical applications of microresonators in optics and photonics*; CRC Press: Boca Raton, FL, 2009.

(9) Yablonovitch, E. Inhibited spontaneous emission in solid-state physics and electronics. *Phys. Rev. Lett.* **1987**, *58*, 2059.

(10) John, S. Strong localization of photons in certain disordered dielectric superlattices. *Phys. Rev. Lett.* **1987**, *58*, 2486.

(11) Krauss, T. F. Photonic crystals: Cavities without leaks. *Nat. Mater.* **2003**, *2*, 777−778.

(12) Foresi, J.; Villeneuve, P. R.; Ferrera, J.; Thoen, E.; Steinmeyer, G.; Fan, S.; Joannopoulos, J.; Kimerling, L.; Smith, H. I.; Ippen, E. Photonic-bandgap microcavities in optical waveguides. *Nature* **1997**, *390*, 143−145.

(13) Sun, H.-B.; Mizeikis, V.; Xu, Y.; Juodkazis, S.; Ye, J.-Y.; Matsuo, S.; Misawa, H. Microcavities in polymeric photonic crystals. *Appl. Phys. Lett.* **2001**, *79*, 1−3.

(14) Ripin, D. J.; Lim, K.-Y.; Petrich, G.; Villeneuve, P. R.; Fan, S.; Thoen, E.; Joannopoulos, J. D.; Ippen, E.; Kolodziejski, L. One-dimensional photonic bandgap microcavities for strong optical confinement in GaAs and GaAs/AlxOy semiconductor waveguides. *J. Lightwave Technol.* **1999**, *17*, 2152.

(15) Baba, T. Photonic crystals and microdisk cavities based on GaInAsP-InP system. *IEEE J. Sel. Top. Quantum Electron.* **1997**, *3*, 808−830.

(16) Solomon, G.; Pelton, M.; Yamamoto, Y. Single-mode spontaneous emission from a single quantum dot in a three-dimensional microcavity. *Phys. Rev. Lett.* **2001**, *86*, 3903.

(17) Benson, T. M.; Boriskina, S. V.; Sewell, P.; Vukovic, A.; Greedy, S. C.; Nosich, A. I. Micro-optical resonators for microlasers and integrated optoelectronics. *Frontiers in planar lightwave circuit technology*; Springer, 2006; pp 39−70.

(18) Md Zain, A. R. M.; Johnson, N. P.; Sorel, M.; De la Rue, R. M. Ultra high quality factor one dimensional photonic crystal/photonic wire micro-cavities in silicon-on-insulator (SOI). *Opt. Express* **2008**, *16*, 12084−12089.

(19) Akahane, Y.; Asano, T.; Song, B.-S.; Noda, S. High-Q photonic nanocavity in a two-dimensional photonic crystal. *Nature* **2003**, *425*, 944−947.

(20) Pavesi, L.; Mazzoleni, C.; Tredicucci, A.; Pellegrini, V. Controlled photon emission in porous silicon microcavities. *Appl. Phys. Lett.* **1995**, *67*, 3280−3282.

(21) Pellegrini, V.; Tredicucci, A.; Mazzoleni, C.; Pavesi, L. Enhanced optical properties in porous silicon microcavities. *Phys. Rev. B: Condens. Matter Mater. Phys.* **1995**, *52*, R14328.
(22) Cazzanelli, M.; Pavesi, L. Time-resolved photoluminescence of all-porous-silicon microcavities. *Phys. Rev. B: Condens. Matter Mater. Phys.* **1997**, *56*, 15264.
(23) Ghulinyan, M.; Oton, C.; Bonetti, G.; Gaburro, Z.; Pavesi, L. Free-standing porous silicon single and multiple optical cavities. *J. Appl. Phys.* **2003**, *93*, 9724−9729.
(24) Pavesi, L.; Panzarini, G.; Andreani, L. All-porous silicon-coupled microcavities: Experiment versus theory. *Phys. Rev. B: Condens. Matter Mater. Phys.* **1998**, *58*, 15794.
(25) De Stefano, L.; Moretti, L.; Rendina, I.; Rossi, A. M. Porous silicon microcavities for optical hydrocarbons detection. *Sens. Actuators, A* **2003**, *104*, 179−182.
(26) Mulloni, V.; Pavesi, L. Porous silicon microcavities as optical chemical sensors. *Appl. Phys. Lett.* **2000**, *76*, 2523−2525.
(27) Reece, P.; Lérondel, G.; Zheng, W.; Gal, M. Optical microcavities with subnanometer linewidths based on porous silicon. *Appl. Phys. Lett.* **2002**, *81*, 4895−4897.
(28) Lehmann, V. *Electrochemistry of Silicon: Instrumentation, Science, Materials and Applications*; Wiley, 2002.
(29) Chen, Y.; Santos, A.; Wang, Y.; Kumeria, T.; Li, J.; Wang, C.; Losic, D. Biomimetic nanoporous anodic alumina distributed bragg reflectors in the form of films and microsized particles for sensing applications. *ACS Appl. Mater. Interfaces* **2015**, *7*, 19816−19824.
(30) Yu, M.; Li, C.; Yang, Y.; Xu, S.; Zhang, K.; Cui, H.; Zhu, X. Cavities between the double walls of nanotubes: Evidence of oxygen evolution beneath an anion-contaminated layer. *Electrochem. Commun.* **2018**, *90*, 34−38.
(31) Yu, M.; Chen, Y.; Li, C.; Yan, S.; Cui, H.; Zhu, X.; Kong, J. Studies of oxide growth location on anodization of Al and Ti provide evidence against the field-assisted dissolution and field-assisted ejection theories. *Electrochem. Commun.* **2018**, *87*, 76−80.
(32) Yu, M.; Cui, H.; Ai, F.; Jiang, L.; Kong, J.; Zhu, X. Terminated nanotubes: Evidence against the dissolution equilibrium theory. *Electrochem. Commun.* **2018**, *86*, 80−84.
(33) Zhao, S.; Xing, J.; Fan, H.; Zhang, S.; Li, D.; Zhu, X. Derivation of a mathematical model for the growth of anodic TiO_2 nanotubes under constant current conditions. *J. Electrochem. Soc.* **2017**, *164*, E187−E193.
(34) Wen, L.; Xu, R.; Mi, Y.; Lei, Y. Multiple nanostructures based on anodized aluminium oxide templates. *Nat. Nanotechnol.* **2017**, *12*, 244−250.
(35) Xu, R.; Wen, L.; Wang, Z.; Zhao, H.; Xu, S.; Mi, Y.; Xu, Y.; Sommerfeld, M.; Fang, Y.; Lei, Y. Three-dimensional plasmonic nanostructures design for boosting photoelectrochemical activity. *ACS Nano* **2017**, *11*, 7382−7389.
(36) Zhan, Z.; Xu, R.; Mi, Y.; Zhao, H.; Lei, Y. Highly controllable surface plasmon resonance property by heights of ordered nanoparticle arrays fabricated via a nonlithographic route. *ACS Nano* **2015**, *9*, 4583−4590.
(37) Lee, J.; Bae, K.; Kang, G.; Choi, M.; Baek, S.; Yoo, D.-S.; Lee, C.-W.; Kim, K. Graded-lattice AAO photonic crystal heterostructure for high Q refractive index sensing. *RSC Adv.* **2015**, *5*, 71770−71777.
(38) Wang, Y.; Chen, Y.; Kumeria, T.; Ding, F.; Evdokiou, A.; Losic, D.; Santos, A. Facile synthesis of optical microcavities by a rationally designed anodization approach: tailoring photonic signals by nanopore structure. *ACS Appl. Mater. Interfaces* **2015**, *7*, 9879−9888.
(39) Shang, G. L.; Fei, G. T.; De Zhang, L. Experimental realization of tunable defect mode in photonic crystal. *J. Phys. D: Appl. Phys.* **2015**, *48*, 435304.
(40) Lee, W.; Schwirn, K.; Steinhart, M.; Pippel, E.; Scholz, R.; Gösele, U. Structural engineering of nanoporous anodic aluminium oxide by pulse anodization of aluminium. *Nat. Nanotechnol.* **2008**, *3*, 234−239.
(41) Yan, P.; Fei, G.-T.; Li, H.; Shang, G.-L.; Wu, B.; Zhang, L.-D. Alumina photonic crystals with defect modes for sensor application. *Chin. J. Chem. Phys.* **2014**, *27*, 121−124.
(42) Ghulinyan, M.; Oton, C. J.; Bonetti, G.; Gaburro, Z.; Pavesi, L. Free-standing porous silicon single and multiple optical cavities. *J. Appl. Phys.* **2003**, *93*, 9724−9729.
(43) Reece, P. J.; Lérondel, G.; Zheng, W. H.; Gal, M. Optical microcavities with subnanometer linewidths based on porous silicon. *Appl. Phys. Lett.* **2002**, *81*, 4895−4897.
(44) Lee, W.; Scholz, R.; Gösele, U. A continuous process for structurally well-defined Al2O3 nanotubes based on pulse anodization of aluminum. *Nano Lett.* **2008**, *8*, 2155−2160.
(45) Lee, W.; Kim, J.-C. Highly ordered porous alumina with tailor-made pore structures fabricated by pulse anodization. *Nanotechnology* **2010**, *21*, 485304.
(46) Lee, W.; Ji, R.; Gösele, U.; Nielsch, K. Fast fabrication of long-range ordered porous alumina membranes by hard anodization. *Nat. Mater.* **2006**, *5*, 741−747.
(47) Santos, A. Nanoporous anodic alumina photonic crystals: Fundamentals, developments and perspectives. *J. Mater. Chem. C* **2017**, *5*, 5581−5599.
(48) Chen, Y.; Santos, A.; Ho, D.; Wang, Y.; Kumeria, T.; Li, J.; Wang, C.; Losic, D. On the generation of interferometric colors in high purity and technical grade aluminum: An alternative green process for metal finishing industry. *Electrochim. Acta* **2015**, *174*, 672−681.
(49) Macias, G.; Ferré-Borrull, J.; Pallarès, J.; Marsal, L. F. 1-D nanoporous anodic alumina rugate filters by means of small current variations for real-time sensing applications. *Nanoscale Res. Lett.* **2014**, *9*, 315.
(50) Zheng, W. J.; Fei, G. T.; Wang, B.; Jin, Z.; Zhang, L. D. Distributed Bragg reflector made of anodic alumina membrane. *Mater. Lett.* **2009**, *63*, 706−708.
(51) Shang, G. L.; Fei, G. T.; Zhang, Y.; Yan, P.; Xu, S. H.; Zhang, L. D. Preparation of narrow photonic bandgaps located in the near infrared region and their applications in ethanol gas sensing. *J. Mater. Chem. C* **2013**, *1*, 5285−5291.
(52) Law, C. S.; Santos, A.; Nemati, M.; Losic, D. Structural engineering of nanoporous anodic alumina photonic crystals by sawtooth-like pulse anodization. *ACS Appl. Mater. Interfaces* **2016**, *8*, 13542−13554.
(53) Nemati, M.; Santos, A.; Law, C. S.; Losic, D. Assessment of binding affinity between drugs and human serum albumin using nanoporous anodic alumina photonic crystals. *Anal. Chem.* **2016**, *88*, 5971−5980.
(54) Santos, A.; Law, C. S.; Chin Lei, D. W.; Pereira, T.; Losic, D. Fine tuning of optical signals in nanoporous anodic alumina photonic crystals by apodized sinusoidal pulse anodisation. *Nanoscale* **2016**, *8*, 18360−18375.
(55) Santos, A.; Pereira, T.; Law, C. S.; Losic, D. Rational engineering of nanoporous anodic alumina optical bandpass filters. *Nanoscale* **2016**, *8*, 14846−14857.
(56) Santos, A.; Law, C. S.; Pereira, T.; Losic, D. Nanoporous hard data: optical encoding of information within nanoporous anodic alumina photonic crystals. *Nanoscale* **2016**, *8*, 8091−8100.
(57) Nemati, M.; Santos, A.; Kumeria, T.; Losic, D. Label-free real-time quantification of enzyme levels by interferometric spectroscopy combined with gelatin-modified nanoporous anodic alumina photonic films. *Anal. Chem.* **2015**, *87*, 9016−9024.
(58) Chen, Y.; Santos, A.; Wang, Y.; Kumeria, T.; Ho, D.; Li, J.; Wang, C.; Losic, D. Rational design of photonic dust from nanoporous anodic alumina films: a versatile photonic nanotool for visual sensing. *Sci. Rep.* **2015**, *5*, 12893.
(59) Kumeria, T.; Rahman, M. M.; Santos, A.; Ferré-Borrull, J.; Marsal, L. F.; Losic, D. Nanoporous anodic alumina rugate filters for sensing of ionic mercury: Toward environmental point-of-analysis systems. *ACS Appl. Mater. Interfaces* **2014**, *6*, 12971−12978.
(60) Law, C. S.; Lim, S. Y.; Santos, A. On the precise tuning of optical filtering features in nanoporous anodic alumina distributed Bragg reflectors. *Sci. Rep.* **2018**, *8*, 4642.
(61) Southwell, W. H. Using apodization functions to reduce sidelobes in rugate filters. *Appl. Opt.* **1989**, *28*, 5091−5094.

DOI: 10.1021/acsanm.8b00494
ACS Appl. Nano Mater. 2018, 1, 4418−4434

Supporting Information

Light-Confining Nanoporous Anodic Alumina Microcavities by Apodized Stepwise Pulse Anodization

Cheryl Suwen Law[a,b,c], Siew Yee Lim[a,b,c], Raeanne M. Macalincag[a], Andrew D. Abell[b,c,d*], and Abel Santos[*a,b,c]

[a]School of Chemical Engineering, The University of Adelaide, Adelaide, SA 5005, Australia
[b]Institute for Photonics and Advanced Sensing (IPAS), The University of Adelaide, 5005 Adelaide, Australia
[c]ARC Centre of Excellence for Nanoscale BioPhotonics (CNBP), The University of Adelaide, 5005 Adelaide, Australia
[d]Department of Chemistry, The University of Adelaide, Engineering North Building, 5005 Adelaide, Australia.

***E-Mails:** andrew.abell@adelaide.edu.au ; abel.santos@adelaide.edu.au

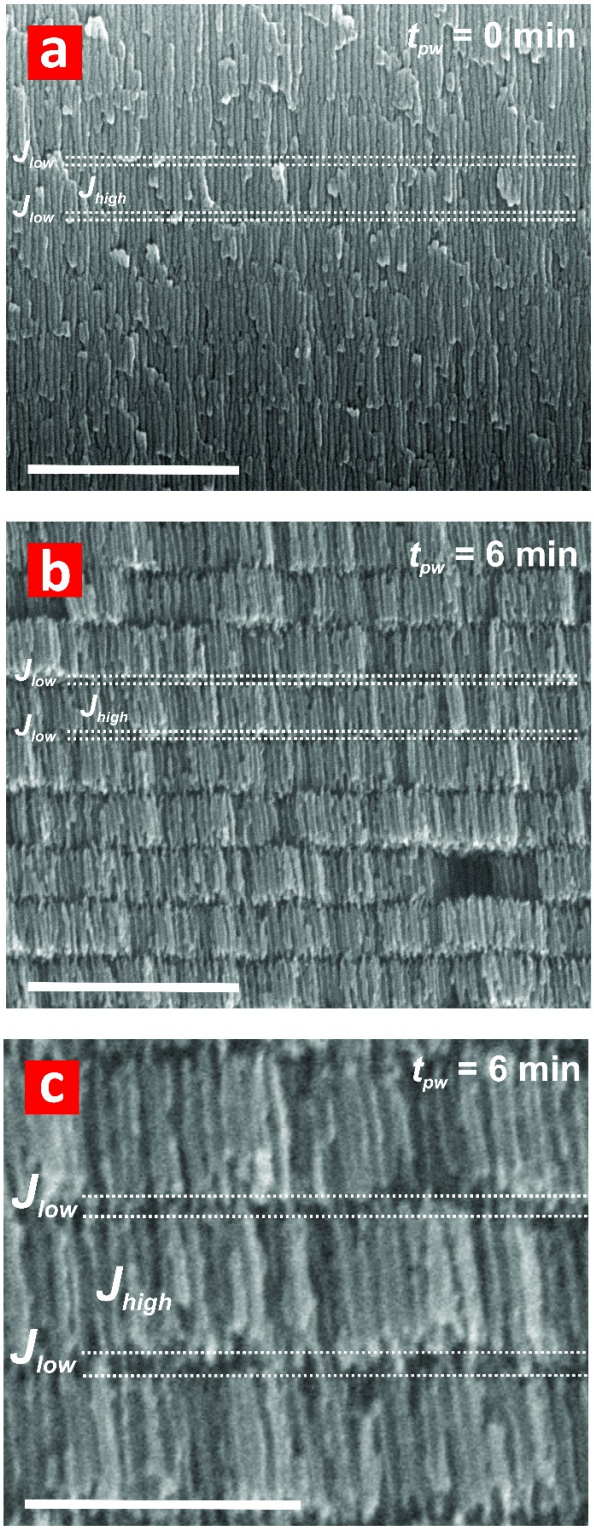

Figure S1. Representative FEG-SEM images demonstrating the differential dissolution rates between NAA layers produced at J_{high} (1.120 mA cm^{-2}) and J_{low} (0.280 mA cm^{-2}) values in NAA-μCVs. a) Cross-sectional FEG-SEM image of a representative NAA-μCV at t_{pw} = 0 min showing layers of NAA produced at J_{high} and J_{low} values (scale bar = 1 μm). b) Cross-sectional FEG-SEM image of the same NAA-μCV at t_{pw} = 6 min (scale bar = 1 μm). c) Magnified view of (b) showing details of the highly porous NAA layers produced at J_{low}, after pore widening treatment for 6 min (scale bar = 500 nm).

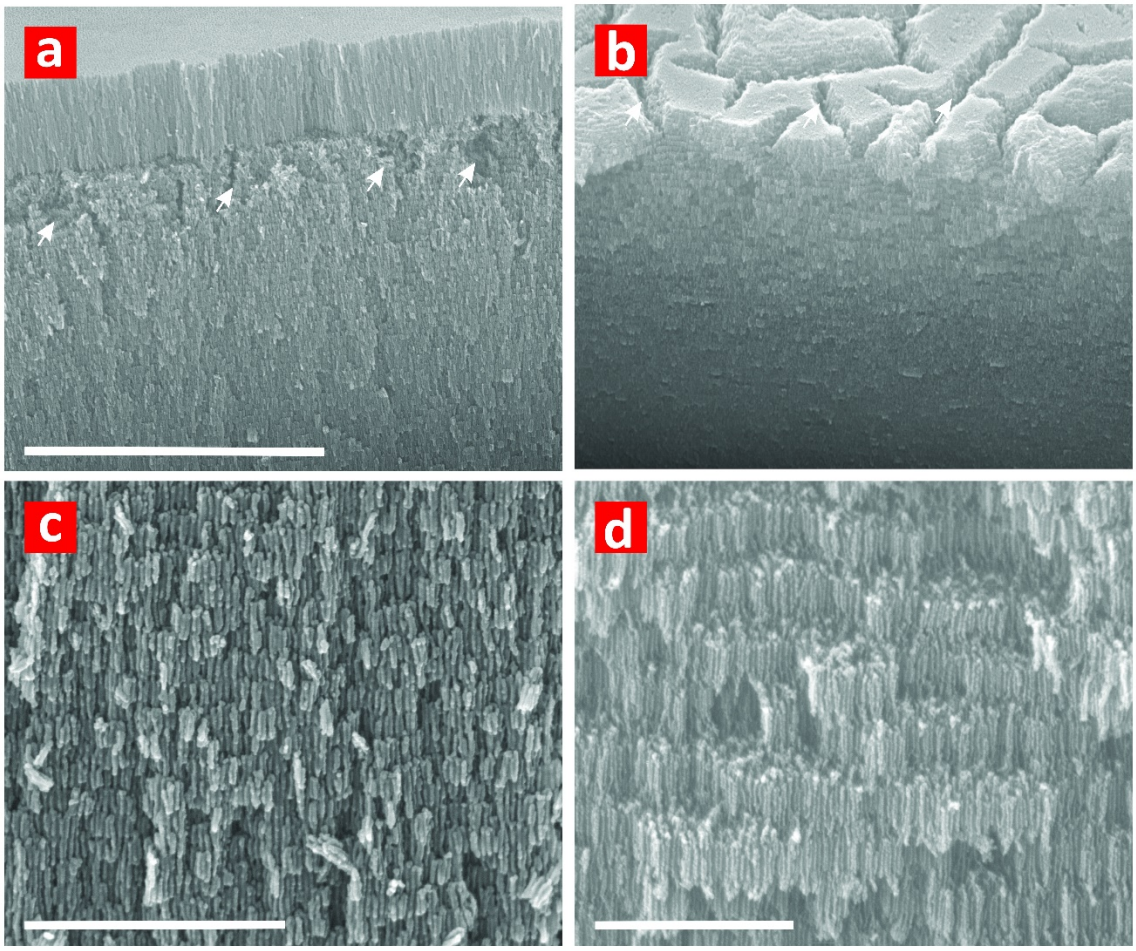

Figure S2. Effect of excessive pore widening time on the structure of NAA-μCVs. a and b) Representative general cross-sectional view FEG-SEM images of a NAA-μCV at t_{pw} = 6 and 8 min, respectively (scale bars = 5 μm) (note: white arrows indicate regions that partially collapse due to excessive pore widening treatment). c and d) Magnified cross-sectional view FEG-SEM images showing details of the porosity between layers in a NAA-μCV at t_{pw} = 6 and 8 min, respectively (scale bars = 1 μm).

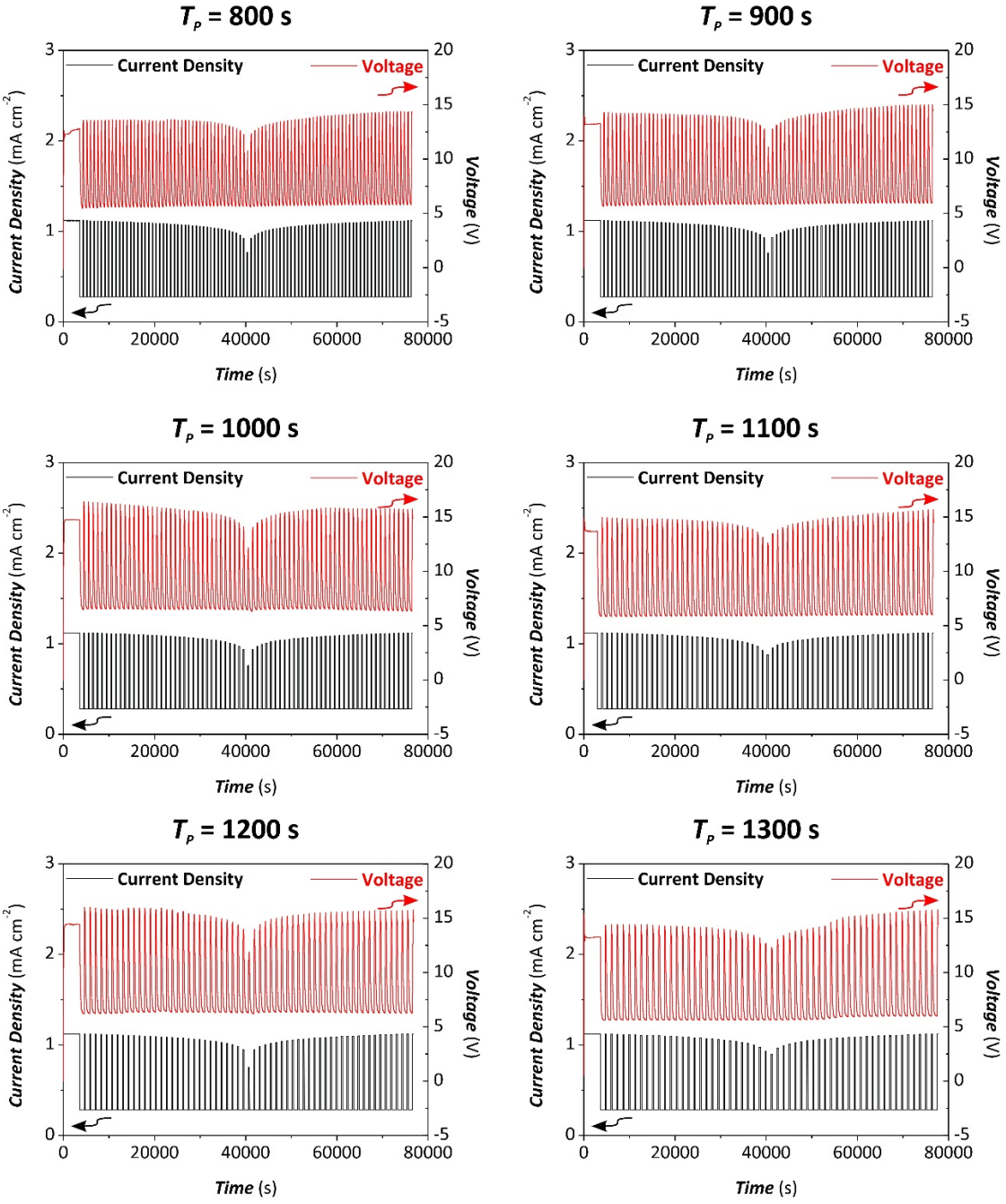

Figure S3. Representative anodization profiles of NAA-μCVs produced by ASPA at different anodization periods, from 800 to 1300 s.

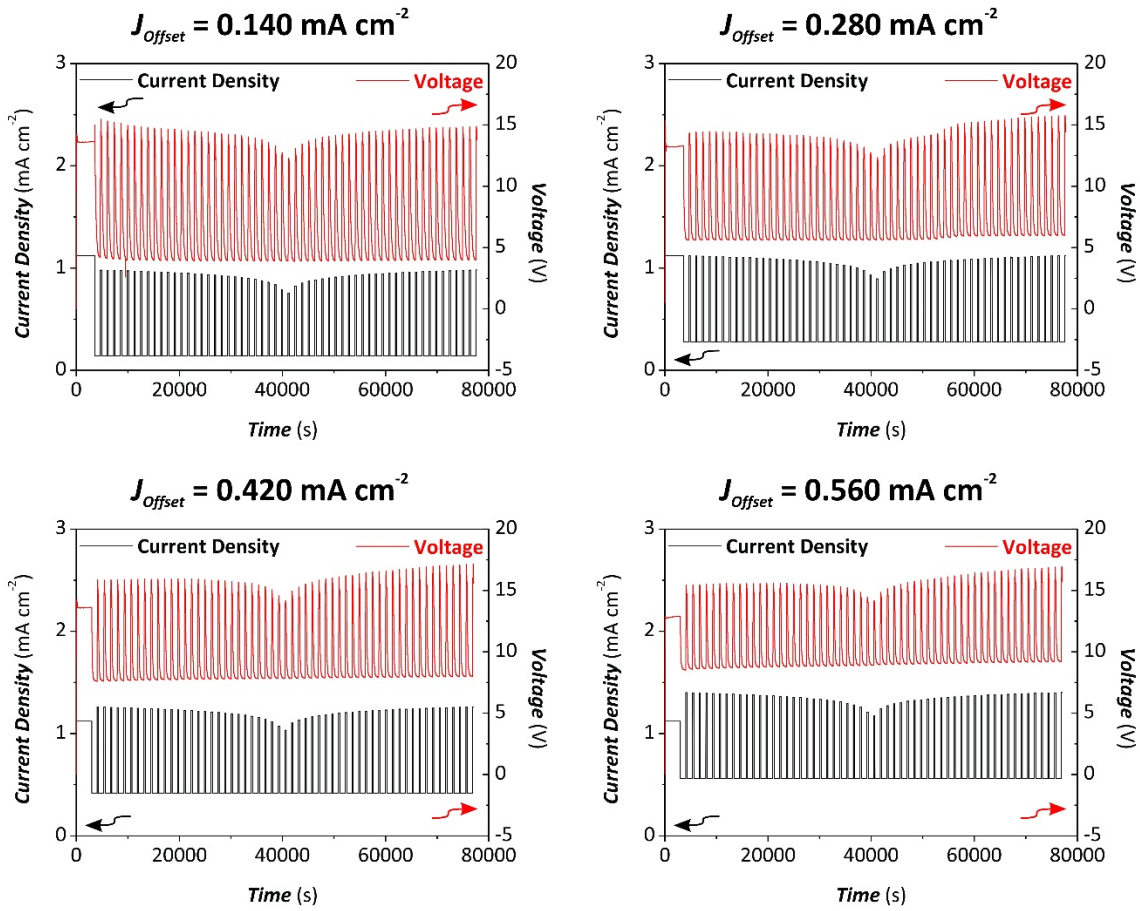

Figure S4. Representative anodization profiles of NAA-μCVs produced by ASPA at different anodization offsets, from 0.140 to 0.560 mA cm^{-2}.

Table S1. Values of the position of resonance band – λ_R, full-width at half maximum – $FWHM_R$, quality factor – Q_C, baseline of Gaussian fitting – y_0, and fitting correlation coefficient – R^2 of NAA-μCVs produced with t_{An} = 5, 10, 15, 20 and 25 h, t_{pw} = 0, 2, 4 and 6 min and T_P = 1200 and 1300 s estimated from Gaussian fittings (note: y_0 in % of transmission units and grey values denote those NAA-μCVs with superior light confining properties than those reported in previous studies).

T_P = 1300 s						T_P = 1200 s					
t_{An} = 5 h						t_{An} = 5 h					
t_{pw} (min)	λ_R (nm)	$FWHM_R$ (nm)	Qc	$y0$ (%T)	R^2	t_{pw} (min)	λ_R (nm)	$FWHM_R$ (nm)	Qc	$y0$ (%T)	R^2
0	725	47	15	60	0.75	0	635	15	41	67	0.99
2	679	50	7	15	0.93	2	596	28	22	27	0.94
4	622	33	19	10	0.92	4	546	23	24	8	0.96
6	444	74	6	30	0.89	6	342	45	8	35	0.83
t_{An} = 10 h						t_{An} = 10 h					
t_{pw} (min)	λ_R (nm)	$FWHM_R$ (nm)	Qc	$y0$ (%T)	R^2	t_{pw} (min)	λ_R (nm)	$FWHM_R$ (nm)	Qc	$y0$ (%T)	R^2
0	691	24	29	60	0.96	0	640	15	43	35	0.92
2	641	22	29	10	0.96	2	609	9.5	64	18	0.98
4	594	13	44	2	0.97	4	564	8	71	3.5	0.99
6	542	17	31	6	0.98	6	501	15	32	3.5	0.98
t_{An} = 15 h						t_{An} = 15 h					
t_{pw} (min)	λ_R (nm)	$FWHM_R$ (nm)	Qc	$y0$ (%T)	R^2	t_{pw} (min)	λ_R (nm)	$FWHM_R$ (nm)	Qc	$y0$ (%T)	R^2
0	702	23	31	29	0.99	0	642	21	30	25	0.89
2	668	17	39	4	0.99	2	623	17	37	6.5	0.96
4	633	17	38	1	0.97	4	588	11	53	1	0.97
6	585	14	41	0.4	0.94	6	539	8	67	0.5	0.95
t_{An} = 20 h						t_{An} = 20 h					
t_{pw} (min)	λ_R (nm)	$FWHM_R$ (nm)	Qc	$y0$ (%T)	R^2	t_{pw} (min)	λ_R (nm)	$FWHM_R$ (nm)	Qc	$y0$ (%T)	R^2
0	709	18	38	10	0.92	0	692	9	75	28	0.94
2	675	11	63	1	0.96	2	665	6	113	7.5	0.98
4	639	17	38	0.4	0.99	4	640	9	74	3.5	0.94
6	586	13	44	1	0.87	6	602	21	29	0.5	0.97
t_{An} = 25 h						t_{An} = 25 h					
t_{pw} (min)	λ_R (nm)	$FWHM_R$ (nm)	Qc	$y0$ (%T)	R^2	t_{pw} (min)	λ_R (nm)	$FWHM_R$ (nm)	Qc	$y0$ (%T)	R^2
0	659	14	47	3.5	0.98	0	651	29	22	2	0.95
2	635	14	45	0.5	0.99	2	617	12	51	0	0.99
4	610	17	35	0	0.96	4	594	15	39	0	0.98
6	575	17	33	0	0.83	6	564	17	32	0.5	0.81

Table S2. Values of the position of resonance band – λ_R, full-width at half maximum – $FWHM_R$, quality factor – Q_C, baseline of Gaussian fitting – y_0, and fitting correlation coefficient – R^2 of NAA-μCVs produced with t_{pw} = 0, 2, 4 and 6 min T_P = 800, 900, 1000, 1100, 1200 and 1300 s estimated from Gaussian fittings (note: y_0 in % of transmission units and grey values denote those NAA-μCVs with superior light confining properties than those reported in previous studies).

T_P = 800 s					
t_{pw} (min)	λ_R (nm)	$FWHM_R$ (nm)	Qc	$y0$ (%T)	R^2
0	396	13	30	3.5	0.97
2	379	17	22	0	0.98
4	350	25	14	0	0.85
6	-	-	-	-	-
T_P = 900 s					
t_{pw} (min)	λ_R (nm)	$FWHM_R$ (nm)	Qc	$y0$ (%T)	R^2
0	478	19	25	2.5	0.93
2	464	22	21	0.5	0.98
4	432	8	57	0.5	0.99
6	402	10	41	0	0.78
T_P = 1000 s					
t_{pw} (min)	λ_R (nm)	$FWHM_R$ (nm)	Qc	$y0$ (%T)	R^2
0	578	10	60	10	0.91
2	569	25	23	1	0.88
4	560	17	32	1	0.96
6	520	12	44	0.4	0.89
T_P = 1100 s					
t_{pw} (min)	λ_R (nm)	$FWHM_R$ (nm)	Qc	$y0$ (%T)	R^2
0	-	-	-	-	-
2	582	10	57	3	0.92
4	539	11	48	0.5	0.99
6	517	21	25	0	0.87
T_P = 1200 s					
t_{pw} (min)	λ_R (nm)	$FWHM_R$ (nm)	Qc	$y0$ (%T)	R^2
0	692	9	75	28	0.94
2	665	6	113	7.5	0.98
4	640	9	74	3.5	0.94
6	602	21	29	0.5	0.97
T_P = 1300 s					
t_{pw} (min)	λ_R (nm)	$FWHM_R$ (nm)	Qc	$y0$ (%T)	R^2
0	709	18	38	10	0.92
2	675	11	63	1	0.96
4	639	17	38	0.4	0.99
6	586	13	44	1	0.87

Table S3. Values of the position of resonance band – λ_R, full-width at half maximum – $FWHM_R$, quality factor – Q_C, baseline of Gaussian fitting – y_0, and fitting correlation coefficient – R^2 of NAA-μCVs produced with t_{pw} = 0, 2, 4 and 6 min and J_{Offset} = 0.140, 0.280, 0.420 and 0.560 mA cm^{-2} estimated from Gaussian fittings (note: y_0 in % of transmission units and grey values denote those NAA-μCVs with superior light confining properties than those reported in previous studies).

J_{Ofsset} = 0.140 mA cm^{-2}					
t_{pw} (min)	λ_R (nm)	$FWHM_R$ (nm)	Qc	$y0$ (%T)	R^2
0	580	9	62	9	0.97
2	556	9	63	2	0.99
4	511	8	65	0.5	0.94
6	477	8	62	0.1	0.97
J_{Ofsset} = 0.280 mA cm^{-2}					
t_{pw} (min)	λ_R (nm)	$FWHM_R$ (nm)	Qc	$y0$ (%T)	R^2
0	709	18.5	38	10	0.92
2	675	11	63	1	0.96
4	639	17	38	0.4	0.99
6	586	13	44	1	0.86
J_{Ofsset} = 0.420 mA cm^{-2}					
t_{pw} (min)	λ_R (nm)	$FWHM_R$ (nm)	Qc	$y0$ (%T)	R^2
0	976	25	39	26	0.97
2	950	34	28	9	0.96
4	929	50	19	6	0.95
6	887	40	22	3.5	0.98
J_{Ofsset} = 0.560 mA cm^{-2}					
t_{pw} (min)	λ_R (nm)	$FWHM_R$ (nm)	Qc	$y0$ (%T)	R^2
0	1096	45	24	34	0.80
2	1067	56	19	20	0.93
4	1046	64	16	23	0.92
6	1003	43	23	23	0.88

Chapter 7

Engineering of Surface Chemistry for Enhanced Sensitivity in Nanoporous Interferometric Sensing Platform

Statement of Authorship

Title of Paper	Engineering of Surface Chemistry for Enhanced Sensitivity in Nanoporous Interferometric Sensing Platforms.
Publication Status	☑ Published ☐ Accepted for Publication ☐ Submitted for Publication ☐ Unpublished and Unsubmitted w ork w ritten in manuscript style
Publication Details	Law, C.S., G.M. Sylvia, M. Nemati, J. Yu, D. Losic, A.D. Abell, and A. Santos, *Engineering of surface chemistry for enhanced sensitivity in nanoporous interferometric sensing platforms*. ACS Applied Materials & Interfaces, 2017. **9**(10): p. 8929-8940.

Principal Author

Name of Principal Author (Candidate)	Cheryl Suwen Law		
Contribution to the Paper	Under the supervision of A. Santos and A. D. Abell, I performed the experiments, interpreted and processed the data and wrote the manuscript.		
Overall percentage (%)	70		
Certification:	This paper reports on original research I conducted during the period of my Higher Degree by Research candidature and is not subject to any obligations or contractual agreements with a third party that would constrain its inclusion in this thesis. I am the primary author of this paper.		
Signature		Date	23/11/2018

Co-Author Contributions

By signing the Statement of Authorship, each author certifies that:

i. the candidate's stated contribution to the publication is accurate (as detailed above);
ii. permission is granted for the candidate in include the publication in the thesis; and
iii. the sum of all co-author contributions is equal to 100% less the candidate's stated contribution.

Name of Co-Author	Georgina M. Sylvia		
Contribution to the Paper	I aided in evaluating the concept of the study and performing the experiments and revising the manuscript. I give consent for Cheryl Suwen Law to present this paper for examination towards the Doctorate of Philosophy.		
Signature		Date	14/11/2018

Name of Co-Author	Mahdieh Nemati		
Contribution to the Paper	I aided in performing the experiments. I give consent for Cheryl Suwen Law to present this paper for examination towards the Doctorate of Philosophy.		
Signature		Date	18/11/2018

Name of Co-Author	Jingxian Yu		
Contribution to the Paper	I aided in evaluating the concept of the study and evaluating final version of manuscript. I give consent for Cheryl Suwen Law to present this paper for examination towards the Doctorate of Philosophy.		
Signature		Date	19/11/2018

Name of Co-Author	Andrew D. Abell		
Contribution to the Paper	I acted as secondary supervisor for the candidate, aided in evaluating the concept of study, revising the manuscript and evaluating the final version of manuscript. I give consent for Cheryl Suwen Law to present this paper for examination towards the Doctorate of Philosophy.		
Signature		Date	23/11/2018

Name of Co-Author	Abel Santos		
Contribution to the Paper	I acted as primary supervisor for the candidate, aided in developing of the experiments, revising the manuscript and evaluating the final version of the manuscript. I give consent for Cheryl Suwen Law to present this paper for examination towards the Doctorate of Philosophy.		
Signature		Date	23/11/2018

7. Engineering of Surface Chemistry for Enhanced Sensitivity in Nanoporous Interferometric Sensing Platforms

7.1 Introduction, Significance and Commentary

The development of sensing platforms with outstanding sensing properties not only depends on the structural optimisation of NAA-PCs, but also their surface chemistry. This chapter aims to optimise the surface chemistry of NAA-PCs by exploring different surface engineering strategies using functional molecules with tuned properties to capture target molecules. NAA-PCs were chemically modified with thiol-containing molecules of different moiety and molecular size in different configurations (i.e. top or inner surface of nanopores) and their sensitivity toward gold ions were assessed in real-time by reflectometric interference spectroscopy (RIfS). The difference in the overall sensitivity demonstrated in this study implies that different molecular features and sensing approach can be used to engineer the sensitivity of NAA-PC platforms with the same chemical selectivity. A rational design of the surface chemistry architecture of NAA-PCs can enhance the sensitivity of these PCs, pushing the development of NAA-PCs based sensor for real-life applications.

7.2 Publication

This section is presented as published research paper by **Law, C.S.**, G.M. Sylvia, M. Nemati, J. Yu, D. Losic, A.D. Abell, and A. Santos, *Engineering of surface chemistry for enhanced sensitivity in nanoporous interferometric sensing platforms*. ACS Applied Materials & Interfaces, 2017. **9**(10): p. 8929-8940.

ACS APPLIED MATERIALS & INTERFACES

Research Article

www.acsami.org

Engineering of Surface Chemistry for Enhanced Sensitivity in Nanoporous Interferometric Sensing Platforms

Cheryl Suwen Law,[†,§] Georgina M. Sylvia,[‡,§,∥] Madieh Nemati,[†] Jingxian Yu,[‡,§,∥] Dusan Losic,[†] Andrew D. Abell,*[,‡,§,∥] and Abel Santos*[,†,‡,§]

[†]School of Chemical Engineering, [‡]Department of Chemistry, [§]Institute for Photonics and Advanced Sensing (IPAS), and [∥]ARC Centre of Excellence for Nanoscale BioPhotonics (CNBP), The University of Adelaide, Adelaide, SA 5005, Australia

Supporting Information

ABSTRACT: We explore new approaches to engineering the surface chemistry of interferometric sensing platforms based on nanoporous anodic alumina (NAA) and reflectometric interference spectroscopy (RIfS). Two surface engineering strategies are presented, namely (i) selective chemical functionalization of the inner surface of NAA pores with amine-terminated thiol molecules and (ii) selective chemical functionalization of the top surface of NAA with dithiol molecules. The strong molecular interaction of Au^{3+} ions with thiol-containing functional molecules of alkane chain or peptide character provides a model sensing system with which to assess the sensitivity of these NAA platforms by both molecular feature and surface engineering. Changes in the effective optical thickness of the functionalized NAA photonic films (i.e., sensing principle), in response to gold ions, are monitored in real-time by RIfS. 6-Amino-1-hexanethiol (inner surface) and 1,6-hexanedithiol (top surface), the most sensitive functional molecules from approaches i and ii, respectively, were combined into a third sensing strategy whereby the NAA platforms are functionalized on both the top and inner surfaces concurrently. Engineering of the surface according to this approach resulted in an additive enhancement in sensitivity of up to 5-fold compared to previously reported systems. This study advances the rational engineering of surface chemistry for interferometric sensing on nanoporous platforms with potential applications for real-time monitoring of multiple analytes in dynamic environments.

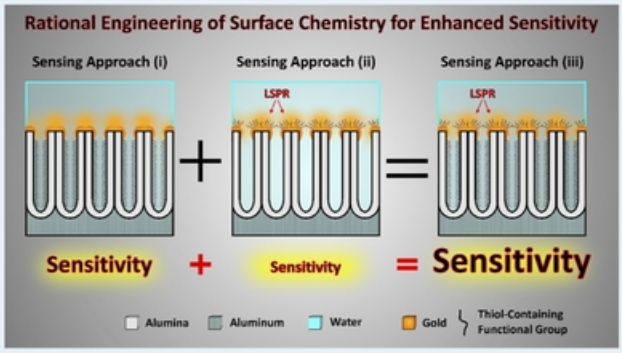

KEYWORDS: *nanoporous anodic alumina, reflectometric interference spectroscopy, surface chemistry engineering, optical sensing, sensing performance*

1. INTRODUCTION

Optical sensors are powerful analytical tools that play vital roles in biomedical research, environmental monitoring, homeland security, and other applications.[1] Advantages of optical sensing systems include immunity to electromagnetic interference, label-free and remote sensing capabilities, and identification of analytes of interest by characteristic spectroscopic signatures.[2,3] Optical sensors collect analytical information through the interaction between light and matter using optical transduction techniques such as surface plasmon resonance (SPR), surface-enhanced Raman scattering (SERS), photoluminescence, and interferometry.[4−7] Among these, interferometric sensors offer a versatile, label-free sensing approach for broad sensing applications.[8−15] The underlying principle of reflectometric interference spectroscopy (RIfS) is based on white light interferometry on solid thin films, which results in the formation of a characteristic interference pattern by the Fabry−Pérot effect.[8,9] Pioneering RIfS systems combined functional polymeric thin films deposited onto glass slides as sensing platforms for gas sensing,[8,10] label-free immunosensing,[10] and biomolecular interaction analysis (BIA).[9,11] The use of nanoporous thin films based on porous silicon as transducer elements opened new opportunities to develop advanced sensing systems for the detection of small organic molecules, DNA, and proteins.[12−15] The nanoporous structure of porous silicon makes it an excellent platform for the development of photonic structures with precisely engineered optical properties such as well-resolved Fabry−Pérot fringes in the RIfS spectrum. Nevertheless, the relatively poor chemical stability in aqueous media of porous silicon leads to unstable optical signals, which is undesirable for practical sensing applications.[16,17] Alternative nanoporous materials, such as nanoporous anodic alumina (NAA), demonstrate similar advantages to those of porous silicon while addressing chemical instability limitations due to the inert nature of alumina (aluminum oxide, Al_2O_3). Versatility of nanopore geometry and surface chemistry, chemical and mechanical stability, and optical properties make NAA an excellent platform for developing interferometric sensing

Received: January 22, 2017
Accepted: February 27, 2017
Published: February 27, 2017

DOI: 10.1021/acsami.7b01116
ACS Appl. Mater. Interfaces 2017, 9, 8929−8940

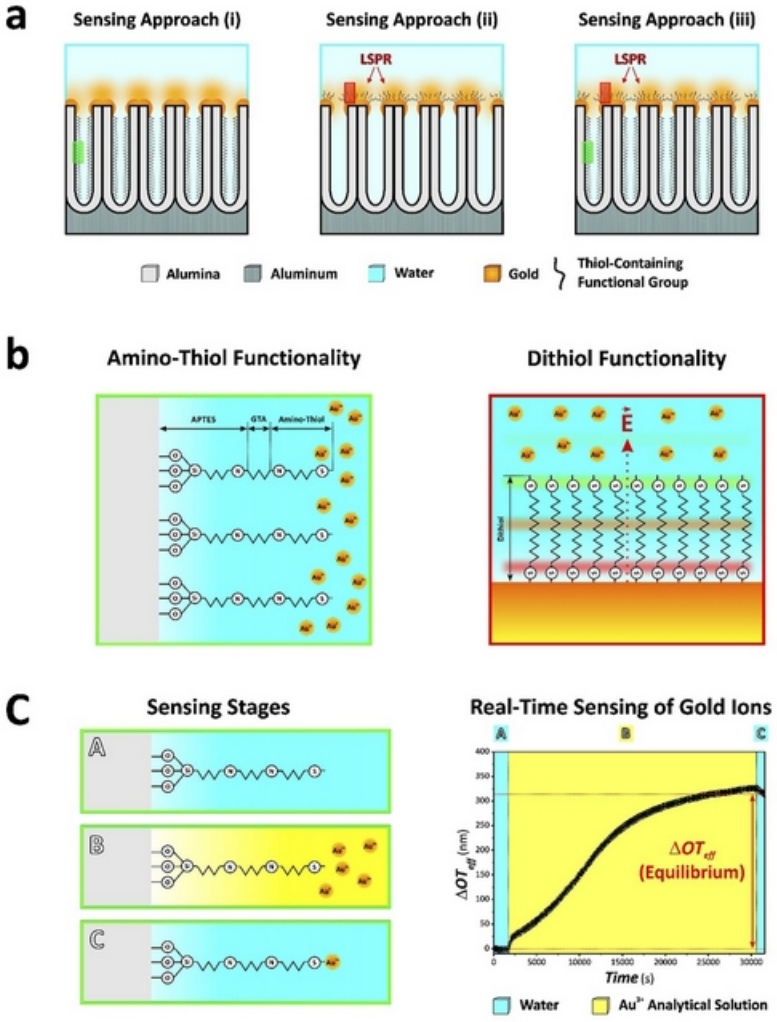

Figure 1. Sensing concepts and surface chemistries of NAA sensing platforms in combination with RIfS. (a) Sensing approaches used in our study: (i) selective functionalization with amino-thiol functional molecules inside the nanopores of NAA platforms, (ii) selective functionalization with dithiol functional molecules on the top surface of NAA platforms, and (iii) selective dual functionalization with amino-thiol and dithiol functional molecules inside the nanopores and on the top surface of NAA platforms, respectively. (b) Details of the surface chemistry structure for amino-thiol (left: magnified view of green rectangle shown in (a)) and dithiol (right: magnified view of red rectangle shown in (b)) functional molecules (note: for dithiol molecules, a localized surface plasmon resonance (LSPR) sensing approach was used, where the sensitivity of the system relies on the electromagnetic field generated in gold-coated NAA platforms, $\vec{E}$). (c) Stages of the sensing approach used in our study (left) and example of real-time sensing of gold ions in NAA platforms based on changes in the effective optical thickness measured by RIfS (note: real sensing for 8-amino-1-octanethiol for $[Au^{3+}]$ = 80 μM).

devices.[18] The combination of RIfS with NAA platforms has recently shown significant and promising potential for qualitative and quantitative detection of a broad range of analytes, such as gases, metal ions, biomolecules, and organic molecules.[19−25]

The sensitivity of interferometric sensors based on NAA and analogous nanoporous materials relies on the magnitude of the interaction between the nanoporous matrix and analyte molecules.[26,27] This interaction is translated into changes in the effective medium of the nanoporous film, the magnitude of which is established by five main factors, including (i) the optical properties of the analyte molecules, (ii) the size of the analyte molecules, (iii) the nature of the medium filling the nanopores (e.g., air or water), (iv) the chemical and physical interaction between the analyte molecules and the surface of the nanoporous matrix, and (v) the effective medium of the sensing platform.[25] The surface of NAA can be chemically modified with different functional molecules in order to attain chemical selectivity toward analytes of interest.[25] This factor is of critical importance, not only to selectively capture targeted analyte molecules but also for the sensitivity of the system, as this is strongly dependent on how surface functional groups interact with analyte molecules. Therefore, a suitable chemical functionalization strategy can result in enhanced sensing performances, which is a critical aspect to consider in the development of optical sensing systems for real-time monitoring of analytes in dynamic environments.

Herein, we demonstrate that a rational engineering of the surface chemistry in NAA interferometric platforms can significantly enhance the overall sensing performance. In this study, the gold−thiol interaction in NAA interferometric platforms was chosen as a sensing binding model to discern the effect of different factors upon the overall sensitivity. NAA platforms were functionalized with different thiol-containing

DOI: 10.1021/acsami.7b01116
ACS Appl. Mater. Interfaces 2017, 9, 8929−8940

Table 1. Summary of the Characteristics of the Different Functional Molecules Used in Our Study

Functional Molecule Name	Functional Molecule Structure	Molecular Parameter	Sensing Approach	Molecular Mass (g mol^{-1})	Contact Angle (^{0})
L-cysteine	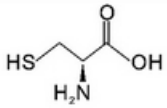	Functional Features	(i)	121.16	36 ± 2
Cysteamine				113.61	39 ± 3
L-cysteine Methyl Ester	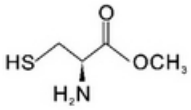			171.65	50 ± 2
AAC	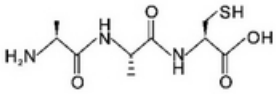			263.42	59 ± 3
3-amino-1-propanethiol		Molecular Length	(i)	127.64	34 ± 2
6-amino-1-hexanethiol				169.72	51 ± 3
8-amino-1-octanethiol				197.77	65 ± 2
1,3-propanedithiol		Molecular Length	(ii)	108.23	105 ± 2
1,6-hexanedithiol	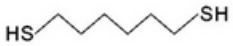			150.31	113 ± 1
1,9-nonanedithiol				192.39	120 ± 5

functional molecules. Three sensing approaches were used to establish the effect of these functional configurations on the sensing performance (Figure 1a). This involved (i) selective chemical functionalization of the inner surface of NAA with amino-thiol molecules of different molecular features and sizes, (ii) selective chemical functionalization of the top surface of NAA with dithiol molecules of different sizes, and (iii) selective chemical functionalization of both the top and inner surface of NAA with amino-thiol molecules and dithiol molecules. Changes in the effective optical thickness of NAA platforms after exposure to analytical solutions containing gold ions (Au^{3+}) are used as the sensing principle (Figure 1b). This process is monitored in real time by RIfS, enabling the real-time assessment of the interaction between thiol functional groups present in NAA platforms and Au^{3+} ions (Figure 1c).

2. EXPERIMENTAL SECTION

2.1. Materials. High purity (99.9997%) aluminum (Al) foils 0.32 mm thick were supplied by Goodfellow Cambridge Ltd. (UK). Oxalic acid ($H_2C_2O_4$), perchloric acid ($HClO_4$), chromium trioxide (CrO_3), 3-aminotrimethoxysilane ($H_2N(CH_2)_3Si(OC_2H_5)_3$, APTES), hydrogen peroxide (H_2O_2), glutaraldehyde ($CH_2(CH_2CHO)_2$, GTA), phosphate buffered saline (PBS), L-cysteine ($C_3H_7NO_2S$), cysteamine hydrochloride ($C_2H_7NS{\cdot}HCl$), 3-amino-1-propanethiol hydrochloride ($C_3H_9NS{\cdot}HCl$), 6-amino-1-hexanethiol hydrochloride ($C_6H_{15}NS{\cdot}HCl$), 8-amino-1-octanethiol hydrochloride ($C_8H_{19}NS{\cdot}HCl$), 1,3-propanedithiol ($C_3H_8S_2$), 1,6-hexanedithiol ($C_6H_{14}S_2$), 1,9-nonanedithiol ($C_9H_{20}S_2$), and gold(III) chloride hydrate ($HAuCl_4{\cdot}H_2O$) were purchased from Sigma-Aldrich (Australia) and used as received, without further purification. L-Cysteine methyl ester hydrochloride ($C_4H_9NO_2S{\cdot}HCl$) was purchased from TCI Co., Ltd., and used as received, without further purification. AlaAlaCys (AAC) was synthesized by stepwise coupling of Fmoc-Cys (Trt) and Fmoc-Ala amino acids through a standard solid phase synthesis with *N*-fluorenylmethyloxycarbonyl/cysteine(trityl) (N-Fmoc/Cys(Trt)) protecting group strategy (see Supporting Information for further details about the synthesis of the tripeptide AAC). Ethanol (C_2H_5OH, EtOH) and phosphoric acid (H_3PO_4) were supplied by ChemSupply (Australia). Ultrapure water Option Q-Purelabs (Australia) was used in the preparation of aqueous solutions for this study.

2.2. Fabrication of Nanoporous Anodic Alumina (NAA) Platforms. Al substrates were anodized through a two-step electrochemical anodization process reported elsewhere.[28−31] In brief, square-like Al chips 1.5 × 1.5 cm^2 were sonicated in EtOH and ultrapure water for 15 min, respectively, and then dried under air stream. Before anodization, Al chips were electropolished in a mixture of EtOH and $HClO_4$ 4:1 (v:v) at 20 V and 5 °C for 3 min. The first anodization step was performed in an aqueous solution 0.3 M oxalic acid at 40 V and 6 °C for 20 h. The resulting NAA layer was subsequently removed by

DOI: 10.1021/acsami.7b01116
ACS Appl. Mater. Interfaces 2017, 9, 8929−8940

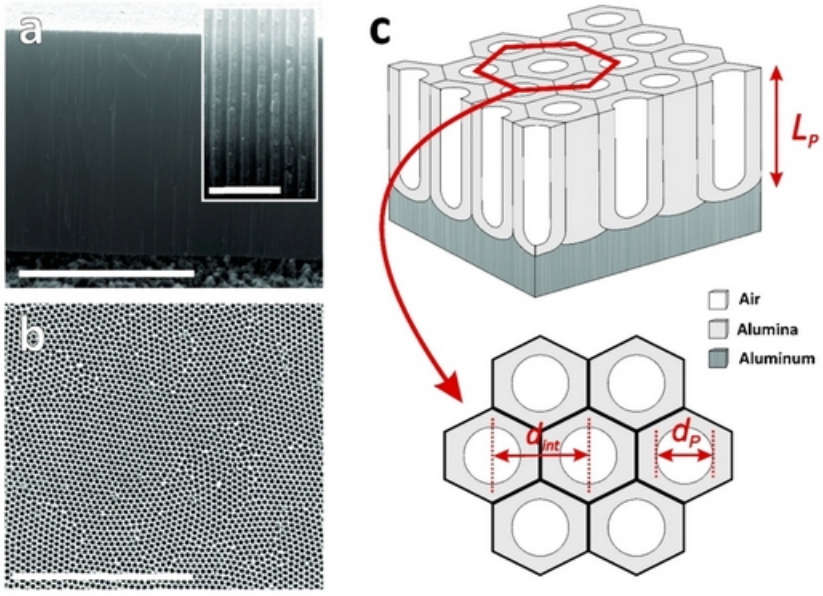

Figure 2. Structural characterization of NAA sensing platforms used in our study. (a) Cross-sectional SEM view of a NAA platform showing straight cylindrical nanopores from top to bottom (scale bar = 5 μm) and inset showing detail of the cylindrical nanopores (scale bar = 500 nm). (b) Top SEM view of a NAA platform featuring characteristic hexagonally arranged cylindrical nanopores across its surface as a result of a two-step anodization process (scale bar = 3 μm). (c) Schematic illustration providing a visual description of the geometric features of NAA platforms with details of the structural parameters (L_p = pore length, d_p = pore diameter, and d_{int} = interpore distance).

wet chemical etching in a mixture of 0.2 M chromic acid (H_2CrO_4) and 0.4 M H_3PO_4 at 70 °C for 3 h. The second anodization step was carried out under the same conditions (0.3 M $H_2C_2O_4$, 40 V and 6 °C) for 2 h. Lastly, the nanoporous structure of these NAA platforms was widened by wet chemical etching in an aqueous solution of H_3PO_4 (5 wt %) at 35 °C for 15 min.

2.3. Surface Chemistry Modification Using Amino-Thiol Functional Molecules: Sensing Approach (i). The functionalization of the inner surface of NAA sensing platforms was carried out via silanization with APTES.[32−35] The as-produced NAA sensing platforms were first hydroxylated by immersion in hydrogen peroxide (30 wt %) at 90 °C for 10 min and then dried under air stream. Next, hydroxylated NAA platforms were functionalized with 3-aminopropyltriethoxysilane by chemical vapor deposition at 110 °C for 3 h and then washed with ethanol and distilled water. To activate the amine terminal group ($-NH_2$) of APTES molecules immobilized onto the inner surface of NAA platforms, these were fully immersed in an aqueous solution of 2.5 vol % glutaraldehyde in PBS for 30 min. GTA-activated NAA sensing platforms were then ready for the immobilization of amino-thiol functional molecules, which was carried out by immersing these platforms into different amino-thiol solutions for 18−20 h. Table 1 summarizes all the thiol-containing functional molecules used in this study. Two parameters of the functional molecules were analyzed using sensing approach (i): namely, the molecular features of amino-thiol molecules and their size. To analyze the former parameter, GTA-activated APTES-functionalized NAA platforms were functionalized with 1 mg mL^{-1} in PBS solution (pH = 7.4) of L-cysteine, cysteamine hydrochloride, L-cysteine methyl ester hydrochloride, and AAC, following the above-mentioned process (*vide supra*). As far as the analysis on the molecular size is concerned, GTA-activated APTES-functionalized NAA platforms were functionalized with 1 mg mL^{-1} in PBS solution of 3-amino-1-propanethiol hydrochloride, 6-amino-1-hexanethiol hydrochloride, and 8-amino-1-octanethiol hydrochloride. Note that amino-thiol-functionalized NAA platforms were washed with ultrapure water and dried under air stream after functionalization. Finally, the amino-thiol-functionalized NAA sensing platforms were coated with an ultrathin layer of gold (i.e., 4−5 nm) using a sputter coater equipped with a film thickness monitor (sputter coater 108auto, Cressington, USA) to enhance light interference.[16,21]

2.4. Surface Chemistry Modification Using Dithiol Molecules: Sensing Approach (ii). The top surface of gold-coated NAA sensing platforms was selectively functionalized with a set of dithiol molecules (Table 1) by direct immersion in a solution of functionalizing molecules over 18−20 h to generate self-assembled monolayers of dithiol molecules onto gold sputtered onto the top surface of NAA platforms. The dithiol solutions used were 1 mg mL^{-1} of 1,3-propanedithiol, 1,6-hexanedithiol, and 1,9-nonanedithiol in EtOH. The dithiol-functionalized NAA platforms were then washed with EtOH and ultrapure water after functionalization to remove physisorbed molecules, dried under air stream, and stored under dry conditions until further use.

2.5. Surface Chemistry Modification Using Both Amino-Thiol and Dithiol Molecules: Sensing Approach (iii). After establishing the most sensitive thiol-containing functional molecules in approaches (i) and (ii) (i.e., amino-thiols and dithiols, respectively), a set of NAA platforms were selectively functionalized with both thiol-terminated molecules, sequentially. In this process, NAA platforms were first hydroxylated, silanized, and activated using the above-mentioned silanization protocol. The GTA-activated APTES-functionalized NAA platforms were then ready for the selective immobilization of amino-thiol molecules onto the inner surface of their nanopores, which was carried out under batch condition (i.e., immersion of NAA platforms in amino-thiol solution for 18−20 h). The amino-thiol-functionalized NAA platforms were then coated with a thin layer of gold, and their top surface was selectively functionalized with dithiol molecules under batch conditions for 18−20 h following the protocol used in approach (ii).

2.6. RIfS System and Detection of Gold Ions (Au^{3+}). Details of our RIfS setup have been reported elsewhere.[20,22] In brief, white light from a tungsten source was directed onto the surface of thiol-functionalized NAA platforms with an illumination spot of 2 mm by a bifurcated optical probe. The collection fiber of the optical probe collected and transferred the reflected light from the illumination spot to a miniature spectrophotometer (USB 4000 + VIS-NIR-ES, Ocean Optics, USA). The optical spectra were obtained in the range 400−1000 nm and saved at intervals of 30 s with an integration time of 20 s, with 20 average measurements. The acquired RIfS spectra were

DOI: 10.1021/acsami.7b01116
ACS Appl. Mater. Interfaces 2017, 9, 8929−8940

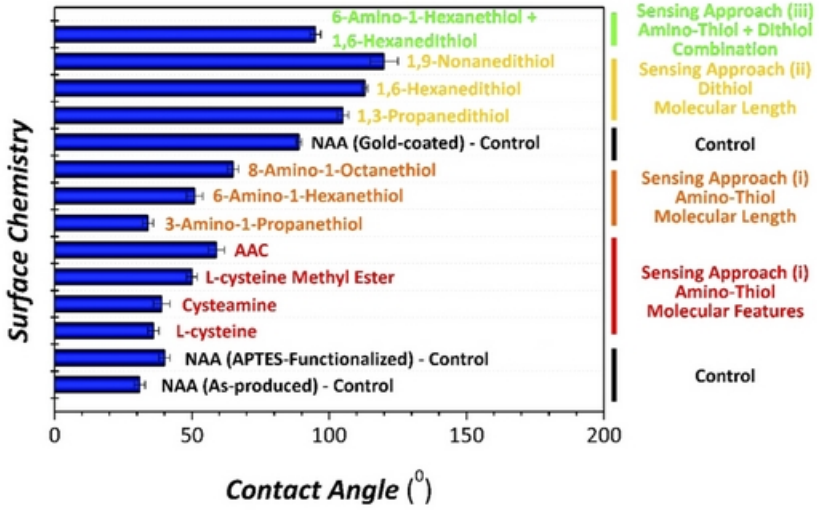

Figure 3. Contact angle characterization for the different surface chemistries assessed in our study.

processed by applying fast Fourier transform using Igor Pro library (Wavemetrics, USA) to estimate the effective optical thickness (OT_{eff}) of the NAA sensing platforms (eq 1):

$$OT_{eff} = 2n_{eff}L_p \cos\theta \quad (1)$$

where OT_{eff} is the effective optical thickness of the film, n_{eff} is the effective refractive index of the NAA platform, L_p is its physical thickness, and θ is the angle of incidence of light (i.e., $\theta = 0°$ in this case).

The sensitivity of thiol-functionalized NAA platforms toward gold ions was assessed by RIfS through changes in OT_{eff} as a function of the concentration of gold ions. This binding process was monitored in real time using a custom-designed flow cell. A stock solution of Au^{3+} ions (1 mM) was prepared by dissolving $HAuCl_4 \cdot H_2O$ in ultrapure water, and analytical solutions of Au^{3+} with concentrations ranging from 20 to 80 μM with an interval of 20 μM were obtained by dilution of the Au^{3+} stock solution. Thiol-functionalized NAA sensing platforms were packed in a custom-made flow cell based on transparent acrylic plastic and analytical solutions were flowed at a rate of 100 μL min^{-1}. This flow rate was maintained throughout the sensing experiments by a peristaltic pump (LongerPump BT100-2J) with an equivalent pumping angular rate of 1.4 rpm. The sensing experiments started with the establishment of stable baseline by flowing ultrapure water. Once a stable baseline was obtained, analytical solutions of Au^{3+} of different concentrations (20, 40, 60, and 80 μM) were introduced into the flow cell. The interaction between Au^{3+} ions present in the analytical solutions and thiol functional groups on the surface of functionalized NAA platforms induced sharp changes (i.e., increment = red-shift) in the OT_{eff} of NAA platforms. After OT_{eff} achieved a stable value, ultrapure water was flowed for 15 min to obtain the total change of OT_{eff} (ΔOT_{eff}) associated with the corresponding concentration of Au^{3+} ions. Note that fresh thiol-functionalized NAA platforms were used to establish the total effective optical thickness change for each analytical concentration of Au^{3+}.

2.7. Structural Characterization of NAA Sensing Platforms. Scanning electron microscopy (SEM) images of NAA sensing platforms were acquired using a field-emission gun scanning electron microscopy (FEG-SEM FEI Quanta 450). These images were used to establish the geometric features of NAA platforms by image analysis using ImageJ (public domain program developed at the RSB of the NIH).[36]

2.8. Contact Angle Measurement in NAA Sensing Platforms. The contact angle for each NAA sensing platforms was measured by a tensiometer (Attension Theta optical tensiometer). The sensile drop technique was used in these experiments, where a water droplet was formed on the end of a syringe, which was descended until the water droplet touched the surface of the sample stage, followed by the withdraw of the needle away from the stage. Image analysis was used to establish the contact angle on the surface of NAA platforms containing functional groups.

3. RESULTS AND DISCUSSION

3.1. Structural Characterization of NAA Sensing Platforms. SEM images of the NAA platforms reveal the characteristic geometric features of NAA produced by a two-step anodization approach (Figure 2). Cross-sectional SEM images of these platforms show vertically aligned straight cylindrical nanopores from top to bottom (Figure 2a). Top SEM images reveal that these nanoporous photonic films feature hexagonally arranged nanopores homogeneously distributed across their surface (Figure 2b) with an average pore diameter (d_p) of 66 ± 6 nm, pore length (L_p) of 6.0 ± 0.1 μm, and interpore distance (d_{int}) of 105 ± 4 nm (Figure 2c).

3.2. Contact Angle Measurements of Functionalized NAA Sensing Platforms. The successful functionalization of NAA platforms with thiol-containing functional molecules using approaches (i) and (ii) was validated and analyzed by contact angle measurements (Figure 3). Note that the purpose of contact angle measurements was to establish the effect of the molecular interaction and conformation among the functionalizing molecules on the hydrophobic character of functionalized NAA platforms. As such, these NAA platforms for sensing approach (i) were not coated with a thin layer of gold to mimic the surface chemistry inside the nanopores. Two samples were used as control references for NAA platforms functionalized following approach (i) (i.e., selective functionalization of the inner surface of the nanopores with amino-thiol functional molecules), being the as-produced and APTES-functionalized NAA platforms. The contact angle of these NAA platforms was found to be 31 ± 2° and 40 ± 2°, respectively. Whereas as-produced NAA platforms have a hydrophilic character, the functionalization of their inner surface with APTES molecules induces a relatively weak hydrophobic character due to the presence of amine terminal groups ($-NH_2$) (Figure 3). As for the effect of the molecular features of cysteine-like molecules, Figure 3 shows that the hydrophobic character of the NAA increases in the following order: L-cysteine (36 ± 2°) < cysteamine (39 ± 3°) < L-cysteine methyl

DOI: 10.1021/acsami.7b01116
ACS Appl. Mater. Interfaces 2017, 9, 8929−8940

ester (50 ± 2°) < AAC (59 ± 3°). These results show that the presence of additional functional groups (e.g., carboxyl, ester, methyl, etc.) has a significant impact on the hydrophobic character of these photonic films (Table 1). For instance, AAC is a tripeptide and thus possesses two amide functional groups. As a result, AAC-functionalized NAA platforms have the strongest hydrophobic character among the cysteine-like functional molecules analyzed in our study. This property in turn determines the surface interaction between analyte molecules (i.e., Au^{3+}) in an aqueous matrix and the surface of the sensing platforms. Another important factor which plays a role in the overall hydrophobic character of functionalized NAA platforms is the length of the functional molecules. To discern the effect of this parameter, we analyzed the contact angle in a set of NAA platforms functionalized with amino-thiol molecules (Figure 3 and Table 1). Our results reveal that the hydrophobic character of NAA platforms increases with the length of the amino-thiol functional molecules in the following order: 3-amino-1-propanethiol (34 ± 2°) < 6-amino-1-hexanethiol (51 ± 3°) < 8-amino-1-octanethiol (65 ± 2°) (Figure 3 and Table 1). As such, the longer the amino-thiol backbone, the more hydrophobic the character of the functionalized surface. It is worthwhile noting that thiol groups (−SH) are hydrophobic. Therefore, the conformation of the functional layer immobilized onto the surface of NAA has a direct effect upon the overall hydrophobic character of these films. This result suggests that functional layers of 8-amino-1-octanethiol molecules immobilized onto the inner surface of GTA-activated APTES-functionalized NAA platforms have a more compact assembly as compared to other functional amino-thiol molecules of shorter backbone structure. As such, more thiol functional terminal groups would be exposed across the surface of NAA, increasing the hydrophobic character of NAA platforms functionalized with 8-amino-1-octanethiol.

Finally, we assessed the contact angle of NAA films functionalized with dithiol molecules following approach (ii). In this case, a gold-coated NAA platform was used as a control, the contact angle of which was found to be significantly more hydrophobic (i.e., 89 ± 1°) than that of noncoated or amino-thiol-functionalized NAA platforms (Figure 3). The hydrophobic character of these NAA platforms was further increased after selective chemical functionalization with dithiol groups following sensing approach (ii) (Figure 1a). We also analyzed the effect of the length of dithiol molecules on the hydrophobic character of NAA platforms. Our results demonstrate that as per the amino-thiol molecules, longer molecules give a more hydrophobic character to the NAA platform in the following order: 1,3-propanedithiol (105 ± 2°) < 1,6-hexanedithiol (112 ± 1°) < 1,9-nonanedithiol (119 ± 5°). Therefore, this result verifies that longer molecules can provide more compact self-assembled monolayers of dithiol functional groups onto the surface of gold-coated NAA platforms.

3.3. Evaluation of Sensitivity in NAA Sensing Platforms Functionalized with Amino-Thiol Functional Molecules. A range of amino-thiol molecules containing a common cysteine-like backbone structure was used to modify the surface chemistry of NAA platforms and discern the effect of molecular functionalities and backbone length on the sensing performance of NAA interferometric sensors. Prior to immobilization, silanization and activation of amine terminal groups were performed. In this process, NAA platforms were pretreated with hydrogen peroxide for hydroxylation of the inner surface of nanopores (i.e., generation of hydroxyl groups). Silanization of these NAA platforms was carried out by chemical vapor deposition of APTES molecules to endow as-produced NAA platforms with amine functionality through the silane layer, inside the nanopores.[37] The amine functional groups of APTES molecules were then activated by GTA molecules, which provides aldehyde functionality, through the immersion of NAA platforms in GTA solution. The immobilization of amino-thiol molecules on the GTA-activated NAA platforms occurred through the amine binding formed between the aldehyde functionality of GTA molecules and the amine group of amino-thiol molecules.[37] A schematic illustration of the immobilization and binding of these molecules onto the inner surface of GTA-activated APTES-functionalized NAA platforms is shown in Figure 1c. Both the inner and top surfaces of the NAA were functionalized with APTES, GTA, and amino-thiol molecules. Note that these amino-thiol-functionalized NAA platforms were coated with a thin layer of gold before they were used as sensing platforms. This layer of gold covered the functional molecules attached onto the top surface of NAA platforms, preventing top surface functional groups from interacting with Au^{3+} ions. Thus, there was no occurrence of binding events on the top surface of NAA platforms, and only amino-thiol molecules functionalized on the inner surface of nanopores were exposed to Au^{3+} ions for binding.

3.3.1. Effect of Molecular Features in Amino-Thiol Functional Molecules. The cysteine-like molecules immobilized onto the inner surface of NAA platforms have similar backbone structure, where they have both amine and thiol groups, but they differ in their functional groups along the molecule (e.g., carboxyl, ester, etc.), as shown in Table 1. These amino-thiol functionalized NAA sensing platforms were combined with RIfS and their sensitivity assessed by measuring changes in the effective optical thickness of the film (ΔOT_{eff}) in response to the binding of Au^{3+} ions present in analytical solutions of different concentration (20, 40, 60, and 80 μM) using sensing approach (i) (Figure 1a). Figure 4a displays representative graphs showing ΔOT_{eff} as a function of time for NAA platforms functionalized with L-cysteine, cysteamine, L-cysteine methyl ester, and AAC. Note that a stable baseline was first obtained in ultrapure water before injection of the analyte solution containing Au^{3+} ions. An increase in OT_{eff} was observed as the Au^{3+} solution was flowed through the system, which indicates the binding between Au^{3+} ions and thiol functional groups immobilized onto the inner surface of these NAA platforms. This observation is true for all cases (i.e., L-cysteine, cysteamine, and AAC) except for L-cysteine methyl ester, where there was a decrease in OT_{eff} at the initial stage of the flowing of Au^{3+} solution. The decrease in OT_{eff} observed might be due to conformational changes upon the interaction between Au^{3+} and L-cysteine methyl ester. Ultrapure water was flowed again through the system for 15 min once the binding between gold ions and thiol groups reached the equilibrium, which was characterized by a plateau in the spectra. In this process, ΔOT_{eff} was found to decrease slightly due to the removal of physisorbed gold ions, which is in good agreement with previous studies using a similar sensing approach.[22] The correlation between ΔOT_{eff} and the concentration of Au^{3+} for cysteine-like molecules with different molecular features is shown in Figure 4b. This analysis reveals a linear dependence of ΔOT_{eff} with $[Au^{3+}]$ for all the cysteine-like molecules within the range of concentrations studied. As the concentration of gold ions in the analytical solution increases, more Au^{3+} ions

DOI: 10.1021/acsami.7b01116
ACS Appl. Mater. Interfaces 2017, 9, 8929−8940

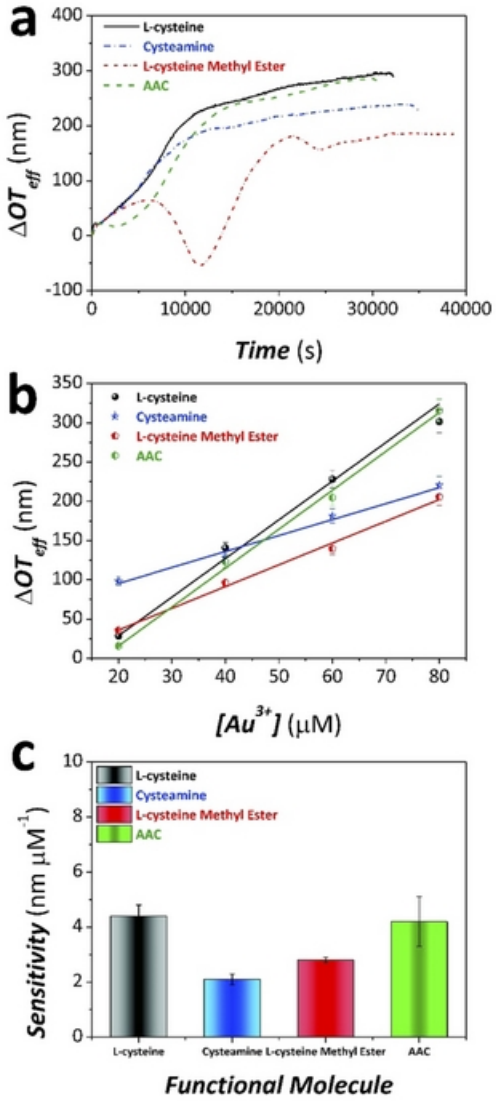

Figure 4. Assessment of optical sensitivity for amino-thiol functional molecules with different molecular features in NAA sensing platforms through the detection of different concentrations of gold ions using sensing approach (i). (a) Representative graph showing the effective optical thickness change in NAA sensing platforms functionalized with L-cysteine, cysteamine, L-cysteine methyl ester, and AAC for a concentration 80 μM of Au^{3+} measured in real time by RIfS. (b) Linear fitting lines for NAA sensing platforms modified with L-cysteine, cysteamine, L-cysteine methyl ester, and AAC used to establish the linear correlation between ΔOT_{eff} and $[Au^{3+}]$ for the range of concentrations 20, 40, 60, and 80 μM. (c) Bar chart summarizing the sensitivities (i.e., slope of linear fittings shown in (b)) for NAA sensing platforms modified with L-cysteine, cysteamine, L-cysteine methyl ester, and AAC.

are available to be bound by thiol functional groups present in the inner surface of NAA platforms, which in turn is translated into greater changes in the effective optical thickness. The slope of these linear fittings corresponds to the sensitivity of the system, expressed in terms of effective optical thickness change per concentration unit (i.e., nm μM^{-1}) (Figure 4c). Our results indicate that L-cysteine and AAC provide approximately the same level of sensitivity to Au^{3+} ions (4.4 $\pm$ 0.4 and 4.2 $\pm$ 0.6 nm μM^{-1}, respectively), whereas NAA platforms functionalized with L-cysteine methyl ester and cysteamine show the least sensitivity (i.e., 2.8 $\pm$ 0.1 and 2.1 $\pm$ 0.2 nm μM^{-1}, respectively). Unlike the other amino-thiol molecules, the only site for cysteamine molecules to interact with Au^{3+} ions is via the thiol terminal group. Thus, the amount of gold ions immobilized onto the inner surface of NAA platforms is approximately equivalent to the number of cysteamine molecules available inside the surface of NAA nanopores. As a result, the low sensitivity achieved by cysteamine-functionalized NAA platforms when detecting gold ions (2.1 $\pm$ 0.2 nm μM^{-1}) could be associated with the lack of other functionalities along its backbone structure, which might provide further sites for binding interactions. Although L-cysteine methyl ester possesses a terminal-ester functional group, the presence of this additional functional group compared to L-cysteine only slightly improves the sensitivity of the NAA platforms toward Au^{3+} ions (2.8 $\pm$ 0.1 nm μM^{-1}), as revealed by the results shown in Figure 4c. In contrast to cysteamine and L-cysteine methyl ester, the carboxylic acid groups of L-cysteine and AAC might be able to interact with gold ions through van der Waals forces, increasing the occurrence of gold ion capturing events inside the nanopores and thus enhancing the overall sensitivity of the system as a result (i.e., 4.4 $\pm$ 0.4 and 4.2 $\pm$ 0.6 nm μM^{-1}, respectively). Carboxylic acid is known as one of the common building blocks for the formation of molecular self-assembled layers on metal surfaces through chemisorption.[38] Therefore, we suggest that L-cysteine and AAC molecules immobilized onto the inner surface of NAA nanopores could also bind to areas that are free of APTES linkage molecules through the direct chemisorption of carboxylic acid on APTES-free aluminum oxide.[39] This would result in an increment in the number of thiol-terminated molecules present on the inner surface of NAA nanopores, which in turn would be translated into a significant enhancement of the sensitivity of the NAA platforms toward Au^{3+} ions. As mentioned before, the size and the refractive index of the functional molecules immobilized onto the inner surface of NAA platforms could also have an impact on the overall sensitivity of the system.[25] It can be observed that whereas cysteamine has the smallest chemical structure among the functional molecules analyzed in this section of our study, the functional molecule AAC has the biggest molecular size, which could contribute to a more sensitive system due to the bigger magnitude of the ΔOT_{eff} in NAA platforms when interacting with Au^{3+} ions.

3.3.2. Effect of Molecular Length in Amino-Thiol Functional Molecules. NAA sensing platforms were functionalized with amino-thiol molecules featuring different backbone lengths by APTES silanization and subsequent immobilization by GTA activation and functionalization of amino-thiol molecules. These NAA platforms were then gold coated before being used as sensing platforms. The amino-thiol molecules used in our study to assess the effect of the molecular length by sensing approach (i) were 3-amino-1-propanethiol, 6-amino-1-hexanethiol, and 8-amino-1-octanethiol. As depicted in Table 1, these molecules possess a terminal amine group ($-NH_2$), which is responsible for attachment to the GTA-activated APTES molecules immobilized onto the inner surface of NAA nanopores. Additionally, a terminal thiol group ($-SH$) is responsible for Au^{3+} ions capture, and the sole variation between these amino-thiol molecules is the length of the carbon chain between the terminal functional groups. Assessment of the sensitivity of these amino-thiol-functionalized NAA platforms was carried out using the protocol outlined

DOI: 10.1021/acsami.7b01116
ACS Appl. Mater. Interfaces 2017, 9, 8929−8940

previously based on sensing approach (i) (Figure 1a). Figure 5a shows an example of real-time sensing in these NAA-

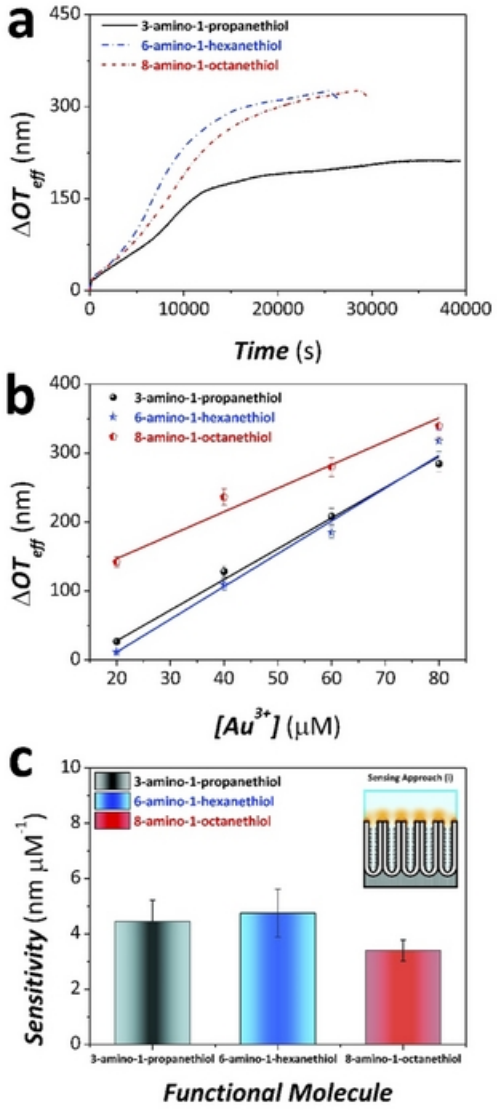

Figure 5. Assessment of optical sensitivity for amino-thiol functional molecules with different molecular lengths in NAA sensing platforms through the detection of different concentrations of gold ions using sensing approach (i). (a) Representative graph showing the effective optical thickness change in NAA sensing platforms functionalized with 3-amino-1-propanethiol, 6-amino-1-hexanethiol, and 8-amino-1-octanethiol for a concentration 80 μM of Au^{3+} measured in real time by RIfS. (b) Linear fitting lines for NAA sensing platforms modified with 3-amino-1-propanethiol, 6-amino-1-hexanethiol, and 8-amino-1-octanethiol used to establish the linear correlation between ΔOT_{eff} and $[Au^{3+}]$ for the range of concentrations 20, 40, 60, and 80 μM. (c) Bar chart summarizing the sensitivities (i.e., slope of linear fittings shown in (b)) for NAA sensing platforms modified with 3-amino-1-propanethiol, 6-amino-1-hexanethiol, and 8-amino-1-octanethiol.

functionalized platforms, while Figure 5b depicts the correlation between Au^{3+} ions concentration and ΔOT_{eff}, establishing the linear dependency of ΔOT_{eff} for amino-thiol-functionalized NAA platforms with $[Au^{3+}]$. It is apparent that the higher the concentration of gold ions in the analyte solution, the more Au^{3+} ions available to interact with amino-thiol molecules immobilized onto the inner surface of NAA nanopores. As such, ΔOT_{eff} increases with the concentration of gold ions, linearly, within the range of analyte concentrations used in our study. The sensitivity provided by these amino-thiol molecules of different molecule length was estimated by the slope of the fitting lines for the respective amino-thiol molecules shown in Figure 5b. An overview of the sensitivity of these amino-thiol molecules is presented in the bar chart of Figure 5c. Our analysis reveals that NAA platforms functionalized with 6-amino-1-hexanethiol have the greatest sensitivity (4.8 ± 0.9 nm μM^{-1}) followed by 3-amino-1-propanethiol (4.4 ± 0.8 nm μM^{-1}). Interestingly, 8-amino-1-octanethiol-functionalized NAA platforms showed the least sensitivity toward Au^{3+} ions (3.4 ± 0.4 nm μM^{-1}). Previous studies indicated that functional molecules of bigger molecular size immobilized onto the inner surface of nanoporous materials can provide more significant changes in the effective optical thickness of the sensing platforms, resulting in a higher sensitivity toward targeted analytes.[26,27] Nevertheless, we found this to be partly true for NAA platforms functionalized with 3-amino-1-propanethiol and 6-amino-1-hexanethiol, where the latter (i.e., 6C) is slightly more sensitive toward Au^{3+} ions as compared to the former (i.e., 3C). However, 8-amino-1-octanethiol was the least sensitive molecule, despite being the longest (i.e., 8C) of those investigated. This might be due to the molecular orientation and conformation of 8-amino-1-octanethiol immobilized onto the inner surface of NAA nanopores. The longer carbon chain length of 8-amino-1-octanethiol might lead to molecules becoming folded or crumpled up inside the nanopores, shielding the thiol functional groups from interacting with Au^{3+} ions. In contrast, the shorter lengths of 3-amino-1-propanethiol and 6-amino-1-hexanethiol molecules could facilitate the orientation and alignment in such a way that the amount of sensing molecules and available thiol functional groups inside the nanopores is higher than that of 8-amino-1-octanethiol molecules. Based on these observations, we postulate that there is an optimal size in terms of overall sensitivity of the system for the functionalizing molecules to be immobilized onto the inner surface of NAA nanopores.

3.4. Evaluation of Sensitivity of NAA Sensing Platforms Functionalized with Dithiols of Different Molecular Sizes toward Au^{3+} Ions. Sensing approach (ii) corresponds to a localized surface plasmon resonance (LSPR) sensing configuration (Figure 1b). It is known that a LSPR approach in NAA sensing platforms can provide high sensitivity and low limit of detection performances due to the disturbance and interaction between the electromagnetic field generated around nanometric metallic structures and analyte molecules.[40,41] In our study, NAA sensing platforms were coated with a thin layer of gold before functionalization with dithiol molecules of different molecular length (i.e., carbon chain). The dithiol molecules used in this study feature different backbone lengths, 1,3-propanedithiol (3C), 1,6-hexanedithiol (6C), and 1,9-nonanedithiol (9C). The chemical structures of the dithiol molecules possess a terminal thiol group at each end of the molecule as shown in Table 1. Unlike the previous sensing approach where the amino-thiol molecules were selectively immobilized inside the NAA nanopores, these dithiol molecules were selectively attached on the top surface of gold-coated NAA nanopore through the well-known affinity interaction between gold on the surface of NAA and one of the thiol groups of the dithiol molecules. The other thiol group remains free to detect Au^{3+} ions during the flow of analyte solutions.

DOI: 10.1021/acsami.7b01116
ACS Appl. Mater. Interfaces 2017, 9, 8929−8940

The attachment of dithiol molecules on the gold-coated surface of NAA is illustrated in Figure 1b. An example of real-time sensing and the resulting linear correlation between the concentration of Au^{3+} ions and ΔOT_{eff} for each dithiol molecule is presented in Figure 6a,b. These results indicate that ΔOT_{eff} increases linearly with the concentration of gold ions present in the analyte solutions. As the concentration of Au^{3+} increases, there are more gold ions available to be captured by dithiol molecules attached on the surface of NAA. As a result, the occurrence of gold−thiol binding events on the gold-coated surface of NAA increases, producing a greater ΔOT_{eff} of the film. Figure 6b shows the linear fittings corresponding to the different NAA sensing platforms functionalized with the dithiol molecules used in our study. These fittings were used to assess the sensitivity of these dithiol molecules toward gold ions using sensing approach (ii). As indicated by the bar chart in Figure 6c, NAA platforms functionalized with 1,6-hexanedithiol are the most sensitive platforms toward Au^{3+} ions, with a sensitivity of 0.9 ± 0.1 nm μM^{-1}, whereas 1,3-propanedithiol and 1,9-nonanedithiol have significantly poorer sensitivity of 0.3 ± 0.1 and 0.2 ± 0.1 nm μM^{-1}, respectively. In the LSPR approach used in our study, the gold−thiol binding events taking place on the gold-coated surface of NAA platforms induce a change in the local refractive index environment, which is measured through changes in effective optical thickness of the film by RIfS. It is worth noting that the electromagnetic fields near the metal surface are greatly enhanced; however, the electromagnetic strength decreases rapidly with the distance from the metallic structure (Figure 1b). Therefore, it is expected that the sensitivity of NAA sensing platforms using sensing approach (ii) will increase if they are functionalized with dithiol molecules of smaller molecular size. Duyne and co-workers demonstrated the reduction of LSPR sensitivity with distance from the surface of metallic structures using self-assembled monolayers of increasing length.[42−44] Dithiols of shorter chain length present the thiol terminal group inside the strongest part of the electromagnetic field generated on the gold-coated surface of NAA (Figure 1b). Therefore, gold−thiol binding events occurring within that part of the localized electromagnetic field can significantly change the overall effective optical thickness of the platform. NAA platforms functionalized with 1,9-nonanedithiol exhibit low sensitivity, and this might be due to the fact that the thiol group responsible for the interaction with Au^{3+} ions is located far from the active zone of the local electromagnetic field, where its strength is poor. Thus, changes in the local refractive index environment due to gold−thiol interaction are not optimal to be translated into changes in the effective optical thickness of the film, as indicated by the low sensitivity achieved in these NAA platforms. In contrast, NAA platforms functionalized with 1,6-hexanedithiol exhibited the highest sensitivity, indicating that the binding between thiol and Au^{3+} ions occurs at a distance where the electromagnetic field presents the highest strength. NAA platforms functionalized with 1,3-propanedithiol had a low sensitivity probably due to the decay in the strength of the electromagnetic field.

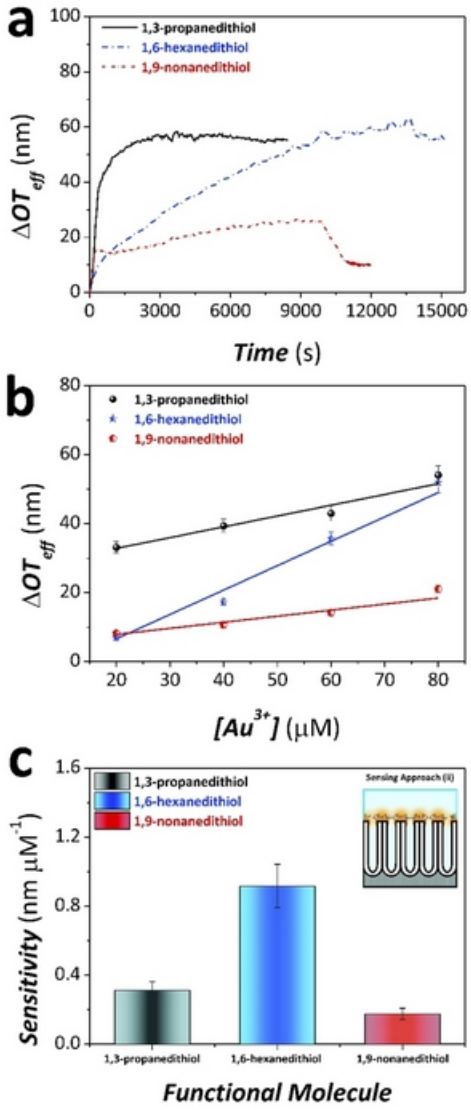

Figure 6. Assessment of optical sensitivity for dithiol functional molecules with different molecular lengths in NAA sensing platforms through the detection of different concentrations of gold ions using sensing approach (ii). (a) Representative graph showing the effective optical thickness change in NAA sensing platforms functionalized with 1,3-propanedithiol, 1,6-hexanedithiol, and 1,9-nonanedithiol for a concentration 80 μM of Au^{3+} measured in real time by RIfS. (b) Linear fitting lines for NAA sensing platforms modified with 1,3-propanedithiol, 1,6-hexanedithiol, and 1,9-nonanedithiol used to establish the linear correlation between ΔOT_{eff} and $[Au^{3+}]$ for the range of concentrations 20, 40, 60, and 80 μM. (c) Bar chart summarizing the sensitivities (i.e., slope of linear fittings shown in (b)) for NAA sensing platforms modified with 1,3-propanedithiol, 1,6-hexanedithiol, and 1,9-nonanedithiol.

It is noteworthy that sensitivities of NAA sensing platforms modified with dithiol molecules using sensing approach (ii) were significantly lower than that of amino-thiol molecules using sensing approach (i). Our results also indicate that the required time for the binding of Au^{3+} ions to dithiol molecules immobilized on the gold-coated surface of NAA platforms to reach equilibrium was shorter than that of amino-thiol molecules selectively immobilized inside the nanopores. This might be associated with the presence of more thiol functional groups on the surface of NAA platforms. The top surface area used in sensing approach (ii) with dithiol molecules is much smaller than that of the inner surface of NAA nanopores used in sensing approach (i) for the immobilization of amino-thiol molecules. As a result, less gold−thiol binding events occur on the gold-coated dithiol-functionalized surface of NAA plat-

DOI: 10.1021/acsami.7b01116
ACS Appl. Mater. Interfaces 2017, 9, 8929−8940

forms, and thus changes in the effective optical thickness of these NAA platforms are smaller, resulting in lower sensitivities.

3.5. Evaluation of Sensitivity of NAA Sensing Platforms with Dual Functionalization. We performed a pioneering set of experiments in order to discern whether the implementation of sensing approaches (i) and (ii) into the same NAA platform results in an additive enhancement of the overall sensitivity of the system. To this end, NAA sensing platforms were functionalized on both the inner surface of NAA nanopores as well as the gold-coated surface of NAA platforms (sensing approach (iii) as illustrated in Figure 1a) using the most sensitive molecules identified from sensing approaches (i) and (ii). 6-Amino-1-hexanethiol (inner surface) and 1,6-hexanedithiol (top surface), with individual sensitivities of 4.8 ± 0.9 and 0.9 ± 0.1 nm μM^{-1}, respectively, were used as sensing molecules for sensing approach (iii). Following hydroxylation and silanization, NAA sensing platforms were functionalized with 6-amino-1-hexanethiol. The amino-thiol modified NAA platforms were then coated with gold before selective functionalization of their top surface with 1,6-hexanedithiol molecules. The dual-functionalized NAA platforms were then used in the detection of gold ions by RIfS. The obtained results presented in Figure 7a,b show that ΔOT_{eff} increases with increasing Au^{3+} in the analyte solution, following a linear relationship between these two parameters. Note that the binding of Au^{3+} to the dual-functionalized NAA platforms took a longer time to reach the equilibrium, which might be due to the presence of functionalizing molecules on the top surface of NAA. The layer of dithiol molecules attached on the top surface of NAA and their interaction with Au^{3+} might act as a hindrance barrier to the flow of Au^{3+} into the nanopores, delaying the occurrence of Au^{3+}–amino-thiol interaction inside the nanopores, thus taking longer time to reach the equilibrium. The sensitivity of NAA platforms using sensing approach (iii) was found to be 5.6 ± 1.0 nm μM^{-1}. Significantly, the combined functionalization of both the inner and top surfaces of NAA platforms provides an almost additive enhancement of the sensitivity compared to that of NAA platforms functionalized with either 6-amino-1-hexanethiol or 1,6-hexanedithiol alone, using sensing approaches (i) and (ii) individually. The sensitivities of these three NAA platforms are compared in Figure 7c. These results indicate that the sensitivity enhancement is approximately additive due to the combined effect of amino-thiol and dithiol molecules selectively immobilized onto NAA platforms. Functionalization of both the inner and top surfaces of NAA nanopores results in more thiol functional groups on the surface of NAA platforms, which are then exposed to gold ions present in the analyte solution. As a result, greater changes in the effective optical thickness of these NAA platforms occur, increasing the overall sensitivity of the system. These results demonstrate that the sensitivity of NAA sensing platforms can be improved by a rational engineering of the surface chemistry. In our case, we found that this rational engineering can make it possible to achieve a 6-fold greater sensitivity than that obtained in previous studies.[21]

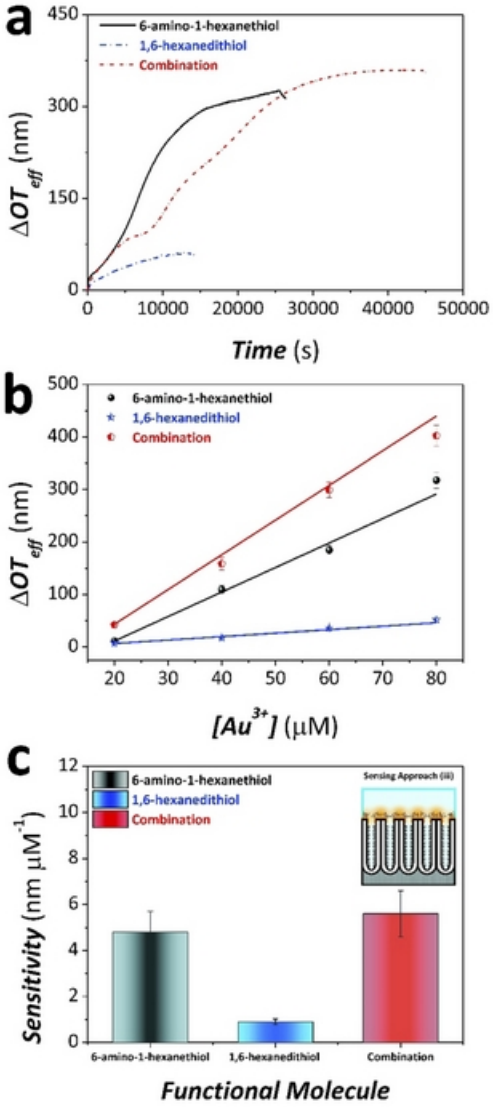

Figure 7. Assessment of optical sensitivity for combined functional molecules in NAA sensing platforms through the detection of different concentrations of gold ions using sensing approach (iii). (a) Representative graph showing the effective optical thickness change in NAA sensing platforms functionalized with 6-amino-1-hexanethiol, 1,6-hexanedithiol, and the combination of both for a concentration 80 μM of Au^{3+} measured in real time by RIfS. (b) Linear fitting lines for NAA sensing platforms modified with 6-amino-1-hexanethiol, 1,6-hexanedithiol, and the combination of both used to establish the linear correlation between ΔOT_{eff} and [Au^{3+}] for the range of concentrations 20, 40, 60, and 80 μM. (c) Bar chart summarizing the sensitivities (i.e., slope of linear fittings shown in (b)) for NAA sensing platforms modified with 6-amino-1-hexanethiol, 1,6-hexanedithiol, and the combination of both.

4. CONCLUSIONS

We have demonstrated for the first time a rationale toward enhancing sensitivity in thiol-modified NAA sensing platforms by surface chemistry engineering. The surface chemistries of NAA sensing platforms were selectively modified using thiol-containing molecules (i.e., amino-thiol and dithiol molecules) with a range of molecular features and backbone sizes and using two different sensing approaches. A series of experiments based on the detection of gold ions were carried out to assess the effect of these functional molecules and the sensing approach on the sensitivity of the system. Changes in the effective optical thickness of these NAA platforms were used as the sensing parameter for the establishment of the overall sensitivity of the system. Our experiments revealed that 6-amino-1-hexanethiol molecules provide the best sensing performance of the amino-thiol modified NAA platforms using sensing approach (i), with

DOI: 10.1021/acsami.7b01116
ACS Appl. Mater. Interfaces 2017, 9, 8929–8940

a sensitivity of 4.8 ± 0.9 nm μM^{-1}. NAA sensing platforms modified with 1,6-hexanedithiol were the most sensitive platform (0.9 ± 0.1 nm μM^{-1}) for dithiol-functionalized NAA platforms using approach (ii). To further enhance the overall sensitivity of the system, NAA sensing platforms were modified using a dual functionalization approach with 6-amino-1-hexanethiol and 1,6-hexanedithiol, as these two molecules offered the best individual sensitivities as compared to other amino-thiol and dithiol molecules. Our results indicated that the sensing performance of the resulting NAA platforms has an additive enhancement of sensitivity (5.6 ± 1.0 nm μM^{-1}) as a result of the combined Au^{3+} ion binding capacity of 6-amino-1-hexanethiol (inner surface) and 1,6-hexanedithiol (top surface).

We have established that the performance of a sensor is dependent on the molecular makeup and backbone length of the functional molecule employed as well as the sensing approach utilized. The sensitivity of a sensing system can be enhanced through a rational engineering of the surface chemistry on the sensing platform, where these interferometric sensing platforms can be functionalized with analyte-specific molecules that respond to the same targeted analytes but may differ in their backbone structures or molecular sizes. Different functional groups or molecular sizes can endow a sensing platform with more sensitivity. In conclusion, our study provides a better understanding and deeper insight into potential optimization pathways through surface chemistry engineering and opens up new opportunities for the development of ultrasensitive sensors, with potential applicability in a broad range of fields and disciplines.

■ ASSOCIATED CONTENT

Supporting Information

The Supporting Information is available free of charge on the ACS Publications website at DOI: 10.1021/acsami.7b01116.

Synthesis process used to produce the cysteine-like compound AAC (PDF)

■ AUTHOR INFORMATION

Corresponding Authors

*(A.D.A.) Phone + 61 8 8313 5652; e-mail Andrew.abell@adelaide.edu.au.

*(A.S.) Phone +61 8 8313 1535; e-mail abel.santos@adelaide.edu.au.

ORCID

Dusan Losic: 0000-0002-1930-072X

Andrew D. Abell: 0000-0002-0604-2629

Abel Santos: 0000-0002-5081-5684

Notes

The authors declare no competing financial interest.

■ ACKNOWLEDGMENTS

Authors thank the support provided by the Australian Research Council (ARC) through the grants DE140100549, CE140100003, DP120101680, and FT110100711 and the School of Chemical Engineering (UoA). Authors thank the Adelaide Microscopy (AM) Centre for FEG-SEM characterization.

■ REFERENCES

(1) Fan, X.; White, I. M.; Shopova, S. I.; Zhu, H.; Suter, J. D.; Sun, Y. Sensitive Optical Biosensors for Unlabeled Targets: A review. *Anal. Chim. Acta* **2008**, *620*, 8−26.

(2) Jeffrey, W. C.; Daniel, M. R. Label-Free Biosensors for Biomedical Applications. In *Optical, Acoustic, Magnetic, and Mechanical Sensor Technologies*; CRC Press: 2012; pp 45−78.

(3) Gauglitz, G.; Moore, D. S. *Handbook of Spectroscopy*; John Wiley & Sons, Inc.: Weinheim, 2010.

(4) McDonagh, C.; Burke, C. S.; MacCraith, B. D. Optical Chemical Sensors. *Chem. Rev.* **2008**, *108*, 400−422.

(5) Borisov, S. M.; Wolfbeis, O. S. Optical Biosensors. *Chem. Rev.* **2008**, *108*, 423−461.

(6) Eggins, B. R. *Chemical Sensors and Biosensors*; John Wiley & Sons: West Sussex, 2008; Vol. *28*.

(7) Santos, A.; Kumeria, T.; Losic, D. Nanoporous Anodic Alumina: A Versatile Platform for Optical Biosensors. *Materials* **2014**, *7*, 4297−4320.

(8) Belge, G.; Beyerlein, D.; Betsch, C.; Eichhorn, K.-J.; Gauglitz, G.; Grundke, K.; Voit, B. Suitability of Hyperbranched Polyester for Sensoric Applications−Investigation with Reflectometric Interference Spectroscopy. *Anal. Bioanal. Chem.* **2002**, *374*, 403−411.

(9) Birkert, O.; Tünnemann, R.; Jung, G.; Gauglitz, G. Label-Free Parallel Screening of Combinatorial Triazine Libraries using Reflectometric Interference Spectroscopy. *Anal. Chem.* **2002**, *74*, 834−840.

(10) Gauglitz, G.; Brecht, A.; Kraus, G.; Mahm, W. Chemical and Biochemical Sensors Based on Interferometry at Thin (Multi-) Layers. *Sens. Actuators, B* **1993**, *11*, 21−27.

(11) Schmitt, H.-M.; Brecht, A.; Piehler, J.; Gauglitz, G. An Integrated System for Optical Biomolecular Interaction Analysis. *Biosens. Bioelectron.* **1997**, *12*, 809−816.

(12) Lin, V. S.-Y.; Motesharei, K.; Dancil, K.-P. S.; Sailor, M. J.; Ghadiri, M. R. A Porous Silicon-Based Optical Interferometric Biosensor. *Science* **1997**, *278*, 840−843.

(13) Dancil, K.-P. S.; Greiner, D. P.; Sailor, M. J. A Porous Silicon Optical Biosensor: Detection of Reversible Binding of IgG to a Protein A-Modified Surface. *J. Am. Chem. Soc.* **1999**, *121*, 7925−7930.

(14) Janshoff, A.; Dancil, K.-P. S.; Steinem, C.; Greiner, D. P.; Lin, V. S.-Y.; Gurtner, C.; Motesharei, K.; Sailor, M. J.; Ghadiri, M. R. Macroporous p-Type Silicon Fabry-Perot Layers. Fabrication, Characterization, and Applications in Biosensing. *J. Am. Chem. Soc.* **1998**, *120*, 12108−12116.

(15) Schwartz, M. P.; Alvarez, S. D.; Sailor, M. J. Porous SiO_2 Interferometric Biosensor for Quantitative Determination of Protein Interactions: Binding of Protein A to Immunoglobulins Derived from Different Species. *Anal. Chem.* **2007**, *79*, 327−334.

(16) Santos, A.; Balderrama, V. S.; Alba, M.; Formentín, P.; Ferré-Borrull, J.; Pallarès, J.; Marsal, L. F. Nanoporous Anodic Alumina Barcodes: Toward Smart Optical Biosensors. *Adv. Mater.* **2012**, *24*, 1050−1054.

(17) Salonen, J.; Laine, E.; Niinisto, L. Thermal Carbonization of Porous Silicon Surface by Acetylene. *J. Appl. Phys.* **2002**, *91*, 456−461.

(18) Chen, Y.; Santos, A.; Wang, Y.; Kumeria, T.; Wang, C.; Li, J.; Losic, D. Interferometric Nanoporous Anodic Alumina Photonic Coatings for Optical Sensing. *Nanoscale* **2015**, *7*, 7770−7779.

(19) Pan, S.; Rothberg, L. J. Interferometric Sensing of Biomolecular Binding using Nanoporous Aluminum Oxide Templates. *Nano Lett.* **2003**, *3*, 811−814.

(20) Alvarez, S. D.; Li, C.-P.; Chiang, C. E.; Schuller, I. K.; Sailor, M. J. A Label-Free Porous Alumina Interferometric Immunosensor. *ACS Nano* **2009**, *3*, 3301−3307.

(21) Kumeria, T.; Santos, A.; Losic, D. Ultrasensitive Nanoporous Interferometric Sensor for Label-Free Detection of Gold (III) Ions. *ACS Appl. Mater. Interfaces* **2013**, *5*, 11783−11790.

(22) Dronov, R.; Jane, A.; Shapter, J. G.; Hodges, A.; Voelcker, N. H. Nanoporous Alumina-Based Interferometric Transducers Ennobled. *Nanoscale* **2011**, *3*, 3109−3114.

Supporting Information

Engineering of Surface Chemistry for Enhanced Sensitivity in Nanoporous Interferometric Sensing Platforms

Cheryl Suwen Law[1,3], Georgina M. Sylvia[2,3,4], Madieh Nemati[1], Jingxian Yu[2,3,4], Dusan Losic[1], Andrew D. Abell[2,3,4*] and Abel Santos[1,2,3*]

[1]School of Chemical Engineering, The University of Adelaide, Engineering North Building, SA 5005 Adelaide, Australia

[2]Department of Chemistry, The University of Adelaide, Physics Building, SA 5005 Adelaide, Australia

[3]Institute for Photonics and Advanced Sensing (IPAS), The University of Adelaide, SA 5005 Adelaide, Australia

[4]ARC Centre of Excellence for Nanoscale BioPhotonics (CNBP), The University of Adelaide, SA 5005 Adelaide, Australia

***E-Mails:** andrew.abell@adelaide.edu.au ; abel.santos@adelaide.edu.au

Synthesis of AlaAlaCys (AAC)

AAC was synthesized using a standard solid phase synthesis with N-Fmoc/Cys(Trt) protecting group strategy. Stepwise coupling of N-Fmoc/Cys(Trt) and Fmoc-Ala amino acids using reagents HATU and DIPEA was conducted on 2-chlorotrityl resin with a 0.4 mmol/g loading capacity. To 2-chlorotrityl resin (1.0 g, 3.2 mmol) in dry DCM (15 mL) with DIPEA (5.6 mL, 32.0 mmol). The solution was transferred into a sintered glass funnel with Teflon stopcock, and allowed to react for 1h, before washing with DCM (3×20 mL), DMF (3×20 mL) and DCM (3×20 mL) to give the amino acid on resin (0.576 mmol/g of resin). Fmoc deprotection was performed using piperidine (25% v/v) in DMF, which was added to the peptide on resin and left to stand for 30 min. The solution was drained and the resin was washed as described above before a TNBS test to confirm the presence of a terminal primary amine. Fmoc-Ala (385 mg, 1.15 mmol) in DMF (3 mL) was added to the peptide on resin followed by 0.5 M HATU/DMF (3mL) and DIPEA (0.8 mL, 4.61 mmol), and the reaction allowed to stir for 1 h before washing. The deprotection and coupling process was repeated again with Fmoc-Ala until the peptide reached 3 amino acid residues in length, with a final Fmoc deprotection. The peptide was then cleaved from resin and the cysteine side chain Trt protecting group was removed in one step using TFA/H_2O/TIPS ($95: 2.5: 2.5$ v/v) for 1 h. The solvent was removed *in vacuuo* to give AAC as a white solid (152 mg). ^{1}H NMR (500 MHz, DMSO-d_6) δ 8.58 (1H, d, N*H*, *J* = 7.5 Hz), 8.25 (1H, d, N*H*, *J* = 7.5 Hz), 8.05 (2H, m, NH_2), 4.44 – 4.38 (2H, m, 2 x Cα*H*), 3.86 (1H, m, Cα*H*), 2.91 - 2.85 (1H, m, C*H*H), 2.80 – 2.74 (1H, m, CH*H*), 1.33 (2H, d, CH_3, *J* = 7.0 Hz), 1.27 (2H, d, CH_3, *J* = 7.0 Hz) ppm; ^{13}C NMR (126 MHz, DMSO-d_6) δ 171.8, 171.3, 169.0, 54.3, 48.1, 48.0, 25.5, 18.1, 17.2 ppm; HRMS-ESI (*m/z*) calculated for $C_9H_{17}N_3O_4S$ $[M + H]^+$ 264.1018, found 264.1009 and $[M + Na]^+$ 286.0837, found 286.0828.

Abbreviations

Fmoc, Fluorenylmethyloxycarbonyl; Trt, Trityl; Ala, Alanine; DMF, dimethylformamide; DIPEA, diisopropylethylamine; HATU, 1-[Bis(dimethylamino)methylene]-1H-1,2,3-triazolo[4,5-b]pyridinium 3-oxid hexafluorophosphate; DCM, dichloromethane; TNBS, trinitrobenzenesulfonic acid; TFA, trifluoroacetic acid.

Chapter 8

Real-Time Binding Monitoring between Human Blood Proteins and Heavy Metal Ions in Nanoporous Anodic Alumina Photonic Crystals

Statement of Authorship

Title of Paper	Real-Time Binding Monitoring between Human Blood Proteins and Heavy Metal Ions in Nanoporous Anodic Alumina Photonic Crystals.
Publication Status	☑ Published ☐ Accepted for Publication ☐ Submitted for Publication ☐ Unpublished and Unsubmitted w ork w ritten in manuscript style
Publication Details	Law, C.S., S.Y. Lim, A.D. Abell, and A. Santos, *Real-time binding monitoring between human blood proteins and heavy metal ions in nanoporous anodic alumina photonic crystals*. Analytical Chemistry, 2018. **90**(16): p. 10039-10048.

Principal Author

Name of Principal Author (Candidate)	Cheryl Suwen Law		
Contribution to the Paper	Under the supervision of A. Santos and A. D. Abell, I performed the experiments, interpreted and processed the data and wrote the manuscript.		
Overall percentage (%)	70		
Certification:	This paper reports on original research I conducted during the period of my Higher Degree by Research candidature and is not subject to any obligations or contractual agreements with a third party that would constrain its inclusion in this thesis. I am the primary author of this paper.		
Signature		Date	23/11/2018

Co-Author Contributions

By signing the Statement of Authorship, each author certifies that:

i. the candidate's stated contribution to the publication is accurate (as detailed above);
ii. permission is granted for the candidate in include the publication in the thesis; and
iii. the sum of all co-author contributions is equal to 100% less the candidate's stated contribution.

Name of Co-Author	Siew Yee Lim		
Contribution to the Paper	I aided in performing the experiments. I give consent for Cheryl Suwen Law to present this paper for examination towards the Doctorate of Philosophy.		
Signature		Date	14/11/2018

Name of Co-Author	Andrew D. Abell		
Contribution to the Paper	I acted as secondary supervisor for the candidate, aided in revising the manuscript and evaluating the final version of manuscript. I give consent for Cheryl Suwen Law to present this paper for examination towards the Doctorate of Philosophy.		
Signature		Date	23/11/2018

Name of Co-Author	Abel Santos		
Contribution to the Paper	I acted as primary supervisor for the candidate, aided in developing of the experiments, revising the manuscript and evaluating the final version of the manuscript. I give consent for Cheryl Suwen Law to present this paper for examination towards the Doctorate of Philosophy.		
Signature		Date	23/11/2018

8. Real-Time Binding Monitoring between Human Blood Proteins and Heavy Metal Ions in Nanoporous Anodic Alumina Photonic Crystals

8.1 Introduction, Significance and Commentary

To further explore the applicability of optical sensing systems based on NAA-PCs and RIfS, this chapter assesses the binding between heavy metal ions and human blood proteins immobilised onto NAA-PCs. The proposed sensing system has provided useful information about the binding kinetics, affinity, mechanisms, and the dynamic conformational changes of the proteins upon their interactions with heavy metal ions. This provides new insights into the fate of metal ions and metal-based drugs in biological systems. This sensing system is a promising complementary technique to conventional analytical methodologies, offering other advantages such as reliability, operational simplicity, and real-time monitoring capabilities under dynamic flow. The presented results demonstrate the potential of this system for functional analytical devices with impact in real-life applications.

8.2 Publication

This section is presented as published research paper by **Law, C.S.**, S.Y. Lim, A.D. Abell, and A. Santos, *Real-time binding monitoring between human blood proteins and heavy metal ions in nanoporous anodic alumina photonic crystals*. Analytical Chemistry, 2018. **90**(16): p. 10039-10048.

analytical chemistry

Article

Cite This: *Anal. Chem.* 2018, 90, 10039−10048

pubs.acs.org/ac

Real-Time Binding Monitoring between Human Blood Proteins and Heavy Metal Ions in Nanoporous Anodic Alumina Photonic Crystals

Cheryl Suwen Law,[†,‡,§] Siew Yee Lim,[†,‡,§] Andrew D. Abell,[*,‡,§,∥] and Abel Santos[*,†,‡,§]

[†]School of Chemical Engineering, The University of Adelaide, 5005 Adelaide, Australia

[‡]Institute for Photonics and Advanced Sensing (IPAS), The University of Adelaide, 5005 Adelaide, Australia

[§]ARC Centre of Excellence for Nanoscale BioPhotonics (CNBP), The University of Adelaide, 5005 Adelaide, Australia

[∥]Department of Chemistry, The University of Adelaide, 5005 Adelaide, Australia

Supporting Information

ABSTRACT: This study reports on the real-time binding assessment between heavy metal ions and blood proteins immobilized onto nanoporous anodic alumina photonic crystals (NAA-PCs) by reflectometric interference spectroscopy (RIfS). The surface of NAA-PCs is chemically functionalized with γ-globulin (GG), transferrin (TFN), and serum albumin (HSA), the major proteins present in human blood plasma. Protein-modified NAA-PC platforms are exposed to analytical solutions of mercury ions of different concentrations. Dynamic changes in the effective optical thickness of protein-modified NAA-PCs in response to heavy metal ions are assessed in real time to evaluate the binding kinetics, affinity, and mechanism. Protein molecules undergo conformational changes upon exposure to mercury ions, with HSA exhibiting the strongest affinity. The combination of protein-modified NAA-PCs with RIfS allows real-time monitoring of protein-heavy metal ions interactions under dynamic flow conditions. This system is capable of detecting dynamic conformational changes in these proteins upon exposure to heavy metal ions. Our results provide new insights into these binding events, which could enable new methodologies to study the toxicity of heavy metal ions and other biomolecular interactions.

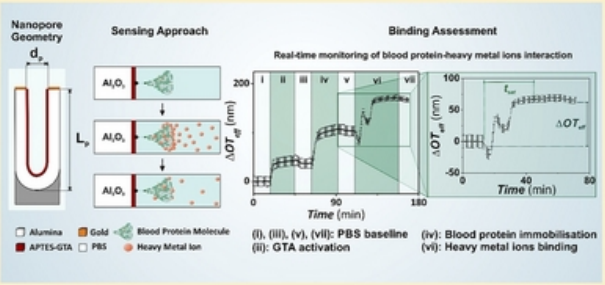

Metal ions play a critical role in biology, the environment, and medicine, particularly as a basis for new metal-based drugs.[1] A deficiency or excess of metal ions in the human body can cause functional disruptions and cellular toxicity.[2] Essential metal ions with critical biological roles include Na^+, K^+, Mg^{2+}, Fe^{2+}, Cu^{2+}, and Zn^{2+}.[3] Conversely, heavy metal ions such as Cd^{2+}, Pb^{2+}, Hg^{2+}, and Cr^{3+} are harmful to the human body, even at minute concentrations.[2] Heavy metal ions generated from mining, metal plating, fertilizers and pesticides production, and batteries industry leach into the ecosystems (i.e., water and soil), accumulate in the biosphere, and enter living organisms (i.e., plants and animals) through the alimentary chain.[4,5] Uptake of heavy metal ions leads to the interaction of these toxic ions with proteins present in the human blood plasma such as albumin, immunoglobulins, transferrin, haptoglobin, and ceruloplasmin.[6,7] Characterization of these protein-heavy metal ions interactions is thus critical to determine associated metabolic and physiological processes that lead to toxicity and to understand the mechanism of bioavailability, assimilation, and excretion of heavy metal ions in the human body.[6]

The interaction between blood plasma proteins and heavy metal ions is assessed by various analytical techniques such as dialysis, chromatography, electrophoresis, inductively coupled plasma mass spectroscopy (ICP-MS), and surface plasmon resonance (SPR).[5,6,8−14] However, these techniques are costly, require laborious preparation processes, and do not provide real-time monitoring capabilities to study protein-heavy metal ions interactions under dynamic conditions. Reflectometric interference spectroscopy (RIfS) presents as a promising complementary technique to characterize a broad range of biomolecular binding events.[15] RIfS provides low cost, sensitivity, operational simplicity, and real-time monitoring features under dynamic flow conditions, making it a very attractive technique to complement benchmark analytical methodologies. RIfS relies on the interaction of white light with a solid thin film (i.e., sensing platform), which generates a characteristic interference pattern due to the Fabry−Pérot effect. Biomolecular interactions in the sensing platform result in shifts in the optical interference pattern due to modifications of the effective refractive index or physical thickness of the thin film. These changes estimated by RIfS can be used as a principle to develop sensing systems.[16−18] The combination of RIfS with nanoporous optical films enhances sensitivity and selectivity as compared to solid thin films due to the increased

Received: June 17, 2018
Accepted: July 25, 2018
Published: July 25, 2018

DOI: 10.1021/acs.analchem.8b02732
Anal. Chem. 2018, 90, 10039−10048

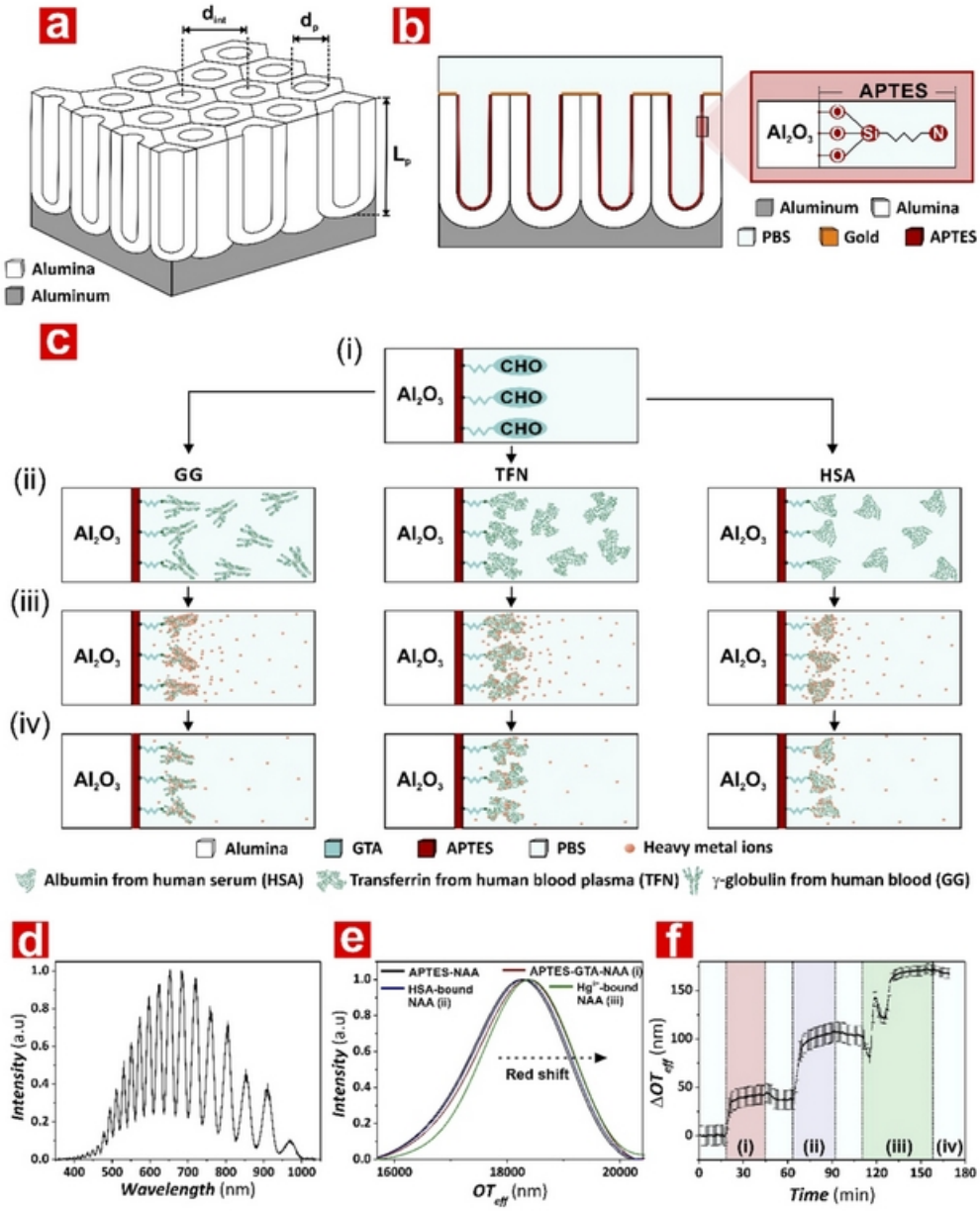

Figure 1. Assessment of binding affinity between blood proteins and mercury ions combining RIfS with NAA-PC platforms. (a) Illustration describing the geometric features of NAA-PCs including the pore length (L_p), interpore distance (d_{int}), and pore diameter (d_p). (b) Schematic showing the inner surface chemistry of gold-coated NAA-PCs modified with APTES. (c) Main stages of the sensing approach used to assess the affinity between blood proteins and mercury ions: (i) activation of APTES-functionalized NAA-PCs with GTA; (ii) immobilization of blood proteins onto the inner surface of NAA-PCs; (iii) exposure of blood protein-modified NAA-PCs to heavy metal ions; and (iv) binding of mercury ions to blood proteins. (d) RIfS spectrum of NAA-PCs produced by two-step anodization used to measure the effective optical thickness (OT_{eff}) by FFT. (e) OT_{eff} of NAA-PC platforms estimated by FFT after the different surface chemistry modifications. (f) Example of real-time monitoring of ΔOT_{eff} at the different sensing stages: (i) GTA activation (red); (ii) human serum albumin immobilization (purple); (iii) binding to Hg^{2+} ions (green); and (iv) final ΔOT_{eff}.

specific surface area to accommodate functional binding groups.[15] Furthermore, the structure of some nanoporous materials can be engineered with precision to control light–matter interactions at the nanoscale to further enhance the sensing performance.[19] Among other materials, nanoporous anodic alumina photonic crystals (NAA-PCs) produced by electrochemical oxidation (i.e., anodization) of aluminum are excellent platforms to develop RIfS-based sensing systems.[20] NAA-PCs provide a versatile nanoporous geometry that can be engineered through different anodization strategies, a surface chemistry that allows chemical modifications for selectivity toward analytes of interest, stable optical signals, and biocompatibility.[21]

Herein, we assess the binding affinity between heavy metal ions and blood proteins using a RIfS sensing system in which protein-modified NAA-PCs are exposed to analytical solutions containing different concentrations of mercury ions under dynamic flow conditions. This sensing concept with the characteristic optical interference pattern and real-time

DOI: 10.1021/acs.analchem.8b02732
Anal. Chem. 2018, 90, 10039−10048

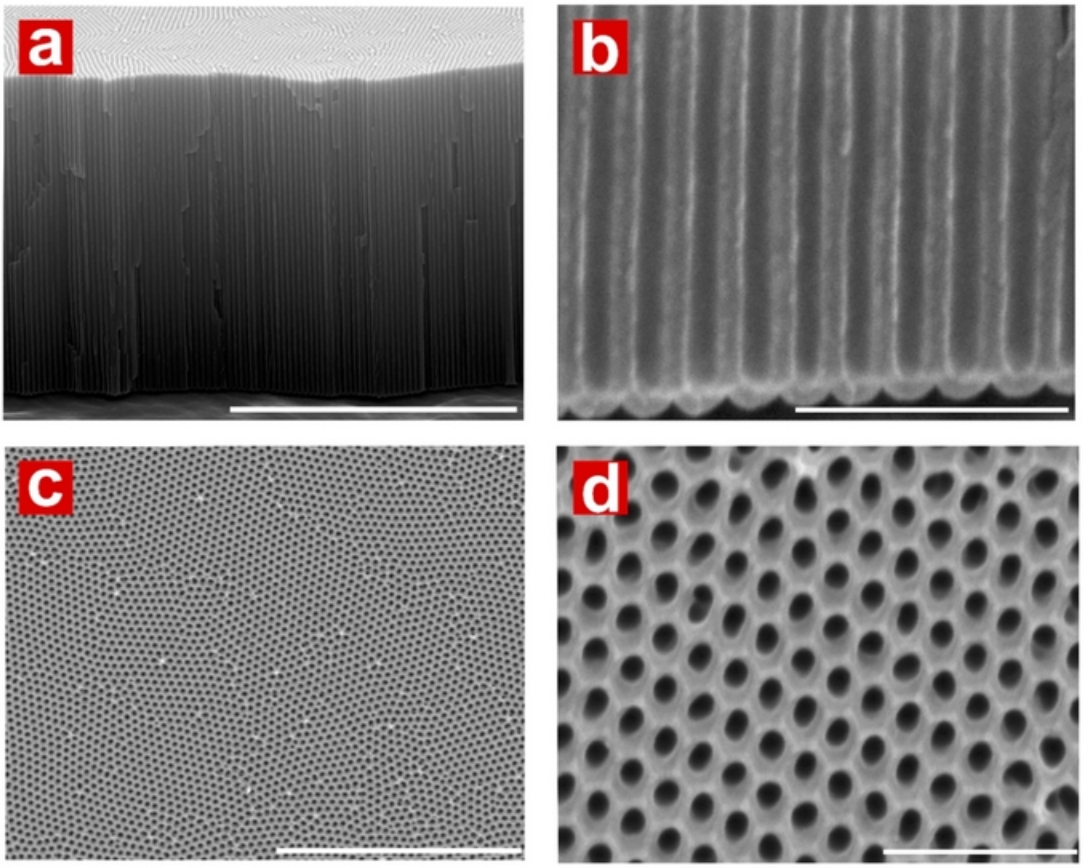

Figure 2. Structural characterization of NAA-PCs produced by two-step anodization. (a) Cross-sectional FEG-SEM view of a NAA-PC featuring straight cylindrical nanopores along the thickness of the film (scale bar = 5 μm). (b) Magnified view of panel a (scale bar = 500 nm). (c) Top FEG-SEM view of hexagonally arranged cylindrical nanopores across the surface of NAA-PCs (scale bar = 3 μm). (d) Magnified view of panel c (scale bar = 500 nm).

monitoring of protein-heavy metal ions binding is illustrated in Figure 1.

EXPERIMENTAL SECTION

Materials. High purity (99.9997%) aluminum (Al) foils 0.32 mm thick were supplied by Goodfellow Cambridge Ltd. (U.K.). Oxalic acid ($H_2C_2O_4$), perchloric acid (HClO4), chromic acid (H_2CrO_4), 3-aminotrimethoxysilane (H_2N-$(CH_2)_3Si(OC_2H_5)_3$, APTES), hydrogen peroxide (H_2O_2), glutaraldehyde ($CH_2(CH_2CHO)_2$, GTA), phosphate buffered saline (PBS), γ-globulin from human blood (GG), transferrin from human blood plasma (TFN), albumin from human serum (HSA), gold(III) chloride hydrate ($HAuCl_4H_2O$), and mercury(II) chloride ($HgCl_2$) were purchased from Sigma-Aldrich (Australia). Ethanol (C_2H_5OH, EtOH) and phosphoric acid (H_3PO_4) were supplied by ChemSupply (Australia). Ultrapure water (18.2 Ω.m) Mili-Q (Australia) was used in the preparation of aqueous solutions.

Fabrication and Functionalization of Nanoporous Anodic Alumina Sensing Platforms. NAA-based Fabry–Pérot interferometers were produced by a two-step electrochemical anodization process reported elsewhere and functionalized with APTES molecules by silanization.[22−24] A detailed explanation of these processes is provided in the Supporting Information.

Assessment of Blood Proteins–Heavy Metal Ions Binding by RIfS. Details of the RIfS setup used in this study and a detailed explanation of the sensing process is provided in the Supporting Information.[25,26] Briefly, RIfS spectra were acquired in the wavelength range of 400−1000 nm and processed by applying fast Fourier transform (FFT) to estimate the effective optical thickness (OT_{eff}) of NAA-PCs according to eq 1.

$$OT_{eff} = 2n_{eff}L_p \cos\theta \quad (1)$$

where OT_{eff}, n_{eff}, and L_p are the effective optical thickness, the effective refractive index, and the physical thickness of the NAA-PC platform, respectively, whereas θ is the angle of incidence of light (i.e., $\theta = 0°$ in this case).

Structural Characterization of NAA-PCs. The structural features of NAA-PC platforms were characterized by field-emission gun−scanning electron microscopy (FEG-SEM, FEI Quanta 450). FEG-SEM images were analyzed using ImageJ.[27]

RESULTS AND DISCUSSION

Structural Characterization of NAA-PCs. Figure 2 shows FEG-SEM images of NAA-PCs produced by two-step anodization. These NAA-PCs feature straight cylindrical nanopores that grow from top to bottom, perpendicularly to the underlying Al substrate (Figure 2a,b). Top view FEG-SEM images reveal an array of hexagonally arranged nanopores that are homogeneously distributed across the surface (Figure 2c,d). The average pore diameter (d_p), interpore distance

DOI: 10.1021/acs.analchem.8b02732
Anal. Chem. 2018, 90, 10039−10048

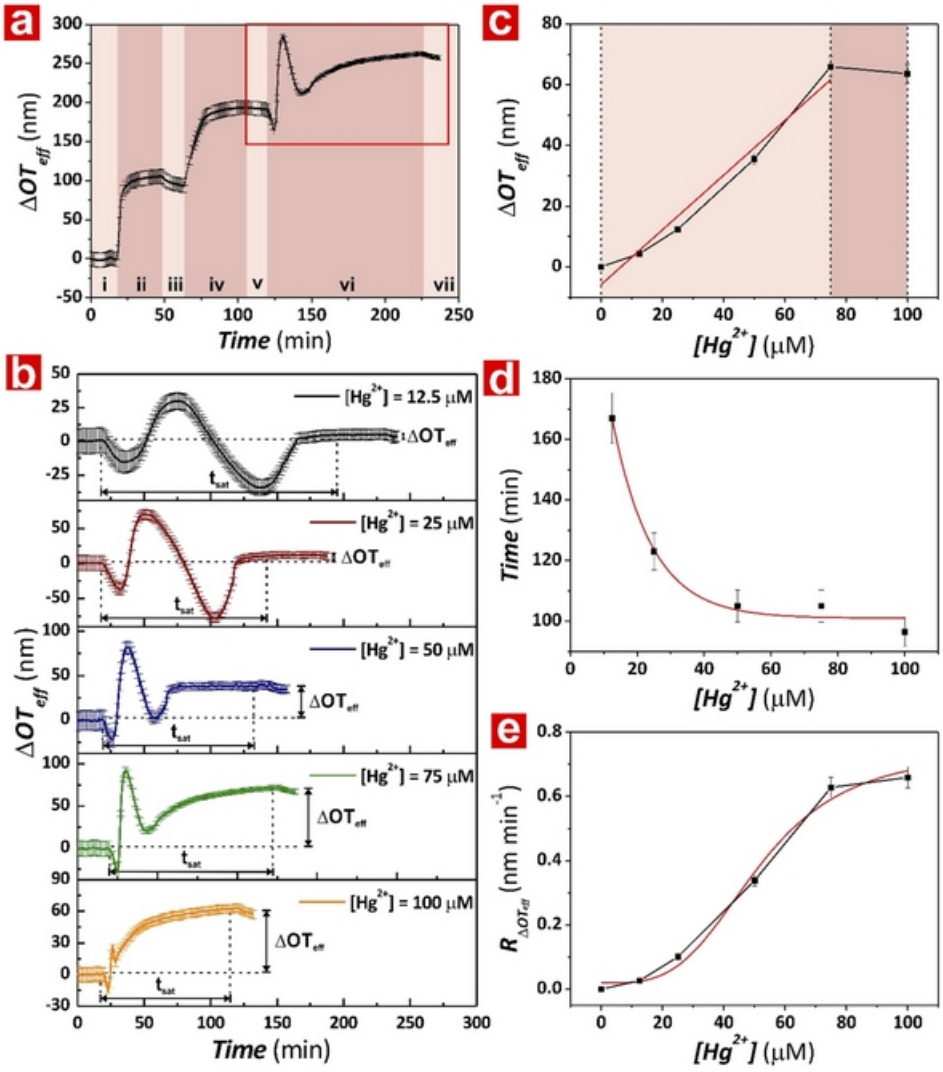

Figure 3. Assessment of the binding affinity between Hg^{2+} ions and GG-functionalized NAA-PCs for different concentrations of Hg^{2+} ions. (a) Example of real-time monitoring of ΔOT_{eff} for the different sensing steps: (i) PBS baseline, (ii) GTA activation, (iii) PBS washing, (iv) GG functionalization, (v) PBS washing, (vi) Hg^{2+} binding, and (vii) PBS washing. (b) Real-time Hg^{2+} binding stage (red square in panel a) for each $[Hg^{2+}]$ (i.e., 12.5, 25, 50, 75, and 100 μM). (c) Correlation between ΔOT_{eff} and $[Hg^{2+}]$ for GG-functionalized NAA-PCs. (d) Correlation of t_{sat} and $[Hg^{2+}]$ for GG-functionalized NAA-PCs. (e) Kinetic rate ($R_{\Delta OT_{eff}}$) for the binding reaction between Hg^{2+} ions and GG-functionalized NAA-PCs for each $[Hg^{2+}]$.

(d_{int}), and pore length (L_p) estimated by FEG-SEM image analysis, were 67 ± 6 nm, 106 ± 5 nm, and 5.5 ± 0.1 μm, respectively.

Functionalization of NAA-PCs. To immobilize blood protein molecules onto the inner surface of nanopores, NAA-PC platforms were hydroxylated in H_2O_2 to increase the number of hydroxyl groups. A layer of APTES molecules was then deposited onto the inner surface of NAA-PCs through chemical vapor deposition to provide amine functional groups.[23] These groups were then activated by GTA via the aldehyde functionality of GTA. Blood protein molecules were selectively immobilized onto the GTA-APTES-activated surface of NAA-PCS via N-terminus covalent binding with the aldehyde functionality, where the amine moiety in the N-terminus of blood proteins reacts with the aldehyde group of GTA to form an imine.[28]

Binding Interaction between Hg^{2+} and Blood Proteins. Hg^{2+} is one of the largest and most dangerous environmental pollutants, with exposure leading to neurological problems and myocardial infraction as well as pulmonary and kidney function impairment.[4,20] Mercury ions bind specifically to sulfhydryl group, causing poisoning of active sites and structural degradation of proteins present in human blood plasma.[6,29,30] Therefore, techniques that enable real-time monitoring of molecular interactions between blood protein molecules and Hg^{2+} ions are critical to understand the toxic effects associated with these ions and implement efficient treatments.

Binding Interaction between Hg^{2+} and γ-Globulin (GG). γ-Globulins are plasma proteins with important roles in humoral (antibody-mediated) immune responses by binding to antigens.[31] GGs contain multiple heavy and light polypeptide chains cross-linked by disulfide bridges, with a molecular

DOI: 10.1021/acs.analchem.8b02732
Anal. Chem. 2018, 90, 10039−10048

weight of 155−160 kDa.[32] The disulfide bonds between cysteine residues in GG are prone to denaturation or reduction due to solvent exposure to form free sulfhydryls, which have significant affinity to soft metal ions.[33,34] GG-functionalized NAA-PCs were exposed to analytical solutions of Hg^{2+} with controlled concentrations. Figure 3a shows an example of real-time measurement of the effective optical thickness changes (ΔOT_{eff}) in NAA-PCs by RIfS associated with each stage of the sensing process (i.e., GTA activation, GG immobilization, and Hg^{2+} exposure). A stable baseline was first obtained by injecting PBS into the flow system containing APTES-functionalized NAA-PCs for 15 min. A 2.5 vol % amount of GTA solution was then flowed through the system for 30 min to activate the amine group of APTES. Next, fresh PBS solution was flowed for 15 min to remove physisorbed GTA molecules from the inner surface of NAA-PCs, which was denoted by a slight blue shift in ΔOT_{eff}. A solution of 1 mg mL^{-1} GG in PBS was then flowed through the system to functionalize the inner surface of NAA-PCs with GG. The immobilization of GG was denoted by an increase in ΔOT_{eff} (i.e., red shift). Saturation of the surface of NAA-PCs with GG was denoted by a plateau in ΔOT_{eff}. Fresh PBS solution was flowed again for 15 min to remove unbound GG molecules. The stable ΔOT_{eff} signal during this stage suggests that GG molecules were strongly immobilized onto the inner surface of NAA-PCs. Binding between Hg^{2+} and GG inside the nanopores of NAA-PCs was established by measuring ΔOT_{eff} over time after exposure to analytical solutions of Hg^{2+} ions. As Figure 3a shows, the exposure of GG-modified NAA-PCs to Hg^{2+} resulted in an initial blue shift in the ΔOT_{eff} signal due to the partial reduction or degradation of disulfide bonds between cysteine residues in immobilized GG. Note that not all disulfide bridges in the GG molecules reduce or denature depending on their position within the GG molecule. Disulfide bonds between cysteine residues either form between different polypeptide chains (i.e., interchain bonds) or within the one polypeptide chain (i.e., intrachain bonds).[35] Intrachain disulfides are buried between two layers of antiparallel β-sheet structured chains and hence more protected from degradation.[32,35] Conversely, interchain disulfide bonds are located at the hinge region of the GG molecule, becoming highly solvent-exposed and contributing to the higher reactivity of the cysteine residues forming the interchain disulfides.[35,36] Degradation of disulfide bonds triggers a conformational change in the hinge region of GG, causing other disulfide bonds to be solvent-exposed to a greater extent and thus increasing their susceptibility to undergo further degradation.[36] Therefore, the initial decrease in ΔOT_{eff} observed during the injection of Hg^{2+} can be associated with the reduction of interchain disulfide bonds into free sulfhydryls. The formation of sulfhydryls groups from the reduction of disulfide bonds after interaction with Hg^{2+} induces a red shift in ΔOT_{eff}. The steep increment of ΔOT_{eff} is due to the presence of readily accessible thiol groups in the GG that strongly bound to Hg^{2+}.[37] A maximum of ΔOT_{eff} is achieved when most of the sulfhydryls in the GG react with Hg^{2+}. However, the ΔOT_{eff} signal is progressively blue-shifted after achieving the ΔOT_{eff} maximum due to the reorientation of immobilized GG. Hg^{2+}-bound GG molecules undergo a second structural conformation change to minimize the steric hindrance and molecular strain. This molecular orientation favors the binding of new Hg^{2+} ions due to exposure of additional functional groups within the GG molecule, leading to a new increment of ΔOT_{eff}. Saturation of these extra functional groups within the GG is reflected by a plateau in ΔOT_{eff}, which denotes no free Hg^{2+} binding sites within the GG molecules. Finally, fresh PBS solution is flowed through the system for 15 min to remove unbound Hg^{2+} ions. This results in a slight blue shift and the establishment of the total ΔOT_{eff} associated with the Hg^{2+}−GG interaction at the equilibrium state of the reaction. Figure 3b shows ΔOT_{eff} resulting after GG-modified NAA-PCs were exposed to different concentrations of Hg^{2+}. The trend in ΔOT_{eff} is similar for all these Hg^{2+}−GG interactions, although to decrease $[Hg^{2+}]$ has several effects on the ΔOT_{eff} trend: (i) the initial decrement of ΔOT_{eff} just after exposure to Hg^{2+} ions is reduced; (ii) the slope of the initial increment of ΔOT_{eff} after effect I decreases; (iii) the width of the parabolic tram of ΔOT_{eff} due to structural conformation changes increases; (iv) the minimum of ΔOT_{eff} after the conformational changes decreases—below the original baseline for 12.5 and 25 μM. These dynamic changes in ΔOT_{eff} due to the interaction Hg^{2+}−GG can be associated with the kinetics and binding mechanism of this chemical reaction. At a lower $[Hg^{2+}]$, the number of Hg^{2+} per unit volume is lesser; thus a longer time is needed for Hg^{2+} to interact and bind with the GG immobilized onto the inner surface of NAA-PCs. The arrows shown in Figure 3b indicate the total ΔOT_{eff} associated with the Hg^{2+}−GG interaction after the equilibrium state is reached for each concentration assessed in our study, using the initial PBS baseline as a reference before and after exposure to Hg^{2+}. Figure 3c summarizes the ΔOT_{eff} estimated for each concentration of Hg^{2+}. It is apparent that ΔOT_{eff} increases linearly with increasing $[Hg^{2+}]$ from 0 to 75 μM.

If the number of sulfhydryl groups present in the GG for Hg^{2+} binding is the same for all the Hg^{2+} concentrations, the higher $[Hg^{2+}]$, the more the Hg^{2+} ions available per unit volume. As a result, increasing the number of Hg^{2+}−GG interactions on the inner surface of GG-functionalized NAA-PCs is translated into larger ΔOT_{eff}. As Figure 3c indicates, this reaction achieves its saturation point at $[Hg^{2+}]$ = 75 μM, which is denoted by a plateau in ΔOT_{eff}. A linear fitting from 0 to 75 μM was used to establish the sensitivity (S_{GG-Hg}) of GG-modified NAA-PCs toward Hg^{2+} ions, the low limits of detection (LoD_{GG-Hg}) of this system, which were 0.901 ± 0.090 nm μM^{-1} and 10.5 ± 1.0 μM, respectively, with a linearity $R^2(GG)$ = 0.967.

The kinetics of the Hg^{2+}−GG reaction in NAA-PCs is characterized by estimating the saturation time (t_{sat}—time at which the equilibrium state is reached) for each $[Hg^{2+}]$ from Figure 3b. Figure 3d reveals that t_{sat} decreases exponentially as $[Hg^{2+}]$ increases. The higher concentration of Hg^{2+} ions inside the nanopores increases exponentially the frequency of binding events with GG molecules immobilized onto the inner surface of NAA-PCs. As a result, a shorter time is required to occupy the available binding sites (i.e., sulfhydryl groups) in the GG. The binding rate $R_{\Delta OT_{eff}}$, calculated as the ratio between ΔOT_{eff} and t_{sat} for each $[Hg^{2+}]$, was estimated to gain a better insight into the kinetics of the Hg^{2+}−GG interaction. Figure 3e shows this relationship, with an apparent sigmoidal kinetics model, where the binding activity of GG increases rapidly with $[Hg^{2+}]$ until equilibrium state is reached. This sigmoidal kinetic behavior suggests several Hg^{2+} binding sites in the GG molecules, which is consistent with the generation of free thiol groups formed during the reduction/degradation of disulfide bonds after exposure to Hg^{2+}. Initial binding of Hg^{2+} ions to

DOI: 10.1021/acs.analchem.8b02732
Anal. Chem. 2018, 90, 10039−10048

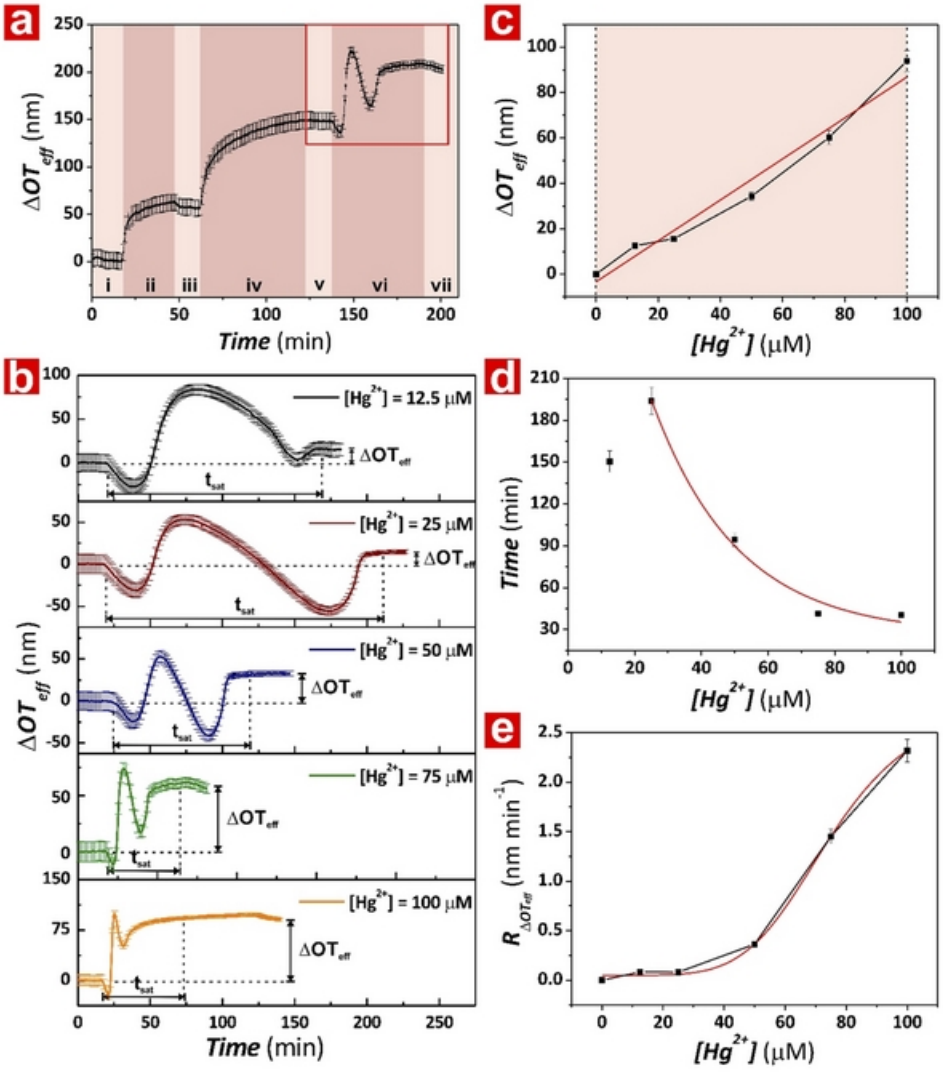

Figure 4. Assessment of the binding affinity between Hg^{2+} ions and TFN-functionalized NAA-PCs for different concentrations of Hg^{2+} ions. (a) Example of real-time monitoring of ΔOT_{eff} for the different sensing steps: (i) PBS baseline, (ii) GTA activation, (iii) PBS washing, (iv) TFN functionalization, (v) PBS washing, (vi) Hg^{2+} binding, and (vii) PBS washing. (b) Real-time Hg^{2+} binding stage (red square in panel a) for each $[Hg^{2+}]$ (i.e., 12.5, 25, 50, 75, and 100 μM). (c) Correlation between ΔOT_{eff} and $[Hg^{2+}]$ for TFN-functionalized NAA-PCs. (d) Correlation of t_{sat} and $[Hg^{2+}]$ for TFN-functionalized NAA-PCs. (e) Kinetic rate ($R_{\Delta OT_{eff}}$) for the binding reaction between Hg^{2+} ions and TFN-functionalized NAA-PCs for each $[Hg^{2+}]$.

thiol groups present in the GG molecules affects the affinity of subsequent Hg^{2+}−GG interactions, inducing an increment in affinity with increasing Hg^{2+} concentration due to molecular conformational changes.[38]

Binding Interaction between Hg^{2+} and Transferrin. Transferrin (TFN) is a glycoprotein composed of a single polypeptide chain with a molecular weight of ~80 kDa.[39] Folding of the polypeptide chain gives TFN a bilobal structure, where the two globular lobes (i.e., N-lobe and C-lobe) are composed of alternating α-helical and β-sheet segments joined by a short peptide chain in the form of a random coil.[40] The lobes possess a metal binding site and are structurally similar. The main function of transferrin is to transport Fe^{3+} within the circulatory system.[41] Fe^{3+} coordinates to the ligands in the metal binding site formed by two tyrosine residues, a histidine and an aspartic acid residue.[40] Binding of Fe^{3+} to TFN occurs with the concomitant binding of a synergistic anion such as carbonate and oxalate. TFN in serum is partially saturated with Fe^{3+}, leaving substantial vacant binding sites available to bind other metal ions present in the bloodstream.[42] TFN can bind to a wide variety of divalent, trivalent, and tetravalent metal ions.[43−47] Nonetheless, the metal binding sites in TFN have the strongest affinity to Fe^{3+}.[39,41,48] Limited studies have reported the binding affinity between TFN and Hg^{2+} ions, but it is known that Hg^{2+} binds to the two tyrosine residues present in TFN molecules to form metallotransferrin complexes.[40,49] Figure 4a presents an example of the real-time monitoring of ΔOT_{eff} in TFN-functionalized NAA-PCs after each sensing stage. Figure 4a shows a slight blue shift in ΔOT_{eff} when TFN-functionalized NAA-PCs are exposed to Hg^{2+}, which is associated with conformational changes of immobilized TFN molecules. The continuous flow of Hg^{2+} ions results in a sharp red shift in ΔOT_{eff}, which indicates a

DOI: 10.1021/acs.analchem.8b02732
Anal. Chem. 2018, 90, 10039−10048

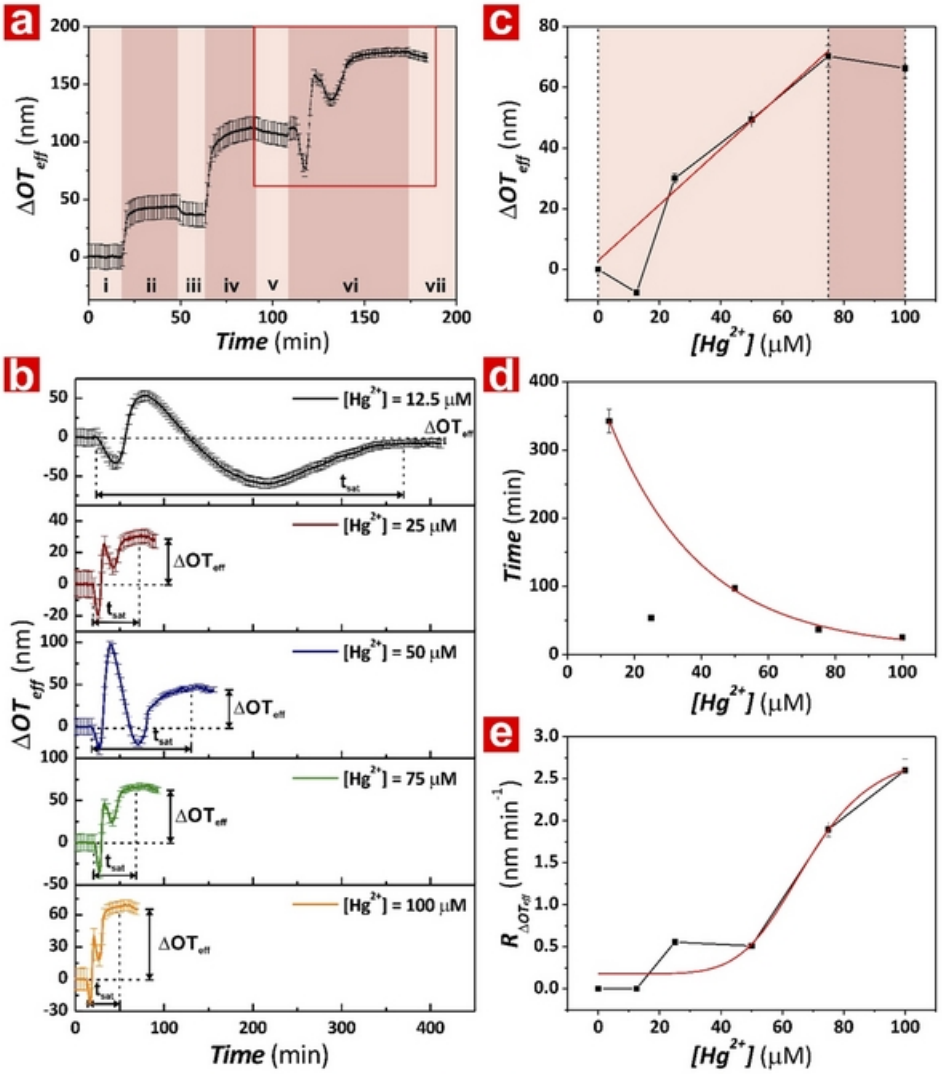

Figure 5. Assessment of the binding affinity between Hg^{2+} ions and HSA-functionalized NAA-PCs for different concentrations of Hg^{2+} ions. (a) Example of real-time monitoring of ΔOT_{eff} for the different sensing steps: (i) PBS baseline, (ii) GTA activation, (iii) PBS washing, (iv) HSA functionalization, (v) PBS washing, (vi) Hg^{2+} binding, and (vii) PBS washing. (b) Real-time Hg^{2+} binding stage (red square in panel a) for each $[Hg^{2+}]$ (i.e., 12.5, 25, 50, 75, and 100 μM). (c) Correlation between ΔOT_{eff} and $[Hg^{2+}]$ for HSA-functionalized NAA-PCs. (d) Correlation of t_{sat} and $[Hg^{2+}]$ for HSA-functionalized NAA-PCs. (e) Kinetic rate ($R_{\Delta OT_{eff}}$) for the binding reaction between Hg^{2+} ions and HSA-functionalized NAA-PCs for each $[Hg^{2+}]$.

strong interaction between TFN and Hg^{2+} ions during this stage.

After the initial conformational change, the binding sites in the N- and C-lobes in the TFN are exposed to the Hg^{2+} ions present in the solution. The tyrosine- and sulfur-containing residues in the metal binding sites of TFN have high affinity to hard metal ions.[42] Hg^{2+} is a divalent metal ion, with relatively acidic character and a relatively high stability constant that favors strong interactions with the tyrosine- and sulfur-containing residues in the TFN molecules.[40,49,50] TFN undergoes a wide-open to closed conformational change upon binding Fe^{3+}.[40,51−54] As Figure 4a reveals, ΔOT_{eff} undergoes a blue shift just after reaching its maximum and then it red shifts again to achieve equilibrium state. This behavior is ascribed to dynamic conformational changes of immobilized TFN. After initial Hg^{2+} binding, TFN molecules switch the lobes from open to closed form (i.e., blue shift).[48,55] However, due to the difference in ionic radius between Hg^{2+} (1.02 Å) and Fe^{3+} (0.65 Å), TFN cannot completely achieve a closed conformation.[48,56] Therefore, TFN molecules undergo a conformation change to accommodate Hg^{2+} ions by a certain degree of domain closure (i.e., red shift).[48] Finally, fresh PBS was flowed through the system after achieving equilibrium state. Figure 4b shows the dynamic ΔOT_{eff} for the Hg^{2+}−TFN interactions at different Hg^{2+} concentrations. This system follows and identical underlying binding mechanism for the range of concentrations studied, from 12.5 to 100 μM. Figure 4c reveals a linear increment of ΔOT_{eff} with $[Hg^{2+}]$ from 0 to 100 μM. The sensing parameters of the TFN-functionalized NAA-PCs were obtained from the linear fitting shown in Figure 4c, with a sensitivity $S_{TFN-Hg} = 0.902 \pm 0.090$ nm μM^{-1}, a low $LoD_{TFN-Hg} = 15.4 \pm 1.5$ μM, and $R^2(TFN) = 0.966$. Figure 4d shows the values of t_{sat} estimated for the TFN-modified NAA-PCs for each $[Hg^{2+}]$, where t_{sat} decreases

DOI: 10.1021/acs.analchem.8b02732
Anal. Chem. 2018, 90, 10039−10048

exponentially from 25 to 100 μM upon exposure to Hg^{2+}. Finally, Figure 4e shows the reaction rate ($R_{\Delta OT_{eff}}$) for this system, estimated as the ratio $\Delta OT_{eff}/t_{sat}$ for each concentration of Hg^{2+}. The sigmoidal kinetics of Hg^{2+}–TFN binding implies a low binding activity of TFN at low [Hg^{2+}] and a drastic increase in binding activity as TFN is exposed to higher [Hg^{2+}]. The sigmoidal curve indicates the existence of two specific metal binding sites in the TFN molecules that allow cooperative binding of Hg^{2+}. The initial binding of Hg^{2+} to the first metal binding site in TFN determines further binding interactions with Hg^{2+} at the secondary metal binding sites, which is consistent with previous studies.[40]

Binding Interaction between Hg^{2+} and Human Serum Albumin. Human serum albumin (HSA) is responsible for maintaining the pH and osmotic pressure of plasma, and facilitating the transportation, distribution, and metabolism of many ligands such as fatty acids, amino acids, metal ions, and drugs.[57,58] HSA is a monomeric multidomain macromolecule of 585 amino acid residues, containing 35 cysteine residues, 17 structural disulfide bonds, one free thiolate (Cys 34), and one tryptophan (Trp 214), in a globular heart-shaped conformation with a molecular weight of ~66 kDa.[57,59,60] The multidomain ligand binding organization of HSA makes it an ideal cargo to transport critical biological components.[61] The binding between HSA and Hg^{2+} ions was assessed in real time using HSA-functionalized NAA-PCs in combination with RIfS. Figure 5a shows an example of real-time monitoring of ΔOT_{eff} in HSA-modified NAA-PCs. The inflow of Hg^{2+} analyte solution into the system generates an initial conformational change of HSA that makes the Cys 34 binding site for Hg^{2+} binding accessible. The loop–link–loop structure of HSA allows it to undergo flexible structural transitions upon exposure to certain molecules.[62] Although the HSA's Cys 34 is located at the surface of the protein, the free sulfhydryl group is facing toward the interior of the molecule and it is shielded by side chains of amino acids, preventing reaction with other external molecules.[58] However, the presence of Hg^{2+} ions triggers an initial conformational change in the HSA (i.e., initial blue shift), where the phenolic side chain of tyrosine turns over to allow Hg^{2+} binding at the Cys 34 site. This conformation modification also shifts the free sulfhydryl group closer to the exterior of the HSA molecule.[58] The enhanced accessibility of Cys 34 promotes the binding of Hg^{2+} to its free sulfhydryl group, as indicated by the red shift of ΔOT_{eff} after initial conformational change. ΔOT_{eff} then rises until it reaches a maximum, indicating that most of the Cys 34 binding sites of HSA molecules are bound to Hg^{2+}.[6,8,63] However, the Hg^{2+}-bounded HSA molecules undergo a new conformational change after achieving the ΔOT_{eff} maximum, which is translated into a blue shift in ΔOT_{eff}. After initial binding, HSA molecules change their conformation to accommodate the captured Hg^{2+} ions. This secondary structural change in HSA is associated with the binding of Hg^{2+} ions to the active donor atoms of amino acid side chains, where the α-helix structure is transitioned into a β-sheet arrangement due to the destabilization of the hydrogen bonds between carbonyl and amide moiety present in the α-helix structure.[8] Finally, a new red shift in ΔOT_{eff} occurs after the secondary structural change is achieved. HSA has other metal binding sites such as N-terminal and multimetal binding sites, which consist of amino acid residues with N and O donor atoms that are capable of binding Hg^{2+} ions.[55] Conformational changes of HSA expose additional molecular binding sites for additional binding interactions with Hg^{2+} until equilibrium state is reached. The process is terminated by flowing fresh PBS solution through the system to establish the total ΔOT_{eff} associated with HSA upon exposure to different [Hg^{2+}] (Figure 5b). Interaction between Hg^{2+} ions and HSA-functionalized NAA-PCs over time monitored through ΔOT_{eff} shows a trend comparable to that observed in GG and TFN systems. Figure 5c summarizes the obtained results for ΔOT_{eff} measured after the equilibrium state is reached for each [Hg^{2+}].

ΔOT_{eff} increases linearly for [Hg^{2+}] from 0 to 75 μm. However, a plateau is reached for [Hg^{2+}] > 75 μM, indicating the complete saturation of binding sites in HSA molecules above that [Hg^{2+}]. Binding of Hg^{2+} ions to HSA significantly affects the secondary and tertiary structure of HSA due to the bonding with active donor atoms of the amino acid residues.[8] More α-helix chains transit to β-turn fractions with increasing [Hg^{2+}]. A linear fitting within the linear range of the Hg^{2+}–HSA reaction was used to establish the sensing parameters of the system (Figure 5c). S_{HSA-Hg}, LoD_{HSA-Hg}, and R^2(HSA) for this reaction were 0.920 ± 0.090 nm μM^{-1}, 11.3 ± 1.1 μM, and 0.984, respectively. As Figure 5d shows, t_{sat} increases linearly with [Hg^{2+}] from 0 to 50 μM and decreases exponentially from 50 to 100 μM. Thus, for [Hg^{2+}] < 50 μM, the saturation of the binding sites of HSA takes longer time with increasing concentration of Hg^{2+}. This phenomenon is associated with concentration-dependent conformational changes in HSA molecules. However, at concentrations above 50 μM, HSA molecules undergo significant structural changes that accelerate binding of Hg^{2+} since more binding sites are exposed. This leads to an exponential decrement of t_{sat} with [Hg^{2+}] since the availability of Hg^{2+} inside the nanopores increases the frequency of binding events. Figure 5e illustrates $R_{\Delta OT_{eff}}$ for the HSA-modified NAA-PC system. The HSA–Hg^{2+} interaction follows a sigmoidal kinetics model, where $R_{\Delta OT_{eff}}$ is slow at low [Hg^{2+}] but it increases rapidly as [Hg^{2+}] increases, suggesting an optimum [Hg^{2+}] range in which $R_{\Delta OT_{eff}}$ is enhanced. The binding of Hg^{2+} to the first binding sites present in HSA enhances its binding affinity due to the exposure of additional binding sites as a result of conformational changes.

■ CONCLUSIONS

This study provides new insights into interactions between blood proteins and heavy metal ions. The combination of blood protein-modified NAA-PCs with RIfS enables real-time, in situ monitoring of these biochemical interactions. This technique makes it possible to detect and quantify dynamic conformational changes in immobilized blood protein molecules upon exposure to analytical solutions of heavy metal ions. The interactions between three model blood proteins with mercury ions were assessed, including γ-globulin (GG), transferrin (TFN), and serum albumin (HSA). HSA showed the highest affinity toward Hg^{2+} followed by TFN and GG (S_{HSA-Hg} = 0.920 nm μM^{-1} > S_{TFN-Hg} = 0.902 nm μM^{-1} > S_{GG-Hg} = 0.901 nm μM^{-1}), using changes in the effective optical thickness of NAA-PCs as sensing parameter. All these blood proteins underwent conformational changes upon exposure to mercury ions, with a binding mechanism that is dependent on the type of blood protein. GG, TFN, and HSA showed a two-stage conformational change when exposed to mercury ions, in which the initial interaction with these ions

DOI: 10.1021/acs.analchem.8b02732
Anal. Chem. 2018, 90, 10039–10048

Supporting Information

Real-Time Binding Monitoring between Human Blood Proteins and Heavy Metal Ions in Nanoporous Anodic Alumina Photonic Crystals

Cheryl Suwen Law[a,b,c], Siew Yee Lim[a,b,c], Andrew D. Abell[b,c,d*], and Abel Santos[a,b,c*]

[a]School of Chemical Engineering, The University of Adelaide, Adelaide, SA 5005, Australia
[b]Institute for Photonics and Advanced Sensing (IPAS), The University of Adelaide, 5005 Adelaide, Australia
[c]ARC Centre of Excellence for Nanoscale BioPhotonics (CNBP), The University of Adelaide, 5005 Adelaide, Australia
[d]Department of Chemistry, The University of Adelaide, Engineering North Building, 5005 Adelaide, Australia.

***E-Mails:** andrew.abell@adelaide.edu.au ; abel.santos@adelaide.edu.au

S-1. Fabrication of Nanoporous Anodic Alumina Sensing Platforms. NAA-based Fabry–Pérot interferometers were produced by two-step electrochemical anodization process. Prior to anodization, aluminum (Al) substrates in the form of 1.5 x 1.5 cm^2 square chips were sonicated in EtOH and ultrapure water for 15 min each and dried under air stream. Al chips were electropolished in a mixture of $HClO_4$ and EtOH 1:4 (v:v) at 20 V and 5 ^{0}C for 3 min before anodized in an electrochemical reactor with a circular window of 1 cm in diameter. The first anodization step was carried out in an aqueous solution of 0.3 M oxalic acid at 40 V and 6 ^{0}C for 20 h. The resulting NAA layer was removed by chemical etching in a mixture of 0.2 M H_2CrO_4 and 0.4 M H_3PO_4 at 70 ^{0}C for 3 h. The second anodization step was performed under the same anodization condition for 2 h. Finally, the NAA-PCs were pore-widened by wet chemical etching in an aqueous solution of H_3PO_4 5 *wt* % at 35 ^{0}C for 15 min.

S-2. Surface Chemistry Functionalization of Nanoporous Anodic Alumina Sensing Platforms. The inner surface of NAA-PCs was chemically functionalized by silanization with APTES following a well-established protocol. In brief, NAA-PC platforms were hydroxylated by immersion in H_2O_2 (30 *wt* %) at 90 ^{0}C for 10 min and dried under air stream. Hydroxylated NAA-PCs were subsequently functionalized with APTES by chemical vapor deposition under vacuum at 110 ^{0}C for 3 h and washed with ultrapure water to remove unbounded APTES molecules. Finally, the top surface of APTES-functionalized NAAPCs was coated with a ~4-5 nm thick gold layer using a sputter coater equipped with a film thickness monitor (sputter coater 108auto, Cressington, USA) for light interference enhancement.

S-3. Optical Set-Up and Assessment of Blood Proteins-Heavy Metal Ions Binding by RIfS in Nanoporous Anodic Alumina Sensing Platforms. White light from a tungsten source with an illumination spot of 2 mm was focused on the surface of NAA-PC platforms by a bifurcated optical probe. The reflected light from the illumination spot was collected and transferred to a miniature spectrophotometer *via* the collection fiber of the optical probe (Flame, Ocean Optics, USA). The optical spectra were acquired in the wavelength range of 400–1000 nm and saved at intervals of 30 s with an integration time of 50 ms and 50 average measurements. The RIfS spectra were processed by applying fast Fourier transform in Igor Pro library (Wavemetrics, USA) to estimate the effective optical thickness (OT_{eff}) of NAA-PCs. The binding between blood proteins and metal ions were assessed in real-time by monitoring the changes in OT_{eff} in response to different concentrations of metal ions using RIfS. APTES-functionalized NAA-PCs were packed in a customized flow cell made of transparent acrylic plastic, GTA activated, modified with blood proteins (GG, TFN and HSA) and exposed to analytical solutions containing controlled concentrations of heavy metal ions. This process was performed in-situ, under dynamic flow conditions by a peristaltic pump (BT100-2J, LongerPump, USA) with a constant angular rate of 1.4 rpm (i.e. 100 µL min^{-1}). First, a stable baseline was established with the injection of PBS solution into the flow cell for 15 min. A 2.5 *vol* % GTA solution in PBS was then flowed into the system for 30 min to activate the amine terminal group (-NH_2) of APTES molecules. Next, fresh PBS solution was flowed through the system for 15 min to wash off any physisorbed GTA molecule. Then, the inner surface of GTA-activated APTES-functionalized NAA-PCs was modified with blood proteins by flowing 1 mg mL^{-1} solutions containing GG, TFN and HSA in PBS. The blood protein solutions were flowed through the system until the change in OT_{eff} reached a plateau, indicating that the inner surface of NAA-PCs was saturated with blood protein molecules. PBS was then flowed into

the system for 15 min to remove physisorbed blood protein molecules. Protein-functionalized NAA-PCs were then exposed to analytical solutions of mercury (Hg^{2+}) ions with different concentrations (i.e. [Hg^{2+}] = 12.5, 25, 50, 75 and 100 µM). These analytical solutions were prepared by dilution of 1 mM $HgCl_2$ stock solution in PBS. Heavy metal ions solutions were continuously flowed through the system until stabilization of OT_{eff}, which indicates that the interaction between blood protein molecules and metals ions has achieved a saturation point. The final step was to flow fresh PBS through the system for 15 min to establish the total change of OT_{eff} resulting from the equilibrium state for blood proteins-metal ions interactions (ΔOT_{eff}).

S-4. Binding Interaction between Au^{3+} and HSA. Gold-based drugs can lead to undesired leaching, diffusion and adsorption of gold ions to various organs, which can induce adverse side effects in patients such as nephrotoxicity, blood disorders and cardiovascular toxicity.[S1] Gold ions can act as a neurotoxin that leads to peripheral neuropathy and lethal gold poisoning. Therefore, it is crucial to understand the binding mechanisms and affinity of gold ions with proteins present in the blood stream. To further understand the metal-binding properties of HSA toward Au^{3+} ions, we assessed HSA-functionalized NAA-PCs upon exposure to analytical solutions of Au^{3+} with controlled concentrations (i.e. [Au^{3+}] = 12.5, 25, 50, 75 and 100 µm). A variety of binding sites is available in HSA for metal ions, with the free thiol group of the Cys 34 providing the primary binding site for Au^{3+}.[S2,S3] However, disulphide bonds present in HSA contain imidazole groups of histidine, which can also bind to Au^{3+} since this ion is fairly soft and can form stable covalent complexes with soft ligands like imidazole.[S4] **Figure S-1a** shows an example of real-time shifts in ΔOT_{eff} corresponding to the different sensing stages (i.e. GTA-APTES activation, HSA immobilization, Au^{3+} binding and final washing)

used to assess the binding affinity between HSA and Au^{3+} ions in NAA-PCs combined with RIfS. A stable baseline in PBS was first obtained prior to activation of APTES functionalized NAA-PC platforms with GTA. HSA molecules were immobilized onto the inner surface of NAA-PCs by flowing a solution 1 mg mL^{-1} of HSA in PBS through the flow system. Note that 15 min washing steps, with fresh PBS, were incorporated in between stages to remove physically bounded molecules. The red shift in ΔOT_{eff} after HSA exposure indicates that the inner surface of the nanopores was completely covered with HSA molecules. Analytical solutions of Au^{3+} prepared by dissolution of gold (III) chloride hydrate ($HAuCl_4H_2O$) were then introduced into flow system and their interaction with immobilized HSA molecules assessed by RIfS in real time. **Figure S-1a** reveals an initial blue shift in ΔOT_{eff} just after HSA-functionalized NAA-PCs are exposed to the Au^{3+} solution, indicating a conformational change in HSA. Exposure to Au^{3+} ions results in an initial structural modification of HSA by which the sulfhydryl group at the Cys 34 terminal becomes closer to the surface of the molecule.[S5] Au^{3+} ions bind covalently to the thiol group of the more accessible Cys 34, which is translated into a continuous red shift in ΔOT_{eff}. Once available binding sites in HSA are saturated with Au^{3+}, the ΔOT_{eff} signal stabilizes, denoting the equilibrium state of the reaction. Finally, fresh PBS is flowed through the system to remove weakly-bound Au^{3+} ions. Binding between HSA and Au^{3+} is demonstrated to be irreversible.[S3] **Figure S-1b** presents ΔOT_{eff} measurements performed in real-time as a function of the concentration of Au^{3+} ions. The pattern shown by the Au^{3+}-HSA interaction through ΔOT_{eff} is the same for any of the concentrations assessed in our study (i.e. initial blue shift followed by a red shift until the equilibrium state is reached). The arrows shown in **Figure S-1b** indicate the ΔOT_{eff} at each [Au^{3+}] after the equilibrium state is reached and **Figure S-1c** summarizes the obtained results. As **Figure S-1b** shows, the initial conformational changes in HSA (i.e. minimum of ΔOT_{eff} achieved after exposure to Au^{3+}) is

more significant with increasing concentration of ions. High [Au^{3+}] can cause a structural transition of HSA from a buried to an exposed configuration (i.e. rearrangement of α-helices). As a result, ΔOT_{eff} increases linearly with [Au^{3+}] since more functional groups are available in the immobilized HSA molecules to bind Au^{3+} ions. The linear fitting shown in **Figure S-1c** reveals a sensitivity ($S_{HSA\text{-}Au}$) of 0.88 ± 0.09 nm μm^{-1} and a limit of detection ($LoD_{HSA\text{-}Au}$) of 22.0 ± 2.2 µM for the Au^{3+}-HSA system. An analysis of the saturation time (**Figure S-1d**) shows that the reaction time for binding between immobilized HSA molecules and Au^{3+} ions decreases exponentially with increasing [Au^{3+}]. For [Au3+] > 25 µM, the functional binding groups present in HSA are saturated with Au^{3+} ions just after the initial conformational change. HSA molecules do not undergo any additional structural change during the exposure to Au^{3+} and the available binding sites can easily accommodate the Au^{3+} ions present inside the nanopores. **Figure S-1e** shows the kinetics rate of the Au^{3+}-HAS interaction as $R_{\Delta OTeff}$ for each [Au^{3+}]. As this graphs reveals, the reaction rate increases exponentially with increasing concentration of ions. This result suggests that the Au^{3+}-HSA interaction follows a second order kinetics, where $R_{\Delta OTeff}$ is affected by either the amount of immobilized HSA molecules and [Au^{3+}].

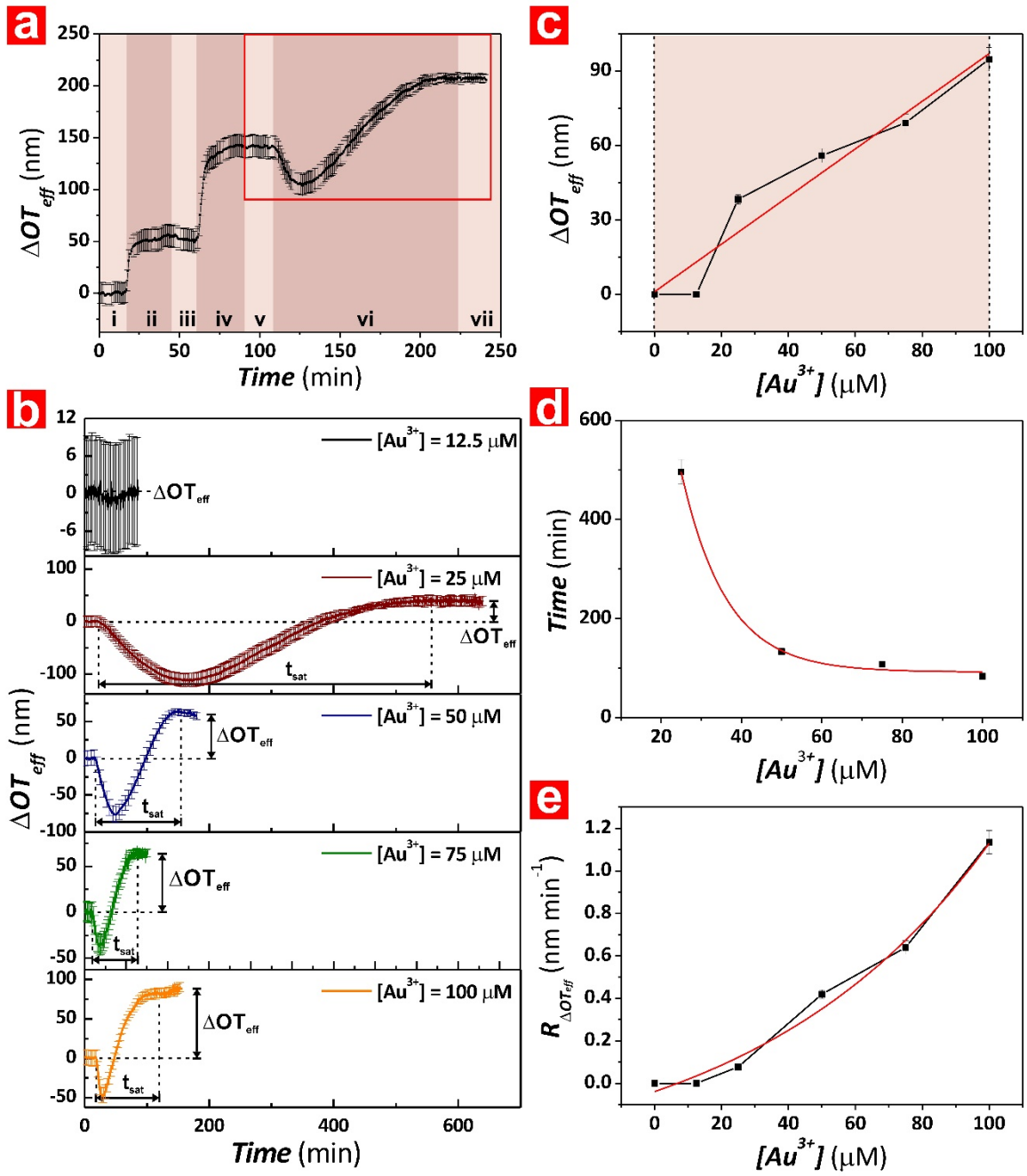

Figure S-1. Assessment of the binding affinity between Au^{3+} ions and HSA-functionalized NAA-PC platforms for different concentrations of Au^{3+} ions. a) Example of real-time monitoring of ΔOT_{eff} for the different sensing steps: (i) PBS baseline, (ii) GTA activation, (iii) PBS washing, (iv) HSA functionalization, (v) PBS washing, (vi) Au^{3+} binding and (vii) PBS washing. b) Real-time Au^{3+} binding stage (red square in (a)) for each [Au^{3+}] (i.e. 12.5, 25, 50, 75 and 100 μM). c) Correlation between ΔOT_{eff} and [Au^{3+}] for HSA-functionalized NAA-PCs. (d) Correlation of t_{sat} and [Au^{3+}] for HSA-functionalized NAA-PCs. e) Kinetic rate ($R_{\Delta OTeff}$) for the binding reaction between Au^{3+} ions and HSA-functionalized NAA-PCs for each [Au^{3+}].

REFERENCES

(S1) Panyala, N. R.; Peña-Méndez, E. M.; Havel, J. Gold and Nano-Gold in Medicine: Overview, Toxicology and Perspectives. *J. Appl. Biomed.* 2009, *7*, 75-91.

(S2) He, X. M.; Carter, D. C. Atomic Structure and Chemistry of Human Serum Albumin. *Nature* **1992**, *358*, 209.

(S3) Bal, W.; Sokołowska, M.; Kurowska, E.; Faller, P. Binding of Transition Metal Ions to Albumin: Sites, Affinities and Rates. *Biochim. Biophys. Acta, Gen. Subj.* **2013**, *1830*, 5444-5455.

(S4) Blundell, T.; Jenkins, J. The Binding of Heavy Metals to Proteins. *Chem. Soc. Rev.* **1977**, *6*, 139-171.

(S5) Sugio, S.; Kashima, A.; Mochizuki, S.; Noda, M.; Kobayashi, K. Crystal Structure of Human Serum Albumin at 2.5 Å Resolution. *Protein Eng.* **1999**, *12*, 439-446.

Chapter 9

Conclusions

9. Conclusions

9.1 Conclusions

The works presented throughout this thesis advance fundamental and applied knowledge in optical sensing, using the combination of RIfS with NAA-PCs as a model sensing system that can be easily implemented into miniaturised and lab-on-a-chip systems for different applications. The critical advance is to engineer NAA-PCs with desirable structural, optical and chemical properties to achieve enhanced sensitivities. This is demonstrated by an extensive study on various anodisation approaches and surface chemistry modification methods. Structural engineering of NAA-PCs enables fine tuning of optical signals across the spectral regions, while surface chemistry modification with functional molecules provides chemical selectivity toward target analytes. A combination of both strategies is demonstrated to be an optimal approach to develop NAA-based RIfS systems with optimal properties. The specific conclusions derived from each work presented in this thesis are summarised as follows.

9.1.1. Design, engineering and optimisation of NAA-PCs

The fabrication of NAA-PCs based on different anodisation profiles was explored to create a broad palette of PC structures with unique properties. The anodisation approaches studied are: (i) sawtooth-like pulse anodisation – where the effective medium of NAA-PCs is engineered in a sawtooth fashion (Chapter 3); (ii) stepwise pulse anodisation for the production of NAA distributed Bragg reflectors (NAA-DBRs) (Chapter 4); (iii) modified sinusoidal pulse anodisation, with an insertion of cavity step at constant current density in between, to create gradient-index NAA microcavities (GIF-NAA-μCVs) (Chapter 5); (iv) modified stepwise pulse anodisation to produce NAA-μCVs based on DBRs (DBR-NAA-μCVs) (Chapter 5); and (v) apodised stepwise pulse anodisation to generate NAA-μCVs (Chapter 6). The manipulation of the anodisation parameters was demonstrated as an effective method to optimise the optical properties of NAA-PCs. An apodisation strategy was introduced and implemented into stepwise pulse anodisation to produce apodised NAA-DBRs. This nanofabrication approach effectively engineers the optical properties of NAA-DBRs.

These works establish the tuneability of the optical properties of NAA-PCs across the UV-visible-NIR spectrum, with maximised optical signal intensity and minimised spectral bandwidth. These features are desired to develop more sensitive sensing platforms with enhanced sensitivity.

9.1.2. Surface chemistry modification of NAA photonic structures

Various surface chemistry engineering approaches were explored to provide NAA photonic structures with chemical selectivity and specificity toward analytes. These include metal sputtering, chemical vapour deposition, and self-assembly of functional monolayers. Deposition of a layer of gold onto NAA-PCs by sputter coating enables the formation of self-assembled monolayers of thiol-containing molecules by binding affinity between thiol and gold (Chapter 3). NAA-PCs can also be modified with small molecules and biomolecules after their pre-treatment with silane molecules by chemical vapour deposition (Chapters 7 and 8). These surface chemistry modification protocols yielded stable functional layers within the inner surface of NAA-PCs, which allow selective detection of target analytes (Chapter 7). Both the inner and top surface of NAA-PCs can be functionalised with molecules to provide desired functionalities. The dual functionalisation strategy demonstrated in Chapter 7 is a feasible method to enhance the sensing capacity of NAA-PCs as sensing platforms.

9.1.3. Optimisation and sensing performance assessment of chemically modified NAA-PCs

The sensing performance of chemically functionalised NAA-PCs was evaluated in real-time using RIfS as a function of change in effective optical thickness upon interaction with analytes of interest. The applicability of the combined RIfS-NAA-PCs system as optical sensor is demonstrated by different binding models, such as gold-thiol interactions (Chapter 3 and 7) as well as human blood proteins and mercury ions (Chapter 8). As established in Chapter 7, the sensitivity can be further enhanced through a rational engineering of the surface chemistry of NAA-PCs, when these platforms are functionalised with analyte-specific molecules that are selective to target analytes. Our results demonstrate that the sensing performance of this system is

dependent on the molecular moiety or size of the functional molecules, which results in different levels of affinity to analytes. Dual functionalisation approach is found to have an additive effect on the sensitivity enhancement of NAA-PCs-based sensing platforms. The proposed optical sensor has shown promising potential in chemical and biosensing for biomedical and environmental applications, offering ultrasensitive performance and capacity to detect and quantify dynamic conformational changes in biomolecules upon interaction with analytes. This system can be readily used to study binding kinetics, affinity and mechanism phenomena. This thesis paves the route to create a new generation of miniaturised sensing devices with ultrasensitive, multiplexed and high-throughput sensing capabilities.

9.2 Recommendations for Future Work

The studies presented in this thesis advance the development of smart sensing devices by providing extensive fundamental research on structural optimisation, surface chemistry engineering, and sensing assessment of NAA-PCs in combination with RIfS. Future studies aiming to translate these systems into rapid, portable, cost-competitive and efficient sensing devices for field and lab-on-a-chip medical, environmental, industrial, security and material science applications should focus on the following possible directions:

1. Even though NAA-based sensing platforms have a higher optical and chemical stability, the spectral bandwidth of NAA-PCs achieved is relatively larger than that of porous silicon-based photonic crystals. This detrimental characteristic has an impact in the overall sensitivity of these sensing platforms. Therefore, further experimental optimisation in terms of anodisation parameters and structural engineering should be performed to produce narrow line-width and high-quality NAA-PCs with complex PC architectures.
2. NAA-PCs based RIfS sensing systems employed in these studies focus on the detection of single analytes, which may limit its translation into fully functional prototypes for real-life applications. The capability of NAA-PCs as sensing platforms can be further advanced by creating microfluidic channels on the surface of these PCs by photolithography, where each channel is imparted with different functionalities by surface chemistry modifications. This will allow NAA-PCs to detect

multiple analytes in different channel to expand the application of this system for multiplexed sensing.

3. More extensive studies should be carried out regarding the surface chemistry modifications of NAA-PCs to ensure that only targeted analytes are bound to the inner surface and prevent biofouling. Molecular species present in complex matrices such as biological fluids and environmental samples are to be analysed.
4. The translation of the proposed sensing system into a working device will require more comprehensive research evaluating the optical response of the system under conditions that mimic real-life scenarios, with the use of real-life samples such as blood, urine, soil, water, industrial emission and effluent.

Appendix

Fine Tuning of Transmission Features in Nanoporous Anodic Alumina Distributed Bragg Reflectors

Law, C.S., Lim, S.Y., and Santos, A. *Fine tuning of transmission features in nanoporous anodic alumina distributed Bragg reflectors*. in *Nanophotonics Australasia 2017*. 2018. International Society for Optics and Photonics.

Statement of Authorship

Title of Paper	Fine tuning of transmission features in nanoporous anodic alumina distributed Bragg reflectors.
Publication Status	☑ Published ☐ Accepted for Publication ☐ Submitted for Publication ☐ Unpublished and Unsubmitted w ork w ritten in manuscript style
Publication Details	Law, C.S., Lim, S.Y., and Santos, A. *Fine tuning of transmission features in nanoporous anodic alumina distributed Bragg reflectors*. in *Nanophotonics Australasia 2017*. 2018. International Society for Optics and Photonics.

Principal Author

Name of Principal Author (Candidate)	Cheryl Suwen Law		
Contribution to the Paper	Under the supervision of A. Santos, I performed the experiments, interpreted and processed the data and wrote the manuscript.		
Overall percentage (%)	70		
Certification:	This paper reports on original research I conducted during the period of my Higher Degree by Research candidature and is not subject to any obligations or contractual agreements with a third party that would constrain its inclusion in this thesis. I am the primary author of this paper.		
Signature		Date	23/11/2018

Co-Author Contributions

By signing the Statement of Authorship, each author certifies that:

i. the candidate's stated contribution to the publication is accurate (as detailed above);
ii. permission is granted for the candidate in include the publication in the thesis; and
iii. the sum of all co-author contributions is equal to 100% less the candidate's stated contribution.

Name of Co-Author	Siew Yee Lim		
Contribution to the Paper	I helped Cheryl Suwen Law with performing the experiments. I give consent for Cheryl Suwen Law to present this paper for examination towards the Doctorate of Philosophy.		
Signature		Date	14/11/2018

Name of Co-Author	Abel Santos		
Contribution to the Paper	I acted as primary supervisor for the candidate, aided in developing of the experiments, revising the manuscript and evaluating the final version of the manuscript. I give consent for Cheryl Suwen Law to present this paper for examination towards the Doctorate of Philosophy		
Signature		Date	23/11/2018

Fine Tuning of Transmission Features in Nanoporous Anodic Alumina Distributed Bragg Reflectors

Cheryl Suwen Law[1,2,3], Siew Yee Lim[1,2,3] and Abel Santos[1,2,3*]
[1]School of Chemical Engineering, The University of Adelaide, Adelaide, Australia
[2]Institute for Photonics and Advanced Sensing (IPAS), The University of Adelaide
[3]ARC Centre of Excellence for Nanoscale BioPhotonics (CNBP), The University of Adelaide, Adelaide
*abel.santos@adelaide.edu.au

ABSTRACT

This study introduces an innovative apodisation strategy to tune the filtering features of distributed Bragg reflectors based on nanoporous anodic alumina (NAA-DBRs). The effective medium of NAA-DBRs, which is modulated in a stepwise fashion by a pulse-like anodisation approach, is apodised following a logarithmic negative function to engineer the transmission features of NAA-DBRs. We investigate the effect of various apodisation parameters such as apodisation amplitude difference, anodisation period, current density offset and pore widening time, to tune and optimise the optical properties of NAA-DBRs in terms of central wavelength position, full width at half maximum and quality of photonic stop band. The transmission features of NAA-DBRs are shown to be fully controllable with precision across the spectral regions by means of the apodisation parameters. Our study demonstrates that an apodisation strategy can significantly narrow the width and enhance the quality of the characteristic photonic stop band of NAA-DBRs. This rationally designed anodisation approach based on the combination of apodisation and stepwise pulse anodisation enables the development of optical filters with tuneable filtering features to be integrated into optical technologies acting as essential photonic elements in devices such as optical sensors and biosensors.

Keywords: Nanoporous Anodic Alumina, Distributed Bragg Reflectors, Apodisation, Filtering Features, Stepwise Pulse Anodisation.

1. INTRODUCTION

Photonic crystals (PCs) are periodic micro/nanostructures that feature a regular distribution of refractive index (or dielectric constant), which can be arranged in either one, two or three dimensions[2-6]. PCs can modify the propagation of electromagnetic waves when photons travel across their structure due to the photonic stop bands that they possess.[7,8] The PCs' photonic stop bands allow or forbid the propagation of photons of certain wavelengths and these light–matter interactions can be precisely engineered by the PCs' structure. Among various fabrication techniques (i.e. lithography[9-13], wet chemical etching[14-15], fiber pulling[16], self-organisation[17,18] and electrochemical etching[19-22]), electrochemical oxidation of metals (anodisation) is a promising method to produce nanostructured PCs based on materials such as silicon, titanium and aluminium. Anodisation enables the in-depth engineering of the porosity of anodic oxides to produce multidimensional PCs with various refractive index profiles such as rugate filters[23-25], microcavities[26,27], waveguides[28-29] and distributed Bragg reflectors.[30,31]

Of all the materials produced by anodisation, nanoporous anodic alumina (NAA) – nanoporous anodic oxide produced by anodisation of aluminium – has superior properties in terms of chemical, mechanical and physical stability. Furthermore, the geometric features of nanopores in NAA can be controlled with versatility and precision by means of the anodisation parameters. NAA is an excellent platform to develop photonic structures since it features stable optical signals without additional passivation steps.[32] NAA can be produced by a cost-competitive, industrially scalable fabrication process, which enables the production of NAA with high degree of regularity, resolution and aspect ratio to guide, reflect, transmit, emit and enhance incident light by engineering its effective medium.[24,32-41] Recent studies have demonstrated that pulse-like anodisation strategies enable the development of a wide range of NAA PCs (i.e. distributed Bragg reflectors, gradient index filters, Fabry-pérot interferometer and microcavities). A careful selection of the anodisation conditions makes it possible to translate complex anodisation profiles such as pseudo-sinusoidal, sawtooth-

Nanophotonics Australasia 2017, edited by James W. M. Chon, Baohua Jia, Proc. of SPIE
Vol. 10456, 1045659 · © 2018 SPIE · CCC code: 0277-786X/18/$18 · doi: 10.1117/12.2282250

like, pseudo-stepwise and multi-sinusoidal into porosity modulations to engineer the NAA's effective medium in depth.[24,34-38,41-60] These NAA PCs possess unique characteristic photonic stop bands that are tuneable across the UV-visible-NIR spectrum.

This study aims to establish a rational anodisation approach to fabricate NAA-based distributed Bragg reflectors (NAA-DBRs) with well-resolved, distinctive and narrow photonic stop bands, where the conceptual illustration is presented in **Figure 1**. NAA-DBRs have a relatively wide photonic stop band with the presence of characteristics sidelobes on both sides of the band due to the sharp truncation of refractive index between adjacent layers within the PC structure.[61,62] These two characteristics of NAA-DBRs can be undesirable in applications that require precise optical filtering of light.[41,55-57] To suppress these redundant sidelobes, the contrast of refractive index profile can be modulated using smooth functions (e.g. Gaussian, sine and Kaiser windows) to minimise the refractive index contrast in NAA-DBRs. Furthermore, since the refractive index contrast of NAA-DBRs defines the width of the photonic stop bands, a low refractive index contrast can be translated into a reduction in the bandwidth.[61] Herein, we adopt an apodisation strategy to engineer and tune the characteristic photonic stop bands of NAA-DBRs. Stepwise pulse anodisation (SPA), as shown in **Figure 1a** (Left), is used to produce NAA-DBRs featured with a distribution of effective refractive index that follows a stepwise profile along the nanopores (**Figure 1b** - left). A logarithmic negative apodisation function is employed to apodise the SPA (**Figure 1a** – right) in order to produce NAA-DRBs with well-resolved and high quality photonic stop bands. Different apodisation parameters, namely anodisation amplitude difference, anodisation period, current density offset and pore widening time are systematically manipulated to assess their effect on the features of the characteristics photonic stop bands of NAA-DBRs (**Figure 1c**). This work further advances NAA-based PCs technology demonstrating that anodisation can provide a precise control over the photonic stop bands, unraveling exciting and promising potential applications in optical sensing, optical filters and photonic devices.

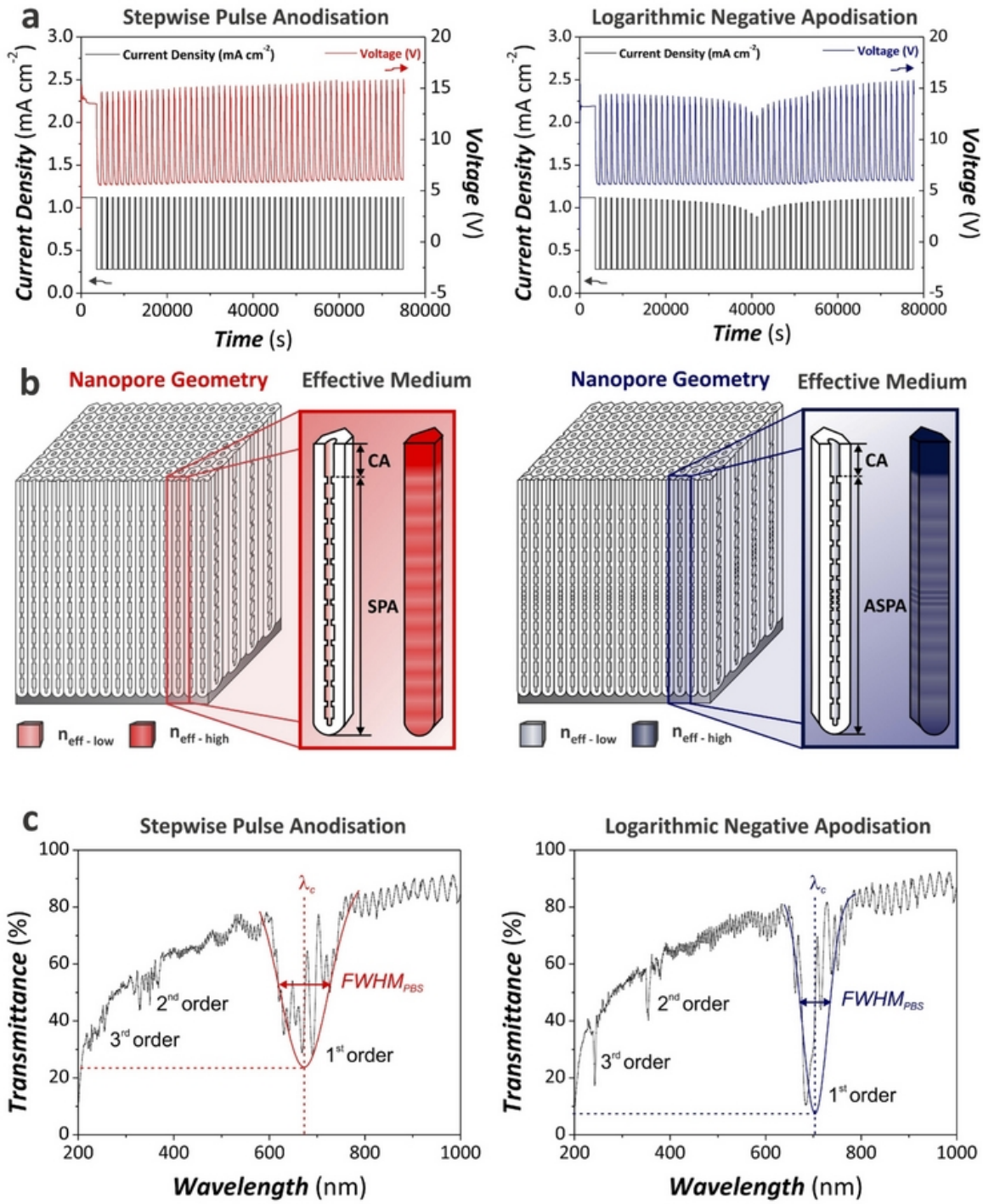

Figure 1. Illustrative concept of fabrication and characterisation of nanoporous anodic alumina distributed Bragg reflectors (NAA-DBRs). (a) Example of stepwise pulse anodisation profile used to produce NAA-DBRs (Right – No apodisation; Left- Logarithmic negative apodisation) (b) Schematic diagram of nanoporous structure of NAA-DBRs with effective medium approximation under non-apodisation (Right) and apodisation (Left) condition. (c) Representative transmission spectra of NAA-DBRs with definitive characteristic parameters (Right – No apodisation; Left- Logarithmic negative apodisation).

2. METHODOLOGY

2.1 Fabrication of NAA-DBRs

Nanoporous anodic alumina-based distributed Bragg reflectors (NAA-DBRs) were produced by apodised stepwise pulse anodisation (ASPA) under galvanostatic conditions. 1.5 x 1.5 cm aluminium (Al) square chips were prepared and cleaned under sonification in ethanol and distilled water for 15 min each, then dried under air stream. Cleaned Al substrates were electropolished in a mixture of ethanol (EtOH) and perchloric acid 4:1 (v:v) at 20 V and 5 ℃ for 3 min. Electropolished chips were then anodised in an electrochemical reactor at -1 ℃ using aqueous solution of 1.1.M of sulphuric acid with 25 v% of EtOH as electrolyte. Note that the anodisation temperature was kept constant throughout the process. The galvanostatic anodisation process started with a constant step at a current density of 1.12 mA cm^{-2} for 1 h to allow the formation of a thin nanoporous layer that facilitates a homogenous pore growth rate prior to ASPA. The anodisation profile was then set to stepwise pulse mode modified with logarithmic negative apodisation function. ASPA profiles were produced by a custom-designed Labview®-based software based on Eq.1.

$$J(t) = 2A_J(t) + J_{offset} \tag{1}$$

where $A_J\ (t)$ is time-dependent current density amplitude based on logarithmic negative apodisation function. Logarithmic negative apodised amplitude is expressed as a function of time, as shown in Eqs. 2 and 3.

For $t \leq t_{an}/2$

$$A(t)_J = A_{\max} + \left(\frac{A_{\min} - A_{\max}}{\log\left(\frac{t_{an}}{2} + 10\right) - 1} \right) \cdot \left(\log(t + 10) - 1\right) \tag{2}$$

For $t > t_{an}/2$

$$A(t)_J = \left(\frac{A_{\max} - A_{\min}}{\log(t_{an} + 10) - \log\left(\frac{t_{an}}{2} + 10\right)} \right) \cdot \left(\log(t + 10) - \log\left(\frac{t_{an}}{2} + 10\right) \right) + A_{\min} \tag{3}$$

where A_{max} and A_{min} are the maximum and minimum amplitudes, whereas t_{an} is the total anodisation time at ASPA.

In order to achieve fine tuning of transmission features of NAA-DBRs, several apodisation parameters, namely anodisation amplitude difference (ΔA_J), anodisation period (T_p), current density offset (J_{offset}) and pore widening time (t_{pw}) were systematically modified from 0 to 0.42 mA cm^{-2} with a step size of 0.21 mA cm^{-2}; from 1100 to 1500 s with a step size of 200 s; from 0.14 to 0.42 mA cm^{-2} with a step size of 0.14 mA cm^{-2}; and from 0 to 6 min with an interval of 2 min, respectively.

2.2 Optical characterisation

To selectively dissolve the remaining aluminium substrate from the back side of these aluminium chips, NAA-DBRs were subjected to chemical etching in an etching cell with a saturated solution of $HCl/CuCl_2$ using an etching mask with a circular window of 5 mm in diameter. Etched NAA-DBRs were then pore widened in an aqueous solution of 5 wt % H_3PO_4 at 35 °C for t_{pw} of 0, 2, 4, and 6 min and optically characterised. The features of the photonic stop band (PSB) of etched NAA-DBRs (position and full width at half maximum – FWHM) were then assessed by measuring their transmission spectra by UV-visible-NIR spectroscopy (Cary 5000, Agilent, USA) for the wavelength range 200–1500 nm at normal incidence (i.e. $\theta = 0^o$) with a resolution of 1 nm. The interferometric colour displayed by NAA-DBRs was

evaluated by digital images acquired using a Canon EOS 700D digital camera equipped with a Tamron 90 mm F2.8 VC USD macro mount lens with autofocus function under natural illumination.

2.3 Structural characterisation

The structural properties of NAA-DBRs were characterised by a field emission gun scanning electron microscope (FEG-SEM FEI Quanta 450). The acquired SEM images were analysed using ImageJ (public domain program developed at RSB of the NIH).

3. RESULTS AND DISCUSSION

3.1 Fabrication and structural characterisation of NAA-DBRs

NAA-DBRs were fabricated by stepwise pulse anodisation (SPA), where the current density was pulsed between high and low current density values in a stepwise fashion after a short constant anodisation (CA) step, as illustrated in **Figure 1a** – left. The nanoporous structure of NAA-DBRs was engineered in depth according to stepwise anodisation waves, yielding stacks of NAA layers with stepwise modulated porosity (**Figure 2b**). As denoted by the white arrows in **Figure 2b**, the length between consecutive NAA layers, which defines the period length (L_{Tp}), corresponds to each stepwise pulse in the anodisation profile and it was found to be 211 ± 6 nm for NAA-DBR produced at an anodisation period of 1300 s. On the other hand, apodised NAA-DBRs were produced by apodising the SPA profile using a logarithmic negative function (**Figure 1b**). The in-depth porosity of NAA-DBRs, as described in **Figure 1b** – left, was directly proportional to the apodisation current density during anodisation.

3.2 Effect of apodisation amplitude difference on the transmission features of NAA-DBRs

Figure 1c shows representative transmission spectra of non-apodised and logarithmic negative apodised NAA-DBRs fabricated under the same anodisation conditions. From the analysis of **Figure 1c**, it is revealed that both non-apodised and apodised NAA-DBRs display not only first order PSB in the range of 650–750 nm, but also second and third order PSBs in the range of 350–400 nm and 250–300 nm, respectively. The intensity of the first order PSB is greater than that of second and third order PSBs. They also display significant ripples in their transmission spectra due to interference fringes. However, the PSB of apodised NAA-DBRs has a narrower width with minimised sidelobes as compared to that of non-apodised NAA-DBRs. The application of apodisation enhances the intensity of PSB in addition to improving the resolution of the PSB, in particular the second and third orders PSBs, resulting in well-resolved and sharper bands. The transmission spectra of non-apodised and apodised NAA-DBRs as a function of t_{pw} in **Figures 2c and d** show the same trend in the effect of t_{pw} on the position of the PSB across the UV-visible-NIR range, where it undergoes a blue shift (i.e. first, second and third order) as the nanoporous structure of NAA-DBRs is widened with increasing t_{pw}. These results are in good agreement with previous studies.[40,57,60] To widen the nanopores of NAA-DBRs enhances the contrast of porosity between consecutives layer of NAA due to the existing gradient dissolution rate between NAA layers produced at different current density levels, resulting in a decrease of the overall effective refractive index of NAA-DBRs. This in turn shifts the position of PSB towards regions of shorter wavelength[40,63]. It was also observed that an increase in t_{pw} results in the broadening of the PSB, as observed in **Figures 2c and d**.

For non-apodised NAA-DBRs, the intensity of first order characteristic PSB increases through pore widening treatment. However, the intensity of second and third order PSB is not affected by pore widening process, as shown in **Figure 2c**. The transmittance baseline, on the other hand, decreases as t_{pw} increases, which can be attributed to the over etching of the nanopores and light scattering effects by the PC structure, as reported in previous studies.[40] Similar to non-apodised NAA-DBRs, the intensity of the characteristic first order PSB of apodised NAA-DBRs increases with increasing t_{pw}. However, in contrast to non-apodised NAA-DBRs, the increase in the intensity of PSB for apodised NAA-DBRs is found to be less significant. Furthermore, a decrease in the intensity of second order and third order PSBs is observed as apodised NAA-DBRs are etched at a longer t_{pw}. The transmittance baseline of apodised NAA-DBRs is maintained despite the increasing t_{pw} from 0 to 4 min (**Figure 2d**). Furthermore, our analysis reveals that apodised NAA-DBRs feature enhanced intensity of the characteristics PSBs as compared to that of pore widening treatment. Thus apodisation is an effective means to tune the width as well as enhancing the intensity of characteristic PSBs.

As displayed in **Figure 1c**, it is observed that the characteristics PSB of non-apodised and apodised NAA-DBRs is similar to a bell-shaped curve, which can be approximated to a Gaussian curve with a central peak wavelength at its

maximum (λ_c) and its full width at half maximum ($FWHM_{PSB}$). λ_c denotes the location of the first order characteristic PSB in the UV-visible-NIR spectrum, whereas $FWHM_{PSB}$ indicates the width of the characteristic PSB. These two parameters, λ_c and $FWHM_{PSB}$, are used to define the quality factor of the PSB (Q_{PSB}) in NAA-DBRs, where a high quality of characteristic stop band is represented by a high value of Q_{PSB}. The expression that correlates λ_c and $FWHM_{PSB}$ to Q_{PSB} is shown in Eq. 4.

$$Q_{PSB} = \frac{\lambda_c}{FWHM_{PBS}} \tag{4}$$

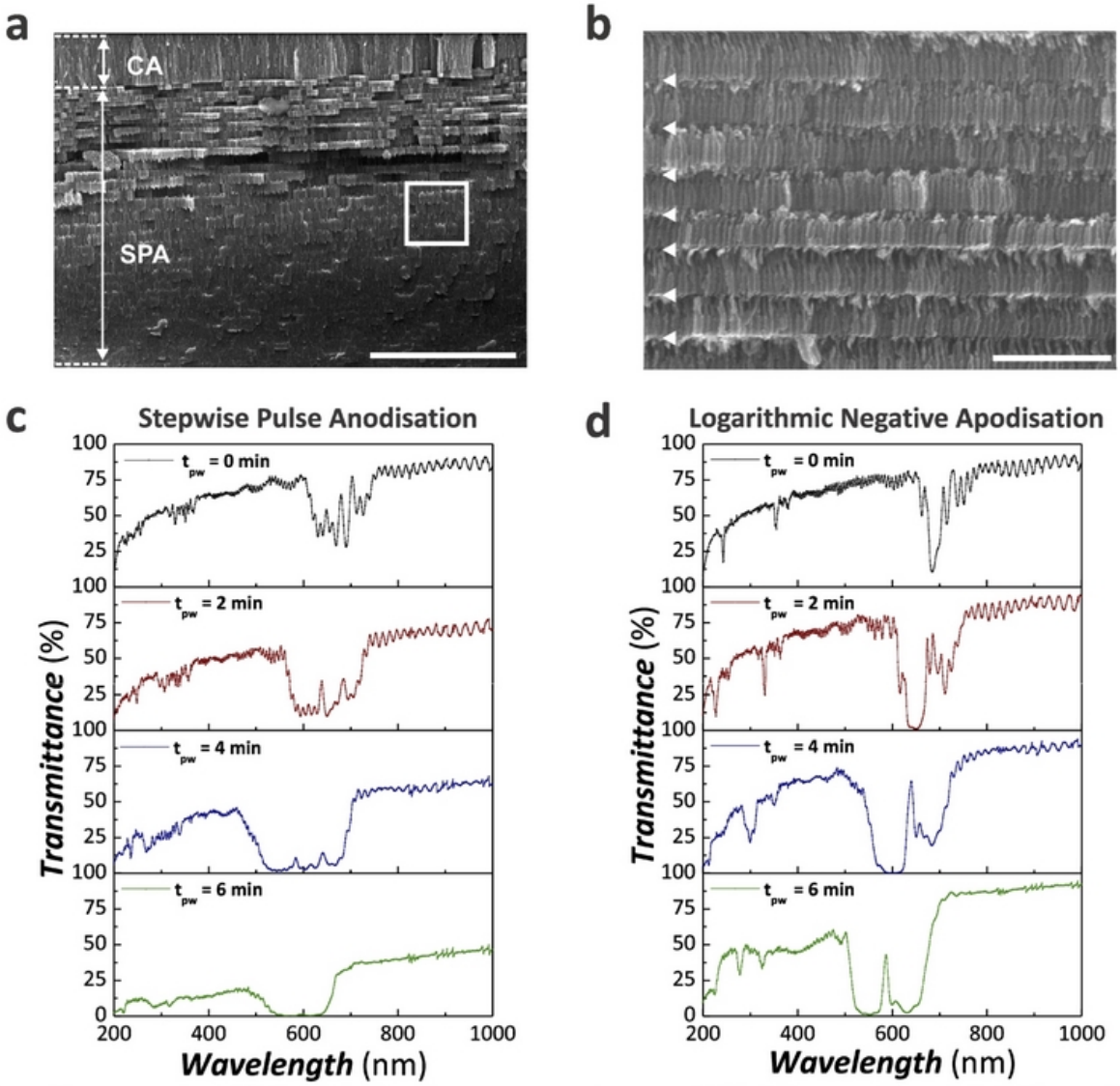

Figure 2. Structural and optical characterisation of nanoporous anodic alumina distributed Bragg reflectors. (a) SEM image showing the cross section of NAA-DBRs produced at ΔA_J = 0 mA cm^{-2}, T_p = 1300 s, J_{offset} = 0.28 mA cm^{-2} and t_{pw} = 6 min (scale bar = 5 µm). (b) Magnified view of white square in (a) showing stacks of NAA layers with the arrows denoting the period length (L_{Tp}) (scale bar = 500 nm). (c) Transmission spectra of NAA-DBRs (ΔA_J = 0 mA cm^{-2}, T_p = 1300 s, J_{offset} = 0.28 mA cm^{-2}) at different t_{pw}. (d) Transmission spectra of logarithmic negative apodised NAA-DBRs (ΔA_J = 0.21 mA cm^{-2}, T_p = 1300 s, J_{offset} = 0.28 mA cm^{-2}) as a function of t_{pw}.

The apodisation amplitude difference (ΔA_J) was systematically modified from 0 to 0.42 mA cm^{-2} with an interval of 0.21 mA cm^{-2} to unveil the effect of this fabrication parameter on the optical properties of NAA-DBRs in terms of λ_c, $FWHM_{PSB}$, Q_{PSB} and interferometric colour. Note that NAA-DBRs produced at ΔA_J = 0 mA cm^{-2} correspond to non-apodised NAA-DBRs, while NAA-DBRs produced at ΔA_J = 0.21 and 0.42 mA cm^{-2} are logarithmic negative apodised with ΔA_J of respective values. The results obtained are shown in **Figure 3** and they are based on the first order PSB as it plays a more significant role on governing the optical properties of NAA-DBRs as compared to the second and third order PSBs. **Figure 3a** shows the correlation of λ_c to ΔA_J for NAA-DBRs at different t_{pw}s, where λ_c is observed to be located within the visible range. When ΔA_J is increased from 0 to 0.21 mA cm^{-2}, there is a slight red shift in λ_c but a slight blue shift when ΔA_J is further increased to 0.42 mA cm^{-2}. It is worthwhile to note that the magnitude of this shift is minimal and thus ΔA_J has a weak influence on λ_c regardless of t_{pw}. Compared to ΔA_J, the effect of t_{pw} on λ_c is more significant as the magnitude of this shift in λ_c is greater. As aforementioned, an increase in t_{pw} induces a blue shift in λ_c. This trend is also observed in **Figure 3a**, where λ_c is shifted to shorter wavelengths as t_{pw} increases. This is observed for all NAA-DBRs produced with different ΔA_J.

λ_c establishes the interferometric colour displayed by NAA-DBRs as λ_c indicates the wavelength at which light is reflected more efficiently by the PC structure. **Figure 3b** depicts the colour properties of NAA-DBRs as a function of ΔA_J and t_{pw}. These NAA-DBRs display colours such as red, orange and yellow as their λ_c are located within the visible range. Non-apodised NAA-DBRs (ΔA_J = 0 mA cm^{-2}) display more distinct colour with stronger intensity as they reflect light more efficiently (i.e. broader band of wavelengths), which is consistent with the results obtained in previous study.[58] On the contrary, the colour of apodised NAA-DBRs are paler than that of non-apodised NAA-DBRs, the brightness of which is observed to decrease as ΔA_J increases. As the difference between minimum and maximum anodisation amplitude is greater, the period length varies to a greater extent in depth along the nanopores. As a result, light is reflected more selectively but in a less efficient manner. For instance, the interferometric colour of apodised NAA-DBRs with ΔA_J = 0 mA cm^{-2} and t_{pw} = 4 min is a blend of light yellow and pale green. The blue shift in λ_c due to an increase in t_{pw} is also reflected in the interferometric colour change of these NAA-DBRs from red-orange to yellow-green when λ_c shifts from the upper range (i.e. when t_{pw} = 0 and 2 min) to mid-range (i.e. when t_{pw} = 4 and 6 min) of the visible spectrum.

The contour map in **Figure 3c** illustrates the effect of ΔA_J and t_{pw} on $FWHM_{PSB}$ of the characteristic bands of NAA-DBRs. The PSBs of NAA-DBRs can be characterised in terms of their $FWHM_{PSB}$, upon which a more selective and sensitive NAA-DBRs have narrow characteristic stop bands with a low value of $FWHM_{PSB}$.[58] ΔA_J has a strong influence on $FWHM_{PSB}$ in non-apodised NAA-DBRs as the field lines at ΔA_J = 0 mA cm^{-2} are relatively close. The distance between the field lines increases as ΔA_J increases to 0.42 mA cm^{-2}, inferring that a greater difference in anodisation amplitude has a weaker effect on $FWHM_{PSB}$. The width of the characteristic PSB of NAA-DBRs decreases as ΔA_J approaches 0.21 mA cm^{-2} from 0 and 0.42 mA cm^{-2}, suggesting that ΔA_J = 0.21 mA cm^{-2} is the optimum apodising parameter in producing narrow stop bands with a $FWHM_{PSB}$ of 32 ± 1 nm. On the contrary, the non-apodised NAA-DBRs (ΔA_J = 0 mA cm^{-2}) counterpart has a $FWHM_{PSB}$ of 130 ± 1 nm, which is ~4 times wider than that of apodised NAA-DBRs. Thus apodisation is demonstrated to be an effective approach in tuning the width of the PSB as a lower $FWHM_{PSB}$ is favourable in producing high quality characteristic stop bands. The equidistant field lines at short t_{pw} (0 and 2 min) as well as the wide field lines at longer t_{pw} (4 and 6 min) reveal that the $FWHM_{PSB}$ has a stronger dependency at shorter t_{pw}. $FWHM_{PSB}$ increases as t_{pw} increases, in spite of the varying ΔA_J.

With the determined λ_c and $FWHM_{PSB}$, the quality of characteristic PSBs (Q_{PSB}) is analysed using Eq. 4 and the distribution of Q_{PSB} as a function of ΔA_J and t_{pw} for apodised and non-apodised NAA-DBRs is shown in **Figure 3d**. The colour fields in **Figure 3d** concentrate at the region of t_{pw} = 0 to 2 min and the distance between the field lines decreases with decreasing t_{pw}. In general, Q_{PSB} increases as t_{pw} decreases and this suggests that pore widening has a negative effect in producing NAA-DBRs with high quality characteristic PSBs. The application of apodisation has a positive impact on Q_{PSB}, as described by the decreasing field line distances when ΔA_J increases from 0 to 0.21 mA cm^{-2}. Further increase of ΔA_J to 0.42 mA cm^{-2} has a slightly less significant effect on Q_{PSB}, denoted by the wider field line distances. This yields a local maximum of Q_{PSB} = 21.3 ± 0.6 at ΔA_J = 0.21 mA cm^{-2} and t_{pw} = 0 min, producing logarithmic negative apodised NAA-DBRs with high quality characteristic PSB. This is ~4.1 times greater than the Q_{PSB} of non-apodised NAA-DBRs (i.e. ΔA_J = 0 mA cm^{-2} and t_{pw} = 0 min) with a value of 5.1 ± 0.2.

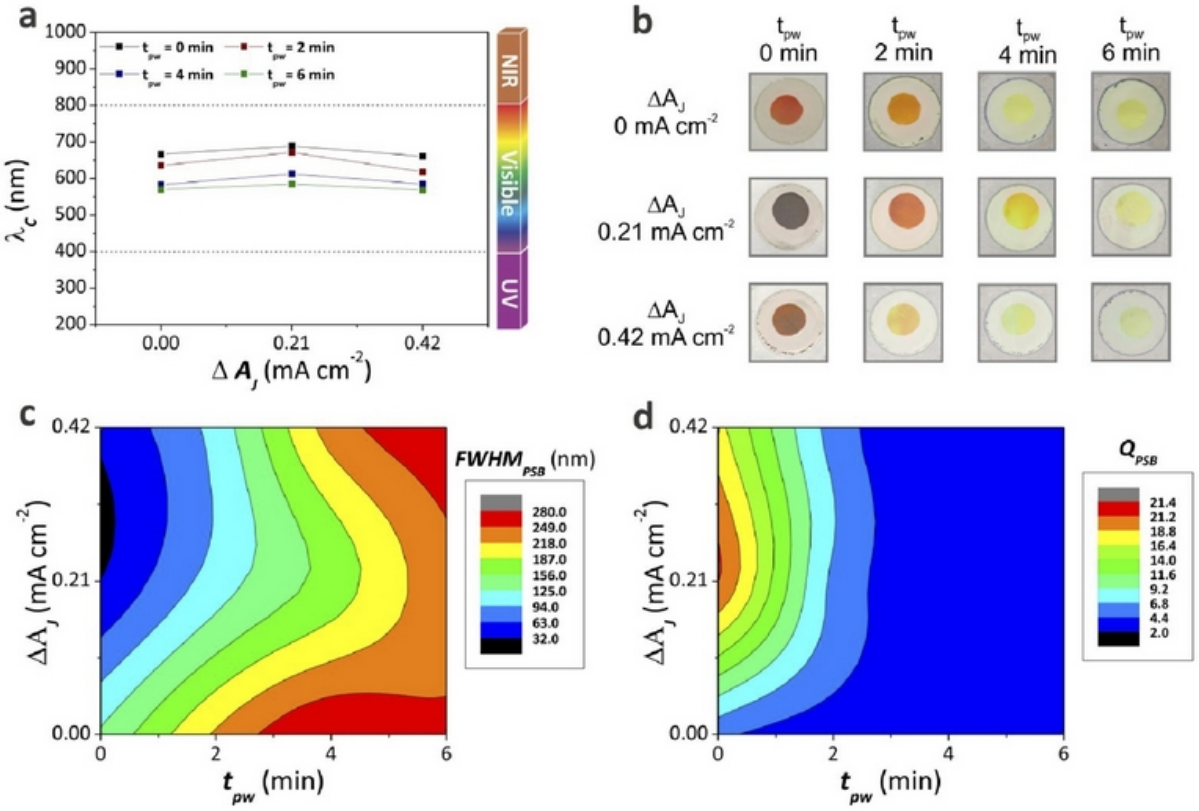

Figure 3. Effect of ΔA_J on the transmission features of NAA-DBRs. (a) Correlation between ΔA_J and the position of central PSB of apodised NAA-DBRs at different t_{pw}. (b) Digital photos of apodised NAA-DBRs (diameter = 1cm) as a function of ΔA_J and t_{pw}. (c) Contour plot showing the distribution of $FWHM_{PSB}$ by the manipulation of ΔA_J and t_{pw}. (d) Contour plot describing the dependence of Q_{PSB} on ΔA_J and t_{pw}. (Note: T_p and J_{offset} were fixed at 1300 s and 0.28 mA cm^{-2}, respectively).

3.3 Effect of anodisation period on the transmission features of NAA-DBRs

As shown in the previous section, NAA-DBRs apodised with ΔA_J = 0.21 mA cm^{-2} are demonstrated to exhibit high quality characteristic PSBs. By keeping ΔA_J constant at 0.21 mA cm^{-2}, the anodisation period (T_p) was modified from 1100 to 1500 s with an interval of 200 s to study the effect of T_p on the transmission features of logarithmic negative apodised NAA-DBRs in terms of λ_c, interferometric colours, $FWHM_{PSB}$ and Q_{PSB}. The transmission spectra of apodised NAA-DBRs produced at different T_p show first, second and third order characteristic PSBs, similar to that in **Figure 2d**. **Figure 4a** shows how the position of λ_c for the first order PSB changes with T_p and t_{pw} across UV-visible-NIR spectrum. For all T_p, the central wavelength of apodised NAA-DBRs is located within the visible range of the spectrum. A linear relationship between T_p and λ_c is established, where the longer the anodisation period, the longer the central wavelength is positioned at. For example, λ_c of as-produced apodised NAA-DBRs with T_p of 1100 s is at 570 ± 1 nm and λ_c shifts to 780 ± 1 nm when T_p increases to 1500 nm. This result is in good agreement with previous studies.[57,58,60] As the anodisation period determines the period length within the nanoporous structure of apodised NAA-DBRs, the longer the anodisation period, the longer the length of NAA layers between consecutive stepwise pulses, resulting in the reflection of light at longer wavelengths. By further increase the anodisation period (i.e. T_p > 1500 s), the position of λ_c can be engineered in the NIR region. T_p is an effective parameter to achieve versatile tuneability of λ_c across the spectral regions. Increasing t_{pw} has the same effect (i.e. blue shift) on λ_c of apodised NAA-DBRs produced with different T_p as to that of different ΔA_J.

Apodised NAA-DBRs display vivid interferometric colours when λ_c is located within the visible range (500 to 800 nm). However, λ_c of apodised NAA-DBR with T_p = 1500 s and t_{pw} = 0 min is located at 780 nm, which is relatively close to the NIR region, and thus these NAA-DBRs are transparent (black colour denoted by the background). There is a red shift in the interferometric colour of apodised NAA-DBRs with T_p from 1100 to 1500 s as depicted in **Figure 4b**. For

example, at t_{pw} = 4 min, apodised NAA-DBRs display turquoise (i.e. λ_c = 520 nm) at T_p = 1100 s and the colour changes to yellow and then orange as λ_c shifts from 600 to 650 nm. The blue shift in λ_c that results from the increase in t_{pw} is also established by the interferometric colour change of apodised NAA-DBRs. However, it is worth nothing that the colour change of apodised NAA-DBRs from the effect of t_{pw} is not as significant as the effect of T_p. Furthermore, the colour intensity of these apodised NAA-DBRs is fairly strong as they are apodised with a moderate value of ΔA_J (i.e. 0.21 mA cm^{-2}).

The analysis of $FWHM_{PSB}$ as a function of T_p and t_{pw} is presented **Figure 4c**. As denoted by the relative wide colour field and distant field lines, $FWHM_{PSB}$ has a relatively weak dependency on T_p. However, a general trend is observed between $FWHM_{PSB}$ and T_p. $FWHM_{PSB}$ increases with T_p, thus apodised NAA-DBRs produced with longer T_p exhibit wider characteristic PSBs due to the increased period length within the PC structure. However, apodised NAA-DBRs with t_{pw} = 6 min show an opposite effect, where $FWHM_{PSB}$ increases as T_p decreases. This might be due to the over-etching after pore widening treatment. For the effect of t_{pw} on $FWHM_{PSB}$, $FWHM_{PSB}$ of apodised NAA-DBRs has a stronger dependence on longer t_{pw}, as conveyed by the shorter field line distances at t_{pw} = 4 and 6 min. Apodised NAA-DBRs produced with various T_p show an increase in $FWHM_{PSB}$ as they are pore widened. This treatment increases the diameter of nanopores of apodised, resulting in wider PSB with higher values of $FWHM_{PSB}$. Therefore, t_{pw} has a greater influence on $FWHM_{PSB}$ than that of T_P. A local minima of $FWHM_{PSB}$ = 32 ± 1 nm is identified in the colour map when the fabrication parameters are set at T_p = 1300 s and t_{pw} = 0 min. Apodised NAA-DBRs produced at these parameters exhibit a narrow characteristic PSB.

The correlation between Q_{PSB} and T_p and t_{pw} is presented in the contour map in **Figure 4d**. The colour field is dense with close field lines at the region of t_{pw} = 0 and 2 min, but the distance between the field lines in the map increases with t_{pw}, denoting that the dependence of Q_{PSB} of apodised NAA-DBRs on t_{pw} is weaker as t_{pw} increases. Furthermore, the quality of characteristic PSB of apodised NAA-DBRs is worsened as they are pore widened, which can be predicted from the values of $FWHM_{PSB}$ based on the inversely proportional relationship between $FWHM_{PSB}$ and Q_{PSB}. Further modification of T_p has a negative effect on enhancing the Q_{PSB} of apodised NAA-DBRs with $t_{pw} \geq 4$ min. Pore widening treatment broadens the characteristic PSB of apodised NAA-DBRs, thus decreasing the Q_{PSB}. The distance between the field lines decreases as T_p is modified from 1100 and 1500 s, suggesting the dependency of Q_{PSB} on T_p increases as T_p approaches to 1300 s. This gives rise to a local maximum with a value of Q_{PSB} of 21.3 ± 0.6 at T_p = 1300 s and t_{pw} = 0 min. The colour fields denote that fabrication at shorter T_p produces apodised NAA-DBRs with better Q_{PSB} than those at longer T_p. Unlike $FWHM_{PSB}$, which depends more on t_{pw} than on T_p, Q_{PSB} of apodised NAA-DBRs shows a stronger dependency on T_p rather than t_{pw}.

3.4 Effect of current density offset on the transmission features of NAA-DBRs

To achieve precise tuning of the transmission features, apodised NAA-DBRs were fabricated at different current density offset (J_{offset}): 0.14, 0.28 and 0.42 mA cm^{-2}. Their transmission spectra and digital photos were measured and analysed, and the results obtained are compiled in **Figure 5**. The correlation between J_{offset} and λ_c of apodised NAA-DBRs at different t_{pw} for the first order PSB is presented in **Figure 5a**. Apodised NAA-DBRs produced at J_{offset} of 0.14 and 0.28 mA cm^{-2} have their characteristics λ_c located within the visible range, whereas λ_c of those at J_{offset} = 0.42 mA cm^{-2} is in the NIR range. λ_c of apodised NAA-DBRs is shown to have a linear relationship with J_{offset}, the higher J_{offset} is the longer λ_c, thus red-shifting λ_c towards the NIR region. This result is consistent with the results obtained in previous studies.[60] It is also observed that the shift in λ_c is greater when J_{offset} increases from 0.28 to 0.42 mA cm^{-2} in spite of the different t_{pw}. The manipulation of t_{pw} has shown the same effect on λ_c; longer t_{pw} induces a blue shift in λ_c due to the decrease in the overall refractive index of apodised NAA-DBRs and the enhanced porosity contrast. The position of λ_c of apodised NAA-DBRs is more affected by the manipulation of J_{offset} than t_{pw}, as established by the magnitude of the shift in λ_c. J_{offset} are demonstrated to be an effective parameter to precisely engineer the transmission PSB of apodised NAA-DBRs across the entire UV-visible-NIR spectrum.

The digital photos showing the interferometric colour of apodised NAA-DBRs produced at different J_{offset} and t_{pw} are shown in **Figure 5b**. Apodised NAA-DBRs fabricated at high J_{offset} (i.e. 0.42 mA cm^{-2}) are found to be transparent as they reflect light of wavelength in the NIR region. On the contrary, apodised NAA-DBRs with J_{offset} of 0.14 and 0.28 mA cm^{-2} display vivid interferometric colours, such as blue, green, yellow and orange, which correspond to their respective first order characteristic PSB in the visible range. The red shift in λ_c due to increasing J_{offset} is also described by the colour change in apodised NAA-DBRs. Apodised NAA-DBRs of J_{offset} = 0.14 mA cm^{-2} has displayed blue-green color as their λ_c are in the mid-range of the visible spectrum, and the colour changes to yellow-red when J_{offset} is increased to 0.28 mA cm^{-2}. Further increase of J_{offset} to 0.42 mA cm^{-2} induces a greater red shift in λ_c towards the NIR range. A blue shift in

the interferometric colours of apodised NAA-DBRs is observed with t_{pw}. The colour displayed by these apodised NAA-DBRs are fairly intense as they are fabricated at moderate $\Delta A_J = 0.21$ mA cm^{-2}.

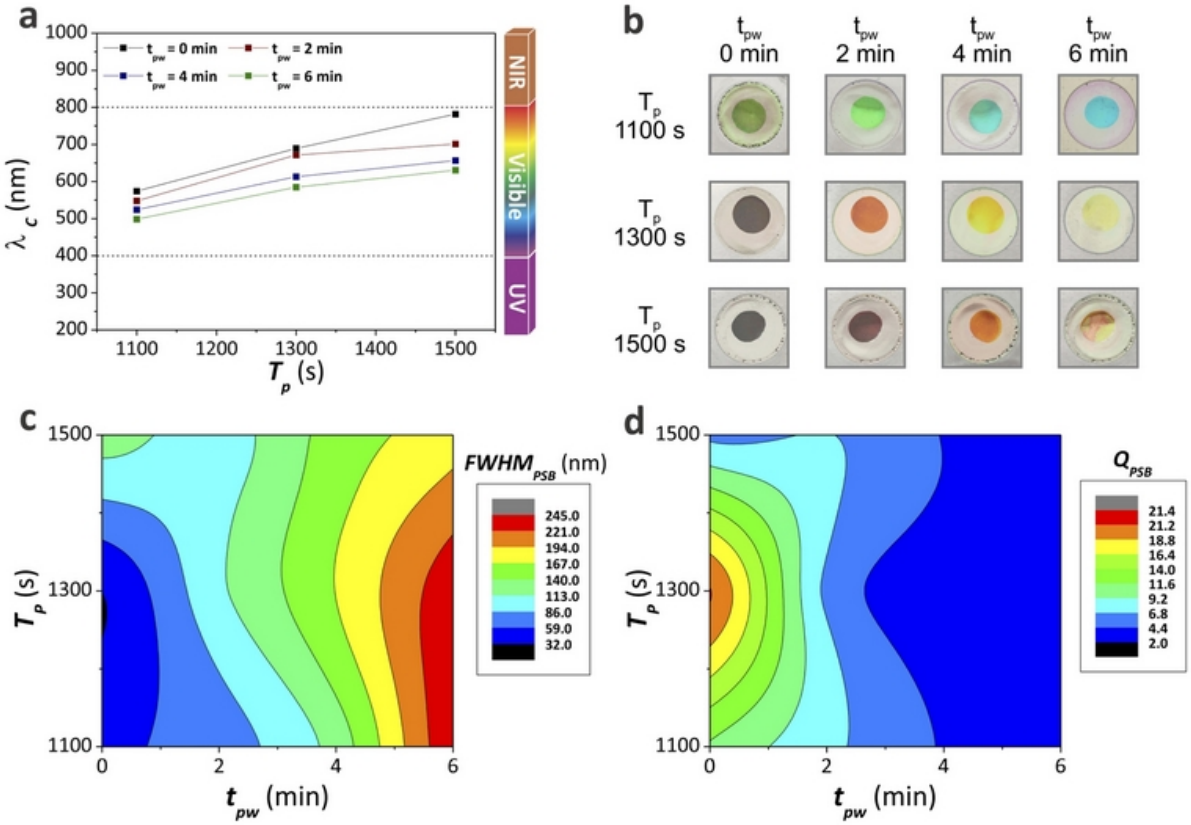

Figure 4. Effect of T_p on the transmission features of logarithmic negative apodised NAA-DBRs. (a) A linear relationship between T_p and λ_c of NAA-DBRs for different t_{pw}. (b) Digital photos of apodised NAA-DBRs of 1 cm diameter illustrating their interferometric colours as a function of T_p and t_{pw}. (c) Contour map showing the dependence of $FWHM_{PSB}$ on T_p and t_{pw}. (d) Contour map describing the effect of T_p and t_{pw} on Q_{PSB}. (Note: ΔA_J and J_{offset} were fixed at 0.21 and 0.28 mA cm^{-2})

Figure 5c shows the distribution of $FWHM_{PSB}$ in terms of J_{offset} and t_{pw}. The closer and equidistant colour lines in the bottom left region of the map indicate that $FWHM_{PSB}$ of apodised NAA-DBRs has a slightly stronger dependence at low J_{offset} and short t_{pw}. Other than that, the rest of the map is of wide colour field and field lines, implying the weak correlation of $FWHM_{PSB}$ to J_{offset} and t_{pw}. However, when comparing the effect of J_{offset} and t_{pw} on $FWHM_{PSB}$, t_{pw} plays a more significant role in $FWHM_{PSB}$ of apodised NAA-DBRs, as described by the closer field lines as well as the colour fields across the x-axis direction (i.e. blue to red). As a consequence from the increment of t_{pw} in the pore widening treatment of apodised NAA-DBRs, their characteristics PSB broadens with increasing $FWHM_{PSB}$, which may not be desirable for applications requiring high sensitivity. The effect of J_{offset} generally causes a slight increase in $FWHM_{PSB}$, as illustrated by the distribution of colour fields along the y-axis. Nonetheless, apodised NAA-DBRs produced at J_{offset} = 0.28 mA cm^{-2} and $t_{pw} = 0$ min have the narrowest characteristic PSB with a $FWHM_{PSB}$ of 32 ± 1 nm, as identified in the colour map.

Q_{PSB} of apodised NAA-DBRs are determined through their correlation to λ_c and $FWHM_{PSB}$, established by Eq. 4, and the results as a function of J_{offset} and t_{pw} are summarised in **Figure 5d**. Similar to **Figures 3d and 4d**, the colour fields concentrate on the region of $t_{pw} < 2$ min. From the closer distance between the field lines at $t_{pw} \leq 2$ min than that of $t_{pw} \geq 2$ min, it is apparent that the dependency of Q_{PSB} on t_{pw} increases as t_{pw} decreases from 6 to 0 min. Furthermore, the evolution of colour field across the x-axis suggests that shorter t_{pw} favours the production of apodised NAA-DBRs with high quality characteristic PSBs. In term of the effect of J_{offset}, by focusing on the region of $t_{pw} = 0$ min, the colour field between 0.14 and 0.28 mA cm^{-2} are denser with closer field lines as compared to the region between 0.28 and 0.42 mA

cm^{-2}. This reveals that Q_{PSB} has a stronger dependency on $J_{offset} \leq 0.28$ mA cm^{-2} as compared to $J_{offset} \geq 0.28$ mA cm^{-2}. This also denotes that apodised NAA-DBRs with $J_{offset} = 0.14$ mA cm^{-2} have a greater Q_{PSB} than those of $J_{offset} = 0.42$ mA cm^{-2}, with a local maximum of Q_{PSB} of 21.3 ± 0.6 at $J_{offset} = 0.28$ mA cm^{-2} and $t_{pw} = 0$ min. On the whole, the contour map demonstrates that J_{offset} has a more substantial effect on Q_{PSB} of apodised NAA-DBRs as compared to t_{pw}. However, pore widening of apodised NAA-DBRs with prolonged t_{pw} has a stronger effect in decreasing Q_{PSB}, despite the manipulation of J_{offset} for the enhancement of the quality of characteristic PSBs.

The comparison between **Figures 3a, 4a and 5a** has revealed that the modification of T_p and J_{offset} can be used to shift λ_c across the entire UV-visible-NIR spectrum efficiently and effectively. This also allows the tuning of the interferometric colours displayed by NAA-DBRs, which is a suitable feature to develop versatile photonic nanotools for visual sensing. In the case of Q_{PSB}, ΔA_J plays a more significant role in the determination of Q_{PSB}, as denoted by the closer field lines in the colour field when **Figures 3d, 4d and 5d** are compared. Regarding $FWHM_{PSB}$, the wide colour fields in **Figures 3c, 4c and 5c** described the relatively weak dependency of $FWHM_{PSB}$ on ΔA_J, T_p and J_{offset}, instead $FWHM_{PSB}$ correlates more to t_{pw}. Another observation is that the combination of apodisation with stepwise pulse anodisation has shown a better result in minimising the bandwidth and maximising the quality of PSB (Q_{PSB} = 21.3 ± 0.6) as compared to sinusoidal pulse anodisation (Q_{PSB} = 4.6 ± 0.4).[58]

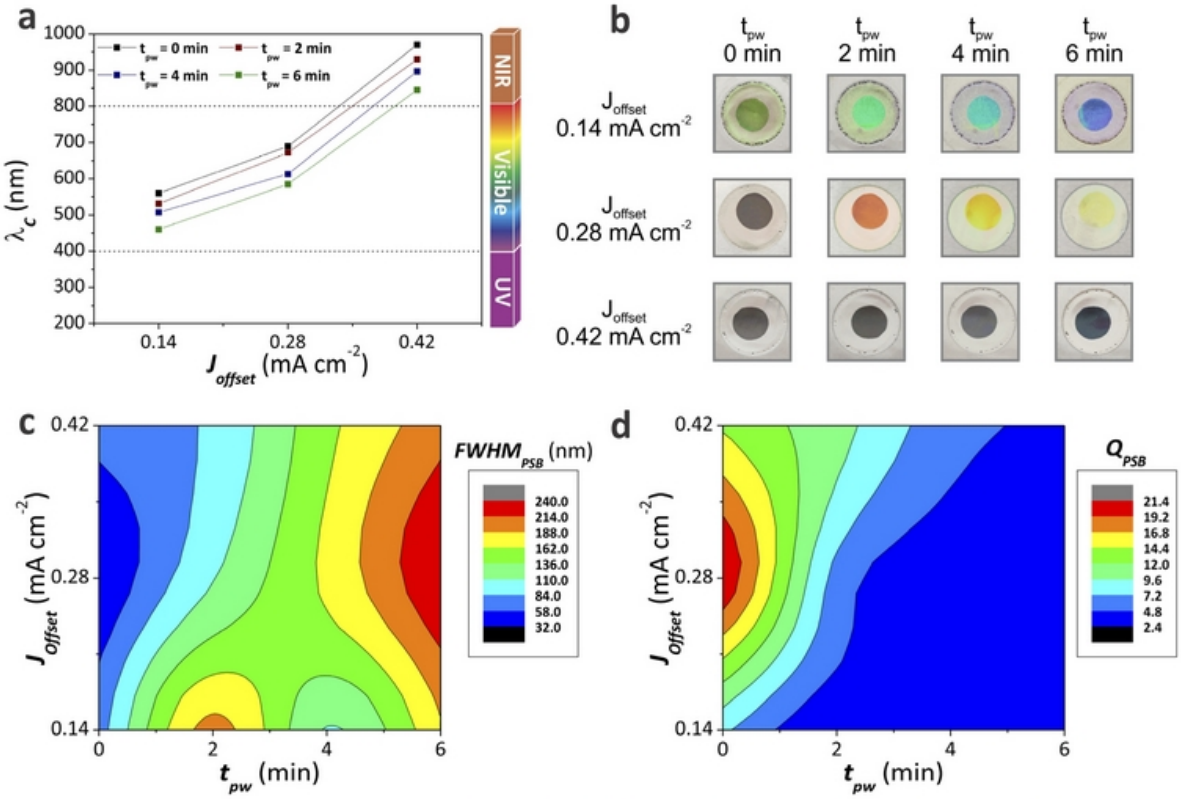

Figure 5. Effect of J_{offset} on the transmission features of logarithmic negative apodised NAA-DBRs. (a) A linear distribution of λ_c of apodised NAA-DBRs as a function of J_{offset} and t_{pw} across the UV-visible-NIR spectrum. (b) Digital photos establishing the colour characteristics of apodised NAA-DBRs with diameter of 1 cm resulting from the effect of J_{offset} and t_{pw}. (c) Dependence of $FWHM_{PSB}$ on J_{offset} and t_{pw} for apodised NAA-DBRs. (d) Dependence of Q_{PSB} of apodised NAA-DBRs as a function of J_{offset} and tpw. (Note: ΔA_J and T_p were fixed at 0.21 mA cm^{-2} and 1300 s)

4. CONCLUSIONS

This study has successfully engineered NAA-based distributed Bragg reflectors by apodised stepwise pulse anodisation using a logarithmic negative function, where their transmission features such as quality and position of photonic stop bands and interferometric colours were systematically assessed. Apodisation based on logarithmic negative function is demonstrated to be effective in narrowing the bandwidth, increasing the intensity and reducing the characteristic sidelobes of the photonic stop bands of NAA-DBRs. Fabrication parameters such as apodisation amplitude difference, anodisation period, current density offset and pore widening time were modified to tune the transmission features of NAA-DBRS and optimise the quality of the photonic stop bands of NAA-DBRs. This study reveals that the manipulation of amplitude difference has a stronger effect on Q_{PSB} than $FWHM_{PSB}$ and λ_c, where the dependency of Q_{PSB} is particularly stronger when the apodisation amplitude difference is at 0.21 mA cm^{-2}. As for the effect of the anodisation period, a red shift in λ_c is observed when anodisation period is altered from 1100 to 1500 s. $FWHM_{PSB}$ has shown a diminished correlation to the anodisation period as compared to that of Q_{PSB}. NAA-DBRs with narrower bandwidth and better quality are produced when their anodisation period is optimised at 1300 s. In addition to that, the effect of increasing current density offset has established a red shift in λ_c. The effect of current density offset on Q_{PSB} is relatively weak, on the contrary, the dependence of Q_{PSB} is stronger and increases as the current density offset approaches 0.28 mA cm^{-2}. Through the systematic modifications of apodisation parameters, the highest value of Q_{PSB} apodised NAA-DBRs achieved is 21.3 ± 0.6, which is 3.5 times greater than apodised rugate filters and 4.1 times greater than non-apodised NAA-DBRs. Another parameter studied was the pore widening time, where it is found out that an increase in t_{pw} has the same effect on the transmission characteristic of NAA-DBRs such as a blue shift in λ_c, an increase in $FWHM_{PSB}$ as well as a decrease in Q_{PSB} regardless of the changing apodisation parameters. The broadening effect on the characteristic bands of NAA-DBRs due to pore widening treatment may enhance the intensity of the characteristics band, but it is unfavourable for the production of narrow line-width NAA-DBRs. Furthermore, NAA-DBRs are demonstrated to display vivid colours across the spectral regions such as green, blue, red, orange and yellow that corresponds to their position of λ_c across UV-visible-NIR spectrum. It is worthwhile to note that among the fabrication parameters assessed in this study, apodisation amplitude difference has a more significant effect on Q_{PSB} of NAA-DBRs, and thus it is a more effective parameter in optimising Q_{PSB}. On the other hand, the fine and precise tuning of λ_c and interferometric colours of NAA-DBRs across the spectrum can be achieved by the manipulation of anodisation period and current density offset. To conclude, this study establishes the use of apodisation as an effective approach to tune the filtering features of NAA-based photonic structures, which could have broad applicability in different fields and disciplines such as sensing and biosensing.

ACKNOWLEDGEMENTS

Authors thank the support provided by the Australian Research Council (ARC) through the grant number DE140100549 and the School of Chemical Engineering (UoA). Authors thank the Adelaide Microscopy (AM) centre for FEG-SEM characterization.

REFERENCES

[1] Santos, A., "Nanoporous anodic alumina photonic crystals: fundamentals, developments and perspectives," J. Mater. Chem. C 5, 5581-5599 (2017).
[2] López. C., "Materials aspects of photonic crystals," Adv. Mater. 15(20), 1679-1704 (2003).
[3] Akahane, Y., Asano, T., Song, B-S. and Noda, S., "High-Q photonic nanocavity in a two-dimensional photonic crystal," Nature, 425(6961), 944-947 (2003).
[4] Noda, S., Tomoda, K., Chutinan, A., and Yamamoto, N., "Full three-dimensional photonic bandgap crystals at near-infrared wavelengths," Science 289 (5479), 604-606 (2000).
[5] Noda, S., Chutinan, A. and Imada, M., "Trapping and emission of photons by a single defect in a photonic bandgap structure," Nature 407 (6804), 608-610 (2000).
[6] Song, B-S., Noda, S., Asano, T., and Akahane, Y., "Ultra high-Q photonic double heterostructure nanocavity," Nat. Mat. 4(3), 207-210 (2005).

[7] Yablonovitch, E., "Inhibited spontaneous emission in solid-state physics and electronics," Phys. Rev. Lett. 58(20), 2059-2062 (1987).
[8] Yablonovitch, E., "Photonic band-gap structures," J. Opt. Soc. Am. B 10(2), 283-295 (1993).
[9] Charlton, M. D. B., Roberts, S. W. and Parker, G. J., "Guided mode analysis, and fabrication of a 2-dimensional visible photonic band structure confined within a planar semiconductor waveguide," Mater. Sci. Eng. B. 49(2), 155-165 (1997).
[10] Gerard, J. M., Izrael, A., Marzon, J. Y., Padjen, R. and Laan, F. R., "Photonic bandgap of two-dimensional dielectric crystals," Solid-State Electron 37(4), 1341-1344 (1994).
[11] Berger, V., Gauthier-Lafaye, O. and Coastard, E., "Fabrication of a 2D photonic bandgap by a holographic method," Electron. Lett. 33(5), 425-426 (1997).
[12] Yi-Yan, A., Wilkinson, C. D. and Laybourn, P. J., "Two-dimensional grating unit cell demultiplexer for thin-film optical waveguide," IEEE J. Quantum Electron. 16, 1089-1092 (1980).
[13] Zengerle, R., "Light propagation in singly and doubly periodic planar waveguides," J. Mod. Opt. 34(12), 1589-1617 (1987).
[14] Little, B. E., Foresi, J. S., Steinmeyer, G., Theon, E. R., Chu, S. T., Haus, H. A., Ippen, E. P., Kimerling, L. C. and Greene, W., "Ultra-compact Si-SiO_2 microring resonator optical channel dropping filters," IEEE Photonics Technol. Lett. 10(4), 549-551 (1998).
[15] Scherer, A., Painter, O., d'Urso, B., Lee, R. and Yariv, A., "InGaAsP photonic band gap crystal membrane microresonators," J. Vac. Sci. Technol. B 16(6), 3906-3910 (1998).
[16] Tonucci, R., Justus, B. L., Campillo, A. J. and Ford, C. E., "Nanochannel glass array," Science 258, 783-785 (1992).
[17] Lawandy, N. M., Balachandran, R. M., Gomes, A. S. L. and Sauvain, E., "Laser action in strongly scattering media," Nature 368(6470), 436-438 (1994).
[18] Holland, B. T., Blanford, C. F., and Stein, A., "Synthesis of macroporous minerals with highly ordered three-dimensional arrays of spheroidal voids," Science 281 (5376), 538– 540 (1998).
[19] Grüning, U., Lehmann, V., Ottow, S. and Busch, K., "Macroporous silicon with a complete two-dimensional photonic band gap centered at 5 μM," Appl. Phys. Lett. 68(6), 747-749 (1996).
[20] Grüning, U., Lehmann, V. and Engelhardt, C. M., "Two-dimensional infrared photonic band gap structure based on porous silicon," Appl. Phys. Lett 66(24), 3254-3256 (1995).
[21] Rowson, S., Chelnokov, A., Cuisin, C. and Lourtioz, J. M., "Three-dimensional characterization of a two-dimensional photonic bandgap reflector at midinfrared wavelengths," IEE Proc.: Optoelectron 145(6), 403-408 (1998).
[22] Lau, H. W., Parker. G. J., Greef, R. and Hölling, M., "High aspect ratio submicron pillars fabricated by photoassisted electrochemical etching and oxidation," Appl. Phys. Lett. 67(13), 1877-1879 (1995).
[23] Ishikura, N., Fuijii, M., Nishida, K., Hayashi, S., and Diener, J., "Porous silicon based extended-bandwidth rugate filters for mid-infrared application," Infrared Phys. Technol. 53(4), 292-294 (2010).
[24] Kumeria, T., Mohammad Mahbubur, R., Santos, A., Ferré-Borrul, J., Marsal, L.F. and Losic, D., "Nanoporous anodic alumina rugate filters for sensing of ionic mercury: towards environmental point-of-analysis systems," ACS Appl. Mater. Interfaces 6(15), 12971-12978 (2014).
[25] King, B. and Sailor, M. J., "Medium-wavelength infrared gas sensing with electrochemically fabricated porous silicon optical rugate filters," J. Nanophoton. 5(1), 051510 (2011).
[26] Pavesi, L., "Porous silicon dielectric multilayers and microcavities," L. Riv. Nuovo Cim. 20(1), 1-75 (1997)
[27] Salem, M. S., Ibrahim, S. M. and Amin, M., "Facile design and stabilization of a novel one-dimensional silicon-based photonic crystal microcavity," J. Appl. Phys. 122(3), 033104 (2017).
[28] Hotta, K., Yamaguchi, A. and Terramae, N., "Nanoporous waveguide sensor with optimized nanoarchitectures for highly sensitive label-free biosensing," ACS Nano 6(2), 1541-1547 (2012).
[29] Loni, A., Canham, L., Berger, M., Arens-Fischer, R., Munder, H., Luth, H., Arrand, H. and Benson, T., "Porous silicon multilayer optical waveguides," Thin Solid Films 276(1), 143-146 (1996).
[30] Argawal, V. and Del Rio, J., "Tailoring the photonic band gap of a porous silicon dielectric mirror," Appl. Phys. Lett. 82(10), 1512-1514 (2003).
[31] Chen, Y., Santos, A., Wang, Y., Kumeria, T., Ho, D., Li, J., Wang, C. and Losic, D., "Rational design of photonic dust from nanoporous anodic alumina films: a versatile photonic nanotool for visual sensing," Sci. Rep. 5, 12893 (2015).

[32] Losic, D. and Santos, A., [Nanoporous anodic alumina: fabrication, structure, properties and applications], Springer, Switzerland (2015).
[33] Busch, K., Lölkes, S., Wehrspohn, R. B., Föll, H., [Photonic crystals: advances in design, fabrication, and characterization], Wiley-VCH Verlag GmbH &Co. KGaA, Weinheim, 63-84 (2006).
[34] Santos, A., Kumeria, T., Wang, Y. and Losic, D., "In situ monitored engineering of inverted nanoporous anodic alumina funnels: on the precise generation of 3D optical nanostructures," Nanoscale 6, 9991-9999 (2014).
[35] Santos, A., Balderrama, V. S., Alba, M., Formentín, P., Ferré-Borrull, J., Pallarès, J. and Marsal, L. F., "Nanoporous anodic alumina barcodes: toward smart optical biosensors," Adv. Mat. 24(12)., 1050-1054 (2012).
[36] Kumeria, T., Mohammad Mahbubur, R., Santos, A., Ferré-Borrul, J., Marsal, L.F. and Losic, D., "Structural and optical nanoengineering of nanoporous anodic alumina rugate filters for real-time and label-free biosensing applications," Anal. Chem. 86(3), 1837-1844 (2014).
[37] Kumeria, T., Santos, A., Mohammad Mahbubur, R., Ferré-Borrul, J., Marsal, L.F. and Losic, D., "Advanced structural engineering of nanoporous photonic structures: tailoring nanopores architecture to enhance sensing properties," ACS Photonics 1(12), 1298-1306 (2014).
[38] Kumeria, T., Santos, A. and Losic, D., "Nanoporous anodic alumina platforms: engineered surface chemistry and structure for optical sensing applications," Sensors 14(7), 11878-11918 (2014).
[39] Kumeria, T., Santos, A. and Losic, D., "Ultrasensitive nanoporous interferometric sensor for label-free detection of gold (III) ions," ACS Appl. Mater. Interfaces 5(22), 11783-11790 (2013).
[40] Rahman, M. M., Marsal, L. F., Pallarès, J. and Ferré-Borrull, J., "Tuning the photonic stop bands of nanoporous anodic alumina-based distributed Bragg reflectors by pore widening," ACS Appl. Mater. Interfaces 5(24), 13375-13381(2013).
[41] Shang, G. L., Fei, G. T., Zhang, Y., Yan, P., Xu, S. H. and Zhang, L. D., "Preparation of narrow photonic bandgaps located in the near infrared region and their applications in ethanol gas sensing," J. Mater. Chem. C 1, 5285-5291(2013).
[42] Santos, A., Kumeria. T. and Losic, D., "Nanoporous anodic alumina: a versatile platform for optical biosensors," Materials 7(6), 4297-4320 (2014).
[43] Santos, A., Kumeria. T. and Losic, D., "Nanoporous anodic aluminum oxide for chemical sensing and biosensors," Trends Anal. Chem. 44, 25-38 (2013).
[44] Chen, Y., Santos, A., Ho, D., Wang, T., Kumeria, T., Li, J., Wang, C. and Losic, D., "On the generation of interferometric colors in high purity and technical grade aluminum: an alternative green process for metal finishing industry," Electrochim. Acta 174, 672-681 (2015).
[45] Wang, Y., Chen, Y., Kumeria, T., Ding, F., Evdokiou, A., Losic, D. and Santos, A., "Facile synthesis of optical microcavities by a rationally designed anodisation approach: tailoring photonic signals by nanopores structure," ACS Appl. Mater. Interfaces 7(18), 9879-9888. (2015).
[46] Santos, A., Kumeria, T. and Losic, D., "Optically optimized photoluminescent and interferometric biosensors based on nanoporous anodic alumina: a comparison," Anal. Chem. 85(16), 7904-7911 (2013).
[47] Macias, G., Ferré-Borrul, J., Pallarès, J. and Marsal, L.F, "1-D nanoporous anodic alumina rugate filters by means of small current variations for real-time sensing applications," Nanoscale Res. Lett. 9(1), 1-6 (2014).
[48] Macias, G., Hernández-Eguía, L. P., Ferré-Borrull, J., Pallarès, J. and L. F. Marsal, "Gold-coated ordered nanoporous anodic alumina bilayers for future label-free interferometric biosensors," ACS Appl. Mater. Interfaces 5(16), 8093-8098 (2013).
[49] Zheng, W. J., Fei, G. T., Wang, B., Jin, Z. and Zhang, D. L., "Distributed Bragg reflector made of anodic alumina membrane," Mater. Lett. 63(8), 706-708 (2009).
[50] Xu, Q., Sun, H-Y., Yang, Y-H., Liu, L-H. and Li, Z-Y., "Optical properties and color generation mechanism of porous anodic alumina films," Appl. Surf. Sci. 258(5), 1826-1830 (2011).
[51] Liu, Y., Wang, H. H., Indacochea, J. E. and Wang, M. L., "A colorimetric sensor based on anodized aluminum oxide (AAO) substrate for the detection of nitroaromatics," Sens. Actuators B160(1), 1149-1158 (2011).
[52] Wang, B., Fei, G. T., Wang, M., Kong, M. G. and Zhang, L. D., "Preparation of photonic crystals made of air pores in anodic alumina," Nanotechnology 18(36), 365601 (2007).
[53] Chen, Y., Santos, A., Wang, Y., Kumeria, T., Wang, C., Li, J. and Losic, D., "Interferometric nanoporous anodic alumina photonic coatings for optical sensing," Nanoscale 7(17), 7770-7779 (2015).
[54] Yao, Z., Zheng, M., Ma, L. and Shen, W., "The fabrication of ordered nanoporous metal films based on high field anodic alumina and their selected transmission enhancement," Nanotechnology 19(46), 465705 (2008).

[55] Santos, A., Pereira, T., Law, C. S. and Losic, D., "Rational engineering of nanoporous anodic alumina optical bandpass filters," Nanoscale 8(31), 14846-14857 (2016).
[56] Sukarno, Law, C. S. and Santos, A., "Realisation and optical engineering of linear bandpass filters in nanoporous anodic alumina photonic crystals," Nanoscale 9(22), 7541-7550 (2017).
[57] Law, C. S., Santos, A., Nemati, M. and Losic, D., "Structural engineering of nanoporous anodic alumina photonic crystals by sawtooth-like pulse anodisation," ACS Appl. Mater. Interfaces 8(21), 13542-13554 (2016).
[58] Santos, A., Law, C.S., Lei, D. W. C., Pereira, T. and Losic, D., "Fine tuning of optical signals in nanoporous anodic alumina photonic crystals by apodized sinusoidal pulse anodisation," Anal. Chem. 88(11), 5971-5980 (2016).
[59] Santos, A., Law, C.S., Pereira, T. and Losic, D., "Nanoporous hard data: optical encoding of information within nanoporous anodic alumina photonic crystals," Nanoscale 8(15), 8091-8100 (2016).
[60] Santos, A., Yoo, J. H., Rohatgi, C. V., Kumeria, T., Wang, Y. and Losic, D., "Realisation and advanced engineering of true optical rugate filters based on nanoporous anodic alumina by sinusoidal pulse anodisation," Nanoscale 8(3), 1360-1373 (2016).
[61] Lorenzo, E., Oton, C. J., Capuj, N. E., Ghulinyan, M., Navarro-Urrios, D., Gaburro, Z. and Pavesi, L., "Porous silicon-based rugate filters," Appl. Opt. 44(26), 5415-5421 (2005).
[62] Ilyas, S., Böcking, T., Killian, K., Reece, P. J., Gooding, J., Gaus, K. and Gal, M., "Porous silicon based narrow line-width rugate filters," Opt. Mater. 29(6), 619-622 (2007).
[63] Rahman, M., Garcia-Caurel, E., Santos, A., Marsal, L., Pallarès, J. and Ferré-Borrull, J., "Effect of anodization voltage on the pore-widening rate of nanoporous anodic alumina," Nanoscale Res. Lett. 7(1), 1-7 (2012).